Theoretical and experimental study of the role of the reed in clarinet playing

Pierre-André Taillard

UNIVERSITE BRETAGNE SCIENCES LOIRE POUR L'INGENIEUR

Le Mans Université

THESE DE DOCTORAT DE

LE MANS UNIVERSITE
COMUE UNIVERSITE BRETAGNE LOIRE

ECOLE DOCTORALE N° 602
Sciences pour l'Ingénieur
Spécialité : *Acoustique*

Par

Pierre-André TAILLARD

Theoretical and experimental study of the role of the reed in clarinet playing

Étude théorique et expérimentale du rôle de l'anche dans le jeu de la clarinette

Thèse présentée et soutenue au Mans, le 2 juillet 2018
Unité de recherche : Laboratoire d'Acoustique de l'Université du Maine – UMR CNRS 6613
Thèse N° : LEMA20181010

Rapporteurs avant soutenance :

Christophe VERGEZ, Directeur de Recherche, LMA, Marseille
Maarten VAN WALSTIJN, Lecturer, Queen's University, Belfast

Composition du Jury :

Président
Jean-François PETIOT, Professeur des Universités, ECN, LS2N, Nantes
Pauline EVENO, Docteure, Présidente Directrice Générale, SYOS, Paris

Directeur de thèse
Jean-Pierre DALMONT, Professeur des Universités, LAUM, Le Mans
Co-directeur de thèse
Bruno GAZENGEL, Professeur des Universités, LAUM, Le Mans

Invité
Jean KERGOMARD, Directeur de Recherche Émérite, LMA, Marseille

A la mémoire de mon père

Remerciements

Qu'il me soit permis de remercier toutes les personnes qui m'ont accordé une confiance inébranlable et qui m'ont permis d'avancer malgré mon isolement géographique. Il n'est pas possible de les mentionner et de les remercier toutes. Que les personnes concernées veuillent bien m'excuser.

Je pense en particulier à **Jean Kergomard** qui a cosigné tous les articles que j'ai publiés jusqu'ici. Il a su prendre le temps nécessaire pour essayer de comprendre les élucubrations de cet illuminé venant des montagnes suisses et essayer de les transcrire dans un langage plus structuré et compréhensible, permettant de publier certaines d'entre-elles.

Je pense bien sûr aussi à **Jean-Pierre Dalmont**, mon interlocuteur de la première heure et mon actuel directeur de thèse. Une connivence particulière fait que c'est l'une des rares personnes de la communauté acoustique "qui me comprend", qui sait lire entre les lignes et compléter ce qu'il manque (bien que ceci lui ait fort souvent demandé de s'arracher quelques cheveux…). Il a le don de la synthèse et c'est lui qui remet généralement mes idées dans le bon ordre. Il convient aussi de remercier son épouse **Véronique** qui m'a souvent invité chez eux et qui a dû faire preuve de beaucoup de patience lorsque je lui enlevais son mari à des heures et des jours indus pour d'interminables séances de travail.

Avec **Franck Laloë**, grand physicien quantiste et clarinettiste amateur, nous avons abondamment échangé, tant sur des sujets scientifiques que musicaux. C'est lui qui a rendu possible l'étude relatée au Chapitre 3 en mettant à ma disposition un labo d'optique au laboratoire Kastler Brosser de l'ENS, à Paris, sous la supervision de **Michel Gross** [83, 66, 84].

Claudia Fritz se souvient certainement encore de l'avalanche de mails assommants que je lui envoyée à l'époque de sa thèse [55, 57, 58, 56]. Je pense à l'équipe de l'IRCAM à Paris avec qui les échanges ont été souvent assez denses lors du projet CAGIMA : **Thomas Hélie, Joël Bensoam, René Caussé, Alain Terrier, David Roze** et **Robert Piéchaud**. Je garde un très bon souvenir des gens du LMA à Marseille. Les échanges ont été particulièrement fructueux avec **Fabrice Silva, Philippe Guillemain, Christophe Vergez, Patrick Sanchez, Sami Karkar, Didier Ferrand, Alexis Guilloteau, Whitney Coyle** et bien sûr **Jean Kergomard** déjà cité. Du côté du LAUM au Mans, outre **Jean-Pierre Dalmont**, il faut tout d'abord remercier mon co-directeur de thèse **Bruno Gazengel**, qui m'a appris la rigueur et l'organisation, tant dans la conduite des expériences que dans la rédaction. Lors de mes nombreux séjours au Mans, en particulier lors du projet SDNS-AIMV, j'ai eu la chance de pouvoir collaborer avec **André Almeida, Baptiste Bergeot, Joël Gilbert, Emmanuel Brasseur, Alfredo Muñoz Arancón** et **Frédéric Ablitzer**. De nombreuses personnes issues d'autres milieux m'ont apporté leur soutien. Parmi celles-ci, mentionnons **Avraham (Mico) Hirschberg**, **Sébastien Ollivier**, **Jean Jeltsch**, **Michael Jousserand**, **Jean-Lou Zimmermann**, **Stefan Siegenthaler**, **Thomas Drescher**, **Martin Kirnbauer**, **Jacques Ditisheim**, **Sylvain Jaccard** et **René Michon**.

Je remercie le jury de thèse et en particulier les deux rapporteurs **Maarten van Walstijn** et **Christophe Vergez** pour son travail et pour les remarques judicieuses prodiguées.

Je suis redevable à la **haute école ARC ingénierie** à Neuchâtel qui m'accueille depuis plusieurs années comme chercheur invité, en me permettant de bénéficier de ses infrastructures, notamment logicielles. Elle a aussi contribué aux débuts de ma formation en acoustique, en m'offrant un cours sur le logiciel CATIA, qui m'a permis d'effectuer mes premières simulations modales 3D. J'aimerais remercier en particulier **Guido Frosio**, **Massimo Monti**, **Philippe Grize**, **Thierry Copponnex**, **Eric Marguet**, **Pierre Pasche** et **Yves Salvadé**.

Je dois aussi surtout remercier mon épouse **Marie-France** et mes enfants **Julien, Florian, Elsa** et **Virgile** qui m'ont si souvent vu absent, perdu dans mes pensées ou travaillant avec acharnement à mon ordinateur ou à mettre au point de nouvelles manips improbables. Je suis particulièrement redevable à mon épouse qui a su assumer les charges nécessaires pour rendre cette thèse possible.

Avant-propos

Ce mémoire de thèse est assez atypique à plusieurs titres. Tout d'abord, il a été rédigé par un musicien (muni d'un simple bac scientifique) qui s'est formé à l'acoustique de manière autodidacte, sans avoir jamais suivi un seul cours sur les bancs des amphithéâtres des universités. Il résume certains travaux menés au cours des 17 dernières années, dont la plupart ont été réalisés sans imaginer qu'ils seraient un jour réunis pour fournir la matière des premiers chapitres de ce mémoire. L'étendue du sujet traité est aussi assez inhabituelle, puisqu'elle concerne en réalité tout le domaine de l'acoustique de la clarinette.

Il convient de relater l'enchaînement de circonstances qui m'ont amené à rédiger ce mémoire.

Mon activité professionnelle au début de ma carrière était essentiellement centrée sur la pratique et l'enseignement de la musique, en particulier autour des instruments historiques. Cependant, depuis l'obtention de mon Baccalauréat en 1982, je n'ai jamais perdu contact avec les activités scientifiques. En particulier, lors de mes études musicales à Bâle, j'ai entretenu une collaboration soutenue avec mon regretté ami, l'archéozoologue Philippe Morel. J'ai réalisé plusieurs études dans des domaines aussi divers que l'ornithologie [1], l'ostéologie [145], l'archéologie [103] et la spéléologie, dont certaines ont fait l'objet de publications. Ces travaux m'ont permis d'acquérir un certain nombre de connaissances scientifiques qui se sont révélées utiles pour mes études acoustiques, notamment les techniques d'analyse statistique (analyse en composantes principales, analyse discriminante, cluster analysis, etc...). Cette période de ma vie a également été marquée par une activité semi-professionnelle en tant que programmeur-analyste, au cours de laquelle j'ai réalisé divers projets :

— Pour Ph. Morel, j'ai développé entre 1986 et 1990 une suite de logiciels d'analyse très performants pour l'époque : Archeos. Ces logiciels ont été réalisés « sur mesure », de manière à optimiser son travail d'acquisition et d'analyse des données ostéologiques. Un grand soin a été accordé pour permettre une saisie des données efficace et j'ai développé langage de programmation et un compilateur permettant de définir des analyses complexes de la banque de données. A l'époque, mon logiciel était environ 100 fois plus rapide à l'analyse que celui utilisé par le Laboratoire de Préhistoire de l'Université de Bâle, grâce à une structure permettant un compactage maximal des données. Ce gain de temps était alors très précieux : une analyse s'effectuait en quelques minutes au lieu de plusieurs heures, pour des fouilles d'une certaine ampleur, comme celle du campement magdalénien de Champréveyres [102].

— En 1988, un projet de l'Université de Berne [179] m'a chargé de développer une carte d'acquisition des cris de chauve-souris (à l'époque, ces cartes étaient d'un prix prohibitif), ainsi que le logiciel autorisant une détermination automatique des espèces, d'après des mesures de fréquence instantanées, au début, lors du maximum d'amplitude et à la fin du cri, ainsi que les durées correspondantes.

— J'ai également développé un logiciel pour la correction des examens propédeutiques de médecine de l'université de Bâle (questionnaires à choix multiples), au moyen d'un lecteur optique. Ce logiciel a permis la correction des épreuves de médecine durant une bonne dizaine d'années. J'ai adapté ce programme pour l'évaluation des examens cantonaux des laborants de chimie.

1. En particulier des études sur les chouettes forestières comme la Chouette de Tengmalm (*Aegolius funereus*) et la Chevêchette d'Europe (*Glaucidium passerinum*), que je poursuis encore actuellement, ayant développé un logiciel assez performant de détection et détermination bioacoustique des chants d'oiseaux.

— En 1989, j'ai participé à l'élaboration d'une carte de santé sécurisée Sanacard. J'ai écrit des logiciels permettant la saisie et le cryptage des données.

Tous ces travaux m'ont permis d'acquérir une certaine rigueur dans le développement de programmes informatiques et dans la structuration des données. En outre, j'ai pu me familiariser avec certaines méthodes mathématiques, mises en application dans mes logiciels.

Le projet Claripatch constitue le tournant décisif qui m'a amené à l'acoustique. L'origine de ce projet remonte à l'an 2000, lorsque la Schola Cantorum Basiliensis (SCB) – institut où j'enseigne la clarinette historique – décide de mettre sur pied un symposium en mai 2001 sur le thème « la clarinette autour de 1800 », en invitant une dizaine de chercheurs et de clarinettistes de premier plan pour y contribuer. Pour ma part, j'ai réalisé une étude musicologique de l'interprétation des œuvres pour clarinette de Carl Maria von Weber, suivie de la construction d'un bec permettant de répondre aux exigences artistiques déduites des témoignages historiques recueillis. En troisième lieu, la SCB m'a chargé de documenter ces recherches par un concert et l'enregistrement d'un CD avec le pianiste Edoardo Torbianelli. Ce CD a obtenu plusieurs distinctions discographiques (Diapason d'or, 10 de Répertoire, nommé deux fois CD du mois). Quelques semaines avant l'enregistrement du CD, en septembre 2001, j'ai eu l'idée décisive qui a permis au projet Claripatch de naître. Comme il était devenu trop risqué de modifier le bec que j'avais mis au point, j'ai imaginé de modifier virtuellement la courbure de la table en insérant une cale entre l'anche et le bec. L'enregistrement a été réalisé avec un patch rudimentaire constitué de deux lames d'acier trempé de 3 centièmes de mm d'épaisseur, fixées au bec avec de la graisse pour liège (je vous laisse imaginer le goût et les traces de rouille laissées sur les anches). Dans les mois qui ont suivi, j'ai développé l'idée, puis déposé un brevet le 31.12.2001 (aidé par la fondation SOVAR pour la promotion économique). Ce brevet (numéro de publication WO2003056543 A1) a été accordé aux Etats-Unis (US 6,921,853 B2), le 26.07.2005. Les demandes de brevet européen et japonais ont été abandonnées en cours de procédure, en raison du modeste succès commercial de l'invention.

Afin de déterminer le profil optimal des différents modèles, j'ai expérimenté plusieurs centaines de prototypes, essayé des dizaines de modèles mathématiques pour tenter de comprendre comment fonctionne une table de clarinette. J'ai pris conscience de l'extrême subtilité de sa courbure et du nombre insoupçonné de formes qu'il est possible de lui donner : des modifications locales de quelque 5 microns produisent des différences de sonorité très audibles. Ainsi sont nés, par approximations successives, les huit modèles de patches commercialisés, après avoir cerné autant de problèmes courants rencontrés avec les anches. L'aventure a continué ensuite sur un terrain plus conventionnel, faisant appel au savoir-faire des écoles techniques et des écoles d'ingénieurs, pour la conception et la réalisation de l'outillage permettant une production industrielle d'une étampe de découpage, d'une boîte de rangement faisant aussi office de boîte à anches, un anneau de positionnement et une « Clarimute » (une sorte de sourdine permettant d'exercer silencieusement son embouchure). En 2004, Stephan Siegenthaler – un client fortuné, enthousiasmé par mon invention - me proposa de fonder une société pour commercialiser ce produit. Ainsi est née l'entreprise Claripatch S.A.

Le développement de ce produit a fait naître chez moi le désir d'étudier de manière scientifique le fonctionnement de cette invention et plus généralement, de comprendre l'acoustique de mon instrument. Une motivation pédagogique m'a également incité à entreprendre cette étude : lors de l'enseignement de la clarinette (et en particulier des instruments historiques), il n'est pas toujours évident de poser un diagnostic correct. Est-ce l'anche, le bec, l'instrument ou la technique de jeu de l'instrumentiste qui est déficient ? Je voulais aussi comprendre pourquoi il était si difficile de trouver des anches répondant en tous points à mes attentes, dans l'espoir que la science permettrait peut-être de répondre à cette question.

Au début de l'année 2003, j'ai commencé à m'intéresser aux travaux réalisés par les acousticiens à propos de la clarinette et rapidement, j'ai pu nouer des contacts réguliers avec les meilleurs spécialistes de la discipline, tout d'abord par courrier électronique, puis je me suis rendu pour la première fois au LAUM en février 2004. En automne 2004, j'ai été sollicité par Claudia Fritz, alors doctorante à l'IRCAM, pour l'aider dans le réglage de la bouche artificielles, dans le cadre des expériences réalisées pour sa thèse. Une collaboration régulière s'est progressivement mise en place, qui a donné lieu, après plusieurs années, à quelques publications dans des revues à comité

de lecture.

Jean-Pierre Dalmont a su trouver les arguments et la persévérance nécessaire (à peu près 5 ans...) pour me pousser à mettre de l'ordre dans mes travaux en pagaille et à en terminer quelques-uns sous forme de mémoire de thèse, en m'incitant à solliciter une validation des acquis professionnels, pour permettre mon inscription à l'université.

Voici l'origine de ce projet insensé, achevé à un âge où on songe ordinairement plus à terminer sa carrière qu'à prendre un nouveau départ.

L'essentiel de mon activité dans le domaine de l'acoustique a été réalisée à titre purement bénévole. J'ai cependant été engagé lors de 2 contrats de type post-doc dans le cadre des projets SDNS-AIMV (Systèmes Dynamiques Non Stationnaires - Application aux Instruments de Musique à Vent) de 2011 à 2013 au LAUM et CAGIMA (Conception Acoustique Globale d'Instruments de Musiques à Anches justes et homogènes), de 2013 à 2015 à l'IRCAM, en collaboration avec l'entreprise Buffet Crampon. Depuis septembre 2012, j'enseigne en outre l'acoustique musicale dans le cadre de la Haute-Ecole de Musique de Genève, site de Neuchâtel.

Abrégé de la thèse

Ce mémoire de thèse est structuré en 5 parties traitant chacune d'un thème de recherche différent. Les 3 premières parties examinent sous différents aspects les relations entre l'anche, l'excitateur et le résonateur. Les 2 dernières parties tentent une synthèse des différents éléments abordés.

Résumé de la Partie I

Cette partie traite de modèles simples analytiques pour des instruments de type clarinette. Le comportement acoustique du résonateur cylindrique se résume à une fonction de réflexion élémentaire - un simple retard - postulant ainsi que les pertes ne dépendent pas de la fréquence. L'anche est réduite à une simple raideur linéaire sans inertie, venant buter sur le bec en obstruant le canal. L'anche du modèle de Raman est si simple que les aspects mécaniques et aérauliques sont complètement confondus. Les sons produits sont bien entendu caricaturaux, puisqu'il s'agit d'une suite de créneaux (signal carré). Malgré cela, le modèle présente un certain intérêt, puisqu'il est capable de prédire correctement les seuils de bifurcation et autorise un traitement analytique permettant de délimiter les divers régimes de fonctionnement. L'excitateur est caractérisé par 2 paramètres essentiels : la raideur (les clarinettistes parlent de "force de l'anche") et l'ouverture à pression d'air nulle. Le modèle établit une relation de récurrence permettant de prévoir l'état acoustique de l'instrument à partir de son état au temps discret précédant, soit celui nécessaire à un aller-retour de l'onde dans le résonateur. Les 2 Chapitres de cette partie sont constitués par des articles publiés en 2010 et 2015.

Le Chapitre 1 revisite l'article de Dalmont et al. [35] "An analytical prediction of the oscillation and extinction thresholds of a clarinet" en ciblant plus particulièrement l'effet des pertes. J'ai en effet remarqué qu'un certain nombre de cas avaient été omis dans l'article initial, notamment lorsque les pertes sont élevées. Il propose en outre une méthode de calcul nouvelle, beaucoup plus concise, développée sur l'idée de mon coauteur, Jean Kergomard. Ce modèle est assez éclairant également pour le musicien, parce qu'il délimite clairement certaines zones de fonctionnement de l'instrument, en fonction de 2 paramètres de jeu contrôlés par l'instrumentiste : l'ouverture à pression d'air nulle et le paramètre de perte (que le clarinettiste peut influencer partiellement au moyen de sa lèvre, mais qui dépend aussi notamment de l'étanchéité des clés ou de la porosité de l'instrument [14]). La connaissance de ces zones est très utile d'un point de vue pédagogique, mais également pour perfectionner sa technique instrumentale.

Le Chapitre est focalisé sur les cycles limites correspondant au régime à 2 états, contrairement à celui du Chapitre 2, focalisé sur les transitoires. Grâce à une formulation basée sur la différence de pression entre la bouche et le bec, l'effet de la fonction non-linéaire sur la production du régime à 2 états peut être analysé et en particulier le rôle des pertes. Un diagramme de fonctionnement a pu être établi, délimitant plusieurs zones. Lorsque le paramètre d'embouchure adimensionné ζ est petit, les pertes peuvent être trop importantes pour autoriser une production sonore. L'article complète cette conclusion en ajoutant que pour $\zeta \geq 1/\sqrt{5}$, lorsque les pertes augmentent, la bifurcation à l'émergence devient inverse, avant que le son ne disparaisse. L'instrument devient alors plus difficile à jouer. Pour ζ plus petit que cette valeur, lorsque les pertes augmentent, on passe directement d'une bifurcation directe à l'émergence, à l'absence de son.

Le Chapitre 2 traite des cartes itérées. Le modèle de Raman y est transcrit sous la forme d'une fonction f qui lie l'onde progressive qui quitte le bec au temps n avec l'onde progressive

suivante, qui quittera le bec au pas de temps suivant, $n + 1$, soit le temps nécessaire à l'onde pour effectuer un aller-retour dans le tuyau cylindrique. Le régime statique est caractérisé par l'équation $x = f(x)$ et le régime auto oscillant ordinaire à 2 états par l'équation $x = f(f(x))$. Ce chapitre étudie la fonction f dans de nombreux cas de figure, en mettant l'accent sur les régimes "exotiques", tels que les doublement de périodes, les cascades sous-harmoniques, les intermittences et les régimes chaotiques.

On trouvera à la fin du Chapitre 2 un résumé en français sous la forme d'un article de congrès qui reprend l'essentiel de l'article sous une forme plus concise.

Résumé de la Partie II

Cette partie traite de la caractérisation de l'excitateur de clarinette, en focalisant les études sur le rôle de l'anche. Il s'agit de décrire de manière objective les différences observées entre anches et de les projeter sur un modèle simplifié.

Le Chapitre 3 examine la question de la mécanique de l'anche d'un point de vue dynamique. Il est constitué par un article paru en 2014. On étudie un panel de 55 anches par holographie. On détecte les fréquences de résonance de l'anche (prise isolément, sans enroulement sur le bec de clarinette) jusqu'à 20 kHz, soit approximativement les 15 premières résonances de l'anche. Deux séries de mesures ont été effectuées, avec un taux d'hygrométrie différent.

Dans la première partie de l'article, on décrit les observations d'un point de vue statistique. Les fréquences de résonance sont souvent hautement corrélées entre elles, particulièrement celles des modes transverses et dans une moindre mesure, celles des modes de flexion. La force nominale de l'anche est étonnamment mieux corrélée avec les fréquences des modes transverses qu'avec celle des modes de flexion. Les modes de flexion à l'intérieur d'une même série de mesure présentent des fréquences relativement peu corrélées. Une analyse en composantes principales (ACP) effectuée sur les fréquences de résonance identifie 4 facteurs capturant 91.2% de la variance de l'échantillon. Les données peuvent donc être reconstituées à partir de 4 facteurs non corrélés. L'effet du changement d'hygrométrie peut apparemment être décrit à l'aide d'un seul facteur.

Dans la deuxième partie de l'article, on tente d'établir un modèle d'anche viscoélastique du matériau composant l'anche qui permettrait d'expliquer les différences observées entre anches. Le modèle numérique autorise une reconstitution satisfaisante des fréquences de résonances, par combinaison linéaire avec des paramètres proches de ceux issus de l'ACP. Le module de Young longitudinal ainsi que le module de cisaillement longitudinal/transverse sont exprimés en fonction de la fréquence, à l'aide du modèle viscoélastique de Zener. Une corrélation élevée (de l'ordre de 0.96 à 0.98) est observée entre les paramètres du modèle et les facteurs ACP. La méthode proposée permet de déterminer 3 paramètres mécaniques caractérisant le matériau composant l'anche, à partir d'une seule série de mesures, effectuée avec une humidité correspondant à celle avec laquelle les anches sont conditionnées à l'usine, dans leurs emballages scellés. Le quatrième paramètre ne peut probablement pas être déterminé de manière reproductible, puisque l'exposition des anches à l'air extrêmement sec du laboratoire d'optique n'a pas été contrôlée. Le même protocole et le même modèle viscoélastique pourrait être utilisé pour mesurer d'autres types d'anches simples (clarinette basse ou saxophone). Le changement de géométrie ne requiert qu'une nouvelle estimation d'une série de coefficients à partir de simulations par éléments finis avec la nouvelle géométrie. Bien que les modes d'ordre élevé ne jouent probablement aucun rôle décisif dans le fonctionnement acoustique de la clarinette, l'étude montre qu'ils permettent de révéler la structure intime du matériau composant l'anche. Ces paramètres pourraient aider à caractériser le comportement des anches de clarinette.

Malheureusement, l'étude perceptive réalisée (de manière assez informelle) sur les anches mesurées n'a pas permis d'établir un lien statistiquement très significatif avec les paramètres dégagés. Cependant, la répétition de résultats « presque significatifs » montre que ces paramètres ont probablement tout de même une relation avec le comportement musical des anches. Cette étude a cependant eu le mérite de préparer le développement de la méthode décrite au Chapitre suivant, qui a permis d'atteindre cet objectif.

Le Chapitre 4 propose une méthode de caractérisation expérimentale statique de l'excitateur

de clarinette. On évalue deux quantités en fonction de la pression de lèvre et d'air appliquée sur l'anche : la déflection mécanique à proximité de la pointe de l'anche et le débit d'air pénétrant par le canal. La méthode utilise une bouteille à laquelle on connecte un bec de clarinette instrumenté. A l'aide des lois de la thermodynamique, on peut évaluer à tout instant la quantité d'air présente dans la bouteille. Lors du cycle de mesure, on crée tout d'abord une dépression dans la bouteille, suffisante pour maintenir l'anche plaquée sur la table du bec durant plusieurs secondes. On mesure ensuite la quantité d'air qui revient dans la bouteille en traversant le canal entre l'anche et le bec. Au bout d'un instant, on observe une ouverture assez soudaine de l'anche et la pression ambiante revient dans la bouteille. Le retour de l'air est cependant suffisamment lent pour qu'on puisse considérer des conditions quasi statiques. La section aéraulique efficace est déduite en fonction du débit mesuré, d'après la loi de Bernoulli. Lors de cette expérience, on mesure également la déflexion mécanique de l'anche par capteur optique.

La méthode "de la bouteille" permet une mesure très satisfaisante des caractéristiques de l'excitateur de clarinette, en termes de précision et de reproductibilité. Un point doit cependant encore être amélioré : la caractérisation des échanges thermiques avec la bouteille, qui a été effectuée ici de manière empirique. Cette amélioration peut aussi passer par le développement d'une bouteille ayant un comportement thermique moins critique pour la mesure.

Résumé de la Partie III

Cette partie traite de la simulation temps-réel du son de l'instrument par modèle physique, en développant un synthétiseur permettant d'évaluer (entre autre) les différences de sonorité en fonction de l'anche. Elle commence par l'élaboration d'un modèle d'anche réaliste, ayant un comportement statique conforme aux mesures (et autorisant une transformation aisée en un modèle dynamique, simple et efficient), puis se concentre sur l'analyse modale de la colonne d'air des instruments à vent (approches 1) impédance d'entrée et 2) guide d'ondes), résultat de ma collaboration au projet CAGIMA. Ma tâche au sein de ce projet consistait à développer les techniques nécessaires au prototypage virtuel des instruments à vent. A partir de la géométrie de l'instrument et des équations qui décrivent le comportement physique de l'instrument dans le domaine spectral, il s'agit de développer une méthode d'estimation modale de l'impédance d'entrée, des fonctions de transfert ou des fonctions des matrices de diffusion qui autorise une simulation temps-réel, tout en garantissant la passivité de l'instrument simulé à toute fréquence. Cette formulation dans le domaine temporel discret autorise une simulation du comportement de l'instrument au moyen d'un synthétiseur. L'un des buts du projet CAGIMA est que le facteur d'instrument puisse tester virtuellement son instrument d'un point de vue musical (justesse, facilité d'émission, timbre) avant de construire un prototype réel.

Le Chapitre 5 propose une modélisation de l'excitateur à partir des mesures mécaniques et aérauliques. Le modèle mécanique statique suppose que la déflection de l'anche en fonction de la pression appliquée est une fonction décroissante et convexe pouvant s'approximer par tronçons paraboliques. Le modèle statique peut être aisément converti en un modèle dynamique, en ajoutant une masse et un amortissement, à l'aide du schéma de contact décrit par [25]. Le temps de calcul lors de la simulation est à peine plus élevé que celui du schéma traditionnel d'oscillateur linéaire à un mode. La section aéraulique est évaluée en fonction de la position de l'anche à partir des mesures, par interpolation.

Le modèle proposé possède 3 propriétés intéressantes : 1) L'estimation des paramètres ne pose aucune difficulté et se base sur des techniques standard d'optimisation. 2) Le modèle reproduit les mesures statiques effectuées sur les anches avec une erreur standard typique de l'ordre de quelques microns. 3) La simulation dynamique est efficiente et bien adaptée pour une simulation temps-réel. Le calcul ne requiert que quelques multiplications et une racine carrée par pas de temps (à part lors des transitions entre sections, où 2 évaluations sont nécessaires). Tous les tronçons de la fonction sont simulés à partir du même historique. Le nombre de tronçons composant la fonction d'approximation n'a pratiquement aucun impact sur le temps de calcul. Le temps de recalcul aux transitions entre deux sections adjacentes est négligeable.

Le Chapitre 6 est constitué par un article soumis en 2017 à "Applied Acoustics". Il est focalisé sur l'estimation modale de l'impédance d'entrée des instruments à vent et aborde en

particulier le cas d'une impédance d'entrée mesurée à l'aide d'un pont d'impédance. Il décrit comment des techniques d'analyse bien connues peuvent être mises en application, en évitant un certain nombre de pièges. Un exemple d'application à la clarinette est donné, en détaillant des algorithmes empiriques simples qui permettent de simuler les transitions entre doigtés et le son externe à partir du son interne calculé dans le bec.

Cet article passe en revue de nombreux aspect liés à une représentation modale de l'impédance d'entrée des instruments à vent. La méthode LSCE (Least Squares Complex Exponentials) est un outil précieux dans ce contexte, mais une application à une impédance mesurée ou analytique requiert certain nombre de précautions. Parmi les difficultés à résoudre, on peut citer : une reconstruction physiquement acceptable en basse fréquence, l'implémentation de points fictifs dans le domaine spectral de manière à assurer la passivité du filtre numérique à toute fréquence, l'utilisation d'une arithmétique haute précision, suivant le nombre de modes demandés pour la simulation. La méthode permet de dériver des filtres numériques précis dans la bande de fréquence mesurée et passifs à toute fréquence, autorisant une synthèse temps-réel. Bien que la méthode ait servi jusqu'ici uniquement à simuler des clarinettes, son efficacité pour l'estimation modale de l'impédance d'entrée d'instruments tels que le saxophone, le cor, la trompette et le trombone a été vérifiée.

Au Chapitre 7, la question de l'estimation modale est étendue au domaine des guide d'ondes. Il propose une structure logicielle permettant la simulation d'instruments à vent en temps réel. Ce logiciel permet de construire un synthétiseur, en assemblant les briques élémentaires de chaque tronçon de l'instrument. Les obstacles principaux ont pu être levés, en utilisant une formulation basée essentiellement sur les fonctions de réflexion et de transmission des matrices de diffusion (ondes progressives), pour lesquelles les techniques développées au Chapitre 6 peuvent être appliquées. On peut ainsi dériver des filtres numériques qui sont à la fois précis dans la bande de fréquence spécifiée et passifs à toute fréquence. Au besoin, ces filtres peuvent être convertis aisément en filtres d'impédance ou d'admittance, moyennant 2 multiplications par pas de temps. La simulation des réflectances de rayonnement est traitée, en cas de pertes linéaires ou non linéaires. Les retards fractionnaires ont pu être éliminés, comme effet collatéral de l'estimation modale, en les intégrant directement aux filtres numériques. Le problème des boucles sans délai a également pu être résolu analytiquement pour chacune des jonctions proposées. Des modèles d'excitateurs, de pavillons, de cheminées, de pistons et de coulisses ont été implémentés. Une architecture logicielle orientée objet - basée sur une simulation segmentée de la colonne d'air, où les segments sont liés au moyen de jonctions répertoriées dans un dictionnaire - y est proposée. Ce dictionnaire implémente plus d'une douzaine de jonctions différentes (plus ou moins sophistiquées, avec ou sans masse acoustique ajoutée, avec pertes linéaires ou non-linéaires). Le logiciel gère également certains aspects pouvant être délicats à contrôler, comme celui des transitions entre doigtés (en régulant le degré d'ouverture de chaque cheminée latérale, ainsi que les conditions d'embouchure nécessaires à la production de chaque note de la gamme).

Bien que le nombre de cas simulés soit assez restreint, le synthétiseur a permis d'obtenir certains résultats musicalement convaincants. Des tests systématiques devraient être menés, qui pourraient amener un lot d'observations intéressantes, comme par exemple celle-ci : l'aisance d'émission du second régime (registre du clairon) est nettement améliorée par le modèle avec pertes non-linéaires, particulièrement lors du jeu de grands intervalles. Ceci peut paraître surprenant au premier abord, mais l'explication est logique. Les pertes non-linéaires contribuent à atténuer la première résonance (à cause du débit élevé engendré dans la cheminée du trou de registre lorsqu'on essaie de jouer le premier régime, ce qui cause des pertes importantes), alors que la seconde résonance n'est pratiquement pas affectée (puisque le trou de registre est situé près d'un nœud de pression du second régime, ce qui cause un débit peu important dans la cheminée de registre et ainsi, des pertes non-linéaires faibles). En d'autre termes, le seuil d'oscillation du premier régime est haussé par les pertes non-linéaires au-dessus de celui du second régime, qui demeure pratiquement inchangé, ainsi l'oscillation démarre plus facilement sur le 2ème régime.

Il serait intéressant d'appliquer la méthode pour examiner une question récurrente des clarinettistes et hautboïstes : pourquoi les anches semblent-elle plus fortes en altitude qu'en plaine ? Le synthétiseur permettrait de vérifier si la différence de densité de l'air est suffisante pour expliquer l'effet constaté. A première vue, il semble que l'influence de ce paramètre devrait principalement concerner les pertes non-linéaires au niveau des cheminées. Une densité plus élevée implique des

pertes accrues, ce qui fait baisser le seuil de saturation, donnant ainsi l'impression que l'anche est plus faible.

L'outil développé offre de nouvelles opportunités pour le développement d'instruments de musique à vent, particulièrement pour les personnes n'ayant pas un bagage acoustique important (musiciens et facteurs d'instruments par exemple). Il permet de simuler la plupart des instruments à vents, notamment ceux de la famille des cuivres et des anches faibles. Divers exemples d'application sont donnés, notamment pour la simulation temps-réel d'une clarinette en sib Buffet Crampon avec 28 tronçons et 22 cheminées latérales avec pertes non linéaires au niveau de chaque trou. Des synthétiseurs peuvent être générés à partir de la géométrie de l'instrument, à l'aide des méthodes décrites, en focalisant l'attention du développeur sur les aspects musicaux (intonation, homogénéité du son et facilité d'émission, par exemple). Le but qui m'a été assigné lors du projet CAGIMA a ainsi pu être atteint : le prototypage virtuel. Une intégration des techniques développées au sein du projet PAFI (plate-forme d'aide à la facture instrumentale) serait souhaitable.

Résumé de la Partie IV

Cette partie tente de faire une synthèse en réunissant les différents développements proposés, par le biais d'une étude sur la jouabilité d'un panel d'anches de clarinette qui confronte mesures physiques, évaluations musicales et synthèse sonore. Une méthode de caractérisation des anches a pu être établie, qui permet de mesurer au moins 4 facteurs corrélés de manière significative avec les évaluations musicales du clarinettiste.

Le Chapitre 8) confronte 3 types de données récoltées à partir d'un panel de 40 anches de clarinette : i) mesures physiques objectives, incluant (pour chaque anche et embouchure) des expériences statiques (mesures aérauliques, déflection mécanique et photographies du canal) et une expérience dynamique (diagramme de bifurcation, établi sur un *crescendo / decrescendo*). ii) évaluation musicales subjectives. L'auteur de ces lignes a joué ces mêmes anches à l'aveugle (avant que les mesures ne soient analysées) et les a notées sur la base de 4 descripteurs différents. iii) données issues de la synthèse sonore. Les modèles physiques développés dans la partie III sont mis en application pour simuler les diagrammes de bifurcation.

Les questions centrales auxquelles répond ce Chapitre sont les suivantes : existe-t-il des informations communes à toutes les données récoltées ? Quelle est leur nature et leur nombre ? Est-ce que les corrélations détectées sont dues au hasard ? Existe-il un lien avéré entre les mesures objectives, les évaluations subjectives et les simulations ? Peut-on proposer aux facteurs d'anches une caractérisation des anches qui repose sur cette base ? On répond à ces questions en appliquant une technique statistique : l'analyse canonique des corrélations.

L'étude démontre le rôle essentiel de la statique de l'anche lors du jeu de l'instrument et détaille la diversité et la complexité des comportements observés. Ces aspects concernent l'excitateur (anche+bec+lèvre) considéré dans son entier et non pas uniquement l'anche seule, prise isolément. Les photos du canal réalisées avec une anche neuve, en variant l'embouchure, ont une valeur prédictive permettant d'envisager un tri des anches à l'usine, au moyen de procédures rapides et automatisées. Ainsi, les facteurs d'anche pourraient proposer une catégorisation basée sur le feed-back de leurs clients. En fonction des mesures effectuées à l'usine et du feed-back renvoyé par les clients, il sera possible d'évaluer l'importance relative pour les musiciens de chaque facteur objectif détecté par l'étude et vérifier s'ils permettent une classification du type bon/mauvais, valide pour la majorité des musiciens ou si les préférences exprimées reflètent plutôt des préférences stylistiques individuelles (ou l'utilisation d'un autre modèle de bec). Il reste encore à montrer que les mesures réalisées immédiatement après fabrication sont bien représentatives de l'état de l'anche une fois arrivée chez le client. En particulier, il faut vérifier si le facteur 2 qui caractérise l'ouverture au repos est déjà mesurable à la fabrication ou s'il résulte d'une maturation du bois post fabrication. Le cas échéant, un simple retablage permettrait de rendre plus jouables un certain nombre d'anches, en ajustant l'ouverture au repos. L'influence des déformations plastiques au cours de la vie de l'anche devrait être analysée. Ceci permettrait probablement d'insuffler une seconde jeunesse à certaines anches devenues trop fermées, qui devraient sinon être éliminées.

L'étude perceptive montre que les 4 descripteurs proposés sont corrélés de manière statisti-

quement significative avec les 4 premiers facteurs objectifs détectés (soit 2 ou 3 de plus que ce qui avait pu être prouvé jusqu'ici à partir de test perceptifs). Ces facteurs correspondent à : 1) la raideur de l'anche, particulièrement dans sa partie médiane, 2) l'ouverture au repos 3) l'évolution de la raideur entre la pointe et l'empeigne de l'anche et 4) les déformations plastiques de l'anche rodée, liées à une différence de raideur entre les côtés et l'axe de l'anche. Les facteurs 5 et 6 sont liés à des antisymétries de l'anche qui n'ont pas été ciblées par des tests perceptifs spécifiques (différence de raideur entre les côtés et torsion (plastique) de l'anche). On relèvera que ce lien significatif a été établi en comparant des mesures objectives (essentiellement *statiques*), réalisées sur des anches **sèches**, au *jeu* par un clarinettiste de ces mêmes anches à l'état **humide**. Les caractéristiques mises à jour permettent de saisir pourquoi des descripteurs vagues comme "qualité globale" ou "brillance" sont mal adaptés, notamment parce qu'ils ne tiennent pas compte des multiples influences (antinomiques) qui entrent en compte. Des descripteurs plus raffinés pourront être proposés, grâce notamment l'utilisation de la synthèse sonore et aux indications précises sur les différences de fonctionnement entre anches fournies par les photos du canal. Ces photos fournissent aussi au clarinettiste des renseignements précieux sur les corrections qu'il est possible d'apporter à l'anche par grattage, soit en construisant son propre banc d'essai (comportant un bec, une lèvre artificielle et un appareil de photo), soit en fonction des différences perceptives notées. Le fabricant de becs peut aussi s'inspirer des techniques développés pour optimiser la forme de la table en fonction d'un modèle d'anche particulier (ou pour développer un intercalaire de type Claripatch permettant d'adapter la table du bec à l'anche jouée).

Les simulations ont permis de valider très grossièrement la pertinence des modèles physiques développés. Une optimisation plus poussée des paramètres permettant une meilleure adéquation entre mesures et simulations doit être réalisée et une comparaison plus fouillée des signaux doit être entreprise. Il s'agit aussi de clarifier quel est l'ingrédient manquant au modèle d'anche pour obtenir une meilleure adéquation avec les CGS des signaux d'anche mesurés. Malgré cela, le modèle d'anche non linéaire 1D proposé semble assez représentatif du comportement réel de l'anche. La modélisation du bec doit également être examinée. L'hypothèse usuelle - qui l'assimile à un cylindre de volume équivalent - doit être révisée, parce que l'évolution spectrale des signaux est mal reproduite par ce modèle simplifié. Les simulations réalisées à partir d'un relevé de perce d'une clarinette Buffet Crampon montre de manière convaincante que le réalisme des signaux synthétisés dépend de manière assez sensible de la géométrie retenue pour simuler le bec.

Le Chapitre 8 présente avant tout des études à caractère exploratoire, réalisée avec un bec "Vandoren M30" et des anches "Vandoren classic". Certaines directions importantes ont pu être mises en évidence, mais elles doivent encore être confirmées et approfondies par une étude plus détaillée et plus rigoureuse, comportant plusieurs types de becs et d'anches. En particulier, une étude de la mécanique de lèvre doit encore être réalisée.

Résumé de la Partie V

Cette partie est consacrée aux conclusions générales et aux perspectives. Elle dresse un bilan rétrospectif des recherches effectuées durant presque deux décennies, relaté au Chapitre 9 et traduit en français *in extenso* ci-après.

Conclusions générales, en forme de postface

Les travaux que menés sur l'acoustique de la clarinette au cours de ces 17 dernières années ont permis d'effectuer un certain nombre de progrès intéressants, non seulement pour l'acoustique mais également pour les musiciens. A l'époque, il me semblait évident que les modèles d'anche développés par les acousticiens (comme celui décrit au Chapitre 1) ne pouvaient pas refléter toute la subtilité du problème de l'anche et que ces modèles ne permettraient pas d'orienter une caractérisation objective des anches différente de celle qui est proposée depuis des décennies par les facteurs d'anches, à savoir par la mesure de la "force" de l'anche. Ce soupçon s'est révélé fondé : une part du mystère qui entourait le problème de l'anche a pu être levé, réconciliant ainsi la perception du musicien avec une modélisation assez réaliste du problème physique, tout en restant relativement simple et efficiente à simuler.

La réalisation de cette tâche n'a pas été facile, parce qu'elle a nécessité tout d'abord des années de formation autodidacte en acoustique, pratiquement sans aide extérieure, essayant de lire et comprendre de nombreux articles et ouvrages, butant parfois des semaines durant sur quelques phrases que je n'arrivais pas à saisir, sur une coquille dans une équation ou sur une notation ambiguë, essayant de refaire certains calculs, avant d'être finalement en état de réaliser ma première étude digne d'intérêt.

Les premiers travaux réalisés sur le modèle de Raman m'ont montré la beauté d'un monde mathématique riche, généré à partir de 2 équations apparemment très simples. L'utilité de ces modèles théoriques pour les musiciens n'est pas évidente à démontrer, parce que les sons produits sont très caricaturaux. S'ils ne permettent pas de faire véritablement la distinction entre le son d'un klaxon et celui d'une clarinette, ils autorisent toutefois un certain nombre de conclusions intéressantes sur les modalités de fonctionnement de ce type d'instruments. Les modèles analytiques permettent d'expliquer pourquoi il est pratiquement impossible de jouer pianissimo avec un instrument comportant des tampons défectueux, ne bouchant pas les cheminées de manière étanche. Ils orientent l'instrumentiste et le pédagogue vers les techniques permettant de maîtriser le "pianissimo magique" caractéristique de l'instrument, en modulant le paramètre de pertes au moyen de la texture et de la position de la lèvre inférieure. La connaissance des modalités physiques régissant le jeu de l'instrument est importante pour comprendre et enseigner correctement certains aspects importants du contrôle du son par l'instrumentiste. La compréhension des raisons précises qui autorisent ou interdisent tel ou tel comportement permet aussi de disculper l'instrumentiste en toute bonne foi, sans obliger celui-ci à se justifier, en rejetant ordinairement la faute sur l'anche. La découverte des sons "exotiques" comme les doublements de période (mis en évidence par divers auteurs bien avant mes travaux) fut aussi pour moi une révélation sur l'utilité musicale de ces modèles théoriques simples.

Mes premières tentatives naïves de simuler certains aspects de la mécanique de l'anche à l'aide du logiciel CATIA m'ont assez rapidement montré que le secret de l'anche ne pouvait pas résider dans une manière particulière de vibrer, par exemple grâce à certaines relations harmoniques privilégiées entre les premières résonances : la moindre modification des conditions aux limites détruisait cet équilibre supposé optimal. Des simulations statiques du contact entre le bec et l'anche ont été bien plus instructives et m'ont fait soupçonner qu'une part de la subtilité du problème de l'anche résidait de ce côté-là. Malheureusement, au lieu de poursuivre mes recherches dans cette direction, j'ai opté pour une étude qui s'est avérée finalement pas très fructueuse : la piste de la viscoélasticité.

L'étude des résonances d'un panel par holographie a permis de révéler tout un bestiaire de déformées, beaucoup moins régulier et symétrique qu'attendu par les simulations par éléments finis, supposant le matériau idéalement homogène. Le modèle viscoélastique proposé permet certes de reproduire certaines différences systématiques entre anches, mais les études exploratoires menées pour tenter de faire un lien avec certains descripteurs musicaux subjectifs n'ont pas conduit à des résultats très probants. La plupart des tests réalisés n'ont pas pu prouver l'existence de liens statistiquement significatifs : la plupart du temps, les résultats étaient situés dans la zone "grise", où il est difficile de se prononcer. Cependant, la répétition de ces résultats "presque significatifs" indique qu'il y a probablement "quelque chose" derrière les paramètres mis en évidence. Le modèle proposé ne tient pas compte de l'inhomogénéité du matériau ni des différences géométriques entre anches, qui sont inévitables, malgré tout le soin apporté à leur manufacture. Il est toutefois possible que certains paramètres (du modèle viscoélastique) puissent influencer le comportement de l'excitateur et ainsi jouer un rôle bien plus important qu'un simple décalage fréquentiel de certains modes d'ordre élevé.

Les années qui ont suivi l'étude holographique ont permis de mettre au point un bec instrumenté performant et de développer des logiciels d'acquisition et d'analyse du jeu de l'instrumentiste en temps réel (non décrits dans ce mémoire), dans le cadre du projet SDNS-AIMV. La méthode mathématique d'approximation des équations différentielles, que j'ai nommée Extended Discrete Singular Convolutions (EDSC), a été mise au point durant cette période. Initialement, cette méthode devait servir à simuler le contact de l'anche avec la table de manière grossière et simplifiée, autorisant un calcul temps-réel. Il s'est avéré qu'elle autorise en outre la résolution numérique d'équations aux dérivées partielles fractionnaires ou un calcul des modes de poutre et de plaque avec une précision inégalée, eu égard à la taille du maillage. Malheureusement,

l'article qui lui a été consacré n'a jamais été finalisé et publié, bien que la majeure partie du travail ait été réalisée. Le peu d'intérêt rencontré par cette méthode aux yeux des acousticiens n'est probablement pas étranger à cet abandon. La publication du texte inachevé en annexe de ce mémoire permettra peut-être de la sauver de l'oubli.

Le projet CAGIMA a orienté ensuite mes recherches dans une direction très différente : l'étude du résonateur, par le biais des outils de l'analyse complexe, des transformées linéaires (Laplace, en particulier), des décompositions modales et des filtres numériques. Les deux premières années du projet ont avant tout constitué un apprentissage de ces méthodes, qui me semblaient initialement hors de ma portée. Avec les moyens du bord, j'ai tenté une approche de ces domaines assez hermétiques à l'intuition. Peu à peu, j'ai saisi comment ces domaines étaient interconnectés et acquis certaines techniques permettant de les aborder avec plus de sûreté. Plus de deux ans après la fin officielle du projet, j'ai finalement réalisé ce qu'on attendait initialement de moi : le développement d'une méthode autorisant le prototypage virtuel des instruments à vent. Bien qu'il reste encore passablement de travail à accomplir pour valider les méthodes développées et achever l'élaboration d'un simulateur grand public, j'espère que mon apport sera finalement utile à la communauté et qu'il pourra aider les facteurs d'instrument à concevoir de nouveaux instruments, plus justes, plus homogènes et faciles à jouer.

Cette épopée s'achève avec la rédaction de ce mémoire, après près de trois années passées en tant que doctorant de l'université du Maine, qui ont permis l'achèvement de certains projets et leur mise au propre. Finalement, le "secret" de l'anche a pu être partiellement percé, en abandonnant la piste quasi métaphysique de la "vibration" de l'anche au profit d'une approche beaucoup plus basique et terre à terre qui consiste à observer son comportement statique. La méthode "de la bouteille" permet une mesure précise et répétable des caractéristiques aérauliques statiques. Cette méthode fonctionne de manière très satisfaisante, bien que certains progrès concernant la maîtrise et la modélisation des échanges de chaleur doivent encore être réalisés. Le bec instrumenté développé quelques années auparavant, les améliorations apportés à la lèvre artificielle mise au point par A. Muñoz et les dispositifs bricolés dans mon garage ont permis une mesure fiable de la déflection de l'anche. Ces mesures ont été complétées par des photographies précises du canal qui se sont révélées très instructives et assez faciles à interpréter, après traitement des images par les méthodes développées. Une variété insoupçonnée de comportements a ainsi pu être observée, accréditant ainsi les témoignages des clarinettistes au sujet de l'importante variabilité des anches à l'intérieur des emballages vendus dans le commerce (d'une même marque, modèle et force).

Une précision s'impose cependant au sujet de la "vibration" de l'anche : l'étude a montré l'importance des aspects statiques, mais cela ne signifie pas pour autant que les aspects dynamiques soient négligeables. Ils sont probablement intimement liés aux aspects statiques, par l'intermédiaire du matériau constituant l'anche. Cet aspect ne doit pas être minimisé lors de la recherche de matériaux alternatifs au roseau : il est important de reproduire non seulement le comportement statique, mais également la fréquence de la première résonance de l'anche en roseau ainsi que son amortissement, sans quoi l'anche ne donnera probablement pas satisfaction. Les propriétés d'amortissement du roseau humide sont vraisemblablement importantes pour atténuer toute vibration parasite de l'anche, sans entraver le maintien de l'oscillation de la colonne d'air.

La mise au point d'un modèle non linéaire d'anche (séparant clairement les aspects mécaniques et aérauliques), conjuguée à l'architecture logicielle développée pour la simulation des guide d'ondes (incluant des effets non linéaires au niveau des orifices et un modèle de bec plus réaliste) a permis de vérifier qu'une partie importante du problème est maintenant scientifiquement sous contrôle. Il reste bien entendu un certain nombre de points à améliorer pour parfaire l'adéquation entre mesures et simulations (dont l'étude de la mécanique de lèvre), mais cet objectif semble maintenant plus aisé à atteindre.

L'analyse canonique des corrélations atteste la présence d'un lien très fort entre toutes les mesures physiques objectives réalisées à l'intérieur d'un panel de 40 anches. L'existence de plus d'une dizaine de facteurs indépendants a pu être prouvée de manière statistiquement significative. La confrontation entre les mesures de bifurcation et les données issues de la synthèse sonore a également montré l'existence de liens solides pour au moins 13 facteurs. L'un des points qui me réjouissent le plus dans toute cette étude est la mise en évidence du fait que les 4 plus importants facteurs objectifs détectés sont corrélés de manière statistiquement significative avec les

évaluations subjectives réalisées par le clarinettiste. Cela ouvre la voie à une sélection automatisée des anches, réalisée directement à l'usine. La nature des descripteurs évalués, la comparaison avec les diagrammes de bifurcation mesurés et les mesures statiques réalisées permettent d'orienter les recherches dans des directions négligées jusqu'ici, mettant en évidence le caractère ambivalent de certains descripteurs, lorsque le contexte d'évaluation n'est pas clairement défini. Ces approches éclairent de manière pertinente l'échec relatif de certaines tentatives de caractérisation des anches au moyen de descripteurs subjectifs trop vaguement définis.

Il reste à espérer que les faits révélés seront pris au sérieux par les fabricants d'anches, qu'ils mettront en œuvre les techniques de caractérisation préconisées, les amélioreront et que bientôt, les clarinettistes pourront sélectionner leurs anches d'une manière beaucoup plus précise et efficace que par le passé. J'espère également que cette étude permettra une mise au point facilitée de nouveaux modèles de becs ou d'anches, notamment lors de la mise en œuvre de matériaux alternatifs au roseau.

Contents

List of Figures

List of Tables

Introduction

The research studies presented in this dissertation are all related to my interrogations about the clarinet reed (exciter) and its relationship with the sound production of the instrument (resonator). Most of these researches have been initiated or realized without imagining that they would be joined together someday as a PhD.

Traditionally, the Introduction consists in presenting the state of art in the concerned topic of research before the beginning of the project. With the present project, this approach makes little sense, because the topic of research is too broad (i.e. the acoustics of wind instruments and of the clarinet in particular) and because the project started too long ago (about 2001). In this dissertation, the state of art is presented succinctly for each subproject, at the beginning of each chapter. The general structure of the project is the subject of this Introduction.

This dissertation is structured in 5 Parts dealing with different topics of research. The first 3 parts examine the relationships between the reed, the exciter and the resonator. The 2 last parts try to do a synthesis of the findings. The global structure can be summarised as follow:

I) Study of the Raman model (considering the reed as a spring without inertia, characterized by a linear stiffness and an opening at rest), investigating more particularly:
   1) Effect of losses
   2) Playing regimes

II) Characterization of clarinet reeds, examined under the following aspects:
   3) Dynamic
   4) Static

III) Real-time simulations by physical model of:
   5) Exciter, according to measurements
   6) Resonator, modeled by its input impedance
   7) Resonator, modeled by waveguides

IV) Attempt of Synthesis:
   8) Study of the playability of a reed panel

V) General conclusions:
   9) Concluding reflections to the project

The first part deals with simple analytical models for clarinet-like instruments. The cylindrical resonator is reduced to an elementary reflection function - a simple delay - postulating that the losses do not depend on the frequency. The reed is reduced to a simple linear stiffness without inertia, beating against the lay of the mouthpiece and obstructing the channel. The reed of the Raman model is so simple that the mechanical and aeraulic aspects are completely undistinguished. The sounds produced are of course caricatural (square signals). Despite this, the model is of some interest since it is able to correctly predict the bifurcation thresholds and allows an analytical treatment to delimit the various operating regimes. The exciter is characterized by 2 essential parameters: the stiffness (the clarinettists say "strength of the reed") and the opening at zero air pressure. The 2 Chapters composing this Part consist of articles published in 2010 and 2015.

Chapter 1 revisits the article by Dalmont et al. [35] *An analytical prediction of the oscillation and extinction thresholds of a clarinet* focusing in particular on the effect of losses. I noticed that

a number of cases had been omitted in the original paper, especially when the losses are high. The paper also proposes a new calculation method, much more concise, developed on an idea of my coauthor, Jean Kergomard. This model is quite enlightening also for the musician, because it clearly delimits certain operating regimes of the instrument, according to 2 playing parameters controlled by the instrumentalist: the opening at zero air pressure and the loss parameter (that the clarinettist can influence partially by means of its under lip, but which also depends in particular on a possible leakage of a keypad or on the porosity of the instrument [14]).

Chapter 2 deals with iterated maps. The Raman model is transcribed in the form of a function f that links the travelling wave that leaves the mouthpiece at time n with the next travelling wave, which leaves the mouthpiece at the next time step, $n + 1$, i.e. the time required for the wave to make a round trip in the cylindrical pipe. The static regime is characterized by the equation $x = f(x)$ and the usual two-state oscillating regime by the equation $x = f(f(x))$. This chapter examines the function f in many cases, with emphasis on "exotic" regimes, such as period doubling, subharmonic cascades, intermittencies and chaotic regimes.

The second Part deals with the characterization of the clarinet exciter, focusing the studies on the role of the reed. Its main goal is to objectively describe the differences observed between reeds and to project them on simplified models.

Chapter 3 examines the question of reed mechanics from a dynamic point of view. It is constituted by an article published in 2014. We study a panel of 55 reeds by holography. The resonance frequencies of the reed (taken alone, without lip and without bending against the mouthpiece lay) are detected up to 20 kHz (approximately the first 15 resonances of the reed). In the first part of the article, the observations are described from a statistical point of view. In the second part, we try to establish a viscoelastic reed model, which would explain the differences observed between reeds.

Chapter 4 proposes a method of experimental characterization of the clarinet exciter. Two quantities are evaluated as a function of the lip and air pressure applied to the reed: the mechanical deflection in the vicinity of the reed tip and the air flow entering through the channel. The method uses a bottle connected to an instrumented clarinet mouthpiece. The thermodynamical laws allows the evaluation of the quantity of air present in the bottle at any moment. The measuring cycle starts with creating a moderate vacuum in the bottle, sufficient to maintain the reed tightly bent against the lay for several seconds. The amount of air returning into the bottle through the channel is measured. After a while, the sudden opening of the reed occurs and the ambient pressure is recovered in the bottle. However, the return of the air is slow enough to consider quasi-static conditions. The effective aeraulic section is deduced from the measured flow, according to Bernoulli's law. During this experiment, the mechanical deflection of the reed is also measured by optical sensors.

The third Part deals with the real-time simulation of wind instrument by physical models and describes a synthesizer allowing to evaluate (among others) the sound expected for each reed. This Part begins with the development of a realistic, static reed model, in accordance with the measurements (and extended to a simple and efficient dynamic model). The next Chapter focuses on the modal analysis of the input impedance of the air column of wind instruments, as a result of my collaboration with the CAGIMA [112, 113, 72, 71, 73, 74, 29, 26, 28, 30, 27, 70] project. My task in this project was to develop the techniques needed for the virtual prototyping of wind instruments. From the geometry of the instrument and the related physical equations in the spectral domain, a method is described for the modal estimation of the input impedance, transfer functions or scattering functions, allowing a real-time simulation, while ensuring the passivity of the simulated instrument at any frequency. This formulation in the discrete time domain allows a simulation of the the instrument by means of a synthesizer. One of the goals of the CAGIMA project is to provide tools to the instrument maker allowing to test virtually its instrument from a musical point of view (intonation, ease of emission and timbre) before building a real prototype.

Chapter 5 proposes a model of the exciter, according to the mechanical and aeraulic measurements. The static, mechanical model assumes that the deflection of the reed (with respect to the applied pressure) is a decreasing, convex function that can be approximated by piecewise-parabolic sections. The static model can be easily converted into a dynamic model, adding mass and damping, using the dynamic contact scheme described in [25]. The computation cost of the

simulation is only slightly higher than that of the traditional one-mode linear scheme. The aeraulic section is evaluated with respect to the position of the reed from the measurements, by interpolation.

Chapter 6 consists of an article submitted in 2017 to "Applied Acoustics". It focuses on the modal estimation of the input impedance of wind instruments and deals in particular with the case of a measured input impedance. It describes the application of well-known analytical techniques, avoiding a number of pitfalls. An example of application to the clarinet is given, detailing simple empirical algorithms that simulate: i) the transitions between fingerings and ii) the external sound from the internal pressure calculated in the mouthpiece.

In Chapter 7, the question of modal estimation is extended to waveguides, in particular for a modal estimation of the scattering matrices. A theory of reflection and transmission functions is developed, focused on the transposition of analytical expressions (in the spectral domain) into digital filters expressed in the discrete time domain. It is shown how these digital filters can be adapted to simulate an impedance or admittance relationship. The simulation of the radiation reflectance is examined in the case of linear and nonlinear losses. An object-oriented software architecture - based on a segmented simulation of the air column, where the segments are linked by means of junctions (listed in a dictionary) - is proposed. This software allows to someone with almost no acoustic knowledge to build its own simulator, by assembling the elementary bricks of each section of the instrument. Simplified procedures simulate the transitions among fingerings, by managing the degree of opening of each lateral chimney. Models of valves and slides are given. This software can simulate the majority of the wind instruments, in particular those of the brass and the weak reed families. Various application examples are given, in particular for the real-time simulation of a Buffet Crampon Bb clarinet, with 28 sections and 22 lateral chimneys (and nonlinear losses at each tonehole).

The fourth Part attempts to summarize the proposed developments, through a study on the playability of clarinet reeds that confronts objective physical measurements, subjective musical evaluations and data from sound synthesis, trying to reproduce an experiment conducted with the artificial mouth.

Chapter 8) confronts 3 types of data collected from a panel of 40 clarinet reeds: i) Objective physical measurements, including (for each reed and embouchure) static experiments (aeraulic measurements, mechanical deflection and channel photographs) and a dynamic experiment (bifurcation diagram, established on a *crescendo* / *decrescendo*). ii) Subjective musical evaluations: the author played these same reeds blind (before analysis of the measurements) and scored them on the basis of 4 different descriptors. iii) Sound synthesis: physical models developed in Part III are used to simulate bifurcation diagrams.

The central questions addressed in this Chapter are the following ones: Are some factors common to all collected data blocks? Which are their nature and number? Are the detected correlations due to chance? Is there a statistically proven link between objective measurements, subjective evaluations and simulations? Can the reeds be characterized on the basis of the detected factors? These questions are answered by applying a statistical technique: the canonical correlation analysis (CCA).

The fifth part, Chapter 9, is devoted to the general conclusions and future work. The conclusions have the character of a postface, reflecting the experience accumulated during this very long project. The factual conclusions are located at the end of each chapter.

Didactic introduction to the field of research

This section is written for readers with limited experience in clarinet acoustics.

The basic operation of the instrument is explained graphically, by simulating the physical behavior of the instrument. These graphs will help the reader to intuitively understand how the instrument works and allow to get an idea about the kind of problems that had to be solved in order to perform such very realistic simulations. Moreover these examples will allow him to grasp the practical utility of the tools developed.

The Fig. 1 presents a simulation of a playing clarinet, which was performed by using most of the methods developed in the present PhD, namely:

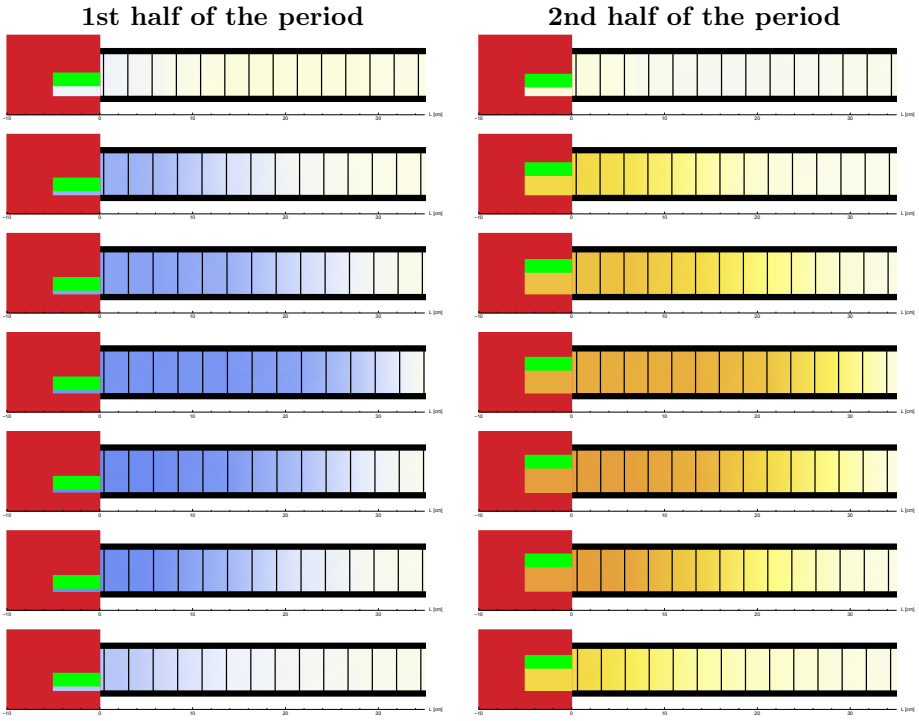

Figure 1 – Simulation of one period of the self-oscillation of a clarinet. The playing frequency is about 238 Hz. The 14 successive pictures schematize the physical state of the instrument in time steps of 1/14 of period (i.e. about 0.3 ms). The pressure in the instrument is indicated by a color code, from red (overpressure of 4200 Pa) to blue (underpressure of -4200 Pa). The blowing pressure in the mouth (red square on the left) is 4200 Pa. The thin vertical black lines delimit air particles having all the same initial volume. The position of the reed is represented by a green rectangle. Below the reed, the channel allows the air to pass from the mouth into the instrument.

— The reed is simulated according to the measurements of a real ("bad") reed from the panel studied in Chapter 8, measured with the method presented in Chapter 4 and simulated with the method presented in Chapter 5.

— The instrument is simulated in real time with the waveguide technique described in Chapter 7, using the modal estimation described in Chapter 6, incorporating nonlinear losses at the output of the instrument, as developed in Appendix A and with the software described in Appendix B.

Actually, the simulated instrument is simply a cylinder of $d = 15$ mm diameter and of length L =35 cm (although the developed methods allow a realistic simulation of a full clarinet). The Fig. depicts one cycle of oscillation (i.e. one period). The pressure $p(t, x)$ in the instrument is indicated by a color code, from red (overpressure) to blue (underpressure). Waves travel inside the instrument at the speed of sound (i.e. much faster than the air particles). A period consists of 4 travels of the wave in the instrument: a round trip of the underpressure wave and a round trip of the overpressure wave. Note that the playing frequency f_{play} =238.36 Hz is reasonably well foreseen by the formula $f_{play} = c/(4(L + 0.8d)) = 239$ Hz, where $c \simeq 346$ m/s is the speed of sound at 25°C (as in the simulation). The displacement of the thin vertical black lines makes it possible to follow the displacement of the air particles in the air column, from which the flow rate $u(t, x)$ can be deduced.

The Fig. 2 presents exactly the same simulation, but the time t is coded by colors (hue) and the longitudinal coordinate x and the physical parameters are represented respectively on the abscissa and ordinate axes. The period is divided in 2 halves (as in the precedent Fig.) which

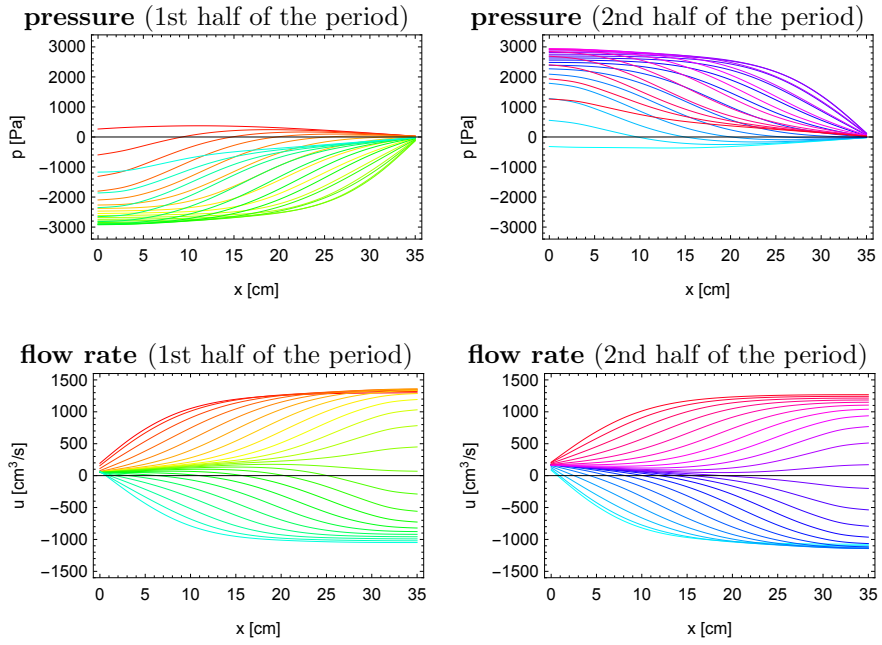

Figure 2 – Same simulation than Fig. 1, with the difference that the time t is coded by a circular code of colors (hue) and the physical parameters are depicted on the ordinate axis. The time elapsed between each successive curve is 0.09 ms. The period is divided in 2 halves as in Fig. 1 (columns of the Fig.). The first row presents the pressure in the instrument $p(t, x)$ as a function of the x coordinate along the instrument ($x = 0$: mouthpiece, $x = 35$ mm: output). Similarly, the 2nd row presents the flow rate in the instrument $u(t, x)$.

form the columns of the Fig. The first and the second rows depict respectively the pressure $p(t, x)$ and the flow rate $u(t, x)$ in the instrument.

The Fig. 3 presents once more the same simulation, but x is coded by the colors of the avocado and the time t and the physical parameters are represented respectively on the abscissa and ordinate axes. The evolution of the following parameters is presented: $p(t, x)$, $u(t, x)$, $z(t)$ (deflection of the reed, 6 mm from tip) and $S(z(t))$ (effective section of the channel through which the air enters into the instrument, also called aeraulic section of the channel).

The simultaneous examination of these 3 Figs. allows to understand intuitively what is happening in the instrument.

Let's first look at the reed. Its position is determined by the difference of pressure between mouth and instrument and also by the embouchure (which is here quite tight: the clarinettist compresses the reed pretty strongly with the lips). When the pressure drop is small (red against orange) the reed is open. It can be seen that it never completely closes the channel, even when the pressure drop across the reed is large (red against blue). A small leak is always present. This leak has a noticeable influence on the efficiency of operation of the instrument: the peak amplitude of the pressure in the mouthpiece is only 70% of that of the blowing pressure (while in the theoretical models, when the reed closes hermetically the channel during half of each period, it should be around 100%, see Chapters 1 and 2). This low efficiency is probably one of the reasons because the clarinettist did not appreciate this reed (R14) for playing the beginning of the Poulenc Sonata or the "Hirt auf dem Felsen" by Schubert (see Chapter 8). When the reed is open, the pressure in the instrument is never exactly equal to the pressure in the mouth: the generated flow helps to compensate the losses in the instrument, so as to maintain the self-oscillation of the instrument. Note that the relationship between pressure $p(t, x = 0)$ and reed deflection z is not always linear: the stiffness of the reed increases when the channel is nearly closed, while the open reed is quite linear. Each movement of the reed is followed by a few (here quasi imperceptible) jolts, at the resonance frequency of the reed. These jolts are clearly

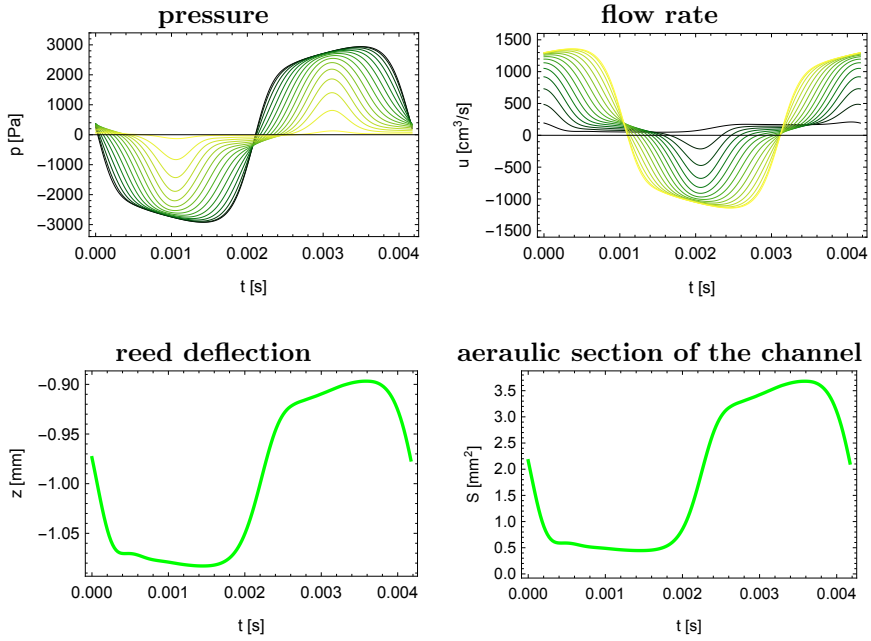

Figure 3 – Same simulation than Fig. 1, with the difference that the time t is represented on the abscissa axis, the physical parameters are depicted on the ordinate axis and the longitudinal coordinate x is coded by the colors of the avocado, from dark (mouthpiece, $x = 0$) to light (output, $x = L$), in steps of 25 mm.

observed on the measurements of the same reed with a looser embouchure on Fig. 8.8 (or the theoretical simulation Fig. 5.3), where it is observed that the resonance frequency varies with the deflection: it is notably higher when the channel is almost closed, because a reed bending against the mouthpiece lay works like a stiffening spring.

Why is the zero position of the reed deflection z situated on the plane of the table of the mouthpiece lay and not at the position where the reed closes the channel, as usual? This is because the position of the reed is measured about 6 mm away from the tip of the reed. The reed is therefore able to bend further inside the mouthpiece window, even if the channel is already closed. The aeraulic section $S(z)$ is considered as a nonlinear function of the reed deflection z. This way, the mechanical problem (i.e. the jolts of the reed) is considered independently of the aeraulic problem (how much air enters into the instrument). This nonlinearity can be observed by comparing z and S on Fig. 3.

We examine now how the air enters into the instrument: it penetrates by blows, mainly when the reed is open and the air flow reaches its highest value when the reed initiates the closing phase. It is determined by the Bernoulli's law from the pressure drop across the reed and the aeraulic section. The mean flow rate in the instrument is about 12 times lower than the maximal flow rate at the output, respectively 0.113 and 1.360 liters per second, which corresponds to an air speed of 0.64 and 7.7 m/s, in a pipe of 15 mm of diameter (i.e. much less than the speed of sound). Note that at the open end of the pipe, the pressure is nearly zero. Fortunately, this pressure is not strictly zero, otherwise no sound would be heard outside [2].

The principal aims of the study are to understand :

— how the reed interacts with the instrument

— what is the influence of the reed on the sound production

— how is it possible to select the reeds that best meet the expectations of the clarinettist

2. In this example, the peak-to-peak amplitude of the pressure signal is about 22.5 times smaller at $x = L$ than at $x = 0$. Notice the similarity between $p(t, x)$ and $u(t + \tau/4, L - x)$, with $\tau = 0.0042$ s, the duration of one period, especially when x is near 0 (dark green pressure curve and yellow flow rate curve in Fig. 3). Note also that $\partial_t u(t, x = L)$ is roughly proportional to $p(t, x = L)$.

General remark about the bibliography

The Chapters 1, 2, 3, 6 and the Appendices E and F have their own bibliography (since their texts have been directly imported as pdf files), while all other parts of the text share a common bibliography, located at the end of the document.

Part I

Simple analytical Models for Clarinet-Like Instruments

Chapter 1

An Analytical Prediction of the Bifurcation Scheme of a Clarinet-Like Instrument: Effects of Resonator Losses

Résumé

Les relations entre les paramètres d'excitation et les régimes d'oscillation sont bien connues pour les instruments à cordes. Une étude similaire a été tentée à propos des instruments à anche, dans l'optique d'en déduire certaines conséquences sur la facilité de jeu. Dans un modèle minimal d'instrument type clarinette, trois paramètres sont pris en compte : i) la pression dans la bouche, ii) l'ouverture de l'anche au repos, iii) la longueur du résonateur présumé cylindrique. Récemment, un paramètre supplémentaire a été ajouté : un paramètre de pertes dans le résonateur (dans le modèle de Raman, on considère que ces pertes sont indépendantes de la fréquence). Ceci permet d'expliquer l'extinction du son, lorsque la pression dans la bouche devient très importante. Nos travaux continuent ceux de Dalmont et al. [35], cherchant à établir un diagramme des régimes d'oscillation en fonction de l'ouverture de l'anche et du paramètre de pertes. Nous avons développé une méthode de calcul alternative qui permet une généralisation plus aisée et qui simplifie nettement les développements analytiques. Un accent particulier a été mis dans l'étude d'un cas apparemment jamais investigué : lors de pertes importantes, la bifurcation à l'émergence peut être inverse, de manière similaire à celle à l'extinction, en cas de faibles pertes. La plupart des calculs sont réalisés de manière analytique et permettent de mettre clairement en évidence l'influence des différents paramètres. Nous avons tenté d'en déduire un certain nombre conséquences musicales à propos des techniques de jeu à conseiller aux clarinettistes.

Cet article [150] est reproduit avec l'autorisation du coauteur et celle de l'éditeur S. Hirzel, du 15 janvier 2018.

Acta Acustica united with Acustica
Vol. 101 (2015) 279 – 291

DOI 10.3813/AAA.918826

An Analytical Prediction of the Bifurcation Scheme of a Clarinet-Like Instrument: Effects of Resonator Losses

P.-A. Taillard[1)], J. Kergomard[2)]

[1)] University of Applied Sciences and Arts Northwestern Switzerland, Musik-Akademie Basel. Academy of Music. Schola Cantorum Basiliensis. Leonhardsstr. 6, 4051 Basel

[2)] LMA, CNRS, UPR 7051, Aix-Marseille Univ, Centrale Marseille, 13402 Marseille Cedex 20, France. kergomard@lma.cnrs-mrs.fr

Summary

The understanding of the relationship between excitation parameters and oscillation regimes is a classical topic concerning bowed string instruments. The paper aims to study the case of reed woodwinds and attempts to find consequences on the ease of playing. In the minimum model of clarinet-like instruments, three parameters are considered: i) the mouth pressure, ii) the reed opening at rest, iii) the length of the resonator assumed to be cylindrical. Recently a supplementary parameter was added: the loss parameter of the resonator (using the "Raman model", that considers resonator losses to be independent of frequency). This allowed explaining the extinction of sound when the mouth pressure becomes very large. The present paper presents an extension of the paper by Dalmont *et al.* (JASA, 2005), searching for a diagram of oscillation regimes with respect to the reed opening and the loss parameter. An alternative method is used, which allows easier generalization and simplifies the calculation. The emphasis is done on the emergence bifurcation: for very strong losses, it can be inverse, similarly to the extinction one for weak losses. The main part of the calculations are analytical, giving clear dependence of the parameters. An attempt to deduce musical consequences for the player is given.

PACS no. 43.75.Ef, 43.75.Pq, 43.75.-z

1. Introduction

The understanding of the relationship between excitation parameters and oscillation regimes is a classical topic concerning bowed string instruments: for instance Shelleng [1], or Guettler [2], or Demoucron *et al.* [3] proposed 2D diagrams with respect to either bow force and bow position, or bow position and bow velocity. For reed instruments, this kind of diagrams are less numerous: in [4], Dalmont *et al.* proposed a diagram with respect to excitation pressure and reed opening, and recently Almeida *et al.* [5] proposed a diagram with respect to blowing pressure and lip force, related to the reed opening.

In the minimum model of reed, clarinet-like instruments, three parameters are considered: i) the mouth pressure, ii) the reed opening at rest, iii) the length of the resonator assumed to be cylindrical. In [4], a supplementary parameter was added: the loss parameter of the resonator (using the "Raman model", that considers resonator losses independent of frequency). This allowed explaining the extinction of sound when the mouth pressure becomes very large. We notice that the agreement of the theoretical results with experimental results was satisfactory (see [6]).

The objective of the present paper is to revisit the paper by Dalmont *et al.* [4]: the focus is the search for a diagram of oscillation regimes of reed instruments with respect to two parameters: the reed opening, and the loss parameter. The choice of these two parameters is justified by the fact that the third parameter, the blowing pressure, is the easiest to modify for the instrumentalist. The elements of this diagram were rather complete in [4], but phenomena occurring for strong losses, especially at the emergence of the sound, were not investigated.

The use of simplified models for the prediction of the oscillation regimes is classical for musical instruments producing self-sustained oscillations. For the calculation of the instability thresholds, linearization was used (see Wilson and Beavers [7] or Silva *et al.* [8]), while for ab initio computation, the iterated map scheme was studied (see Mc Intyre *et al.* [9], Maganza *et al.* [10], Taillard *et al.* [11]). The interest of the model chosen in the present paper is that analytical formulas are possible, given clear dependence of the parameters (for other models, numerical calculations could be possible by using similar basic ideas, using for instance continuation methods [12] or time-domain methods [13, 14]).

Received 03 January 2014,
accepted 15 May 2014.

The analytical calculations presented hereafter are slightly different from those of [4]. They also are limited to the limit cycles corresponding to the two-state oscillating regime, but are based upon a generalization of the fact that for this regime, when no losses are present, the flow rate is a constant. This regime is the most similar to what musicians consider as a "normal" sound. In particular the method allows studying the character of the emergence and extinction bifurcations of this regime, which are important properties related to the possibility to play pianissimo or not, and more generally to the ease of playing. In [4] it was shown that the extinction bifurcation can be direct or inverse (supercritical and subcritical, respectively, see Refs; [15, 16, 17]); here it is shown that this is true also for the emergence bifurcation.

In Section 2, the basic model of [4] is reminded (see also [18]), and a treatment of the problem based upon a unique quantity, the pressure difference Δp, is presented in Section 3. This leads to a simple graphical analysis of the two-state regime, explained in Section 4, yielding a proof that it cannot exist with reverse flow, and an easy calculation method. Then some blowing pressure thresholds (stability, existence, ...) are calculated with respect to the parameters of interest (loss, reed opening).

In Section 5 the thresholds related to the instability of the regimes are calculated. Then by making two thresholds equal, the mouth pressure can be eliminated and limits of existence and stability of the static and two-state regimes are found in Section 6: this allows drawing the diagram sought. Finally a discussion is proposed concerning the existence of oscillating regimes (Section 7), with an attempt to consider more realistic models and a discussion about musical consequences.

2. The model and its parameters

We briefly remind the basic elements of the model, the non-linear characteristic of the exciter, and the origin of the iteration method, thanks to a simplified treatment of the resonator.

2.1. Nonlinear characteristics of the entering flow

In a quasi static regime, the flow U entering the resonant cavity is modeled with the help of an approximation of the Bernoulli equation, as discussed e.g. in [19]. Comparison with experiment can be found in [20]. We note P_{int} the acoustic pressure inside the mouthpiece, assumed to be equal to the one at the output of the reed channel, P_m the pressure inside the mouth of the player. For small values of the difference,

$$\Delta P = P_m - P_{int}, \tag{1}$$

the reed remains close to its equilibrium position, and the flow U is proportional to $\mathrm{sign}(\Delta P)\sqrt{|\Delta P|}$; for larger values of this difference, the reed moves and, when the difference reaches the closure pressure P_c, it completely blocks the flow (the reed is beating). These two effects are included by assuming that if $\Delta P \leq P_c$ the flow U is proportional to $sign(\Delta P)\sqrt{|\Delta P|}\,[P_c - \Delta P]$, and if $\Delta P > P_c$, the flow vanishes. Introducing the dimensionless quantities

$$\begin{aligned} p &= P_{int}/P_c, \quad u = U Z_c/P_c \\ \gamma &= P_m/P_c, \quad \gamma_c = P_c/P_c = 1, \end{aligned} \tag{2}$$

where $Z_c = \rho c/S$ is the characteristic acoustic impedance of the cylindrical resonator, having the cross section S (ρ is the density of air, c the velocity of sound), we obtain

$$u = \zeta f(\Delta p), \tag{3}$$

with

$$\Delta p = \Delta P/P_c = \gamma - p, \tag{4}$$

$$f(\Delta p) = 0 \quad \text{if} \quad \Delta p > 1, \tag{5}$$

$$f(\Delta p) = \mathrm{sign}\big(\Delta p\big)\,(1-\Delta p)\sqrt{|\Delta p|} \text{ if } \Delta p < 1. \tag{6}$$

The parameter ζ characterizes the intensity of the flow and is defined as

$$\zeta = \frac{cS_{op}}{S}\sqrt{\frac{2\rho}{P_c}}, \tag{7}$$

where S_{op} is the opening cross section of the reed channel at rest. ζ is inversely proportional to square root of the reed stiffness, contained in P_c. In real clarinet-like instruments, typical values of the parameters are $\gamma \in [0, 1.5]$; $\zeta \in [0.1, 0.5]$; values $\zeta > 1$ will not be considered here, since they correspond to multi-valued functions to be solved (see [11]), and this case does not seem very realistic in practice for clarinet-like instruments. The function $f(\Delta p)$ is obviously non-analytic; it is made of three separate analytic pieces, with a singular point at $\Delta p = 0$, and its derivative is discontinuous at $\Delta p = 1$.

2.2. Resonator model

The resonator of length ℓ is assumed to be cylindrical, with zero terminal impedance. Using the d'Alembert decomposition, a change in variables at the entry of the resonator can be chosen as

$$p(t) = p^+(t) + p^-(t), \quad u(t) = p^+(t) - p^-(t), \tag{8}$$

with the following relationship between incoming wave $p^-(t)$ and outcoming wave $p^+(t)$:

$$p^-(t) = -\lambda p^+(t - 2\ell/c), \tag{9}$$

where λ is the loss parameter, assumed to be independent of frequency. This is a strong assumption, necessary to obtain square signals: for certain initial conditions, all quantities remain constant in the time interval $2n\ell/c < t < 2(n+1)\ell/c$. The approximation is rough for certain characteristics of the signal, such as the spectrum, but it is useful for the study of the existence, stability and amplitude

of the produced sound. With this assumption, the resonator is characterized by a unique (recurrence) relation,

$$p_n^- = -\lambda p_{n-1}^+, \tag{10}$$

where $2\ell/c$ is the time unit. As discussed further in Section 4.2.5, losses can occur either at the extremity (radiation) or during propagation (e.g. in the boundary layers): in the latter case, if α is the attenuation constant per unit length, $\lambda = \exp(-2\alpha\ell)$, and the dimensionless input impedance at zero frequency is

$$\mu \stackrel{\text{def}}{=} \tanh(\alpha\ell) = \frac{1-\lambda}{1+\lambda}, \quad \text{or } \lambda = \frac{1-\mu}{1+\mu}, \tag{11}$$

while the input impedance at the operating frequency is $1/\mu$. In what follows, the losses are characterized by the parameter μ, varying between 0 (no losses) and 1 (very strong losses, no wave reflection). This parameter, the reed opening ζ and the mouth pressure γ are the three parameters of the problem. Several combination parameters will be useful,

$$\beta \stackrel{\text{def}}{=} \zeta\mu, \quad \beta_1 \stackrel{\text{def}}{=} \zeta^{-1}\mu \quad \text{or } \zeta^2 = \beta/\beta_1, \quad \mu^2 = \beta\beta_1. \tag{12}$$

β is proportional to the input impedance at zero frequency, while β_1 is proportional to the input admittance at the operating frequency. Two pairs of parameters can be used: either (ζ, μ) or (β, β_1). Notice that because ζ and μ are smaller than unity, $\beta < 1$ and $\beta < \beta_1$, and $\beta\beta_1 = \mu^2 < 1$. Other parameters will be useful[1],

$$\beta_2 \stackrel{\text{def}}{=} \frac{2\beta_1}{1+\beta\beta_1} = \frac{\tanh 2\alpha\ell}{\zeta}, \quad \beta_3 \stackrel{\text{def}}{=} \frac{1}{2\beta} - \frac{3\beta_1}{2}. \tag{13}$$

3. Equations for transients and limit cycles

3.1. Recurrence for the pressure difference

Using Equations (3), (8) and (11), the recurrence relation (10) can be rewritten with respect to the quantities $\Delta p_n \stackrel{\text{def}}{=} \gamma - p_n$ and u_n. The result is

$$2\gamma = (1+\mu)(\Delta p_n + u_n) + (1-\mu)(\Delta p_{n-1} - u_{n-1}). \tag{14}$$

Because the flow rate $u = \zeta f(\Delta p)$ is a function of the pressure difference Δp, this relation is a recurrence for the quantity Δp, equivalent to the recurrence used in [11] for the quantity p^+,

$$\Delta p_n = H^{-1}\left[K(\Delta p_{n-1})\right], \tag{15}$$

with $H(x) = x + \zeta f(x)$,

$$K(x) = \gamma(1+\lambda) - \lambda\big(x - \zeta f(x)\big). \tag{16}$$

The inverse of function H can be found in [11] (see Appendix).

[1] In [4], the parameters γ and ζ are with dimension, except in the appendix, and are denoted p_m and u_A, respectively. β, β_1 and β_2 are defined in the same way as in the present paper.

3.2. Basic equations for the static regime

Equation (14) is interesting in particular for the calculation of the limit cycles. For the static regime, Δp is a constant, then

$$\gamma = \Delta p + \beta f(\Delta p) \stackrel{\text{def}}{=} h(\Delta p). \tag{17}$$

It is possible to calculate Δp from the value of γ, or vice-versa. Concerning the stability, if the iteration function is denoted $g(x) = H^{-1}[K(x)]$, the classical stability condition is $|g'(\Delta p)| < 1$. Because $K(x) = H[g(x)]$, $\mathrm{d}K/\mathrm{d}x = (\mathrm{d}H/\mathrm{d}g)(\mathrm{d}g/\mathrm{d}x)$, and the condition can be written as[2]

$$\left[\lambda\frac{1-\zeta f'(\Delta p)}{1+\zeta f'(\Delta p)}\right]^2 < 1 \tag{18}$$

$$\text{or} \quad \left[f'(\Delta p) + \beta_1\right]\left[1+\beta f'(\Delta p)\right] > 0 \tag{19}$$

(see Equation 12).

3.3. Basic equations for the two-state regime

For the two-state regime, because $\Delta p_{n+1} = \Delta p_{n-1}$, the following expression is found by eliminating γ from Equation (14) written for the pairs $(n+1, n)$ and $(n, n-1)$

$$h_1(\Delta p_n) = h_1(\Delta p_{n-1}) \tag{20}$$

$$\text{with} \quad h_1(X) \stackrel{\text{def}}{=} \beta_1 X + f(X). \tag{21}$$

An important property of the two-state regime is the square shape of the signal, which can be decomposed into the sum of a mean value p_{mean} (zero frequency component) and an acoustic component p_{ac} (sum of the odd harmonics of the operating frequency), with zero mean value

$$p_n = p_{mean} + p_{ac} \text{ with } p_{mean} = \frac{1}{2}(p_n + p_{n-1})$$

$$\text{and} \quad p_{ac,n} = \frac{1}{2}(p_n - p_{n-1}). \tag{22}$$

Notice that $p_{ac,n} = -p_{ac,n-1}$, and that a similar equation can be written for the flow rate. Equation (20) generalizes the result obtained when losses are ignored ($\mu = 0$), i.e. the constant flow rate, and it is nothing else than the input impedance relation for the acoustic component

$$\mu(p_n - p_{n-1}) = u_n - u_{n-1}. \tag{23}$$

It is possible to calculate the values of the two states without knowledge of γ, starting e.g. with the value of Δp_n: $\Delta p_{n\pm1}$ and γ are successively deduced from Equations (20) and Equation (14). Adding the two equations (14) for the pairs $(n+1, n)$ and $(n, n-1)$, it is obtained

$$\gamma_{ij} = \frac{1}{2}\left[h(\Delta p_i) + h(\Delta p_j)\right], \tag{24}$$

$$\text{or} \quad \gamma_{ij} = \frac{1}{2}(\Delta p_i + \Delta p_j)(1-\beta\beta_1) + \beta h_1, \tag{25}$$

[2] Notice that $|A/B|^2 < 1$ is equivalent to $(A-B)(A+B) < 0$.

with $h_1 = h_1(\Delta p_i) = h_1(\Delta p_j)$ and $i = n$, and $j = n \pm 1$. Similarly for regimes with more than two states, it could be possible to start the calculation from a given state, and to deduce the other states, the prior knowledge of γ being unnecessary. Equation (24) is the input impedance relation for the mean value component: $p_n + p_{n-1} = \mu(u_n + u_{n-1})$.

For the two-state regime, the stability condition is $|g'(\Delta p_i)g'(\Delta p_j)| < 1$, and after some algebra, the result of [4] is found (see Equation 13),

$$C < \beta_2 \text{ or } C > \frac{1}{\zeta^2 \beta_2}, \tag{26}$$

$$\text{with} \quad C = -\frac{f'(\Delta p_i) + f'(\Delta p_j)}{1 + \zeta^2 f'(\Delta p_i) f'(\Delta p_j)}. \tag{27}$$

4. Existence of the static and two-state regimes

The previous results can be applied whatever the shape of the function $f(\Delta p)$. The present section investigates the existence of the static and two-state regimes for the particular shape of the function given by Equations (5) and (6).

4.1. Static regime

For negative Δp, the function $f(\Delta p)$ is negative too, therefore the static regime does not exist for negative flow (and positive excitation pressure γ). For $\Delta p > 1$, the static regime exists for $\gamma = \Delta p > \gamma_c = 1$. The pressure $p = \gamma - \Delta p$ vanishes: this is obvious because the reed closes the input of the resonator.

Otherwise, for a non-beating reed, the study of the function in the right-hand side of Equation (17) shows that it increases from 0 to 1 when Δp increases from 0 to 1. Therefore a unique solution[3] exists for $0 < \gamma < 1$.

4.2. Two-state regime

4.2.1. Number of solutions

For the two-state regime, two values of Δp, with the same value of the function $h_1(X)$ are sought. They do not depend on the impedance at zero frequency, i.e. on the value of β. The study of $h_1(X)$ leads to the following results (see Figure 1): for negative X, the derivative $h_1'(X)$ is always positive, while for positive X, it is positive up to $X = \Delta_M$, where $\sqrt{X}$ is the positive root of the equation

$$3X - 2\beta_1\sqrt{X} - 1 = 0, \quad \text{i.e.} \tag{28}$$

$$X = \Delta_M \quad \text{with} \quad \Delta_M = \frac{1}{9}\left[\beta_1 + \sqrt{\beta_1^2 + 3}\right]^2. \tag{29}$$

[3] The expression for the static pressure in the mouthpiece is

$$p_s = \gamma - \frac{1}{9}\left[\frac{1}{\beta} + 2\sqrt{3 + \frac{1}{\beta^2}}\,\sin\left[\frac{1}{3}\arcsin(\kappa)\right]\right]^2$$

$$\text{with} \quad \kappa = \left[-2 + 9(-1+3\gamma)\beta^2\right] / \left[2(1+3\beta^2)^{3/2}\right].$$

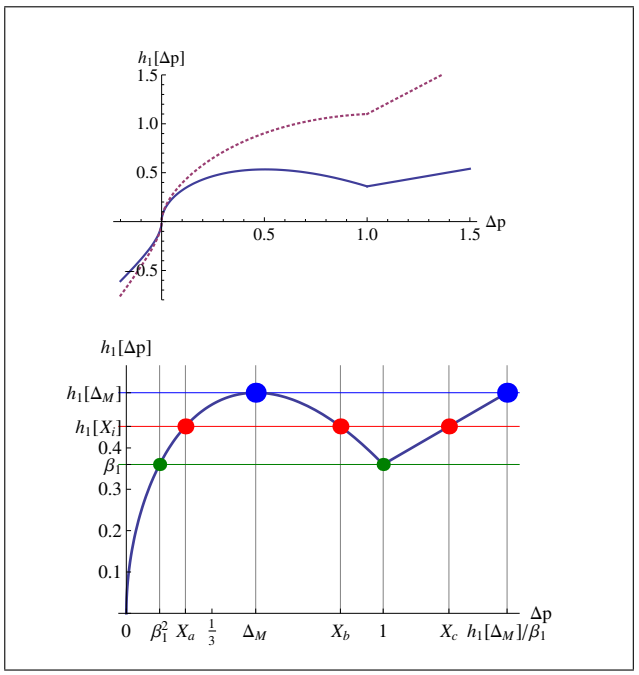

Figure 1. Top: Function $h_1(\Delta p)$ for two values of β_1. Dotted line: $\beta_1 = 1.1$ (monotonous variation). Solid line: $\beta_1 = 0.36$. Bottom: Zoom for the second case. A maximum value exists at $P_M = (\Delta_M, h(\Delta_M))$. The middle horizontal line corresponds to $h_1(X) = 0.452$, with the 3 solutions X_a, X_b, X_c.The two other horizontal lines exhibit the limits of existence of the two-state regime.

For $X > 1$ (beating reed), the value of the derivative is β_1, and is positive. Two cases need to be distinguished: if $\Delta_M > 1$, i.e. if $\beta_1 > 1$, the derivative is always positive and it is impossible to find two values of X with the same value $h_1(X)$. On the contrary, for

$$\beta_1 < 1, \tag{30}$$

the function decreases from $h_1(\Delta_M)$ to β_1 when X increases from Δ_M to 1, then re-increases. Solutions of Equation (20) can be found in this case only, and the corresponding value of the function is necessarily larger than β_1. A consequence is that Equation (20) has no solution for $h_1(X) < \beta_1$, and this is true in particular for negative $h_1(X)$. Therefore no two-state regime can be found with negative flow. This conclusion is compatible with the general result obtained for all possible regimes in [11]. Because of this result, the paper is now focused on positive pressure differences Δp.

For $h_1(X) \in [\beta_1, h_1(\Delta_M)]$, three values of X, defined as $X_a < X_b < X_c$ lead to the same value of the function (see Figure 1), and three two-state regimes are possible, which can be either non-beating (for the pair $[X_a, X_b]$) or beating (for the pairs $[X_a, X_c]$ and $[X_b, X_c]$). The intervals of the three solutions are as follows: $X_a \in \left[\beta_1^2, \Delta_M\right]$; $X_b \in [\Delta_M, 1]$; $X_c \geq 1$.

From the solution of Equation (20), the corresponding excitation pressure γ for the two-state regime is given by Equation (24), for the three pairs of solutions $(\Delta p_i, \Delta p_j) = (X_i, X_j)$. For the particular case of the

beating-reed regime, when $h_1 = \beta_1 \Delta p_c$, and $i = a, b$, the expression can be also written as

$$\gamma_{ic} = \frac{1}{2}\left[h(\Delta p_i) + \frac{h_1(\Delta p_i)}{\beta_1}\right] \quad (31)$$

$$= \Delta p_i + \frac{f(\Delta p_i)}{\beta_2} \stackrel{\text{def}}{=} h_2(\Delta p_i). \quad (32)$$

4.2.2. Existence, beating, saturation and extinction thresholds

- At the limit of existence, when $h_1'(\Delta p)$ vanishes,

$$\Delta p_a = \Delta p_b = \Delta_M. \quad (33)$$

Therefore the existence threshold γ_{th} of the two-state regime is

$$\gamma_{th} = \Delta_M + \beta f(\Delta_M) = h(\Delta_M). \quad (34)$$

The solutions can be either stable or unstable, i.e. the bifurcation can be direct or inverse. This is discussed hereafter in Section 5.2.2.

- Another limit of existence is given by $X_b = 1$. Using Equation (31), this yields: $\gamma = \gamma_c = 1$. The solutions can be either stable or unstable, i.e. the bifurcation can be direct or inverse. This is discussed hereafter in Section 5.2.1.
- The beating threshold γ_b appears when one solution is $X = 1$, $h_1(X) = \beta_1$, thus the pair of solution is: $X_a = \beta_1^2$, $X_b = 1$; therefore, using Equation (31),

$$\gamma_b = h_2(\beta_1^2). \quad (35)$$

Because $\beta_1^2 < 1$, and $0 < \beta < \beta_1$, the threshold γ_b can be shown to be always smaller than the closure threshold $\gamma_c = 1$.

- The saturation threshold is obtained for the beating regime, with $dp_a/d\gamma = 0$, with $p_a = \gamma - X_a$, i.e. $dX_a/d\gamma = 1$, therefore $X_a = 1/3$, $\gamma_{sat} = h_2(1/3)$, and

$$p_a = \frac{2}{3\sqrt{3}\beta_2}, \qquad u = f\left(\frac{1}{3}\right) = \frac{2\zeta}{3\sqrt{3}} = u_{\max}. \quad (36)$$

At the saturation value, the flow rate is maximum: $u = u_{\max}$. For $\beta_1 > 1/\sqrt{3}$, the saturation threshold is the beating threshold, because for $\beta_1^2 = 1/3$, $\gamma_{sat} = \gamma_b$: the amplitude of the pressure decreases from the beating threshold.

- Finally the overcritical (extinction) threshold γ_e is given by $d\gamma/d\Delta p_i = 0$ in Equation (31). This condition yields to the result

$$3\Delta p_a - 2\beta_2\sqrt{\Delta p_a} - 1 = 0, \quad (37)$$

$$\text{or} \quad \Delta p_a = \frac{1}{9}\left[\beta_2 + \sqrt{\beta_2^2 + 3}\right]^2 = \Delta p_e \quad (38)$$

$$\text{and} \quad \gamma_e \stackrel{\text{def}}{=} h_2(\Delta p_e). \quad (39)$$

Because $\Delta p_e < 1$, it exists if $\beta_2 < 1$ only. As explained in [4], when losses tend to 0 (β_2 tends to 0), the extinction threshold tends to infinity. The threshold γ_e is always larger than $\gamma_c = 1$, because $\sqrt{\Delta p_e} - \beta_2 = (1 - \Delta p_e)/(2\sqrt{\Delta p_e})$, thus

$$\gamma_e - \gamma_c = \frac{1}{\beta_2}\frac{(1 - \Delta p_e)^2}{2\sqrt{\Delta p_e}} \geq 0. \quad (40)$$

4.2.3. Subcritical threshold at emergence (non-beating reed)

Results (34) to (38) were obtained with other, equivalent methods in [4]. However another threshold can exist for the non-beating case ($i = a$, $j = b$): for certain values of the parameters, the emergence bifurcation can be inverse, and the threshold of oscillation is different for crescendo and decrescendo playing. The subcritical threshold γ_{sc} can be calculated by using the change in variables defined in [4]

$$\Sigma \stackrel{\text{def}}{=} \sqrt{X_a} + \sqrt{X_b}, \quad \Pi \stackrel{\text{def}}{=} \sqrt{X_a}\sqrt{X_b}. \quad (41)$$

Equation (20) implies

$$\Pi = \Sigma^2 - \beta_1\Sigma - 1 \quad (42)$$

(this change in variables is related to the decomposition into dc and acoustic components, see Equation 22). The threshold can be calculated by writing $d\gamma/d\Sigma = 0$ in Equation (24), which can be written as a polynomial in Σ (see Equation (A17) in [4]) [4] For our purpose, it is convenient to write this equation as follows (denoting $\gamma = \gamma_{ab}$)

$$\gamma = \beta(\varphi - \beta_3)(\varphi^2 - 1) + \gamma_b \quad \text{with} \quad \varphi \stackrel{\text{def}}{=} \Sigma - \beta_1, \quad (43)$$

where β_3 is given by Equation (13). Notice that for the beating threshold $\varphi_b = 1$. The derivative $d\gamma/d\varphi$ vanishes for $\varphi = \varphi_{sc}$

$$3\varphi_{sc}^2 - 2\beta_3\varphi_{sc} - 1 = 0 \quad (44)$$

$$\text{or} \quad 2\varphi_{sc}(\varphi_{sc} - \beta_3) = 1 - \varphi_{sc}^2 \quad (45)$$

$$\text{or} \quad \varphi_{sc} = \frac{1}{3}\left[\beta_3 + \sqrt{\beta_3^2 + 3}\right]. \quad (46)$$

Therefore, φ_{sc} is always positive, and combining Equations (43) and (45), it is shown that the threshold γ_{sc} is always smaller than the beating-reed threshold

$$\gamma_{sc} = \gamma_b - \frac{\beta}{2\varphi_{sc}}(1 - \varphi_{sc}^2)^2. \quad (47)$$

[4] The equation is

$$\gamma = \beta\Sigma^3 - (1 + 3\beta\beta_1)\Sigma^2/2 + (\beta_1 - \beta)\Sigma + 1.$$

The two solutions for φ are (see Equation 13):

$$\varphi_n = \frac{1}{3}\left(\beta_3 + 2\delta\cos\left[\frac{1}{3}\left(\arccos(\Phi) + 2n\pi\right)\right]\right)$$

$$\text{where} \quad \Phi = \frac{2\beta\beta_3\left(\delta^2 - 12\right) + 27\left(\gamma - \gamma_b\right)}{2\beta\delta^3}$$

$$\text{and} \quad \delta = \sqrt{3 + \beta_3^2}, \quad n = 0 \text{ or } 2.$$

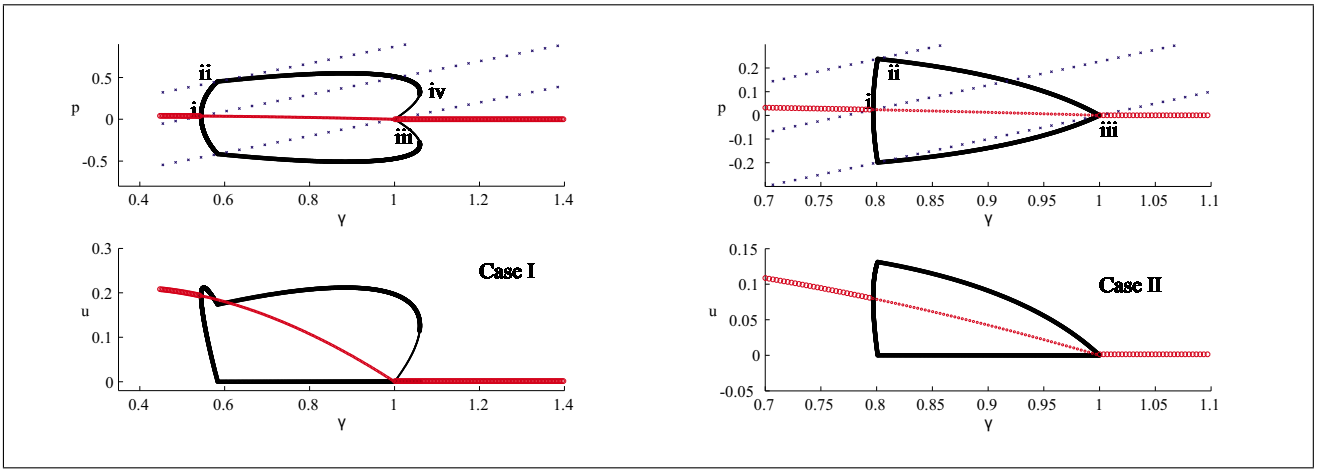

Figure 2. Two examples of bifurcation schemes for the pressure (γ, p) and the flow rate (γ, u). The emergence bifurcation is direct. The three dotted (blue in the online version), increasing straight lines indicate the three domains of solutions X_a, X_b, and X_c. **Case I, left**: $\zeta = 0.55$, $\mu = 0.2$. The solid curve corresponds to a two-state regime, which is stable (thick line) or unstable (thin line): the emergence bifurcation is direct, while the extinction bifurcation is inverse. The pale (red in the online version), decreasing line corresponds to the static regime, which is stable (thick line) or unstable (thin line). The point i indicates the instability threshold γ_{th} of the static regime; the point ii the beating threshold γ_b of the two-state regime; the point iii is the closure threshold $\gamma_c = 1$, the point iv is the extinction threshold γ_e of the two-state regime. **Case II, right**: $\zeta = 0.4$, $\mu = 0.3$. Both emergence i and extinction bifurcations iii are direct. The point ii indicates the beating threshold γ_b of the two-state regime. Because $\beta_1 = .75 > 1/\sqrt{3}$, saturation occurs at the beating threshold γ_b.

4.2.4. Solutions

The direct solution of the cubic equation (43) is possible (see footnote 4). In the present paper we propose a method based upon Equations (20) and (25). Starting from a value of $X_a \in \left[\beta_1^2, \Delta_M\right]$, the solution X_c (above unity) is obtained by $X_c = h(X_a)/\beta_1$, and the solution X_b is deduced by solving the equation $h_1(X_b) = h_1(X_a)$ for $X_b \in [\Delta_M, 1]$. The latter equation is cubic in $\sqrt{X_b}$. It has a solution already known, $\sqrt{X_a}$, therefore $\sqrt{X_b}$ can be deduced as the positive solution of a quadratic equation[5], as

$$x^2 - (\beta_1 - \sqrt{X_a})x - \frac{h_1(X_a)}{\sqrt{X_a}} = 0, \quad \text{where} \quad x = \sqrt{X_b}.$$

$$X_b = \frac{1}{4}\left[\beta_1 - \sqrt{X_a} + \sqrt{(\beta_1 + \sqrt{X_a})^2 + \frac{4f(X_a)}{\sqrt{X_a}}}\right]^2. \quad (48)$$

From the knowledge of the three solutions of $h_1(X) = h_1(X_a)$, the three values of γ_{ij} are deduced from Equation (25). Figures 2 and 3 show 4 examples of bifurcation schemes for different cases. The calculation is done by varying the starting value X_a and was verified using the iterated map algorithm ([11]), which obviously gives stable solutions only. The three straight lines $p = \gamma - \beta_1^2$, $p = \gamma - \Delta_M$, and $p = \gamma - 1$ delimit the three domains of solutions, X_a, X_b and X_c. The solution is non-beating for the pair $[X_a, X_b]$) or beating, for the pairs $[X_a, X_c]$ and $[X_b, X_c]$), see Figure 1.

[5] According to Vieta's formula, the sum of the three solutions is β_1, their product is $-h$. Notice that the third solution differs from $\sqrt{X_c}$, because X_c corresponds to a beating reed.

Figure 4 shows the diagram $(\Delta p, \gamma)$ for the case I of Figure 2. This allows exhibiting the function $h(\Delta p)$, given by Equation (17), for the static regime and the function $h_2(\Delta p)$, given by Equation (31), for the beating, two-state regime. The one-state regime is stable from $\{0, 0\}$ to $\{\Delta_M, \gamma_{th}\}$ and above $\{1, 1\}$. The non-beating two-state is given by Equations (24) and (48), the beating two-state is given for $X_a < 1$ by the function $h_2(X)$. The bifurcation at emergence is direct, the oscillation is stable from $\{\Delta_M, \gamma_{th}\}$ to $\{\beta_1^2, \gamma_b\}$. The beating two-state is stable from $\{\beta_1^2, \gamma_b\}$ to $\{\Delta p_e, \gamma_e\}$ and unstable between $\{\Delta p_e, \gamma_e\}$ and $\{1, 1\}$. The oscillation amplitude is at a maximum at $\{1/3, \gamma_s\}$, where the slope of $h_2(X)$ is unity.

4.2.5. Radiated sound

The radiation losses are small at low frequencies, therefore it is very simple and classical to deduce them by perturbation from the output flow rate, considering a monopole radiation. Two cases have to be distinguished: losses occur at the output, or losses occur during propagation into the tube. Both cases give the same input impedance, but not the same transfer functions between input and output. The latter case is more realistic, and is considered here. If the output impedance is 0, and losses due to boundary layers only, the output acoustic flow rate is given by the standard transmission lines relationships: $u_{out} = \sinh(j\omega\ell/c + \alpha\ell)p_{ac}$, where $\omega\ell/c = \pi/2$ (see Section 3.2). Therefore the amplitude relationship is

$$|u_{out}| = |p_{ac}| \,/\, \cosh(\alpha\ell)$$
$$= |p_{ac}|\sqrt{1-\mu^2} = |u_{ac}|\frac{\sqrt{1-\mu^2}}{\mu}.$$

The maximum output acoustic flow rate is obtained for the saturation threshold; at the saturation threshold, because

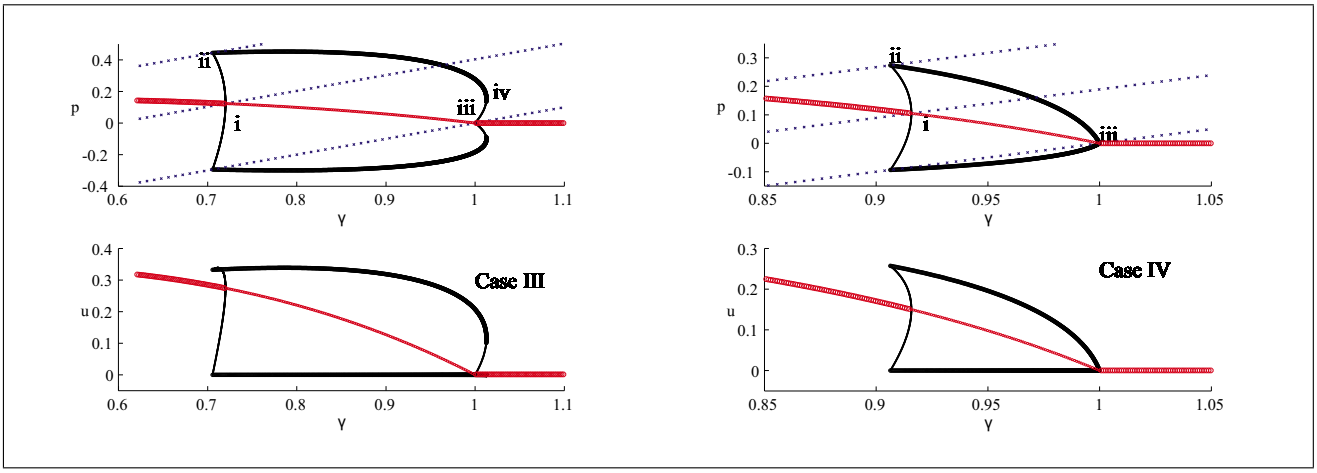

Figure 3. Two examples of bifurcation schemes for the pressure (γ, p) and the flow rate (γ, u). The emergence bifurcation is inverse. The three dotted (blue in the online version), increasing straight lines indicate the three domains of solutions X_a, X_b, and X_c. **Case III, left**: $\zeta = 0.88$, $\mu = 0.45$. Both emergence and extinction bifurcations are inverse. The point *iv* indicates the overcritical (extinction) threshold γ_e of the two-state regime, and the point *iii* the closure threshold $\gamma_c = 1$ of the static regime. **Case IV, right**: $\zeta = 0.88$, $\mu = 0.7$. The extinction bifurcation is direct.

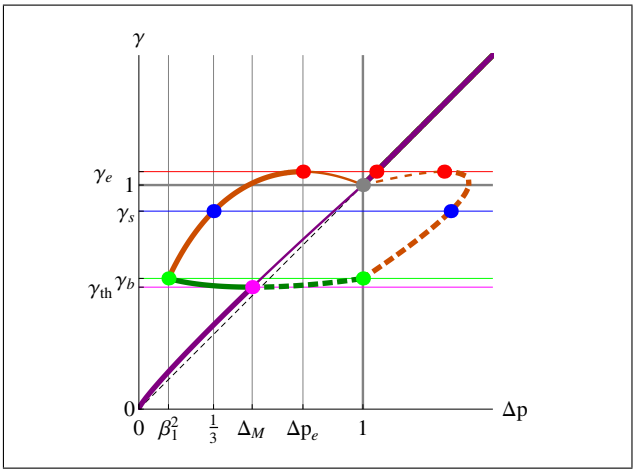

Figure 4. Representation for $(\Delta p, \gamma)$. The function $h(\Delta p)$ is used for the static regime (black curve, purple in the online version) and the function $h_2(\Delta p)$ for the beating, two-state regime (grey curve, brown in the online version). The non-beating two-state (light grey, green in the online version) is given by Equations (24) and (48). Thick lines: stable regime, thin lines: unstable regime. Dashed lines: solution of the 2-state regime with the high value of Δp. The points signal the transitions at the different thresholds.

the reed is beating, $|u_{ac}| = (u_{\max} + 0)/2 = \zeta/(3\sqrt{3})$,(see Equation 36). For $\beta_1 = \mu/\zeta < 1/\sqrt{3}$, the saturation threshold is the beating threshold (see Section 4.2.2), and $p_{ac} = (1 - \beta_1^2)/2$, therefore

$$|u_{out}|_{\max} = \frac{\sqrt{1-\mu^2}}{3\sqrt{3}\beta_1} \quad \text{if} \quad \beta_1 > \frac{1}{\sqrt{3}}; \tag{49}$$
$$|u_{out}|_{\max} = \frac{1}{2}(1-\beta_1^2)\sqrt{1-\mu^2} \quad \text{if} \quad \beta_1 < \frac{1}{\sqrt{3}}.$$

For a given value of ζ, this is monotonously decreasing function of μ; for a given value of μ, this is an increasing function of ζ.

5. Calculation of instability thresholds

The stability conditions (18) and (26) are calculated using the expression of the derivative $f'(\Delta p)$

$$f'(\Delta p) = \frac{1 - 3\Delta p}{2\sqrt{\Delta p}} \quad \text{if} \quad \Delta p < 1,$$
$$f'(\Delta p) = 0 \quad \text{if} \quad \Delta p > 1. \tag{50}$$

5.1. Instability of the static regime

The condition (18) generalizes the condition $f'(\Delta p) > 0$, as discussed in [21] for the lossless case (see page 349). For the (static) beating reed case, which exists for $\gamma > \gamma_c = 1$ (see previous section), $f'(\Delta p) = 0$, thus the static regime is always stable. For the non-beating reed case, the first factor of Inequality (18) is equal to $h_1'(\Delta p)$, thus it vanishes when Δp satisfies Equation (28), i.e. $\Delta p = \Delta_M$. For this value, Δ_M, the second factor of Inequality (18) is $(1 - \beta\beta_1)$, which is positive[6]. Thus (29) together with Equations (17) gives the threshold γ_{th}, given by Equation (34).

Therefore the condition $h_1'(\Delta p) = 0$ gives both the limit of existence of the two-state regime (see Equation 34), and the instability threshold of the static regime. Nevertheless the nature (direct or inverse) of the bifurcation between the two regimes is not yet solved by this result[7]. The term $\beta f(\Delta_M)$ is the static pressure p_s in the mouthpiece; the presence of the parameter β indicates that the threshold depends on the impedance at zero frequency.

[6] Another threshold can be sought when the denominator of Equation (18) vanishes: this leads to the solution of either $1 = 0$ when $\Delta p > 1$, or $f'(\Delta p) = -1/\beta$, with $0 < \Delta p < 1$. These two equations have no solution.

[7] In [4], β was assumed to be very small in practice, and Equation (34) was simplified in $\gamma_{th} = \Delta_M$, but the complete equation (34) was given for the threshold of existence for the two-state regime.

5.2. Instability of the two-state regime

5.2.1. Beating-reed case: overcritical (extinction) threshold

For the beating regime $f'(X_c) = 0$, with $X_i < 1$, thus, using Condition (26), $C = -f'(X_i)$ for $i = a$ or b. Because $C < 1$, and because $\zeta^2\beta_2 = \zeta \tanh 2\alpha\ell < 1$, the second inequality (26) is never valid. Therefore the stability is defined by the condition $C < \beta_2$.

When $\beta_2 > 1$, this condition is always satisfied, and the beating two-state regime is stable (no overcritical threshold γ_e exists, as noticed in Section 4.2.2).

When $\beta_2 < 1$, Equation (37) is used, yielding $\beta_2 = (3\Delta p_e - 1)/(2\sqrt{\Delta p_e})$. The function $(3x-1)/(2\sqrt{x})$ being always increasing for positive x, the inequality $C < \beta_2$ holds if $X_i < \Delta p_e$, or $p_i > p_e = \gamma - \Delta p_e$. This distinguishes in the (γ, p) plane the two branches separated by the overcritical threshold: the upper one is stable, while the lower one is unstable[8]. The unstable branch is the branch joining the static regime, because the two regimes cannot be stable for the same value of the parameter γ when they converge to the same point. This can be explained with mathematical arguments, based upon either a perturbation method (see [15]) or the topological degree (see [16]). This can be also studied by using Inequalities (26), as done in [4].

It can be noticed that because γ_e is larger than unity, the beating, two-state regime is always stable for $\gamma_b < \gamma < \gamma_c = 1$, whatever the value of β_2.

5.2.2. Non-beating case: period doubling and subcritical (emergence) threshold

i) For the non-beating regime ($i = a$, $j = b$), an expression of the instability threshold was given in [4] and it was explained that the threshold is given by $1/C = \zeta^2\beta_2$. Some errors were done in the derivation, and they are corrected in appendix A of the present paper. When the excitation pressure is larger than this threshold, here denoted γ_{ins}, period doubling can occur, then a complex bifurcation scenario (see [11]).

ii) Otherwise, it can be checked that the second condition $C = \beta_2$ leads to the subcritical emergence threshold γ_{sc}: it separates two branches in the (γ, p) plane, the upper one being stable while the lower one is unstable. This is similar to what happens for the overcritical threshold. When it exists, the emergence bifurcation is as follows: when playing crescendo, the oscillation starts for $\gamma = \gamma_{th}$, while playing decrescendo, the oscillation stops for $\gamma = \gamma_{sc}$.

When this subcritical threshold can exist? From Equations (43) and (44), it is found that

$$\gamma_{th} - \gamma_{sc} = \beta(\varphi_{th} - \varphi_{sc})^2 \left[\frac{1}{2\varphi_{sc}} + \frac{\varphi_{sc}}{2} + \varphi_{th}\right], \qquad (51)$$

[8] It is possible to show that the interesting solution in this discussion is $X_i = X_b$: because $\beta_2 > \beta_1$, the solution Δp_e at the overcritical threshold is larger than Δ_M, thus it is always larger than X_a. Instability occurs for the pair (X_b, X_c).

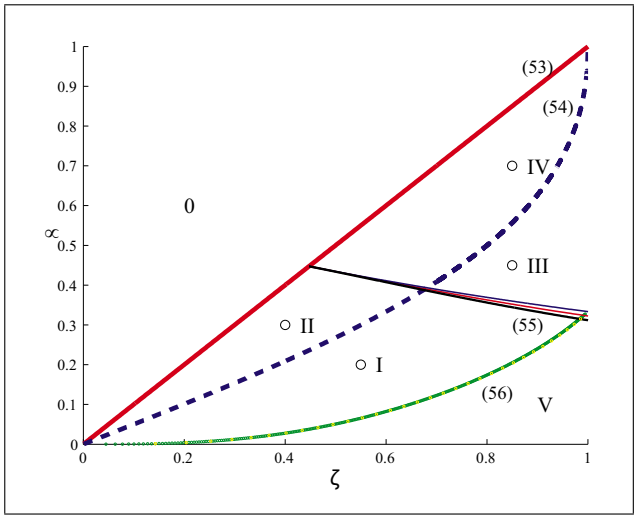

Figure 5. Plane (ζ, μ). The four Regions I to IV correspond to the different cases presented for the examples shown in Figs. 2 and 3. The chosen values for the examples are indicated by a circle. In Region V period doubling or other regimes can exist, in Region 0 no sound is possible. The numbers refer to the equation number. Above line (53), no sound is possible. Curve (54) distinguishes the extinction bifurcation (direct above, inverse below). Curve (55) distinguishes the emergence bifurcation (direct above, inverse below). Below curve (56), complicated regimes can appear by destabilization of the two-state regime. The two curves close to the curve (55) correspond to Equations (59), and (60), from to the top to the bottom (see Section 6.3).

where $\varphi_{th} = \Sigma_{th} - \beta_1$ and $\varphi_{th} - \varphi_{sc} = \Sigma_{th} - \Sigma_{sc}$, with

$$\Sigma_{th} = 2\sqrt{\Delta_M} = \frac{2}{3}\left(\beta_1 + \sqrt{\beta_1^2 + 3}\right). \qquad (52)$$

Two cases are possible:

- $\Sigma_{sc} > \Sigma_{th}$: the emergence bifurcation is direct: stable solutions exist for $\gamma > \gamma_{th}$.
- $\Sigma_{sc} < \Sigma_{th}$: the emergence bifurcation is inverse, and stable solutions exist for $\gamma > \gamma_{sc}$.

When Σ_{sc} continues to decrease below Σ_{th}, the bifurcation remains inverse, but the subcritical threshold γ_{sc} becomes the beating threshold γ_b. This happens when $\Sigma_{sc} = \Sigma_b = 1 + \beta_1$, or $\varphi_{sc} = \varphi_b = 1$ (notice that the inequality $\Sigma_b \leq \Sigma_{th}$ always holds). The discussion is extended in Section 6.3.

6. Limits of regimes in the plane (μ, ζ)

From the different expressions of the thresholds, it is possible to deduce the limits separating different domains in the plane (μ, ζ), as shown in Figure 5. Above the diagonal (region 0), no two-state regime can exist. Other regions of the plane are defined by the nature of the emergence and extinction bifurcations: they are named by the number of the four cases shown in Figures 2 and 3: in Regions I and III, the extinction bifurcation is inverse, while in Regions II and IV, it is direct. What is new in this paper is the separation between Regions I and II, with direct emergence bifurcation, and regions III and IV, with

inverse emergence bifurcation. Finally, in Region V, the two-state regime can be unstable, and can be replaced by more complicated regimes, with period doubling, chaos, intermittences, etc... (see [11]).

6.1. Emergence and extinction bifurcations

- When the instability threshold γ_{th} (Equation 34) of the static regime reaches the closing threshold $\gamma_c = 1$, the static regime becomes stable whatever the values of all parameters, and no sound can be expected. This happens[9] for $\beta_1 > 1$, and this confirms the result explained in Section 4.2.1 that no two-state regime can exist (this discussion is extended in the next section). The condition for the existence of sound can be also written as

$$\mu < \zeta \quad \text{or} \quad \lambda > \frac{1-\zeta}{1+\zeta}. \tag{53}$$

- When the overcritical threshold γ_e (Equation 38) reaches the closure threshold of the static regime $\gamma_c = 1$ (Equation 35), the extinction bifurcation becomes direct instead of inverse, as explained in the previous section. For $\beta_2 < 1$, the bifurcation is inverse: this is probably the most frequent case for real clarinets and clarinettists, and corresponds to

$$\zeta > \tanh 2\alpha\ell = \frac{2\mu}{1+\mu^2} \quad \text{or} \quad \lambda > \sqrt{\frac{1-\zeta}{1+\zeta}}. \tag{54}$$

  Between the two limits (53) and (54), the extinction bifurcation is direct (Regions I and IV).
- When the subcritical threshold γ_{sc} (Equation 46) reaches the instability threshold of the static regime γ_{th} (Equation 34), the emergence bifurcation becomes direct. From Equation (51), this happens when $\varphi_{sc} = \varphi_{th}$. The bifurcation is direct in Regions I and II, with the condition

$$\beta < \frac{\Sigma_{th} - \beta_1}{\beta_1 \Sigma_{th} + 3}. \tag{55}$$

6.2. Limit of instability of the two-state, non-beating regime

Finally, when the instability threshold γ_{ins} of the oscillating regime given by the condition $1/C = \zeta^2\beta_2$ (see Section 5.2.2) reaches the beating threshold γ_b, the limit was given in [4] (with a small error). The formula can be obtained from Equation (26), for $X_a = \beta_1^2$, and $X_b = 1$, $f'(X_b) = -1$. The limit ζ_i is given by the equation

$$\frac{1-f'}{1-\zeta^2 f'} = \frac{1}{\zeta^2\beta_2}, \quad \text{where} \quad f' = f'(X_a) = \frac{1-3\beta_1^2}{2\beta_1}. \tag{56}$$

This leads to a second order equation in ζ^2,

$$\beta_1^2(1-3\beta_1^2)\zeta^4 + (4\beta_1^2 - 3\beta_1 + 1)(\beta_1+1)\zeta^2 - 2\beta_1 = 0. \tag{57}$$

[9] The equation $\gamma_{th} = 1$ has two solutions: $\Delta_M = 1$, and $\sqrt{\Delta_M} = 1/\beta$. Because β is necessarily less than unity, the latter solution is larger than unity.

A particular value is $\beta_1 = 1/3$, $f' = 1$, $\zeta_i = 1$, $\mu = 1/3$, $\lambda = 1/2$. For a given loss coefficient μ ($< \zeta$), the two-state regime is always stable when $\zeta < \zeta_i$. For the sake of simplicity, we remark that an excellent approximation of the limit, better than 1%, is based upon the fact that for small losses, the coefficient $\beta = \zeta^2\beta_1$ is small, therefore $\beta_2 \simeq 2\beta_1$

$$\zeta_i^2 \simeq \frac{1}{2\beta_1(1-f') + f'}. \tag{58}$$

6.3. Limits related to the beating threshold

Another limit is reached when the subcritical threshold γ_{sc} becomes the beating-reed threshold γ_b, thus the stable two-state regime is always beating. However the unstable branch is non-beating (see Figures 2 and 3). Using Equation (47), it is found to be given by $\varphi_{sc} = \beta_3 = 1$, i.e.

$$\beta < \frac{1}{3\beta_1 + 2}. \tag{59}$$

A last limit is reached when the instability threshold of the static regime γ_{th} (34) reaches the beating threshold of the two-state regime γ_b, i.e. when $\varphi_{th} = \Sigma_{th} - \beta_1 = \beta_3$ in Equation (43),

$$\beta = \frac{1}{\beta_1 + 2\Sigma_{th}}. \tag{60}$$

For both limits given by Equations (59) and (60), the corresponding curves are therefore within Regions III and IV of Figure 5. They are very close to the limit given by Equation (55), corresponding to the change in nature of the emergence bifurcation. The three limits are even equal for $\beta_1 = 1$, $\beta = 1/5$, $\mu = \zeta = 1/\sqrt{5}$. For a given ζ, when losses are small (μ small), the emergence bifurcation is direct. Then, when β reaches the limit (55), the bifurcation becomes inverse, with a non-beating reed. Then, when β reaches the limit given by Equation (59), the bifurcation remains inverse, but the reed becomes always beating in the two-state regime.

Figure 6 shows details of the bifurcation scheme $(\Delta p, \gamma)$ near the subcritical threshold for different cases between the non-beating case $\gamma_{th} < \gamma_b$ and the beating case $\gamma_b < \gamma_{th}$ (for the latter case, the beating threshold is the subcritical threshold, as for the points III and IV). The corresponding values of the parameters (ζ, μ) are extremely close together.

7. Influence of losses on the existence of the two-state regime

When losses tend to infinity (μ tends to unity), no sound is possible whatever the value of ζ: this is in accordance with the intuition that if no reflection exists at the input of the resonator, no self-sustained oscillation can happen. Nevertheless, we do not prove that other types of regimes cannot exist, such as four-state, eight-state, ... In this section, this issue is discussed together with the influence of the choice of the model. Moreover, some musical consequences are discussed.

7.1. Possibility of existence of other oscillating regimes

When the static regime is always stable ($\beta_1 > 1$), it has been proved that the two-state regime cannot exist. It is probable that other types of regimes do not exist, but the general proof is difficult. Using the calculation of the successive iterate functions for different values of the initial condition (see [11]), we verified that when $\beta_1 > 1$, the successive iterates converge to the unique point that is the limit cycle of the static regime, thus no other regime can exist. This can be done for every set of parameter values, $\gamma, \zeta, \mu < \zeta$: if the convergence is always to a unique state, then it is sure that no other regime than the static one can exist. Obviously, this verification is not possible in practice, but the verification has been done for some set of parameter values.

We conclude that no oscillating regime exists for $\beta_1 > 1$, even if the rigorous sentence should be: no oscillating regime exists by destabilization of the static regime. A similar discussion could be done for the destabilization of the two-state regime into more complicated regimes (see Section 6.2).

7.2. Influence of the choice of the model

7.2.1. Model for the beating reed

The method used in the present paper can also be used for any shape of the nonlinear characteristic, at least numerically (the condition being that a nonlinear characteristic is static). All equations of sections 2 and 3 remain valid when modifying the nonlinear function $f(\Delta p)$. In particular if a smooth beating transition is chosen with no singularity, Figure 1 shows that the condition (30), $\beta_1 < 1$, can be generalized into the following condition: the function $h_1(\Delta p)$ goes through both a maximum and a minimum.

7.2.2. Frequency dependence of losses

The Raman model is interesting because all quantities can be determined analytically, but it is not very realistic. It is based upon two important assumptions: losses do not depend on frequency, and the reed has no dynamics. A generalization of the present study is out of the scope of the present paper, but it is interesting to note that the condition $\beta_1 < 1$ can be easily generalized when these assumptions are not done, as explained hereafter.

When losses depend on frequency, it is possible to use the characteristic equation obtained by linearizing the nonlinear equation around the pressure of the static regime p_s, and writing the approximation of the first harmonic

$$u = F(p) \simeq F(p_s) + (p - p_s)F'(p_s), \tag{61}$$

$$u = Y_1 p, \tag{62}$$

where Y_1 is the admittance of the fundamental frequency. The characteristic equation is written as

$$F'(p_s) = Y_1. \tag{63}$$

As it is well known (see [22]), this gives the condition $Im(Y_1) = 0$, thus the playing frequency f_p at the threshold

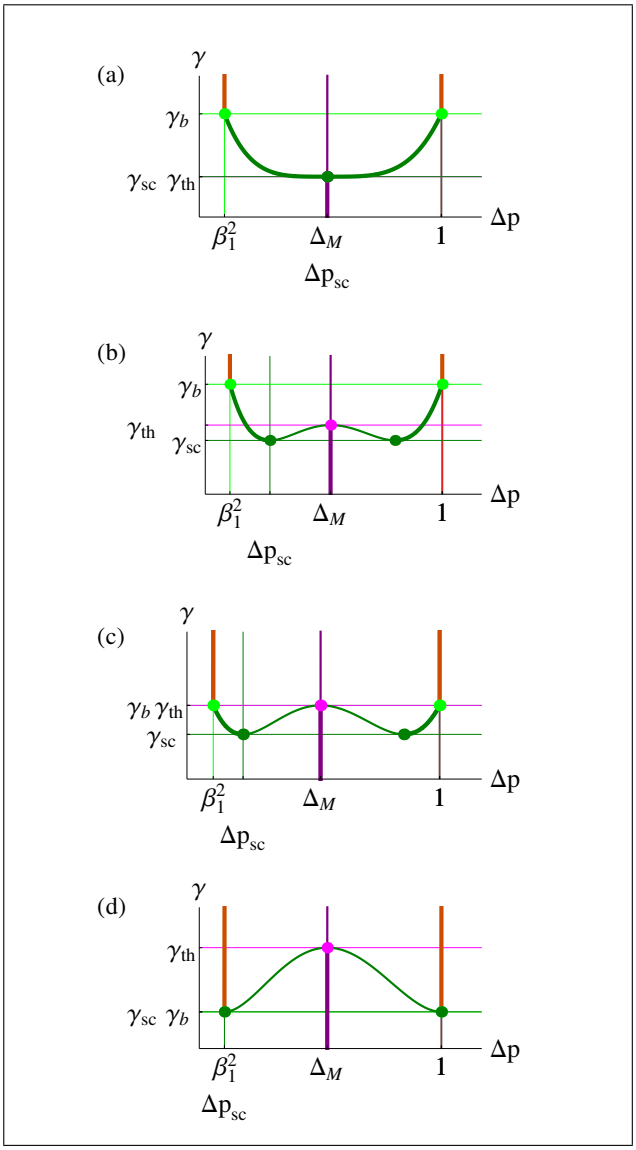

Figure 6. Zoom of bifurcation diagrams with sub-critical threshold. $\beta_1 = 0.68$ (a) $\gamma_{sc} = \gamma_{th}$, $\beta = 0.24419$; (b) $\gamma_{sc} < \gamma_{th} < \gamma_b$, $\beta = 0.24532$; (c) $\gamma_{th} = \gamma_b$, $\beta = 0.24584$; (d) $\gamma_{sc} = \gamma_b$, $\beta = 0.24752$.

can be deduced. Moreover, if at this frequency, $\beta_1 \overset{\text{def}}{=} Y_1/\zeta$, the pressure threshold is given by

$$f'(\Delta p_s) = -\beta_1 \tag{64}$$

because $F(p) = \zeta f(\Delta p)$. Therefore Δp_s satisfies Equation (28),

$$\Delta p_s = \Delta_M \quad \text{and} \quad \gamma_{th} = \Delta_M + p_s, \tag{65}$$

as expected in Section 5.1. As a consequence, when the losses depend on frequency, the value of the threshold is the same as for the Raman model, and the limit of existence of the two-state regime $\beta_1 = 1$ is unchanged. Nevertheless the hypothesis has been done that the small oscillations are sinusoidal (on this subject, see [23], [22] or [24]), and this is not true for inverse bifurcations. When several harmonics interact, the problem becomes much more

intricate, especially because of resonance inharmonicity. Moreover taking into account the frequency dependence of the losses leads to a distinction between the threshold of the fundamental regime and the "overblown" regimes (see [12]): this distinction does not exist with the Raman model, which allows a distinction based upon the initial conditions only.

As a summary, it can be said that if we suppose that the impedance peak of the operating frequency is higher than the other ones, the emergence bifurcation is direct and the limit $\beta_1 = Y_1/\zeta = 1$ is valid. This is true in particular for the first register of a clarinet and a part of the second register. The large increase of radiation losses at higher frequency due to the open toneholes lattice (see e.g. [25]) does not affect the highest peak, therefore the main result of the present paper can be extrapolated to a large number of notes of a real clarinet.

7.2.3. Effect of the reed dynamics

When the reed dynamics is taken into account as that of a 1 dof oscillator, the following characteristic equation has been obtained by Silva *et al.* [8]:

$$Y_1 = \zeta\sqrt{\gamma}\left[\frac{1}{1+\mathrm{j}\theta/Q_r-\theta^2}-\frac{1-\gamma}{2\gamma}\right], \tag{66}$$

where $\theta = \omega/\omega_r$, ω_r is the reed-resonance angular frequency, and Q_r its quality factor. The threshold pressure and frequency can be deduced from this equation, and were studied in this paper; here we are interested in the limit for which the static regime becomes always stable, i.e. when $\gamma = 1$. If the input impedance of the resonator is considered around a resonance frequency ω_1, it is possible to write

$$Y = Y_1\left[1+\mathrm{j}Q_1\left(\frac{\omega}{\omega_1}-\frac{\omega_1}{\omega}\right)\right],$$

where Q_1 is the quality factor of the resonance. For $\gamma = 1$, the real part of Equation (66) leads to the result

$$\beta_1 = \frac{1}{1-\theta^2+Q_r^{-2}\frac{\theta^2}{1-\theta^2}}. \tag{67}$$

For a lossless reed, $\beta_1 = 1/(1-\theta^2) > 1$: the limit of the losses in the tube allowed for having a sound is increased by the reed dynamics, which favors the sound production. But the effect of the reed losses is to decrease the limit. It can be concluded that reed losses and resonator losses act in the same sense concerning the range of parameter allowing sound production (this conclusion is valid for the direct-bifurcation case).

7.3. Discussion about musical consequences for the player

The previous results can be useful in order to understand and teach important aspects of the sound control by the instrumentalist. Such an objective knowledge should largely increase the pedagogical efficiency. Otherwise the approach of the problems remains more subjective and the explanations can be lengthy and less clear. One of the most useful aspects is about *pianissimo* playing. The bifurcation diagrams show that the players have two possibilities: near the emergence and near the extinction. The first possibility is used for playing *dolce*, with a quasi monochromatic sound, but the sound is noisy and cannot be sustained for a long time, due to high value of the airflow u (see Figure 2, case I). The dynamic is not easy to control because of the steepness of the bifurcation diagram near γ_{th}. The second possibility, near γ_e, conducts to a clean pianissimo, with a sound richer in high harmonics. This can however only be achieved by crossing the curve (54) in Figure 5, in order to reach the region II where the extinction bifurcation is direct.

This property is usually unknown by the players (the ability of playing such a "magical" pianissimo is often attributed exclusively to the "quality" of the reed). The beginners reduce the reed opening (ζ) by "biting" the reed and this causes unwanted effects: the pitch rises considerably, due to the decrease of the effect of the reed flow rate (see [26], and such a bending stress can cause a plastic (irreversible) deformation of the reed). The skilled player can reach region II by increasing the damping due to the lip and use a high blowing pressure near the extinction threshold, playing in the reverse way (decreasing the mouth pressure for playing louder, see Figure 2, case II). The lip comes very near to the tip of the reed, with a moderate lip pressure. This effect is probably similar to an increase of β_1, resulting in a displacement of the playing parameters on the (μ, ζ) plane exactly in the wanted direction, increasing the value of μ and decreasing the value of the parameter ζ proportionally to $\sqrt{\beta_1}$. The decrease in ζ is probably due to an increase of the reed stiffness. Decreasing ζ without "biting" too much could also be achieved by modifying the hydrodynamics of the airflow entering the channel, in order to increase the *vena contracta*, but to our knowledge no experimental evidence shows that the player can indeed modify significantly the *vena contracta*. Conversely, it seems that the parameter β cannot be significantly controlled by the player (in another way than by modifying the length of the air column). In real life, this parameter of static airflow resistance may not be determined only by the length and the diameter of the bore but certainly also by hydrodynamic effects near the channel, due to the viscosity of the air. This acts in a similar but possibly stronger way than the static resistance of the bore. Practical tests show that the effects predicted in the zones III and IV are indeed observed in some pathological situations, despite the fact that our theoretical model would require many meters of a tube of small diameter to obtain such high values of β.

To include the musician mouth in the model is obviously rather complicated, even if at low frequencies, the effect of the vocal tract is not important. Therefore the previous analysis requires some conjectures. Besides the problems of bifurcation, the analysis of the Raman model permits establishing some facts useful for the musician:

- The calculation of the mean flow shows that the most economical blowing pressure is near the beating threshold in Region I (corresponding to normal playing). This explains that skilled players can sustain the sound significantly longer than beginners.
- The transients are much faster if ζ is large (see [18]); weak reeds help doing this, as well as using a moderate lip pressure. This simplifies the staccato learning.
- The effects of leaks in the air column (misplacement of a finger, defective pads) increase the value of β_1, so that regions 0, and probably III or IV can be possibly visited (see Section 7.2.2). Almost any control can be destroyed over the dynamics (or at least rendering the dynamic control more difficult), despite of the attempts of the clarinettist to supply more energy to the instrument by opening the embouchure, increasing ζ.

8. Conclusion

The present paper is focused on limit cycles corresponding to two-state regimes, and is a complement to the paper [11], which was focused on transients. Thanks to a formulation focused on the pressure difference between mouth and mouthpiece, the effect of the nonlinear function on the production of the two-state regime can be analyzed, and especially the role of the losses. The map shown in Fig 5 can certainly be improved by using more complex models, but we think that some results are robust. When the reed opening at rest is very small or when the reed stiffness is very large (i.e. when the dimensionless parameter ζ is very small), losses can be too large and the sound production becomes impossible. A complement to this conclusion is the following: for ζ larger than $1/\sqrt{5}$, when losses increase, the emergence bifurcation becomes inverse before the sound disappears, and the instrument becomes more difficult to play. For ζ smaller than this value, when losses increase, there is a direct passage from the direct emergence bifurcation to the absence of sound.

Appendix

A1. Correction to [4]

The instability threshold γ_{ins} of the oscillating regime is given by the condition $1/C = \zeta^2\beta_2$ (see Inequalities (26), it is the limit of unstable solutions toward period-doubling of the two-state regime). This leads to the following equation, if Σ and Π are defined by Equation (41),

$$\frac{4\Pi}{\zeta^2} + (1+3\Pi)^2 - 3\Sigma^2 = \frac{4\beta_1}{1+\beta\beta_1}\Sigma(3\Pi - 1). \qquad \text{(A1)}$$

Together with Equation (42) leads to a fourth-order equation in Σ; from the solution Σ the value the threshold of instability γ_{ins} is deduced by using Equation (43). Another method is to start from certain values of the parameter β_1 and of the solution Σ, then to deduce Π using Equation (42), then β, which is solution of a second order equation.

In [4], Equation (A23) was correct, but a factor 4 was missing in Equation (A24), the correct equation being the present Equation (A1). Then Equation (A25) needs to be corrected by introducing a factor 4 on the right-hand side, and the factor $(2+3\Pi)$ needs to be replaced by $(12\Pi - 1)$ in Equation (A28) and similarly $(2+3\Pi_0)$ needs to be replaced by $(12\Pi_0 - 1)$ in Equation (A30).

Concerning the limit $\gamma_{ins} = \gamma_b$, Equations (A32) to (A34) of [4] are corrected in Section 6.2 of the present paper. The last equation gives the coefficient β_1 as a series expansion of the limit ζ_i,

$$\beta_1 = \frac{\zeta^2}{2}\left[1 - \zeta^2 + \frac{5}{4}\zeta^4 - \zeta^6\right]. \qquad \text{(A2)}$$

This expression corrects Equation (A34) of the previous paper (the correction is small, because the order 6 in ζ only is concerned), but this approximation is much less accurate than the present Equation (58).

Acknowledgements

This work was supported by the French National Agency ANR within the SDNS-AIMV and CAGIMA projects. We thank also the high school ARC-Engineering in Neuchâtel. Finally we wish to thank Philippe Guillemain and Christophe Vergez for fruitful discussions. Moreover this work has been carried out in the framework of the Labex MEC (ANR-10-LABX-0092) and of the A*MIDEX project (ANR-11-IDEX-0001-02), funded by the "Investissements d'Avenir" French Government program managed by the French National Research Agency (ANR)

References

[1] J. C. Schelleng: The bowed string and the player. J. Acoust. Soc. Am. **53** (1973) 26–41.

[2] K. Guettler: On the creation of the helmholtz movement in the bowed string. Acta Acustica united with Acustica **88** (2002) 970–985.

[3] M. Demoucron, A. A., R. Caussé: Measuring bow force in bowed string performance: Theory and implementation of a bow force sensor. Acta Acustica united with Acustica **95** (2009) 718–732.

[4] J.-P. Dalmont, J. Gilbert, J. Kergomard, S. Ollivier: An analytical prediction of the oscillation and extinction thresholds of a clarinet". J. Acoust. Soc. Am. **118** (2005) 3294–3305.

[5] A. Almeida, J. Lemare, M. Sheahan, J. Judge, R. Auvray, K. S. Dang, S. John, J. Geoffroy, J. Katupitiya, P. Santus, A. Skougarevsky, J. Smith, J. Wolfe: Clarinet parameter cartography: automatic mapping of the sound produced as a function of blowing pressure and reed force. Proceedings of the International Symposium on Music Acoustics, Sydney, Australia, 2010.

[6] J.-P. Dalmont, C. Frappé: Oscillation and extinction thresholds of the clarinet: Comparison of analytical results and experiments. J. Acoust. Soc. Am. **122** (2007) 1173–1179.

[7] T. A. Wilson, G. S. Beavers: Operating modes of the clarinet. J. Acoust. Soc. Am. **56** (1974) 653–658.

[8] F. Silva, J. Kergomard, C. Vergez, J. Gilbert: Interaction of reed and acoustic resonator in clarinetlike systems. J. Acoust. Soc. Am. **124** (2008) 3284–3295.

[9] M. E. McIntyre, R. T. Schumacher, J. Woodhouse: On the oscillations of musical instruments. J. Acoust. Soc. Am. **74** (1983) 1325–1345.

[10] C. Maganza, R. Caussé, F. Laloë: Bifurcations, period doubling and chaos in clarinetlike systems. Europhysics letters **1** (1986) 295–302.

[11] P.-A. Taillard, J. Kergomard, F. Laloë: Iterated maps for clarinet-like systems. Nonlinear Dynamics **62** (2010) 1–19.

[12] S. Karkar, C. Vergez, B. Cochelin: Oscillation threshold of a clarinet model: A numerical continuation approach. J. Acoust. Soc. Am. **131** (2012) 698–707.

[13] P. Guillemain, J. Kergomard, T. Voinier: Real-time synthesis of clarinet-like instruments using digital impedance models. J. Acoust. Soc. Am. **118** (2005) 483–494.

[14] T. K., H. Kodama, A. Nakajima, T. Tachibana: Numerical study on multi-stable oscillations of woodwind single-reed instruments. Acta Acustica united with Acustica **95** (2009) 1123–1139.

[15] G. Iooss, D. D. Joseph: Elementary stability and bifurcation theory. Undergraduate texts in Mathematics. Springer Verlag, 1980.

[16] D. H. Sattinger: Topics in stability and bifurcation theory. Lecture notes in mathematics. Springer Verlag, 1973.

[17] S. H. Strogatz: Nonlinear dynamics and chaos: with applications in Physics, Biology, Chemistry, and Engineering. Addison-Wesley, Reading, MA, 1994.

[18] J. Kergomard: Elementary considerations on reed-instrument oscillations. – In: Mechanics of musical instruments, Vol. 335. CISM Courses and Lectures. A. Hirschberg, J. Kergomard, G. Weinreich (eds.). Springer-Verlag, Wien, 1995, 229–290.

[19] A. Hirschberg, R. W. A. Van de Laar, J. P. Marrou-Maurires, A. P. J. Wijnands, H. J. Dane, S. G. Kruijswijk, A. J. M. Houtsma: A quasi-stationary model of air flow in the reed channel of single-reed woodwind instruments. Acustica **70** (1990) 146–154.

[20] J.-P. Dalmont, J. Gilbert, S. Ollivier: Nonlinear characteristics of single-reed instruments: quasistatic volume flow and reed opening measurements. J. Acoust. Soc. Am. **114** (2003) 2253–2262.

[21] N. Fletcher, T. Rossing: The physics of musical instruments. Springer Verlag, 1991.

[22] N. Grand, J. Gilbert, F. Laloë: Oscillation threshold of woodwind instruments. Acta Acustica **1** (1997) 137–151.

[23] W. E. Worman: Self-sustained nonlinear oscillations of medium amplitude in clarinet-like systems. PhD thesis, Case Western Reserve University, 1971.

[24] B. Ricaud, P. Guillemain, J. Kergomard, F. Silva, C. Vergez: Behavior of reed woodwind instruments around the oscillation threshold. Acta Acustica united with Acustica **95** (2009) 733–743.

[25] E. Moers, J. Kergomard: On the cutoff frequency of clarinet-like instruments. Geometrical versus acoustical regularity. Acta Acustica united with Acustica **97** (2011) 984–996.

[26] J.-P. Dalmont, P. Guillemain, P. A. Taillard: Influence of the reed flow on the intonation of the clarinet. Acoustics 2012, Nantes, 2012, 1173–1177.

Chapter 2

Iterated maps for clarinet-like systems

Résumé

Mc Intyre et coll. (1983) ont montré que l'on peut ramener le calcul des oscillations d'une clarinette à une simple itération, dans un modèle où le résonateur est cylindrique avec des pertes indépendantes de la fréquence et où l'anche est vue comme un ressort sans inertie. Pour cela on choisit le couple d'ondes aller/retour comme variables de base. Le système peut alors se ramener à l'itération d'une fonction $f(x)$ qui relie les amplitudes de ces ondes, conduisant à des oscillations en signaux carrés. Dans cet article, nous étudions cette fonction de manière plus approfondie et en déduisons un encadrement des valeurs des paramètres d'excitation pour lesquelles l'anche peut battre, ou encore pour lesquelles le signe du débit peut s'inverser. Les cartes itérées de la fonction f(x) renseignent notamment sur la stabilité des régimes périodiques, ou aident à comprendre l'existence de régimes chaotiques, de fenêtres de périodicité ou d'intermittences.

Cet article [151] est reproduit avec l'autorisation des coauteurs et celle de l'éditeur Springer, du 11 janvier 2018. Notons qu'un résumé de ce travail est disponible en français [152], figurant à la fin de ce Chapitre.

Nonlinear Dyn (2010) 62: 253–271
DOI 10.1007/s11071-010-9715-5

ORIGINAL PAPER

Iterated maps for clarinet-like systems

P.-A. Taillard · J. Kergomard · F. Laloë

Received: 12 December 2009 / Accepted: 29 March 2010 / Published online: 29 April 2010

Abstract The dynamical equations of clarinet-like systems are known to be reducible to a non-linear iterated map within reasonable approximations. This leads to time oscillations that are represented by square signals, analogous to the Raman regime for string instruments. In this article, we study in more detail the properties of the corresponding non-linear iterations, with emphasis on the geometrical constructions that can be used to classify the various solutions (for instance with or without reed beating) as well as on the periodicity windows that occur within the chaotic region. In particular, we find a regime where period tripling occurs and examine the conditions for intermittency. We also show that, while the direct observation of the iteration function does not reveal much on the oscillation regime of the instrument, the graph of the high order iterates directly gives visible information on the oscillation regime (characterization of the number of period doubligs, chaotic behaviour, etc.).

P.-A. Taillard
Conservatoire de Musique Neuchâtelois, Avenue Léopold-Robert 34, 2300 La Chaux-de-Fonds, Switzerland

J. Kergomard (✉)
Laboratoire de Mécanique et d'Acoustique, CNRS UPR 7051, 31 Chemin Joseph Aiguier, 13402 Marseille Cedex 20, France
e-mail: kergomard@lma.cnrs-mrs.fr

F. Laloë
Laboratoire Kastler-Brossel, ENS, UMR 8552 CNRS, ENS, et UMPC, 24 rue Lhomond, 75005 Paris, France

Keywords Bifurcations · Iterated maps · Reed musical instruments · Clarinet · Acoustics

1 Introduction

Non-linear iterated maps are now known as an universal tool in numerous scientific domains, including for instance mechanics, hydrodynamics, and economy [1–5]. They often appear because the differential equations describing the dynamics of a system can be reduced to non-linear iterations, with the help of Poincaré recurrence maps for instance. The resulting iterations combine a great mathematical simplicity, which makes them convenient for numerical simulations, with a large variety of interesting behaviours, providing generic information on the properties of the system. In particular, they are essential to characterize one of the routes to chaos, the cascade of period doublings [6, 7].

In musical acoustics, Mc Intyre et al. have given, in a celebrated article [8], a general frame for calculating the oscillations of musical instruments, based upon the coupling of a linear resonator and a non-linear excitator (for reed instruments, the flow generated by a supply pressure in the mouth and modulated by a reed). In an appendix of their article they show that, within simplified models of self-sustained instruments, the equations of evolution can also be reduced to an iterated map with appropriate non-linear functions. For resonators with a simple shape such as

a uniform string or a cylindrical tube, the basic idea is to choose variables that are amplitudes of the incoming and outgoing waves (travelling waves), instead of usual acoustic pressure and volume velocity in the case of reed instruments. If the inertia of the reed is ignored (a good approximation in many cases), and if the losses in the resonator are independent of frequency, the model leads to simple iterations; the normal oscillations correspond to the so called "Helmholtz motion", a regime in which the various physical quantities vary in time by steps, as in square signals. Square signals obviously are a poor approximation of actual musical signals, but this approach is sufficient when the main purpose is to study regimes of oscillation, not tone-color.

In the case of clarinet-like systems, the idea was then expanded [9], giving rise to experimental observations of period doubling scenarios and to considerations on the relations between stability of the regimes and the properties of the second iterate of the non-linear function; see also [10] and especially [11] for a review of the properties of iterations in clarinet-like systems and a discussion of the various regimes (see also [12]). More recent work includes the study of oscillation regimes obtained in experiments [13, 14], computer simulation [15] as well as theory [16, 17].

The general form of the iteration function that is relevant for reed musical instruments is presented in Sect. 3. It is significantly different from the usual iteration parabola (i.e. the so-called logistic map). Moreover, it will be discussed in more detail that the control parameters act in a rather specific way, translating the curve along an axis at 45° rather than acting as an adjustable gain.

The purpose of the present article is to study the iterative properties of functions having this type of behaviour, and their effect on the oscillation regimes of reed musical instruments. We will study the specificities and the role of the higher order iterates of this class of functions, in particular in the regions of the so called "periodicity windows", which take place beyond the threshold of chaos. These windows are known to contain interesting phenomena [2, 3, 18, 19], for instance period tripling or a route to intermittence, which to our knowledge have not yet been studied in the context of reed musical instruments. Moreover, the iterates give a direct representation of the zones of stability of the different regimes (period doublings for instance), directly visible on the slope of the corresponding iterate.

For numerical calculations, it is necessary to select a particular representation of the non-linear function, which in turn requires to choose a mathematical expression of the function giving the volume flow rate as a function of the pressure difference across the reed. A simple and realistic model of the quasi-static flow rate entering a clarinet mouthpiece was proposed in 1974 by Wilson and Beavers [20], and discussed in more detail in 1990 by Hirschberg et al. [21]. This model provides a good agreement with experiments [22] and leads to realistic predictions concerning the oscillations of a clarinet [23]. Using this mathematical representation of the flow rate, we will see that iterations lead to a variety of interesting phenomena. Our purpose here is not to propose the most elaborate possible model of the clarinet, including all physical effects that may occur in real instruments. It is rather to present general ideas and mathematical solutions as illustration of the various class of phenomena that can take place, within the simplest possible formalism; in a second step, one can always take this simple model as a starting point, to which perturbative corrections are subsequently added in order to include more specific details.

We first introduce the model in Sect. 2, and then discuss the properties of the iteration function in Sect. 3. The bifurcations curves are obtained in Sect. 4 and, in Sect. 5, we discuss the iterated functions and their applications in terms of period tripling and intermittence. In particular, we see how the graph of high order iterates give visible information on the regime of oscillation (number of period doublings for instance) or the appearance of a chaotic regime, while nothing special appears directly in the graph of the first iterate. Two appendices are added at the end.

2 The model

We briefly recall the basic elements of the model, the non-linear characteristics of the excitator, and the origin of the iterations within a simplified treatment of the resonator.

2.1 Nonlinear characteristics of the entering flow

In a quasi static regime, the flow U entering the resonant cavity is modelled with the help of an approximation of the Bernoulli equation, as discussed, e.g.

in [21]. We note P_{int} the acoustic pressure inside the mouthpiece, assumed to be equal to the one at the output of the reed channel, P_m the pressure inside the mouth of the player; for small values of the difference:

$$\Delta P = P_m - P_{\text{int}}, \tag{1}$$

the reed remains close to its equilibrium position, and the conservation of energy implies that U is proportional to $\eta_p\sqrt{|\Delta P|}$, where $\eta_p = \pm 1$ is the sign of ΔP (we ignore dissipative effects at the scale of the flow across the reed channel); for larger values of this difference, the reed moves and, when the difference reaches the closure pressure P_c, it completely blocks the flow. These two effects are included by assuming that if $\Delta P \leq P_c$ the flow U is proportional to $\eta_p\sqrt{|\Delta P|}[P_c - \Delta P]$, and if $\Delta P > P_c$, the flow vanishes. Introducing the dimensionless quantities:

$$\begin{aligned} p &= P_{\text{int}}/P_c, \\ u &= U Z_\infty/P_c, \\ \gamma &= P_m/P_c, \\ \Delta p &= \Delta P/P_c = \gamma - p, \end{aligned} \tag{2}$$

where $Z_\infty = \rho c/S$ is the acoustic impedance of an infinitely long cylindrical resonator having the same cross section S than the clarinet bore (ρ is the density of air, c the velocity of sound), we obtain:

$$u = 0 \tag{3}$$

if $\Delta p > 1$ i.e. $p < \gamma - 1$;

$$u = \zeta(p + 1 - \gamma)\sqrt{\gamma - p} \tag{4}$$

if $0 < \Delta p < 1$ i.e. $\gamma - 1 < p < \gamma$;

$$u = -\zeta(p + 1 - \gamma)\sqrt{p - \gamma} \tag{5}$$

if $\Delta p < 0$ i.e. $p > \gamma$.

The parameter ζ characterizes the intensity of the flow and is defined as:

$$\zeta = \frac{c S_{\text{op}}}{S}\sqrt{\frac{2\rho}{P_c}}, \tag{6}$$

where S_{op} is the opening cross section of the reed channel at rest. One can show that ζ is inversely proportional to square root of the reed stiffness,[1] contained in P_c. In real instruments, typical values of the parameters are $\gamma \in [0, 1.5]$; $\zeta = [0.1, 0.5]$; values $\zeta > 1$ will not be considered here, since they correspond to multi-valued functions $u(p)$, a case that does not seem very realistic in practice. Figure 1 shows an example of function defined in (3) to (5). It is obviously non-analytic; it is made of three separate analytic pieces, with a singular point at $p = \gamma$. The derivative of the function $u(p)$ is discontinuous at $p = \gamma - 1$ (point M_b in Fig. 1, the index b being used for the limit of possible beating); a smoothing of the resulting angle of the function could easily be introduced at the price of a moderate mathematical complication, but this is not necessary for the present discussion.

2.2 Iteration

Waves are assumed to be planar in the quasi one dimensional cylindrical resonator. Any wave can be expanded into an outgoing wave $p^+(t - z/c)$ and an incoming wave $p^-(t + z/c)$, where t is the time and z the abscissa coordinate along the axis of the resonator; at point $z = 0$ (at the tip of the reed), the acoustic pressure and flow[2] are given by

$$p(t) = p^+(t) + p^-(t); \qquad u(t) = p^+(t) - p^-(t) \tag{7}$$

or

$$p^+(t) = \frac{1}{2}[p(t) + u(t)]; \qquad p^-(t) = \frac{1}{2}[p(t) - u(t)]. \tag{8}$$

We will use variables $p^\pm(t)$ instead of $p(t)$ and $u(t)$. If we assume that the impedance at the output of the resonator is zero (no external radiation, the output pressure remains the atmospheric pressure), we obtain the reflection condition:

$$p^-(t) = -p^+(t - 2\ell/c), \tag{9}$$

where ℓ is the resonator length and c the sound velocity. This equation expresses that the reflected wave has

[1] The reed remains close to its equilibrium position; the acoustic flow is then independent of the stiffness of the reed. Equation (4) then provides $U Z_\infty/P_c \simeq \zeta\sqrt{(P_m - P_{\text{int}})/P_c}$, or $U \simeq (\zeta\sqrt{P_c}/Z_\infty)\sqrt{(P_m - P_{\text{int}})}$; but P_c is roughly proportional to the reed stiffness, so that the independence of the flow with respect to the stiffness requires that ζ is inversely proportional to the square root of this stiffness.

[2] The flow is related to the pressure via the Euler equation: $\partial P/\partial z = -\rho S^{-1}\partial U/\partial t$.

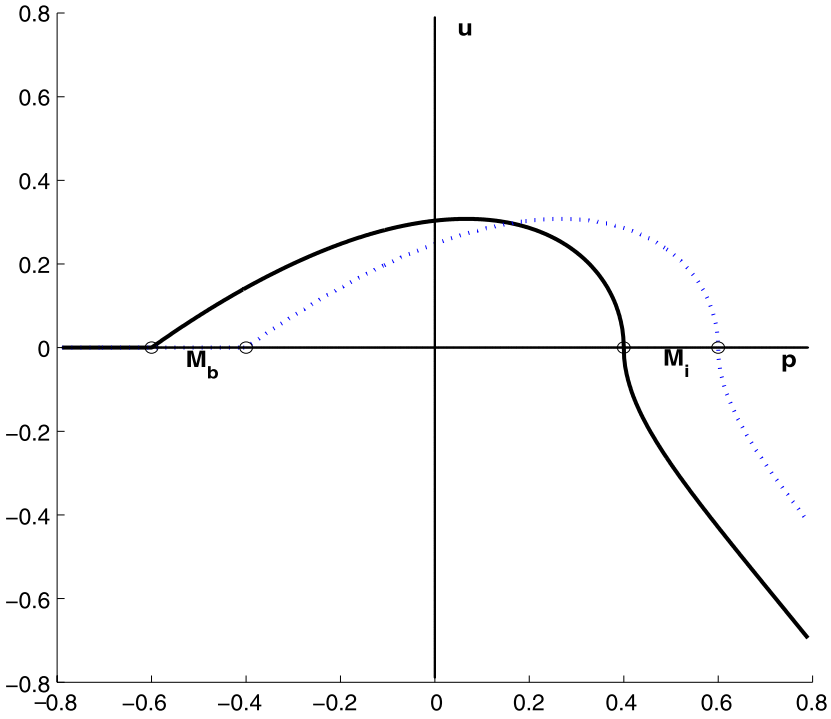

Fig. 1 Graph showing the air flow rate u entering the resonator of a clarinet as a function of the internal pressure p (pressure in the mouthpiece). All physical quantities are expressed in dimensionless units, as explained in the text. M_b corresponds to the contact point where the internal pressure in the mouthpiece bends the reed sufficiently to close the channel, so that the flow vanishes; it remains zero in all region $p < \gamma - 1$. M_i is the inversion point where $p = \gamma$ and where the acoustic flow changes sign. The full line corresponds to $\gamma = 0.4$, the broken line to $\gamma = 0.6$. Here, $\zeta = 0.8$

the same amplitude than the incoming wave. Losses are not included in this relation, but one can also introduce them very easily by replacing (9) by

$$p^-(t) = -\lambda p^+(t - 2\ell/c), \tag{10}$$

which amounts to introducing frequency independent losses; a typical value is $\lambda = 0.9$. For a cylindrical open tube with no radiation at the open end so that losses only occur inside the tube, $\lambda = \exp(-2\alpha\ell)$, where α is the absorption coefficient. Of course, this is an approximation: real losses are frequency dependent[3] and radiation occurs, but since losses remain a relatively small correction in musical instruments, using (10) is sufficient for our purposes.

We now assume that all acoustical variables vanish until time $t = 0$, and then that the excitation pressure in the mouth suddenly takes a new constant value γ; this corresponds to a Heaviside step function for the control parameter. Between time 0 and time $2l/c$, according to (10), the incoming amplitude $p^-(t)$ remains zero, but the outgoing amplitude $p^+(t)$ has to jump to value p_1^+ in order to fulfil (3) to (5). At time $t = 2l/c$, the variable $p^-(t)$ jumps to value $-\lambda p_1^+$, which immediately makes $p^+(t)$ jump to a new value p_2^+, in order to still fulfil (3) to (5). This remains true until time $t = 4l/c$, when $p^-(t)$ jumps to value $-\lambda p_2^+$ and $p^+(t)$ to a value p_3^+, etc. By recurrence, one obtains a regime where all physical quantities remain constant in time intervals $2nl/c < t < 2(n+1)l/c$, in particular p_n for the pressure and u_n for the flow, with the recurrence relation:

$$p_n^- = -\lambda p_{n-1}^+. \tag{11}$$

In what follows, it will be convenient to use $2l/c$ as a natural time unit. We will then simply call "time n" the time interval $(n-1)2l/c \le t < n2l/c$. Notice that in order to get higher regimes (with, e.g. triple frequency), the previous choice of transient for γ needs to be modified (see, e.g.[11]).

Now, by combining (3) to (5) and (7), one can obtain a non-linear relation g between p_n^+ and p_n^-:

$$p_n^+ = g(p_n^-)\,, \tag{12}$$

which, combined with (11), provides the relation:

$$p_n^+ = g(-\lambda p_{n-1}^+) = f(p_{n-1}^+), \tag{13}$$

with, by definition: $f(x) \equiv g(-\lambda x)$. The equation of evolution of the system are then equivalent to a simple mapping problem with an iteration function $f(x)$.

[3]The value of α depends on both frequency f and radius R. For normal ambient conditions (20°C), $\alpha = 2.96 \times 10^{-5}\sqrt{f}/R$ (see, e.g. [24]).

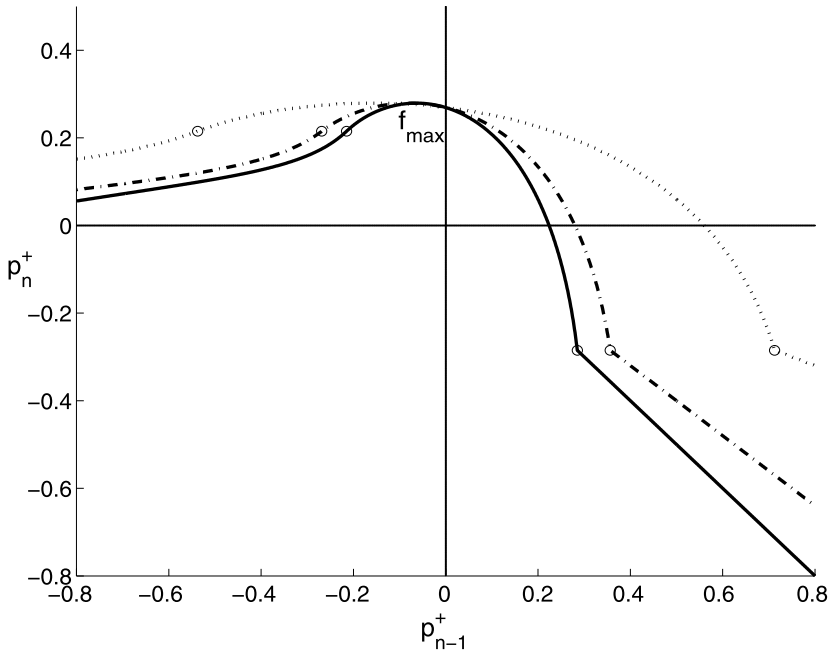

Fig. 2 Iteration function f for $\zeta = 0.8$ and $\gamma = 0.43$ *Solid line* $\lambda = 1$ (no loss in the resonator); *mixed line* $\lambda = 0.8$; *dotted line* $\lambda = 0.4$. The *circles on the right* indicate the contact point M_b, *those on the left* the flow inversion point M_i

The graph of this function is obtained by rotating the non-linear characteristics of Fig. 1 by 45° (in order to obtain g), then applying a symmetry (to include the change of sign of the variable) and finally a horizontal rescaling by a factor $1/\lambda$; the result is shown in Fig. 2. This provides a direct and convenient graphical construction of the evolution of the system [9]; Figure 3 shows how a characteristic point 1 is transformed into its next iterate 2, etc. by the usual construction, at the intersection of a straight line with the iteration curve, i.e. by transferring the value of $f(x)$ to the x axis and reading the value of the function at this abscissa in order to obtain $f[f(x)]$.

In what follows, we consider γ as the main control parameter of the iteration; it corresponds to a change of pressure in the mouth of the instrumentalist. A second control parameter is ζ, which the player can also change in real time by controlling the lip pressure on the reed. For a given note of the instrument, parameter λ remains fixed, but of course depends on which lateral holes of the clarinet are closed, in other words on the pitch of the note.

The oscillations where the functions remain constant and jump to a different value at regular interval of times are reminiscent of the Raman regime for the oscillation of bowed strings [25]. McIntyre et al. have indeed noticed that, if one replaces the non-linear function by that corresponding to a bowed string, one obtains the Raman oscillation regime of a string bowed at its center [8].

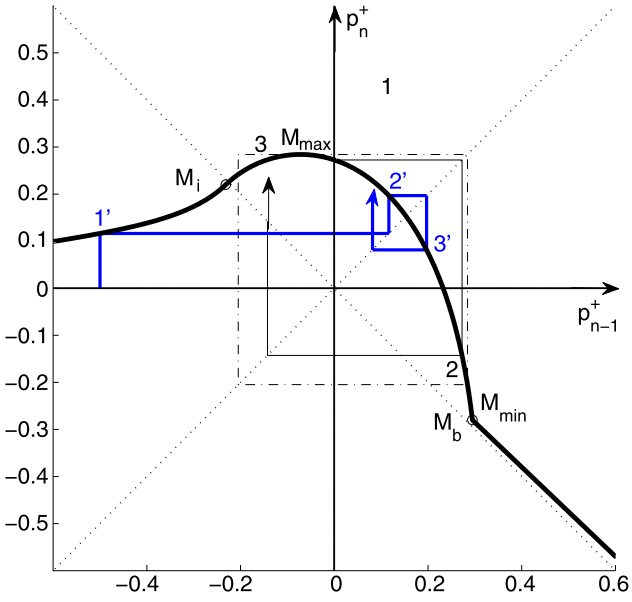

Fig. 3 Graphical illustration of the iteration, where an initial point 1 is iterated into point 2, 3, etc. (similarly for the point 1', 2', 3',...). Since the non-linear iteration function has a maximum $f_{\max}$, after a few steps the iteration remains inside an "iteration square" shown in *broken lines*. This square has its upper side tangent to the maximum of the function, at point $M_{\max}$, which after one iteration becomes point $M_{\min}$ defining the lowest side of the square (ordinate $f_{\min}$). Depending on the parameters, the iteration square contains or does not contain the contact point M_b and the flow inversion point M_i. Here, $\gamma = 0.44$, $\zeta = 0.8$, $\lambda = 0.95$

3 Properties of the iteration

The analytical expression of the iteration function is given in Appendix A. Figure 2 shows the function for given values of the parameters γ and ζ, and three different values of the loss parameter λ.

In the literature, the most commonly studied functions have the following properties (see, e.g. Collet and Eckman [4, 5] or Bergé et al. [2, 3]):

- They are defined on a finite interval and map this interval into itself;
- They are continuous;
- They have a unique maximum;
- their Schwarzian derivative is negative.

A function verifying these properties will be called a "standard" function; the function $f(x)$ of interest in our case does not fulfil all these requirements.

Domain of iteration Usually, the iteration function defines an application of the interval $0 \leq x \leq 1$ over itself. Here, $f(x)$ is defined on an infinite interval $[-\infty, +\infty]$ even if, obviously, very large values of the variables are not physically plausible. Nevertheless, analyzing the different cases corresponding to (3) to (5), one can show that the function $f(x)$ has a maximum $f_{\max}$ obtained for:

$$x_{\max} = -\frac{1}{\lambda}\left[\frac{\gamma}{2} - \frac{5}{18} - \chi\left(\zeta - \frac{5}{3\zeta}\right)\right] \tag{14}$$

with value:

$$\begin{aligned} f_{\max} &= \frac{\gamma}{2} + A_\zeta \quad \text{with} \\ A_\zeta &= \chi\left(\zeta + \frac{1}{3\zeta}\right) - \frac{1}{18}, \end{aligned} \tag{15}$$

where χ is defined by:

$$\chi = \frac{1}{9}\left[\sqrt{3 + \frac{1}{\zeta^2}} - \frac{1}{\zeta}\right]. \tag{16}$$

It can be shown that this maximum is unique for large value of ζ ($\zeta > 1/\sqrt{3}$); for smaller values, a second maximum exists at a very large negative values of x, i.e. for very large negative flow, but we will see below that such values of the flow cannot be obtained after a few iterations. Therefore, we focus our attention only on the maximum $f_{\max}$, which varies slowly as a function of ζ because A_ζ increases monotonically from 0 for $\zeta = 0$ to a small value (5/54, for $\zeta = 1$).

The geometrical construction of Fig. 3 shows that, after a single iteration, the characteristic point M necessarily falls at an abscissa $x \leq f_{\max}$. Let us call $f_{\min} = f(f_{\max})$ the ordinate of the point on the iteration function with abscissa $f_{\max}$. The two vertical lines $x = f_{\min}$ and $x = f_{\max}$, together with the two horizontal lines $y = f_{\min}$ and $y = f_{\max}$, define a square in the x, y plane, from which an iteration cannot escape as soon as the iteration point has fallen inside it.[4] Conversely, since every characteristic point has at least two antecedents, the iteration can bring a point that was outside the square to inside. In other words, the square determines a part of the curve which is invariant by action of the function. For usual initial conditions, such as $p_0^- = 0$, the starting point already lies within the square, so that all points of the iteration keep this property. We have checked that, even if one starts with very large and un-physical pressure differences (positive or negative), the iterations rapidly converge to the inside the square. In what follows, we call it the "iteration square".

The net result is that, if we do not consider transients, we can consider that the function defines an application of the interval $[f_{\min}, f_{\max}]$ over itself. We are then very close to the usual mapping situation, except that here the interval depends on the control parameters (since the value of $f_{\max}$ depends on γ and ζ), but with a relatively slow variation.

Singularities An interesting feature of the iteration function is the discontinuity of its first derivative occurring at the beating limit point M_b at $x = x_b$, given by:

$$x_b = \frac{1-\gamma}{2\lambda}; \qquad f(x_b) = \frac{\gamma - 1}{2}. \tag{17}$$

When the reed closes the channel ($p^+ = p^-$, $p^+ + p^- < \gamma - 1$), $x > x_b$, $f(x) = -\lambda x$, the iteration function is linear.

Another singularity, i.e. a discontinuity of the second derivative, is obtained at the crossover between positive and negative flow, the inversion point M_i where sign of the flow changes. Its abscissa $x = x_i$ is

[4] We assume that $f(f_{\min}) > f_{\min}$, which means that the iteration curve crosses the left side of the square, as is the case in Fig. 3.

given by

$$x_i = -\frac{\gamma}{2\lambda}; \qquad f(x_i) = \frac{\gamma}{2}. \tag{18}$$

For $0 < \gamma < 1$, x_i is negative and x_b positive: therefore, the initial point of the iteration ($x = 0$) lies in the interval $[x_i, x_b]$, with neither contact with the mouthpiece nor negative flow, as one could expect physically.

Schwarzian derivative The Schwarzian derivative [4, 5] of $f(x)$ is equal to:

$$Sf = \frac{f'''}{f'} - \frac{3}{2}\left[\frac{f''}{f'}\right]^2, \tag{19}$$

where f', f'', and f''' indicate the first, second, and third derivatives of $f(x)$, respectively. If $x > x_b$, it is zero; if $x_i < x < x_b$, using the change of variables given in Appendix A, Sf can be shown to be equal to

$$Sf = \frac{8\lambda^2}{Y'^4(Y'-2)^2}\left[Y'''Y'(Y'-2) - 3Y''^2(Y'-1)\right], \tag{20}$$

where Y is a function of X—see (27) to (29). Therefore, its sign does not depend on the loss parameter λ. After some calculations, the Schwarzian derivative is found to be negative for all $x \in [x_i, x_b]$ when $\zeta < 1/\sqrt{5}$. Otherwise, it is negative up to a certain value, then positive up to $x = x_b$. The calculation of Sf for the case $x < x_i$ shows that it is positive, except for a small interval. The iteration function therefore differs from a standard function because of the sign of the Schwartzian derivative; this is related to the nature of the bifurcation at the threshold of oscillation [26], which can be either direct or inverse.

Beating and negative flow limits In Fig. 3, we see that, depending whether the contact point M_b and flow inversion point M_i of the iteration curve fall inside or outside the iteration square, a beating behavior of the reed and a sign inversion of the air flow are possible or not.

Point M_b falls inside the iteration square if its abscissa x_b given by (17) is smaller than $f_{\max}$, which leads to:

$$\gamma > \gamma_b \equiv \frac{1 - 2\lambda A_\zeta}{1+\lambda}. \tag{21}$$

The limiting value γ_b is less than unity (it tends to 1/2 when ζ tends to 0 and λ tends to unity). This necessary condition is completely independent of the nature of the limit cycle, and less stringent than the limit γ_{b2s} obtained in [17], for a 2-state cycle:

$$\gamma_{b2s} = 1/2\left[1 + \beta\beta_1 + \beta_1^2(1 - \beta\beta_1)\right], \tag{22}$$

where $\beta = \zeta(1-\lambda)/(1+\lambda)$ and $\beta_1 = \beta/\zeta^2$. Figure 4 gives a comparison between the two limits. Similarly, a necessary condition for possible inversions of the sign of the air flow is that point M_i falls inside the iteration square of Fig. 3, in other words that x_i is larger than $f_{\min}$. We show in Appendix B that this happens if:

$$\gamma_{i1} < \gamma < \gamma_{i2}. \tag{23}$$

The expression of the two limits γ_{i1} and γ_{i2} are given in the appendix and can be seen on Fig. 4. They are solutions of $x_i = f_{\min}$, and exist only if the following condition holds:

$$\lambda > \frac{1}{1 + 2A_\zeta}. \tag{24}$$

Therefore, for a given ζ, negative flow is possible only above a certain value of λ; this value is $27/32 = 0.84$ for $\zeta = 1$, and tends to unity when ζ tends to zero. Using a more realistic shape for the function $f(x)$ with a rounding of the kink at x_b (no discontinuity of the derivative) should lead to a shorter range of negative flow, making the phenomenon even less likely, as illustrated in Fig. 4.

Of course, the two above conditions (21) and (23) are necessary, but not sufficient; they do not ensure that either beating or flow inversion will indeed take place, since this will be true only if the corresponding regions of the non-linear curve are reached during the iterations. Generally speaking, this will have more chance to occur in chaotic regimes, where many points are explored in the iterations, than in periodic regimes. Since no observation of negative flow has been reported in the literature, it is not clear whether this actually happens in real instruments.

In conclusion of this section, the iteration function is similar to those usually considered in the context of iterated maps, without really belonging to the category of "standard" functions. The major difference is actually the effect of the control parameters on the function, since usually the control parameters acts as a

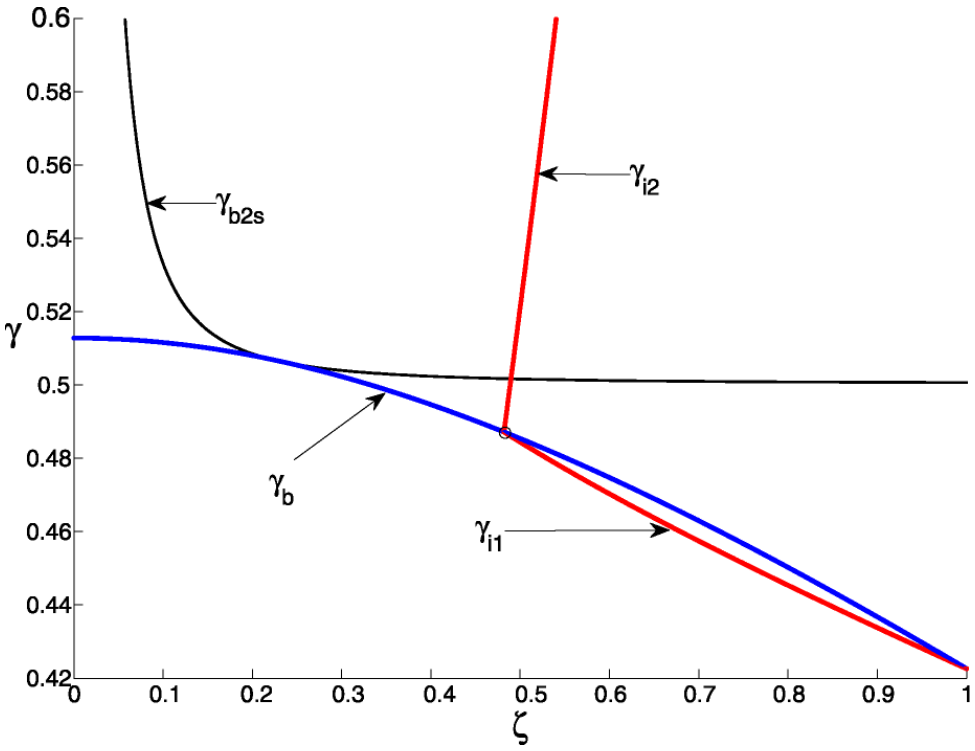

Fig. 4 In the plane of the control parameters γ and ζ, the line representing γ_b gives a border between the upper region, where reed beating may occur, and the lower region where it cannot—see (21). As a point of comparison, the line labelled γ_{b2s} correspond to the limit obtained in [17] for the particular case of a 2-state regime, and given by (22). The figure also shows the line γ_{i1} and γ_{i2} associated with the possibility of negative flow (the first one turns out to be very close to that associated with reed beating). Small values for the losses have been assumed ($\lambda = 0.95$)

gain, expanding the vertical axis of the graph; here, the parameter γ (pressure in the mouth of the instrumentalist) translates the iteration function along an axis at 45° of the coordinate axis, while the other control parameter ζ (the pressure of the lip on the reed) expands the function along the perpendicular axis. It is therefore not surprising that we should find a parameter dependence of the dynamical behaviours that is significantly different from the standard results.

4 Bifurcation curves

Figure 5 shows an example of bifurcation curves, for $\lambda = 0.95$ and $\zeta = 0.8$, and illustrates the relative complexity of the possible regimes. The upper curve corresponds to the outgoing amplitude p^+ (or x), the middle curve to acoustic pressure p, and the lower curve to the acoustic flow u. The three curves show the last 20 values obtained after computing 400 iterations for each value of the mouth pressure γ. By calculating 2,000 iterations for a given value of the parameter γ, we have checked that the limit cycle is then reached. Obviously, this method leads to stable regimes only.

When the control parameter γ increases, the beginning of these curves follows a classical scenario of successive period doublings, leading eventually to chaos; as expected, high values of the parameters ζ and λ favour the existence of chaotic regimes, as well as beating reed or negative flow. When γ continues to increase, another phenomenon takes place: chaos disappears and is replaced by a reverse scenario containing a series of frequency (instead of period) doublings. We call this phenomenon a "backward cascade" (in order to distinguish it from the usual "inverse cascade", which takes place within periodicity windows inside chaos [2, 3]); this backward cascade is a consequence of the specificities of the effect of the control parameter on the iteration function in our model, and of the particular shape of the iteration function (for instance a straight line beyond the beating limit point). As a matter of fact, different kinds of cascades have been studied in the literature (see, e.g. [27] and [28], in particular Fig. 5).

In Fig. 5, the variations of γ correspond to a "crescendo": for a given value of γ, the initial value for the iteration, p_0^+, is chosen to be equal to the last value p_{400}^+ obtained with the previous value of γ. But we have also studied the "decrescendo" regime and observed that, in the chaotic regimes, the plotted points differ from the crescendo points; on the other hand, they remain the same in the periodic regimes, indicating a direct character of the bifurcations (no hysteresis). We have found an exception to this rule: be-

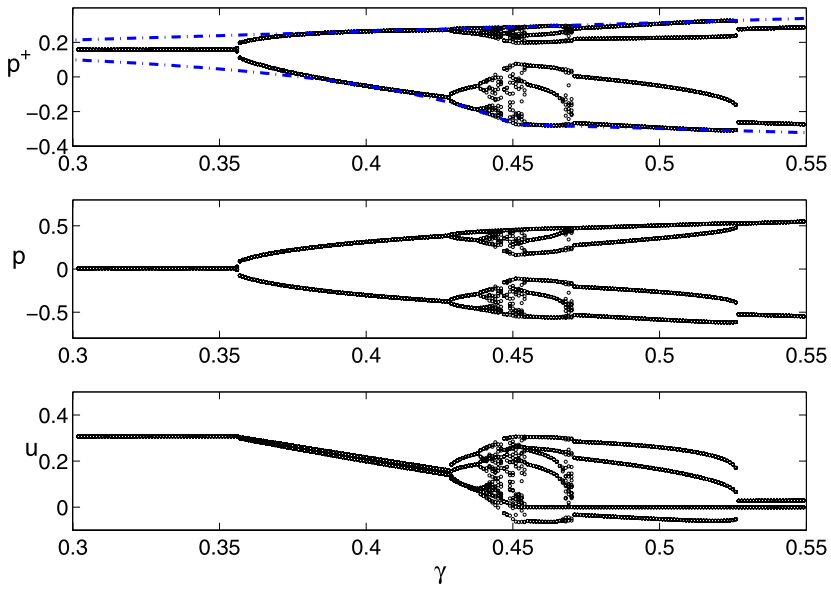

Fig. 5 Bifurcation curve for $\lambda = 0.95$ and $\zeta = 0.8$. For increasing values of the abscissa γ (blowing pressure), corresponding to a crescendo, the curve show the values after 400 iterations of the outcoming wave p^+ (*top*) the pressure p in the mouthpiece (*middle*), and the volume flow u (*bottom*). Above $\gamma \simeq 0.45$, the flow can be negative and the reed can beat. The *top figure* also shows $f_{\max}(\gamma)$ and $f_{\min}(\gamma)$ (*mixed lines*) associated to the "iteration square"

tween values $\gamma = 0.5$ and $\gamma = 0.53$, 2-state and 4-state regimes coexist, indicating an inverse bifurcation. Another inverse bifurcation, between a 2-state regime and a static regime, occurs beyond the limit of the figure, the two regimes coexisting between $\gamma = 1$ and $\gamma = 6.3544$; this is not shown here (the shape of the curve can be found in Ref. [17], see upper Fig. 4).

The two limits of the function $f(x)$, $f_{\max}$, and $f_{\min}$, are also plotted in the upper figure (p^+) showing that, as expected, the corresponding values remain inside the iteration square (Sect. 3). In the figure at bottom, the results for the flow u exhibit lower limits for negative flow and for beating, which are very close to the theoretical limits, respectively, $\gamma_{i1} = 0.4454$ and $\gamma_b = 0.4503$, and are located within the chaotic regime. Negative flow disappears at the bifurcation between the 4-state and the 2-state regime, $\gamma = 0.5262$, a much lower value than the higher limit for negative flow $\gamma_{i2} = 1.189$.

Table 1 shows the critical values of γ corresponding to changes of regime. Up to the first chaotic regime ($\gamma = 0.4409$), the behaviour follows the usual period doubling cascade scenario. Between $\gamma = 0.4467$ and $\gamma = 0.4479$, a "periodicity windows" [2, 3] is obtained, with 6-state, then 12-state and 24-state regimes (but no 3-state regime). Above the value $\gamma = 0.4409$ for which chaos starts, an "inverse cascade" type scenario is observed, then intermittences occur, chaos again, and finally the "backward cascade" to the static regime. We did not try to obtain the same accuracy for the values of all different thresholds, because the ranges for γ have very different widths; for some values of γ, it has been necessary to make up to 2,000 iterations, and sometimes it is not obvious to distinguish between a chaotic regime, a long transient, or an intermittency regime.

5 Iterated functions

We now discuss how the iterated functions can be used to study the different regimes and their stability. We write $f^{(2)}(x)$ the second iterate of f, and more generally $f^{(n)}(x)$ its iterate of order n; the derivative of f with respect to x is $f'(x)$. Around the fixed point x^* of the first iterate $f(x)$, a Taylor expansion gives

$$\begin{aligned} f(x) &= f(x^*) + (x - x^*) f'(x^*) + \cdots \\ &= x^* + (x - x^*) f'(x^*) + \cdots , \end{aligned}$$

which provides the well-known stability condition for a fixed point x^* of $f(x)$:

$$|f'(x^*)| < 1. \tag{25}$$

Since the derivative of the iterate of order n is given by:

$$f^{(n)\prime}(x^*) = f'(x^*) f^{(n-1)\prime}(x^*)$$

one can show by recurrence that, when $x = x^*$, it is equal to the nth power of the derivative of f, so that

$$f^{(n)}(x) = x^* + (x - x^*)[f'(x^*)]^n + \cdots \tag{26}$$

Table 1 Values of the parameter γ at the *lower* limit of the different regimes, corresponding to Fig. 5. I = intermittencies; C = crescendo; D = decrescendo; PW = periodicity windows

From $\gamma =$	Regime	Comments	From $\gamma =$	Regime	Comments
0	1-state		0.4540	24-state	
0.3545	2-state		0.4542	12-state	
0.4272	4-state		0.4544	6-state	
0.4384	8-state		0.466216	I	
0.4403	16-state		0.4664	chaos	
0.4408	32-state		0.46945	60-state	
0.4409	chaos	$\gamma_{i1} = 0.4454$	0.4695	20-state	
0.4467	6-state	PW	0.4696	chaos	
0.4474	12-state	PW	0.46985	4-state	
0.4476	24-state	PW	0.5000	2-state (D)	
0.4479	chaos	$\gamma_b = 0.4503$	0.53	2-state (C)	
0.4538	36-state		1.	1-state (D)	$\gamma_{i2} = 1.189$
0.4539	chaos		6.3544	1-state (C)	

If the fixed point is stable (resp. unstable) with respect to $f(x)$, it is also stable (resp. unstable) with respect to any iterate. If x is a vector, instead of a scalar, this linearized approach leads to the Floquet matrix, and $f'(x)$ should be replaced by the eigenvalues of the matrix.

5.1 Stability of the period doubling regimes

Examples of iterated functions of order 1, 2, and 4 are shown in Figs. 6 and 7, with the same values of ζ and λ as in Fig. 5; in the former, the blowing pressure γ is 0.31, in the latter, γ is 0.42. The first iterate has a unique fixed point, $M^* = (x^*, x^*)$, located by definition on the first diagonal. The fixed point is stable if the absolute value of the derivative at M^* is smaller than unity, in other words if the tangent line lies between the first diagonal (with slope $+1$) and its perpendicular (with slope -1). When $\gamma = 0.31$, we see in Fig. 6 that the fixed point M^* is stable, so that no oscillation takes place. When γ increases, M^* becomes instable and, at the same time, gives rise to three fixed points of $f^{(2)}$. For $\gamma = 0.42$, Fig. 7 shows that the tangent is outside the angle between the diagonal and its perpendicular, so that the fixed point is now unstable; on the other hand, the second iterate $f^{(2)}$ now has two more fixed points $M_1^{(2)}$ and $M_2^{(2)}$ with slopes less than 1 (in absolute value): we therefore have a stable 2-state regime.

The same scenario then repeats itself when γ continues to increase: at some value, points $M_1^{(2)}$ and $M_2^{(2)}$ become instable in turn (the corresponding slope exceeds 1 in absolute value), and both points $M_1^{(2)}$ and $M_2^{(2)}$ divide themselves into three fixed points of $f^{(4)}$; the two extreme new points have small slopes for this iterate, which leads to a 4-state stable regime. By the same process of successive division of fixed points

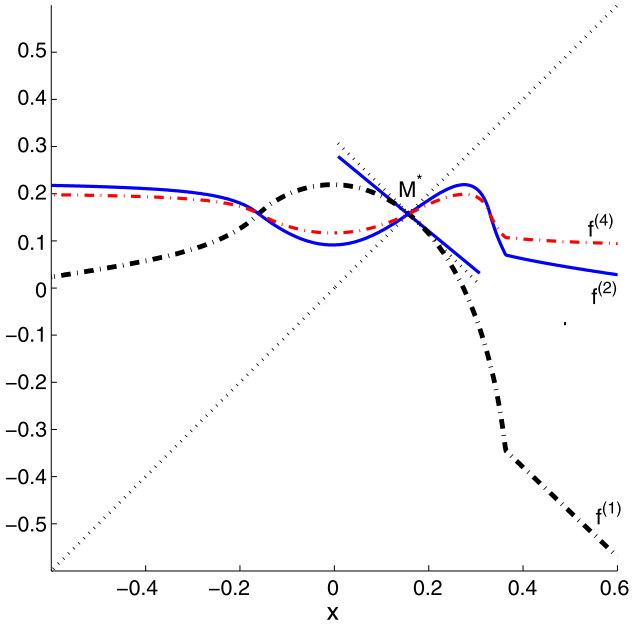

Fig. 6 Iteration functions for $\lambda = 0.95$, $\gamma = 0.31$, and $\zeta = 0.8$. The 1st iterate $f(x)$ is shown with a *mixed line*, the 2nd iterate $f^{(2)}(x)$ with a *solid line*, and $f^{(4)}(x)$ with a *thin mixed line*. The *dotted lines* are the first diagonal and the straight line perpendicular at the fixed point M^* of $f(x)$, solution of $f(x) = x$. The tangent lines to iterate 1 at the point M^* is shown with a *solid line*

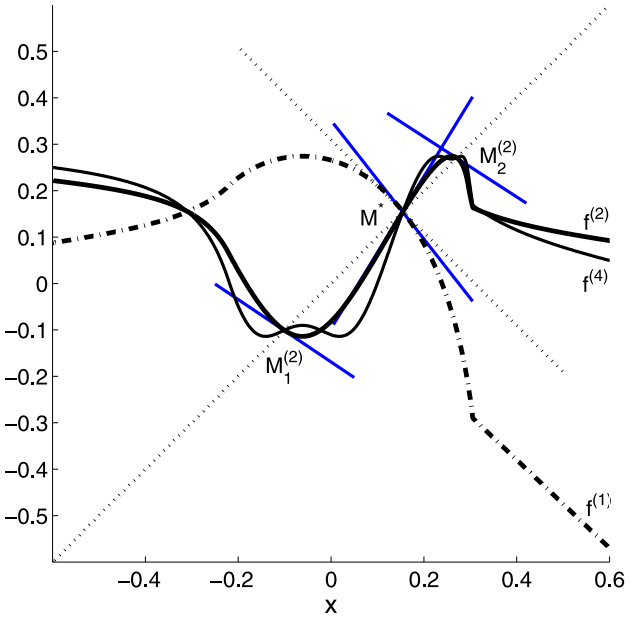

Fig. 7 Iterates for $\lambda = 0.95$, $\gamma = 0.42$, and $\zeta = 0.8$, with the same plots that in Fig. 6. The tangent lines at the new fixed points of $f^{(2)}(x)$, $M_1^{(2)}$, and $M_2^{(2)}$, are also shown

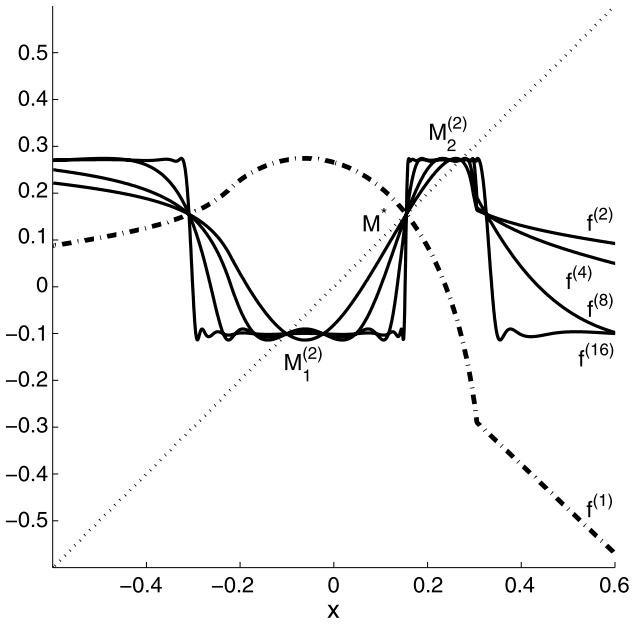

Fig. 8 Iterates for $\lambda = 0.95$, $\gamma = 0.42$ and $\zeta = 0.8$, of order 1, 2, 4, 8 and 16. The convergence to the 2-state regime is visible

of higher and higher iterates, one obtains an infinite number of period doublings, until eventually chaos is reached. This is the classical Feigenbaum route to chaos.

Some general remarks are useful to understand the shape of the iterates in the figures:

- If the value of $f(x)$ for the abscissa x verifies $f(x) = f(x^*)$, i.e. if the point $M(x,\ f(x))$ is on a horizontal line $y = x^*$, all iterates go through the same point;
- The extrema of $f^{(2)}(x)$ verify either $f'(x) = 0$ (i.e. $x = x_{\max}$) or $f^{(2)}(x) = f_{\max}$, because $df^{(2)}(x)/dx = f'[f(x)]f'(x)$; therefore, the extrema of $f^{(2)}(x)$ are at either the same abscissa or the same ordinate as those of $f(x)$;
- More generally, for $n > 1$, if $f^{(n-1)}(x) = x_{\max}$, then $f^{(n)}(x) = f_{\max}$, and it is at a maximum (its first derivative vanishes and the second one is negative), and if $f^{(n-1)}(x) = f_{\max}$, then $f^{(n)}(x) = f_{\min}$, and it is at a minimum (its first derivative vanishes and the second one is positive);
- The kink of the first iterate (beating limit point) is also visible on the iterates;
- A well-known property of the Schwarzian derivative is as follows. If the Schwarzian derivative of $f(x)$ is negative, the Schwarzian derivatives of all iterates are negative as well.

Figure 8 shows the higher order iterates (of order 4, 8 and 16) in the same conditions as Fig. 7. We observe that the iterates become increasingly close together when their order increases, with smaller and smaller slopes at the fixed points corresponding to the 2-state regime. Moreover, they resemble more and more a square function, constant in various domains of the variable. This was expected: in the limit of very large orders, whatever the variable is (i.e. whatever the initial conditions of the iteration are) one reaches a regime where only two values of the outgoing wave amplitude are possible; these values then remain stable, meaning that the action of more iterations will not change them anymore. So, one can read directly that the limit cycle is a 2-state on the shape of $f^{(16)}$, which has two values; it would for instance have 4 in the limit cycle was a 4-state regime for these values of the parameters. For the clarity of the figure, we have shown only iterates with orders that are powers of 2, but it is of course easy to plot all iterates. For a 2-state regime, even orders are sufficient to understand the essence of the phenomenon, since odd order iterates merely exchange the two fixed points $M_1^{(2)}$ and $M_2^{(2)}$.

In Table 1, the existence of two different stable regimes for the same value of the parameters signals an inverse bifurcation; Figure 9 shows an example of such a situation. For $\gamma = 1.2$, both the static and

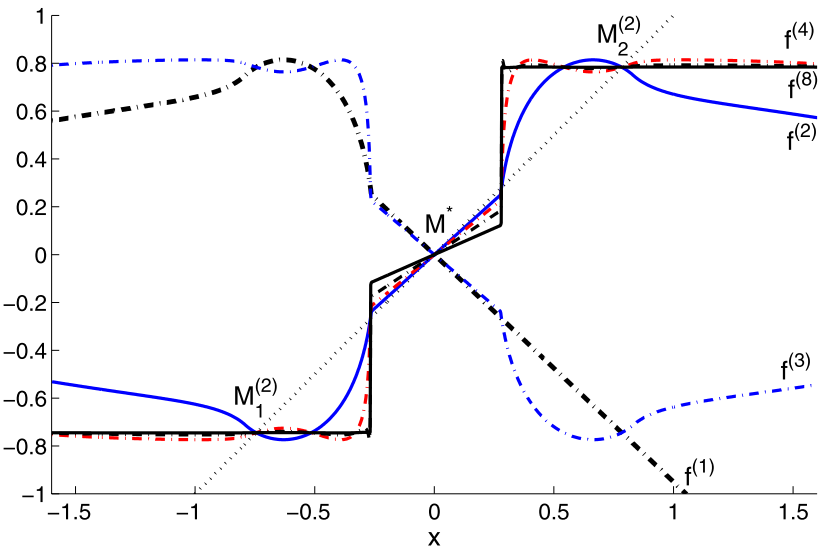

Fig. 9 Iterates for $\lambda = 0.95$, $\gamma = 1.5$, and $\zeta = 0.8$, of order 1, 2, 3, 4, and 8. The curves of $f^{(8)}$ and $f^{(16)}$ are almost perfectly superimposed. Around $x = 0$, the convergence to the static regime appears to be very slow. On the contrary the convergence to the 2-state regime is rapid

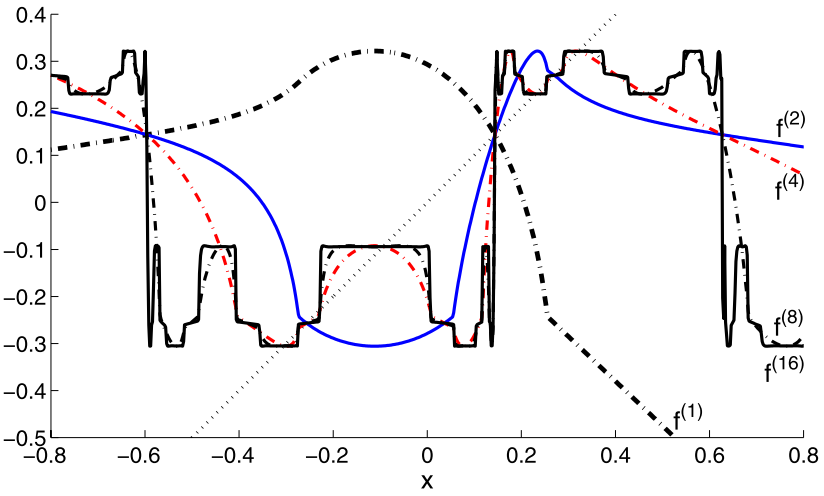

Fig. 10 Iterates for $\lambda = 0.95$, $\gamma = 0.515$ and $\zeta = 0.8$, of order 1, 2, 4, 8, and 16.

2-state regimes are then stable, depending on the initial conditions. For the static regime, the curve $f^{(1)}$ coincides with the second diagonal $y = -x$, a case in which the fixed point is presumably stable (the stability becomes intuitive when one notices that the tangents of the higher order curves lie within the angle of the two diagonals). For the 2-state regime, the state of positive pressure value corresponds to a beating reed.

Finally, Fig. 10 shows another case of existence of two different regimes for the same value of the parameters. A 2-state regime can occur, as well as a 4-state regimes can occur. It appears that the second one is more probable than the first one, when initial conditions are varied.

5.2 Periodicity windows; intermittencies

We now investigate some regimes occurring in a narrow range of excitation parameter γ.

(i) We first examine a chaotic regime occurring just before a 6-state regime (period tripling) and the transition between the two regimes. Figure 11 shows the iterated functions of order 1, 2, 6, and 12. The 6th iterated function crosses the first diagonal at the same points than the first and the second iterates only, which means that no 6-state regime is expected. By contrast, the 12th iterate cuts the diagonal at more points, but with a very high slope, indicating that the corresponding fixed points cannot be stable. This combined with the fact that no convergence to a square function (constant by domains), such as $f^{(16)}$ in Fig. 8, suggests an aperiodic behavior; the time dependent signal shown in Fig. 12 looks indeed chaotic (nevertheless the flow always remains positive). The periodic/chaotic character of the signal can be distinguished by examining the time series, but a complementary method is the computation of an FFT. For the signal of Fig. 12,

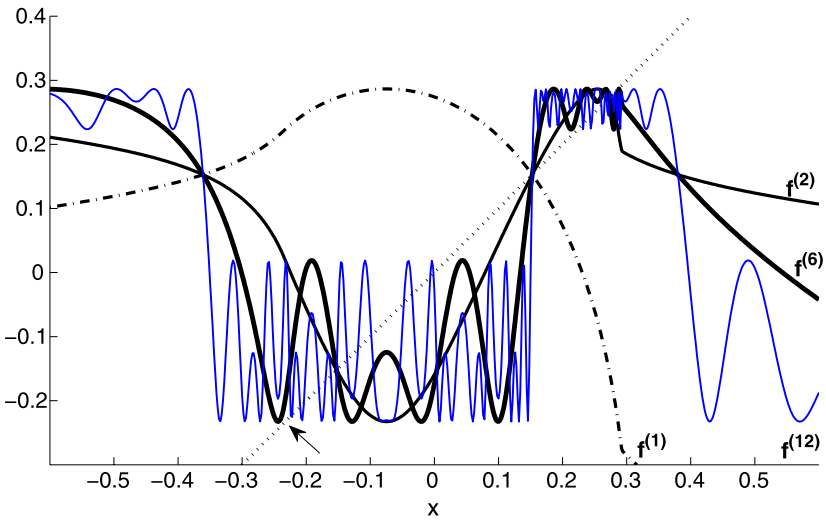

Fig. 11 Iterates for $\lambda = 0.95$, $\gamma = 0.4445$, and $\zeta = 0.8$, of order 1, 2, 6, and 12. A convergence to an aperiodic regime is visible. The arrow indicates a region where $f^{(6)}(x)$ is very close to the first diagonal, but does not yet cross it

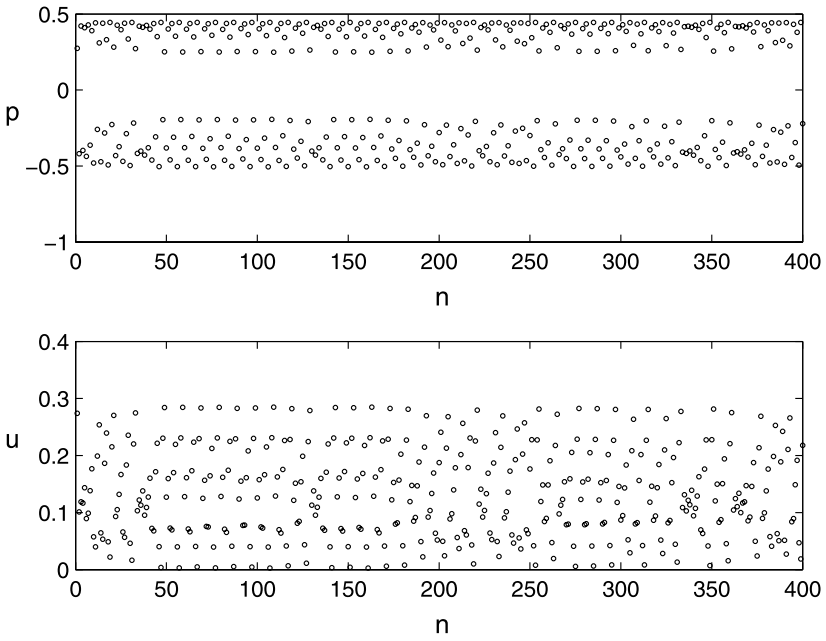

Fig. 12 Iteration from $n = 0$ for $\lambda = 0.95$, $\zeta = 0.8$, $\gamma = 0.4445$, $p_0^+ = 0$; the *upper part* shows the pressure p, the *lowest part* the values of the flow u. The regime looks chaotic

the spectrum is more regular than the spectrum of a 6-state periodic regime. Nevertheless, the frequencies of the latter (the "normal" frequency f_2 of the 2-state regime with the frequencies $f_2/3$ and $2f_2/3$) remains visible in the spectrum of the first one, as it is often the case for signals corresponding to very close values of the parameter. A consequence is that these frequencies clearly appear when listening the sound.

Figure 13 is similar to Fig. 11, but with a slightly larger value of γ (0.4469 instead of 0.4445). In the region indicated by the arrow, one notices that the 6th iterated function now cuts the first diagonal. They are 12 points of intersection (plus 1 common point with the first iterate as well as two common points with the second iterate, all unstable); the slope of the tangent shows that 6 of them are stable, so that one obtains a 6-state, periodic, regime. The variations of higher order iterates, e.g. $f^{(12)}$, remain very fast; the convergence to the limit cycle is then much slower than for Fig. 8, except if the initial point is close to a limit point (e.g. that shown by an arrow: it turns out that the 12th iterated function is very close to the 6th one). As a consequence, the initial transient to the 6-state regime can be rather chaotic, as shown in Fig. 14, but convergence to a periodic regime does occur later. This existence of periodic regimes above the threshold for chaos is

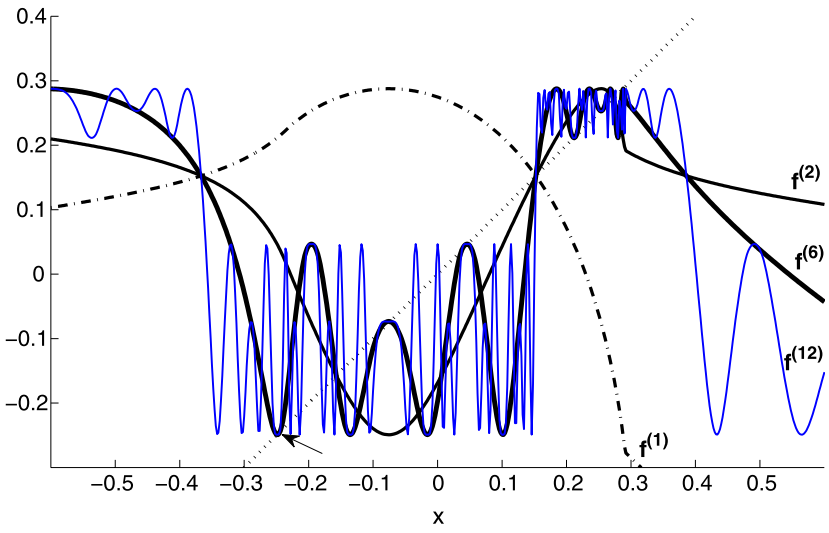

Fig. 13 Iterates for $\lambda = 0.95$, $\gamma = 0.4469$ and $\zeta = 0.8$, of order 1, 2, 6 and 12. A convergence to a 6-state regime is observed. The *arrow* indicates a region where $f^{(6)}(x)$ cuts the first diagonal

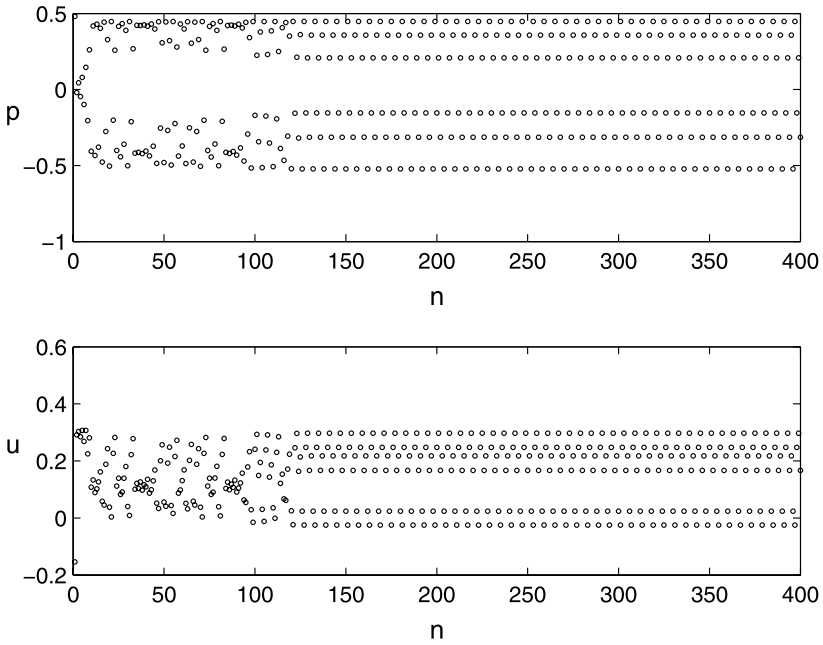

Fig. 14 Iteration from $n = 0$ for $\lambda = 0.95$, $\zeta = 0.8$, $\gamma = 0.4469$, $p_0^+ = -0.3347$. The regime is periodic (6-state)

called "periodicity windows", which appears as a narrow whiter region in Fig. 5. A difference with the usual 2^n-state regimes (when γ is below the chaotic range), for instance corresponding to Fig. 7, is that one obtains 2^n intersections with the diagonal, stable or unstable; by contrast, for the 6-state regime, they are 6 stable and 6 unstable points.

(ii) We now examine the transition between a 6-state regime and a 4-state regime through chaotic regimes or intermittency regimes. For $\gamma = 0.4544$, a 6-state regime is obtained. Figure 15 shows the iterates of order 1, 2, 4, and 6. The 4th and 6th iterates have common intersections with the first and second iterates, since both 4 and 6 are multiples of 2. The 6th iterate intersects the first diagonal at 12 other points, while the 4th cuts the diagonal at 4 points only. These 4 points are unstable, thus no 4-state regime can exist. On the contrary, for the 6th iterate, half of the 12 points are stable (i.e. with a small slope of the tangent line), so that one obtains a 6-state stable regime.

What happens for a higher value of γ, namely 0.472 corresponding to a 4-state regime is shown in Fig. 16, with again the iterates of order 1, 2, 4, 6. The 4th iterate curve crosses the diagonal for the same number of points than previously, but the 4 points

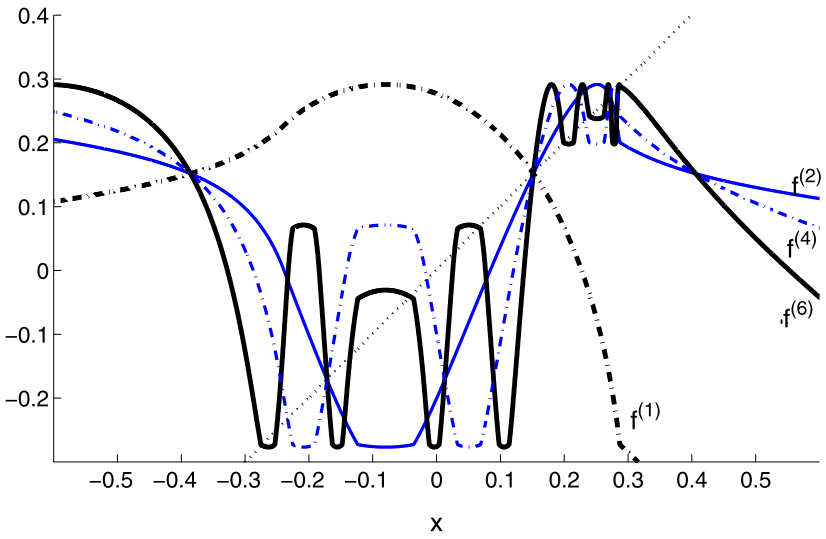

Fig. 15 Iterates for $\lambda = 0.95$, $\gamma = 0.4544$ and $\zeta = 0.8$, of order 1, 2, 4, and 6. A convergence to a 6-state regime is observed

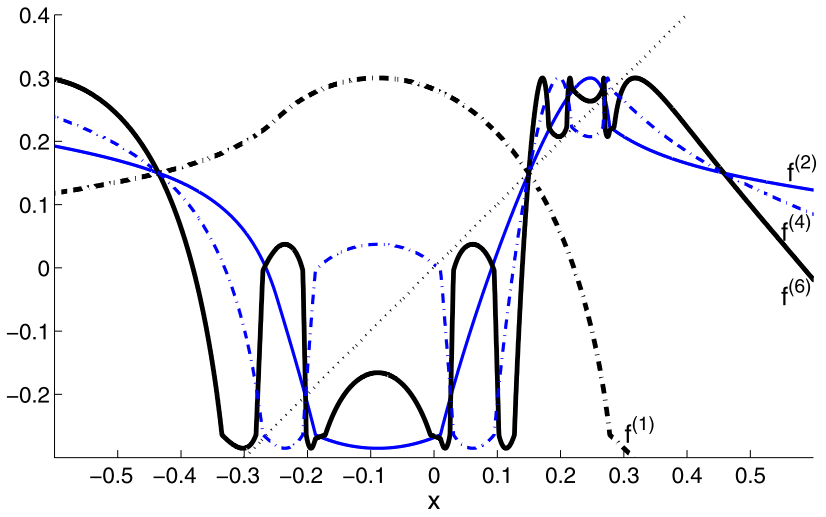

Fig. 16 Iterates for $\lambda = 0.95$, $\gamma = 0.472$, and $\zeta = 0.8$, of order 1, 2, 4, and 6. A convergence to a 4-state regime is observed

are now stable. The 6th order iterate does not intersect the diagonal, except at the common points with the two first iterates. Between the two preceding values of the parameter γ, both chaotic and intermittent regimes can exist. For $\gamma = 0.46623$, Fig. 17 shows intermittencies between a chaotic and a 6-state behaviours (upper curve), and Fig. 18 shows that the 6th iterate is tangent to the first diagonal in 6 points, so that the resulting permanent regime can be interpreted as a kind of "hesitation" between two behaviours. The 4 intersections of the 4th iterate remain unstable.

The lower curve in Fig. 17 shows another, more visible, example of intermittencies, obtained with slightly different values of the parameters, between a chaotic regime and a 4-state one (actually it is a 8-state one, very close to a 4-state regime).

6 Conclusion

The study of the iteration model of the clarinet should not be limited to the first iterate: higher order iterates give interesting information on possible regimes of oscillation. In the limit of very high orders, their shape gives a direct indication of the number of states involved in the limit regime, or of chaotic behavior. One can also predict an intermittent regime of the iterations, which takes place when an iterate is almost tangent to the first diagonal, so that the iterations are "trapped" for some time in a narrow channel. The phe-

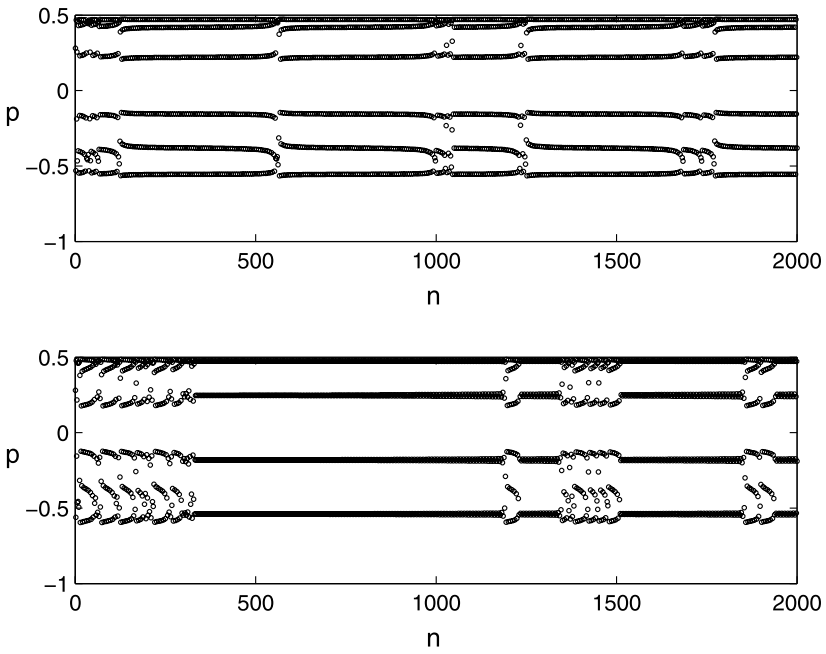

Fig. 17 Iteration from $n = 0$ for $\lambda = 0.95$, $\zeta = 0.8$, $\gamma = 0.46623$, $p_0^+ = 0$ (*upper curve*): Intermittencies between chaos and a 6-state regime are observed. However, the *lower curve* (for $\lambda = 1$, $\zeta = 0.8$, $\gamma = 0.467$, $p_0^+ = 0$) shows a more clear situation of intermittencies between chaos and a 4-state regime

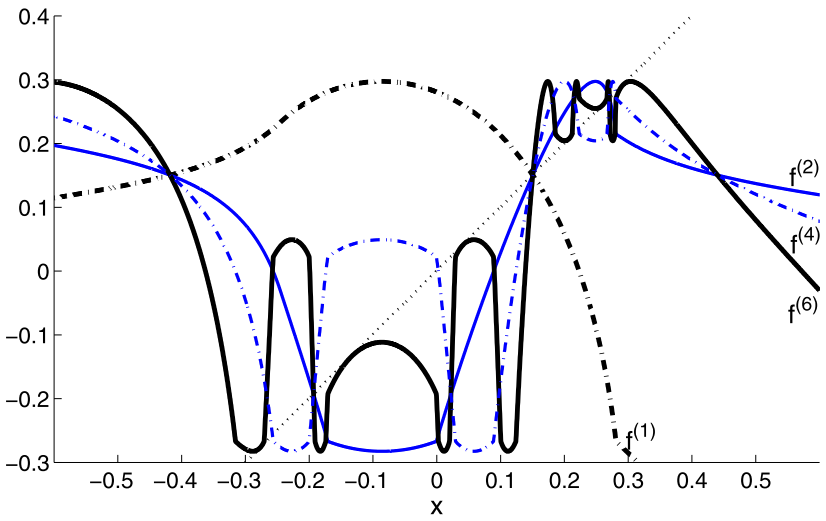

Fig. 18 Iterates for $\lambda = 0.95$, $\gamma = 0.46623$, and $\zeta = 0.8$, of order 1, 2, 4, and 6, corresponding to intermittencies. The sixth iterate is tangent to the diagonal

nomenon might be related to some kinds of multiphonic sounds produced by the instrument. It is true that this phenomenon takes place only in a rather narrow domain of parameters, but this is also the case of the period doubling cascade, which has been observed experimentally. One can therefore reasonably hope that the present calculations will be followed by experimental observations.

Acknowledgements This work was supported by the French National Agency ANR within the CONSONNES project. We thank also the Conservatoire neuchâtelois and the high school ARC-Engineering in Neuchâtel. Finally, we wish to thank Sami Karkar and Christophe Vergez for fruitful discussions.

Appendix A: Analytical iteration function

A.1 Derivation of the equations

Our purpose is to obtain an analytical expression of the iteration function $p_n^+ = f(p_{n-1}^+)$. From the basic model (Eqs. (3 to 5, 7, 11)), the following quantities can be defined:

$$X = \gamma - p_n = \gamma - p_n^+ - p_n^- = \gamma - p_n^+ + \lambda p_{n-1}^+;$$

$$Y = u_n + X = \gamma - 2p_n^- = \gamma + 2\lambda p_{n-1}^+.$$

$p_n^+ = g(\ p_n^-)$ can be obtained from the knowledge of the function $X(Y)$, given by the solving of:

$$Y = X \quad \text{(beating reed, } X > 1\text{);} \tag{27}$$

$$Y = X + \zeta(1-X)\sqrt{X} \quad \text{(non-beating reed, positive flow, } 0 < X < 1\text{);} \tag{28}$$

$$Y = X - \zeta(1-X)\sqrt{-X} \quad \text{(non-beating reed, negative flow, } X < 0\text{).} \tag{29}$$

For the non-beating reed case, the study of function $Y(X)$ leads to a direct analytical solution, as explained below, at least if $\zeta < 1$ (otherwise it is a multi-valued function).

Finally, with the notation $x = p_{n-1}^+$ and $f(x) = p_n^+$, if $\mathcal{Y}(X)$ is the Heaviside function, the iteration function is obtained as

$$f(x) = \gamma - X(Y) + \lambda x, \text{ with } Y = \gamma + 2\lambda x \text{ and} \tag{30}$$

$$Y(X) = X + \zeta sign(X)\,\mathcal{Y}(1-X)(1-X)\sqrt{|X|}. \tag{31}$$

A.2 Non-beating reed, positive flow ($0 \leq Y \leq 1$)

For this case, both X and Y are positive and smaller than unity, because $\zeta < 1$. Writing $Z = \sqrt{X}$, (28) is written as

$$G_1(Z) = Y,$$
$$\text{where } G_1(Z) = -\zeta Z\left[Z^2 - \frac{Z}{\zeta} - 1\right]. \tag{32}$$

The study of function $G_1(Z)$ shows that it is monotonously increasing from 0 to 1 when Z increases from 0 to 1. Therefore, the equation $G_1(Z) = Y$ has a unique solution when $0 \leq Y \leq 1$. With this condition, it appears that the equation has three real solutions, and that the interesting solution (located between 0 and 1) is the intermediate one. As a conclusion, it is possible to use the classical formula for the solution of the cubic equation:

$$\sqrt{X} = Z = -\frac{2}{3}\eta \sin\left[\frac{1}{3}\arcsin\left(\frac{\psi-\mu}{\zeta\eta^3}\right)\right] + \frac{1}{3\zeta};$$
$$\psi = \frac{1}{\zeta^2}; \quad \eta = \sqrt{3+\psi}; \quad \mu = \frac{9}{2}(3Y-1).$$

A.3 Non-beating reed, negative flow ($Y \leq 0$)

For this case, both X and Y are negative. Writing $Z = \sqrt{-X}$, Equation (29) is written as follows:

$$G_2(Z) = Y, \quad \text{where } G_2(Z) = -\zeta Z\left[Z^2 + \frac{Z}{\zeta} + 1\right]. \tag{33}$$

The study of the function $G_2(Z)$ shows that it is monotonously decreasing from 0 when Z increases from 0. Therefore, the equation $G_2(Z) = Y$ has a unique real, positive solution when $Y \leq 0$. The two other solutions are either real and negative or complex conjugate, with a negative real part, because the sum of the three solutions is negative ($-1/\zeta$). As a conclusion, the solution can be written by using the following formulae:

If the discriminant is positive

$$\text{discr} = q^3 + r^2 > 0, \quad \text{where}$$
$$q = \frac{1}{9}[3-\psi]; \quad r = -\frac{\psi+\mu}{27\zeta}.$$
$$\sqrt{-X} = Z = s_1 - \frac{q}{s_1} - \frac{1}{3\zeta}; \quad s_1 = \left[r + \sqrt{\text{discr}}\right]^{1/3}.$$

If the discriminant is negative

$$\text{discr} = q^3 + r^2 < 0$$
$$\sqrt{-X} = Z = \frac{2}{3}\eta' \cos\left[\frac{1}{3}\arccos\left(-\frac{\psi+\mu}{\zeta\eta'^3}\right)\right] - \frac{1}{3\zeta};$$
$$\eta' = \sqrt{-3+\psi}.$$

Appendix B: Negative flow limit

The condition of existence of negative flow is given by $x_i > f_{\min}$. This is equivalent to the condition on the antecedents, $x_i' < f_{\max}$, where x_i' is the larger antecedent of x_i, such as $x_i' > x_{\max}$, because $f(x)$ is decreasing for all $x > x_{\max}$ (see Fig. 2). Therefore, the volume flow is negative at time $n+1$.

In order to determine the limit value γ_i, the following equations are to be used:

$$X = \gamma - x_i + \lambda x_i' = \frac{\gamma}{2\lambda}(1+\lambda)^2 + \lambda A_\zeta; \tag{34}$$

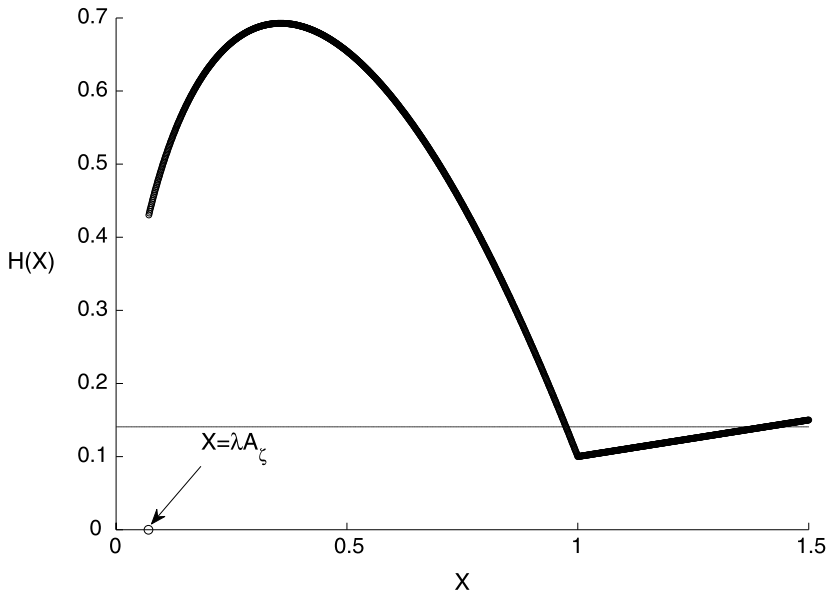

Fig. 19 Function $H(X)$ given by (37) and constant line $\delta = 2\lambda A_\zeta$. Two solutions $X > \lambda A_\zeta$ exits for this case ($\lambda = 0.9$, $\zeta = 0.9$), because condition (24) is satisfied

$$Y = \gamma + 2\lambda x_i' = \gamma(1+\lambda) + \lambda 2A_\zeta. \tag{35}$$

γ being positive (a reasonable hypothesis for the normal playing), the unknown X needs to be larger than the quantity λA_ζ. Eliminating γ in the above equations implies the following equation, with $X > \lambda A_\zeta$:

$$Y(X) - X = \frac{(\lambda-1)X + 2\lambda A_\zeta}{1+\lambda},$$

or

$$H(X) = \delta, \tag{36}$$

with

$$H(X) = (1+\lambda)[Y(X) - X] + (1-\lambda)X$$
$$\text{for } X > \lambda A_\zeta;\ \delta = 2\lambda A_\zeta. \tag{37}$$

An example of function $H(X)$ is shown in Fig. 19. It appears that no solutions exist if $H(1) > \delta$ and two solutions exist if $H(1) < \delta$, i.e. if inequation (24) holds. The two solutions can be obtained analytically. However, for sake of simplicity, we give the exact solution for the larger one, γ_{i2}, and an approximation for the smaller one, γ_{i1}, obtained at the first order in $\varepsilon = 1 - X$:

$$\gamma_{i2} = \frac{2\lambda^2 A_\zeta}{1-\lambda^2}; \tag{38}$$

$$\gamma_{i1} \simeq \frac{2\lambda}{(1+\lambda)^2}[1 - \lambda A_\zeta - \varepsilon], \tag{39}$$

$$\text{with } \varepsilon = \frac{\lambda - 1 + 2\lambda A_\zeta}{(\lambda+1)\zeta + \lambda - 1}. \tag{40}$$

This error is found to be less than 1% in comparison with the exact value. Condition (24) can be shown to be necessary and sufficient. We do not give the entire proof, but it can be shown that another necessary condition for having two solutions is $H'(1^-) < 0$, or $\zeta(\lambda+1) + \lambda - 1 > 0$, but it is implied by condition (24).

Figure 4 shows that the first negative flow threshold γ_{i1} is very close to the threshold γ_b, and slightly smaller. For a given λ, the limit value of ζ such as $\lambda > 1/(1+2A_\zeta)$ corresponds to the equality between the beating reed threshold and the negative flow one. For a given ζ, negative flow is possible above a certain value of λ. For rather strong losses, if $\lambda < 0.84$, no negative flow can occur. For a cylindrical resonator, this implies that $\alpha\ell > 0.085$.

References

1. May, R.M.: Simple mathematical models with very complicated dynamics. Nature **261**, 459–467 (1976)
2. Bergé, P., Pomeau, Y., Vidal, C.: Order within Chaos. Wiley/Hermann, New York (1986)
3. Bergé, P., Pomeau, Y., Vidal, C.: L'ordre dans le chaos. Hermann, Paris (1984)
4. Collet, P., Eckmann, J.P.: Properties of continuous maps of the interval to itself. In: Osterwalder, K. (ed.) Mathematical Problems in Theoretical Physics. Springer, Heidelberg (1979)

5. Collet, P., Eckmann, J.P.: Iterated Maps on the Interval as Dynamical Systems. Birkhäuser, Basel (1980)
6. Feigenbaum, J.: The universal metric properties of nonlinear transformations. J. Stat. Phys. **21**, 669–706 (1979)
7. Feigenbaum, J.: The metric universal properties of period doubling bifurcations and the spectrum for a route to turbulence. Ann. N.Y. Acad. Sci. **357**, 330–336 (1980)
8. McIntyre, M.E., Schumacher, R.T., Woodhouse, J.: On the oscillations of musical instruments. J. Acoust. Soc. Am. **74**, 1325–1345 (1983)
9. Maganza, C., Caussé, R., Laloë, F.: Bifurcations, period doubling and chaos in clarinetlike systems. Europhys. Lett. **1**, 295–302 (1986)
10. Brod, K.: Die Klarinette als Verzweigungssytem: eine Anwendung der Methode des iterierten Abbildungen. Acustica **72**, 72–78 (1990)
11. Kergomard, J.: Elementary considerations on reed-instrument oscillations. In: Hirschberg, A., Kergomard, J., Weinreich, G. (eds.) Mechanics of Musical Instruments. CISM Courses and Lectures, vol. 335, pp. 229–290. Springer, Wien (1995)
12. Lizée, A.: Doublement de période dans les instruments à anche simple de type clarinette, Master degree thesis, Paris (2004). http://www.atiam.ircam.fr/Archives/Stages0304/lizee.pdf
13. Idogawa, T., Kobata, T., Komuro, K., Masakazu, I.: Nonlinear vibrations in the air column of a clarinet artificially blown. J. Acoust. Soc. Am. **93**, 540–551 (1993)
14. Gibiat, V., Castellengo, M.: Period doubling occurences in wind instrument musical performances. Acustica United Acta Acustica **86**, 746–754 (2000)
15. Kergomard, J., Dalmont, J.P., Gilbert, J., Guillemain, P.: Period doubling on cylindrical reed instruments. In: Proceedings ot the Joint Congress CFA/DAGA'04, pp. 113–114, Strasbourg, 22–25th March 2004
16. Ollivier, S., Kergomard, J., Dalmont, J.-P.: Idealized models of reed woodwinds. Part II: On the Stability of "Two-Step" Oscillations. Acta Acustica United Acustica **91**, 166–179 (2005)
17. Dalmont, J.-P., Gilbert, J., Kergomard, J., Ollivier, S.: An analytical prediction of the oscillation and extinction thresholds of a clarinet. J. Acoust. Soc. Am. **118**, 3294–3305 (2005)
18. Vallée, R., Delisle, C.: Periodicity windows in a dynamical system with delayed feedback. Phys. Rev. A **34**, 309–3018 (1986)
19. Stefanski, K.: Universality of succession of periodic windows in families of 1D-maps. Open Syst. Inf. Dyn. **6**, 309–324 (1999)
20. Wilson, T.A., Beavers, G.S.: Operating modes of the clarinet. J. Acoust. Soc. Am. **56**, 653–658 (1974)
21. Hirschberg, A., Van de Laar, R.W.A., Marrou-Maurires, J.P., Wijnands, A.P.J., Dane, H.J., Kruijswijk, S.G., Houtsma, A.J.M.: A quasi-stationary model of air flow in the reed channel of single-reed woodwind instruments. Acustica **70**, 146–154 (1990)
22. Dalmont, J.-P., Gilbert, J., Ollivier, S.: Nonlinear characteristics of single-reed instruments: quasistatic volume flow and reed opening measurements. J. Acoust. Soc. Am. **114**, 2253–2262 (2003)
23. Dalmont, J.-P., Frappé, C.: Oscillation and extinction thresholds of the clarinet: Comparison of analytical results and experiments. J. Acoust. Soc. Am. **122**, 1173–1179 (2007)
24. Caussé, R., Kergomard, J., Lurton, X.: Input impedance of brass musical instruments—comparison between experiment and numerical model. J. Acoust. Soc. Am. **75**, 241–254 (1984)
25. Raman, C.V.: On the mechanical theory of vibrations of bowed strings [etc.]. Indian Assoc. Cultiv. Sci. Bull. **15**, 1–158 (1918)
26. Mayer-Kress, G., Haken, H.: Attractors of convex maps with positive Schwarzian derivative in the presence of noise. Physica D **10**, 329–339 (1984)
27. Parlitz, U., Englisch, V., Scheffczyk, C., Lauterborn, W.: Bifurcation structure of bubble oscillators. J. Acoust. Soc. Am. **88**, 1061–1077 (1990)
28. Scheffczyk, C., Parlitz, U., Kurz, T., Knop, W., Lauterborn, W.: Comparison of bifurcation structures of driven dissipative nonlinear oscillators. Phys. Rev. A **43**, 6495–6502 (1991)

10ème **C**ongrès **F**rançais d'**A**coustique

Lyon, 12-16 Avril 2010

Cartes itérées appliquées à un instrument de type clarinette

Pierre-André Taillard[1], Jean Kergomard[2], Franck Laloë[3], Sami Karkar[2]

[1] Conservatoire de musique, Avenue Léopold-Robert 34, 2300 La Chaux-de-Fonds, Suisse, taillard@hispeed.ch

[2] LMA, CNRS UPR 7051, 31, Chemin J. Aiguier - 13402 Marseille Cedex 20, {kergomard, karkar}@lma.cnrs-mrs.fr

[3] Laboratoire Kastler Brossel, ENS, UMR CNRS 8552, 24 Rue Lhomond, F-75231 Paris Cedex 05, laloe@lkb.ens.fr

Mc Intyre et coll. (1983) ont montré que l'on peut ramener le calcul des oscillations d'une clarinette à une simple itération, dans un modèle où le résonateur est cylindrique avec des pertes indépendantes de la fréquence, et où l'anche est vue comme un ressort sans inertie. Pour cela on choisit le couple des ondes aller et retour comme variables de base, et le système peut se ramener à l'itération d'une fonction f(x) qui relie les amplitudes de ces ondes, conduisant à des oscillations en signaux carrés. Nous donnons une étude plus approfondie de cette fonction et en déduisons un encadrement des valeurs des paramètres d'excitation pour lesquelles l'anche peut battre, ou encore pour lesquelles le signe du débit peut s'inverser. Les fonctions itérées de la fonction f(x) renseignent notamment sur la stabilité des régimes périodiques, ou aident à comprendre l'existence de régimes chaotiques, de fenêtres de périodicité ou d'intermittences.

1 Introduction

Clarinette et cartes itérées Dans leur article bien connu, Mc Intyre et coll. [1] ont proposé pour les instruments de musique auto-oscillants un modèle générique très simple reposant sur deux éléments : une fonction non linéaire (excitation) et une impédance d'entrée (résonateur, corde ou tuyau). Dans le cas d'un instrument cylindrique à anche simple, de type clarinette, ces deux éléments relient pression dans le bec et débit d'entrée dans le résonateur ; plusieurs articles ont traité d'un cas très simple, où le résonateur est sans pertes ou avec pertes indépendantes de la fréquence (l'anche est vue comme un simple ressort), en calculant des cycles limites à deux états (signaux carrés) et leur stabilité [2, 3, 4, 5, 6]. Dans une annexe, Mc Intyre et coll. remarquent que avec ces hypothèses, si on utilise une fonction de réflexion - onde retour/onde aller - pour caractériser le résonateur, le modèle se ramène à un simple modèle de cartes itérées. La valeur de l'onde aller à deux instants distants de $2\ell/c$ (temps d'aller et retour dans le tuyau, c étant la vitesse du son, et ℓ la longueur) se déduit par simple itération d'une fonction non linéaire. Cette dernière est obtenue par transformation de la fonction non linéaire physique (débit/pression), appelée caractéristique non linéaire et notée ci-après $\mathcal{C}$, supposée quasi-statique.

C'est cette idée que nous avons souhaité développer, en poussant l'utilisation des itérées plus loin que celles d'ordre 2, les itérées d'ordre plus élevé donnant des informations utiles sur les régimes d'oscillation possibles.

Caractéristique non linéaire $\mathcal{C}$ débit-pression Le choix de la caractéristique $\mathcal{C}$ aujourd'hui le plus courant repose sur un modèle simplifié d'équation de Bernoulli pour l'écoulement dans le canal entre anche et bec, et la création d'un jet à sa sortie [7] (cf fig. 1). La comparaison expérience-théorie a été menée avec succès [8] pour l'amplitude de la pression acoustique dans le bec dans le cas de sons "normaux", dont l'approximation est un signal carré de fréquence fondamentale $c/4\ell$.

Ceci justifie le choix de cette forme de caractéristique pour l'étude avec les cartes itérées. Cette forme se divise en trois parties :

1. pour les grandes différences de pression entre la bouche de l'instrumentiste et le bec, l'anche plaque (ou bat[1]) et le débit est nul (expérimentalement il ne l'est pas tout à fait, mais on peut se contenter de ce modèle) ;

2. pour les différences de pression plus faibles mais positives, le vitesse dans le canal anche-bec croît comme la racine carrée de la différence de pression (équation de Bernoulli), et donc aussi le débit, mais ce dernier décroît ensuite en raison de la force de rappel de l'anche, jusqu'à s'annuler ;

3. enfin, si la pression dans la bouche est inférieure à celle dans le bec, le débit est négatif ; cette partie du modèle n'a en fait jamais été confrontée à l'expérience. Elle semble surprenante, puisque la source d'énergie est bien la surpression dans la bouche du musicien ; nous discutons cet aspect plus loin.

La figure 1 montre ces trois parties. Elles sont délimitées par les points de contact M_b et d'inversion M_i. Il y a trois paramètres, que nous choisissons sans dimensions, avec les notations d'articles précédents :

1. la pression dans la bouche, supposée constante, notée γ ; elle est toujours positive, et vaut 1 à la limite de placage de l'anche en régime statique ;

2. le débit maximum qui peut entrer dans le tuyau, lié notamment à l'ouverture du canal d'anche au repos et sa raideur, noté ζ ; les expériences montrent qu'il se

[1] Nous employons le terme "plaquer" pour le régime statique, l'anche ne décollant pas, et "battre", en régime dynamique.

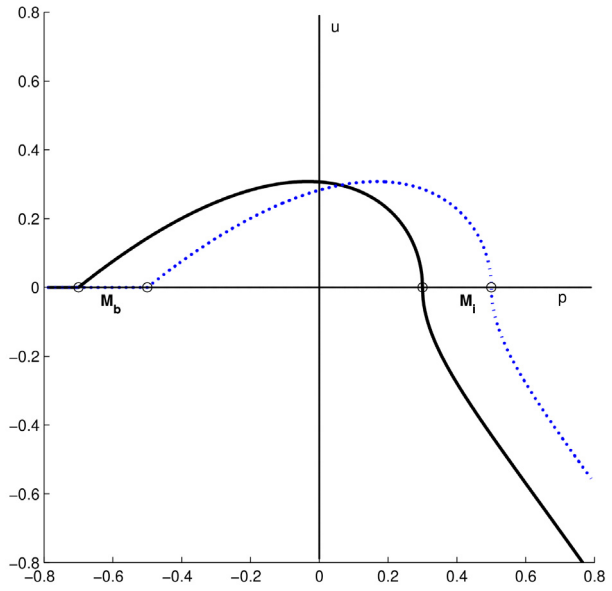

FIG. 1: Caractéristique non linéaire (débit entrant/pression dans le bec) pour une valeur donnée de la pression dans la bouche, supposée constante, $\gamma = 0.3$ (trait plein) et 0.5 (pointillé). Le paramètre $\zeta = 0.8$, n'est qu'un facteur multiplicatif. La fonction physique est en fait une fonction de la différence de pression (bouche - bec) ; augmenter la pression dans la bouche γ revient donc à translater cette courbe vers la droite. Les deux cercles marquent les limites entre les trois parties de la courbe : la limite de contact anche-bec, M_b, et le point d'inversion du débit, M_i.

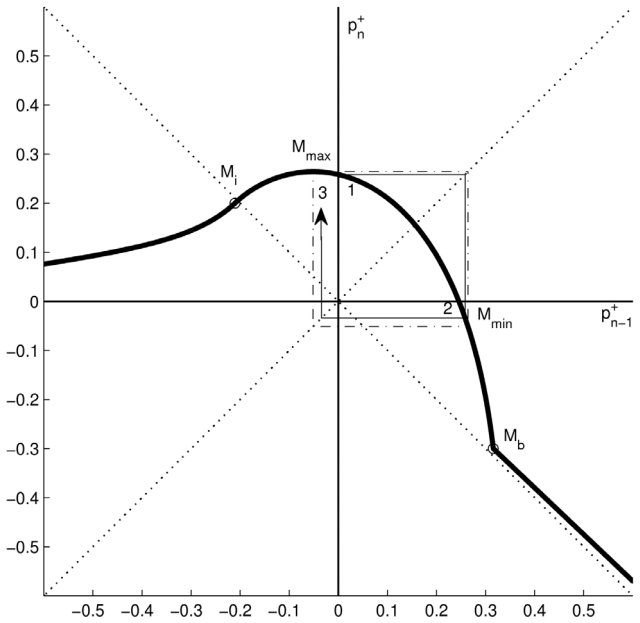

FIG. 2: Fonction non linéaire reliant l'onde aller à l'instant t, notée p_n^+ à l'onde aller à l'instant $t-2\ell/c$, p_{n-1}^+. Les paramètres sont $\gamma = 0.4$ $\zeta = 0.8$ $\lambda = 0.95$ En pointillé le carré limité par les valeurs f_{min} et f_{max} pour l'abscisse et l'ordonnée. Nous montrons aussi le début d'une itération pour une condition initiale donnée (points 1, 2, 3)

situe en général entre $0,2$ et $0,4$, mais ce sont les valeurs élevées qui peuvent produire des régimes "anormaux" (on suppose cependant qu'il est toujours inférieur à l'unité) ;

3. le paramètre de pertes λ, rapport des amplitudes des ondes (retour/aller), des valeurs typiques étant $0,9$ à $0,95$. Il correspond aux pertes près des parois et par rayonnement, la variation en fréquence étant ignorée.

La simple étude de la fonction non linéaire déduite de la caractéristique $\mathcal{C}$ (cf figure 2) permet de trouver des conditions pour que l'anche puisse battre ou que le débit devienne négatif. C'est l'objet du paragraphe 3, le paragraphe 2 montrant comment on calcule les cartes itérées. Ayant montré un exemple de schéma de bifurcation obtenu par expérience numérique, nous montrons au § 4 l'intérêt des fonctions itérées pour l'étude de la convergence, c.-à-d. de la durée des transitoires, et de la stabilité des régimes (cycles limites).

2 Cartes itérées (calcul ab initio)

La caractéristique $\mathcal{C}$ relie débit u entrant dans le résonateur et pression p dans le bec. D'après la décomposition de d'Alembert, la pression est à chaque instant la somme de l'onde aller p^+et l'onde retour p^-dans le tuyau, tandis que le débit est leur différence (compte tenu de l'adimensionnement). À l'instant initial, on suppose que la pression dans la bouche saute brutalement de $t = 0$ à la valeur notée γ puis reste constante. Pendant la durée $\tau = 2\ell/c$, temps d'un aller-retour dans le tuyau, il n'y a pas d'onde retour, et on a donc $p = u = p^+$, ce qui avec la caractéristique non linéaire donne la condition initiale, inchangée pendant la durée τ. Puis l'onde retour arrive à l'entrée :

$$p^-(t) = -\lambda p^+(t-\tau). \tag{1}$$

Le signe $-$ vient de la simplification de la condition aux limites (pression nulle). On peut donc en déduire les grandeurs acoustiques pendant l'intervalle $[\tau, 2\tau]$, et ainsi de suite. Il est alors légitime de discrétiser le temps, et de ne considérer que les instants $n\tau$. L'équation (1) est notée :

$$p_n^- = -\lambda p_{n-1}^+. \tag{2}$$

On peut la transformer en une relation entre pression et débit, qui n'est autre qu'une condition d'impédance (transformée dans le domaine temporel, et déduire à chaque instant les valeurs des grandeurs physiques grâce à la caractéristique $\mathcal{C}$, qui lie u_n à p_n. Ceci est utile en particulier pour rechercher les cycles limites. Mais pour s'intéresser aux transitoires, mieux vaut conserver l'éq. (2) et transformer la fonction non linéaire, en recherchant la fonction liant p_n^+et p_n^-. On tire alors de ces deux équations la relation de base de la méthode :

$$p_n^+ = f(p_{n-1}^+). \tag{3}$$

L'onde aller est donc obtenue par un simple calcul d'itération de la fonction f, ou carte itérée. La fonction f est obtenue simplement à partir de $\mathcal{C}$, et l'éq. (3) pour le modèle considéré est une équation du 3^e degré. Dans le cas sans pertes ($\lambda = 1$), la fonction est obtenue par

simple rotation de 45° de $\mathcal{C}$. Partant de la condition initiale, on peut donc calculer un transitoire (cf figure 2) ou, en faisant un varier le paramètre principal, la pression dans la bouche γ, un schéma de bifurcation avec par exemple 1000 pas de temps, c.-à-d. 1000 itérations : pour ce faire, on doit admettre que la convergence a bien eu lieu, ce qui bien entendu n'est pas vrai pour les régimes chaotiques, ou les transitoires très longs.

Un exemple de régime chaotique est montré par la figure 3. Il apparaît comme une sorte succession de différents régimes à 6 états. La figure 4 montre le spectre FFT pour ce régime : on voit qu'il y a une superposition d'un spectre continu et d'un spectre de raies, contenant principalement la raie principale (fréquence $c/2\ell$). Ceci est classique, car on entend toujours la fréquence du régime de base (à deux états) dans un régime chaotique. La même figure compare ce spectre à celui d'un régime périodique à 6 états, obtenu pour une valeur très proche du paramètre d'excitation γ : on n'a pas non plus exactement un spectre de raies, mais ceci est dû à la troncature du signal.

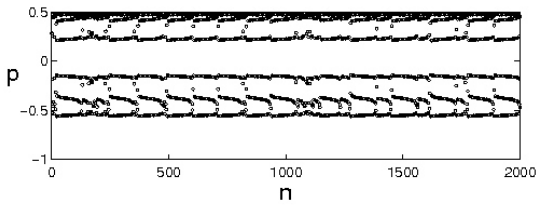

FIG. 3: Valeurs de la pression pour 2000 itérations. On a l'impression d'une succession de régimes à 6 états, la figure 4 montrant que le régime est chaotique. ($\gamma = 0.4664$ $\zeta = 0.8$ $\lambda = 0.95$)

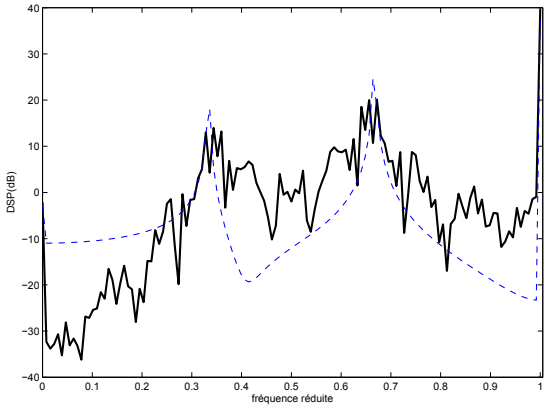

FIG. 4: Spectre de la pression pour le cas montré par la figure 3 en trait plein, comparé à un régime périodique à 6 états, en pointillé ($\gamma = 0.4467$ $\zeta = 0.8$ $\lambda = 0.95$). La fréquence 1, c.-à-d. la fréquence normale de jeu, $c/4\ell$, est très présente.

La figure 5 montre un exemple de schéma de bifurcation : on remarque que le débit peut s'annuler et devenir négatif. La première partie du schéma, jusque environ $\gamma = 0.44$ est un schéma classique de route vers le chaos par doublement de période [9, 10, 11]. Il a été montré que ceci n'est possible qu'avec un grand paramètre ζ, et de faibles pertes. Expérimentalement un doublement de période a pu être observé sur certains instruments (cromorne, basson [12]).

À l'intérieur de la plage de régimes chaotiques, on trouve les classiques fenêtres de périodicités, avec des régimes à 6 états (nous n'avons pas trouvé de régimes à 3 états) ; ensuite on trouve une "cascade à l'envers", qui ramène à des régimes périodiques simples, à 4 états, 2 états ou un état. Ceci s'explique par la dépendance particulière des paramètres de la fonction, les régimes à deux états en anche battante, pour de grandes pressions γ, étant toujours stables. Notons que cette cascade à l'envers doit être distinguée d'une cascade inverse, plus classique, et que l'on trouve dans la plage de régimes chaotiques.

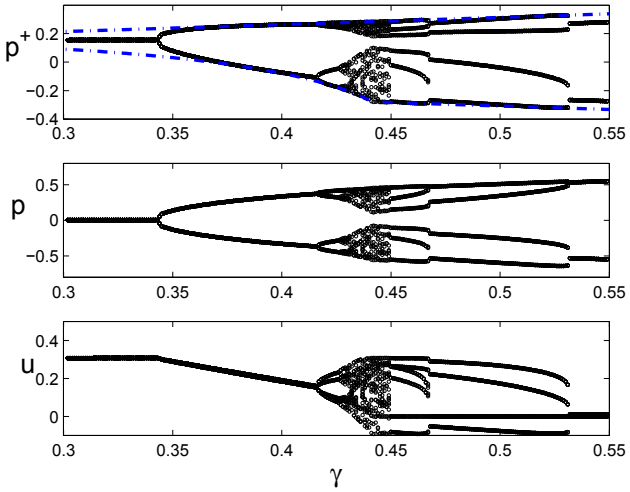

FIG. 5: Schéma de bifurcation obtenu par expérience numérique de 400 itérations pour des valeurs croissantes de la pression dans la bouche γ. En haut l'onde aller p_n^+, avec en pointillé les valeurs de f_{min} et f_{max}, au milieu la pression p_n, en bas le débit u_n.

3 Propriétés de la fonction non linéaire f (itérée d'ordre 1)

La fonction f présente un maximum $f_{\max}$ voisin de $\gamma/2$, qui est unique pour les valeurs de ζ supérieures à $1/\sqrt{3}$. On a $f_{\max} = \gamma/2 + A(\zeta)$, où $A(\zeta)$ est une fonction croissante de ζ ($A(0) = 0$, $A(1) = 5/54$). Pour les valeurs inférieures de ζ, il existe un maximum pour les très faibles valeurs de x, qui sont irréalistes, et à partir de quelques itérations, on arrive toujours en pratique dans le carré représenté sur la figure 4. On montre que les limites de ce carré sont $f_{\min} = f(f_{\max})$, à condition que la fonction coupe le carré sur son côté gauche ($f(f_{\min}) > f_{\min}$). La figure 5 montre en pointillé les deux valeurs $f_{\min}$ et $f_{\max}$ qui encadrent les valeurs de l'onde aller p^+.

Un résultat intéressant est alors obtenu en cherchant à quelle condition portant sur γ, les points de contact M_c et d'inversion M_i sont situés dans le carré. L'anche

ne peut battre qu' à la condition suivante :

$$\gamma > \frac{1 - 2\lambda A(\zeta)}{1 + \lambda}. \quad (4)$$

On peut montrer que cette limite est inférieure à celle qui est appelée "seuil d'anche battante" dans des articles récents (voir par ex. [6]), qui ne considèrent que les régimes à deux états. Pour d'autres types de régimes, l'anche peut battre pour une pression dans la bouche plus faible. C'est ce que l'on voit sur les diagrammes déjà publiés [3]. Précisons que la condition (4) n'est pas suffisante pour que l'anche batte : il faut en outre que les régions correspondantes de la courbe soient effectivement explorées, et tout ce que l'on peut dire est qu'elles ont plus de chances de l'être en régime chaotique.

Ceci est un résultat nouveau simple, de même que celui qui concerne la condition pour que le débit puisse être négatif. Deux cas existent :

- $\lambda < 1/[1 + 2A(\zeta)]$. Les pertes ne sont pas très faibles. Le débit ne peut jamais être négatif, on peut montrer que c'est le cas le plus courant ;
- $\lambda > 1/[1 + 2A(\zeta)]$. Il existe pour γ une limite inférieure, très légèrement inférieure à celle donnée par (4), et une limite supérieure, entre lesquelles le débit peut être négatif. Là encore, les conditions pour que le débit soit négatif sont encore plus restrictives pour un régime à deux états.

Notons que la fonction $f(x)$ a une discontinuité de dérivée première en M_b. Notons enfin que la fonction $f(x)$ n'a en général pas les propriétés des fonctions les plus étudiées par les mathématiciens (cf par exemple [11]), ce que nous avons détaillé dans [13].

4 Emploi des itérées pour l'analyse des régimes d'oscillations

Nous commençons par rappeler quelques propriétés des fonctions itérées, notées $f^{(n)}(x) = f\left[f^{(n-1)}(x)\right]$. Si x^* est un point fixe de $f(x)$, c.-à-d. si $f(x^*) = x^*$, il est aussi point fixe de toutes les itérées. Ainsi sur la figure 6, l'itérée d'ordre 1 a un point fixe, et les itérées d'ordre 2 et 4 en ont trois.

Le régime correspondant à un point fixe est stable si la dérivée de $f(x)$ en ce point est en valeur absolue inférieure à l'unité. La figure 6 montre ainsi le point fixe 0 de l'itérée d'ordre 1 : le régime correspondant est le régime statique (à un seul état), et pour la valeur de γ choisie, il est instable parce que la tangente à la courbe n'est pas située entre les deux diagonales tracées en ce point. En revanche les points 1 et 2, qui sont les points fixes de l'itérée d'ordre 2, donnent lieu à un régime stable à deux états, puisque les tangentes sont bien situées par rapport aux diagonales. Toujours sur la même figure, on voit que l'itérée d'ordre 4 ne coupe pas la diagonale en d'autres points que celles d'ordre 1 et 2, et donc il ne peut exister de régimes à 4 états, stables ou non.

D'autres propriétés sont aisées à démontrer : ainsi toutes les itérées passent par le point $(x, f(x))$, situé sur la droite horizontale passant par x^*. Les extremums de l'itérée d'ordre 2 sont soit à la même abscisse, soit à la même ordonnée que ceux de l'itérée d'ordre 1. Le coin au point M_b (discontinuité de la dérivée) est également visible sur les itérées.

La figure 7 montre pour les mêmes valeurs des paramètres les itérées d'ordre 8 et 16. Pour une valeur de x donnée, donc pour une condition initiale donnée, on peut voir la convergence vers le régime périodique à 2 états quand le nombre d'itérations augmente. Comme nous n'avons choisi que des valeurs paires des ordres d'itérées, on ne voit pas l'alternance entre les points 1 et 2. Mais ceci permet de voir la rapidité de convergence, indépendamment de la condition initiale.

Pour terminer, nous analysons une situation plus complexe, celle de régimes chaotiques ou proches du chaos. La figure 8 nous montre, pour les valeurs des paramètres de la figure 3, que l'itérée d'ordre 12, pour l'exemple choisi, présente beaucoup plus d'oscillations que l'itérée d'ordre 6, ce qu'on peut mettre en relation avec le caractère chaotique du régime. Cependant l'analyse doit être très fine, car de tous petits changements peuvent aboutir à d'autres types de régime. Ainsi on remarque que l'itérée d'ordre 6 est presque tangente à la première diagonale en 6 points. En revanche quand cette itérée traverse la diagonale, elle la coupe donc en 12 points, et la moitié de ces points est nécessairement stable, ce qui explique le régime (stable) à 6 états. Le cas intermédiaire est le suivant : quand l'itérée d'ordre 6 est parfaitement tangente, on a un régime d'intermittences entre le régime chaotique, et le régime à 6 états. Il va de soi que l'observation expérimentale de ce type de transition est difficile, les régimes de ce genre n'existant que sur une très faible plage de paramètres. Pour un instrumentiste, c'est chose quasiment impossible, mais une expérience courante est que en choisissant des doigtés de fourches, donc un résonateur plus complexe que celui étudié dans cette communication, on peut obtenir une très grande variété de régimes, y compris des régimes à modulation de fréquence, en changeant progressivement le paramètre d'excitation. Un schéma de bifurcation complexe est donc une expérience courante ressentie par les instrumentistes [14].

5 Conclusion

Les cartes itérées permettent à la fois une interprétation des transitions de régimes, et un calcul simple de leur stabilité. Et l'étude de la fonction elle-même, ou itérée d'ordre 1, peut être très instructive pour analyser le comportement de modèle, comme ici le modèle de caractéristique non linéaire.

Remerciements

Ce travail a été réalisé dans le cadre du projet ANR CONSONNES. Nous remercions aussi Christophe Vergez pour ses remarques très utiles.

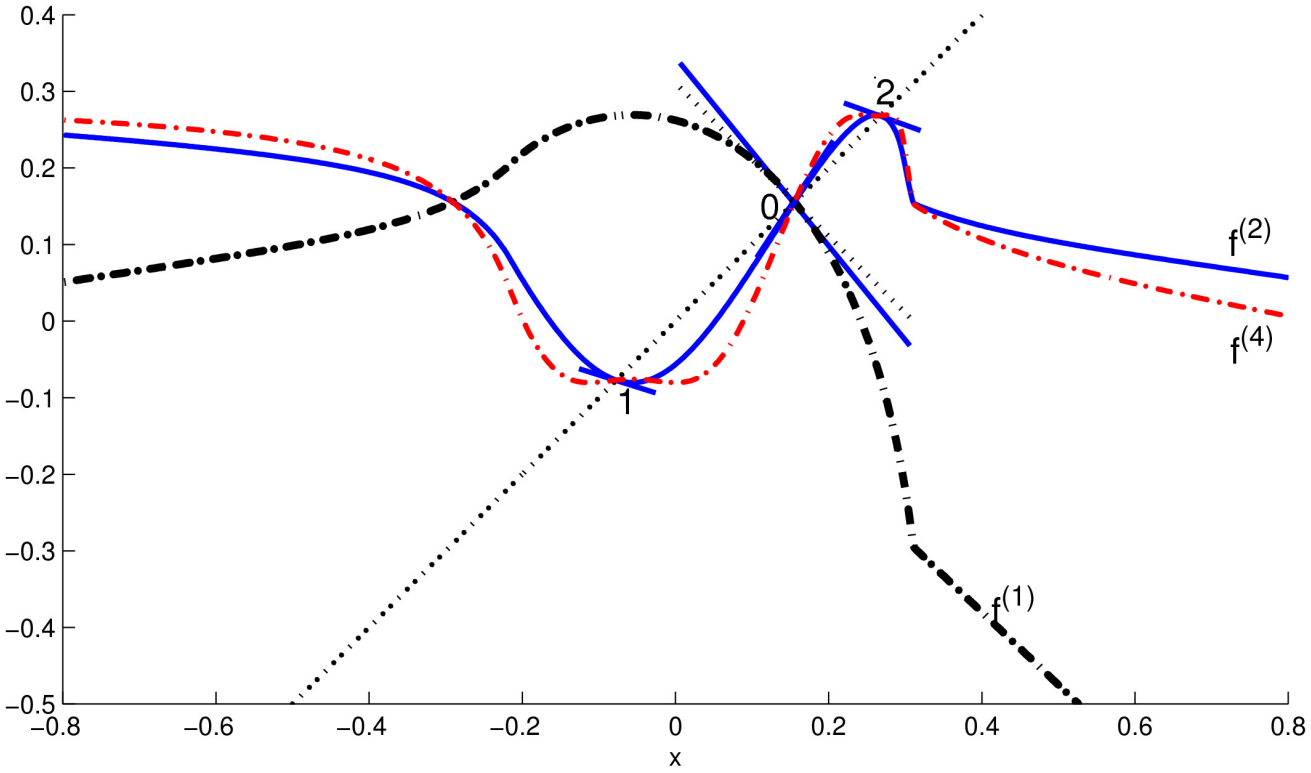

FIG. 6: Itérées d'ordre 1 , 2 et 4 pour des valeurs des paramètres correspondant à un régime à 2 points (1 et 2) stable, et un régime à 1 point (0) instable. $\gamma = 0.41$, $\zeta = 0.8$, $\lambda = 0.95$. Les points fixes des fonctions sont par définition sur la première diagonale. On a fait figurer les tangentes aux points fixes, ainsi que la deuxième diagonale au point 0.

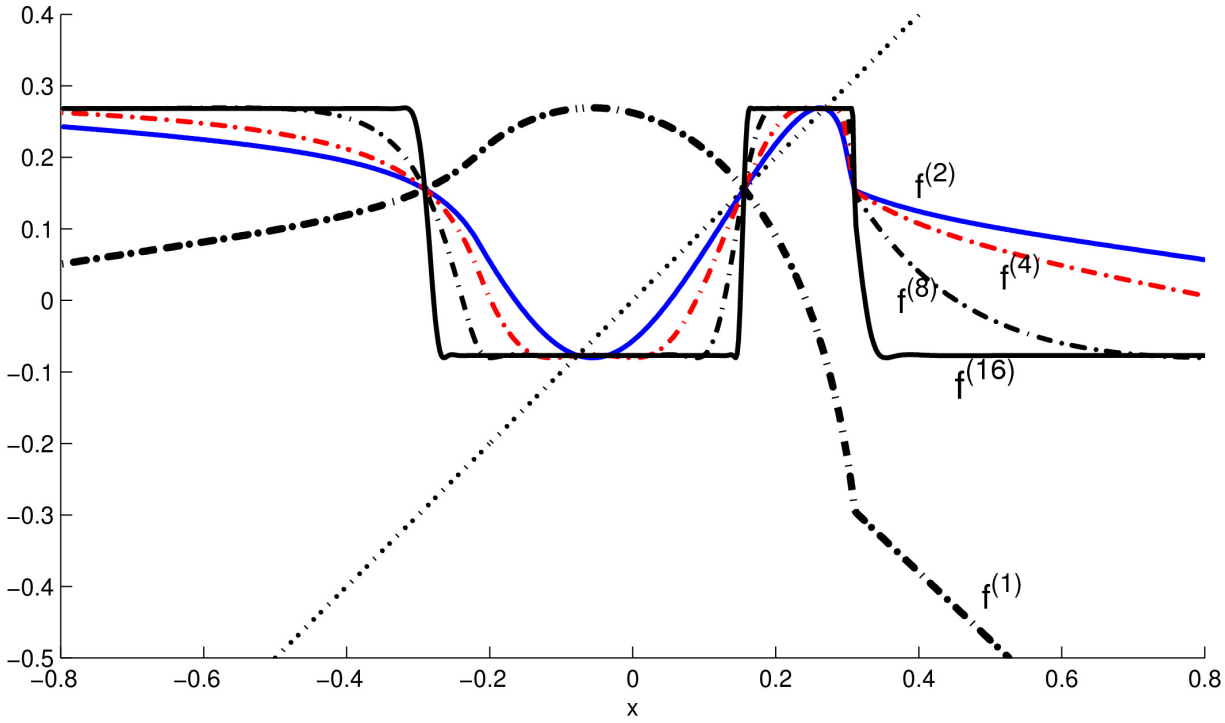

FIG. 7: Figure identique à la figure 6, avec en outre les itérées d'ordre 8 et 16. La convergence vers le régime à deux états est très rapide, quelle que soit la condition initiale (abscisse x).

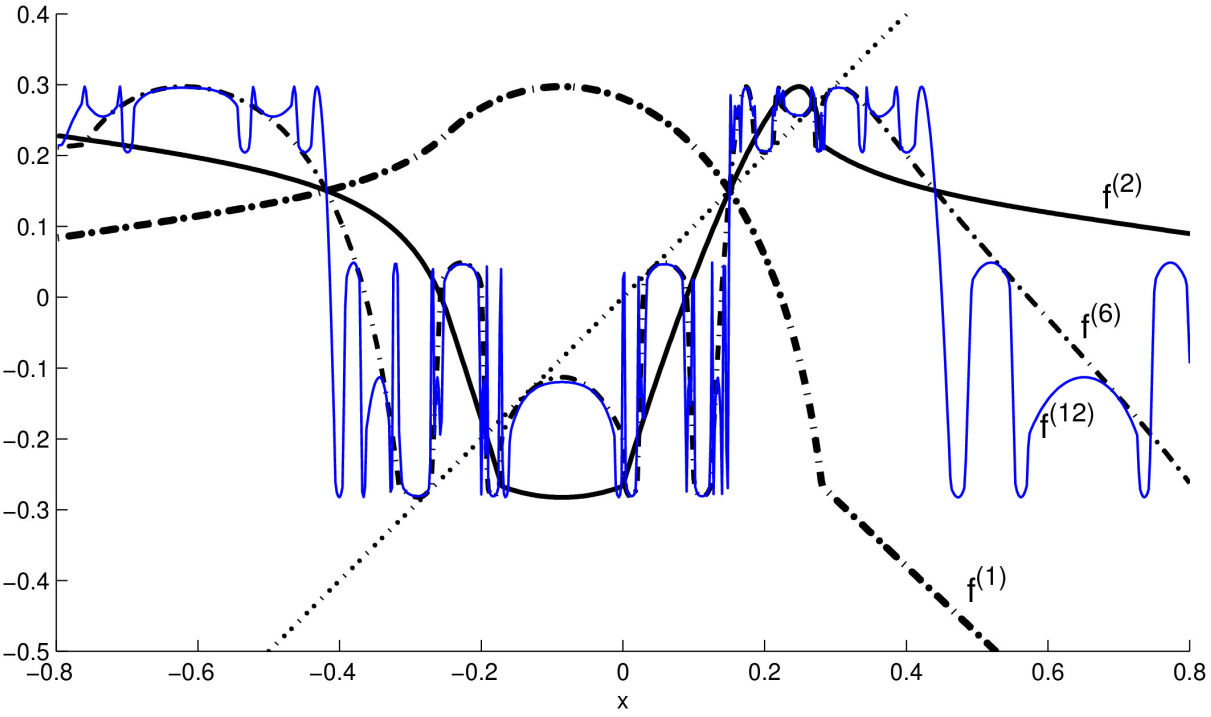

FIG. 8: Itérées d'ordre 1 ,2, 6 et 12 pour les paramètres de la figure 3. La fonction d'ordre 12 présente un grand nombre d'oscillations, qui peuvent expliquer la nature chaotique, c.-à-d. la très forte dépendance des conditions initiales du résultat.

Références

[1] McIntyre, M. E. , Schumacher, R. T., and Woodhouse, J. . On the oscillations of musical instruments. *J. Acoust. Soc. Am*, 74, 1983, 1325–1345.

[2] Maganza, C., Caussé, R. and Laloë, F. . "Bifurcations, period doubling and chaos in clarinetlike systems", *Europhysics letters* 1, 1986, 295–302.

[3] Kergomard, J., "Elementary considerations on reed-instrument oscillations". In *Mechanics of musical instruments*, vol. **335** (A. Hirschberg/ J. Kergomard/ G. Weinreich, eds),of *CISM Courses and Lectures*, pages 229–290. Springer-Verlag, Wien, 1995.

[4] Kergomard, J., Dalmont, J.P. , Gilbert, J. and Guillemain, Ph. . "Period doubling on cylindrical reed instruments". *In Proceedings ot the Joint congress CFA/DAGA'04,* pages 113–114, Strasbourg, 22th 25th March 2004.

[5] Ollivier, S. , Kergomard, J. and Dalmont, J.-P. "Idealized models of reed woodwinds. Part II : On the Stability of "Two-Step" Oscillations". *Acta Acustica united with Acustica*, 91, 2005, 166–179.

[6] Dalmont, J.-P. , Gilbert, J., Kergomard, J. and Ollivier, S. "An analytical prediction of the oscillation and extinction thresholds of a clarinet". *J. Acoust. Soc. Am.*, 118, 2005, 3294–3305.

[7] Hirschberg, A. , Van de Laar, R. W. A. , Marrou-Maurires, J. P. , Wijnands, A. P. J., Dane, H. J. , Kruijswijk, S. G. and Houtsma, A. J. M. "A Quasi-stationary Model of Air Flow in the Reed Channel of Single-reed Woodwind Instruments". *Acustica*, 70, 1990, 146–154.

[8] Dalmont, J.-P. and Frappé, C.," Oscillation and extinction thresholds of the clarinet : Comparison of analytical results and experiments". *J. Acoust. Soc. Am.*, 122, 2007, 1173–1179.

[9] May, R. M., "Simple mathematical models with very complicated dynamics", *Nature* 261, 1976, 459-67.

[10] Bergé, P. , Pomeau, Y. and Vidal, C., *L'ordre dans le chaos*, Hermann, Paris, 1984.

[11] Collet, P. and Eckmann, J.P. , "Properties of Continuous Maps of the Interval to Itself", *Mathematical Problems in Theoretical Physics*, K. Osterwalder (ed.), Springer-Verlag, Heidelberg, 1979; *Iterated Maps on the Interval as Dynamical Systems*, Birkhäuser, Basel, 1980.

[12] Gibiat, V. and Castellengo, M. . "Period doubling occurences in wind instrument musical performances", *Acustica united with acta acustica*, 86, 2000, 746–754.

[13] Taillard, P.A., Kergomard, J., Laloë, F., "Iterated maps for clarinet-like systems", *Nonlinear Dynamics*, 2009 (soumis).

[14] Kergomard, J.,"Instruments de musique à vent; comment éviter le chaos pour faire de la musique ?", Acoustique et Techniques, 9, 1997, 15-22.

Part II

Experimental Characterization of the Clarinet Exciter

Chapter 3

Statistical Estimation of Mechanical Parameters of Clarinet Reeds Using Experimental and Numerical Approaches

Résumé

Lors de cette étude, un échantillon de 55 anches de clarinette a été observé par holographie, en collectant 2 séries de mesures, réalisées avec un taux d'hygrométrie différent. Les fréquences de résonance des 15 premiers modes ont été déduites de ces observations. Une analyse statistique révèle de bonnes corrélations entre les 2 séries, mais aussi des différences significatives. A l'intérieur d'une même série, les fréquences des modes de flexion sont relativement mal corrélées, ce qui n'était pas attendu. Une analyse en composantes principales montre que la variance de chaque série peut être capturée à 90% à l'aide de 3 facteurs. Le premier facteur est lié aux modes transverses, le second aux modes de flexions de fréquence élevée et le 3ème au 1er mode de flexion. Un 4ème facteur est nécessaire pour prendre en compte une sensibilité divergente par rapport au taux d'humidité entre les 2 séries. Des simulations par éléments finis 3D ont été menées, à partir d'un modèle orthotrope et de la géométrie de l'anche. Une analyse de sensibilité révèle que, mis à part la densité, les fréquences de résonance théoriques dépendent principalement de 2 paramètres : E_L et G_{LT} (module de Young longitudinal et module de cisaillement longitudinal/transverse). Une formule analytique approximative est donnée pour calculer les fréquences de résonance en fonction de ces deux paramètres. Le désaccord entre les fréquences observées et calculées suggère que les modules élastiques des anches mesurées dépendent de la fréquence. Un modèle viscoélastique est alors développé, dont les paramètres sont calculés par régression linéaire à partir de 4 composantes orthogonales, ajustées par moindres carrés, ce qui permet de caractériser de manière objective le matériau composant l'anche (canne de Provence, *Arundo donax* L.)

Cet article [153] est reproduit avec l'autorisation des coauteurs et celle de l'éditeur S. Hirzel, du 15 janvier 2018.

ACTA ACUSTICA UNITED WITH ACUSTICA
Vol. 100 (2014) 555 – 573

DOI 10.3813/AAA.918735

Statistical Estimation of Mechanical Parameters of Clarinet Reeds Using Experimental and Numerical Approaches

Pierre-André Taillard[1], Franck Laloë[2], Michel Gross[3], Jean-Pierre Dalmont[4], Jean Kergomard[5]

[1] Conservatoire de musique neuchâtelois, Avenue Léopold-Robert 34, 2300 La Chaux-de-Fonds, Switzerland. taillard@hispeed.ch

[2] Laboratoire Kastler Brossel – UMR 8552 Ecole Normale Supérieure, UPMC, CNRS, 24 rue Lhomond, 75231 Paris Cedex 05, France

[3] Laboratoire Charles Coulomb - UMR 5221 CNRS-UM2, Université Montpellier, II place Eugène Bataillon, 34095 Montpellier, France

[4] Laboratoire d'Acoustique de l'Université du Maine - UMR CNRS 6613, Université du Maine, 72085 Le Mans, France

[5] Laboratoire de Mécanique et d'Acoustique - CNRS, UPR 7051, Aix-Marseille Univ, Centrale Marseille, 13402 Marseille Cedex 20, France

Summary

A set of 55 clarinet reeds is observed by holography, collecting 2 series of measurements made under 2 different moisture contents, from which the resonance frequencies of the 15 first modes are deduced. A statistical analysis of the results reveals good correlations, but also significant differences between both series. Within a given series, flexural modes are not strongly correlated. A Principal Component Analysis (PCA) shows that the measurements of each series can be described with 3 factors capturing more than 90% of the variance: the first is linked with transverse modes, the second with flexural modes of high order and the third with the first flexural mode. A forth factor is necessary to take into account the individual sensitivity to moisture content. Numerical 3D simulations are conducted by Finite Element Method, based on a given reed shape and an orthotropic model. A sensitivity analysis revels that, besides the density, the theoretical frequencies depend mainly on 2 parameters: E_L and G_{LT}. An approximate analytical formula is proposed to calculate the resonance frequencies as a function of these 2 parameters. The discrepancy between the observed frequencies and those calculated with the analytical formula suggests that the elastic moduli of the measured reeds are frequency dependent. A viscoelastic model is then developed, whose parameters are computed as a linear combination from 4 orthogonal components, using a standard least squares fitting procedure and leading to an objective characterization of the material properties of the cane *Arundo donax*.

PACS no. 43.75.-z, 43.75.Ef, 43.75.Pq

1. Introduction

Clarinettists experience every day the crucial importance of clarinet reeds for the quality of sound. Their characterization is a real challenge for musicians who wish to obtain reeds that are suited to their personal needs. The present paper addresses this complex field of research. Its scope is restricted to the development of an objective method for a mechanical characterization of single reeds of clarinet type. From the shape and the resonance frequencies of each individual reed (measured with heterodyne holography), we intend to deduce the mechanical properties of the material composing it. A subsequent study should then examine how these mechanical properties are correlated with the musical properties of the reeds.

Generally, the physicist chooses a model in order to validate it by observations. In the present study, the complexity of the problematic forced us to adopt the reverse attitude: We observe the mechanical behavior of clarinet reeds with a statistically representative sample and exploit afterwards the statistical results for establishing a satisfactory mechanical model designed with a minimal number of parameters.

Natural materials, such as wood or cane, are often orthotropic and exhibit a different stiffness along the grain (longitudinally) than in the others directions. The problem is then obviously multidimensional. Nevertheless, reed makers classify their reeds by a single parameter: the nominal reed "strength" (also called "hardness"), in general

Received 9 September 2009,
accepted 17 February 2014.

from 1 to 5, which basically reflects the stiffness of the material (cane, *Arundo donax L.*), since all reeds of the same model have theoretically the same shape. The method of measurement is generally not publicized by manufacturers, but this "strength" is probably related to the static Young modulus in the longitudinal direction E_L.

"Static" (i.e. low frequency) measurements of the elastic parameters of cane are available in the literature, for instance Spatz *et al.* [1]. A viscoelastic behavior has been reported in experimental situations (see e.g. Marandas *et al.* [2], Ollivier [3] or Dalmont *et al.* [4]) and this fact seems generally well accepted in wood sciences and biomechanics (for instance Speck *et al.* [5, 6]). Marandas *et al.* proposed a viscoplastic model of the wet reed. Viscoelastic behavior for cane was already demonstrated by Chevaux [7], Obataya *et al.* [8, 9, 10, 11] and Lord [12]. These authors study only the viscoelasticity of the longitudinal Young modulus E_L, leaving aside the case of the shear modulus in the longitudinal/tangential plane G_{LT}. Furthermore, they give no really representative statistics about the variability of the measured parameters.

The observation of mechanical resonance frequencies can be achieved by different methods. The methods used by Chevaux, Obataya and Lord are destructive for the reed, which cannot be used for further musical tests. On the contrary, holography is a convenient non-destructive method, the reed being excited by a loudspeaker. For instance Pinard *et al.* [13] measured with this method the frequency of the 4 lowest resonances and focused their attention on the musical properties of the reeds.

The digital Fresnel holography method was used by Picart *et al.* [14, 15] and Mounier *et al.* [16] to measure high amplitude motion of a reed blown by an artificial mouth. Guimezanes [17] used a scanning vibrometer.

Recent technological developments provide very efficient and convenient measurements with holography, without having to manually identify the modes of resonance and to be satisfied with a single picture of their vibration: in a few minutes hundreds of holograms are acquired showing the response of a reed for many frequencies. The temperature and the moisture content can be considered as constant during a measurement series[1]. The Sideband Digital Holography technique provides additional facilities (see 2.1.1).

Different authors (among them Casadonte [18, 19], Facchinetti *et al.* [20, 21] and Guimezanes [17]) modeled the clarinet reed by Finite Elements Method (FEM) and computed the first few eigenmodes. They chose appropriate values of the elastic parameters in the literature, ignoring however viscoelastic behavior. The goodness of fit between observations and model was of secondary importance, except for Guimezanes. This latter author built a 2-D elastic model of the reed with longitudinally varying parameters. He fitted his model quite adequately with his observations (only 5 resonances were measured), but the fitted parameters seem not really plausible physically. His model didn't respect the assumption of a radial monotonically decreasing stiffness from the outer side to the inner side of the cane. Under such conditions, the frequency of the first resonance would increase in comparison to homogeneous material, and not decrease, as observed experimentally.

In section 2 the measurement method is presented. The experimental setup is described in section 2.1 and the method for observing resonance frequencies is detailed in 2.2. The results for 55 reeds are given in section 3 (statistics, Principal Component Analysis (PCA)[22]).

In section 4, the development and the selection of a satisfactory mechanical model with minimal structure is described. First, a numerical analysis of the resonance frequencies of a reed assumed to be perfectly elastic is done by Finite Element Method (FEM), and a metamodel computing the resonance frequencies from elastic parameters is given in section 4.3. This allows solving the inverse problem in a fast way. However, because the elastic model is not very satisfactory, viscoelasticity has to be introduced and some parameters are added to the model in section 4.4. The viscoelastic model has however too many degrees of freedom, according to PCA. Consequently, the viscoelastic parameters of the model are assumed to be correlated and PCA indicates that these parameters can be probably reconstructed from 4 orthogonal components, as a linear combination, by multiple regression (section 5). The relationships between the components and the viscoelastic parameters is given, and finally the resulting values for these parameters are discussed in section 5.3 and compared with the results in the literature.

2. Observations by Sideband Digital Holography

2.1. Experimental setup

2.1.1. Holographic setup

The experimental setup is shown schematically in Figure 1. A laser beam, with wavelength $\lambda = 650\,\text{nm}$ (angular frequency ω_L) is split into a local oscillator beam (optical field E_{LO}) and an illumination beam (E_I); their angular frequencies ω_{LO} and ω_I are tuned by using two acousto-optic modulators (Bragg cells with a selection of the first order diffraction beam) AOM1 and AOM2: $\omega_{LO} = \omega_L + \omega_{AOM1}$ and $\omega_I = \omega_L + \omega_{AOM2}$, where $\omega_{AOM1,2} \simeq 2\pi \times 80\,\text{MHz}$. The first beam (LO) is directed via a beam expander onto a CCD camera, while the second beam (I) is expanded over the surface of the reed, which vibrates at frequency f . The light reflected by the reed (field E) is directed toward the CCD camera in order to interfere with the LO beam (E_{LO}). 4 phases were used (phase shifting digital holography) and we select the first sideband of the vibrating reed reflected light by adjusting $\omega_{AOM1,2}$ to fulfil the condition: $\omega_{AOM1} - \omega_{AOM2} = 2\pi(f + f_{CCD})/4$, where f_{CCD} is the CCD camera frame frequency. The complex

[1] The significantly lower correlations between resonance frequencies (compared to our data) shows that it was probably not the case in Pinard's study. This fact may also reflect an unprecise determination of the resonance frequencies.

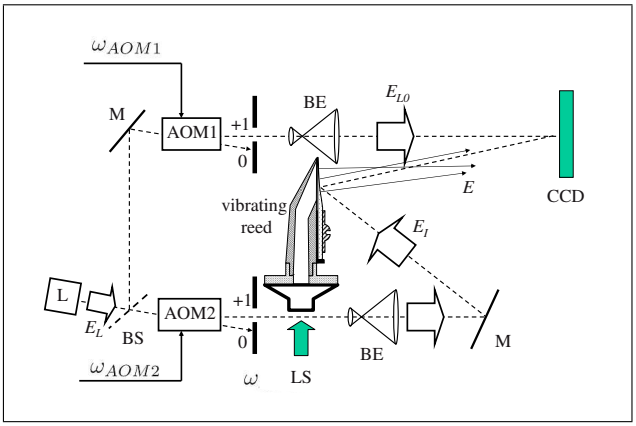

Figure 1. Holographic setup. L: main laser; AOM1, AOM2: acousto-optic modulators; M: mirror; BS: beam splitter; BE: beam expander; CCD: CCD camera; LS: loudspeaker exciting the clarinet reed through the bore of a clarinet mouthpiece at frequency $f = \omega/2\pi$.

hologram signal H provided by each pixel of the camera, which is proportional to the sideband frequency component of local complex field E, is obtained by 4-phases demodulation: $H = (I_0 - I_2) + \mathrm{j}(I_1 - I_3)$ where $I_0 \ldots I_3$ are 4 consecutive intensity images digitally recorded by the CCD camera, and $j^2 = -1$.

From the complex hologram H, images of the reed vibration are reconstructed by a standard Fourier holographic reconstruction calculation [23]. These holographic reconstructed images exhibit bright and dark interference fringes. Counting these fringes provides the amplitude of vibration of the object (in the direction of the beam), which depends on the wavelength λ of the laser, and on the first Bessel function J_1, for instance ±95nm for the first, ±770nm for the 5^{th} and $\pm 1.6\,\mu$m for the 10^{th} maximum (bright fringes) [24, 25][2].

This method has 3 main advantages:

1. The time for data acquisition is very short, about 3 minutes for recording 184 holograms, including holographic reconstruction.
2. The signal to noise ratio is significantly better than with traditional technology, particularly through the elimination of signal at zero frequency.
3. The visualization of large-amplitude vibration (order of magnitude: 0.1 mm) is possible by using high harmonics orders (up to several hundred times the excitation frequency).

2.1.2. Reed excitation

The reed was excited by a tweeter loudspeaker screwed onto an aluminium plate, connected to a clarinet mouthpiece. The lay of this mouthpiece was modified to be strictly flat. A plastic wedge of uniform thickness has been inserted between the lay and the reed, longitudinally to the same height as the ligature (Vandoren Optimum), allowing free vibrations of the entire vamp (length: about 38 mm), see Figure 1. This ensures precise boundary conditions, avoiding any dependence on deformations of the reed. The repeatability of the longitudinal placing of the wedge and of the reed was ensured by a Claripatch ring [26].

This setup requires some comments:

1. The reed is excited exclusively through the bore of the mouthpiece.
2. The pressure field in the chamber of the mouthpiece was not measured. As for a real instrument, the edges of the reed (protected by the walls of the chamber) are subject to a pressure field, which is probably lower than the pressure acting on the rest of the vamp.
3. The boundary conditions are very different from those of a real instrument (no curved lay, no contact with the lip). In addition, the reed was not moistened for the measurement.
4. The excitation device is almost closed. The acoustical resonances of the excitation device are unknown, but may quite easily be deduced by comparing different measurements, because they are always present at the same frequency.

2.2. Observation of resonance frequencies

2.2.1. Experimental protocol

55 clarinet reeds of model Vandoren V12 were purchased in a music shop: 12, 12, 20 and 11 reeds of nominal strengths 3, $3\frac{1}{2}$, 4 and $4\frac{1}{2}$, respectively. 29 reeds were used for two preliminary studies in order to develop the measurement protocol. Each of these reeds was played a total of some tens of minutes, spread over several weeks before measurement with the final protocol. The other 26 reeds were strictly new by measurement, which was performed immediately after package opening (for 21 of them with the new hermetically sealed package by Vandoren, ensuring a relative humidity between 45 and 70%, according to the manufacturer), without moistening the reed.

Each reed was subject to 2 series of measurements:

- **Series A** (asymmetrical excitation: see Figure2): the right half of the mouthpiece chamber was filled with modeling clay to ensure a good excitation of antisymmetrical modes. 184 holograms were made ranging from 1.4 to 20 kHz (sinusoidal signal), by steps of 25 cents. The amplitude of the excitation signal was exponentially increased in the range 1.4 to 4 kHz, from 0.5 to 16 V, then kept constant at 16 V up to 20 kHz. This crescendo limits the amplitude of vibration of the first two resonances of the reed. The temperature was not measured (about 20°C).
- **Series B** (symmetrical excitation: see Figure3): the modeling clay was removed. The protocol is otherwise identical to this of the first series. The reeds were inadvertently exposed during one night to the very dry and warm air from the optical laboratory between the two series of measurements. The reeds lost between 2 and 4% of their mass. In what follows we try to interpret the influence of this fact. The temperature was around 23-25°C.

[2] The original notation from the cited paper is kept. This notation is only valid for this paragraph.

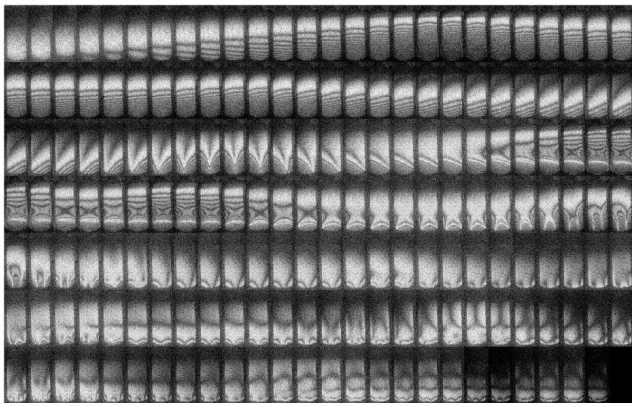

Figure 2. Typical holographic patterns of series A (asymmetrical sinusoidal excitation: the left side of the reed is more strongly excited than the right side). Frequency range: 1.4 to 20 kHz by steps of 25 cents (181 pictures ordered from left to right, continued on the next row; the tip of the reed is down on each picture). Some modes are easily identified: $F1$ (1st row, 19th picture), $T1$ (3rd row, 10th picture), $F2$ (4th row, 7th picture), $T2$ (4th row, penultimate picture), $X1$ (5th row, 5th picture) etc... Modes $T3$ and $F3$ are almost at the same frequency (6th row, 4th and 5th pictures, probably). The last picture of the 3rd row corresponds to an acoustic resonance of the excitation device. It is present on all holograms of both series at the same frequency (examine Figure 3). The excitation amplitude exponentially increases until the 73rd picture (3rd line, 21th picture), being held constant beyond.

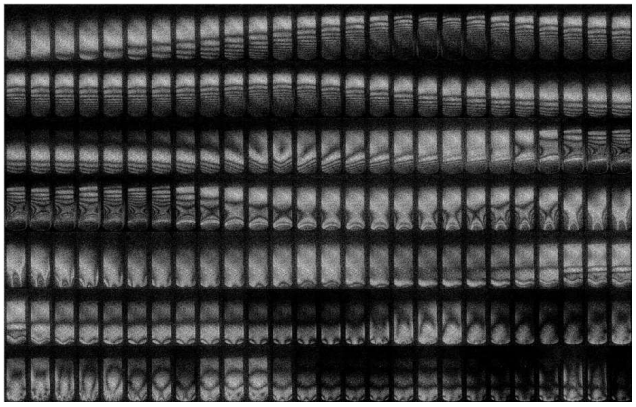

Figure 3. Typical holographic patterns of series B (symmetrical sinusoidal excitation). The modes $X1$ and $T3$ cannot be distinguished anymore. Notice that $T1$ is less marked than under asymmetrical excitation (for some reeds even difficult to identify) and that the pattern has a significant flexural component, strongly dependent on the lateral placing of the reed on the mouthpiece. Notice that the symmetry of the patterns near $T1$ depends on the excitation frequency.

2.2.2. Nomenclature of normal modes

Distinguishing 3 morphological classes, we classify the modes of a clarinet reed as follow : i) The "flexural" (or "bending", or "longitudinal") modes, listed below F, whose frequencies mainly depend on the longitudinal Young modulus (E_L) and polarized mainly in the z axis, ii) the "transverse" (or "torsional", or "twisting") modes, listed below T, mainly dependent on the shear modulus in the longitudinal / tangential plane (G_{LT}), and iii) the

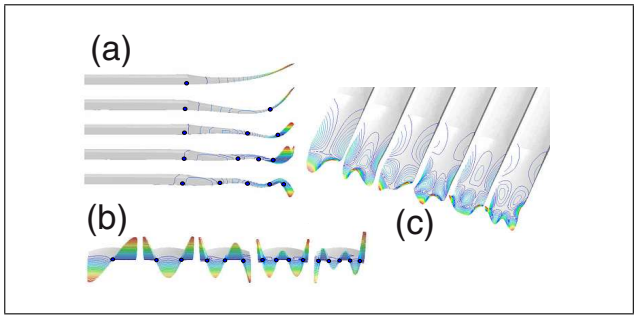

Figure 4. (a) Flexural modes $F1$, $F2$, $F3$, $F4$ and $F5$. Side view. (b) transverse modes $T1$, $T2$, $T3$, $T4$, $T5$. Front view. (c) Generic modes: $X1$, $X2$, $X3$, $X4$, $X5$ and $X6$. View from above. The intersections of nodal lines with the sides of the reed are symbolized by the dark dots.

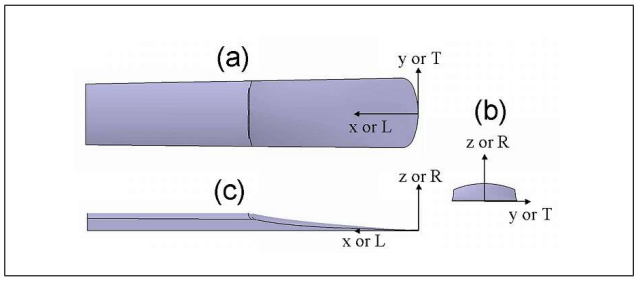

Figure 5. The clarinet reed: coordinates system. (a) top view, (b) front view, (c) side view. x, y, z: Cartesian axes of the object. L, T, R: axes of the orthotropic material (L: longitudinal, T: tangential, R: radial). In the software Catia used for the simulations, the orthotropic model is Cartesian and not cylindrical. Therefore an exact equivalence between x, y, z, and L, T, R respectively can be assumed since we observed no important deviation between the direction of the grain and the axis of symmetry of the reed.

"generic" (or "mixed") modes, listed below X, sensitive to both moduli E_L and G_{LT} (see Figure 4). A subclass of flexural modes may be distinguished: the "lateral" modes (listed below L), polarized mainly in the y axis (see Figure 5). These modes were not observed in our study.

The modes have been numbered after the order of increasing frequencies from a preliminary modal analysis we performed. In our analysis, however, the identification of a mode is based upon morphological criteria. As a matter of fact, the mode number and the order of observed frequencies are not necessarily identical for all reeds.

Strictly speaking, the optical method only allows us to observe the resonance frequencies of the reed and not the eigenfrequencies. Therefore the observed deformation patterns are a priori not identical to the eigenmodes of the reed. Nevertheless in practice no major differences have be found between the computed eigenmodes (see section 4) and the observed or computed deformation for a forced asymmetrical excitation at the corresponding frequency. For this reason we use the terminology "mode" for the maximum amplitude of the response of the reed to a forced excitation. This is somewhat abusive, because the small shift between the resonance frequencies due to damping and the eigenfrequencies computed by FEM,

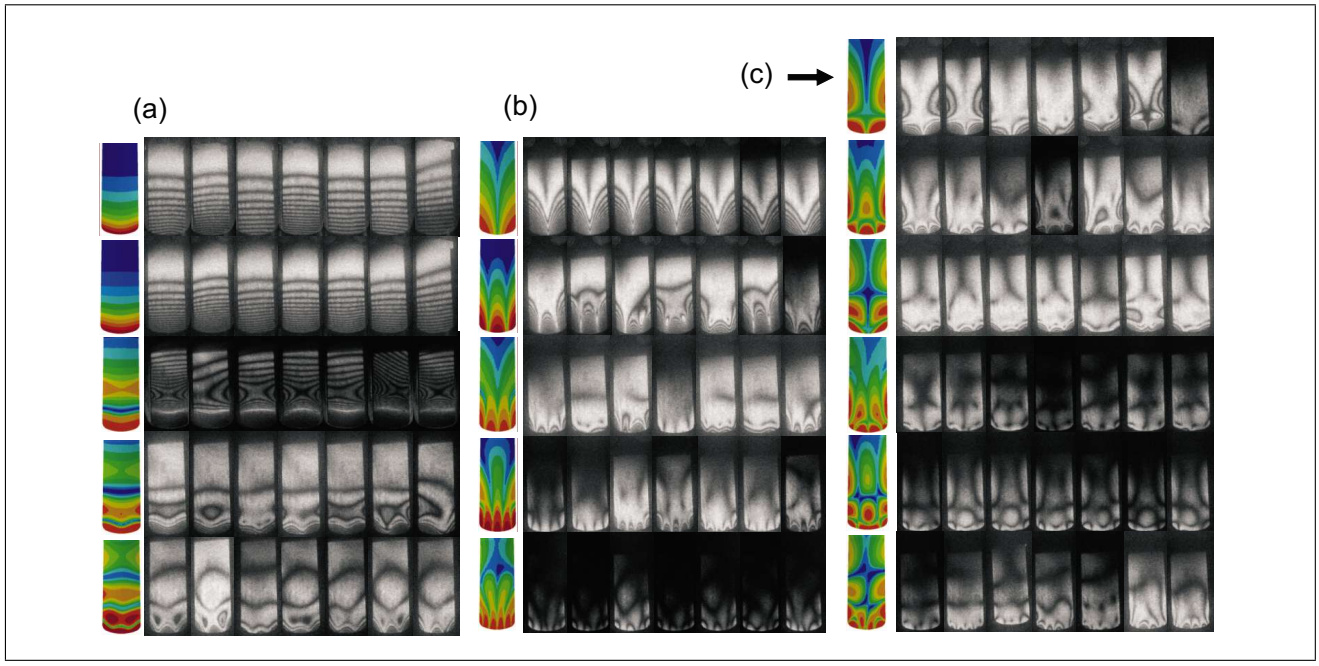

Figure 6. Qualitative comparison with FEM computation, and typical variability of the experimental results. (a) First row: Quasi-static pattern (at 605 Hz, with strong excitation by the LS). 2nd to 5th row: Flexural modes $F1$, $F2$, $F3$ and $F4$. Leftmost column: numerical simulation of eigenmodes by FEM. Columns 2 to 7: Arbitrary selection representing the observed variability (The first two rows correspond to the same selection of reeds). Notice the marked asymmetries and the differences in the curvature of the interference fringes near the tip of the reed. (b) Rows 1 to 5: transverse modes $T1$, $T2$, $T3$, $T4$ and $T5$ (probably). Columns: see (a). (c) Rows 1 to 6: Generic modes $X1$, $X2$, $X3$, $X4$, $X5$ and $X6$. The identification with $X6$ is sometimes unlikely. Columns: see (a).

without damping, is ignored. Besides damping, the acoustic load is also able to shift the resonance frequencies. We assume that this discrepancy is approximately the same for all reed.

2.2.3. Analysis of holograms; mode identification

More than 30000 holograms were made for this study and analyzed as follows: The picture where the number of interference fringes is locally maximum is determined. For some cases, we chose the hologram that is most similar to our numerical simulations (by Finite Element Method, see section 4) or to other holograms (see Figure 6). The holograms corresponding to an acoustical resonance of the system, present at the same frequency (4309 Hz) for all reeds, have been eliminated. The identification of the different patterns to those calculated by FEM was often quite simple. Exceptions have been encountered for $F3$ and $T3$, whose frequencies were often so close that our identification is sometimes uncertain. More sophisticated techniques would certainly solve this problem. Notice that other boundary conditions (e.g. with clamping closer to the tip of the reed) would also easily separate these two modes. The frequency of some higher modes could not always be measured, either because their frequency was beyond 20 kHz, or because their pattern could not be clearly identified.

3. Statistical analysis of resonance frequencies

4 flexural, 5 transverse, and 6 generic modes have been identified, namely all 15 first modes of the reed, excluding lateral modes. This number is significant, compared to the 4 modes detected by Pinard *et al.* [13]. The 6th mode ($L1$) could not be identified, as it is a lateral mode (flexural mode moving mainly in the y axis), not excited by our loudspeaker. We tried to observe it by rotating the mouthpiece to the side, without success. Notice that higher modes could probably be identified using an ultrasonic loudspeaker.

3.1. Statistics

The statistics are displayed on Figure 7 and detailed in Appendix A1, with the analysis of correlations. For 14 measurements of resonance frequencies of the two series, identification of the total number of reeds (55) has been done. For other measurements, identification has been done only for a part of this number. The value of the ratio of the standard deviation σ to the mean value μ, i.e. the relative standard deviation, is found to be between 2 and 5% (about 1/3 tone). If we admit Gaussian distribution for the measured frequencies, 99% of the observations typically range about ±1 tone (±200 cents) around the mean value (i.e. $\mu \pm 3\sigma$), for all frequencies.

The identification of the mode $X6$ is uncertain: it seems to appear for frequencies lower than those of our simulations. Mode $T5$ is on the limit of the range we studied: this explains the small value of the standard deviation.

Between series A and B, the flexural modes $F1$ to $F4$ decrease their average frequency, while the transverse modes slightly increase it. The difference between the two series probably lies mainly in the drying of the reeds, and

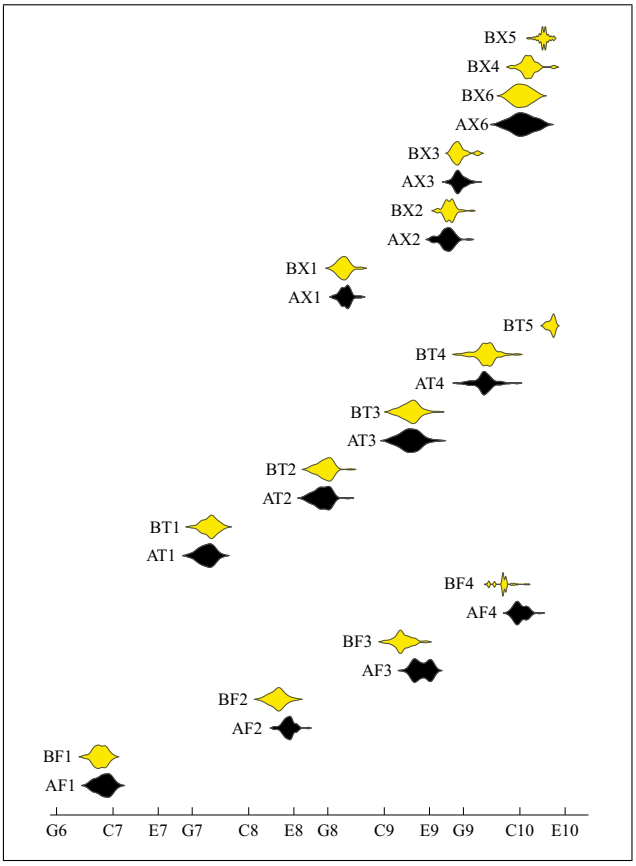

Figure 7. Observed resonance frequencies for the different reeds of each series, according to the results of Table A1. AF1 signifies mode F1, series A. The series A is in black, and the series B in white (yellow online). In abscissa the frequencies in logarithmic (musical) scale (so the musical intervals appear clearly). From the left to the right, the different notes correspond to the following frequencies: 1568, 2093, 2637, 3136, 4186, 5274, 6272, 8372, 10548, 12544, 16744, 21096 Hz

this seems to have a statistically significant effect. This is surprising, because drying decreases the density of the reed, and theoretically this should proportionally increase all frequencies. In addition, according to Obataya *et al.* [11], drying is expected to increase E'_L (at least around 400 Hz), which should also increase the resonance frequencies. However Chevaux [7] observed that drying diminishes E'_L for material extracted from the inner side of the cane and augments slightly E'_L for material extracted nearer from the outer side (for cane suitable for oboe reeds), at least in the frequency range 100-500 Hz.

The hypothesis of an influence of the excitation method on the resonance frequencies seems unlikely, as well as the hypotheses of a poor reproducibility of the position of the reed on the mouthpiece between measurements or of the modification of the acoustic load, due to the modeling clay.

3.2. Principal component analysis

Principal Component Analysis (PCA) is mathematically defined as an orthogonal linear transformation transforming the data to a new coordinate system, such that the greatest variance by any projection of the data comes to lie on the first coordinate (called the first principal component or first factor), the second greatest variance on the second coordinate, and so on [27]. Theoretically PCA is the optimum linear transform for given data in terms of least squares. PCA is based upon the calculation of the eigenvalue decomposition of the covariance (or of the correlation) matrix (see e.g. [22]).

A PCA has been performed using the FACTOR module of SYSTAT [28]. The 14 variables (observed frequencies) presenting complete measurements for all reeds have been selected (all variables having 55 identified pattern, N_A or $N_B = 55$, see Table A1). Frequencies are rated in cents.

The 4 largest eigenvalues have been selected. They capture 91.2% of the total variance of our sample (respectively 53.6%, 21.4%, 10.8% and 5.4% for each factor). A fifth factor would capture only 2.5% variance more. The 14-dimensional data have been linearly projected onto a 4-dimensional factor space.

The factor space can afterwards be orthogonally rotated, for instance for maximizing the correlations between rotated factors and observed variables. In the studied case, no a priori knowledge about the orientation of the factor space is available. For an easy comparison, using the VARIMAX algorithm, we choose to maximize the correlations between rotated factors and all available variables (observed resonance frequencies and theoretical components from the model described hereafter in section 5.2).

We performed also a PCA separately for each measurement series (A and B: 9 and 5 variables, respectively). From series A we detected 3 important factors capturing 90.8% of the variance (56.9, 23.0, 11.0%, respectively). From series B we detected also 3 important factors capturing 94.1% of the variance (54.0, 26.8, 13.3%, respectively). A 4th factor would capture only 3.6% more for series A and 3.4% for series B. One factor seemingly disappeared, compared with the PCA performed on both series. A hypothesis is that this factor is related to the hygrometric change between the two series.

From Table I, we see that all transverse and generic modes are well correlated with $factor_1$; $factor_2$ correlates with high frequency flexural modes of both series (however notably better with those of series A); $factor_3$ well correlates with $F1$ of both series (and somewhat with other low frequency modes: AT1, BT1 and AF2), whereas $factor_4$ correlates quite well with high frequency flexural modes of series B.

3.3. Conclusions from the statistical analysis

Fifteen modes of vibration of the clarinet reed have been observed, while previous studies investigated 4 to 5 modes only [17, 13]. The observed resonance frequencies are often highly correlated, especially those among the "transverse" modes and, to a lesser extent, those among the "flexural" modes. The nominal reed strength is surprisingly better correlated with the frequencies of "transverse" modes as with those of "flexural" modes. The flexural modes within the same series are poorly correlated.

Table I. Correlation (loadings) between rotated factors from PCA and : i) variables (measured resonance frequencies) or ii) components from viscoelastic model ($\boldsymbol{e}[n]$, see section 5.2), for comparison, sorted in reverse order of magnitude. In **bold:** greater correlation for each variable.

	factor_1	factor_2	factor_3	factor_4
AT2	**0.973**	0.054	0.078	-0.008
BT2	**0.953**	0.055	-0.025	0.085
AT3	**0.898**	0.198	-0.237	-0.032
AX2	**0.853**	0.273	-0.073	-0.123
AT1	**0.776**	0.017	0.577	0.087
BT1	**0.762**	-0.033	0.541	0.177
AX3	**0.761**	0.472	0.090	0.217
AX1	**0.740**	0.451	0.356	0.115
AF3	0.223	**0.891**	0.076	0.080
AF2	0.143	**0.791**	0.519	0.064
AF1	0.085	0.360	**0.870**	-0.141
BF1	0.104	0.385	**0.835**	0.209
BF3	0.059	0.596	0.050	**0.755**
BF2	0.147	0.561	0.290	**0.710**
e_1	**0.958**	-0.080	0.105	0.005
e_2	0.059	**0.969**	0.082	0.098
e_3	-0.075	-0.073	**0.971**	0.042
e_4	-0.009	-0.081	-0.039	**0.979**

A principal component analysis of the resonance frequencies identifies 4 main factors, capturing 91.2% of the variance of the sample. The data can therefore be reconstructed with 4 uncorrelated factors only (error: RMSD = 21.8 cents, see Appendix A3.2 and A4). The effect of hygrometric change between both measurement series can seemingly be described with 1 factor only.

These statistical facts offer a guidance for modeling appropriately the mechanics of the clarinet reed.

4. Development of a mechanical model

4.1. Choice of a viscoelastic model

In the present study our concern is to develop a model with a minimal number of physically related components, that adequately reconstructs the observed resonance frequencies of our reeds. We presume that these components offer an objective characterization of the material composing each reed. A sensitivity analysis by FEM calculation assuming an orthotropic, elastic material has been conducted, and showed that the longitudinal Young modulus E_L and the longitudinal / transverse shear modulus G_{LT} play a leading role. Nevertheless taking into account the previous result of 4 factors given by PCA, we will see that an elastic model is not sufficient to establish a satisfactory model with 2 degrees of freedom only (i.e. variables E_L and G_{LT} per series. Therefore a viscoelastic model is sought.

It is well known that the stiffness of natural materials like wood or cane varies with the frequency of the applied stress and with the temperature. The material is stiffer at low temperature and at high frequency. At low frequency or high temperature the material is almost perfectly elastic and reaches the rubbery modulus. At high frequency or at low temperature the glassy modulus is reached; the material is almost perfectly elastic, also, but stiffer. At mid frequency or mid temperature, the apparent modulus (called storage modulus, i.e. the real part of the complex Young modulus for this frequency) is between the two values. For a particular frequency, called relaxation frequency, the storage modulus is exactly at the average of glassy and rubbery moduli. Around this frequency dissipation is maximum. Once the characteristic curve is known (for given temperature and different frequencies, or for given frequency and different temperatures), the Arrhenius equation[3] offers usually an adequate estimate of the stiffness for any frequency and any temperature, within a quite broad range [29].

The determination of the mechanical parameters of a natural material requires determination for each axis of the orthotropic material of the value of 3 parameters (Young modulus, shear modulus and Poisson's ratio). These 9 parameters may exhibit viscoelastic behavior, requiring theoretically for each one the fit of a viscoelastic model, such as the general linear solid (also called Zener model or 3-parameter model, see [29, 30, 31, 32])[4]. The chosen model is based on 6 parameters (3 parameters for both variables E_L and G_{LT}). Therefore the viscoelastic model (section 4.4) has many degrees of freedom (6, for each of the 2 series of measurements, compared to the 4 factors detected by PCA for both series), for solving adequately the inverse problem (see section 5 for the reduction of the number from 12 to 4).

4.2. Computation method

Considering viscoelasticity leads to complex modes with complex eigenfrequencies. Compared to the non-dissipative, elastic case computed by FEM, the main consequence of viscoelasticity, besides dissipation, is that stress and strain are not in phase. For sake of simplicity, we limit the computation to eigenfrequencies only, and assume that they depend on the storage moduli only (i.e. dissipation has a negligible influence). Having reduced the viscoelastic problem to an associated elastic one, the elastic solution may be used (see e.g. Ref. [29]). In order to compute the resonance frequency ω_r after an elastic model, according to Ref. [32], we admit that $E \simeq E'(\omega_r)$, where $E'(\omega_r)$ is the real part of the complex modulus in the frequency

[3] The shift in relaxation time is: $Ln(\text{shift}) = (E_a/R)(1/T - 1/T_{ref})$, where E_a is the activation energy, R is the gas constant (8.314 J/K mol) and T and T_{ref} the absolute temperatures in K. For instance, a shift of +10°C from a reference temperature of 20°C decreases the relaxation time by 16%, if E_a is 13 kJ/mol.

[4] Other multidimensional viscoelastic models could be also considered. In order to fit a wide range of frequencies (more than 2 decades), a 4-parameter model with fractional derivative would be required [32]. In addition, these parameters are known to be sensitive to moisture content. Moreover, the cane is not homogeneous. The stiffness varies in radial direction [7] and local irregularities may be important, as shown by J.-M. Heinrich [33].

Table II. One-At-a-Time sensitivity study by FEM: Averaged ratio between relative change in frequency and relative change for each elastic coefficient (i.e. ±10%), sorted by decreasing order of magnitude, for the first 16 eigenmodes. F: flexural modes ($F1$ to $F4$), T: transverse modes ($T1$ to $T4$), X: generic modes ($X1$ to $X6$), L: lateral modes ($L1$ and $L2$; these modes were not observed in our study), All modes: averaged ratio over all modes. In **bold**: maximum absolute value for each coefficient of the orthotropic material: E_L, E_T and E_R: Young moduli; ν_{LT}, ν_{LR} and ν_{TR}: Poisson coefficients; G_{LT}, G_{LR} and G_{TR}: shear moduli.

Coefficient	F	T	X	L	All modes
E_L	**0.4087**	0.1053	0.1835	0.2093	0.2235
G_{LT}	0.0140	**0.2681**	0.1962	0.1067	0.1575
E_T	0.0076	**0.0976**	0.0741	0.0166	0.0562
G_{LR}	0.0438	0.0131	0.0257	**0.0818**	0.0341
E_R	0.0176	0.0120	0.0135	**0.0662**	0.0207
G_{TR}	0.0046	0.0092	0.0077	**0.0215**	0.0091
ν_{TR}	0.0015	0.0009	0.0015	**0.0054**	0.0019
ν_{LT}	0.0018	**-0.0031**	0.0004	0.0007	-0.0001
ν_{LR}	0.0009	0.0002	0.0005	**0.0013**	0.0007

domain. This hypothesis implies that the calculation of the eigenfrequencies from the values of the storage modulus is done by an iteration procedure, and allows use of a FEM software (Catia) which does not allow computing with frequency-dependent coefficients.

Therefore we first present results of FEM simulations (section 4.3), assuming an elastic and orthotropic behavior of the reed (modeled in section 4.3.1). This helps to identify the modes in experiments, and allows obtaining a fit formula (section 4.3.3) for computing the 11 lower resonance frequencies with respect to two parameters only, E_L and G_{LT}, detected after a sensitivity analysis (section 4.3.2). The fit formula, called "metamodel", is then used in the iterative procedure for the computation of the viscoelastic model. It allows a great reduction of computation time, compared to the FEM, and this is very useful for the inverse problem. Such a metamodel could be directly computed for the viscoelastic model with an appropriate software, but starting with the elastic model simplifies the fitting procedure.

4.3. Elastic model

4.3.1. Modeling the reed

The clarinet reed is defined in a Cartesian axis system x, y, z (see Figure 5). The origin is located in the bottom plane, at the tip of the reed. The material is defined as 3D orthotropic and assumed to be homogeneous, whose longitudinal direction L is parallel to the x axis, the tangential direction T parallel to the y axis and the radial direction R parallel to the z axis[5].

The dimensions in the xy plane are consistent with the measurements given by Facchinetti *et al.* [21]. The heel of the reed is made out of a cylinder section, diameter 34.8 mm, maximum thickness 3.3 mm. The shape of the reed is defined in section A2.

During playing, the reed has two contact surfaces with the ligature. For the present simulations, the reed is clamped in the same way than for normal playing, on two rectangular surfaces 23 × 1 mm, spaced laterally by 5 mm, 38.2 mm from the tip of the reed, simulating the contact surfaces on the Vandoren Optimum ligature. However, unlike normal playing, the whole vamp of the reed is free to vibrate (see Figure 1).

For the simulations, the "Generative Part Structural Analysis" module by Catia v.5.17 (Dassault Technologies) is used, with mesh Octree3D, size 2 mm, absolute sag 0.1 mm, parabolic tetrahedrons. The generated mesh involves 5927 points, allowing both a good accuracy and a reasonable computing time (around 35 seconds).

4.3.2. Sensitivity analysis of elastic coefficients

For selecting the most relevant parameters, we conducted a One-At-a-Time sensitivity analysis [34], varying each coefficient by ±10% and computing the first 16 modes, based on the following reference values: E_L =14000 MPa, $E_T = E_R$ = 480 MPa, $\nu_{LT} = \nu_{LR} = \nu_{TR}$ = 0.22, G_{LT} = 1100 MPa, $G_{LR} = G_{TR}$ = 1200 MPa. The density ρ was set to 520 kg/m^3, according to the estimation by Guimezanes [17]. The results are shown in Table II. Notice that E_L and G_{LT} plays a decisive role, while E_T plays a marginal role and all other parameters have an almost negligible influence on the resonance frequencies. As a consequence, the moduli E_L and G_{LT} are the variables retained in the model. The approximate value of E_T has been estimated according to the morphology of the patterns of higher order modes. This value is consistent with measurements given by Spatz *et al.* [1].

Notice that these results show the validity of a 2D approach, the reed being modeled as a thin plate. This should be used for further studies.

4.3.3. Metamodel approximating the resonance frequencies

The following analytic formula ("metamodel") predicts quickly and efficiently the resonance frequencies of a clamped/free clarinet reed. It was established in the following way: Frequencies of the first 16 modes were computed by FEM, according to a network of 92 separate

[5] Do not confuse the morphological mode classes $L1$, $L2$, $T1$, $T2$, $T3$ and $T4$ with the axes L and T of the orthotropic material.

pairs of values for E_L and G_{LT}, ranging from 8000 to 17000 MPa and 800 to 1700 MPa, respectively. The other elastic coefficients were held constant, according to the reference values cited above. For the range of simulation values, this arbitrary formula (developed by trial and error) provides a very good fit (generally better than ±5 cents, see Table A3). Expected resonance frequencies f are first found in *cents* (FC) from the note F6 (1396.9 Hz), and finally in Hz:

$$\begin{aligned} f(m, E_L, G_{LT}) &= 1396.9 \cdot 2^{FC/1200}, \\ \text{where} \quad FC &= a_{m,0} + a_{m,1}\, E_p + a_{m,2} G_p \\ &\quad + a_{m,3}\, E_p\, G_p + a_{m,4}\, E_p^2 + a_{m,5} G_p^2, \\ E_p &= {E_L}^{-0.66643} \text{ and } G_p = {G_{LT}}^{0.7627}. \end{aligned} \tag{1}$$

The index m is the number of the mode defined in Table A5, Table A3, where the values of the coefficients $a_{m,q}$ are given (E_L and G_{LT} are expressed in MPa).

The influence of the density is easy to predict: frequencies vary proportionally to $\rho^{-1/2}$. The computing cost of this metamodel is about 10^7 times lower than with FEM, largely simplifying the inverse problem.

4.3.4. Efficiency of the metamodel

Equation (1) can be used to estimate the values of E_L and G_{LT}, providing a faithful reconstruction of the observed resonance frequencies. Theoretically these values could be computed for any pair of modes, after their respective observed frequencies. Unfortunately, this method gives no consistent results. A least squares fit is a more robust technique for such a computation. This leads however to systematic errors in the predicted frequencies: low-order modes are systematically overestimated, while high-order modes are underestimated. This can be corrected by adjusting the coefficients $a_{m,0}$ (from Table A3), but this cannot explain the bad correlation among flexural modes within the same series (see Table VI). According to the elastic model, these correlations should be in all cases greater than 0.998. A hypothesis for resolving this contradiction is that the moduli are varying with the frequency in an individual way for each reed. Thus in the next paragraph we consider a viscoelastic model, where E_L and G_{LT} are frequency dependent. This leads to the addition of some parameters, which are to our mind more important that the other elastic coefficients. The fit of such a model requires many observations at different frequencies, in order to reduce the influence of measurements errors and of local irregularities in the structure of cane.

Alternative hypotheses could be considered in this context, such as damping, acoustic load [21], local variations in stiffness or in density, local deviations in thickness, compared to the assumed theoretical model. However, these hypotheses are probably unable to explain the hygrometric-induced individual variations we observed for each reed, thus our preference for the viscoelastic hypothesis.

4.4. Viscoelastic model

In this section, a Zener model is considered (see e.g. [29, 30, 31, 32]). This model is applied to both moduli E_L and G_{LT}. The scheme of the standard viscoelastic solid is presented in Figure 8, with two springs E_1 and E_2 and a dashpot E_3[6]. At low frequencies, E_2 and E_3 have practically no effect (the rubbery modulus E_1 dominates). At high frequencies, E_3 has practically no effect (the glassy modulus $E_1 + E_2$ dominates). In the frequency range near $E_2/(2\pi E_3)$ the dissipation due to E_3 is maximal and the apparent modulus (storage modulus) is in the mid-range. The stress σ and the strain ε are related by the constitutive equation,

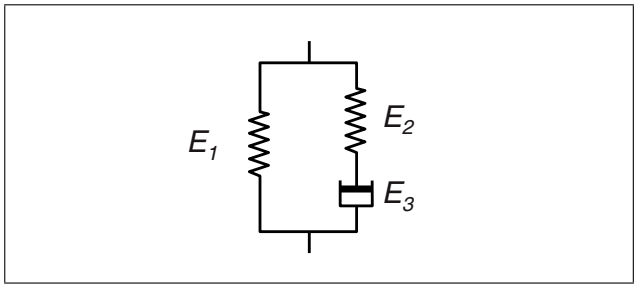

Figure 8. Schematic representation of the standard linear solid: two springs E_1, E_2 and a dashpot E_3.

$$\sigma + \tau_1 \dot{\sigma} = E_1(\varepsilon + \tau_2 \dot{\varepsilon}), \tag{2}$$

in which $\tau_1 = E_3/E_2$ is called the relaxation time and $\tau_2 = E_3(E_1 + E_2)/(E_1 E_2)$ the retardation time. E_1 is called rubbery modulus and $E_1 + E_2$ glassy modulus. In harmonic regime, for an angular frequency ω, the Young modulus is complex,

$$\begin{aligned} E^*(\omega) &= E_1 + E_2 - \frac{E_2^2}{E_2 + \mathrm{j}\omega E_3} \\ &= E_1 + E_2 + \frac{-E_2 + \mathrm{j}\omega E_3}{1 + (\omega E_3/E_2)^2}. \end{aligned} \tag{3}$$

The second formulation separates the real part ($E'(\omega)$: storage modulus) and the imaginary part ($E''(\omega)$: loss modulus) of $E^*(\omega)$. The storage modulus can thus be written as

$$E'(\omega) = E_1 + E_2 - \frac{E_2^3}{E_2^2 + \omega^2 E_3^2} = E_1 \frac{1 + \omega^2 \tau_1 \tau_2}{1 + \omega^2 \tau_1^2}. \tag{4}$$

Notice the properties:

$$\begin{aligned} E'(0) &= E_1, \quad E'(1/\tau_1) = E_1 + E_2/2 \\ E'(\infty) &= E_1 + E_2, \quad \frac{\partial E'}{\partial \omega}\left(\frac{1}{\tau_1}\right) = \frac{E_3}{2}. \end{aligned}$$

For the sake of simplicity, the parameters corresponding to E_L and G_{LT} are denoted E_1, E_2, E_3, and G_1, G_2, G_3, and the storage moduli given by equation (4) $E'(\omega)$ and $G'(\omega)$, respectively. Therefore for each reed (and each series), the model requires 6 parameters instead of 2 (while

[6] This notation allows us to write the parameters of the model as a vector, as required by the computations, but unfortunately it hides the fact that the nature of E_3 (dashpot) is physically different from E_1 and E_2 (springs).

experiments gave 4 main factors only for the whole set of results).

From the knowledge of the 6 parameters, the resonance frequencies can be deduced by an iteration procedure. For each mode the starting point of the iteration is the mean value $f^{(0)}$ of the experimental resonance frequency (see Table A1), then the storage moduli are deduced from equation (4), then a new value $f^{(1)}$ by using equation (1), etc... The convergence of the iteration method is fast, actually one iteration is enough. This can be understood by the fact that the derivative of the iterated function is small (notice that the two first rows of Table II correspond to the derivative of E_L and G_{LT} with respect to frequency). If we give an arbitrary value, for instance $f^{(0)} = 6000$, one iteration more is required for a comparable precision. In all hypotheses (see Appendix A3.6), we used one iteration only. This procedure allows the determination of $f(m)$ from the coefficients E_1, E_2, E_3, G_1, G_2, G_3 for a given reed and a given series.

5. Inverse problem and selection of a robust model

5.1. Simplification of the model by multiple regression

In order to solve the inverse problem for each reed (and each series), we use a classical Mean Squared Deviation method, from the experimental values of the 11 resonance frequencies listed in Table A3 (see Table A5). The results are given and discussed in section 5.3.

However for each reed the viscoelastic model provides 12 parameters, i.e., 12 DoF, and the PCA showed that this number needs to be reduced. Actually this model conducts sometimes to non-physical results (negative rubbery modulus, for instance). This problem comes out because the observed resonance frequencies are far from 0, so the rubbery modulus E_1 cannot be estimated precisely. For that purpose multiple regression (see Appendix A3 for details) is used, by introducing correlations among parameters and reducing the degrees of freedom to a number of 4, called "components", which are linearly related to the parameters. The 4 components are very similar to the 4 factors computed by the PCA, but, because equations (1) and (4) are nonlinear, a small deviation is inevitable for optimal results. Factors and components are consequently strongly correlated (>0.95, see Table I).

We tested different hypotheses to establish a satisfactory robust model (denoted H1 to H9 and described in Appendix A3), together with the detailed computation method. Each hypothesis leads to a given number of components related to the parameters through the regression coefficients. Notice that the parameters and components depend on both the reed and series, while the regression coefficients which correlate the parameters are independent of the reed and the series. A constant value elastic model (the parameters are fixed, and do not depend on the reed or the series, Hypothesis H1) is not sufficient. Similarly a 2-parameter elastic model (E_L and G_{LT}, independent of the series, Hypothesis H2) is not sufficient as well. Conversely a linear model without constraints (with 60 independent coefficients, corresponding to a matrix of order 12(4+1) elements[7], Hypothesis H7) is not necessary, because many coefficients are very small. Eventually a 9 coefficient linear model (H4) has been found to be very satisfactory and is described in section 5.2. The following ideas were applied: after eliminating the very small coefficients and fitting the observations with the remaining coefficients, it is observed that the predictive quality of the model is almost not affected by the simplification. This was done step by step. The problem of non-physical values for certain parameters can be corrected by setting the damping parameters E_3 and G_3 constant, independent of the reeds and of the series (typical values: $E_3 = 0.28$ and $G_3 = 0.02$). There remain 4 parameters for each series and reed, E_1, E_2 and G_1, G_2 (i.e. 8 parameters for each reed). This ensures generally that these parameters fall in a plausible range, when fitting the model. Moreover a hierarchical structure can be introduced in the model, isolating the hygrometric component, bringing the remaining 3 components to a common basis (section 5.2) and simplifying the problem (reduced to only 9 regression coefficients) and giving some insight in the data structure.

The RMSD (Root Mean Square Deviation, see Appendix A3.2) is found to be 30.4 cents for Hypothesis H4, very close to 29.8 cents for H5 with 9 coefficients more. Moreover the standard deviation of the residuals for Hypothesis H4 (and also Hypothesis H5) varies very little over the different resonance frequencies (all around 30 cents).

The fit quality cannot be considered as a perfect and definitive proof that our model reflects the true values of the corresponding storage moduli. The influence of some missing parameters in the model should be examined (for instance differences in thickness between reeds, non constant modulus E_T, non constant density ρ or radial variation of E_L). Anyway, the presented model reflects real mechanical differences between the reeds, very similar to those objectively detected by the PCA.

5.2. Robust estimation of the parameters of the viscoelastic model (Hypothesis H4)

Hypothesis H4 is chosen so that no coefficient can be removed without impacting notably the quality of fit. It can be thought of as the minimal structure allowing an adequate reconstruction of the observed resonance frequencies, in conjunction with the viscoelastic model (equation 4) and the metamodel (equation 1). This minimal structure makes the model more robust against measurements errors, even if it probably introduces some bias.

As a first step, our concern is to eliminate the influence of the moisture content and to bring both series of measurements to a common basis (i.e. predict the effect of drying on the viscoelastic parameters of series B, the series A

[7] For this example, the component vector has 4 elements to be determined, plus a fifth element, which is a constant.

being taken as a reference). $e_1[n]$, $e_2[n]$, $e_3[n]$ and $e_4[n]$ are the 4 independent components characterizing the mechanical properties of the reed n. The choice of the notations is as follows: $e_k[n]$ is the kth element of the vector $\mathbf{e}[n]$., which depends on n. These components are conditioned similarly to PCA as orthogonal factors: mean 0, standard deviation 1 and intercorrelation 0. The elimination of the moisture content can be achieved by reducing the components to a number of 3 for each series $s = 1$ (series A) and $s = 2$ (series B): for reasons explained in Appendix A3.4, these components are denoted $\check{e}_1[s,n]$, $\check{e}_2[s,n]$ and $\check{e}_3[s,n]$.

For series A, the components remain unmodified (series A is taken as reference),

$$\begin{aligned} \check{e}_1[s=1,n] &= e_1[n], \\ \check{e}_2[s=1,n] &= e_2[n], \\ \check{e}_3[s=1,n] &= e_3[n]. \end{aligned} \tag{5}$$

For series B, the effect of drying on the components is predicted by

$$\begin{aligned} \check{e}_1[s=2,n] &= c_{10} + e_1[n], \\ \check{e}_2[s=2,n] &= c_{20} + \frac{1}{2}(e_2[n] + e_4[n]), \\ \check{e}_3[s=2,n] &= c_{30} + e_3[n]. \end{aligned} \tag{6}$$

With this choice of components, the viscoelastic parameters of the model for series s and reed n can then be estimated as

$$\begin{aligned} E_1 &= d_{10} + d_{12}(\check{e}_2[s,n] + \check{e}_3[s,n]), \\ E_2 &= d_{20} + d_{12}(2\check{e}_2[s,n] - \check{e}_3[s,n]), \\ E_3 &= d_{30}, \\ G_1 &= d_{41}(6 + \check{e}_1[s,n]), \\ G_2 &= 2d_{41}(3 + \check{e}_1[s,n] - \check{e}_3[s,n]), \\ G_3 &= d_{60}. \end{aligned} \tag{7}$$

This implies some other interesting relationships,

$$\begin{aligned} E_1 + E_2 &= d_{10} + d_{20} + 3d_{12}\check{e}_2[s,n], \\ G_1 + G_2 &= d_{41}(12 + 3\check{e}_1[s,n] - 2\check{e}_3[s,n]), \\ 2E_1 - E_2 &= 2d_{10} - d_{20} + 3d_{12}\check{e}_3[s,n], \\ 2G_1 - G_2 &= 2d_{41}(3 - \check{e}_3[s,n]). \end{aligned} \tag{8}$$

Notice that the glassy modulus of E_L (i.e., $E_1 + E_2$) depends linearly only on $\check{e}_2[s,n]$. The quantities $2E_1 - E_2$ and $2G_1 - G_2$ depend linearly only on $\check{e}_3[s,n]$, however with opposed signs.

The values of the 9 coefficients are: c_{10}=1.011, $c_{20} = -2.197$, $c_{30} = 0.8294$, $d_{10} = 10300$, $d_{12} = 640.5$, $d_{20} = 7309$, $d_{30} = 0.2822$, $d_{41} = 115.7$, $d_{60} = 0.02038$. The coefficients in equation (1) are adjusted (in order to remove systematic errors) by adding to $a_{m,0}$ (from Table A3) the following values, for $m = 1$ to 11: −26.27, 32.24, −50.05, 4.80, −26.87, −65.28, −48.64, 0.07, −52.98, −76.61 and −111.55 cents.

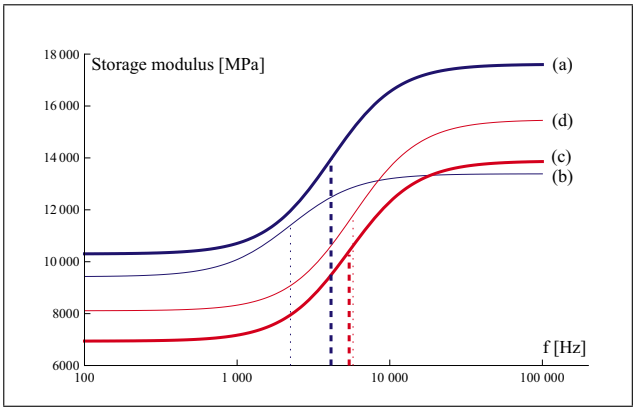

Figure 9. Hypothesis H4: plot of the storage moduli $E'_L(\omega)$ and $G'_{LT}(\omega)$ [in MPa], according to equations (4) to (7), computed for the mean value of all reeds. (a): E'_L series A, (b): E'_L series B, (c): G'_{LT} series A and (d): G'_{LT} series B. For G'_{LT}, the moduli are multiplied by 10. The abscissa of the relaxation frequencies [in Hz] is denoted by dashed lines (series A) and dotted lines (series B). The corresponding numerical values are listed in Tables IV and V. Only the portions of the curves between 2 and 18 kHz could be fitted adequately. The curves outside this range are purely hypothetical: we have no measurements.

Table III. Optimal 9-coefficients model (hypothesis H4): Statistics of the frequency-dependent increase in storage modulus (for Series A or B and E_L or G_{LT}), between the 1st and the 4th flexural mode: $1 - E'(2\pi f_{F1})/E'(2\pi f_{F4})$ or $1 - G'(2\pi f_{F1})/G'(2\pi f_{F4})$, with $f_{F1} = 1996$ Hz and $f_{F4} = 16784$ Hz. Between both series, the correlation is 0.83 for E_L and 1 for G_{LT} (as a consequence of the simplification of the model).

	E_L		G_{LT}	
	Series A	Series B	Series A	Series B
Mean	31%	16%	38%	36%
Stand. dev.	5%	6%	10%	9%
Minimum	20%	1%	13%	15%
Maximum	44%	32%	52%	49%

The change in density between the two series of measurements was not measured precisely (about −2 to −4%). In the model, density is considered as constant.

Figure 9 shows an approximation of the frequency dependence of E_L and G_{LT}, computed for the mean value of all reeds. For Series A, the storage modulus $E'(\omega)$ increases from 11700 MPa at 2 kHz ($F1$) to 17200 MPa at 16.8 kHz ($F4$), while for Series B, it increases from 11100 to 13300 MPa. Therefore under "normal" hygrometry the reed bends in a notably viscoelastic manner, whereas the ultra-dry reed bends in an more elastic manner. For G_{LT}, the reed is generally notably viscoelastic, according to our model. The corresponding values are: 783 to 1290 MPa for Series A, and 896 to 1436 MPa for Series B. Corresponding statistics are displayed on Table III. Drying seems to increase G_{LT} and decrease E_L (except around 2300 Hz), explaining the good correlation between the variables AF1 and BF1.

This simplified model permits interesting conclusions about the structure of our data:

- The component e_1 is related exclusively to G_{LT};
- e_2 is related exclusively to E_L;
- e_3 increases proportionally to the rubbery modulus of E_L (and not its glassy modulus), and decreases proportionally to the glassy modulus of G_{LT} (and not its rubbery modulus); it regulates therefore the viscous component common to E_L and G_{LT}[8];
- e_4 takes into account the variation in moisture content between series A and B.

Notice that the product of the rubbery moduli for the series A, $E_1 G_1$ is correlated at 72% with the nominal reed strength. Individually, these moduli correlate only at 50% and 55% with the nominal reed strength, respectively.

5.3. Results and discussion

Tables IV and V show our results for hypotheses H4 and H5. A comparison with results by other authors is difficult or even quite impossible, because of the disparate structure of the measurements. Such a comparison requires the reconstruction of the measurement data (when possible), the fit of a viscoelastic model or the extrapolation of the values, in order to reach the frequency and temperature range of our measurements. The validity of such a highly speculative task is questionable. For the storage modulus E'_L, all reconstructed values from other authors fall in the range around the average of our measurements ±3 times the standard deviation, however most of the time in the lower range. This probably shows that the selected value for the density ρ is somewhat too high. No representative statistics are available by the other authors.

The most important disagreement, compared with our model (hypotheses H4 and H5), is about the relaxation frequency. The explanation is probably because the studied frequency range was not same. For G_{LT}, we found no viscoelastic measurements by other authors. Our results are summarized in Tables IV and V. For E'_L, between hypotheses H4 and H5, f_r and E'_L at 4 kHz agree well, whereas E_1 and E_2 diverge by about 1-2 SD. This divergence comes because the observed frequency range was not broad enough. For the shear modulus, G_1 and G_2 are in good agreement for both hypotheses (and consequently f_r and G'_L at 4 kHz also).

Our model is valid only for "ambient dry" reeds (since the ultra-dry conditioning was not controlled), in a frequency range which should not exceed one decade. We checked that a fractional derivative model after Gaul *et al.* [32] is not necessary in our narrow frequency range. Such models are however really efficient to cover a broad frequency range. For instance, the data by Lord for dry material [12] could be fitted very well ($E_0 = 8108$ MPa, $E_1 = 2964$ MPa, $p = 0.298$ MPa·s$^\alpha$, $\alpha = 0.546$). Notice that the order of the derivative (α) is 1 in our viscoelastic model.

[8] The parameter E_2 (respectively G_2) determines the influence of the Maxwell arm in the Zener model, since E_3 (respectively G_3) is constant in our simplified model; if $E_2 = 0$ the model is perfectly elastic and the viscous component disappears

Our viscoelastic model is able to partially explain the bad correlations observed between flexural modes. In Table VI, the correlations are compared among observed resonance frequencies and computed modal frequencies, according to the viscoelastic model (hypothesis H4 and H5). It seems that additional hypotheses (such as an irregular thickness) should perhaps be considered for improving the model. However, we should remember that the determination of resonance frequencies carries some uncertainties, especially for the modes $F3$ and $T3$.

In order to clarify this issue, let us examine if the residuals (observed resonance frequencies *minus* computed modal frequencies with hypothesis H5[9]) contain some pertinent information. A PCA shows that perhaps 2 residual factors contain some interesting information (explaining 30% and 18% of the residual variance). The first residual factor is correlated with AT3 (0.86), BT2 (0.74), AT2 (0.73) and AX2 (0.66). All these modes depend strongly on G_{LT}. An adjustment of the coefficient $a_{m,2}$ from the metamodel for the transverse modes could probably cancel this systematic bias (remember that the coefficients $a_{m,q}$ are computed from a theoretical model, which is probably also biased). Indeed, an increase by 14, 21, 16 and 11% of this coefficient affecting the modes $T1$, $T2$, $T3$ and $T4$ makes the RMSD drop from 29.8 to 28.5 cents. The second residual factor is correlated with AF1 (0.36), AF2 (0.29), AT2 (−0.29), BF1 (0.28) and BT1 (−0.23). This probably reveals a competition between flexural and transverse modes when fitting the model. The bias probably comes from the coefficient $a_{m,1}$, regulating the linear dependence to E_L in the metamodel. Adjusting the coefficients $a_{m,1}$ for all modes and the coefficients $a_{m,2}$ for all transverse and generic modes makes the RMSD drop down to 26.2 cents, reaching the size of the measurement steps (25 cents). The adjustments of $a_{m,1}$ are very small for the flexural modes $F1$ to $F4$: -6, 1, 6 and 1%.

This shows that the most important bias depends linearly on the 2 most important parameters (E_L and G_{LT}) of our FEM computations. No supplementary parameter is required until this bias is removed (theoretically down to a RMSD of 21.8 cents, according to H10). For hypothesis H4, the same linear adjustment of the metamodel lets the RMSD drop from 30.4 down to 27.0 cents.

6. Conclusion

The numerical model is satisfactory. From the statistical analysis discussed in section 3.3, it allows selection of the most important parameters describing the mechanical behavior of a reed.

The efficient elastic metamodel can be extended to a viscoelastic behavior of the reeds, approximating the resonance frequencies from the longitudinal Young modulus E_L and the longitudinal / transverse shear modulus G_{LT}

[9] Because H5 is probably less biased than H4 with its minimal structure

Table IV. Summary of our results for hypotheses H4 and H5 about the viscoelastic behavior of the longitudinal Young modulus E_L in cane. E_1, E_2 and f_r (relaxation frequency): parameters from Zener model. E'_L at 4 kHz: storage modulus at 4 kHz [in MPa]. SD: standard deviation (the value preceding SD is the average). The model is valid only between 2 and 18 kHz.

Model	Storage Young modulus $E'_L(\omega)$ at about 20°C			
	E_1 [MPa]	E_2 [MPa]	f_r [Hz]	E'_L at 4 kHz
Hypothesis H4, series A	10300, SD 906	7309, SD 1432	4123, SD 808	13781, SD 897
Hypothesis H5, series A	9377, SD 844	8336, SD 1552	4027, SD 750	13449, SD 839
Hypothesis H4, series B	9423, SD 784	3964, SD 1109	2236, SD 626	12338, SD 885
Hypothesis H5, series B	7844, SD 753	5459, SD 1217	1947, SD 434	12168, SD 882

Table V. Summary of our results for hypotheses H4 and H5 about the viscoelastic behavior of the shear modulus in longitudinal / tangential plane G_{LT} in cane. G'_{LT} at 4 kHz: storage modulus at 4 kHz. Same structure as Table IV. The model is valid only between 2 and 18 kHz.

Model	Storage Shear modulus $G'_{LT}(\omega)$ at about 20°C			
	G_1 [MPa]	G_2 [MPa]	f_r [Hz]	G'_{LT} at 4 kHz
Hypothesis H4, series A	694, SD 116	694, SD 327	5420, SD 2555	926, SD 102
Hypothesis H5, series A	752, SD 119	628, SD 328	6310, SD 3296	924, SD 105
Hypothesis H4, series B	811, SD 116	736, SD 327	5749, SD 2555	1042, SD 99
Hypothesis H5, series B	774, SD 119	769, SD 328	5622, SD 2401	1022, SD 103

Table VI. Correlations of resonance frequencies between flexural modes within the same series, after observations and viscoelastic models H4 and H5. $AF1$, $AF2$, $AF3$, $BF1$, $BF2$ and $BF3$: correlations with modal frequencies $F1$, $F2$ and $F3$ within series A or series B. Lines: corresponding flexural mode between which the correlations are computed.

Model	Mode	$AF1$	$AF2$	$AF3$	Mode	$BF1$	$BF2$	$BF3$
observations	$AF2$	0.73			$BF2$	0.63		
	$AF3$	0.34	0.75		$BF3$	0.43	0.84	
	$AF4$	0.28	0.65	0.74	$BF4$	0.00	0.43	0.45
H4	$AF2$	0.93			$BF2$	0.79		
	$AF3$	0.69	0.90		$BF3$	0.62	0.97	
	$AF4$	0.56	0.81	0.98	$BF4$	0.36	0.82	0.91
H5	$AF2$	0.90			$BF2$	0.69		
	$AF3$	0.57	0.87		$BF3$	0.52	0.98	
	$AF4$	0.43	0.77	0.98	$BF4$	0.26	0.84	0.92

and considering the hypothesis of their frequency dependence. A reconstruction of the observed resonance frequencies can be achieved with a good accuracy, estimating for each reed only 4 components, from which the parameters of a viscoelastic model are computed as a linear combination. The selected model (according to hypothesis H4) is probably slightly biased, but it is more robust against measurement errors than more refined models.

Table I shows that these components are highly correlated to the factors computed by PCA (0.96 to 0.98).

The proposed method allows the determination of 3 mechanical parameters characterizing the material composing each reed, with a single series of measurements, using equations (1), (4) and (7). The reed should be conditioned with a relative humidity corresponding to the one ensured by the hermetically sealed package by Vandoren (about 55%). The fourth parameter cannot be determined in a reproducible way, since the exposure of the reeds to the ultra-dry air of the optical laboratory was not controlled. The same protocol and the same viscoelastic model can be used for other kinds of single reeds (bass clarinet, saxophone). Only the coefficients of Table A3 have to be recomputed after a FEM simulation of the corresponding reed shape.

Despite the fact that the eigenmodes of higher order probably play no important role in the acoustics of the clarinet, the present study shows that they reveal the inner structure of the material building the tip of the reed, so a new step could be done for an objective mechanical characterization of the clarinet reed. A subsequent study should examine if the obtained components are correlated with some musical qualities of the reeds. This could help the reed makers to gain a better control on their products.

Appendix

A1. Statistics and correlations

Table A1 gives the detailed statistics. Linear correlations have been computed between all possible couples

Table A1. Observed resonance frequencies, sorted by frequency (in Hz). N_A (resp. N_B): Number of identified pattern for each mode of series A (resp. B). μ: Mean value of the resonance frequency, σ: Standard deviation, min: Minimum, max: Maximum. Total: total number of identified patterns for each series.

	Series A					Series B				
Mode	N_A	μ	σ	min	max	N_B	μ	σ	min	max
F1	55	1996	77	1838	2154	55	1960	66	1812	2093
T1	55	3377	132	3091	3676	55	3436	129	3136	3729
F2	55	5130	161	4767	5669	55	4856	189	4435	5351
T2	55	6108	261	5587	6939	55	6193	247	5669	7040
X1	55	6869	198	6455	7458	45	6801	217	6363	7458
T3	55	9571	500	8617	11014	54	9590	458	8742	11014
F3	55	10146	419	9262	10857	55	9213	414	8372	10396
X2	55	11521	387	10701	12187	54	11688	379	10857	13098
X3	55	12294	368	11502	13482	11	12290	471	11839	13482
T4	53	14011	756	12186	16503	54	14111	763	12186	16503
F4	45	16784	552	15803	18524	54	15363	663	14079	17484
X6	41	16984	972	15133	18793	30	16888	734	15577	18258
X4	24	18497	518	17234	19067	23	17544	772	16033	19911
X5	0					54	18896	501	17484	19911
T5	0					14	19668	329	19067	19911
Total	658					668				

of variables in the usual way (all the variables from Table A1, except $X5$ and $T5$ of series A, i.e. 13 variables for series A and 15 for series B, plus the nominal reed strength). Results of series A for the mode $F1$ are denoted AF1, and similarly for the other results. The following 12 pairs have a correlation greater than 0.9: AF1/BF1[10], AT1/BT1, AT2/BT2, AT3/AT4, AT3/BT3, AT3/BT4, BT3/BT4, AT4/BT3, BX1/BX3, AT4/BT4, BT4/BX6 and BX3/BX4. 54 pairs of variables have a correlation between 0.8 and 0.9, 50 other pairs between 0.7 and 0.8 and 262 other pairs, below 0.7.

Between the two series, the correlation is excellent for corresponding transverse modes ($T1$ (i.e. AT1/BT1): 0.97, $T2$: 0.97, $T3$: 0.96 and $T4$: 0.98), and generally good for corresponding generic modes ($X1$: 0.87, $X2$: 0.84, $X3$: 0.87 and $X4$: 0.55). For flexural modes, the correlation is good for $F1$ and progressively lower for increasing mode order ($F1$: 0.92, $F2$: 0.66, $F3$: 0.57 and $F4$: 0.47).

Within the same series, on the contrary, there is a poor correlation between AF1 and all measurements of series A, and similarly for BF1 and series B. This is striking: the two best correlated variables are AF2 and AX1 (0.73 and 0.49, respectively) for AF1 and BF2 and BT1 (0.63 and 0.49, respectively) for BF1. Moreover, these correlations are quite low among all flexural modes: see Table VI. This fact is discussed in section 5.3.

The nominal reed strength correlates at 0.7 with AT1 and AX4. We expected a better correlation with $F1$ (only 0.6). This is surprising, since the reeds were probably sorted by a quasi-static bending method by the manufacturer. This would mean that the storage modulus of E_L at very low frequency is not well correlated with its value at the frequencies of the measured resonances. The influence of density has also to be considered. However, Obataya *et al.* [9] observed a good correlation between density and E_L. This point has to be investigated (see also section A3.4 in Appendix A3).

[10] AF1/BF1 means AF1 *versus* BF1. The correlations are computed between $AF1[n]$ and $BF1[n]$, for $n = 1$ to N, where $N = 55$; missing observations are deleted.

Table A2. Network of points for interpolating the thickness of the vamp. See explanations in the text.

x [mm]	s_0 [mm] y=0 mm	s_1 [mm] y=4mm	s_2 [mm] y=6mm
0	0.074	0.080	0.042
5	0.343	0.293	0.197
10	0.648	0.542	0.377
15	1.047	0.847	0.571
20	1.451	1.135	0.745
25	1.926	1.527	1.078
30	2.540	2.084	1.589
35	3.351	2.817	2.256

A2. Defining the shape of the reed

The thickness of the vamp at point (x, y) is interpolated as follows: first, we interpolate 3 points at y=0, 4 and 6mm, with 3 cubic splines, according to Table A2. These three points ($s_0(x)$, $s_1(x)$ and $s_2(x)$) define a biquadratic polynomial,

$$\text{vamp}(x, y) = p_0(x) + p_1(x)\, y^2 + p_2(x)\, y^4,$$

with $p_0(x) = s_0(x)$,
$p_1(x) = (-65\, s_0(x) + 81\, s_1(x) - 16\, s_2(x))/720$ and $p_2(x) = (5\, s_0(x) - 9\, s_1(x) + 4\, s_2(x))/2880$, allowing an interpolation on the y axis. The network of points above was estimated using a least squares fit, based on a network of

Table A3. Coefficients of the metamodel, equation (1). The maximum negative and positive deviations of the model (compared to the values calculated by FEM) are given by $\delta-$ and $\delta+$ [in cents]. The mode $L1$ (6th mode) has been deleted from the Table, since we didn't observe it.

mode	m	$a_{m,0}$	$a_{m,1}$	$a_{m,2}$	$a_{m,3}$	$a_{m,4}$	$a_{m,5}$	$\delta-$	$\delta+$
$F1$	1	2334.56	-1165877	0.2763	-21.99	145883795	-0.000324	-2	4
$T1$	2	1481.70	-642027	5.0725	569.69	83451520	-0.005886	-3	3
$F2$	3	3651.79	-1060625	0.7082	-123.77	130061359	-0.000786	-2	5
$T2$	4	2403.82	-493591	3.8130	501.70	64716271	-0.003741	-9	5
$X1$	5	3153.73	-822597	3.1425	604.29	105032670	-0.003785	-3	4
$F3$	6	4669.87	-1009348	0.7623	-101.18	122741172	-0.000877	-3	6
$T3$	7	3015.77	-275531	3.5285	250.00	29933670	-0.003016	-2	1
$X2$	8	3874.44	-633268	2.0921	589.25	83462866	-0.001958	-9	6
$X3$	9	4381.85	-926543	1.9907	730.31	122925338	-0.002593	-3	3
$T4$	10	2659.08	588457	6.6088	-1269.38	-120493740	-0.005269	-19	26
$F4$	11	6450.01	-1689363	-2.5544	1282.75	247738162	0.001631	-32	42

12×24 thickness measurements, achieved with a dial indicator and a coordinates-measuring table (estimated accuracy: $\pm 5\,\mu$m in z, $\pm 50\,\mu$m in x and y). We measured twenty reeds and select a particularly symmetrical one as reference. This method allows the reconstruction of the measurement network with an accuracy of $\pm 10\mu$m.

The thickness of the heel is defined to be

$$\text{heel}(y) = -14.1 + \sqrt{17.4^2 - y^2}.$$

The contour of the reed in the xy-plane is defined by

$$\text{contour}(x) = \begin{cases} 0 & \text{for } x < 0 \text{ or } x \geq 67.5, \\ \sqrt{(24.4 - x)x} & \text{for } x < 1.13196, \\ 4.08044 + \sqrt{-5.31 + 6.8x - x^2} & \text{for } x < 2.94661, \\ \dfrac{263}{40} - \dfrac{11}{900}x & \text{for } x < 67.5. \end{cases}$$

The thickness of the reed at point (x, y) is defined by

$$\text{thickness}(x, y) = \begin{cases} \min\left[\text{heel}(y), \text{vamp}(x, y)\right] & \text{for } Abs(y) < contour(x), \\ 0 & \text{otherwise.} \end{cases}$$

A3. Development and selection of a simplified viscoelastic model

In this section we describe how the proposed model was developed and selected. Alternate options are presented.

A3.1. Data structure

We need a specific notation for denoting our complicated multivariate data structure as arrays, after a list of indices (see Table A4). The 11 modes are defined after Table A3 (from 1 to 11: $F1$, $T1$, $F2$, $T2$, $X1$, $T3$, $F3$, $X2$, $X3$, $T4$, $F4$).

Table A4. List of indices.

Indice	from	to	numbering
n	1	N=55	reeds
s	1	S=2	series of measurements A (s=1) and B (s=2)
m	1	M=11	modes
q	0	Q=5	coefficients for equation (1)
i	1	I=2	moduli E_L (i=1) or G_{LT} (i=2)
j	1	J=3	viscoelastic parameters
k	0	K=2,3 or 4 or 12	components (factors)

We define a variable $v_{n,s,i,j}$ holding all parameters of our viscoelastic model,

$$\begin{aligned} v_{n,s,1,j} &= E_j \quad \text{and} \\ v_{n,s,2,j} &= G_j \text{ for reed } n \text{ and series } s. \end{aligned} \tag{A1}$$

The array $r_{n,s,m}$ holds the reconstructed resonance frequencies computed for all reed, series and modes, with the parameters $v_{n,s,i,j}$ of our viscoelastic model (see section 4.4).

A3.2. Mean Squared Deviation

As a cost function to minimize, we define the Mean Squared Deviation MSD (also called Mean Squared Error) between reconstructed and measured resonance frequencies $o_{n,s,m}$,

$$\text{MSD} = \frac{1}{NSM} \sum_{n=1}^{N} \sum_{s=1}^{S} \sum_{m=1}^{M} (o_{nsm} - r_{nsm})^2. \tag{A2}$$

With equation (A2), the components of array $\mathbf{v}$ can be fitted by any appropriate algorithm for minimizing a multivariate function. All available measurements can be utilized for fitting the models[11]. Missing observations $o_{m,s,n}$ are then eliminated while computing MSD.

Our model allows a quite good reconstruction of the resonance frequencies, with a $\sqrt{\text{MSD}} \equiv$ RMSD (Root Mean

[11] This was not the case with PCA.

Square Deviation) smaller than 20 cents (it is very small for lower modes, and always smaller than 25 cents). This corresponds to the hypothesis named H9 (all hypotheses H1 to H11 are presented and commented in section A3.6), but, as explained in section 5, the values of the coefficients are not always plausible physically. In section A3.3, we examine how to regulate this drawback by multiple regression.

A3.3. Estimating the parameters of the viscoelastic model by multiple regression

Multivariate linear regression consists in projecting linearly a n dimensional space on a onedimensional space. The generic equation is

$$y = a_0 + \sum_{n=1}^{N} a_n x_n = \sum_{n=0}^{N} a_n x_n, \quad \text{if } x_0 = 1. \tag{A3}$$

Equation (A3) can be generalized for multiple regression as

$$\mathbf{y} = \mathbf{A}\mathbf{x}, \tag{A4}$$

where $\mathbf{x}$ and $\mathbf{y}$ are column vectors and $\mathbf{A}$ a matrix. In what follows, in order to use conventional vectors and matrices (with respectively one and two dimensions), we use the following notation: $v_j[n, s, i] = v_{n,s,i,j}$ is the jth element of the column vector $\mathbf{v}[n, s, i]$.

In our case, we have no prior knowledge about the relationships among the parameters of our model. We assume that each parameter in the model can be computed as a linear combination of some unknown independent components by multiple regression. The multiple regression formula can be written as

$$v_j[n, s, i] = \sum_{k=0}^{K} M_{jk}[s, i] \cdot e_k[n]. \tag{A5}$$

In conventional vectors and matrices notation, equation (A5) reads

$$\boldsymbol{v}[n, s, i] = \boldsymbol{M}[s, i] \cdot \boldsymbol{e}[n],$$

where $\boldsymbol{e}[n]$ is the vector of the orthogonal components for each observed reed n, $\boldsymbol{M}[s, i]$ is the regression matrix, independent of the reed number, depending on the series and the kind of modulus (E_L or G_{LT}). $\boldsymbol{v}[n, s, i]$ is the vector of the parameters of the viscoelastic model.

We have only to choose an arbitrary number of components, for instance $K = 4$, referring to our PCA. We introduce arbitrary constraints in order to obtain more comparable results: over the different reeds, we state that the components must be orthogonally normalized (mean 0, standard deviation 1 and intercorrelation 0). The matrix of components $\boldsymbol{e}$ has consequently to satisfy

$$\boldsymbol{e} \cdot \boldsymbol{e}^T = \begin{pmatrix} N & 0 & 0 & 0 & 0 \\ 0 & N-1 & 0 & 0 & 0 \\ 0 & 0 & N-1 & 0 & 0 \\ 0 & 0 & 0 & N-1 & 0 \\ 0 & 0 & 0 & 0 & N-1 \end{pmatrix}. \tag{A6}$$

Each individual column vector $\mathbf{e}[n]$ from this matrix is written as (for the component $e_0[n] = 1$: see equation A3)

$$\boldsymbol{e}[n] = \begin{pmatrix} 1 & e_1[n] & e_2[n] & e_3[n] & e_4[n] \end{pmatrix}^T. \tag{A7}$$

The components of $\boldsymbol{M}$ are fitted by minimizing MSD in equation (A2). As starting value for the orthogonal components we set : $e_k[n] = factor_k[n]$, where $factor_k[n]$ are the factors computed by PCA (see Section3.2). After a first estimation of $\boldsymbol{M}$, it is possible to release the approximation about $\boldsymbol{e}$: all components and all coefficients in the matrices can be fitted by the fitting procedure. However the number of variables to fit is probably much higher than allowed by most algorithms of function minimizing. The fitting procedure has to be carried "by hand" with subsets of variables. The procedure we used is described below.

For $K = 4$ (the dimension of vector $\boldsymbol{e}[n]$ being 5), and some supplementary choices, the model works very well.

A3.4. Empirical simplification of a 4-parameter model

We observed that the effect of hygrometric changes between both measurements series can be taken into account with one parameter only, practically without drop in quality of fit. This effect can be isolated on component $e_4[n]$ and the remaining components can be transformed linearly, so the further computations can be achieved from a common basis. Equation (A5) is then structured as

$$\boldsymbol{M}[s, i] = \hat{\boldsymbol{M}}[i] \cdot \check{\boldsymbol{M}}[s]. \tag{A8}$$

The reasoning considers the situation where the two series of observations are independent, with a number of components in vector $\check{\boldsymbol{e}}[s, n] = \check{\boldsymbol{M}}[s] \cdot \boldsymbol{e}[n]$ reduced to $\check{K} = K - 1 = 3$. As a consequence the number of rows of matrix $\check{\boldsymbol{M}}[s]$ is 4, as well as the number of columns of $\hat{\boldsymbol{M}}[i]$. This approach, which allows separating hygrometry effects, offers a comfortable way to test different hypotheses, without changing the structure of the computation, by setting some coefficients in the matrices at some arbitrary values or by introducing some linear relationship between coefficients. We get fewer "active" coefficients to fit in the model: the fitting procedure is much faster and this raises the probability to find the best possible fit.

We tried to minimize the number of coefficients different from zero in the matrices, without substantial drop in quality of fit. The model was fitted "by hand", using the solver of Excel (Microsoft Office). We found empirically that a quite sparse setup still gives a good fit[12]:

$$\hat{\boldsymbol{M}}[EL] = \begin{pmatrix} d_{10} & 0 & d_{12} & d_{13} \\ d_{20} & 0 & d_{22} & d_{23} \\ d_{30} & 0 & 0 & 0 \end{pmatrix}, \tag{A9}$$

[12] The fitting process was realized by repeatedly performing four kinds of procedures, in an arbitrary order:

1. Fit the active coefficients in model, without adjusting the coefficients $a_{m,0}$.
2. Fit the active coefficients in model and adjust the coefficients $a_{m,0}$ (or fit all coefficients: $a_{m,q}$).
3. Fit the $e_{n,k}$ components (individually for each reed, irrespective of equation A6), then then normalize and orthogonalize components (in order to satisfy equation A6), finally rotate components (for improving the fit).

Table A5. Synthesis of some hypotheses tested with our model. K: Number of components for each reed n; **model**: elastic, viscoelastic or multiple regression (with the elastic model, E_L and G_{LT} are independent from frequency; the elastic model is computed after the viscoelastic one by setting very small values for the coefficients affecting E_2, E_3, G_2 and G_3, in order to avoid division by 0; multiple regression (see equations A14 and A15); **#ActiveCoef**: number of active coefficients in the matrices $\boldsymbol{M}$ or $\hat{\boldsymbol{M}}$ and $\check{\boldsymbol{M}}$ (fitted through the fitting procedure); **#OtherCoef**: number of other coefficients estimated in model ($a_{m,0}$: adjusted so that the mean error for each mode m and both series is zero, $W_{s,m,k}$: computed analytically, otherwise: fitted through the fitting procedure); RMSD [in cents] after equation (A2): this is a measure of goodness of fit (remember that the vibration patterns of the reeds were observed in steps by 25 cents).

Hypothesis	K	model	#ActiveCoef	#OtherCoef	RMSD
H1	0	elastic	2	$a_{m,0} \to 11$	76.2
H2	2	elastic	4	$a_{m,0} \to 11$	54.8
H3	3	elastic	7	$a_{m,0} \to 11$	43.9
H4	4	viscoelastic	9	$a_{m,0} \to 11$	30.4
H5	4	viscoelastic	18	$a_{m,0} \to 11$	29.8
H6	4	viscoelastic	44	$a_{m,0} \to 11$	29.1
H7	4	viscoelastic	60	$a_{m,0} \to 11$	28.6
H8	4	viscoelastic	60	$a_{m,q} \to 66$	23.2
H9	12	viscoelastic	-	$a_{m,q} \to 66$	19.8
H10	4	regression	-	$W_{s,m,k} \to 110$	21.8
H11	4	regression	4	$\hat{W}_{m,k} \to 44$	24.7

$$\hat{\boldsymbol{M}}[GLT] = \begin{pmatrix} d_{40} & d_{41} & 0 & 0 \\ d_{50} & d_{51} & 0 & d_{53} \\ d_{60} & 0 & 0 & 0 \end{pmatrix}, \tag{A10}$$

$$\check{\boldsymbol{M}}[SeriesA] = \begin{pmatrix} 1 & 0 & 0 & 0 & 0 \\ 0 & 1 & 0 & 0 & 0 \\ 0 & 0 & 1 & 0 & 0 \\ 0 & 0 & 0 & 1 & 0 \end{pmatrix}, \tag{A11}$$

$$\check{\boldsymbol{M}}[SeriesB] = \begin{pmatrix} 1 & 0 & 0 & 0 & 0 \\ c_{10} & 1 & 0 & 0 & 0 \\ c_{20} & 0 & c_{22} & 0 & c_{24} \\ c_{30} & 0 & 0 & 1 & 0 \end{pmatrix}. \tag{A12}$$

This corresponds to the hypothesis named H5. Furthermore some coefficients may be proportional to others, without noticeable drop in quality of fit. This diminishes the number of active coefficients in the different matrices from 18 to 9 (hypothesis H4),

$$\begin{aligned} d_{22} &= 2d_{12}, & d_{13} &= d_{12} = -d_{23}, \\ d_{40} &= d_{50} = 6d_{41} & d_{51} &= 2d_{41} = -d_{53}, \\ c_{22} &= c_{24} = 1/2. \end{aligned} \tag{A13}$$

A3.5. Adjusting coefficients for removing systematic errors

After fitting the different models, we observed some systematic deviations in the resonance frequencies between model and observations. This error has probably two different origins: an inevitable inaccuracy in the FEM computation (and in our metamodel) and an error for parameters not included in the model. A straightforward way to minimize the residuals is to fit the coefficients $a_{m,0}$ in equation (1)[13]. Fitting all coefficients in equation (1) is doubtless a more questionable way to reduce this error (hypotheses H8 and H9). This can reduce the mean deviation between model and observations, but greatly increase the number of coefficients in the model (see however the discussion in Section5.3).

A3.6. Testing different hypotheses

We tested different hypotheses with our model, in order to select a particularly efficient model. Some of them are summarized in the Table A5.

Hypotheses H1 to H3 (elastic model) present a poor fit; the adjustments for coefficients $a_{m,0}$ are large, compensating partially for the missing viscoelastic components. All viscoelastic models are notably better and exhibit smaller adjustments for $a_{m,0}$. Frequency dependence for E_L and G_{LT} seems evident. Hypothesis H4 shows a good accuracy, with only 9 fitted coefficients (and 11 adjustments). Increasing the number of coefficients up to 60 brings only a marginal contribution (H5 to H7). Adjusting the other coefficients of equation (1) in H8 and H9 improve the model, especially for the higher modes (Notice that no multiple regression is used for H9). Our FEM computations (and consequently our metamodel) are probably affected by systematic errors in this frequency range. The influence of E_T should possibly be considered. Between H8 and H9, the total number of components ($N \times K$) increases from 220 to 660. The adjustments within morphological classes are related: "flexural" modes shows systematically lower values than neighboring "transverse" modes.

4. Eliminate some active coefficients (set them as 0, 1 or some other constant value; set some arbitrary linear dependence from other coefficients)

[13] These coefficients can be fitted through the fitting procedure (some constraints have however to be introduced, to avoid an important deviation from their theoretical values) or merely adjusted *a posteriori*, so that the total averaged deviation for each mode and both series is 0.

A3.7. Backward random validation

Following a suggestion by a referee, we applied a principal component analysis to simulated data computed after hypothesis H5: we assigned randomly a value for the 4 components and 55 reeds, following a normal distribution. We repeated this operation ten times. As expected, the PCA detected 4 factors capturing 91.2% (Standard Deviation 1.3%) of the variance of the simulated data (mean: 42.6, 20.9, 16.2 and 11.5% for each factor). This seems compatible with the analysis performed on the observed frequencies (section 3.2): 4 factors: 91.2% of the variance (53.6, 21.4, 10.8 and 5.4% for each factor).

A4. Reconstructing observed resonance frequencies by multiple regression

The scheme of our viscoelastic model is:
⟨vector $\boldsymbol{e}$⟩ → {multiple regression, equation (A5)} → ⟨viscoelastic coefficients $\boldsymbol{v}$⟩ → {viscoelastic model, equation (4)} → ⟨ moduli E'_L and G'_{LT}⟩ → {metamodel, equation (1)} → ⟨ reconstructed resonance frequencies $\boldsymbol{r}$⟩.

It has a very interesting property: the same model of cane can be used for any kind of reeds (for instance bass clarinet or saxophone) or for any other boundary conditions. Only equation (1) has to be changed (or at least, the coefficients $a_{m,q}$ have to be recomputed).

Within our particular setup, the viscoelastic model is however not required for reconstructing the observed resonance frequencies: PCA is theoretically the optimal linear scheme, in terms of least mean square error, for compressing a set of high dimensional vectors into a set of lower dimensional vectors and then reconstructing the original set by multiple regression. The shortened scheme is merely: ⟨vector **factor**⟩ → {multiple regression} → ⟨reconstructed resonance frequencies $\boldsymbol{r}$⟩.

Let us examine this option. For this purpose we use the array $factor_{n,k}$ computed in section 3.2, holding our 4 principal components (factors). As before (section A3.3), we set $factor_{n,0} = 1$. The array of reconstructed resonance frequencies $r_{n,s,m}$ can be computed by multiple regression using an array of matrices $W_{s,m,k}$,

$$\boldsymbol{r}[n, s] = \boldsymbol{W}[s] \cdot \mathbf{factor}[n]. \tag{A14}$$

As before (section A3.4), we have also the option to reduce the dimensionality from K to $\check{K}$, using the previously defined array of matrices $\check{\boldsymbol{M}}[s]$ and then use a unique matrix $\hat{W}_{m,\check{k}}$ to operate the multiple regression,

$$\boldsymbol{r}[n, s] = \hat{\boldsymbol{W}} \cdot \check{\boldsymbol{M}}[s] \cdot \mathbf{factor}[n]. \tag{A15}$$

We call these two options: hypotheses H10 and H11. For H11, we performed a small orthogonal rotation of the factors to concentrate the information about the hygrometric material properties in $factor_{n,4}$, for a better fit. The results are summarized in Table A5.

Multiple regression is an accurate way to retrieve our measurements, comparable to H8 and H9. With only 48 coefficients, H11 is very efficient, even better for "transverse modes" than H10. The results of the regressive model are more difficult to interpret than those of the viscoelastic model. As $e_{n,4}$ before, $factor_{n,4}$ serves uniquely to adjust $factor_{n,2}$ relatively to series B. As expected, $factor_{n,1}$ influences mainly the "transverse modes" and $factor_{n,2}$ the "flexural modes". Their respective coefficients in the matrix $\hat{\boldsymbol{W}}$ reflect this antinomy. "Transverse" and "flexural modes" are affected by $factor_{n,3}$ in a quite similar way, but the slope is not same.

Acknowledgement

We express gratitude for the financial aid from association DEPHY of the "département de physique de l'ENS", and to Fadwa Joud for her help during the experiments. The Haute-Ecole ARC (Neuchâtel, Berne, Jura) provided the software for simulation and calculation, and offered helpful instructions. The Conservatoire neuchâtelois partially supported this study for nearly 3 years. We also thank Morvan Ouisse and Emmanuel Foltête for fruitful discussions, Bruno Gazengel and the referees for careful reading and constructive suggestions.

References

[1] H. Spatz, H. Beismann, F. Brüchert, A. Emanns, T. Speck: Biomechanics of the giant reed Arundo donax. Philosophical Transactions of the Royal Society of London. Series B: Biological Sciences **352** (1997) 1.

[2] E. Marandas, V. Gibiat, C. Besnainou, N. Grand: Caractérisation mécanique des anches simples d'instruments à vent. J. Phys. IV France **4** (1994) C5–633.

[3] S. Ollivier: Contribution à l'étude des oscillations des instruments à vent à anche simple: Validation d'un modèle élémentaire. Dissertation. Université du Maine, Le Mans, France., 2002.

[4] J. Dalmont, J. Gilbert, S. Ollivier: Nonlinear characteristics of single-reed instruments: Quasistatic volume flow and reed opening measurements. The Journal of the Acoustical Society of America **114** (2003) 2253.

[5] O. Speck, H. Spatz: Mechanical Properties of the Rhizome of Arundo donax L. Plant biol (Stuttg) **5** (2003) 661–669.

[6] O. Speck, H. Spatz: Damped oscillations of the giant reed Arundo donax (Poaceae). American journal of botany **91** (2004) 789.

[7] P. Chevaux: Améliorations de la durée de vie des anches doubles en roseau pour instruments à vents. Diploma Thesis. Institut National des Sciences appliquées de Lyon, France, 1997.

[8] E. Obataya: Physical properties of cane used for clarinet reed. Wood Res. Tech. Notes **32** (1996) 30–65.

[9] E. Obataya, T. Umezawa, F. Nakatsubo, M. Norimoto: The effects of water soluble extractives on the acoustic properties of reed (Arundo donax L.). Holzforschung **53** (1999) 63–67.

[10] E. Obataya, M. Norimoto: Mechanical relaxation processes due to sugars in cane (Arundo donax L.). Journal of Wood Science **45** (1999) 378–383.

[11] E. Obataya, M. Norimoto: Acoustic properties of a reed (Arundo donax L.) used for the vibrating plate of a clarinet. The Journal of the Acoustical Society of America **106** (1999) 1106–1110.

[12] A. Lord: Viscoelasticity of the giant reed material Arundo donax. Wood Science and Technology **37** (2003) 177–188.

[13] F. Pinard, B. Laine, H. Vach: Musical quality assessment of clarinet reeds using optical holography. The Journal of the Acoustical Society of America **113** (2003) 1736.

[14] P. Picart, J. Leval, F. Piquet, J. Boileau, T. Guimezanes, J. Dalmont: Tracking high amplitude auto-oscillations with digital Fresnel holograms. Optics Express **15** (2007) 8263–8274.

[15] P. Picart, J. Leval, F. Piquet, J. Boileau, T. Guimezanes, J. Dalmont: Study of the Mechanical Behaviour of a Clarinet Reed Under Forced and Auto-oscillations With Digital Fresnel Holography. Strain **46** (2010) 89–100.

[16] D. Mounier, P. Picart, J. Leval, F. Piquet, J. Boileau, T. Guimezanes, J. Dalmont: Investigation of clarinet reed auto-oscillations with digital Fresnel holography. The Journal of the Acoustical Society of America **123** (2008) 3240.

[17] T. Guimezanes: Etude expérimentale et numérique de l'anche de clarinette. Dissertation. Université du Maine, Le Mans, France, 2007.

[18] D. Casadonte: The perfect clarinet reed? Vibrational modes of realistic clarinet reeds. The Journal of the Acoustical Society of America **94** (1993) 1807.

[19] D. Casadonte: The clarinet reed: an introduction to its biology, chemistry and physics. Dissertation. Ohio State University, 1995.

[20] M. Facchinetti, X. Boutillon, A. Constantinescu: Application of modal analysis and synthesis of reed and pipe to numerical simulations of a clarinet. The Journal of the Acoustical Society of America **108** (2000) 2590.

[21] M. Facchinetti, X. Boutillon, A. Constantinescu: Numerical and experimental modal analysis of the reed and pipe of a clarinet. The Journal of the Acoustical Society of America **113** (2003) 2874.

[22] I. Jolliffe: Principal component analysis. Springer Verlag, 2002.

[23] U. Schnars, W. Jüptner: Direct recording of holograms by a CCD target and numerical reconstruction. Applied Optics **33** (1994) 179–181.

[24] F. Joud, F. Laloë, M. Atlan, J. Hare, M. Gross: Imaging a vibrating object by Sideband Digital Holography. Optics express **17** (2009) 2774–2779.

[25] F. Joud, F. Verpillat, F. Laloë, M. Atlan, J. Hare, M. Gross: Fringe-free holographic measurements of large-amplitude vibrations. Optics Letters **34** (2009) 3698–3700.

[26] Claripatch SA website. http://www.claripatch.com, 2012.

[27] Wikipedia. http://en.wikipedia.org/wiki/Principal_component_analysis, 2012.

[28] Systat. http://www.systat.com, 2012.

[29] D. Roylance: Engineering viscoelasticity in 3.11 OpenCourseWare . Departament of Materials Science and Engineering Massachusetts Institute of Technology, Cambridge (2001).

[30] A. Chaigne, J. Kergomard, X. Boutillon: Acoustique des instruments de musique. Belin, 2008.

[31] E. Dill: Continuum mechanics: elasticity, plasticity, viscoelasticity. CRC, 2006.

[32] L. Gaul, A. Schmidt: Experimental Determination and Modeling of Material Damping. VDI-Berichte; Schwingungsdämpfung **2003** (2007) 17–40.

[33] J. M. Heinrich: Recherches sur les propriétés densitométriques du matériau cane de Provence et ses similaires étrangers; relation avec la qualité musicale; étude associée d'une mesure de dureté. Technical report Ministère de la Culture, Direction de la Musique et de la Danse, France, 1991.

[34] A. Saltelli, M. Ratto, T. Andres, F. Campolongo, J. Cariboni, D. Gatelli: Global sensitivity analysis. the primer. John Wiley & Sons Chichester, England.

Chapter 4

Static Characterization of the Clarinet Exciter

Résumé

Ce Chapitre propose une méthode originale pour mesurer la caractéristique non linéaire statique de l'excitateur de clarinette, qui lie le débit d'air entrant dans la clarinette en fonction du saut de pression Δp à travers l'anche et de l'embouchure (pression de lèvre appliquée sur l'anche). Ce méthode utilise un bec de clarinette instrumenté, muni d'une anche et d'une lèvre artificielle dont la position ψ est contrôlée par une vis micrométrique. Le bec est connecté à une bouteille dans laquelle on génère un vide modéré en début d'expérience, puis l'air revient peu à peu dans la bouteille à travers le canal (fente entre le bec et l'anche). Après un certain laps de temps, l'anche s'ouvre et la pression ambiante est rétablie dans la bouteille. Les lois thermodynamiques en conditions isochores permettent de calculer à chaque instant le débit entrant dans la bouteille à travers le bec, à partir des mesures de pression. Cette mesure du débit permet d'estimer la section aéraulique efficace $S(\Delta p, \psi)$ à l'aide de la loi de Bernoulli.

4.1 Introduction

Backus was a pioneer in investigating the opening of the channel in playing situation [8] and developed an empirical model used by some early authors. Among them [178, 51, 52, 53, 111, 122, 10] should be mentionned. Hirschberg, Zon and col. established the foundations of the aeraulic model, which is now generally used for the calculation of the airflow entering through the channel. [81, 173, 174, 86, 65, 54]. Ollivier [115] and Dalmont [36] developed a measurement device on this this background, which was used for instance by [32, 33, 39]. The measurement technique proposed in this Chapter is a continuation of this work. The main goal of the present development is to enhance the precision of the measurements, especially at high Δp, when the flow rate is low and difficult to measure with the method described in [115]. Other works should be mentioned on this topic, for instance [21, 1, 118].

This chapter describes an experimental device [148] measuring the static characteristics of the clarinet exciter (consisting of a mouthpiece, a reed and a lip). This device measures the quantity of air entering the instrument, according to the deflection of the reed caused by the applied pressure (lip + air). Chapter 3 is devoted to dynamical measurements, while the present Chapter is devoted exclusively to static measurements. This limitation is justified by a personal belief that has slowly grown up over the years: I am now convinced that the most important concerns about clarinet reeds are related to subtleties in the contact with the lay. We have to relativise the importance of the traditional dynamic approach, which states that a good reed has a good "vibration". In my mind, a good clarinet reed must above all not interfere negatively with the operation of the instrument, so as not to hinder the vibration of its air column. The higher modes of vibration of the reeds play probably a quite anecdotal role in the operation of the

instrument (except perhaps the first torsion mode, which can be excited quite easily, according to my experimental observations). The dynamical problem consists essentially in determining the mass and the damping of a 1D oscillator with nonlinear stiffness. In the playing situation, this task is complicated by the fact that the lip is an integral part of the exciter and that it continuously modulates the dynamic parameters of mass and damping, while its elasticity varies, according to its muscular tension, modifying the "mask" of the instrumentalist. I renounced to study the question of lip mechanics (for this topic, see the attempts in [63, 75]), approximating mass and damping by optimization, comparing measurements and simulations (see Chapter 8).

4.2 Principle of measurement

The device measures the airflow entering the instrument in function of the exciter, with respect to the pressure exerted by the lip on the reed and to the pressure drop across the reed. From this flow rate measurement, the effective aeraulic section is determined by Bernoulli's law. The measuring device consists of an instrumented clarinet mouthpiece connected to a bottle of known volume. The measurement principle is relatively simple: a moderate vacuum (about -15 kPa) is created in the bottle, using a vacuum cleaner. The depression is measured by a piezoelectric sensor. From the knowledge of the initial conditions, from the evolution of the pressure recovery in the bottle and according to the thermal behavior of the bottle, the thermodynamical laws allow to deduce at any moment the quantity of air present in the bottle, and thus measuring the air flow penetrating through the channel (slot between the mouthpiece and the clarinet reed). Very low flow rates can be measured with remarkable precision thanks to the integrating effect of the bottle. A measurement in quasi-static condition requires to avoid any self oscillation of the device. For this purpose, a diaphragm is inserted between the mouthpiece and the bottle, which greatly increases the losses, preventing generally any oscillation [115, 36].

When the depression is large, the reed bends tightly against the mouthpiece lay and the air returns very slowly into the bottle, then, as the depression decreases, this quantity of air becomes more important, and after a while, the sudden opening of the reed occurs, typically during a tenth of a second. The speed of the discharge is slow enough, so that quasi-static conditions can be considered.

4.3 Measurement Bench

The measurement bench is designed to allow several types of measurements (static and dynamic), while ensuring a good reproducibility, without requiring any modification of the embouchure between two experiments of different natures. Fig. 4.3 gives an overview of the experimental setup.

4.3.1 Instrumented mouthpiece

Sensors

The instrumented mouthpiece is made from a Vandoren clarinet mouthpiece model M30, in which different sensors are installed:

— a pressure sensor (Model Endevco 8507C-2) measures the pressure (relatively to the atmospheric pressure, *via* a capillary duct) into the mouthpiece bore at 65 mm from the tip of the mouthpiece.

— 2 optical sensors (reflection coupler ITR8307, consisting of an infrared LED (light source) and a phototransistor (actual sensor)) are installed in the mouthpiece chamber (baffle) about 6 mm from the tip of the mouthpiece, at the left and right edges of the window. The average distance between the reed bent against the lay and the sensor is about 2.5 mm.

The optical sensors were installed by hand in the mouthpiece. Their positions are not perfectly symmetrical.

Conditioning and acquisition of signals

The pressure signals are conditioned by the Endevco amplifier, model 126 and the optical signals by the operational amplifier OP491GPZ.

The signals are acquired using a National Instruments NI9222 acquisition card, at the maximum sampling rate (500 kHz), then downsampled at 10 kHz (in real time) by averaging over 50 successive samples. This procedure reduces the measurement noise considerably, without significant aliasing problems, given the low amplitude of the signals measured above 5 kHz. The reed displacement is obtained (at relatively low speed) with an estimated accuracy of the order of 100-200 nm. The precision is of the order of one micron for fast movements (the reduction of the measurement noise is less efficient).

Immobilization of the mouthpiece

The instrumented mouthpiece is secured in a vise, the jaws of which have been machined and corked, to allow a stable immobilization, without damaging the mouthpiece (see Fig. 4.1). The reeds are attached to the mouthpiece by a Vandoren Optimum ligature, exactly as in a playing situation. The precision of the longitudinal and lateral positioning of the reeds is ensured by two positioning stops, against which the heel of the reed abuts. To improve the reproducibility of positioning, the reeds are pressed against the left guide before clamping the ligature, since the width of each reed is slightly different and varies moreover with the hygrometry.

4.3.2 Artificial lip

The artificial lip consists of a silicone parallelepiped of approximate dimensions 11 X 13 X 10 mm. The lip is glued on a steel rod 3 mm in diameter (artificial teeth), maintained by a metal stirrup. The lip has been glued in such a way that the face in contact with the reed is approximately parallel to the surface of the reed vamp, ensuring however that the side near to the reed tip comes first into contact with the reed, so as to avoid as much as possible the nonlinearity caused by a progressive longitudinal bending of the lip on the surface of the reed. The artificial lip is screwed to the spindle of a digital dial gauge. The vise and the dial gauge are fixed to the frame of an old 2-axis milling machine. Stoppers keep the vise stationary in the axes x (longitudinal) and y (transverse). A toggle lever allows to lift the dial gauge (with the artificial lip) to mount the reeds to be tested. A stop allows a precise repositioning of the lip (of the order of one micron) in the z axis (vertical). A micrometric screw is used to finely adjust the displacement of the artificial lip in the vertical axis, denoted ψ, while checking its position with the digital dial gauge (resolution of the display: 0.001 mm). The zero is fixed arbitrarily approx. 0.3 mm before contact of the lip with the reed. The longitudinal and transverse position of the lip was not modified during all the experiments. The axis system is illustrated in Fig. 5 of the paper presented in Chapter 3. Fig. 4.4 presents the artificial lip in a measurement situation.

Issues

Preliminary tests revealed several problems related to the artificial lip: a very pronounced viscoelastic behavior was observed. It turned out that this is due to the lateral and longitudinal deformation of the silicone under pressure. Because of friction with the reed, the relaxation is not instantaneous and remains measurable for several minutes. The silicone migrates gradually on the surface of the reed, releasing the tension. Another problem has annoying consequences (see Fig. 4.2): the reed is relatively transparent to infrared [1]. The optical signal therefore also depends on the reflection due to the lip and its state of deformation. A remedy could be found for these two problems: a piece of aluminized Mylar is glued on the face of the lip in contact with the reed. This eliminated practically all traces of viscoelasticity, except that intrinsic to the reed, which proved to be much weaker than that due to the lip. The reflective aluminum surface improves also significantly the quality and reliability of the optical signals.

1. The relative transparency of the reed also works in the opposite direction: we must guarantee constant lighting throughout the measurement. This problem is particularly sensitive in cloudy weather: changes in brightness affect the reproducibility of measurements, so a darkening of the windows was necessary.

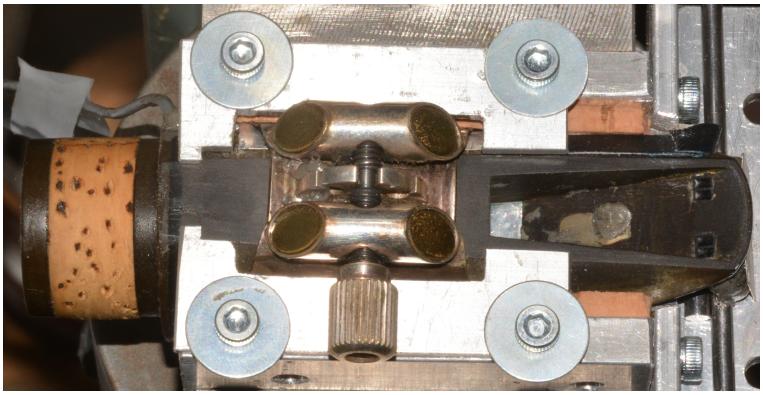

Figure 4.1 – Instrumented mouthpiece. Observe the vise with corked jaws immobilizing the instrumented mouthpiece and the ligature, the 2 optical sensors at the tip of the mouthpiece and the 2 positioning stops, against which the heel of the reed abuts. The gray mass fills an experimental hole (drilled in the mouthpiece for the installation of a pressure sensor).

Figure 4.2 – Reed mounted on the instrumented mouthpiece showing by transparency the 2 illumination spots of the infrared LEDs of the optical sensors (the photo camera is sensitive to near-infrared).

Figure 4.3 – Overview of the experimental device during aeraulic measurements. Compare with the scheme of the same device in Fig. 4.5. From left to right: the thermally insulated bottle (about 3L), the plug, the cock valve, the connection joint (with insulating foam), the vise immobilizing the instrumented mouthpiece, the digital dial gauge to which the artificial lip is attached, the micrometric adjustment screw, the frame of the old milling machine, the camera with macro lens (for the calibration of the optical sensors).

4.3.3 Bottle

The bottle is a mechanically rigid container, hermetically closed, thermally insulated and opaque to light. Since the measurement principle is based on the thermodynamical laws, the dynamics of the heat exchange between the bottle and the air inside the bottle has to be well controlled. Two antinomic variants can be envisaged to optimize the measurement accuracy:

1. Insulating version: the insulation between the walls of the bottle and the air inside the bottle is optimized, so a quasi adiabatic situation can be considered.
2. Thermostatic version: according to the advice of A. Hirschberg (pers. comm.), the bottle

Figure 4.4 – View of the instrumented mouthpiece and the artificial lip in measurement situation. Observe the instrumented mouthpiece immobilized in the vise, one of the positioning stops (lateral and longitudinal) of the reed, the ligature, the reed, the millimeter scale, the artificial lip and its stirrup screwed to the spindle of a digital dial gauge. The elastic counterbalance the spring of the dial gauge, so as to press the spindle of the dial gauge against the micrometer screw.

is filled with fine steel wool, so that the return to room temperature is fast, after each pressure variation.

Tests were carried out using a container of about 100 liters filled with 6 kg of steel wool. It turned out that this rather complicates the problem of heat exchange. I did not experiment if the use of a fan inside the container would allow a better homogenization of the air masses, which could facilitate the modeling of the thermal behavior.

The bottle used in the experiments is made of glass with relatively thick walls. Its volume is 3.178 liters. The neck of the bottle is capped with a plastic plug, allowing a tight connection with the neck. An Endevco 8507C-2 pressure sensor is installed in the plug and also a cock valve, connected to a vacuum cleaner. To avoid the problems caused by the airflow in front of the sensor, a thin flexible tube (inner diameter about 1 mm) is connected, so that the sensor measures the pressure inside the bottle. Calibrated diaphragms can be inserted into a cylindrical slot drilled in the center of the plug.

This bottle has an intermediate thermal behavior (between the two variants mentioned), relatively easy to model empirically. However, the kinetics of the airflow inside the bottle must be taken into account, which can accelerate the heat exchange at the walls.

4.3.4 Connection joint between mouthpiece and bottle

A cylindrical pipe, 9.1 mm long and 16 mm inner diameter, joins the instrumented mouthpiece and the bottle. The additional volume provided by this pipe retards slightly the pressure recovery (when the pressure difference across the diaphragm is large), which improves slightly the accuracy of the measurements. This additional volume may promote unwanted reed squeaks, which must be damped with absorbing foam, thus constituting a kind of low-pass filter. However, the DC resistance to the airflow should kept relatively low by inserting a pipe of small diameter (about 5 mm), passing through the foam from one side to the other.

4.4 Calibration of Diaphragms (1) and Air Flow Measurement (2)

Before proceeding with flow measurements, the diaphragm must first be calibrated. The process is divided in 2 phases: 1) calibration of the diaphragm, 2) measurement of the nonlinear characteristics of the reeds. The underlaying thermodynamic problem must be solved for each phase.

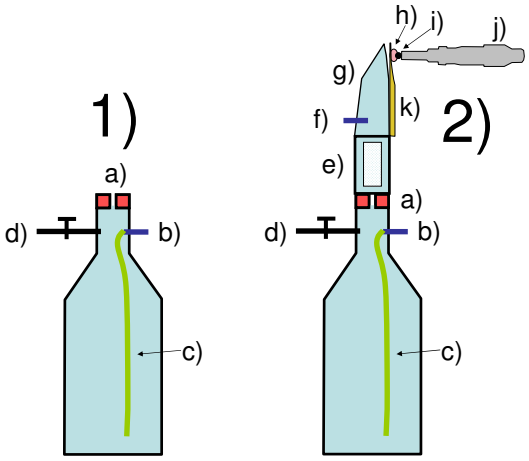

Figure 4.5 – Schematic setup of the problems 1) and 2). a) diaphragm, b) piezoelectric pressure sensor (bottle), c) thin tube (about 1 mm inner diameter), d) cock valve, e) adaptation barrel with absorbing foam (damping the acoustical oscillations), f) piezoelectric pressure sensor (mouthpiece), g) clarinet mouthpiece, h) artificial lip (silicon 10 mm thick), i) steel rod (diameter 3 mm) glued to the artificial lip, j) micrometer screw (controlling the position ψ of the artificial lip), k) clarinet reed

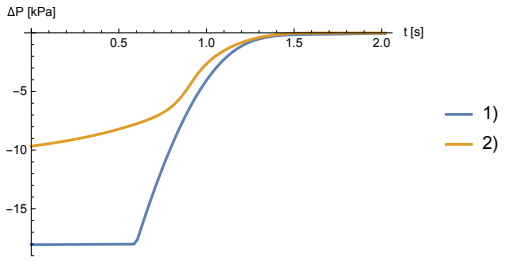

Figure 4.6 – Typical measurements of ΔP during the discharge (zoom) for Problems 1) and 2): 1) diaphragm of 1.5mm diameter. 2) reed measured with a moderately tight embouchure.

Problem 1): discharge through a diaphragm

A diaphragm is connected to the bottle. A moderate vacuum (about 15-20 kPa) is generated in the bottle trough a cock valve at the beginning of the experiment (while the diaphragm is closed). After about 1 minute (allowing the observation of the heat exchange with the bottle), the diaphragm is quickly opened and the discharge starts (the air comes back into the bottle). The pressure in the bottle is measured with a piezoelectric sensor. See Fig. 4.5.

The purpose is to determine the effective aeraulic section of the diaphragm S_{dia} from the pressure measurement (via the computation of temperature and flow rate).

Problem 2): discharge through a varying aeraulic section

The setup of Problem 1) is completed by a clarinet mouthpiece and a reed. An artificial lip (silicon) compresses the reed against the lay of the mouthpiece. The position of its support (stirrup holding the artificial teeth) is denoted ψ and is controlled by a micrometer screw. The reed is not moistened before measurement, in order to avoid a bias in the measurement due to drying.

The purpose is to determine the effective aeraulic section of the channel (slit between reed and mouthpiece) in quasistatic conditions from the pressure measurement inside the mouthpiece p and the aeraulic section of the diaphragm S_{dia} calibrated with Problem 1). The measurement of the pressure in the bottle serves only as a control for the computations. This way the delicate problem of pairing between sensors can be avoided and the precision and the reproducibility of the measurements is increased.

Typical discharge measurements for problems 1) and 2) are depicted on Fig. 4.6. The total duration of one experiment is about 90 s.

4.5 Thermodynamical model

4.5.1 Laws of thermodynamics

This subsection recalls some laws of thermodynamics, using mainly the traditional notations. These laws are well known and can be found in every book about thermodynamics and also in every handbook of chemistry and physics, for instance in the one of my regretted father [116].

Constants and parameters

Description	Identifier	Typical value	Unit
Ideal gaz constant	R	8.314	J/mol/K
Constant for diatomic gazes	γ	1.4	adim
Density of air	ρ		kg/m^3
Viscosity of air	ν	15.6×10^{-6} (at $25°C$)	m^2/s
Pressure	P		Pa
Atmospheric pressure	P_0	101300	Pa
Pressure drop	$\Delta P = P - P_0$		Pa
Volume	V	0.003178	m^3
Flow rate	U		m^3/s
Aeraulic section	S		m^2
$R\times$number of moles of gaz	$N = nR$		J/mol/K
Absolute temperature	T		K
Ambient temperature	T_0	295	K
Temperature of the jet	T_{jet}		K
Temperature of the thermostat	T_{th}		K
Constant of the thermostat	r		
Heat capacity at constant volume	$C_v = N/(\gamma - 1)$		J/mol/K
Internal energy	E		J
Work	W		J
Heat	Q		J/K
Sample rate	f_s	10000	Hz
Time	t		s
Time step	$t_s = 1/f_s$	0.0001	s

Identifiers written with uppercase generally refer to values inside the bottle. In lowercase the same identifiers refer to the value inside the mouthpiece.

Laws

Ideal gas law

$$P\,V = N\,T = n\,R\,T \tag{4.1}$$

and its differential form:

$$dP\,V + P\,dV = dN\,T + N\,dT \tag{4.2}$$

First principle of thermodynamics:

$$dE = dW + dQ \tag{4.3}$$

Newton's empirical law of cooling (thermostat):

$$dT_{th}/dt = -r(T - T_0) \tag{4.4}$$

r is a positive constant, which has to be determined experimentally.

Bernoulli's law:

$$U = \text{sign}(\Delta P)\,S\,\sqrt{2/\rho|\Delta P|} \tag{4.5}$$

This Eq. is valid valid for incompressible fluids and large ducts, comparatively to the aeraulic section S, for Reynolds numbers $Re \simeq U/(\nu\sqrt{\pi S}) > 2000$. For compressible fluids the equation is approximately valid for the conditions at the output of the jet.

4.5.2 Isochoric model

The heat variation due to the thermostatic effect of the bottle is:

$$dQ = C_v\,dT_{th} \tag{4.6}$$

The work of small air volume dV leaving the jet outgoing the diaphragm with a temperature T_{jet} and a pressure P is $dW = dV\,P = dN\,T_{jet}$. On the other side, the variation of energy is $dE = 1/(\gamma - 1)((N + dN)(T + dT) - (dN\,T_{jet} + N\,T))$. Applying Eqs. 4.1, 4.3, 4.4 and 4.6, we obtain the equation of our thermodynamic model in isochoric conditions (*i.e.* at constant volume):

$$dN = \frac{dP\,V + N\,r\,(T - T_0)dt}{\gamma\,T_{jet}} \tag{4.7}$$

Considering an adiabatic expansion in the jet, the temperature of the air leaving the jet is $T_{jet} = T_0\,(P/P_0)^{\frac{\gamma-1}{\gamma}}$.

4.5.3 Discrete time scheme for Problem 1

During an experiment, the pressure in the bottle $P[t]$ is measured with time steps $t_s : P_m = P[m\,t_s]$. We have to deduce from the equations above the temperature T_m and the number of moles ($\times R$) of air in the bottle, N_m.

Initialization

At time step $m = 0$ (before generating the vacuum), the air in the bottle is at ambient temperature T_0 and atmospheric pressure P_0. Applying Eq. 4.1, the initial quantity of air in the bottle is: $N_0 = P_0 V/T_0$.

Iterations for $m > 0$

$$\begin{aligned} dN &= \frac{V(P_m - P_{m-1}) + N_{m-1}\,r\,t_s\,(T_{m-1} - T_0)}{\gamma\,T_{jet}} \\ N_m &= N_{m-1} + dN \\ T_m &= P_m V/N_m \\ U_m &= dN\,T_m/(P_m\,t_s) \end{aligned} \tag{4.8}$$

4.5.4 Validation with known diaphragms

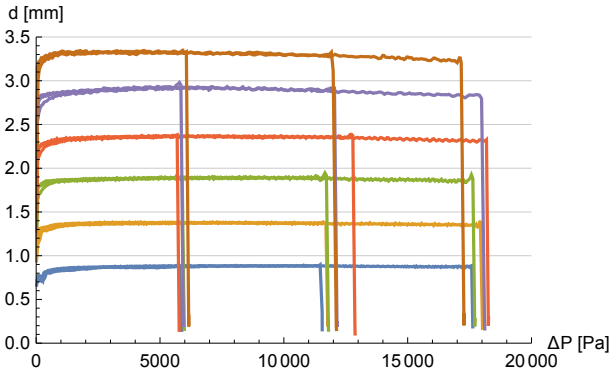

Figure 4.7 – Color lines: effective aeraulic diameter of the tested diaphragms computed with the isochoric scheme Eq. 4.8. Each diaphragm is measured 3 times with different initial conditions. Thin dark thin lines: nominal diameter of the diaphragms.

A validation of the model was performed with a series of chamfered diaphragms of nominal diameters 1, 1.5, 2, 2.5, 3 and 3.5mm. Eq. 4.5 allows the computation of the equivalent aeraulic section S from U, ρ (in the bottle) and ΔP, from which we deduce the equivalent aeraulic diameter of the diaphragms.

Fig. 4.7 depicts the results. The following values of r were determined by optimization (among 3 tests with different initial depressions for each diaphragm): 0.25, 0.32, 0.39, 0.46, 0.54, 0.61, for the diameters 1 to 3.5mm. This accounts approximately for the greater heat exchange with the bottle when the flow rate through the diaphragm is high. Before the discharge $r = 0.20$ (measured value in static conditions).

The aeraulic section of the diaphragm S_{dia} used in Problem 2) is calibrated with this method (in our case 2.9mm). The adaptation barrel with absorbing foam (damping the acoustic oscillations) belongs formally to the diaphragm (like every aeraulic resistance downstream the mouthpiece sensor).

4.5.5 Discrete time scheme for Problem 2

This problem is subdivided in 2 subproblems:
A) compute the net mass flow dn entering into the mouthpiece
B) compute the net mass flow dN entering into the bottle

The total mass flow entering trough the channel is $dN_{ch} = dn + dN$, from which $U_{ch} = T_0 \, (p/P_0)^{\frac{\gamma-1}{\gamma}} \; dN_{ch}/(p \, dt)$ and its corresponding aeraulic section S_{ch} is deduced with Eq. 4.5.

Subproblem A) The mouthpiece is treated with Eq. 4.8 in which the variables of the mouthpiece replace those of the bottle ($P \to p$, $U \to u$, and so on). An adiabatic approximation can be used for this case : $dQ = 0$, thus $r = 0$.

Subproblem B) the combination of Eq. 4.7 with Bernoulli's law Eq. 4.5 enables the calculation of the pressure in the bottle P_m (at discrete time m) from the corresponding measurement of the pressure in the mouthpiece, denoted p_m.

Initialization Like Problem 1), additionally: $p_0 = P_0$.

Iterations for $m > 0$

$$\begin{aligned}
\delta p &= p_{m-1} - P_{m-1}, \quad \rho = (M\,N_{m-1})/V \\
dN &= \text{sign}(\delta p)\,P_{m-1}\,S_{dia}\,\sqrt{|2\delta p/\rho|}\,t_s/T_{m-1} \\
dP &= (N_{m-1}\,r\,t_s\,(T_0 - T_{m-1}) + dN\,\gamma\,T_{jet})/V \\
N_m &= N_{m-1} + dN \\
P_m &= P_{m-1} + dP \\
T_m &= P_m V/N_m \\
U_m &= dN\,T_m/(P_m\,t_s)
\end{aligned} \tag{4.9}$$

with $M = 0.028965/R = 0.00348388$ for the air.

This scheme is not very critical toward the duration of the time step t_s, because it used with measured values: deviations are naturally corrected by the scheme (it "waits" until physically plausible conditions are recovered). In principle it is expected that: $t_s \leq 0.001$ s.

4.6 Examples of measurements

The Figs. 4.8 to 4.13 depicts the results of the aeraulic measurements performed on 4 reeds selected from the panel studied in Chapter 8 (see §8.3.2 and the Table of symbols 8.1) and treated with the methods described in the present Chapter. These Figs. depicts respectively the channel height $h(\psi, y)$, the reed deflection left and right $z_L(\Delta p, \psi)$ and $z_R(\Delta p, \psi)$, the aeraulic section $S(\Delta p, \psi)$ and the nonlinear characteristic $u(\Delta p, \psi)$. These 4 reeds were selected here because they are typical for the CCA factor 1 (stiffness, called "reed strength" by the clarinettists, reeds R06 and R07) and factor 2 (opening at rest, reeds R02 and R05). Observe their locations on the factor plot of *staticF*, Fig. C.2, top left graph.

The measurements of the soft reed (R06) differs essentially from that of the stiff reed (R07) in the following points:

— The channel h is more closed for all embouchures ψ. This is also the case for the reed deflection z and the aeraulic section S at $\Delta p = 0$.

— The maximal height of the nonlinear characteristic u is much lower.

— The difference of stiffness appears clearly (at low Δp) on the graph of the reed compliance z' (and also on the gradient of h and z).

— The main "elbow" in z or S occurs for a much lower value of Δp. The beating threshold is therefore much lower (observe the graph of u).

The measurements of the closed reed (R02) differs essentially from that of the open reed (R05) in the following points:

— The channel h is more closed for the loose embouchure (orange), but not for the tight embouchure (blue). This is also the case for the reed deflection z and the aeraulic section S at $\Delta p = 0$. This difference is especially important for the reed at rest, without contact with the lip (not illustrated on the graphs).

— The aeraulic section S and the nonlinear characteristic u exhibits a very broad elbow at closure, unlike the theoretical characteristic (see Eq. (5) and (6) in Chapter 1). At the contrary, R05 exhibits curves that are more closely related to the theoretical characteristic.

A general property of S appears clearly for all reeds: an increase of displacement of the support of the artificial lip ψ causes a shift of the curve in direction of the negative Δp. This is observed on Fig. 4.13 which depicts S as a function of z, by eliminating Δp. Basing on this observation, a simplified model of the exciter is proposed in the next Chapter, which hypothesizes a linear equivalence between Δp and ψ.

Note that the slope of the curves is practically the same for all reeds, except when the channel is nearly closed. In other words, when the channel is more or less widely open, the width is constant for all reeds (about 20 mm), in a rectangular model of the channel. See also 8.5.6 for this topic.

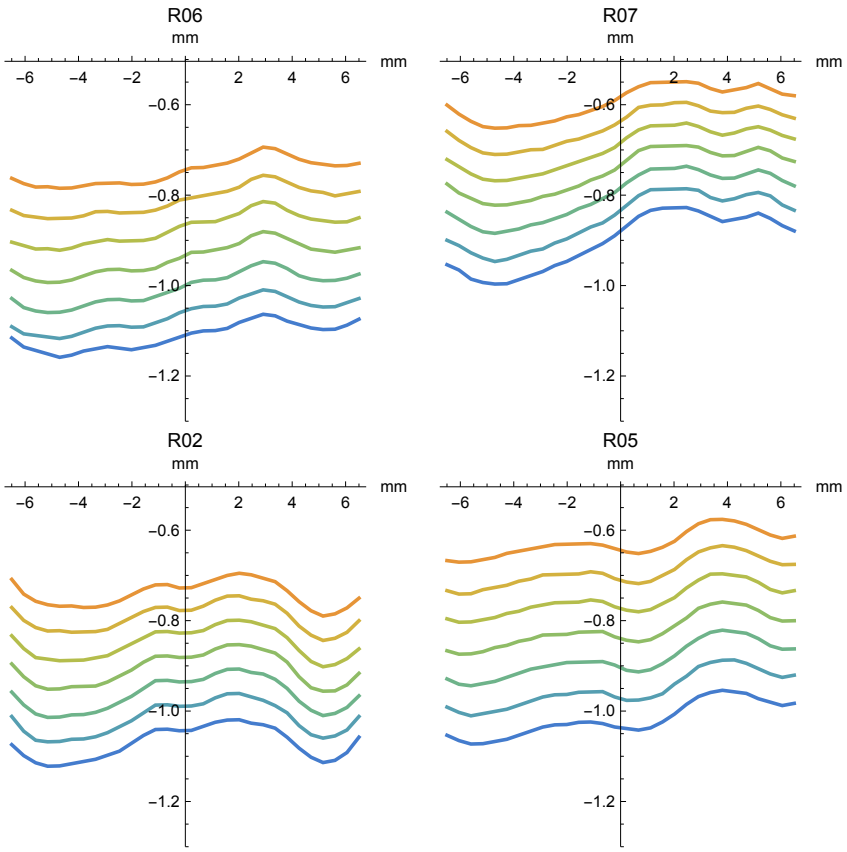

Figure 4.8 – Channel height $h(\psi, y)$ measured by photo (see §8.3.1) for 4 different reeds and 7 embouchures selected from the panel studied in Chapter 8. The 7 embouchures tested are encoded by the colors from orange (loose embouchure, $\psi = 1.750$ mm) to blue (tight embouchure, $\psi = 2.500$ mm).

4.7 Conclusions and future work

The measurement of the static characteristics of the exciter with the "bottle method" provides very satisfactory results in terms of accuracy and reproducibility.

One point was not investigated: the transition between turbulent and laminar flow at very low pressure. The device is not well suited for a precise measurement of this transition. The aeraulic section is approximated from the optical signals at very low pressure. It is well known that the viscosity is the main parameter in this pressure range (cf. Poiseuille flow). This point is not very relevant for the simulation of a clarinet, but it may be important for stability issues in the simulation of a saxophone (pers. comm. Ph. Guillemain).

An other point needs to be improved: the characterization of thermal exchanges with the bottle, which has been carried out empirically. This improvement can also be realized through the development of a bottle having a thermal behavior which is less critical. The temperature could also be measured, for instance by evaluating the speed of sound in the bottle during the most critical moments: when the pressure inside the bottle slowly varies. During these moments, it is difficult to separate the effects of temperature exchange and variation of air quantity. The measurement of the phase shift between the signals of an emitting loudspeaker and a receiving microphone located at opposite sides in the bottle would probably work, because only variations of the speed of sound relative to ambient conditions have to be measured, in order to deduce the temperature. This way, the main drawback related to the quasi-adiabatic case could be probably resolved.

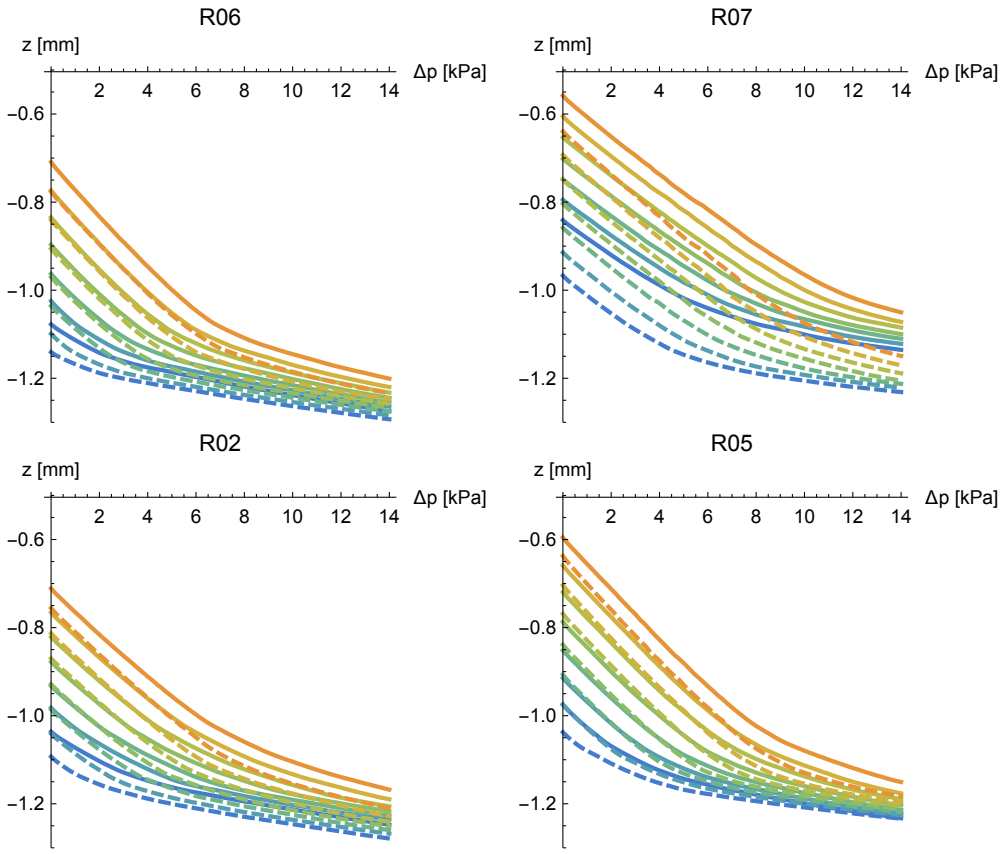

Figure 4.9 – Reed deflection at the tip measured by optical sensors, for 4 different reeds and 7 embouchures selected from the panel studied in Chapter 8. The 7 embouchures tested are encoded by the colors from orange (loose embouchure, $\psi = 1.750$ mm) to blue (tight embouchure, $\psi = 2.500$ mm). Plain lines: left sensor, $z_L(\Delta p, \psi)$. Dashed lines: right sensor $z_R(\Delta p, \psi)$. Observe that the right sensor is situated on the left side of the photo of the channel illustrated on Fig. 4.8.

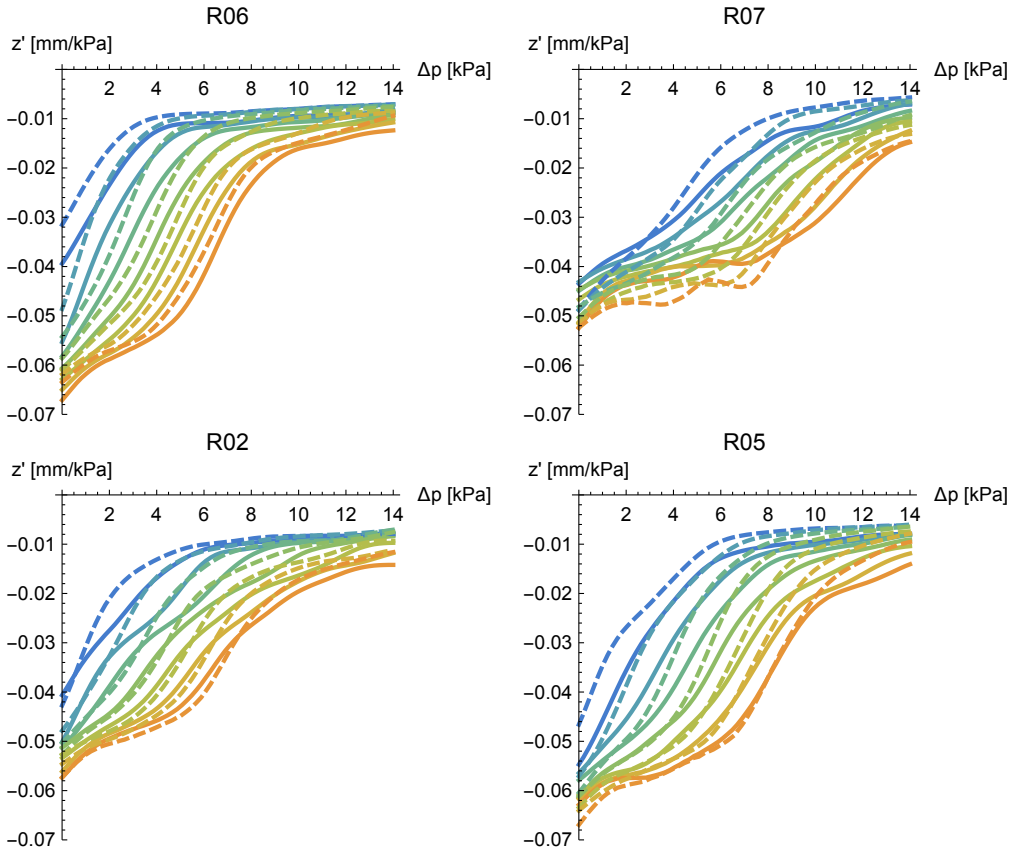

Figure 4.10 – Reed compliance (derivative of z_L and z_R with respect to Δp) corresponding to the deflection illustrated on Fig. 4.9, depicted with the same color code.

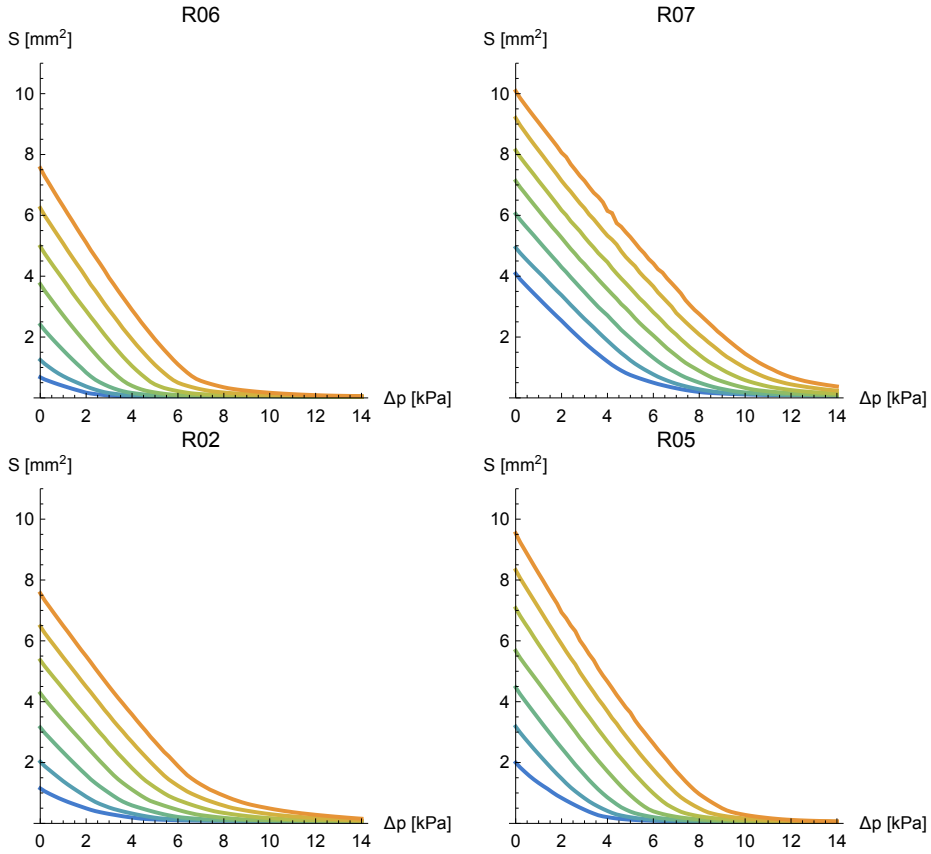

Figure 4.11 – Aeraulic section $S(\Delta p, \psi)$ determined with Eqs. 4.5 and 4.9 for 4 different reeds and 7 embouchures selected from the panel studied in Chapter 8. The 7 embouchures tested are encoded by the colors from orange (loose embouchure, $\psi = 1.750$ mm) to blue (tight embouchure, $\psi = 2.500$ mm). Below 1 kPa, S is approximated from the signal measured by the optical sensors inside the mouthpiece.

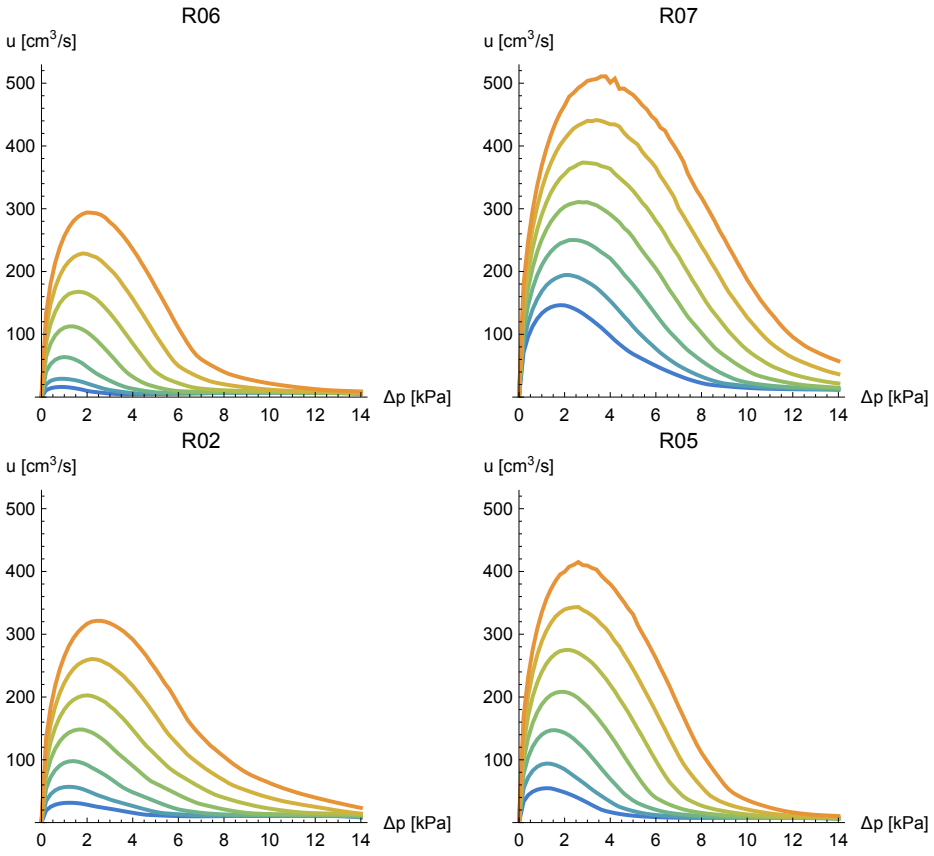

Figure 4.12 – Nonlinear characteristic $u(\Delta p, \psi)$ associated to the aeraulic section illustrated on Fig. 4.11, depicted with the same code of colors.

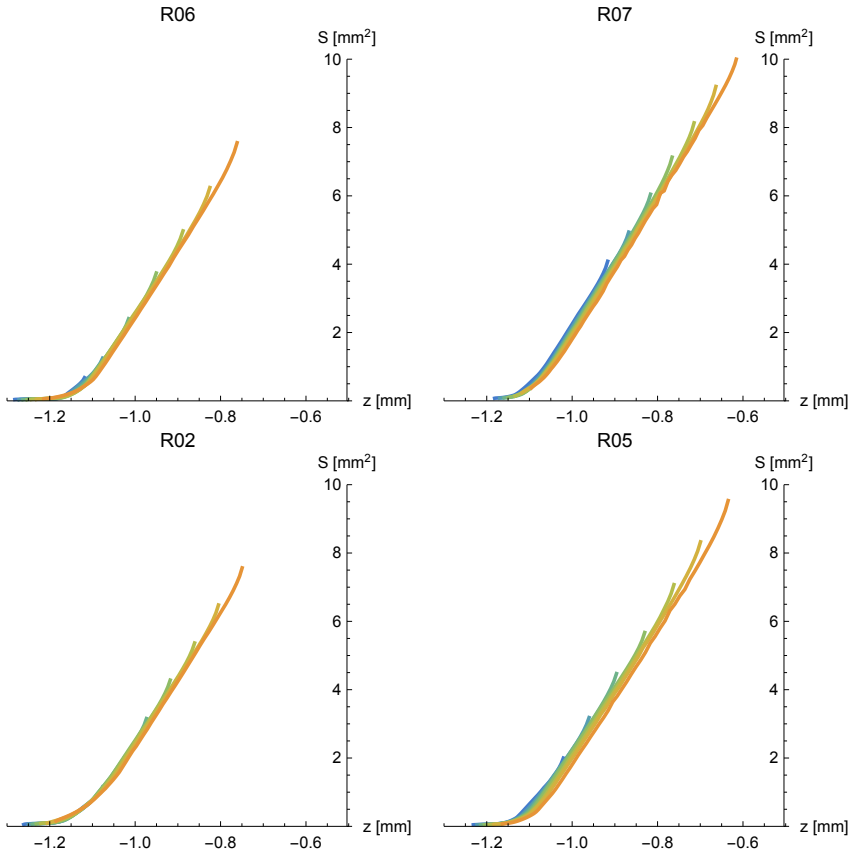

Figure 4.13 – Aeraulic section S as a function of the mean reed deflection at the tip z (mean of the measures of the optical sensors). This graph combines the Figs. 4.9 and 4.11, by eliminating Δp.

Part III

Simulation of Wind Instruments

Chapter 5

Nonlinear Model of the Clarinet Exciter

Résumé

Ce Chapitre propose un modèle simplifié d'excitateur basé sur les mesures expérimentales réalisées avec les techniques décrites au Chapitre 4.

Dans un premier temps, ce modèle simule les caractéristiques mécaniques non linéaires de l'excitateur (mesurées ici par capteur optique). Pour ce faire, on établit un modèle de raideur non linéaire purement statique, en formulant certaines hypothèses simplificatrices. Ce modèle est ensuite transformé en un modèle dynamique 1D relativement simple, en ajoutant des effets inertiels et amortissants, en combinant le modèle de contact développé par [25] et le schéma numérique proposé par van Walstijn et Guillemain [69, 171]. Le modèle suppose que la masse et l'amortissement ne varient pas en fonction de la position de l'anche. La validité de cette hypothèse sera évaluée en partie IV) en comparant simulations et diagrammes de bifurcation mesurés.

Dans un deuxième temps, la section aéraulique est interpolée à partir de la position mécanique de l'anche, en faisant l'hypothèse que la relation statique mesurée entre ces deux paramètres est également valide en régime dynamique.

5.1 Introduction

A reed attached to a clarinet mouthpiece (exciter) behaves mechanically like a stiffening spring, while closing the channel with the lip or air pressure. In the open position, the reed can be modeled as an unilaterally clamped plate having a nearly linear elasticity [17]. Similarly, in the closed position, it behaves like a clamped plate on one side and simply supported plate on the other sides and its elasticity is again almost linear (but its stiffness is significantly higher than in open position). Between these 2 positions, the contact surface between reed ans lay increases with the pressure, then, the tip of the reed comes into contact with the lay, usually somewhat asynchronously between the right and left side and the channel closes progressively. This behavior is attested by the photographs of the channel presented in Chapter 8 (see Fig. 8.3).

Among the various 1D reed models (lumped models) proposed in the literature, many locate the center of mass at the tip of the reed [144, 142, 170, 7, 20, 22, 13, 30, 19], although it is physically quite unrealistic to assume that the reed is instantaneously stopped at the moment of contact with the table (inelastic shock). Other models consider a "phantom" reed penetrating "inside" the mouthpiece, with constant linear stiffness [69]. A more realistic model considers that the equivalent mass is concentrated further away from the tip, in the plane of symmetry of the reed. No inelastic shock is required, since the equivalent mass is concentrated somewhere in the middle of the window and can therefore penetrate inside the mouthpiece chamber: a progressive increase in stiffness of the 1D model is sufficient to take into account most of the observed phenomena. The resonance frequency of the reed thus increases gradually while bending, as

observed experimentally.

Van Walstijn [170, 171] proposes a nonlinear 1D reed model. His numerical scheme unfortunately does not have the required stability, because it does not separate the mechanical and the aeraulic effects, in my opinion. Chaziioannou [17] proposes a model of a 2D reed, simulating the contact with the lay, which is by nature not well adapted for a simulation in real time. To overcome this drawback, he proposes a 1D approximation of his model, [17, 23], which still does not separate the mechanical and the aeraulic effects. These two authors propose in 2015 a conservative scheme allowing a real-time simulation of the contact dynamics [25, 24]. This model was adopted by Muñoz [105] for the clarinet reed. I propose a piecewise adaptation of the model, allowing a simulation based on measurements, by splitting the measured range into a succession of sections, each of them being simulated by the cited contact model. Moreover my model separates the mechanical and the aeraulic problems, reducing this way drastically the numeric instabilities in the simulations.

The present model should be considered as a "work in progress": the stability of the numerical scheme remains largely uninvestigated (although no noticeable problems related with the numerical stability were observed during all performed simulations). The principal aim of the present study is to develop a pragmatic model which is able to:

1. simulate the static, mechanical and aeraulic behavior of reeds according to measurements
2. allow a stable dynamic simulation in usual playing conditions

5.2 Static mechanical model

We seek to define a nonlinear, static 1D model to approximate the mechanical stiffness of the reed. The deflection of the reed y is a function of the position of the lip holder ψ and of the air pressure drop Δp across the reed. This model results from the observation (see Fig. 4.11) that the measurements for the different embouchures are quasi perfectly superimposed, when the origin of the pressures is shifted in a suitable way (at least when the lip is positioned relatively forward on the reed, see Fig. 4.4). This offset depends quite linearly on ψ. The proposed model satisfies a number of constraints, based on simplifying assumptions, and possess the following properties:

1. Given these experimental observations, a linear relation is assumed between ψ and Δp, through an equivalent pressure x, of the form

$$x = \Delta p + \mu(\psi - \psi_0) \tag{5.1}$$

   where μ is a positive constant that depends on the elasticity of the lip and ψ_0 is an arbitrary reference embouchure (usually a moderately tight embouchure, here $\psi_0 = 2.125$ mm).
   If desired, the model can be refined by adding a 2nd order term in ψ, so as to better fit the experimental data.
2. The static model should be easily converted into a dynamic model. For this purpose, a "reverse" definition is preferable: the equivalent pressure x is defined according to the mechanical deflection of the reed y:

$$x = f(y) \tag{5.2}$$

3. The origin and position at which y is measured is arbitrary. Here, y corresponds to the distance between the plane of the mouthpiece lay and the point measured by optical sensor, about 6 mm from the tip of the reed (after averaging this distance between the 2 sensors, calibrating y according to the photos of the channel).
4. The function $f(y)$ is decreasing and convex (stiffening spring, closing under pressure): its second derivative $f''(x)$ is non-negative (i.e. positive or zero).
5. The function $f(y)$ is a piecewise function. The discrete points (y_n, x_n), $0 \leq n \leq N$ constitute the junctions between the pieces. At the junctions, we have: $x_n = f(y_n)$.
6. Typically, $3 \leq N \leq 20$, depending on the precision of the measurements and on the refinement that one wishes to give to the model.

7. The function $f(y)$ is linear for $x \leq x_0$.
8. For $x > x_0$, each piece is parabolic.
9. The junctions between the pieces are of type $\mathcal{C}^1$: the function f and its derivative f' are continuous.
10. The parabola of the section number n ($x_n \leq x \leq x_{n+1}$) is defined using 2 stiffness constants (k_n and κ_n), a constant of height at the origin, h_n (i.e. at $x = 0$) and by the equation [1]

$$x = f_n(y) = k_n(h_n - y) + \kappa_n \lfloor y_n - y \rfloor^2 \tag{5.3}$$

Observe that $f_n(y_n) = x_n = k_n(h_n - y_n)$. The constraints on the decrease and convexity of f imply: $k_n \geq 0$, $\kappa_n \geq 0$. Within the section n, these constraints imply; $y_n \geq y \geq y_{n+1}$.

11. The discrete points are chosen to be representative of the measurements made on the same reed and different embouchures. The mesh can be set arbitrarily in one of the dimensions (for example x_n) and the coordinates in the other dimension (in this example, y_n) are estimated by least squares, according to the measurements and respecting the constraints on k_n and κ_n. The evaluation of the parameters from x_n and y_n is described below.
12. Given the constraints, the inverse function is written:

$$y = f_n^{-1}(x) = \begin{cases} Y_n(x) & x \leq x_n \\ y_n + \frac{k_n - \sqrt{k_n(k_n + 4\kappa_n(y_n - Y_n(x)))}}{2\kappa_n} & x > x_n \end{cases} \tag{5.4}$$

$$Y_n(x) = h_n - \frac{x}{k_n} \tag{5.5}$$

Notice that: $Y_n(x = 0) = h_n$, $Y_n(x = x_n) = y_n = f_n^{-1}(x_n)$ et $y_n - Y_n(x > x_n) \geq 0$.

13. The deflection of the reed y with respect to x (equivalent pressure applied on the reed) is defined by the function:

$$y = f^{-1}(x) = \begin{cases} Y_0(x) & x \leq x_0 \\ f_n^{-1}(x) & x_n < x \leq x_{n+1} \end{cases} \tag{5.6}$$

Note that the function $f_n(y)$ formally corresponds to the equation (C.7) of Muñoz (model K_{NL}) defining the behavior of a reed without mass and damping, with parabolic stiffness, after correcting the sign of ΔP (compare with Eq. (C.4)) and performing the following substitutions: $y \to y(t)$, $y_n \to y_c$, $k_n \to K$, $\kappa_n \to K_c$, $h_n \to H$ and $x \to \Delta P(t)$.

5.2.1 Parameter evaluation

First section

On the first section ($y_0 \geq y \geq y_1$), the parameters of f_0 are evaluated by solving the system of 3 equations: $f_0(y_0) = x_0$, $f_0(y_1) = x_1$ and $f_0(y_2) = x_2$.

Solution:

$$\begin{aligned} \kappa_0 &= \frac{y_2(x_1 - x_0) + y_1(x_0 - x_2) + y_0(x_2 - x_1)}{(y_0 - y_1)(y_0 - y_2)(y_1 - y_2)} \\ k_0 &= \frac{-\kappa_0(y_0 - y_1)^2 - x_0 + x_1}{y_0 - y_1} \\ h_0 &= y_0 + \frac{x_0}{k_0} \end{aligned} \tag{5.7}$$

Next sections

On the section n ($y_n \geq y \geq y_{n+1}$), the parameters of f_n are evaluated by solving the system of 3 equations: $f_n(y_n) = x_n$, $f_n(y_{n+1}) = x_{n+1}$ and $f_n'(y_n) = f_{n-1}'(y_n)$.

1. The notation $\lfloor \cdot \rfloor = (\cdot)\text{Heaviside}(\cdot)$ is already introduced here, but for now, $\lfloor \cdot \rfloor$ could be replaced with $(\cdot)$

Solution:

$$\begin{aligned} k_n &= -f'_{n-1}(y_n) \\ \kappa_n &= \frac{-k_n(y_n - y_{n+1}) - x_n + x_{n+1}}{(y_n - y_{n+1})^2} \\ h_n &= y_n + \frac{x_n}{k_n} \end{aligned} \tag{5.8}$$

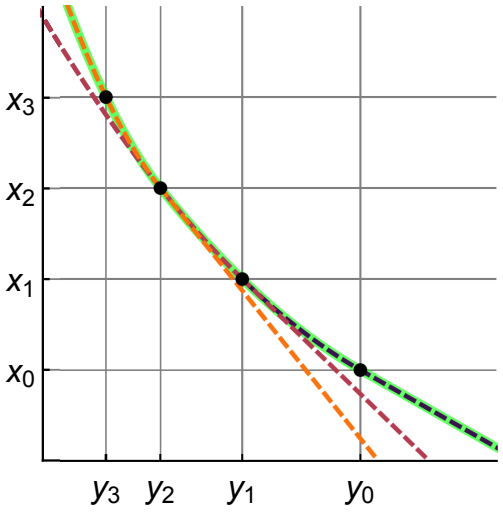

Figure 5.1 – Example of a nonlinear stiffness, represented by the convex, decreasing function $x = f(y)$, modeled piecewise with $N = 3$ parabolic sections. The functions f_0, f_1 and f_2 are shown in broken lines, from black to orange. The function f is depicted in thick green continuous line. The discrete points (y_n, x_n) are in black, from which the parameters k_n, κ_n and h_n of the different pieces of the function f are calculated.

A didactic example with $N = 3$ is illustrated in Fig. 5.1.

Notes: With this evaluation scheme, the first 2 sections have the same curvature κ_n and can therefore be merged into a single section ranging from x_0 to x_2. For the last section, the model can be evaluated beyond x_N, if necessary.

In the simulations described in Chapter 8, the model has $N = 20$ sections. The error between model and measurements rarely exceeds 0.01 mm, regardless of the embouchure. The standard deviation of the error is of the order of 4 microns. An example if given on Fig. 5.2 for 4 selected reeds. The reeds R06 and R07 differ principally by the stiffness (CCA factor 1 of *objectiveF*, see §8.5). The reeds R02 and R05 differ principally by the opening at rest (CCA factor 2 of *objectiveF*). The simulations of the bifurcation diagrams in Chapter 8 for these reeds rely on this segmentation of $f(y)$.

5.3 Dynamic mechanical model

The nonlinear, static model Eq. 5.3 is converted to a nonlinear dynamic 1D model, having a mass m and a damping r. Its differential equation reads (see Chatziioannou [23], Eq 3 or Muñoz Eq C.50):

$$m\,\ddot{y}(t) + r\,\dot{y}(t) + k_n(y(t) - h_n) = -x(t) + \kappa_n \lfloor y_n - y(t) \rfloor^2 \tag{5.9}$$

Basing on the original paper by Chatziioannou *et al.* [25], Muñoz [105] gives a numerical scheme to solve this equation in discrete time, by operating a bi-linear transform (see Eq C.61). With our notations, his numerical scheme reads (at discrete time i):

$$Y_n[i] = -b_{n,1}y[i-1] - b_{n,2}y[i-2] - \Lambda_n(x[i] + 2x[i-1] + x[i-2]) + \beta_n \tag{5.10}$$

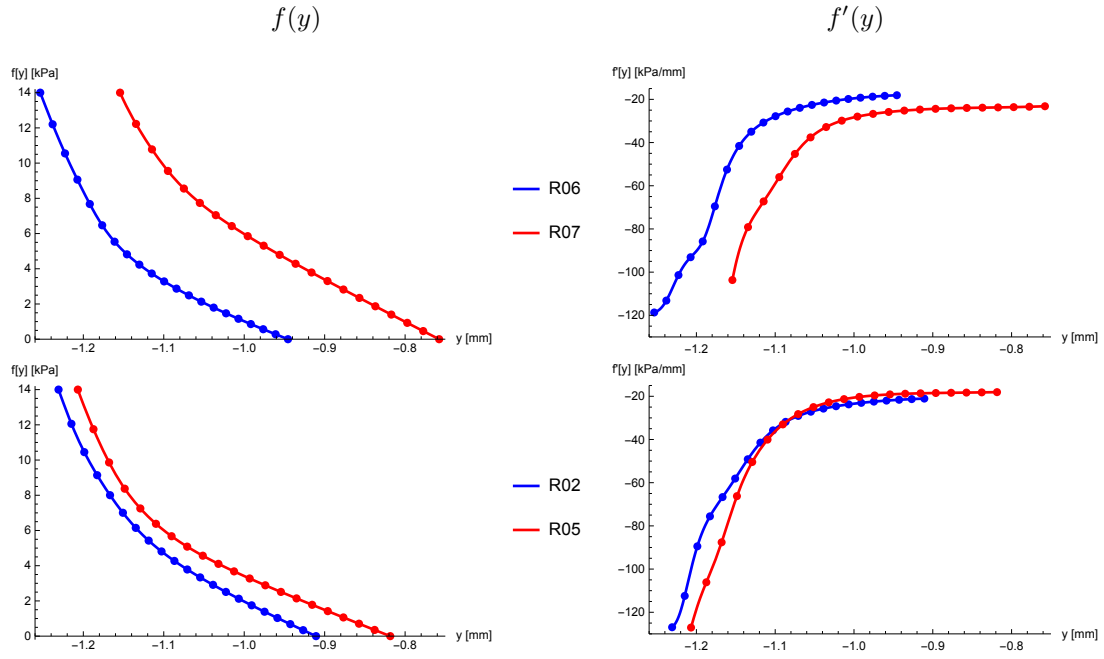

Figure 5.2 – Examples of discrete points (y_n, x_n) used for the piecewise definition of the function $f(y)$, for the 4 different reeds illustrated on Figs. 4.8 to 4.12. The derivative of f with respect to y is depicted in the right column.

$$y[i] = \begin{cases} Y_n[i] & Y_n[i] \geq y_n \\ \frac{1-\sqrt{4\kappa_n\Lambda_n(-\kappa_n\Lambda_n((y[i-2]-y_n)^2+2(y[i-1]-y_n)^2)-Y_n[i]+y_n)+1}}{2\kappa_n\Lambda_n} + y_n & Y_n[i] < y_n \end{cases} \tag{5.11}$$

with $\beta_n = h_n(1 + b_{n,1} + b_{n,2})$, $\Lambda_n = \frac{1}{k_n+2f_sr+4f_s^2m}$, $b_{n,1} = \Lambda_n(2k_n - 8f_s^2m)$ and $b_{n,2} = \Lambda_n(k_n - 2f_sr + 4f_s^2m)$, where f_s is the sampling frequency.

For the linear component (Eq. 5.10), instead of the bi-linear scheme, I propose to use an explicit scheme with a zero instantaneous response developed by Walstijn and Guillemain [69, 171]. This scheme has the great advantage of relying only on past values of x. The coupling with the air column can be solved much more easily, as explained in the article cited. With the explicit scheme, the linear component is written:

$$Y_n[i] = -b_{n,1}y[i-1] - b_{n,2}y[i-2] - a_nx[i-1] + \beta_n \tag{5.12}$$

with $a_{n,1} = -\frac{2}{2mf_s^2+rf_s}$, $b_{n,1} = a_{n,1}\left(2mf_s^2 - k_n\right)$ and $b_{n,2} = \frac{1}{2}f_sa_{n,1}\left(r - 2mf_s\right)$. The resonance pulsation of the linear oscillator n is given by: $\omega_n = \sqrt{k_n/m}$ and the quality factor by: $q_n = r/\sqrt{k_nm}$.

For the quadratic component, Eq. 5.11 is used, with $\Lambda_n = -a_{n,1}/4$.

This alternative scheme is not proved to be well posed in energetical terms. The simulations exhibit no really noticeable difference with the bi-linear scheme (the difference does not exceed 0.1 % of the total amplitude, for the example illustrated in Fig. 5.3). The fact that the resonance frequency of the clarinet reed is usually much smaller than f_s reduces the difference between the two schemes.

5.3.1 Simulation of the dynamic model

Algorithm Before the simulation, initialize $i = 0$ and the excitation signal $x[-1]$, $x[0]$, according to the initial values of ψ and Δp. The position of the reed is determined from its static position, given by Eq. 5.6 : $y[-1] = y[0] = f(x[0])$. Determine $\hat{n}$ such that $y_{\hat{n}} \geq y[0] \geq y_{\hat{n}+1}$.

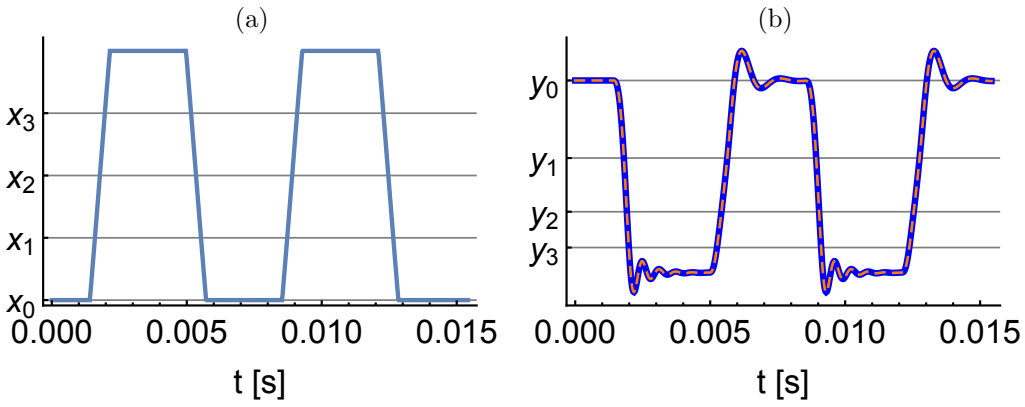

Figure 5.3 – Example of dynamic simulation (680 discrete points) with an arbitrary pressure signal. The corresponding static nonlinear stiffness is shown in Fig. 5.1. (a) excitation signal $x[i]$. (b) dynamic response $y[i]$ of the nonlinear 1D oscillator. In solid blue line, scheme according to Eq. 5.10. In broken orange line, scheme according to Eq. 5.12.

The simulation is performed with the following pseudo-code:

1. Increment i
2. Compute $y[i]$ with $n = \hat{n}$, Eqs. 5.12 and 5.11
3. If $y[i] > y_{\hat{n}}$ and $\hat{n} > 0$, decrement $\hat{n}$, then goto 6.
4. Else if $y[i] < y_{\hat{n}+1}$ and $\hat{n} < N - 1$, increment $\hat{n}$, then goto 6.
5. Otherwise Goto 7 (because $\hat{n}$ remained unchanged)
6. compute $y[i]$ with (the new value) $n = \hat{n}$, Eqs. 5.12 and 5.11
7. Determine the excitation $x[i]$ then goto 1.

As already mentioned, the great advantage of the explicit scheme is that the excitation $x[i]$ can be computed once $y[i]$ is known. With the bi-linear scheme, $x[i]$ must be determined before calculating $y[i]$.

This pseudo-code expects that the reed motion is slow enough to visit the sections one after another, which is usually true. The violations of this principle have generally no consequence, since (in the playing situation) the motion of the reed is, most of the time, relatively slow, either in the open position or in the closed position (see Fig. 5.3). These violations occur only during the transitions and are quickly resorbed, without significant numerical instability, because the potential instabilities on the mechanical simulation have only a minor influence on the aeraulic section which drives the acoustical part of the simulation, which itself determines finally the mechanical force acting on the reed.

An example of a dynamic simulation is given in Fig. 5.3, with $N = 3$. The excitation signal corresponds very schematically to the one observed in the playing situation. Note the change in resonance frequency, according to the position of the reed y. This characteristic is typically observed in the experimental measurements.

5.4 Model of Aeraulic Section

In the proposed model, the mechanical position of the reed (situated in the middle of the reed, a few mm away from the tip, as measured by the optical sensors) determines the effective aeraulic section (area of the slit between the mouthpiece lay and the reed at the periphery of the reed, including the *vena contracta* effect). As already explained, this model presents valuable properties for the stability of the simulations, since the mechanical and the aeraulic problems are well separated: the point determining the mechanical position of the reed is not situated at the periphery of the reed (like in the usual models described in the literature). Thus the

mechanical behavior can be modeled as observed experimentally by the optical sensors and the aeraulic behavior can be modeled as observed experimentally by the bottle method, according to the corresponding mechanical position of the reed, determined by the optical sensors.

More precisely, the amount of air entering the instrument through the channel depends on the embouchure ψ, on the pressure drop across the reed Δp, and on the exciter (i.e. on the reed and mouthpiece used, on the lip position and how the reed is mounted). For each couple $(\psi, \Delta p)$, the airflow entering the instrument through the exciter can be measured in quasi-static conditions as described in §4.2. Bernoulli's law allows the computation of the effective aeraulic section S corresponding to the measured flow. A function can be determined, which links the mechanical position of the reed y (measured at some arbitrary point, such as that located approximately 6 mm from the tip of the reed, measured by optical sensors) and the aeraulic section $S(y)$. In the model proposed here, the quasi-static relationship is assumed to be also valid in dynamic conditions.

The function $S(y)$ is generally convex and increasing, but this is not always the case in the measurements. In the high pressure range (high negative values of y), the reed reopens slightly, because of the sharp angles of the mouthpiece window. The only imperative condition is that $S(y) \geq 0$.

Any interpolation function may be suitable for evaluating $S(y)$ according to measurements (polynomials, splines, etc.). I used the piecewise parabolic interpolation proposed in §5.2, based on a mesh of discrete points optimized by least squares. By construction, the function is linear above y_0, but the parabolic continuation cannot be used below y_N (because it is not physical). A straightforward solution (with $\mathcal{C}^0$ continuity) consists in keeping the function constant below y_N, with value x_N. A crossfade to a constant value (performed with a sigmoid ramp) could also be considered for the last piece of the interpolation function (in order to preserve a $\mathcal{C}^1$ continuity).

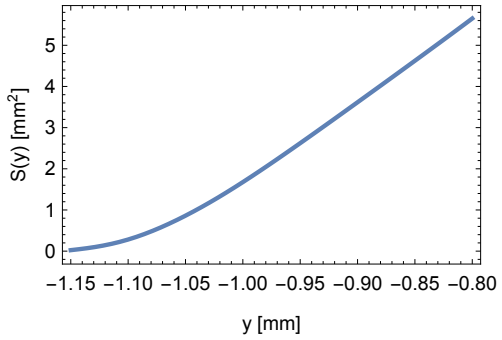

Figure 5.4 – Example of least squares approximation of the function $S(y)$ linking the position of the reed y and the aeraulic section S, according to the measurements of the reed R14, for different embouchures ψ. The function is optimized for the reference embouchure $\psi_0 = 2.125$ mm.

The Fig. 5.4 illustrates the shape of the function $S(y)$ determined by least squares fit for the reed R14. Compare with the measurements for the reeds R02, R05, R06 and R07 depicted on Fig. 4.13.

An alternative solution consists in fitting by least squares the second derivative of $S(y)$ with the EDSC method (Appendix E), using the kernel

$$\delta(x) = \begin{cases} -\frac{1}{16}\left(x^2-1\right)^2\left(7x^2-16\right) & -1 < x < 1 \\ 0 & \text{Otherwise} \end{cases} \tag{5.13}$$

The second antiderivative of the kernel builds an "elbow" function:

$$\delta^{(-2)}(x) = \begin{cases} 0 & x \leq -1 \\ -\frac{1}{128}(x+1)^4\left(x^4-4x^3+2x^2+12x-19\right) & -1 < x < 1 \\ x & x \geq 1 \end{cases} \tag{5.14}$$

This δ kernel is suited for realtime applications and the nonnegativity and the convexity of $S(y)$

are guaranteed if the weights found by least squares are nonnegative (which can be set as a constraint for the fitting procedure).

5.5 Conclusions

The proposed model exhibits 3 interesting properties: 1) The estimation of the parameters is straightforward and rely on standard optimization techniques. 2) The model reproduces the static measurements with a typical error of the order of a few microns. 3) The dynamic simulation is very efficient, apparently stable and suited for real time applications. The computations requires only a few multiplications and a square root per time step (except during the transitions between sections, where 2 evaluations are necessary). All sections are simulated on the basis of the same history ($x[i]$, $y[i]$). The number of simulated sections thus has no impact on the computation time. The recalculation time at the transitions between two adjacent sections, is negligible.

Chapter 6

Modal Analysis of the Input Impedance of Wind Instruments. Application to the Sound Synthesis of a Clarinet

Résumé

Cet article traite de l'analyse modale des instruments à vent examinés à partir de l'entrée de leur colonne d'air. Outre le traitement des modèles analytiques, un accent particulier est mis sur l'estimation modale d'une impédance d'entrée mesurée. Cela nécessite un soin particulier car les mesures ne couvrent qu'une bande de fréquence limitée et sont affectés par des erreurs difficiles à évaluer. Cet article décrit comment les techniques classiques de l'analyse de Prony et des Least Squares Complex Exponentials (LSCE) peuvent être utilisées dans ce contexte, en décrivant notamment comment les pièges principaux peut être évités lors de l'analyse. Une méthode permettant une reconstruction physiquement acceptable de la bande des basses fréquences est proposée. Une technique utilisant des points fictifs dans la gamme des hautes fréquences est développée de manière à assurer la passivité du résonateur dans l'intégralité de la bande de fréquence simulée. Un exemple d'application permettant une synthèse temps-réel de sons de clarinette à partir d'une représentation modale du résonateur est présenté. On y traite notamment des questions de la gestion modale durant les transitions entre les doigtés et de celle de la simulation du son externe. Un exemple musical significatif illustre les possibilités de l'analyse modale appliquée aux instruments à vent.

Cet article a été soumis à Applied Acoustics en date du 12 avril 2017. Il a été accepté pour publication le 15 juillet 2018, soit 2 semaines après la soutenance de la présente thèse. Il est reproduit ici, y compris la section 6.3 et la Fig. 8 dont la suppression a été exigée par l'un des reviewers, alors que les deux rapporteurs de cette thèse ont unanimement salué cette section comme étant l'une des plus enrichissantes de ce chapitre.

D'autre part, Esteban Maestre m'a aimablement signalé une référence en relation avec le sujet de l'article, dont j'ignorais l'existence lors de la rédaction de l'article [95], ainsi que 2 références postérieures au dépôt initial de l'article, [97, 96].

Cette contribution a été réalisée dans le cadre du projet CAGIMA, entre 2013 et 2016.

Modal analysis of the input impedance of wind instruments. Application to the sound synthesis of a clarinet

P.-A. Taillard[a], F. Silva[b,*], Ph. Guillemain[b], J. Kergomard[b]

[a] *FNHW, Schola Cantorum Basiliensis, Leonhardsstrasse 6, 4051 Basel, Switzerland*
[b] *Aix Marseille Univ, CNRS, Centrale Marseille, LMA, Marseille, France*

Abstract

This paper investigates the modal analysis of wind instruments as seen from the input of their air column. Beside the treatment of analytical models, a particular emphasis is given to the analysis of measured input impedances. This requires special care because the measurements cover only a limited frequency band and are affected by some unknown errors. This paper describes how the Prony analysis and the Least Squares Complex Exponential (LSCE) classical techniques can be used in this context and how the main pitfalls can be avoided in their application. A physically acceptable method of reconstruction of the low frequency band is proposed. A technique using fictitious points in the high frequency range is described in order to ensure the passivity of the resonator in the whole frequency band. The principles of a real-time synthesis of clarinet sounds based on the modal representation of the resonator is given as an application, with a method to efficiently handle the modal representation during the transition between fingerings. A musically relevant example finally illustrates the possibilities of the modal analysis applied to wind instruments.

Keywords: Wind Instruments; Modal Analysis; Sound Synthesis.

1. Introduction

Analysis-synthesis of musical sounds produced by self-sustained oscillations in wind instruments is a difficult task, not yet fully attained for some synthesis models. This goal has been achieved for decades for some linear models, despite the difficulty to control such simple models. However, when the synthesis model relies on the physics of the functioning of the instrument, it may include strong nonlinearities that make the estimation of the parameters from the analysis of natural sounds challenging. The synthesis model incorporates playing parameters that generally remain unknown, unless they can be measured simultaneously with the sound. Many subsystems are present (excitation, nonlinear coupling by the input flow, resonator with a complex geometry, nonlinear effects at loud level) and the target is also difficult to define (radiated sound, mouthpiece pressure). The approach proposed in this paper aims at modeling precisely one of these subsystems, the resonator, from experimental data. The resonator is assumed to be linear (its features are independent of the sound level) and is coupled to a classical simple production model. Moreover this allows, by comparison with naturally produced sounds, to collect information on the shortcomings of both the production and the radiation models.

*Corresponding author
Email addresses: taillard@hispeed.ch (P.-A. Taillard), silva@lma.cnrs-mrs.fr (F. Silva), guillemain@lma.cnrs-mrs.fr (Ph. Guillemain), kergomard@lma.cnrs-mrs.fr (J. Kergomard)

Following the pioneering work of Helmholtz [1], sound production in wind instruments is explained as the mutual coupling of a resonator and an exciter, such that it is often enough to know the behavior of the acoustical resonator as seen from the coupling point only. For this reason, the bore is often characterized, experimentally or theoretically, by its input impedance. For example, the latter has been extensively used for the prediction of the oscillation frequency of the full instrument based on the resonance frequencies [2], or transformed either into the impulse response [3] or into the reflection function [4] to be used in numerical schemes for sound synthesis. Another usage relates to the prediction of the steady state periodic regime by means of the harmonic balance method [5]. To the best of our knowledge, Ref. [6] is the first to explore the modal analysis of woodwinds with the parametrization of the reflection function in damped exponentials, with an application to the simulation of some regimes of the *tenora* [7]. According to McIntyre *et al* [8], using the reflection function is allegedly more efficient than the impulse response for time-domain simulation. However, this is only true for schemes involving convolutions. Ref. [9] shows that the modal representation of the input impedance replaces the convolution by lightweight IIR filters and enables synthesis schemes that are at least as efficient. The modal series can then be used directly for time-domain simulations of self-sustained oscillations (as in Ref. [10]) or the estimation of oscillation thresholds [11].

Experimental modal testing is a broad topic in acoustics and vibration. It usually benefits from the observation of the quantities of interest (e.g., displacement, velocity, acceleration, acoustic pressure) at several locations, but also from the use of multiple actuators (*multiple-input-multiple-output*, MIMO) to efficiently excite and identify the various modal shapes and frequencies [12]. In fact, the modal poles are intrinsic characteristics of the tested system and are therefore common to all observations. As a consequence, the redundancy of the information improves the robustness of the identification techniques. Modal analysis using *single-input-single-output* (SISO) configurations entails particular difficulties, some of which relate to the loss of redundancy. This is the case of wind instruments characterized solely by their input impedance. Similarly to Ref. [13] which showed the way to acceptable estimations of reflection function, the present paper aims at exposing the possible pitfalls of the modal analysis of wind instruments and how to avoid them.

In the case of an analytical model for the acoustic resonator, the modal parameters can be theoretically derived from the poles of the input impedance, but it generally accounts for an infinite number of modes due to the transcendental equations arising from the modeling of the wave propagation in the bore. The truncation of the modal series leads to a degraded reconstruction of the impedance, as explained in Ref. [9] and again in Sec. 3. This also applies for the modal analysis of systems modeled by partial differential equations and discretized by the finite elements methods, such as the approach used by the Modalys software [14]. The structural dynamics community proposes several methods to compensate for the effect of neglected modes on the low-frequency range (known as *static condensation techniques*, see, e.g., Ref. [15]) which is not typically relevant in the field of acoustics. Dynamic condensation methods try to restore the inertial effect of the deleted modes but result in a nonlinear problem in order to determine the modal frequencies and shapes.

Modal analysis is usually performed for wind instruments as an optimization process that minimizes the error between the measured impedance and the impedance reconstructed from the finite modal series. The optimized variables may be the poles and the modal coefficients (see Refs. [16, 11]) or the poles only (Ref [17], where the modal coefficients are explicitly determined within the evaluation of the cost function). Both these methods rely on an iterative procedure that requires a decent initialization to guarantee feasibility and a fast convergence.

The main goal of this paper is to propose an efficient method for the parametrization of theoretical or measured input impedances of acoustic waveguides in order to make them suitable for, e. g., the real-time

physics-based synthesis of the sound of wind instruments or for the analysis of their functioning using methods from the dynamical systems community [11]. The parametrization must preserve the passivity of the resonator over the full frequency range, while the above mentioned applications additionally require the models to introduce a low number of parameters (here a reasonable number of modes to be taken into account).

This paper is organized as follows: Sec. 2 reviews the basis of acoustic waveguides and of the modal analysis. Sec. 3 exposes the problems related to the truncation of the modal series of a transfer function. Sec. 4 treats the case of fitting a given transfer function to a modal series. Sec. 5 describes an application of the fitting method to the modeled or measured acoustic resonator. Sec. 6 shows how the results of the modal analysis can be used for sound synthesis and, in particular, how the transition between fingering can be handled. It also includes a musical example based on measurements of the input impedance of a clarinet, followed by a conclusion in Sec. 7.

2. Modal analysis in acoustic waveguides

2.1. Input impedance and reflection coefficient

Within linear acoustic theory, when the acoustic wavelength is large compared to the cross section dimensions of the bore, it is usual to consider one-dimensional models where acoustics is described in terms of the flow rate $u(t,x)$ and the pressure $p(t,x)$, or on their frequency-domain counterparts $U(\omega,x)$ and $P(\omega,x)$, respectively. These only depend on the angular frequency ω and on the axial abscissa x in the waveguide.

At the input of the duct ($x=0$), the flow rate $U(\omega)=U(\omega,0)$ and the pressure $P(\omega)$ are related by the dimensionless input impedance $Z_{in}(\omega)$ or the input admittance $Y_{in}(\omega)$, both being frequency-dependent

$$Z_{in}(\omega)=\frac{1}{Y_{in}(\omega)}=\frac{P(\omega)}{Z_c U(\omega)}. \tag{1}$$

The characteristic impedance $Z_c=\rho c/S_{in}$ depends on the density of air ρ, the speed of sound c and the cross section area at the input of the pipe S_{in}. The reflection coefficient $R(\omega)$ is defined as follows

$$R(\omega)=\frac{Z_{in}(\omega)-1}{Z_{in}(\omega)+1} \quad \Leftrightarrow \quad Z_{in}(\omega)=\frac{1+R(\omega)}{1-R(\omega)}. \tag{2}$$

The inverse Fourier transforms of the input impedance and the reflection coefficient are called the impulse response $h(t)$ and the reflection function, respectively.

Traditional wind instruments are passive device as there is no energy production within the bore. Acoustical energy can only be dissipated. This implies that the energy flux at the input is positive, which is ensured by the constraint $\mathrm{Re}[Z(\omega)]\geq 0$, or, equivalently, $|R(\omega)|\leq 1$, over the full frequency range. In addition, some other properties are commonly found in waveguides. At very low frequencies, the duct is mainly resistive: the flow behaves as a slowly-varying laminar one and the flow rate responds in phase with the input pressure in a way similar to that of the Poiseuille flow. The input impedance may even be assumed to vanish at zero frequency, as is the case in this paper. Conversely, at very high frequencies, dissipation becomes strong enough to damp any resonance, so that Z_{in} approaches 1 (i.e., R approaches 0). This applies approximately for woodwind instruments and for brass instruments (when one removes the mouthpiece that would otherwise lead to an instantaneous reflection at the input of the bore.)

2.2. *Example: the cylindrical pipe*

Consider a cylindrical pipe with radius r and length ℓ. Following Ref. [19], the visco-thermal boundary layer losses are taken into account by means of the first-order approximation of the propagation constant Γ

$$\Gamma(\omega) = \frac{j\omega}{c} + \frac{3.10^{-5}}{r}\sqrt{\frac{j\omega}{\pi}}, \tag{3}$$

where R and the ω are expressed in MKS units, $j = \sqrt{-1}$ is the imaginary unit. The value of the characteristic impedance is assumed to be the lossless value $Z_c = \rho c/(\pi r^2)$ as explained in [19]. In Eq. (3), the term $\sqrt{j\omega}$ could lead to difficulties related to its branch cut [20]. However for visco-thermal losses, the use of the complete formula by Zwikker and Kosten leads to functions having only poles (see [21, 22]). Therefore Eq. (3) is an excellent approximation except at extremely low frequencies, so we assume that the calculation of the poles at higher frequencies is satisfactory.

At the open end, the radiation is modeled by the dimensionless radiation impedance Z_R given by Silva *et al* [23] (see also [24]) as a fraction of two polynomials $N_R(\omega)/D_R(\omega)$. Then, accounting for the transfer matrix between the input and the output of the pipe, the dimensionless input impedance can be expressed as the ratio of two functions $Z(\omega) = N(\omega)/D(\omega)$, N and D having zeros only (i.e., no poles)

$$\begin{pmatrix} N(\omega) \\ D(\omega) \end{pmatrix} = \begin{pmatrix} \cosh\left(\Gamma(\omega)\ell\right) & \sinh\left(\Gamma(\omega)\ell\right) \\ \sinh\left(\Gamma(\omega)\ell\right) & \cosh\left(\Gamma(\omega)\ell\right) \end{pmatrix} \begin{pmatrix} N_R(\omega) \\ D_R(\omega) \end{pmatrix}. \tag{4}$$

This can easily be extended to other geometries like pipes with tone holes or branched tubes.

Fig. 1 shows an example of the input impedance representation for a clarinet-like bore. It is evident that the waveguide is passive ($|\arg\left(Z(\omega)\right)| \leq \pi/2 \Rightarrow \mathrm{Re}[Z(\omega)] \geq 0$) and that the modulus of the reflection coefficient monotonically decreases with ω. A strong feature of wind instrument bores is the existence of weakly damped resonances visible on the modulus of the input impedance, that enable the musician to produce stable and clear tones. For most woodwind bores, the resonances are approximately harmonic, which influences the tuning and timbre of the self-sustained oscillations (see, e.g., [16]).

2.3. *Modal analysis*

As mentioned in the introduction, a parametrization of the input impedance or of the reflection coefficient is required for numerical studies such as real-time simulation, or bifurcation analysis. A classical method is based upon the identification of the resonances in terms of angular frequencies ω_m, quality factors Q_m and magnitude Z_m. We prefer the more general parametrization in terms of poles s_m and modal coefficients C_m to reconstruct the impedance as a series of modal contributions

$$Z_{in}(\omega) = \sum_m \frac{Z_m}{1 + jQ_m\left(\frac{\omega}{\omega_m} - \frac{\omega_m}{\omega}\right)} = \sum_m \frac{C_m}{j\omega - s_m}. \tag{5}$$

For a bore with a high number of resonances M, the parametrization relies on $2M$ complex quantities, C_m and s_m, which may become computationally prohibitive. A model reduction can be achieved by truncating the series to account only for the resonances that are significant in the frequency range of interest.

Resonance frequencies above some cutoff frequency F_{cut} are discarded, and the frequency range above F_{cut} is referred to as the *stop band*, similar to the stop band of lowpass analog and digital filters. This definition has nothing to do with the distinction introduced by Benade [25] about the effects of a tone hole lattice on the input impedance of wind instruments. In addition, we denote F_{min} the lower bound for which the model or measurement is valid, and the frequency range between F_{min} and F_{cut} is referred to as the

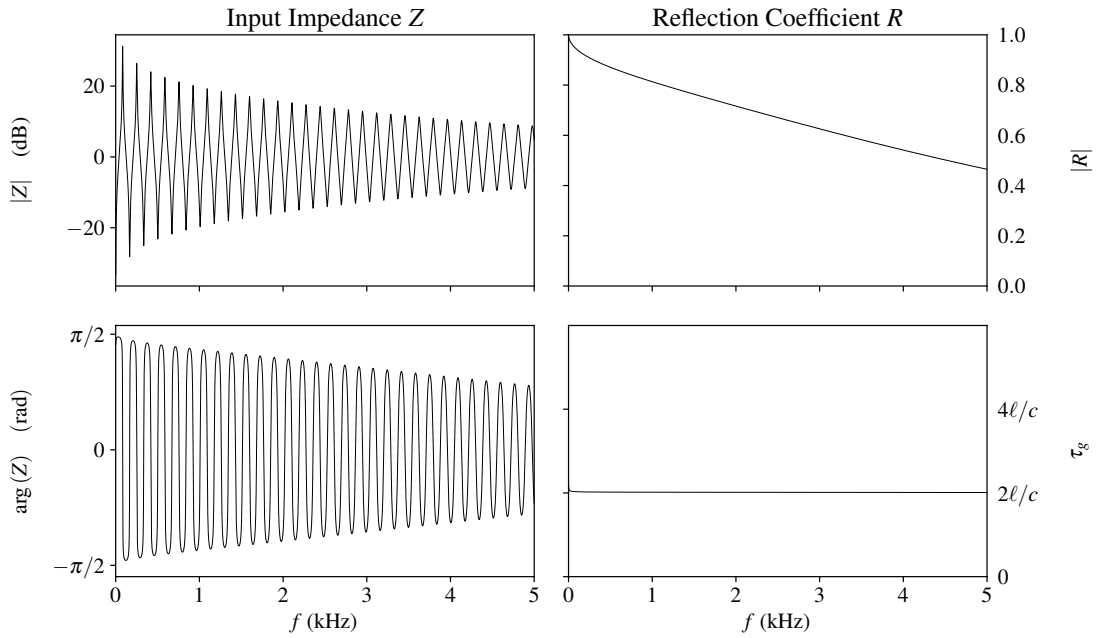

Figure 1: Modulus and argument of the input impedance Z (top left and bottom left, respectively), modulus of the reflection coefficient R (top right) and group delay $\tau_g = -d(\arg(R))/d\omega$ (bottom right) from the analytical model (Eq. (4)). $\ell = 1\,\mathrm{m}$, $r = 1\,\mathrm{cm}$.

pass band. Finally, from the zero frequency to the lower bound F_{min}, the model or the measurement has to be extrapolated according to some physically acceptable rules. This frequency range is thus named the *reconstructed band*.

3. Effect of the truncation of a modal series

The purpose of this section is to highlight the influence of the truncation of the modal series. This truncation is required as only a finite number of modes can be dealt with numerically. To remove any bias from measurements, the analysis is performed on an input impedance calculated by classical analytical models. It is thus possible to compute a theoretically exact modal expansion using complex analysis. This is of limited utility as the models are not valid across the entire frequency range, and cumbersome in that it requires the model to be extended to the Laplace domain, i.e., as a function of the Laplace variable s. However it is useful to demonstrate the consequences of the truncation.

Considering the input impedance $Z_{in}(s) = N(s)/D(s)$ of the cylindrical pipe (see Sec. 2), there are an infinite number of poles s_m, i.e., of roots of $D(s)$. The application of the Cauchy's integral theorem shows that the poles s_m have negative real parts, so that the corresponding time-domain functions $\exp(s_m t)$ decrease with time. The application of the residue calculus [26] to the input impedance yields

$$Z_{in}(s) = \sum_{m\in\mathbb{N}} \frac{C_m}{s - s_m} \text{ with } C_m = \frac{N(s_m)}{D'(s_m)}, \tag{6}$$

where the C_m are the residues of Z_{in} at the poles s_m, assuming the poles to be simple (i.e., of order one). The denominator $D'(s_m)$ of the residue is the derivative of D with respect to the variable s at the pole s_m.

A finite number of poles are estimated numerically using the Newton-Raphson method. For each of the first M poles with a positive imaginary part, the iterative algorithm is initialized using one of the resonance frequency of the input impedance $Z_{in}(s = j\omega)$ evaluated on the frequency axis. The resulting poles are shown in Fig. 2, and evidence that eigenfrequencies $\mathrm{Im}[s_m]$ are almost odd multiples of the first one, and that damping increases with frequency.

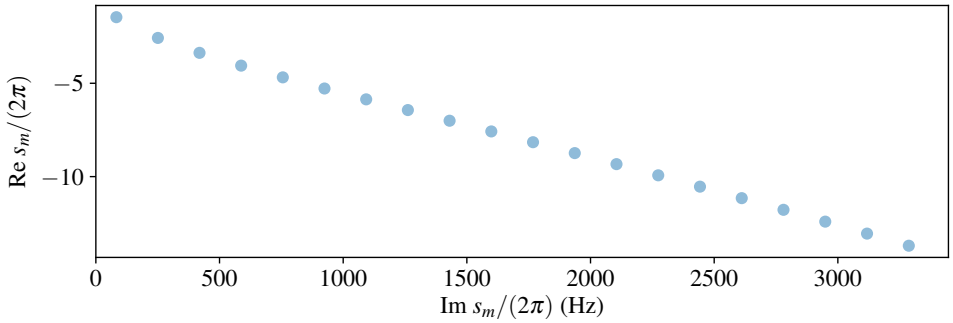

Figure 2: Location of the poles s_m of the input impedance of a cylindrical pipe ($r = 1\,\mathrm{cm}$ and $\ell = 1\,\mathrm{m}$) with radiation and boundary layer losses in the complex plane.

The residues C_m can be analytically derived using the expressions of the radiation impedance and of the propagation constant, and the modal expansion of the input impedance is computed using Eq. (6) considering the M first poles (indexed from zero)

$$Z_{\text{modal}}(s) = \sum_{m=0}^{M-1} \frac{C_m}{s - s_m} + \frac{C_m^*}{s - s_m^*} = 2 \sum_{m=0}^{M-1} \frac{s\,\mathrm{Re}[C_m] - \mathrm{Re}[C_m s_m^*]}{s^2 - 2s\,\mathrm{Re}[s_m] + |s_m|^2}. \tag{7}$$

The resulting impedance and the related reflection coefficient evaluated on the frequency axis (i.e., for $s = j\omega$) are displayed in Fig. 3. Several drawbacks can be mentioned. First the modal impedance restores the resonant behaviour in the vicinity of the first resonances and then slowly decays to 0 with a $-\pi/2$ argument. This induces a reflection coefficient that asymptotically tends to unity above the last resonance frequency taken into account. The resulting resonator thus poorly dissipates power at high frequencies. Furthermore, the poles/residues expansion is exact when considering the infinite summation. Its truncation still preserves the resonances of the input impedance but the anti-resonances are perturbed due to the missing inertial contribution of the ignored higher frequency poles. This may have strong consequences (for example on the magnitude of the even harmonics of the mouthpiece pressure) and results from the choice of the elementary functions in Eq. (5) that essentially focuses on the resonances, the reconstruction out of the resonances being a by product that is only correct when accounting for the infinite set of poles. This is also visible on the modulus of the reflection coefficient that is correct at the resonance frequencies but oscillates in-between with a deviation that comes close to 1 near the truncation limit.

As a conclusion, the theoretical modal expansion is a powerful mathematical tool but it shows practical limitations due to the truncation of the series. In regard to the constraint of the finite number of poles that can be represented numerically, the poles/residues decomposition has to be adapted, for example, by allowing the poles s_m to deviate from the analytical ones. This reverts to a fitting procedure as the one described in the next sections.

Other options are possible, for example, adding a corrective term such as the one introduced by Guillemain and Silva [9] in the specific case of a clarinet-like bore. It is designed as a high-pass filter that is able

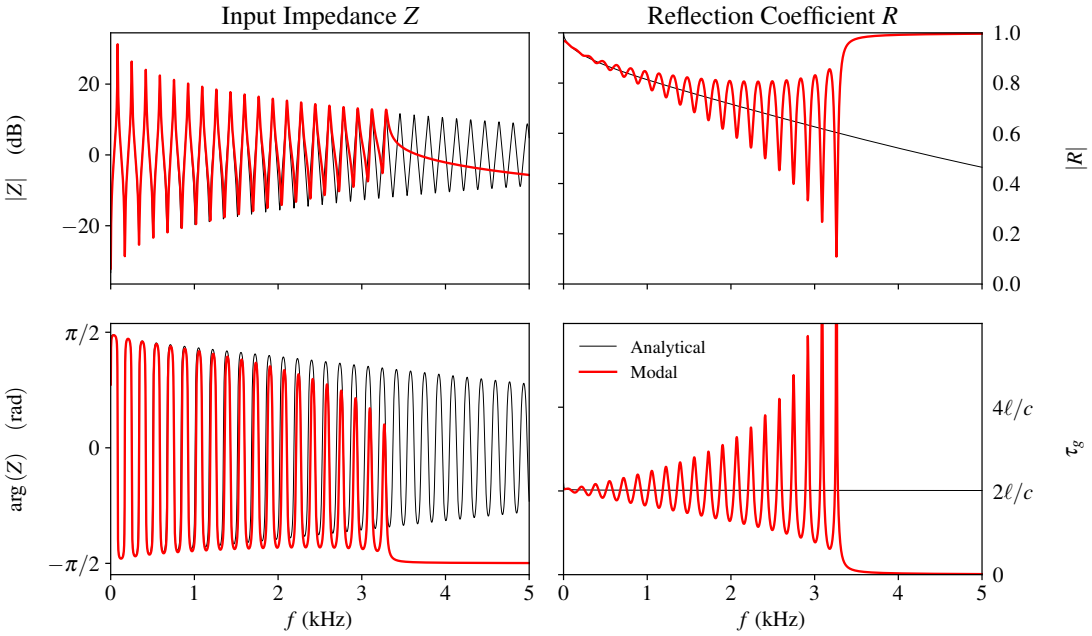

Figure 3: Modulus and argument of the input impedance Z (top left and bottom left, respectively), modulus of the reflection coefficient R (top right) and group delay $\tau_g = -d(\arg(R))/d\omega$ (bottom right) from the analytical model (Eq. (4), thin black line, same as Fig. 1) and from the modal expansion truncated to 20 modes (see Sec. 3, Eq. (7), thick red line). $\ell = 1\,\mathrm{m}$, $r = 1\,\mathrm{cm}$.

to restore the contribution of the ignored higher order poles in the low or mid frequency range and, as a consequence, the position of the anti-resonances. It also tends to the characteristic impedance above the frequency of truncation and thus ensures that the reflection coefficient decays to zero in the high frequency range. The parameters are determined based only on the analytical expression. The generalization of this method is outside the scope of the current paper. In the next section, a fitting procedure is proposed.

4. Fitting a given transfer function to a finite modal expansion

4.1. Prony analysis

Prony analysis, from the name of the French mathematician who developed the method in the late 18th century, is the transposition of the Fourier analysis for damped oscillations. It relies on the assumption that a given causal signal $h(t)$ expands on a series of damped sinusoids

$$h(t) = \text{Heaviside}(t) \sum_{m=0}^{M-1} C_m e^{s_m t}, \tag{8}$$

or, considering the Laplace transform $H(s)$ of the signal

$$H(s) = \sum_{m=0}^{M-1} \frac{C_m}{s - s_m}, \tag{9}$$

where the modal frequencies s_m and the modal coefficients C_m are such that the frequency response $H(s = j\omega)$ is hermitian symmetric, or, equivalently, that $h(t)$ is a real function. This applies when $H(s)$ is an input impedance and $h(t)$ the related impulse response.

A measured signal, sampled with a time step T and assumed to vanish for negative time is expressed as

$$\forall n \geq 0,\ h[n] = \sum_{m=0}^{M-1} C_m y_m^n \equiv \sum_{m=0}^{M-1} C_m e^{n s_m T}, \tag{10}$$

for $y_m = e^{s_m T}$ or, equivalently, $s_m = \left(\log|y_m| + j \arg(y_m)\right)/T$. This expansion implies that the signal $h[n]$ is autoregressive, i.e., there exists a set of coefficients $(\beta_0, \beta_1 \ldots \beta_{M-1}, \beta_M = 1)$ such as

$$\forall n \geq M, h[n] + \sum_{k=1}^{M} \beta_{M-k} h[n-k] = 0. \tag{11}$$

In fact it is possible to build an M-order polynomial with roots y_m. Its coefficients are denoted as β_k (with leading coefficient $\beta_M = 1$), so that $\forall n \geq M$

$$\sum_{k=0}^{M} \beta_{M-k} h[n-k] = \sum_{k=0}^{M} \beta_k h[n+k-M] = \sum_{k=0}^{M} \beta_k \sum_{m=0}^{M-1} C_m y_m^{n+k-M} = \sum_{m=0}^{M-1} C_m y_m^{n-M} \underbrace{\sum_{k=0}^{M} \beta_k y_m^k}_{=0} = 0. \tag{12}$$

The evaluation of Eq. (11) for $n \in [M, 2M-1]$ defines the matrix equation

$$\underbrace{\begin{bmatrix} h[M] \\ h[M+1] \\ \vdots \\ h[2M-1] \end{bmatrix}}_{\boldsymbol{h'}} = -\underbrace{\begin{bmatrix} h[0] & h[1] & \ldots & h[M-1] \\ h[1] & h[2] & \ldots & h[M] \\ \vdots & \vdots & & \vdots \\ h[M-1] & h[M] & \ldots & h[2M-2] \end{bmatrix}}_{\boldsymbol{A}} \cdot \underbrace{\begin{bmatrix} \beta_0 \\ \beta_1 \\ \vdots \\ \beta_{M-1} \end{bmatrix}}_{\boldsymbol{\beta}}. \tag{13}$$

The basic idea of the Prony analysis is that the poles s_m derive from the roots y_m of a polynomial whose coefficients are the β_k which in turn can be obtained by numerically solving Eq. (13).

4.2. Least squares complex exponentials (LSCE)

The Prony method can deal with noisy data by considering more than M evaluations of the autoregressive equation (11), e.g. for $n \in [M, M+N'-1]$ with $N' > M$. The matrix $\boldsymbol{A}$ is then rectangular and the matrix equation $\boldsymbol{A\beta} = -\boldsymbol{h'}$ is overdetermined. It is solved using the least squares Moore-Penrose pseudoinverse of $\boldsymbol{A}$. This extension of the Prony analysis is the so-called *Least squares complex exponentials* method (LSCE, see, e.g., Ref. [12]).

4.3. Evaluation of modal coefficients

The coefficients C_m can be estimated from Eq. (10) for $0 \leq n < M$

$$\underbrace{\begin{bmatrix} h[0] \\ h[1] \\ h[2] \\ \vdots \\ h[M-1] \end{bmatrix}}_{\boldsymbol{h}} = \underbrace{\begin{bmatrix} 1 & 1 & \ldots & 1 \\ y_0 & y_1 & \ldots & y_{M-1} \\ y_0^2 & y_1^2 & \ldots & y_{M-1}^2 \\ \vdots & \vdots & & \vdots \\ y_0^{M-1} & y_1^{M-1} & \ldots & y_{M-1}^{M-1} \end{bmatrix}}_{\boldsymbol{B}} \cdot \underbrace{\begin{bmatrix} C_0 \\ C_1 \\ \vdots \\ C_{M-1} \end{bmatrix}}_{\boldsymbol{C}} \tag{14}$$

where $\boldsymbol{B}$ is a Vandermonde matrix and is invertible for simple poles. This equation can be problematic if h is obtained using a discrete Fourier transform (see last paragraph in Sec. 4.4).

An evaluation in the spectral domain is usually preferable. The coefficients C_m can be obtained from Eq. (9) by using the frequency response function (FRF) $H_n = H(s = jn\Delta\omega)$ measured on a regularly sampled frequency grid

$$\boldsymbol{B'} \cdot \boldsymbol{C} = \boldsymbol{H'} \tag{15}$$

where $\boldsymbol{H'} = \begin{bmatrix} H_{-N'+1} & \dots H_{N'-1} \end{bmatrix}^T$ and $\boldsymbol{B'}$ is a $(2N'-1) \times M$ matrix with generic term $\boldsymbol{B'}_{nm} = 1/\left(j(n-N')\Delta\omega - s_{m+1}\right)$. This includes the evaluation of the FRF for both positive and negative frequencies, spanning from low frequencies to the cutoff frequency, so that $\Delta\omega = 2\pi F_{cut}/(N'-1)$. In order to make the estimation robust with respect to noise, the number N' of computed or measured frequencies is generally much larger than M. The matrix $\boldsymbol{B'}$ is thus rectangular and the system has to be solved again in the least squares sense, using the pseudo inverse of $\boldsymbol{B'}$.

Taking the z-transform of Eq. (10)

$$H(z) = \sum_{n\geq 0} h[n] z^{-n} = \sum_{m=0}^{M-1} \frac{C_m}{1 - y_m z^{-1}}, \tag{16}$$

the same procedure as Eq. (15) can be applied considering the frequency-domain characterization of the discrete-time transfer function, i.e., $H(z)$ evaluated on the unit circle ($z = e^{j(n-N')\Delta\omega T}$ for $n \in [1, 2N'-1]$). The generic term of the matrix $\boldsymbol{B'}$ is

$$\boldsymbol{B'}_{nm} = \frac{1}{1 - y_m e^{j(n-N')\Delta\omega T}}. \tag{17}$$

4.4. Numerical considerations

The methods proposed in the previous sections need to be treated carefully from a numerical perspective. First, the calculations involve exponentiation and high orders polynomials (see, e.g., Eqs. (12) and (14)) which is known to be problematic. Furthermore, when some modes are highly damped or when the C_m span on many orders of magnitude, rounding errors may degrade the numerical accuracy of the computations. The use of high precision arithmetic is necessary essentially in the evaluation of the poles. Once this evaluation is done, the remaining operations do not need to be performed in high precision.

A second point concerns the fact that unstable poles (poles s_m with positive real part) may emerge as roots of the polynomial defined by the coefficients β_m. They may result from an overestimate of the number of modes M: the Prony analysis then uses the additional degrees of freedom to overfit noisy data. They have no physical meaning and can lead to growing exponentials in the modal synthesis. Once the poles have been estimated using Eq. (12), values of y_m such that $|y_m| > 1$ are discarded.

There is also a visible violation of the Nyquist-Shannon sampling theorem as the modal expansion in Eq. (9) has an unlimited bandwidth. Although the Prony's method is somewhat resilient to moderate violations of the sampling theorem, the estimation is improved if the transfer function $H(\omega)$ is guaranteed to converge towards zero instead of a finite non zero value. This may require a shift of the transfer function $H \to H - H(\omega \to \infty)$ which corresponds to an additional pole $s_m \to -\infty$ such that $y_m = 0$, i.e., a Dirac impulse in $h(t)$.

Another important issue concerns Eqs. (15) and (17): the frequencies considered in the estimation of the modal coefficients only span the pass band. Without any additional constraint, the least squares fit may lead to unwanted behaviors in the stop band, for example violating the passivity property at high frequencies. This can be problematic when using the modal series for synthesis with a sampling frequency F_s is much

higher than the cutoff frequency F_{cut}. It is thus necessary to enforce fictitious target points between F_{cut} and $F_s/2$ in order to guarantee the passivity, without degrading the fit in the pass band. This is done by extending the matrix $\boldsymbol{B'}$ and the vector $\boldsymbol{H'}$ by N'' fake values $\hat{H}_n$ for angular frequencies $\hat{\omega}_n > 2\pi F_{cut}$ and their N'' corresponding hermitian symmetric counterparts $\hat{H}_{n+N''} = \hat{H}_n^*$ and $\hat{\omega}_{n+N''} = -\hat{\omega}_n$.

$$\underbrace{\begin{bmatrix} \boldsymbol{H'} \\ \hline \hat{H}_1 \\ \vdots \\ \hat{H}_{2N''} \end{bmatrix}}_{\boldsymbol{H''}} = \underbrace{\begin{bmatrix} \boldsymbol{B'} \\ \hline \left(1 - y_0 e^{j\hat{\omega}_1 T}\right)^{-1} & \dots & \left(1 - y_{M-1} e^{j\hat{\omega}_1 T}\right)^{-1} \\ \vdots & & \vdots \\ \left(1 - y_0 e^{j\hat{\omega}_{2N''} T}\right)^{-1} & \dots & \left(1 - y_{M-1} e^{j\hat{\omega}_{2N''} T}\right)^{-1} \end{bmatrix}}_{\boldsymbol{B''}} \cdot \boldsymbol{C}. \tag{18}$$

The choice of the fictitious points $(\hat{\omega}_n, \hat{H}_n)$ for the case of the modal analysis of wind instruments is discussed in Sec. 5.

Finally, in musical acoustics, the measurements are usually performed in the spectral domain. As extensively explained in Ref. [13], when the impedance $Z(\omega)$ is not purely resistive at the maximum measured frequency f_{cut} (i.e., the impedance does not coincide with a resonance or an antiresonance at that frequency), strong ripple appears on the time-domain signals $r(t)$ and $h(t)$ obtained by the discrete inverse Fourier transform. This is known to lead to simulations with no physical sense. In the present problem, the ripple can also interfere with the evaluation of the modal coefficients C_m by means of the Eq. (14). Conversely, the evaluation in the spectral domain as in Eqs. (15) and (18) does not suffer from this phenomenon.

5. Modal analysis of an acoustic resonator

The method described in the previous section is now applied to the input impedance of an acoustic resonator, first in the case where the impedance is known over the full frequency range (Sec. 5.1), and then when the measurements needs to be preprocessed (Sec. 5.2). The passivity over the stop band is constrained using fictitious points as described in Sec. 5.3, before an example of application is given in Sec. 5.4.

5.1. Analysis of an input impedance known over the pass band

When the input impedance is sampled from DC to the desired sampling frequency, we apply the LSCE method to the shifted variant of the impedance $H = Z_{in} - 1$ in agreement with the requirement of a transfer function decreasing to 0 when the frequency increases. The procedure is as follows:

1. Shift the input impedance so that H decreases to 0 for growing frequencies: usually $H = Z_{in} - 1$.
2. Sample the frequency response $H_n = Z_{in}(n\Delta\omega) - 1$ for $-N' < n < N'$.
3. Compute the discrete-time inverse Fourier transform $h[n]$ from the values H_n.
4. Assemble matrix $\boldsymbol{A}$ and vector $\boldsymbol{h'}$ from Eq. (13), and solve for $\boldsymbol{\beta}$.
5. Compute the roots y_m of the polynomial $P(X) = \sum_{k=0}^{M} \beta_k X^k$.
6. Append pole $y_0 = 0$ to account for the shift of the input impedance.
7. Add fictitious points and solve Eq. (18) for $\boldsymbol{C}$.
8. Add 1 to the modal coefficient C_0, in order to cancel the shift in Z_{in}.
9. Check whether the passivity is respected over the full frequency range. If not, correct the modal coefficient C_0 related to the shift, or update the set of fictitious points and solve Eq. (18) again.

It is also possible to apply the procedure to the reflection coefficient R without the shift (steps 2 to 7 and 9). Even if the reflection coefficient does not have visible resonances, the method can parametrize it as a modal series (as in Eq. (9)), generally with highly damped poles. As this is a smoother function of the frequency, the matrix B'' should be better conditioned. Furthermore, a better balance is maintained between impedance and admittance peaks than when applying LSCE to the shifted input impedance (which attaches more importance to the impedance peaks). However, there is a drawback as the results must be converted back to modal parameters for the impedance. This is done by searching the roots of the high order polynomial $R - 1$ (see Eq. (2)) which requires high precision arithmetics again.

5.2. Analysis of an input impedance with missing data in the low frequency range

The case of measured input impedances requires special care because the measurements may be noisy and/or available and reliable only on a partial range of the frequency domain. The proposed procedure is as follows:

Extrapolation steps. It is known that the input impedance measurements are have limited validity at very low frequencies and the LSCE analysis appears to be very sensitive to the physical plausibility of the reconstruction in the low range. Therefore an extrapolation is required below the lower bound F_{min} of the acceptable data. According to our experience, the reflection coefficient is a smoother function than the input impedance, and is the most suitable for its modulus and its argument to be approximated by low order polynomials.

1. Compute the reflection coefficient R_{meas} from the measured input impedance, using Eq. (2).
2. Select a frequency range $[F_{min}, F_{max}]$ where R_{meas} has an acceptable signal-to-noise ratio (typically from 120 to 230 Hz, depending on the signal-to-noise ratio of the measurement).
3. Fit an even polynomial $q_{even}(\omega)$ to the modulus $|R_{meas}|$ on the selected frequency range. The order is typically set to 10, with the lowest coefficient set to 1 to enforce an input impedance vanishing at zero frequency.
4. Fit an odd polynomial $q_{odd}(\omega)$, typically of order 11, to the unwrapped argument of $(-R_{meas})$.

Merging measured and extrapolated data. The two previous steps lead to the function

$$R_{extrap}(\omega) = -q_{even}(\omega)e^{jq_{odd}(\omega)} \tag{19}$$

that is hermitian symmetric and is used in the $[0, F_{min}]$ frequency range. In order to overcome noisy measurements in the pass band and a possible too high frequency resolution (i.e., $\Delta\omega$ too small, leading to huge dimensions of the matrix $\boldsymbol{B'}$), a smoothing downsampling is desirable in the pass band.

5. The reflection coefficient is reconstructed in the low frequency range as follows:

$$R(\omega) = \begin{cases} R_{extrap}(\omega) & \text{for } 0 \leq \omega < 2\pi F_{min}; \\ \text{crossfade } (R_{extrap}, R_{meas}) & \text{for } 2\pi F_{min} \leq \omega < 2\pi F_{max}; \\ R_{meas}(\omega) & \text{for } 2\pi F_{max} \leq \omega \leq 2\pi F_{cut}; \\ R(-\omega)^* & \text{for } \omega < 0; \end{cases} \tag{20}$$

where the crossfade is performed using the sigmoid function:

$$\text{crossfade } (R_{extrap}, R_{meas}) = R_{extrap} + \frac{R_{meas} - R_{extrap}}{1 + \exp\left[-2a\left(\omega - \pi(F_{min} + F_{max})\right)\right]}. \tag{21}$$

a is chosen so that the sigmoid equals 1% and 99% at $2\pi F_{min}$ and $2\pi F_{max}$, respectively.

Downsampling data.

6. Define a downsampling factor d_s so that the frequency resolution becomes typically $\Delta\omega/2\pi = 0.2\,\mathrm{Hz}$ after downsampling.
7. The smoothing downsampling filtering is applied on the samples of $R(\omega)$ in the pass band: consider $4d_s + 1$ samples, fit a low-order polynomial (typically order 3) on these samples and retain the evaluation of the polynomial at the center frequency of the frame. Advance d_s samples, and repeat the procedure. It can be described as a *moving average* process applying on frequency-domain frames of length $4d_s + 1$ with a $3d_s + 1$ overlap.

Modal analysis on the reconstructed data.

8. Compute Z_{in} using Eq. (2).
9. Apply Sec. 5.1 on Z_{in}.

Modal analysis can again be performed on the reflection coefficient R with the drawback mentioned above. In our experience, the analysis of measured reflection coefficient requires an additional pole $y_0 = 0$ as for the input impedance (step 6 in Sec. 5.1) even without any shift of the data.

5.3. Choice of the fictitious points

In most cases, this issue is not complicated to solve for clarinet-like instruments. According to our experience, the fictitious points in the stop band should be spaced about $20\Delta\omega$ to $200\Delta\omega$ apart from another.

A crude initialization is $\hat{H}_n^{(0)} = 0$, for which the least squares solution of Eq. (18) usually is a convenient solution $\boldsymbol{C}^{(0)}$. The stop band constraint is weakened in a second step by choosing new fictitious values $\hat{H}_n^{(1)}$ from the last $2N''$ values of $\boldsymbol{B''} \cdot \boldsymbol{C}^{(0)}$. Again solve Eq. (18) for vector $\boldsymbol{C}^{(1)}$, this time with source term $\boldsymbol{H''}^{(1)}$.

A known difficult case is that of brass instruments measured with their mouthpieces. Because of the small cavity of the mouthpiece, the damping of the acoustic waves is low and R exhibits a modulus near to unity, even at high frequency. Thus more care is required for the initialization in order to preserve the passivity in the stop band. Notice that $\boldsymbol{B''}^{-1}$ has to be computed only once, which means that many "guesses" can quickly be tested in a trial and error process. Providing a general methodology for such a search is beyond the scope of this paper.

5.4. Example of application

The input impedance of the fingering $F_3^\sharp$ of a professional clarinet was measured with a CTTM impedance head [27]. The measurements are processed according to Sec. 5.2. Typical values provided in previous sections were adopted for this analysis.

Fig. 4 shows the reconstruction of the reflection coefficient in the low frequency range. Fig. 5 depicts the result of the modal analysis performed on the reconstructed data, according to Sec. 5.1. The modulus of the reconstructed impedance deviates from the measurement with a standard error of $0.19\,\mathrm{dB}$, the maximal error being obtained for the first antiresonance ($1.5\,\mathrm{dB}$ local error). This is probably related to a lower signal-to-noise ratio of the measurements at the deepest antiresonance as also visible in Fig. 4. Concerning the argument, the standard deviation is $0.02\,\mathrm{rad}$ with a maximal error of $0.1\,\mathrm{rad}$ at the first and third antiresonance. The corresponding reflection coefficient R is illustrated in Fig. 6, including fictitious points, extrapolated up to $F_s/2$.

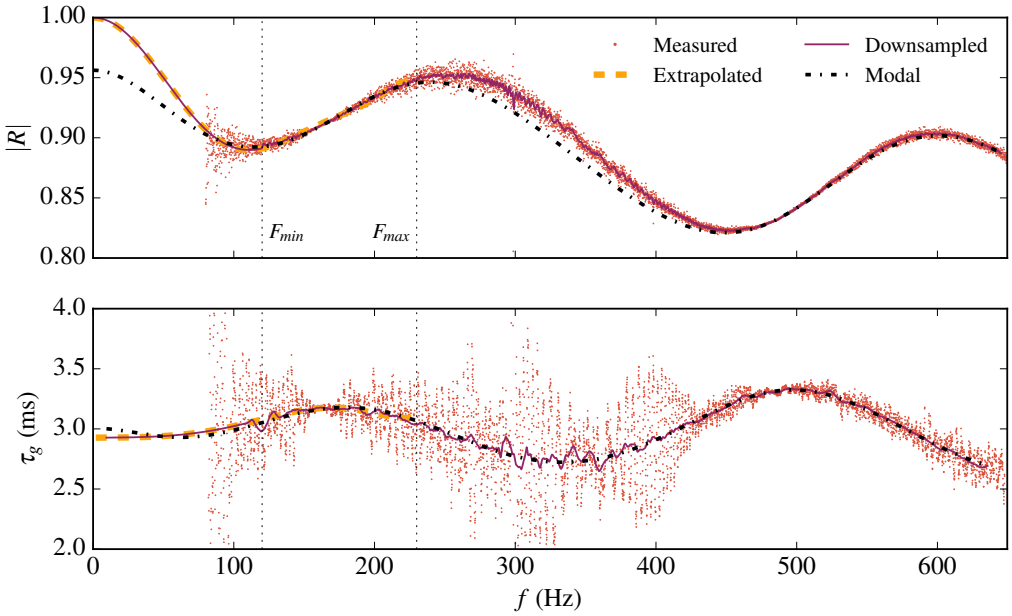

Figure 4: Reconstruction of the reflection coefficient in the low frequency range. Modulus of the reflection coefficient (top) and group delay (bottom) of the measured data (dots), the extrapolated data (thick dashed line), the reconstructed downsampled data (thin line) and of the result of the modal analysis (dash-dotted line). The bounds of the frequency range used for the extrapolation step are also shown (vertical dotted lines).

6. Application to sound synthesis

6.1. Principles of modal synthesis

A direct application of modal analysis of the input impedance (or reflection coefficient) of wind instruments lies in the design of algorithms for real-time sound synthesis. In fact, the functioning of wind instruments is classically viewed as the coupling of an acoustic resonator and a nonlinear excitation system, and this physics-based modeling paradigm can be used for sound synthesis (see Ref. [28] for a review). The numerical scheme then relies on two discrete-time models, one for the exciter and one for the acoustic resonator.

Accounting for the bore, the transposition of the continuous time model to the discrete time is performed in order to preserve the impulse response. The continuous time impulse response $h(t)$ is obtained by the inverse Fourier transform of the modal series in Eq. (5) and the discrete time impulse response $h[n]$ equals $h(t)$ at the positive sampled times

$$h(t \geq 0) = \sum_m C_m e^{s_m t} \Rightarrow h[n \geq 0] = h(nT_s) = \sum_m C_m e^{n s_m T_s} = \sum_m C_m x_m^n \tag{22}$$

where $x_m = e^{s_m T_s}$ and $T_s = 1/F_s$ are related to the sampling frequency F_s. The latter is in general higher than the cutoff frequency F_{cut}. Typical values for F_s and F_{cut} are $4\,\mathrm{kHz}$ and $44.1\,\mathrm{kHz}$, respectively. The z-domain impedance is then

$$H(z) = \sum_m \frac{C_m}{1 - x_m z^{-1}}.$$

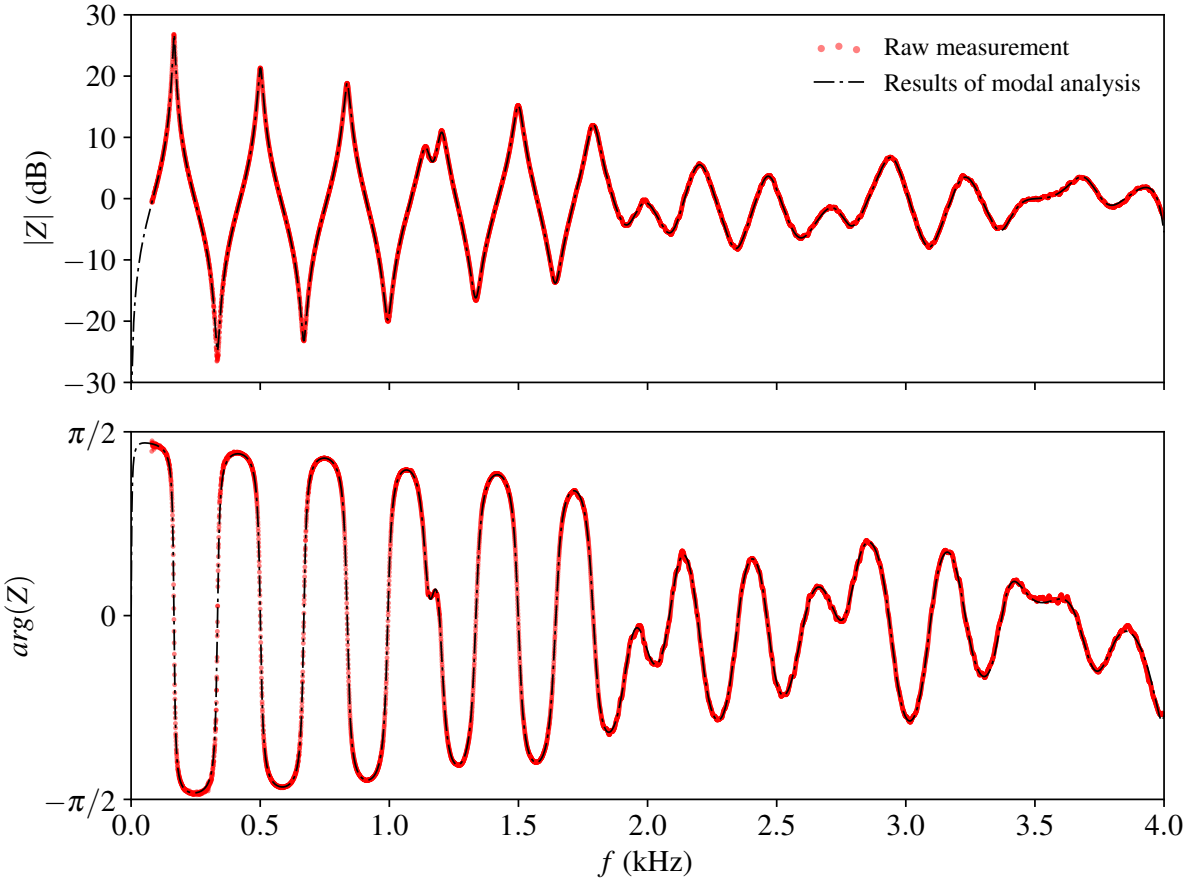

Figure 5: Input impedance Z_{in} of the fingering $F_3^\sharp$ of a professional clarinet (top: modulus, bottom: argument). The raw measurements are shown by the red points ($\Delta w = 2\pi \times 0.047\,\mathrm{rad\,s^{-1}}$) and the results of the modal analysis as used for sound synthesis (following the procedure in Sec. 5.2) are denoted by the thin dashed-dotted line.

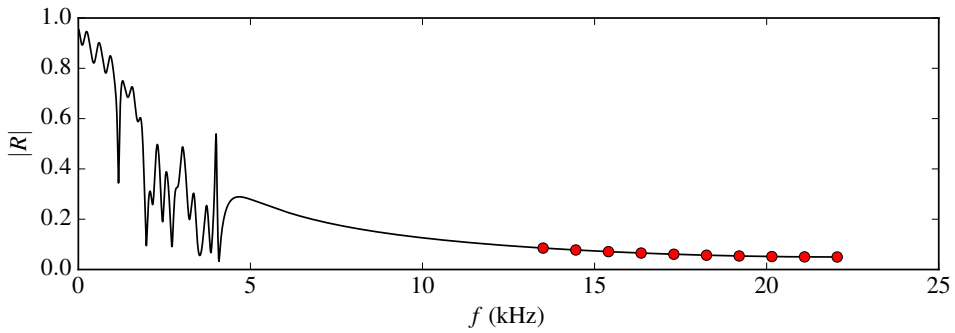

Figure 6: Modulus of the reflection coefficient of the fingering $F_3^\sharp$ from the modal analysis, including the extrapolation in the stop band necessary for the sound synthesis, up to $F_s/2$. The final values $\hat{H}_n^{(1)}$ of the fictitious points determined by the least squares fit are depicted with red dots. These points were set to 0 at the beginning of the procedure.

Because $h(t)$ is real, the coefficients s_m must be either real (monopole) or complex conjugates (bipole), in order to respect the Hermitian symmetry. The same applies to the discrete-time response $h[n]$ and the coefficients x_m. Nevertheless, since a monopole and a discrete Dirac are degenerate bipoles, we can use the generic 2nd order IIR digital filter [29]

$$H(z) = \sum_{\substack{m \\ \mathrm{Im}[s_m] \geq 0}} H_m(z) \text{ with } H_m(z) = \frac{b_{m,0} + b_{m,1} z^{-1}}{1 + a_{m,1} z^{-1} + a_{m,2} z^{-2}} \tag{23}$$

where the values of the coefficients $b_{m,0}$, $b_{m,1}$, $a_{m,1}$ and $a_{m,2}$ are computed from the poles s_m and the modal coefficients C_m according to Table 1. This filter design combines the contributions of complex conjugate poles s_m and s_m^* into a single bipole.

Type	Root	$b_{m,0}$	$b_{m,1}$	$a_{m,1}$	$a_{m,2}$
Dirac	$x_0 = 0$	C_0	0	0	0
Monopole	$x_m > 0$	C_m	0	$-x_m$	0
Bipole	(x_m, x_m^*)	$2\,\mathrm{Re}[C_m]$	$-2\,\mathrm{Re}[C_m x_m^*]$	$-2\,\mathrm{Re}[x_m]$	$\lvert x_m \rvert^2$

Table 1: Coefficients of the digital filters with respect to x_m and C_m.

It is also important to note that the time steps used in measurements (T in Eq. (10)) and in the synthesis (T_s in Eq. (22)) usually differ. This implies that the roots $y_m = \exp(s_m T)$ of the former have to be converted into $x_m = \exp(s_m T_s)$. There may exist roots y_m on the negative real axis ($\mathrm{Re}[y_m] < 0$ and $\mathrm{Im}[y_m] = 0$, i.e., a contribution oscillating at the cutoff frequency), and they have to be split into a pair of complex conjugate values x_m and x_m^*, increasing the number M of poles. As a consequence, when applying the procedure described in Sec. 5, the modal coefficients C_m must be evaluated (step 7. in Sec. 5.1 after converting y_m into x_m.

The filter $H(z)$ enables the evaluation of the pressure $p[n]$ at the input of the waveguide when it is excited by the flow rate $u[n]$. The pressure is the sum of the partial pressures $p_m[n]$, each one accounting for a real pole s_m or a pair of complex conjugate poles (s_m, s_m^*) and obeying the difference equation

$$p_m[n] = b_{m,0} u[n] + b_{m,1} u[n-1] - a_{m,1} p_m[n-1] - a_{m,2} p_m[n-2]. \tag{24}$$

It is possible to arrange the relations so that the (total) pressure at the input of the bore at the current time depends on the current flow rate value and on some previous values

$$p[n] = \sum_m p_m[n] = V_1 u[n] + V_2$$
$$\text{with } \begin{cases} V_1 = \displaystyle\sum_m b_{m,0}, \\ V_2 = \displaystyle\sum_m b_{m,1} u[n-1] - a_{m,1} p_m[n-1] - a_{m,2} p_m[n-2]. \end{cases} \tag{25}$$

This representation of the pressure at the input of the resonator is more convenient to couple with the classical representation of the exciter. The latter is generally described by a nonlinear time-domain relationship $u[n] = F(p[n])$ that may account for unsteady effects. In the general case, the coupling would require an iterative solution to the following problem

$$p[n] = V_1 u[n] + V_2 \text{ and } u[n] = F(p[n]) \tag{26}$$

at each time step n. However, some discrete-time models of the exciter, such as the one given in Appendix A, have an explicit solution. The current pressure $p[n]$ and flow rate $u[n]$ can be efficiently obtained and real-time implementation is achievable.

6.2. Transitions between fingerings

In real instruments, when the instrumentalist changes the pitch from some note A to another note B, he opens and/or closes one or many holes at the same time. According to Ref. [30], a simple crossfade model between the input impedances at the beginning and at the end of the transition is shown to lead to perceptually satisfactory simulations of the transitions between fingerings. This model is only required to be able to simulate the response of the bore for the initial and the final states during the N_r time steps of the transition. The partial pressures $p_{m,A}$ and $p_{m,B}$ are computed simultaneously for the two configurations. At time step $n \in [N_0, N_0 + N_r]$, the pressure $p[n]$ is the result of the linear crossfade

$$p[n] = \sum_m p_{m,A}[n] + \frac{n - N_0}{N_r} \left(p_{m,B}[n] - p_{m,A}[n] \right) . \tag{27}$$

as if the two pipes were simultaneously excited with the same flow rate. This can still be written as $p[n] = V_1 u[n] + V_2$. Consequently the synthesis scheme remains unmodified. At the beginning of the transition, the pipe B is assumed to be silent (i.e. $p_m[N_0 - 1] = 0$ and $p_m[N_0 - 2] = 0$ for all m). Coupling through the flow transfers some energy from the pipe A to the pipe B.

We tested the refinement proposed by Guillemain and Terroir [30] on the basis of the input impedances of a clarinet measured with a tone hole being progressively closed. Their measurements show that the first resonance frequency varies gradually, like a *glissando*, while the amplitude of the peak decreases to a minimal value before increasing to the final value, approximately following the shape of a parabola. This behavior can be simulated in real-time for the most important peaks, such as the one that sustains the oscillation (so-called *master mode*, indexed as $\bar{m}$) and, optionally, the peaks that are strongly excited in the playing situation. The modal coefficient $C_{\bar{m}}$ follows a parabola-like evolution between the initial value $C_{\bar{m},A}$ and the final value $C_{\bar{m},B}$ while the pole $s_{\bar{m}}$ varies linearly from $s_{\bar{m},A}$ to $s_{\bar{m},B}$. The transition for less important peaks is still simulated using the simple crossfading algorithm at a lower computational cost. This algorithm is acceptable for simulating relatively small musical intervals (e.g., opening a single tone hole, as in Ref. [30]). During big jumps, the *glissando*-like transition sometimes sounds strange [31]. Such transitions are known by clarinetists to be difficult to achieve with a good *legato*. In some cases, different playing techniques are used to overcome this difficulty on the real instrument (such as: opening some holes earlier than others; half closed holes; *glissando*-like opening and closing of some holes working acoustically as "speaker keys"; subtle adaptations of the embouchure and the air pressure during the jump; special tuning of some resonances of the vocal tract; modification of the glottis using the crico-thyroid muscle; and others, according to the practice of the first author as a professional clarinetist). However, the MIDI wind controllers used to interface with the synthesizer do not allow such subtle controls.

A pragmatic solution consists of injecting some energy in the mode $\bar{m}$ of note B in order to initiate a bifurcation. At the beginning of the transition, all modes of the pipe B are silent, except mode $\bar{m}$ whose history is set to $p_{\bar{m}}[N_0 - 1] = c_{jump}\, p[N_0 - 1]$ and $p_{\bar{m}}[N_0 - 2] = c_{jump}\, p[N_0 - 2]$. The constant c_{jump} controls the amount of injected energy. With $c_{jump} = 0$, the simulated instrument sounds like the playing of an inexperienced beginner unable to control the jumps (but the *legato* between neighboring notes sounds good), whereas with $c_{jump} = 1$ the jumps are much more secure (but the *legato* sounds strange because every note starts with a small accent). The good balance is about $0.4 < c_{jump} < 0.7$, depending on the piece being played.

The second concern deals with the computational cost, a critical factor for real-time implementations when the number of modes M is large. The simulation of low pitched wind instruments is particularly sensitive to this problem. In Eq. (27), both pipes are played in parallel. Therefore, the computational cost doubles during the transition. This issue is resolved using the algorithm depicted in Fig. 7. Prior to the simulation, the modes of each fingering are classified as primary modes (from 0 up to about $M/2$) and secondary modes (from about $M/2+1$ up to M). The contribution of the latter to the input impedance is marginal, while the primary modes have either a big amplitude or are necessary to ensure the passivity of the filter. The transition begins with a *decrescendo al niente* of the secondary modes of fingering A, followed by the transition Eq. (27) applied to the primary modes of both fingerings and ends with a *crescendo* of the secondary modes of fingering B. The *decrescendo* and the *crescendo* are realized by multiplying the partial pressure of the secondary modes by a coefficient progressively varying respectively from 1 to 0 and from 0 to 1. Typically, the duration of each phase of the transition is 2 ms, 20 ms and 2 ms, respectively. With this algorithm, the computing cost remains approximately constant at every time step.

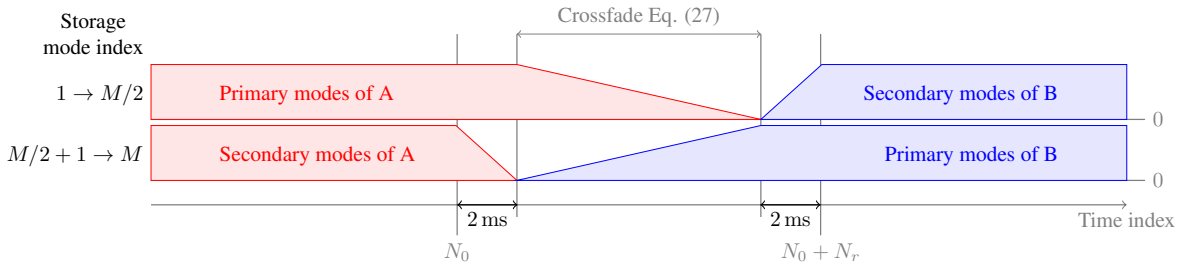

Figure 7: Diagram illustrating the processing of the primary and secondary modes of the initial (A) and final (B) configurations during a transition between two fingerings.

6.3. An example: sound synthesis of a clarinet

This section shows how the modal analysis performed on measured input impedances of a real instrument can be used to achieve the real-time synthesis of a musically relevant illustration, an excerpt of the Brahms Sonata Op. 120 no. 2 (see Fig. 8a).

The input impedance of a professional clarinet has been measured for each fingering used in the excerpt using the device described in Ref. [27], and the data was processed according to Sec. 5.2. The motion of the reed tip (see Ref. [32]) and the pressure in the mouth and in the mouthpiece were then measured while an experienced musician played the excerpt on the same instrument. These signals are used to provide the rough estimation of the control parameters γ and ζ, as defined in Appendix. A. This is known to be a difficult task as many quantities involved in the computation of the control parameters are still unavailable (see, e.g., Ref. [33] for clarinet and Refs. [34][35] for brass instruments). However, their time evolutions are estimated using the short-term average (10 ms frames) of the measured signals and then arbitrarily scaled to the dimensionless control parameters γ and ζ shown in Fig. 8b. This simplistic procedure should provide acceptable estimates for steady-state oscillations, but decreases the bandwidth of the signals which results in slower attack transients. The timings of the transition between fingerings had also to be retrieved from the recorded sound, which may introduce some mismatch between the measured and the synthesized sounds.

For real instruments, the transfer function between the mouthpiece pressure and the external pressure is different for each fingering. This would introduce another series of modal coefficients, thereby increasing the memory storage requirements and computing time. Appendix B gives the details of the design of an

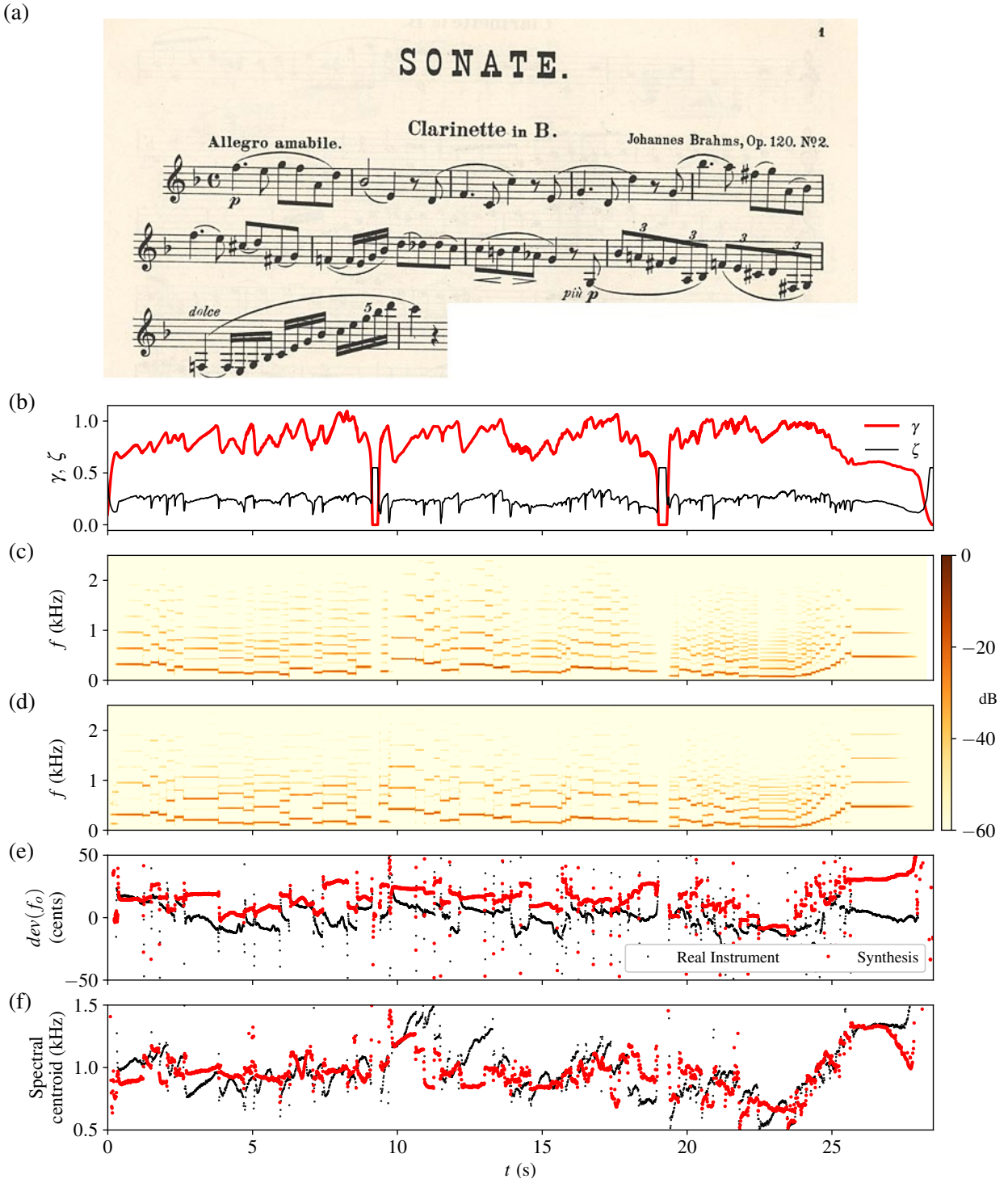

Figure 8: a: Excerpt of the first edition (1895) of Brahms Sonata Op 120 no. 2 that is played on a professional clarinet made in 1981. b: Control parameters γ and ζ estimated from measurements of the mouth pressure and of the reed motion (with an optical sensor) while playing the excerpt. c-d: Spectrograms of the external pressure obtained by applying the radiation filter (see Appendix B) to the mouthpiece pressure (c) measured on the real instrument or (d) produced by the synthesis model described in Sec. 6 using the estimated signals γ and ζ. e-f: Deviation from the tempered scale (e) and spectral centroid (f) calculated on the reconstructed external pressures for the real instrument (black thin markers) and for the synthesis (red thick markers). The parameters used in the synthesis are $\omega_r = 2\pi \times 1340\,\mathrm{rad\,s^{-1}}$, $q_r = 0.3$, and $c_{jump} = 0.7$.

empirical transfer function. It is applied to the mouthpiece pressure measured on the real instrument and on the synthesized mouthpiece pressure signal, in order to produce comparable external sound estimates.

The real-time implementation in Max/MSP of the sound synthesis scheme (accounting for the resonator, the exciter and the radiation) requires no more than 25% of CPU time on a modern personal computer. Many aspects of the simulations are satisfactory (see Fig. 8, and sound files available as supplementary material[1]). The proposed algorithm performs the excerpt noticeably well, without any unwanted squeaks, wrong notes, or absent notes, despite the difficult bindings and jumps in the excerpt. The spectral content of the synthesized external sound (Fig. 8d) is also quite similar to the real one (Fig. 8c).

Fig. 8e provides some insights on the oscillation frequency and the deviation in cents. The musician performance has a mean deviation close to zero (0.5 ± 10 cents), with smooth variations of the playing frequency within almost all notes. The modal-based sound synthesis exhibits a higher overall deviation (15 ± 11 cents) without modulation within the notes. This has implications for the expressiveness of the musical performance [36] and relates to the artificial nature of the sound that can be perceived by experienced listeners. This is also noticeable in Fig. 8f, where the spectral centroid of the synthesized signal exhibits the same note-to-note trends as the reference, but lacks the variations within the notes.

The synthesis inherits problems relating to measurement inaccuracies such as the difference in temperature between the measurement and playing situations, or the use of an adapter that replaces the mouthpiece for the the input impedance measurements. These elements, in addition to the approximate control parameters, could explain the differences between the oscillation frequencies of the original and the synthesized sounds. The simulation of the nonlinear behavior of the tone holes, a more realistic model of the reed, the inclusion of a vocal tract and the treatment of the sound radiation will likely make the synthesized model more closely resemble the real one.

7. Conclusions

This paper investigates many aspects related to the modal representation of the input impedance of wind instruments. The LSCE method is a powerful tool in this context, but a careful treatment of its application to measured or analytical input impedance is necessary. The possible issues include: physically acceptable reconstruction of the impedance in the low range, implementation of fictitious points in the spectral domain ensuring the passivity of the digital filter at every frequency, use of high precision arithmetics depending of the required number of simulated modes, for instance. The described method allows to derive valuable digital filters for real-time synthesis. Though the usefulness of the method is only demonstrated on a clarinet model, the authors have investigated the relevance of the modal analysis on other wind instruments, notably on saxophone, french horn, trumpet and trombone.

Acknowledgments

The authors thank Joël Bensoam, Louis Delebecque, Christophe Vergez for useful discussions, Anneke Scott and Erik Petersen for proofreading, and the He-Arc Ingénierie (Neuchâtel, Switzerland) for the facilities granted. This work is supported by the French ANR research project CAGIMA (ANR-11-BS09-0022).

[1] Note to compositor: please add here a link to supplementary material

Appendix A. Excitation model used in the sound synthesis scheme

The reed displacement is modeled as a single degree of freedom oscillator with natural angular frequency ω_r and damping q_r, driven by the dimensionless difference $\Delta p(t) = \gamma(t) - p(t)$ between the mouth pressure $\gamma(t)$ and the mouthpiece pressure $p(t)$

$$\frac{1}{\omega_r^2}\frac{d^2y(t)}{dt^2} + \frac{q_r}{\omega_r}\frac{dy(t)}{dt} + y(t) = -\Delta p(t) \tag{A.1}$$

when the reed channel is open, and with an additional unilateral contact force ensuring

$$\frac{dy(t)}{dt} = 0 \tag{A.2}$$

when the channel is closed ($y \leq -1$). The flow rate which excites the acoustic resonator takes into account the Bernoulli flow $u_b(t)$, proportional to a dimensionless embouchure parameter $\zeta(t)$ (related to the maximum flow rate that can enter the mouthpiece, see, e.g., Ref. [19]), as well as the flow rate $u_r(t)$ induced by the reed motion (with a factor λ)

$$\begin{aligned} u(t) = u_b(t) + u_r(t) \quad \text{with} \quad u_r(t) = \lambda\frac{dy(t)}{dt}, \\ \text{and } u_b(t) = \zeta(t)(1 + y(t))\text{sgn}(\Delta p(t))\sqrt{|\Delta p(t)|}. \end{aligned} \tag{A.3}$$

A discrete implementation is proposed by Coyle *et al* [37]. It uses a finite difference method for the reed displacement and the induced flow rate that are explicit:

$$y[n] = a_1 y[n-1] + a_2 y[n-2] - b_1\Delta p[n-1] \quad \text{and} \quad u_r[n] = \lambda\left(y[n] - y[n-1]\right), \tag{A.4}$$

with $b_1 = 1/(\kappa+\nu)$, $a_1 = (2\kappa-1)b_1$, $a_2 = (\nu-\kappa)b_1$, $\kappa = 1/(T_s^2\omega_r^2)$ and $\nu = q_r/(2T_s\omega_r)$. In Eq. (A.4), the current displacement $y[n]$ is independent of $p[n]$. This implies that the current Bernoulli flow $u_b[n]$ and pressure $p[n]$ are related by

$$p[n] = V_1\left(u_b[n] + u_r[n]\right) + V_2, \tag{A.5}$$

$$u_b[n] = W\text{sgn}(\gamma - p[n])\sqrt{|\gamma - p[n]|}, \tag{A.6}$$

where $W = \zeta f_{reg}\left(1 + y[n]\right)$ is the smoothed channel opening accounting for the regularization function $f_{reg}(\theta) = \frac{1}{2}\left(\theta + \sqrt{\varepsilon + \theta^2}\right)$ where ε is typically set to 0.04. This function is similar to the one provided in Ref. [38] (Sec. V.E) and operates when the reed beats against the lay. It follows that the Bernoulli flow $u_b[n]$ solves a simple 2nd order polynomial such that

$$u_b[n] = \frac{1}{2}\text{sgn}\left(\gamma - V_2 - V_1 u_r[n]\right)\left(-V_1W^2 + W\sqrt{(V_1W)^2 + 4\Big|\gamma - V_2 - V_1u_r[n]\Big|}\right), \tag{A.7}$$

and, finally, Eq. (A.5) can be used to compute $p[n]$.

Appendix B. Filter used to estimate the external pressure

Sound radiation is certainly important for the musical quality of an instrument. Until now, this aspect was largely neglected by the musical acoustics community due to the complexity of the radiated field and the fact that it exerts only a minor influence on the functioning of the instrument. The literature offers expressions for the transfer function between the velocity at the open end of a waveguide and the radiated pressure in free space only for academic configurations: the plane and spherical wave approximations (see, e.g., Refs. [19] and [39], respectively), the radiation of a semi-infinite circular pipe that is either unflanged [40], infinitely flanged [41], or partially flanged [42]. The case of waveguides with several orifices is even more complex as the orifices radiate in a common space and external interaction can then not be ignored. Ref. [19] (Sec. 14.5) explains the role of the tone hole lattice and Ref. [43] provides an illustration of real instruments with finite elements computations.

In the context of real-time synthesis, we seek a very simplified model of radiation characterized by low computational cost; a single model common to all the fingerings; and one that creates perceptually realistic sounds. Simple models of radiation are available in the literature, but fail to satisfy the last requirement.

We made an attempt to derive such a model from experimental data: for all the fingerings of a professional clarinet, we measured the internal pressure in the mouthpiece $p(t)$ and the external pressure $p_{ext}(t)$ on a microphone situated about 1.5 m in front of the player, in the practice room of a musician (i.e., not in an anechoic room [44]).

The signals $p(t)$ and $p_{ext}(t)$ were averaged over all fingerings. The global transfer function was computed by dividing the discrete Fourier transforms of both averaged signals. The phase was eliminated in the computation of the impulse response by taking the discrete inverse Fourier transform of the modulus of the transfer function. The human ear is known to be practically insensitive to the phase [45]. The simplified discrete time impulse response g_k, shown in Fig. B.9(a), is obtained by truncation in the vicinity of a zero crossing and multiplication by a Gaussian window. The external pressure can then be approximated by a discrete convolution of the internal pressure with the impulse response g_k. The resulting simplified transfer function G is depicted in Fig. B.9(b). Notice that the symmetry of g_k divides by 2 the computing cost of the convolution.

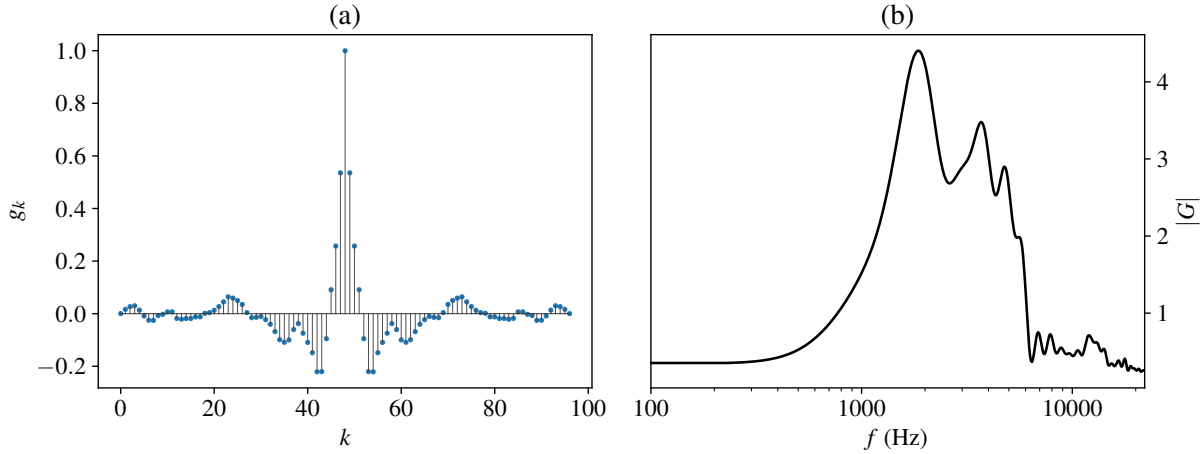

Figure B.9: Simplified impulse response g_k and transfer function G and (for $F_s = 44.1\,\text{kHz}$).

References

[1] von Helmholtz H., *On the sensations of tone*. Dover Publications New York, ch. A VII, 5388, 1954.

[2] Nederveen C. J., *Acoustical aspects of woodwind instruments*. Northern Illinois, DeKalb, 1998.

[3] Schumacher R. T., *Self-Sustained Oscillations of the Clarinet: An Integral Equation Approach*. Acustica 40, 198, 1978.

[4] Schumacher R. T., *Ab initio calculations of the oscillations of a clarinet*. Acustica 48, 71-85, 1981.

[5] Kergomard J., Ollivier S. and Gilbert J., *Calculation of the spectrum of self-sustained oscillators using a variable truncation method: application to cylindrical reed instruments*. Acustica 86, 685-703, 2000.

[6] Agulló J. and Barjau A., *The reflection function $r(t)$: a matrix approach versus FFT^{-1}*. J. Sound Vib. 106(2), 193-201, 1986.

[7] Barjau A. and Gibiat V., *Study of woodwind-like systems through nonlinear differential equations. Part II: Real geometry*. J. Acoust. Soc. Am. 102, 30323037, 1997.

[8] McIntyre M. E., Schumacher R. T. and Woodhouse J., *On the oscillations of musical instruments*. J. Acoust. Soc. Am. 74(5), 1325-1345, 1983.

[9] Guillemain Ph. and Silva F., *On the use of the modal expansion for the sound synthesis in real-time: pitfalls and solutions* (original title: *De lutilisation de la décomposition modale pour la synthèse sonore temps réel : écueils et solutions*). 10ème Congrès Français d'Acoustique, Lyon, 2010.

[10] Silva F., Vergez Ch., Guillemain Ph., Kergomard J. and Debut V., *MoReeSC: a framework for the simulation and analysis of sound production in reed and brass instruments*. Acta Acust. united Ac. 100(1), 126-138, 2014.

[11] Velut L., Vergez Ch., Kergomard J. and Silva F., *Numerical Simulation of the Production of Pedal Notes in Brass Instruments*. Proc. Int. Symp. Mus. Acous., Le Mans, 2014.

[12] Maia N. and Silva J., *Theoretical and experimental modal analysis*. Engineering Dynamics Series, Research Studies Press, Baldock, England, 1997.

[13] Gazengel B., Gilbert J. and Amir N. *Time domain simulation of single-reed wind instrument. From the measured input impedance to the synthesis signal. Where are the traps?* Acta acustica 3, 445-472, 1995.

[14] Ellis N., Bensoam J. and Caussé R., *Modalys demonstration*. Proc. Int. Comp. Music Conf. (ICMC05), 101102, 2005.

[15] Qu. Z.-Q. *Model Order Reduction Techniques*. Springer-Verlag London, 2004.

[16] Doc J.-B., Vergez Ch. and Missoum S., *A minimal model of a single-reed instrument producing quasi-periodic sounds*. Acta Acust. united Ac. 100(3), 543-554, 2014.

[17] Maestre E., Scavone G. and Smith J. O., *Design of recursive digital filters in parallel form by linearly constrained pole optimization*. IEEE Signal Proc. Lett. 23(11), 1547-1550, 2016. Acta Acust. united Ac. 100(1), 126-138, 2014.

[18] Meurisse Th., Mamou-Mani A., Benacchio S., Chomette B., Finel V., Sharp D. and Caussé R., *Experimental demonstration of the modification of the resonances of a simplified self-sustained wind instrument through modal active control*. Acta Acust. united Ac. 101(3), 581-593, 2015.

[19] Chaigne A. and Kergomard J., *Acoustics of musical instruments*. Springer-Verlag New York, 2016.

[20] Hélie Th. and Matignon D., *Representations with poles and cuts for the time-domain simulation of fractional systems and irrational transfer functions*. Signal Processing 86(10), 2516-2528, 2006.

[21] Kergomard J., *General equivalent circuits for acoustic horns*. J. Audio. Eng. Soc. 36, 948-955, 1988.

[22] Bilbao S., Harrison R., Kergomard J., Lombard B. and Vergez Ch., *Passive models of viscothermal wave propagation in acoustic tubes*. J. Acoust. Soc. Am. 138, 555-558, 2015.

[23] Silva F., Guillemain Ph., Kergomard J., Mallaroni B. and Norris A., *Approximation of the acoustic radiation impedance of a cylindrical pipe*. J Sound Vib. 322(1-2), 255-263, 2009.

[24] Kergomard J., Lefebvre A. and Scavone G., *Matching of fundamental modes at a junction of a cylinder and a truncated cone; Application to the calculation of some radiation impedances*. Acta Acust. united Ac. 101(6), 1189-1198, 2015.

[25] Benade A. H. *Fundamentals of musical acoustics*. 2nd edition, Dover, 1990.

[26] Markushevich A. I. and Silverman R. A., *Theory of functions of a complex variable*. Am. Math. Soc. (ed), 2005.

[27] Le Roux J.-C., Pachebat M. and Dalmont J.-P., *A new impedance sensor for industrial applications*. Acoustics, Nantes, 2012.

[28] Välimäki V., Pakarinen J., Erkut C. and Karjalainen M., *Discrete-time modelling of musical instruments*. Rep. Prog. Phys. 69(1), 1-78, 2006.

[29] J.O. Smith, *Introduction to Digital Filters with Audio Applications*, W3K Publishing, 2007.

[30] Terroir J. and Guillemain Ph., *A simple dynamic tonehole model for real-time synthesis of clarinet-like instruments*. Proc. ICMC, Barcelona, Spain, 2005.

[31] Chen J.-M., Smith J. and Wolfe J., *Pitch bending and glissandi on the clarinet: Roles of the vocal tract and partial tone hole closure*. J. Acoust. Soc. Am. 126, 1511-1520, 2009.

[32] Taillard P.-A. and Sanchez P., *Comparison of two clarinets separated by 200 years of evolution* (original title: *Comparaison de deux clarinettes séparées par deux cent ans dévolution : tentative dhybridation amusante et instructive entre facture instrumentale, modèles physiques et synthèse sonore*). 13ème Congrès Français d'Acoustique, Le Mans, 2016.

[33] Perichon L., Carriere O., Hermant J.-P. and Guillemain Ph., *Control parameters inversion using genetic algorithms applied to numerical impedance synthesis for woodwinds*. J. Acoust. Soc. Am. 120(5), 3333, 2006.
[34] D'Haes W. and Rodet X., *A new estimation technique for determining the control parameters of a physical model of a trumpet*. 6th Int. Conf. Digital Audio Effects, London, 2003.
[35] d'Andréa-Novel Br., Coron J.-M. and Hélie Th., *Asymptotic State Observers for a Simplified Brass Instrument Model*. Acta Acust. united Ac. 96(4), 733-742, 2010.
[36] Barthet M., Kronland-Martinet R., Ystad S. and Depalle Ph., *The effect of timbre in clarinet interpretation*. Int. Comp. Music Conf. Copenhagen, 2007.
[37] Coyle W., Guillemain Ph., Kergomard J. and Dalmont J.-D., *Predicting playing frequencies for clarinets: a comparison between numerical simulations and simplified analytical formulas*. J. Acoust. Soc. Am. 138, 2770-2781, 2015.
[38] Kergomard J., Guillemain Ph., Silva F. and Karkar S., *Idealized digital models for conical reed instruments, with focus on the internal pressure waveform*. J. Acoust. Soc. Am. 139(2), 927-937, 2016.
[39] Hélie Th. and Rodet X., *Radiation of a pulsating portion of a sphere: application to horn radiation*. Acta Acust. united Ac. 89(4), 565-577, 2003.
[40] Levine H. and Schwinger J., *On the radiation of sound from an unflanged circular pipe*. Phys. Rev. 73(4), 383-406, 1948.
[41] Norris A. N. and Sheng I. C., *Acoustic radiation from a circular pipe with an infinite flange*. J. Sound Vib. 135(1), 85-93, 1989.
[42] Dalmont J.-P., Nederveen C. J. and Joly N., *Radiation impedance of tubes with different flanges: numerical and experimental investigations*. J. Sound Vib. 244(3), 505-534, 2001.
[43] Lefebvre A., Scavone G. and Kergomard J., *External tonehole interactions in woodwind instruments*. Acta Acust. united Ac. 99(6), 975-985, 2013.
[44] Benade A. H., *From instrument to ear in a room: direct or via recording*. J. Audio. Eng. Soc. 33, 218-233, 1985.
[45] Plomp R. and Steeneken H. J. M., *Effect of phase on the timbre of complex tones*. J. Acoust. Soc. Am. 46(2B), 409-421, 2005.

Chapter 7

Simulation of Wind Instruments with Waveguides in Real Time

Résumé

Ce Chapitre décrit les méthodes nécessaires à la simulation temps réel du comportement physique de de la colonne d'air des instruments à vent au moyen de guide d'ondes. Le modèle est développé essentiellement sur une estimation modale des matrices de scattering de chaque segment composant le guide d'onde. On montre comment les techniques décrites au Chapitre 6 peuvent être appliquées à ces matrices, pour obtenir des filtres précis dans la bande passante et passifs à toutes fréquences. Au besoin, les filtres numériques peuvent être facilement convertis en filtres d'impédance et d'admittance. Un dictionnaire composé d'une douzaine de jonctions de différents types permet d'incorporer des excitateurs, de concaténer des tronçons et d'inclure des dérivations latérales (cheminées). Pour chacune de ces jonctions, le problème des boucles sans retard a été résolu analytiquement. L'estimation modale est également utilisée pour simuler le comportement des réflectances des orifices (pavillon ou trous latéraux), soit de manière linéaire, soit de manière non linéaire (faisant intervenir la loi de Bernoulli). Le modèle non linéaire proposé se différencie par le fait qu'il tend vers le modèle linéaire en petites oscillations, contrairement aux modèles usuels, qui tendent vers une réflection sans pertes. Des modèles de piston et coulisse sont implémentés. Le problème des délais fractionnaires a été solutionné en les incorporant directement lors de l'estimation modale.

Une architecture logicielle écrite dans un langage orienté objet (C++) permet de construire tous type d'instrument à vent de la famille des cuivres ou des instruments à anche faible, de manière très intuitive (en assemblant des pièces, à la manière d'un jeu de construction), sans grandes connaissances acoustiques préalables, grâce à une formulation reposant entièrement sur le domaine temporel discret. Le logiciel prend en charge certains aspects pouvant être délicats à contrôler, comme les transitions entre doigtés ou les adaptations d'embouchure en fonction de la note souhaitée. Quelques exemples d'utilisation sont donnés, incluant la simulation temps-réel d'une clarinette en sib Buffet Crampon avec 28 tronçons et 22 cheminées latérales avec pertes non linéaires au niveau de chaque trou.

7.1 Introduction

Since Helmholtz [176], the sound production in wind instruments is explained as the mutual coupling of a resonator (bore of the instrument) and an exciter (mouthpiece, reed and lips). Schumacher [129, 130] and McIntyre [98] proposed the first calculations of the self-sustained oscillation of a clarinet using time domain discretization of the equations. They showed the superiority of the reflection function over the impulse response (respectively the reciprocals of the input reflectance and the input impedance in the time domain) for the simulation of such instruments, because they have a much shorter support. This approach was adopted for instance

by Gazengel [59, 62] and Vergez [175, 2] for time domain simulations based upon measurements of the input impedance. The computation of convolutions are however an obstacle for the efficiency of real time simulations. The digital waveguide method was initiated in this field of research by Smith [140, 141], followed by Välimäki [167, 168], Scavone [123, 128, 127, 126, 131, 124], Berners [11], Ducasse [44], van Walstijn [170, 7, 171], Hélie [77], Mignot [99], Silva [133, 132, 23, 138, 134, 50, 137, 121, 49, 155, 136], Debut [40], Chatziioannou [17, 18, 20, 22, 19] and Hézard [80] for instance. This approach considers generally the incoming and outgoing waves (traveling waves) at the junctions of the segments composing the pipe, although a formulation based on the physical state variables p (pressure) and u (flow rate) is also possible. Guillemain [67, 69] and Meastre [95, 97, 96], for instance, proposed the use of digital impedance models for real time simulations.

In my point of view, the main benefit of the waveguide implementation (over the input oriented implementation proposed in Chapter 6) is that non linear interactions can be easily simulated at any location in the instrument. This point is crucial for a realistic simulation of a clarinet, with nonlinear losses at each tonehole, as we will see. Of course this advantage is related to a drawback: the computing cost can be critical for real time applications, especially when the number of segments is important. We will see however that a simulation of a full clarinet in real time is possible (on a standard PC) without using special programming techniques.

The present work completes the contribution of the author to the CAGIMA project, initiated in 2013 by two and a half years of collaboration with IRCAM in Paris. One of the main goals of this project is to develop methods for the virtual prototyping of wind instruments, so that instrument makers and musicians can virtually play the instrument and optimize some of its characteristics (like intonation or ease of emission), before a real prototype is build by the instrument maker. This chapter proposes a general framework and practical solutions for the virtual prototyping and waveguide simulation of wind instruments in real time from a given geometry.

The contribution of the present study to the state of art can be summarized as follow:

— Develop a general framework for the simulation of wind instruments with digital filters based on travelling waves

— Show that these filters are well suited for this task, as they can simulate indifferently impedance or admittance relationships

— Demonstrate that an efficient and precise implementation of such filters is quite straightforward. The coefficients can be determined with the proposed application of the LSCE (Least Square Complex Exponential) method, combining 2 main goals: precision in the low frequency range and passivity at all frequencies. The issues related to the passivity are easier to solve than with the formulation based on an impedance relationship. Moreover the behaviour of the filter in the stop band can be designed to mimic the general shape of the computed curves.

— Eliminate the need of fractional delays (except for slides and other length varying segments).

— Solve the problem of delay-free loops.

— Establish a dictionary of junctions, solving the coupling problem at the junctions.

— Implement a software (written in Mathematica) for the computation of the filter coefficients (simulating the transfer functions of each segment), according to the geometry.

— Implement a software (written with the object oriented programming language C++) for the real-time simulation of waveguides.

This chapter is organised as follows: the terminology and a mono-dimensional acoustical model is recalled in Sec 7.2 and 7.3. In Sec. 7.4, a general method is proposed for the design of passive digital filters implementing the reflectance and transmittance functions of the scattering matrices, followed in Sec. 7.5 by a dictionary of junctions and a software impementation (reported in Appendix A and B). The conclusions end this chapter in Sec. 7.6.

7.2 Terminology and background

This paragraph reviews the terminology, the background and defines some basic elements in relation with the implementation of waveguides for the simulation of wind instruments.

7.2.1 Bore

The bore of an axisymmetric pipe is defined as a function of the radius of the pipe $r(x)$ at the curvilinear coordinate x along the wall of the pipe (this is required by the acoustical model: see §7.3.1). Optionally, one may define the radius of the pipe with the axial coordinate ξ, denoted $\underline{r}(\xi)$. Both quantities are related by the equation:

$$x(\xi) = \int_0^\xi \sqrt{1 + \underline{r}'(z)^2}\mathrm{d}z \tag{7.1}$$

and $\underline{r}(\xi) = r(x(\xi))$. By convention, the bore of a pipe of length L begins at $x = 0$ and ends at $x = L$. L is measured in curvilinear coordinates.

7.2.2 Segmentation of a pipe

We refer to a segment of pipe with two indices designating the coordinates of the extremities of a segment (sections), for instance g and d (like *gauche* and *droite*) for a segment of pipe beginning upstream at $x = x_g$ and ending downstream at $x = x_d$. Each segment can itself be composed as a concatenation of subsegments. For instance, the first segment of a clarinet begins at the mouthpiece and ends at the first side tonehole. This segment may be composed of the subsegments: mouthpiece chamber, mouthpiece bore, barrel, upper joint. Generally, the subsegments have a constant curvature and are connected together with a $\mathcal{C}^1$ regularity, (i.e. $r(x)$ and $r'(x)$ are continuous functions). The segmentation seeks to minimize the number of segments. The junctions between segments are positioned in function of time varying commands (like opening and closing toneholes) or of nonlinear interactions. In principle, linear time invariant segments are merged together by concatenation.

The minimal length $\ell = x_d - x_g$ of a segment is imposed by the sampling frequency F_s of the simulation: $\ell \geq c/F_s$. Typically, for $F_s = 44100$ Hz, $\ell \geq 7.79$ mm. This way, the segments can be decoupled, since the propagation time of the waves through the segment is at least one discrete time step.

7.2.3 Physical state variables

In a mono-dimensional model, the physical state variables $p(x,t)$ (pressure) and $u(x,t)$ (flow rate also called volume velocity) are related to their mean value across the section of the pipe $S(x) = \pi r(x)^2$.

7.2.4 Travelling waves

Travelling wave variables ($p^{+/-}$ or $\phi^{+/-}$) may substitute the physical variables $p(x,t)$ and $u(x,t)$. The key idea behind this variable substitution is that the pipe may be approximated as a concatenation of cylindrical segments of infinitesimal length. Therefore, the mean pressure and flow rate across the section $S(x)$ may be approximated locally with plane waves. The substitution can be expressed in 2 different ways:

$$\begin{pmatrix} p^+(x,t) \\ p^-(x,t) \end{pmatrix} = \frac{1}{2}\begin{pmatrix} 1 & z_c \\ 1 & -z_c \end{pmatrix} \cdot \begin{pmatrix} p(x,t) \\ u(x,t) \end{pmatrix} \tag{7.2}$$

or

$$\begin{pmatrix} \phi^+(x,t) \\ \phi^-(x,t) \end{pmatrix} = \frac{r(x)}{2}\begin{pmatrix} 1 & Z_c(x) \\ 1 & -Z_c(x) \end{pmatrix} \cdot \begin{pmatrix} p(x,t) \\ u(x,t) \end{pmatrix} \tag{7.3}$$

where $Z_c(x) = \frac{\rho c}{S(x)}$ is the characteristic impedance, ρ the density of air and c the speed of sound.

The first substitution projects the acoustical variables onto plane waves in an hypothetical reference cylinder of arbitrary characteristic impedance z_c. The second substitution projects the acoustical variables onto plane waves in a cylinder of cross section $S(x)$. The projection is valid on an infinitesimal length (see Ducasse [44]).

7.2.5 Laplace domain

Many analytical solutions of the governing equations of acoustical systems are known only in the frequency domain. The Laplace transform is often used in this context. The Laplace transform of a function $f(t)$, using the Laplace variable s is defined as follows:

$$\mathcal{L}\{f\}(s) = \int_0^\infty f(t)e^{-st}\mathrm{d}t \tag{7.4}$$

For instance, the Laplace transform of a delayed Dirac impulse $\delta(t-\tau)$ is:

$$\mathcal{L}\{\delta(t-\tau)\}(s) = e^{-\tau s} \tag{7.5}$$

Frequently, the solution cannot be converted analytically back to the time domain (with the inverse Laplace transform). In this case, the solution is approximated for instance with a modal estimation, which can be converted back to the time domain. A digital filter can also be designed to perform this conversion in the discrete time domain.

The Fourier transform is equivalent to the bilateral Laplace transform with imaginary argument $s = j\omega$, with $j = \sqrt{-1}$. The imaginary axis of the Laplace transform correspond therefore to the frequency axis of the Fourier transform.

7.2.6 Impedance

The impedance $Z(x,s)$ defines the relationship between the pressure and the flow rate in the frequency domain [85, 64, 31]:

$$Z(x,s) = \frac{P(x,s)}{U(x,s)} \tag{7.6}$$

$Z(x=0,s)$ and $Z(x=L,s)$ are called respectively the input impedance and the output impedance of a pipe of length L. For an open pipe, the output impedance is called the radiation impedance. The impedance $Z(x,s)$ is often adimensioned by division by the characteristic impedance $Z_c(x)$

7.2.7 Reflectance

The reflectance $R(x,s)$ defines the relationship between the incoming and outgoing travelling waves in the frequency domain:

$$R(x,s) = \frac{p^-(x,s)}{p^+(x,s)} = \frac{\phi^-(x,s)}{\phi^+(x,s)} \tag{7.7}$$

$R(x=0,s)$ and $R(x=L,s)$ are called respectively the input reflectance (or reflection coefficient) and the output reflectance of a pipe of length L. For an open pipe, the output reflectance is called the radiation reflectance.

The reflectance is related to the impedance by:

$$R(x,s) = \frac{Z(x,s) - Z_c(x)}{Z(x,s) + Z_c(x)} \quad \Leftrightarrow \quad \frac{Z(x,s)}{Z_c(x)} = \frac{1+R(x,s)}{1-R(x,s)}. \tag{7.8}$$

The inverse Laplace transforms of the input impedance and of the input reflectance are called the impulse response and the reflection function, respectively.

Reflectance of a cylindrical orifice I propose a new approximation of the output reflectance of a cylindrical orifice (more accurate than that proposed in [132, 135]), based on the exact computations by Levin and Schwinger [94] (unflanged case) and by Zorumski [180] (flanged case):

$$R(s) = \sum_{n=1}^{4} \frac{c_n}{(s+s_n)^{n+1}} \tag{7.9}$$

with

	c_1	c_2	c_3	c_4
Unflanged	-8.04398	8.47733	82.8937	28388
Flanged	-7.31824	9.06885	101.345	35481

	s_1	s_2	s_3	s_4
Unflanged	1.34120	1.56315	3.26795	8.84056
Flanged	1.18055	1.46214	3.27813	9.44612

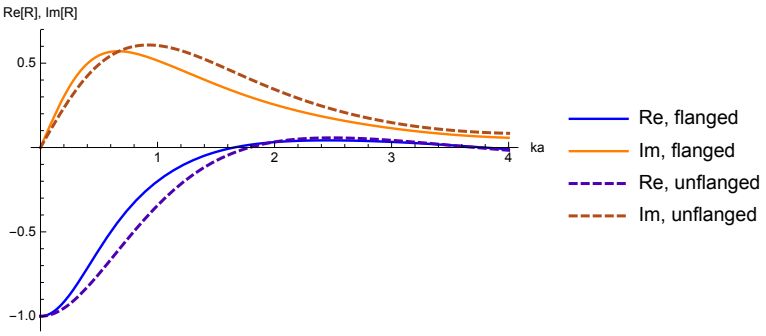

Figure 7.1 – Real and imaginary parts of the reflectance of a cylindrical orifice, approximated with Eq. 7.9, for the flanged (continuous lines) and unflanged (dashed lines) cases. In abscissa, the reduced frequency ka=$\omega a/c$, where a is the radius of the orifice.

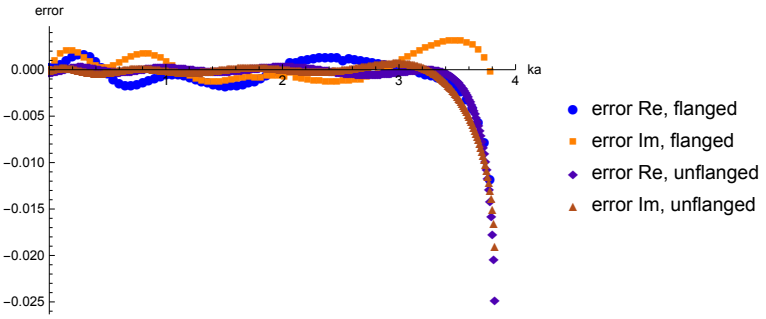

Figure 7.2 – Real and imaginary parts of the error between the exact reflectance of a cylindrical orifice and the approximation with Eq. 7.9, for the flanged and unflanged cases. The cutoff frequency of the exact model (planar mode) is located at ka=3.832 (1st zero of the Bessel function J_1).

These approximations are depicted on Fig. 7.1.

The reflection function $\tilde{r}(t)$ (inverse Laplace transform of Eq 7.9) is:

$$\tilde{r}(t) = \sum_{n=1}^{4} \frac{c_n\, t^n e^{-s_n\, t}}{n!} \tag{7.10}$$

These formulas apply for the reduced frequency: $s \to aj\omega/c$, where a is the radius of the

opening and c is the speed of sound. They approximate the exact results with a precision better than 0.5% (except near to the cutoff frequency: $\omega > 3.5$, see Fig. 7.2).

A modal estimation based on other geometries can be performed, according to [48].

Polynomial low frequency estimation The following formula proposes a low frequency ($0 < \mathrm{ka} < 0.5$) polynomial approximation of the reflectance of cylindrical orifices from the exact computations (planar mode).

$$R(\mathrm{ka}) = -1 + \left(\sum_{n=1}^{4} b_n \, (-1)^{n+1} \, j^n \, \mathrm{ka}^n \right) + O(\mathrm{ka}^5) \tag{7.11}$$

with $\mathrm{ka}{=}a\,\omega/c$.

	b_1	b_2	b_3	b_4
Unflanged	1.25587	1.29000	1.24326	1.28836
Flanged	1.51025	2.13417	1.51404	2.13449

7.2.8 Causality

The causality principle states that an effect cannot precede a cause. The travelling waves preserves the principle of causality: the incident wave is scattered into two components: a reflected component and a transmitted component. These components cannot precede the incident wave.

Computations can be performed in the Laplace domain without respecting the principle of causality. However, the final solution can be approximated in the time domain with a stable digital filter only if the causality principle is respected.

7.2.9 Representative matrices

In the context of wavegides, the generic term "representative matrix" refers to a matrix linking the state variables in two different locations of an acoustical system (c.f. quadripole). These two locations are typically the extremities (sections) of a segment of pipe. Depending on the kind of the state variables involved, the matrix is called admittance matrix, transfer matrix or scattering matrix, for instance. In this chapter, these 3 kinds of representative matrices are used. Let us define them and describe how they are related.

Admittance matrix

The admittance matrix $\boldsymbol{A}^{(g,d)}$ for the segment of pipe x_g to x_d links the pressure and the flow rate at both extremities of the segment:

$$\begin{pmatrix} u_g \\ u_d \end{pmatrix} = \boldsymbol{A}^{(g,d)} \cdot \begin{pmatrix} p_g \\ p_d \end{pmatrix} \tag{7.12}$$

where $p_i = p(x_i, s)$, $u_i = u(x_i, s)$ and $A_{1,2}^{(g,d)} = -A_{2,1}^{(g,d)}$.

Transfer matrix for travelling waves

Using Eqs. 7.3 and 7.12, the transfer matrix for travelling waves $\boldsymbol{C}^{(g,d)}$ reads:

$$\begin{pmatrix} \phi_d^+ \\ \phi_d^- \end{pmatrix} = \boldsymbol{C}^{(g,d)} \cdot \begin{pmatrix} \phi_g^+ \\ \phi_g^- \end{pmatrix} \tag{7.13}$$

where

$$\boldsymbol{C}^{(g,d)} = \frac{1}{a_4} \begin{pmatrix} a_1 + a_2 - a_3 + 1 & a_1 - a_2 - a_3 - 1 \\ a_1 - a_2 + a_3 + 1 & a_1 + a_2 + a_3 - 1 \end{pmatrix}$$

$Z_g = Z_c(x_g)$, $Z_d = Z_c(x_d)$, $a_1 = -Z_g A_{1,1}$, $a_2 = Z_d A_{2,2}$, $a_3 = Z_g Z_d \left(A_{1,2}^2 + A_{1,1}A_{2,2}\right)$ and $a_4 = 2\sqrt{Z_g Z_d} A_{1,2}$. Notice that $C_{1,1} = \frac{1+C_{1,2}C_{2,1}}{C_{2,2}}$.

For sake of conciseness, the indices g and d are not explicitly written when referring to the elements of a matrix (here the admittance matrix $\boldsymbol{A}^{(g,d)}$), provided that the other matrix bear the same indices (here $\boldsymbol{C}^{(g,d)}$).

In a segment of pipe of arbitrary profile, $\boldsymbol{C}^{(g,d)}$ can itself be expressed as the concatenation of subsegments, computing the product of the transfer matrices of each subsegment in reverse order:

$$\boldsymbol{C}^{(g,d)} = \boldsymbol{C}^{(d-1,d)} \cdot \boldsymbol{C}^{(d-2,d-1)} \cdot \ldots \cdot \boldsymbol{C}^{(g+1,g+2)} \cdot \boldsymbol{C}^{(g,g+1)} \tag{7.14}$$

Notice that the transfer functions of this matrix are not causal: they cannot be transposed in the time domain with stable filters.

Scattering matrix for travelling waves

Finally, the scattering matrix for travelling waves $\boldsymbol{\Phi}^{(g,d)}$ is obtained from $\boldsymbol{C}^{(g,d)}$:

$$\begin{pmatrix} \phi_g^- \\ \phi_d^+ \end{pmatrix} = \boldsymbol{\Phi}^{(g,d)} \cdot \begin{pmatrix} \phi_g^+ \\ \phi_d^- \end{pmatrix} \tag{7.15}$$

$$\boldsymbol{\Phi}^{(g,d)} = \begin{pmatrix} -\frac{C_{2,1}}{C_{2,2}} & \frac{1}{C_{2,2}} \\ \frac{1}{C_{2,2}} & \frac{C_{1,2}}{C_{2,2}} \end{pmatrix} = \begin{pmatrix} R_g & T \\ T & R_d \end{pmatrix}$$

The scattering matrix respects the principle of causality and is composed of two propagators $T = T_{g,d} = T_{d,g}$ and two reflectors R_g and R_d.

Notice that:

$$\boldsymbol{C}^{(g,d)} = \begin{pmatrix} T - \frac{R_g R_d}{T} & \frac{R_d}{T} \\ -\frac{R_g}{T} & \frac{1}{T} \end{pmatrix}$$

$$\boldsymbol{A}^{(g,d)} = \begin{pmatrix} \frac{\pi r_g^2 \left(T^2 + R_d - R_g(R_d+1)+1\right)}{c\rho(-T^2+R_d+R_g(R_d+1)+1)} & -\frac{2\pi T r_g r_d}{c\rho(-T^2+R_d+R_g(R_d+1)+1)} \\ \frac{2\pi T r_g r_d}{c\rho(-T^2+R_d+R_g(R_d+1)+1)} & \frac{\pi r_d^2 \left((R_g+1)(R_d-1)-T^2\right)}{c\rho(-T^2+R_d+R_g(R_d+1)+1)} \end{pmatrix}$$

with $r_i = r(x_i)$.

7.2.10 Digital IIR filters

A generic transfer function $H(z)$ may be approximated by modal estimation (see Chapter 6). This approximation relies on the LSCE (Least Squares Complex Exponential) method, as a least squares fit in the low frequency range, up to some cut frequency F_{cut}. The filter is required to be passive at all frequencies (notably above the cutoff frequency, in the stop band of the filter, up to half the sampling frequency F_s). In the z-domain (counterpart of the Laplace domain, for discrete time), this approximation takes the form:

$$H(z) = \sum_m \frac{C_m}{1 - x_m z^{-1}}. \tag{7.16}$$

with [1] $x_m = e^{s_m T_s}$. $T_s = 1/F_s$ is the sampling period and s_m are the poles of the transfer function in the Laplace domain $H(s)$. Because the corresponding impulse response $h(t)$ is real, the coefficients s_m must be either real (monopole) or complex conjugates (bipole) in order to respect the Hermitian symmetry. Since a monopole and a discrete Dirac are degenerate bipoles, $H(z)$, they may be simulated with a generic 2nd order IIR digital filter:

$$H(z) = \sum_{\substack{m \\ \mathrm{Im}(s_m) \geq 0}} H_m(z) \text{ with } H_m(z) = \frac{a_{m,0} + a_{m,1} z^{-1}}{1 + b_{m,1} z^{-1} + b_{m,2} z^{-2}} \tag{7.17}$$

where the values of the coefficients $a_{m,0}$, $a_{m,1}$, $b_{m,1}$ and $b_{m,2}$ are computed from the poles s_m and the modal coefficients C_m according to Table 7.1.

1. We preserve the original notations of Chapter 6. x_m is in this paragraph a pole in the z-domain.

Type	Root	$a_{m,0}$	$a_{m,1}$	$b_{m,1}$	$b_{m,2}$
Dirac	$x_0 = 0$	C_0	0	0	0
Monopole	$x_m > 0$	C_m	0	$-x_m$	0
Bipole	(x_m, x_m^*)	$2\,\mathrm{Re}(C_m)$	$-2\,\mathrm{Re}(C_m x_m^*)$	$-2\,\mathrm{Re}(x_m)$	$\lvert x_m\rvert^2$

Table 7.1 – Coefficients of the digital filters with respect to x_m and C_m.

In order to fix the ideas, let us assume that $H(z)$ represents the input impedance of an hypothetical pipe. The filter $H(z)$ enables the evaluation of the current pressure $p[n]$ at the input of the waveguide when it is excited by the flow rate $u[n]$. The pressure is the sum of the partial pressures $p_m[n]$, each one accounting for a real pole s_m or a pair of complex conjugate poles (s_m, s_m^*) and obeys the difference equation:

$$p_m[n] = a_{m,0}u[n] + a_{m,1}u[n-1] - b_{m,1}p_m[n-1] - b_{m,2}p_m[n-2]. \tag{7.18}$$

It is possible to arrange the relations so that the (total) pressure at the input of the bore at the current time depends on the current flow rate value and on some history:

$$p[n] = \sum_m p_m[n] = V_1 u[n] + V_2$$
$$\text{with } \begin{cases} V_1 = \sum_m a_{m,0}, \\ V_2 = \sum_m a_{m,1}u[n-1] - b_{m,1}p_m[n-1] - b_{m,2}p_m[n-2]. \end{cases} \tag{7.19}$$

This way the filter is easier to couple with other elements like an exciter or with another filter.

Application to travelling waves

The application of digital filters to travelling waves is straightforward: the transfer function $H(z)$ corresponds now to the input reflectance $R(z)$ (in order to fix the ideas). We need only to operate the substitution $p \to p^-$ and $u \to p^+$. Let us substitute additionally $V_i \to v_i$. Eq 7.19 reads then:

$$p^-[n] = v_1 p^+[n] + v_2 \tag{7.20}$$

Besides the "natural" excitation with an incoming wave p^+, the filter can easily be converted as an impedance filter. According to Eq 7.2:

$$p[n] = \frac{z_c(1+v_1)}{1-v_1}u[n] + \frac{2v_2}{1-v_1} = \hat{V}_1 u[n] + \hat{V}_2 \tag{7.21}$$

or as an admittance filter:

$$u[n] = \frac{1-v_1}{z_c(1+v_1)}p[n] - \frac{2v_2}{z_c(1+v_1)} = \check{V}_1 p[n] + \check{V}_2 \tag{7.22}$$

Notice that the structure of Eq. 7.19 is recovered and that only one additional multiplication is required, in order to compute $\hat{V}_2$, compared to the impedance filter case (because $\hat{V}_1$ is a constant). The solution of the coupling problem with a clarinet mouthpiece (Eq. A.7 in Chapter 6) can therefore be directly applied. The excitation of the filter is obtained by:

$$p^+[n] = \frac{z_c u[n] + v_2}{1-v_1} = \frac{p[n] - v_2}{1+v_1} \tag{7.23}$$

Similarly, the filter:

$$\phi^-[n] = \nu_1 \phi^+[n] + \nu_2 \tag{7.24}$$

is converted as an impedance filter according to Eq 7.3:

$$p[n] = \frac{(\nu_1 + 1)\, Z_c}{1 - \nu_1} u[n] + \frac{2\nu_2}{(1 - \nu_1)\, r} = \acute{V}_1 u[n] + \acute{V}_2 \tag{7.25}$$

or as an admittance filter:

$$u[n] = \frac{1 - \nu_1}{(\nu_1 + 1)\, Z_c} p[n] - \frac{2\nu_2}{(\nu_1 + 1)\, r Z_c} = \grave{V}_1 p[n] + \grave{V}_2 \tag{7.26}$$

The excitation of the filter is obtained by:

$$\phi^+[n] = \frac{r\, Z_c\, u[n] + \nu_2}{1 - \nu_1} = \frac{r\, p[n] - \nu_2}{\nu_1 + 1} \tag{7.27}$$

7.2.11 Differentiators and Integrators

Differentiators obey to the difference equation:

$$\text{output}[n] = k\, F_s(\text{input}[n] - \text{input}[n-1]) \tag{7.28}$$

The output of the filter is an approximation of k times the derivative of the input (F_s is the sampling frequency and k is the gain of the filter).

Similarly, integrators obey to the difference equation:

$$\text{output}[n] = \text{output}[n-1] + k/(2\, F_s)(\text{input}[n] + \text{input}[n-1]) \tag{7.29}$$

The output of the filter is an approximation of k times the integral of the input.

For sake of simplicity, differentiators and integrators are treated as reflectors, because of the delay-free response and because they can be written with the IIR filter structure (as degenerated bipoles).

7.3 Mono-dimensional acoustical model

Let us summarise briefly the linear, mono-dimensional acoustical model for axisymmetric ducts. Detailed explanations can be found in Mignot [99], chapters 1 and 2.

7.3.1 The Webster-Lokshin and Euler equations

The Webster-Lokshin equation [78, 100] describes the behavior of the acoustic pressure waves $p(x,t)$ in an 1D axisymmetric duct

$$\left(\partial_x^2 + \frac{2r'(x)}{r(x)}\partial_x\right) p(t,x) = \left(\frac{1}{c^2}\partial_t^2 + \frac{2}{c^{\frac{3}{2}}}\epsilon(x)\partial_t^{3/2}\right) p(t,x) \tag{7.30}$$

This model considers a linear propagation of the acoustical waves with viscothermal losses near the walls. The flow rate $u(x,t)$, dual quantity to the pressure, is described by the Euler equation

$$-\frac{\rho}{S(x)}\partial_t u(t,x) = \partial_x p(t,x) \tag{7.31}$$

with parameters $\epsilon(x) = \kappa_0\sqrt{1 - r'(x)^2}/r(x)$, coefficient of viscothermal losses, and $\kappa_0 \simeq 3.5 \times 10^{-4}$ m$^{1/2}$.

7.3.2 Analytical expression of the admittance matrix

For a segment where the loss parameter $\epsilon(x)$ can be approximated by a constant and with constant curvature $\Upsilon = \frac{r''(x)}{r(x)}$, the admittance matrix can be expressed analytically (formula from [100], with simplification and rectification of the typographical errors):

$$\boldsymbol{A}^{(g,d)} = \begin{pmatrix} \frac{\pi r_g^2(\zeta_g + \coth(L\Gamma(s))\Gamma(s))}{s\rho} & -\frac{\pi r_g r_d \operatorname{csch}(L\Gamma(s))\Gamma(s)}{s\rho} \\ \frac{\pi r_g r_d \operatorname{csch}(L\Gamma(s))\Gamma(s)}{s\rho} & \frac{\pi r_d^2(\zeta_d - \coth(L\Gamma(s))\Gamma(s))}{s\rho} \end{pmatrix} \tag{7.32}$$

with $L = x_d - x_g$, $\zeta_i = r'(x_i)/r(x_i)$ and $\Gamma(s) = \sqrt{\left(\frac{s}{c}\right)^2 + 2\epsilon\left(\frac{s}{c}\right)^{\frac{3}{2}} + \Upsilon}$.

7.3.3 Analytical expression of the scattering matrix

For a segment with approximatively constant $\epsilon(x)$ and constant curvature Υ, the propagator T and the reflectors R_g and R_d of the scattering matrix $\boldsymbol{\Phi}^{(g,d)}$ are approximated with following expressions:

$$\begin{aligned} T &= \frac{2\,c\,s\,\Gamma(s)\,\operatorname{csch}(L\,\Gamma(s))}{d_1} \\ R_g &= \frac{(s - c\,\zeta_g)\,(s - c\,\zeta_d) - d_2}{d_1} \\ R_d &= \frac{(s + c\,\zeta_g)\,(s + c\,\zeta_d) - d_2}{d_1} \\ d_1 &= (s + c\,\zeta_g)\,(s - c\,\zeta_d) + 2c\,s\,\Gamma(s)\,\coth(L\,\Gamma(s)) + d_2 \\ d_2 &= c^2\,\Gamma(s)\,((\zeta_g - \zeta_d)\,\coth(L\,\Gamma(s)) + \Gamma(s)) \end{aligned} \tag{7.33}$$

In the case of a cylinder, the analytic solution simplifies to:

$$\begin{aligned} T &= \breve{D}(s)\,\exp(-L\,s/c) \\ R_g &= R_d = 0 \\ \breve{D}(s) &= \exp(-\breve{\epsilon}\,\sqrt{s}), \quad \breve{\epsilon} = \epsilon(x)\,L/\sqrt{c} \end{aligned} \tag{7.34}$$

Observe that this is not merely a simplification of Eq. 7.33. The inverse Laplace transform of $\breve{D}(s)$ is:

$$\breve{d}(t) = \mathcal{L}^{-1}\{\breve{D}\}(t) = \frac{\breve{\epsilon}}{2\sqrt{\pi\,t^3}}\exp\left(-\frac{\breve{\epsilon}^2}{4\,t}\right), \quad t > 0. \tag{7.35}$$

The delay $\exp(-L\,s/c)$ is implemented with a delay line (c.f. Eq. 7.5). See however §7.4.1 if the delay is not commensurable to the sampling period.

7.4 Modal estimation

This section presents an estimation algorithm optimized for travelling waves. The method of modal estimation is detailed in Chapter 6.

A modal estimation can be performed on all causal transfer functions related to travelling waves (i.e. propagators, reflectors and reflectances) with a single algorithm. The issues associated to the passivity of the filters are less severe than in the case of impedance relationships. The analytical expression of these functions in the spectral domain can be found in the literature, for instance [99, 100, 135, 79].

7.4.1 Elimination of fractional delays

The propagation delay should be eliminated from the propagators (and also from the reflectors and reflectances, when the pipe begins with a cylindrical portion), by multiplication with $\exp(\tau s)$.

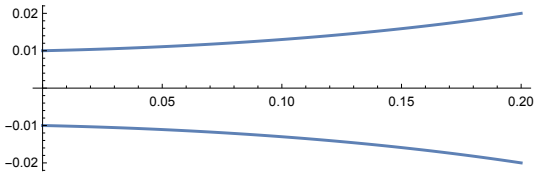

Figure 7.3 – Simulated flared duct with constant curvature ($r_g = 10$ mm, $r_d = 20$ mm, $L = 200$ mm, $\Upsilon = 30$).

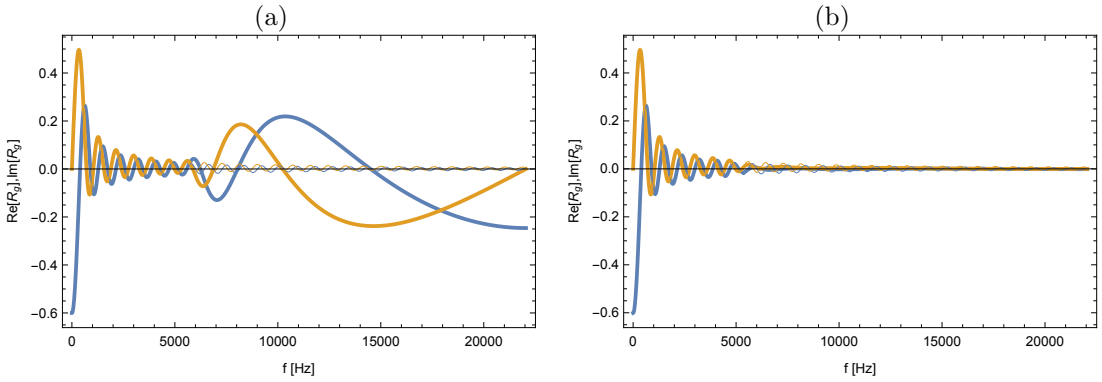

Figure 7.4 – Modal estimation (with 15 dipoles) of the reflector R_g of the scattering matrix $\mathbf{\Phi}^{(g,d)}$ of a flared duct illustrated on Fig. 7.3. Blue: Re(R_g), Orange: Im(R_g). Thick lines: modal estimation, thin lines: analytical function. The modal coefficients C_m are fitted by least squares in the following frequency bands: (a) 0 to F_{cut}, (b) 0 to $3\,F_{cut}$, $F_{cut} = 5000$ Hz.

If the delay is not commensurable to the sampling period T_s, τ should be chosen slightly smaller than this delay, typically $\tau = T_s \max\left(\left\lfloor \frac{L}{T_s c} \right\rfloor - 2, 1\right)$. The modal estimation of a generic transfer function $H(s)$ is then operated on $H'(s) = \exp(\tau s) H(s)$. This procedure automatically eliminates the need of fractional delays. A delay of at least 1 sampling period decouples the junctions. The Fig. 7.7 depicts the modal estimation of a propagator T with and without partial elimination of the propagation delay.

7.4.2 Estimation of the discrete time impulse response

In the LSCE method, the poles are estimated from the discrete time impulse response $h_n = h[nT_{\text{cut}}]$ (respectively $h'[nT_{\text{cut}}]$, if the propagation delay has been eliminated), with sampling period $T_{\text{cut}} = 1/(2F_{\text{cut}})$. The samples h_n are obtained by following algorithm:

1. Oversample $H(s)$ up $k_{os}F_{\text{cut}}$, with oversampling factor typically $k_{os} = 16$.
2. Compute the discrete time impulse response by inverse Discrete Fourier Transform
3. Downsample the discrete time impulse response down to F_{cut} with respect to its integral, in order to obtain the samples h_n

Discussion of the downsampling process A centered estimation of the integral is not optimal, despite of the fact that the error is minimal in the low frequency band (when taking the Discrete Fourier Transform of h_n), because the error increases exponentially up to F_{cut}. This characteristic is not optimal in order to guarantee the passivity of the filter at all frequencies, when fitting the modal coefficients C_m. A forward estimation works better, because the absolute value of the error exhibits a parabola shape: the error is small around $F = 0$ and small again around $F = F_{\text{cut}}$. This way a precise, passive filter is easily obtained. The following method works fine for estimating the integral: h_0 is taken as the sum of the k_{os} first samples of the oversampled discrete time impulse response, and so on. This procedure eliminates practically all ripples from

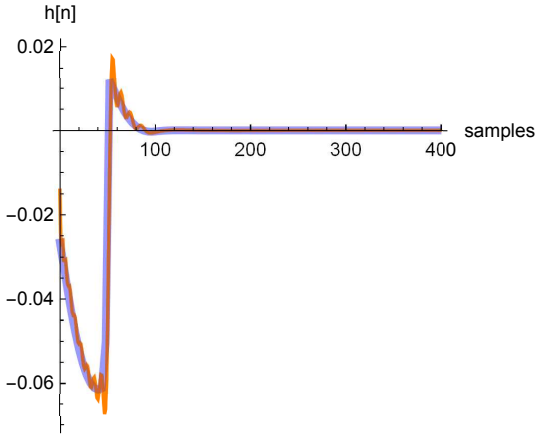

Figure 7.5 – Discrete impulse response of the reflector R_g of the flared duct depicted on Fig. 7.3. Blue: after oversampling / downsampling of the analytical function, as discussed in §7.4.2. Orange: discrete impulse response of the filter illustrated on Fig. 7.4 (b). The Gibbs phenomenon is a consequence of the frequency band limitation (see Appendix E). The amplitude of the ripples has to be controlled by the least squares fit in such a way that the simulated scattering matrix remains i) passive at every frequency and ii) accurate in the pass band.

the impulse response (see Fig. 7.5). Usually the LSCE method do not detect any poles x_m with real negative values (corresponding to components oscillating at the frequency F_{cut}. These poles (if any) should be eliminated before estimating the modal coefficients.

7.4.3 Estimation of the modal coefficients

An exemple of a modal estimation is given for the flared duct depicted on Fig. 7.3. The modal estimation of the reflector is illustrated on Fig. 7.4 (spectral domain) and Fig. 7.5 (discrete time domain). The corresponding poles are shown in Fig. 7.6, as well as the propagator in Fig. 7.7.

The modal coefficients are estimated in the z-domain as described in in Chapter 6 (Eq. 18). Usually, no fictitious points are required in order to guarantee the passivity of the filter at all frequencies. The requirements to the filter can be specified in a more flexible way than with impedance filters. With a sampling grid up to about 0.95 to 1.0 F_{cut}, the precision of the estimation is optimal in the pass band (but it must be verified that the filter is still passive). An uneven sampling grid may be specified in order to enhance the precision of the filter in some frequency band. The sampling grid may be extended into the stop band. This way the response in the stop band mimics the general shape of the transfer function (see Fig. 7.4). This behavior is however obtained at the cost of a reduced precision in the pass band.

Passivity

The passivity of each individual filter is not a sufficient condition to guarantee the passivity of the waveguide. It must be checked at the extremity of each segment that the energy of the scattered waves do not exceed that of the incident wave. In other words, it must be verified that input impedance (upstream) of the scattering matrix remains passive at any frequency, when a lossless impedance is connected to the output (downstream). If required, the modal coefficients of the filters are reduced proportionally [2].

2. Instead of this coarse and straightforward treatment, a more careful and refined procedure should be developed.

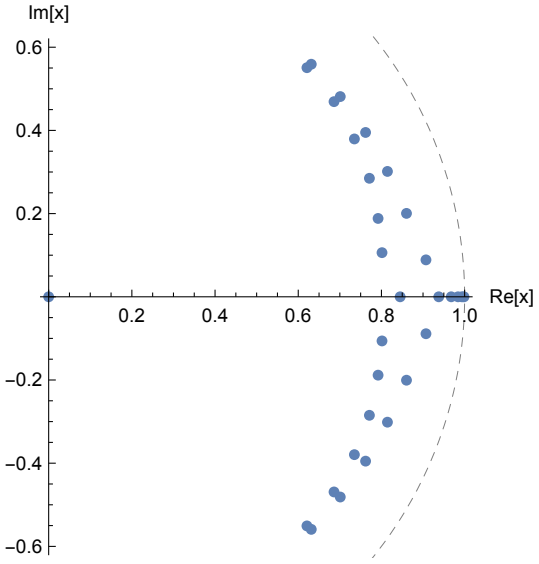

Figure 7.6 – Poles x_m (in the unit circle of the z plane) of the modal estimation of the reflector R_g of the flared duct depicted on Fig. 7.3.

7.4.4 Estimation *via* the poles of the analytical function

Alternatively, the poles may be determined directly from the analytical functions. This may be done for instance with the NSolve procedure of Mathematica, applied to a limited portion of the complex plane (because the number of poles is infinite). These poles have an imaginary part situated in the vicinity of the odd multiples of $2\pi c/(4L)$, except the first poles which depend strongly on the geometry. The poles of the transfer function $H(s)$ are found by the Mathematica request (limited here to a portion of the real negative and imaginary positive quadrant):

$$\text{NSolve}\left[\frac{1}{H(s)} = 0 \wedge -5F_{\text{cut}} \leq \text{Re}(s) \leq 0 \wedge 0 \leq \text{Im}(s) \leq 2\pi F_{\text{cut}}, s\right]$$

The modal coefficients are estimated as already described. However a direct estimation is not satisfactory. A precise estimation can be done only up to $f_{\text{cut}}/2$. Unfortunately this causes severe problems with the passivity in the stop band. An empirical recipe can however be formulated to overcome this issue:

1. Take the set of analytical poles up to F_{cut} (in the Laplace domain). Restore the hermitian symmetry, if necessary.
2. Add (to this set) a copy of these poles with a higher damping (i.e. multiply the real part of the poles by an arbitrary coefficient, typically between 2 and 5).
3. Add a few (1 to 3) real negative poles (for instance $\{-200, -2000, -20000\}$), in order to enhance the precision of the filter in the very low frequency band and also in order to mimic the behavior of the transfer function in the stop band.
4. Estimate the modal coefficient (according to §7.4.3) associated with this set of poles (after conversion of the poles into the z-domain). A fit is possible also for the full frequency band, up to $F_s/2$. The same set of poles is used for all transfer functions of the scattering matrix (because they share the same set of analytical poles; this remains true also after the (partial) elimination of the delay in the propagator).

Notice that this procedure generates poles which are approximatively those of the modal estimation (see Fig. 7.6). This procedure cannot be applied to a modal estimation of Eq.7.34, because it has no poles (but it has a branch cut). The poles of Eq.7.33 can be used instead, but an estimation via §7.4.2 is usually more economical, in terms of computational efficiency of the derived filter.

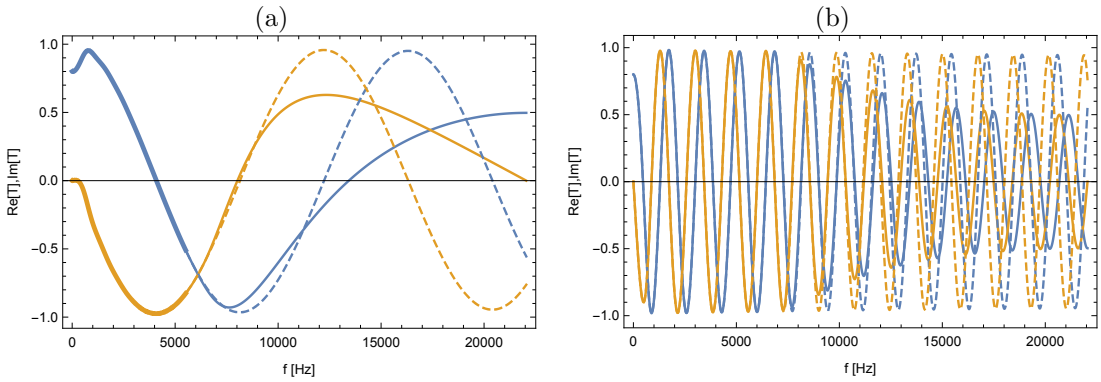

Figure 7.7 – Modal estimation (with 15 dipoles) of the propagator T of the scattering matrix $\mathbf{\Phi}^{(g,d)}$ of the flared duct depicted on Fig. 7.3. Blue line: Re(T), Orange line: Im(T). Thick lines: frequency band over which the fit by least squares was performed, medium lines: modal estimation, dashed lines: analytical function. (a) fitted function, after partial removal of the propagation delay (23 samples, instead of $f_s\, L/c = 25.683$ samples, which would require a fractional delay line for the simulation), (b) frequency response of the simulated propagator T (including delay line).

7.4.5 Discussion

It should be examined if a more economical recipe can be formulated with approximately the same accuracy. The proposed recipe shows that a simulation with waveguides is about 4-8 times more demanding in terms of computer power than the linear simulation of the sole input impedance. Indeed, the corresponding transfer functions for a segment of pipe of same length have approximatively the same number of analytical poles. The difference is explained by: 1) simulation of 4 transfer functions instead of 1 (plus radiation reflectance), 2) solving the coupling problem at each junction, and 3) difference in the number of additional poles that are necessary to account for the truncation of the modal series and to ensure the passivity. This is however not true for cylindrical pipes, for which the waveguide formulation is generally more economical than the impedance formulation, because: 1) only 2 propagators have to be simulated, 2) the total number of poles of the digital filters of both propagators and of the radiation reflectance is generally lower than that of the input impedance filter, 3) this number do not depend on the length of the pipe, 4) the frequency response of the waveguide is accurate practically up to $F_s/2$ and 4) no coupling problem has to be to solved at the output of the pipe. The most efficient linear implementation of a cylindrical pipe is however done with a single reflectance filter and a delay line, which requires approximately the same number of poles than a single propagation filter (see implementation in B.3.1).

The extremely light implementation proposed by Guillemain [68] should be mentioned in this context. It is however inaccurate in the high frequency range (because of the shift of the impedance peaks) and requires a pipe length commensurate with the sampling frequency.

7.5 Dictionary of junctions and Architecture of the synthesizer

A dictionary of junctions is proposed in Appendix A. This Appendix treats some technical aspects related to the junctions, like analytical solution of the coupling problem for different kind of junctions or the incorporation of nonlinear losses in the toneholes.

The software structure and the technical issues related to the implementation and the simulation of digital instruments are described in Appendix B.

An exemple of simulation is given on Fig. 7.8 for a Buffet Crampon Clarinet, model Prestige,

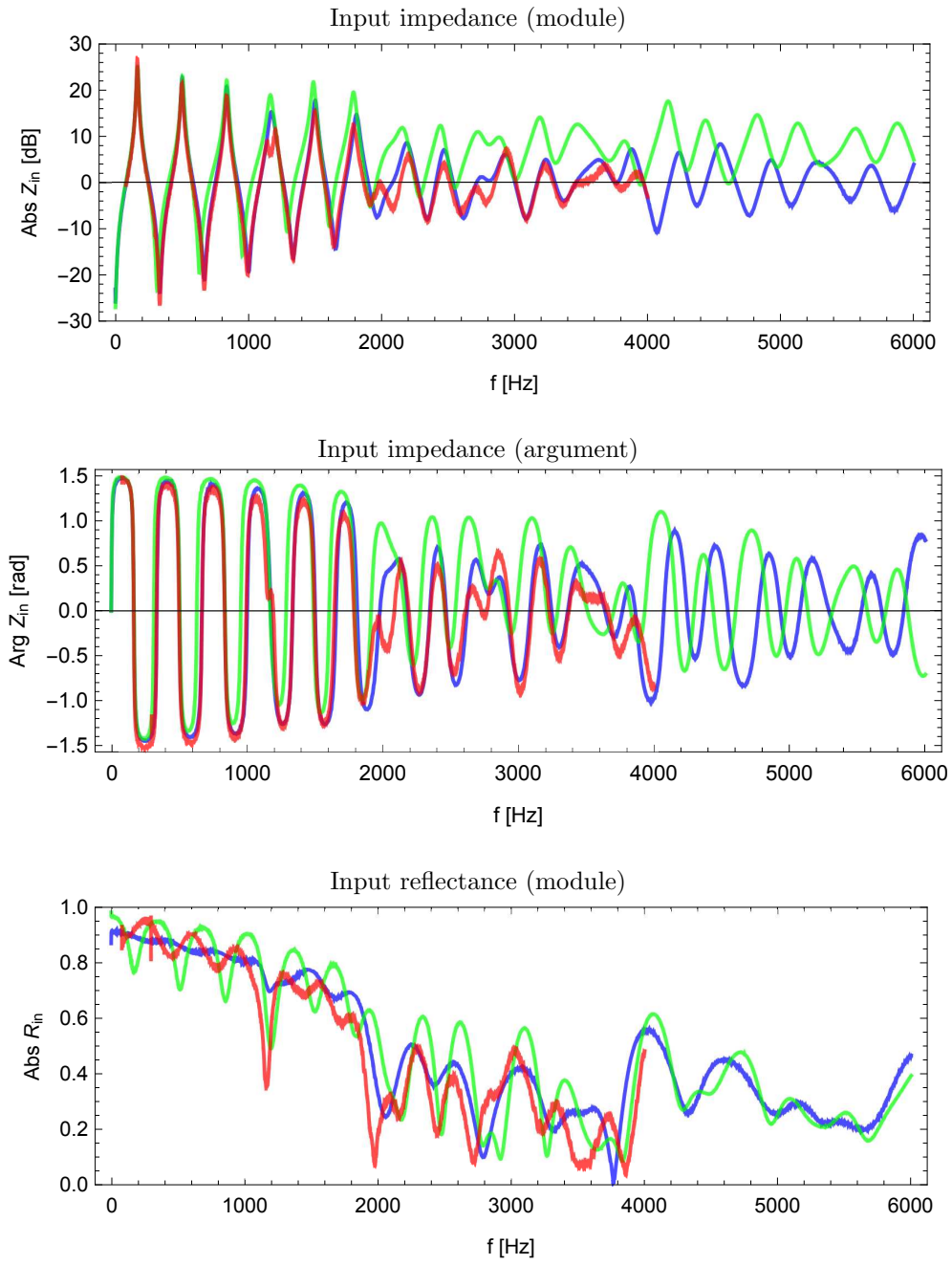

Figure 7.8 – Input impedance and input reflectance of the fingering F#3 of a Buffet Crampon clarinet, model Prestige. Red: measurement. Blue: waveguide simulation with a cylindrical mouthpiece bore (corresponding to the adaptation piece with which the instrument was measured). Green: waveguide simulation with a conical mouthpiece bore, as as described in 8.3.4. The input impedance is adimensioned by the characteristic impedance of a circular section of 15 mm diameter in the 3 cases, in order to allow an absolute comparison of the magnitudes.

simulated with 28 segments and 22 lateral toneholes (with linear losses, in order to allow a comparison with the linear measurements), see §B.3.3. The geometrical dimensions of this instrument are given in [154]. Minor modifications of the geometry were necessary in order to respect the minimal length imposed to the segments (see §7.2.2). The toneholes labeled *trille2* and *Mib3 F*

in "Tableau 2" were suppressed and the toneholes *Mib3 C* and *Si2F* were located respectively at 203.1 and 281.0 mm, instead of 199.8 and 279.0 mm.

The numerical filter corresponding to the fingering F#3 is excited by a discrete impulse and the input impedance Z_{in} is computed by Fourier transform of the impulse response. This exercice is repeated for 2 different geometries of the mouthpiece bore:

1. Cylindrical bore (diameter 15.0 mm, length 64.5 mm) corresponding to the interior volume of the mouthpiece and also to the adaptation piece with which the input impedance of the instrument was measured at LMA Marseille (in collaboration with P. Sanchez).
2. Conical bore as described in 8.3.4.

In the Fig. the simulated input impedances are compared with the measured input impedance. Compare also with the modal estimation of this measurement in Chapter 6, Fig. 5.

7.6 Conclusions and future work

This chapter proposes a software structure (based on the concept of waveguides) for the simulation of wind instruments in real time. The main obstacles could be overcome, using a formulation relaying essentially on the reflection and transmission functions of the scattering matrices (traveling waves), for which the techniques described in Chapter 6 could be applied. So, accurate digital filters (in some specified pass band) could be designed, which are passive at all frequencies. If required, digital filters can be easily converted into impedance or admittance filters. Fractional delays have been eliminated as a side effect of the modal estimation, integrating them directly into the digital filters. The problem of delay free loops could be solved analytically for each of the proposed junctions. Models of exciters, bells, horns, chimneys, valves and slides are implemented. The software architecture (written in C++) is designed for a simulation of the instrument in segments, which can be concatenated by the mean of a dictionary of junctions. The dictionary implements a dozen of junctions (more or less sophisticated, with or without added acoustic mass, with linear or nonlinear losses). The software supports also some tricky aspects of the synthesis, such as the transitions between fingerings or embouchure adaptations depending on the played note.

So far, the simulations seem convincing, although the number of simulated cases is still relatively small. Systematical tests should be conducted and could possibly lead to interesting observations, like the following one: the ease of emission in the second regime of the clarinet (clarion register) is notably better with the nonlinear loss model, especially while playing large intervals. This may be surprising at first glance, but the explanation is logical. The nonlinear losses contribute to attenuate the first resonance peak (due to the high flow rate generated in the register hole when the instrument plays a 2nd register-fingering in the first regime, causing high nonlinear losses), whereas the second peak is practically unaffected (since the register hole is located near a pressure node of the second regime, causing a low flow rate in the chimney, so the nonlinear losses are negligible). In other words, the oscillation threshold of the first regime is increased by the nonlinear losses above that of the second regime, which remains practically unchanged, so the oscillation starts on the second regime.

It would be interesting to apply the method to examine a recurring question of clarinettists and oboists: why do the reeds seem stronger at altitude than in the plains? The developed synthesizer allows to check if the difference in air density is sufficient to explain the effect. At first sight, it seems that the influence of this parameter should mainly concern nonlinear losses at the chimneys. A higher density implies increased losses, which lowers the saturation threshold, giving the impression that the reed is weaker.

This tool opens new opportunities for the design of wind instruments, especially for people who are not really skilled in acoustics (musicians and instrument maker, for instance). Synthesizers can be implemented from the geometry of the instrument with the described methods, focussing the attention of the designer on the musical aspects (intonation, homogeneity of sound, ease of emission, for example), achieving thus the principal aim set for my participation to the CAGIMA project: the virtual prototyping. An interaction with the PAFI (plate-forme d'aide à la facture instrumentale) project should be considered [45].

The potential of the software remains for the moment completely under exploited and numerous improvements are still needed to make it fully operational:

— The implemented models must be validated in detail, in particular the model of nonlinear losses in chimneys.

— Presently, the modal estimation is implemented only in the Mathematica language. An implementation in C ++ would be desirable for a broader use and for a faster recalculation of the filters, after each modification of the geometry of the instrument.

— A development effort is needed to facilitate the automated design of the filters. Currently, some parameters (like the number of modes or some constraints imposed to the fit by least squares) must be optimized by hand.

— The filter optimization must be improved with respect to passivity, especially for short segments, where the losses are very low. Accuracy and passivity aspects are then critical to balance.

— The low frequency optimization needs to be reviewed. In this frequency range (where the losses are very small), the preservation of the relative precision between the filters is more important than the absolute precision of each filter. Otherwise, aberrant results may occur, such as the simulation of a larger main flow in the speaker hole than in the main bore.

— An interface with standard synthesizers (like Max MSP) has yet to be realized.

— Different software objects are not yet implemented, for example: alternative exciter models, exciters for other instruments like flutes, radiation models computing the external sound perceived at any point in the space [125], interactions between toneholes due to external radiation [101, 87, 90, 88, 117, 93].

Part IV

Playability of Clarinet Reeds

Chapter 8

Study of a Panel of Clarinet Reeds confronting Objective Measurements, Subjective Evaluations and Sound Synthesis

Résumé

Ce Chapitre réalise une synthèse entre les éléments développés lors des chapitres précédents, en confrontant 3 types de données récoltées à partir d'un panel de 40 anches de clarinette: i) *Mesures physiques objectives*: pour chaque anche (et différentes embouchure), les données collectées comportent des expériences statiques (mesures aérauliques, déflection mécanique et photographies du canal) et une expérience dynamique (diagramme de bifurcation, établi sur un *crescendo / decrescendo*). ii) *Evaluations musicales subjectives*: un clarinettiste a joué ces mêmes anches à l'aveugle (avant que les mesures ne soient analysées) et les a notées sur la base de 4 descripteurs différents. iii) *Synthèse sonore*: les modèles physiques développés dans la partie III) sont mis en application pour simuler les diagrammes de bifurcation.

L'analyse canonique des corrélations atteste la présence d'un lien très fort entre toutes les mesures physiques objectives réalisées à l'intérieur du panel d'anches étudié. L'existence de plus d'une dizaine de facteurs indépendants est prouvée de manière statistiquement significative. La confrontation entre les mesures objectives et les données issues de la synthèse sonore montre l'existence de liens indubitables pour au moins 13 facteurs. Les 4 plus importants facteurs objectifs détectés sont corrélés de manière statistiquement significative avec les évaluations subjectives réalisées par le clarinettiste. Cela ouvre la voie à une sélection automatisée des anches, réalisée directement à l'usine.

8.1 Introduction

This study aims at summarizing the work done in recent years and described in the Parts II and III, by investigating a reed panel through various approaches (acoustics, music, sound synthesis, statistics). Its main purpose is to verify the solidity of the link between the physical measurements acquired from this panel of reeds and the subjective musical evaluation of these same reeds, blindly, by a clarinettist. The second aim of the study is to check summarily the relevance of the physical models developed, by confronting them with the experimental data acquired by playing this panel of reed by an artificial mouth.

This study is conducted in three successive phases: In the first phase, 3 categories of data are collected, namely:

— objective physical measurements

— subjective musical evaluations

— simulations by physical model

The second phase consists of confronting these data on a statistical basis, by canonical correlation analysis and to verify the statistical significance of the correlations found. In the third phase the acoustic and musical results are interpreted in the light of the statistically significant correlations found between canonical factors. Incidentally, it will also be necessary to check if the objective measurements made on dry reeds (in ambient conditions, without prior humidification) are well representative of the behavior of the wet reed, in playing situation.

The present study establishes also a link with the initial sparkle that conducted me to acoustics in 2001: the invention of the Claripatch system [1]. To develop the range of commercially available models, I performed a perceptive study by Principal Component Analysis (PCA) in 2002, using a panel of about thirty reeds. On the basis of the determined factors, I selected 8 reeds located at the extremes of the first 4 factors and I empirically tried to improve their functioning, according to the thickness profile conferred to the patch.

Since then, many authors have performed perceptual studies on simple reeds and have tried to find a connection with objective measurements. Pinard [120, 46], Stetson [143], Mukhopadhyay [104], Casadonte [15], Kolesik [89], Obataya [114], Gazengel [60, 61], Petiot [119] and Muñoz [108, 107, 106, 109] can be cited. A good summary of these works can be found in the first chapter of Muñoz's thesis [105]. The studies - whose statistical significance has been evaluated - have come to the conclusion that the reeds can be classified on the basis of 2 descriptors (playability and timbre). This is for instance the case of the study described in the cited thesis, Chapter 3, as well as that of Gazengel [61]. Muñoz has evaluated 20 reeds of 4 different brands, using a panel of 7 musicians. Large differences were found between musicians: some discern reliably the differences between reeds, others do not. There is no general consensus about the analyzed descriptors: a musician has evaluated the same descriptor in a way that is reproducible but very different from the other musicians, whom evaluations are more coherent among themselves. The descriptors "ease of playing" and "timbre" are correlated to 0.95. No canonical correlations analysis has been made, so it is not possible to know if more than one statistically significant canonical factor could be highlighted by this panel of musicians. The only significant factor is correlated with the stiffness of the reed at low pressure (linear component of the stiffness of the reed at rest). In order to allow a fair comparison, Muñoz's data should be analyzed with the methods proposed in this Chapter.

The investigations comparing a synthesis model and experimental measurements are not very numerous and are generally based on the study of a single reed, which prohibits any validation on a statistical basis, among which [17] and [105] can be cited. In this sense, the proposed approach is innovative.

The study of Guillemain [9] comparing perceptively the sounds generated by a synthesis model should be mentioned, as well as a study of scraping techniques for correcting the function of the reed [147].

The experimental setup is described in Sec. 8.2 and the collected data are detailed in Sec. 8.3. The methods of analysis are presented in Sec. 8.4, with which the data is analysed, in Sec. 8.5, then an interpretation of the detected factors is attempted in Sec 8.6, followed by the conclusions in Sec. 8.7.

8.2 Experimental setup

The measuring bench is described in §4.3. The physical symbols related to the measurements are listed in Table 8.1.

1. This system allows the clarinetist to regulate the behavior of his reeds by modifying the shape of the mouthpiece lay, by the mean of a wedge (patch). This wedge has a variable thickness, precisely defined, which modifies the bending of the reed against the lay [146].

8.2.1 Reed panel

40 "Vandoren classic" clarinet reeds were purchased in a music shop, of strength 2, 2.5, 3, 3.5 (10 of each). The reeds were randomly numbered from R00 to R39. In principle, all reeds should have the same geometry, since they were all manufactured in the same way. Theoretically, only the stiffness and the homogeneity of the wood differs, but in reality, the machining is not as regular as supposed, as showed a preliminary (unpublished) study on a panel of 15 reeds. Significant differences in geometry were found, which correlate with aeraulic measurements. The geometry of the reeds of the studied panel has not (yet) been measured.

During the measurements, the reeds undergo all the same "aging" protocol and have an equivalent hydric history (see §8.3.6). However, it is questionable whether this treatment is comparable to a normal playing situation.

8.2.2 Photographs of the channel

The photographs of the channel (slot between reed and mouthpiece through which the air enters into the instrument) were made by a Nikon D5200 SLR camera attached to a tripod and equipped with a macro lens [2] Micro Nikkor AF, 105 mm 1/2.8 D. The focal plane of the device is approx. 32 cm away from the tip of the mouthpiece, frontally to the channel. This relatively large distance comparatively to the about 1 mm height of the channel, allows to neglect the effects of parallax.

The size of the pixel at the tip of the reed is determined by a millimeter scale (4.15 microns). The origin of the coordinate system is defined by the intersection between the plane of the mouthpiece lay and the median plane of symmetry of the reed, at the tip (see Fig. 3 in Chapter 3). The reference line - corresponding on the photos to the plane of the mouthpiece lay - is determined photographically, by clamping on the lay a flat, reed-like metal plate. The pictures are deliberately overexposed, so as to optimize the exposure of the reed. The illumination is provided by the flash of the camera.

8.2.3 Artificial mouth

The measuring bench was transformed into an artificial mouth in "suction" (i.e. working with a negative pressure in the instrument) by connecting a 261 mm long PVC tube (15.5 mm inner diameter) to the instrumented mouthpiece. The end of the tube was inserted (in airtight manner) into a circular hole made in the smallest face of a parallelepipedic container (volume: about 100 liters). The hole was off centered by a few centimeters from the center of the face, to avoid unwanted acoustical effects due to symmetry.

The dimensions of the container (410 × 510 × 600 mm) have been optimized so as to spread the first acoustic resonances as evenly as possible. Pieces of carpet were glued on all interior walls, so as to dampen these resonances. An Endevco sensor was introduced through a small orifice to measure the pressure in the container. A cock valve allows to establish a moderate vacuum in the container, using a vacuum cleaner.

8.3 Collected data

8.3.1 Channel height

Several thousands photographs were made to determine the height of the channel $h(\psi, y)$, as a function of the embouchure ψ and the transverse coordinate y [3]. Only two series of photos (denoted PhotoNew and PhotoBreakIn) were included in the analysis.

For PhotoNew, 16 embouchures were measured for the position of the lip support ψ ranging from 3.400 to 0.400 mm, in 0.200 mm increments, plus 2 photos without lip contact, before

2. This professional lens was kindly lent by the naturalist and wildlife photographer Jean-Lou Zimmermann, whom I thank warmly.

3. Since y is the transverse coordinate, the deflection of the reed (traditionally denoted y, like in Chapter 5) is now denoted z, in this Chapter.

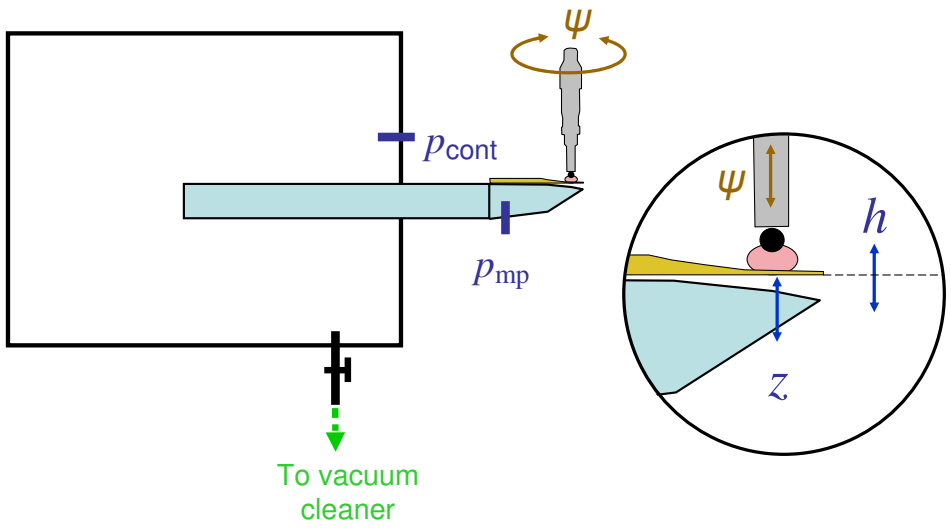

Figure 8.1 – Scheme of the artificial mouth in "suction" for the bifurcation measurements. The position ψ of the artificial lip support is regulated by a micrometer screw. The measured parameters are: p_{mp} (pressure in mouthpiece), p_{cont} (pressure in container), h (height of the channel, measured by photo), z (deflection of the reed tip, measured by optical sensor, calibrated with h and $p_{cont} = 0$). The reference plane for h and z (plane of the mouthpiece lay) is indicated by a dashed line. The zero for ψ is fixed arbitrary about 0.3 mm before contact between the artificial lip and the reed.

and after measurement. For PhotoBreakIn, 25 embouchures were measured for ψ ranging from 3.750 to 0.750 mm, in 0.125 mm increments, plus 2 photos without lip contact before and after measurement.

Note that the term "channel height" (or "reed height") is used abusively (for sake of brevity) to refer to the distance between the tip of the reed and the plane of the mouthpiece lay.

Treatment of the photos

The photos were subjected to image processing, from which 30 measurements of the channel height are extracted per photo, evenly distributed over the entire width of the reed.

The photos were processed in the following way: First, the pictures are centered according to a reference picture, to take into account the small offset (a few hundredths of a millimeter) due to manual shooting[4]. The outer front edge of the mouthpiece is painted in light blue with fine Indian ink dots, which facilitates the automated image centering (accuracy: $\simeq$ 0.01 mm), maximizing the correlations between reference and photo, from 3 target areas of about 1.2 $\times$ 1.2 mm.

The area of interest of the picture is converted to black-white by substraction between the "Brightness" component (HSB decomposition) and the "Yellow" component (MCYK decompo-

4. A remote trigger would minimize this problem, as would the use of a more stable and massive stand.

p_{atm}	atmospheric pressure ($p_{atm} = 0$)
p_{mp}	pressure measured in mouthpiece
p_{cont}	pressure measured in the container
Δp	$= p_{atm} - p_{mp}$ (pressure drop across the reed)
p_{supply}	$= p_{atm} - p_{cont}$ (corresponds to the blowing pressure in the usual situation)
y	transverse coordinate (channel)
ψ	position of the micrometer screw attached to the support of the artificial lip
$h(\psi, y)$	measured channel height (by photo of the channel)
$z_L(\Delta p, \psi)$	measured reed deflection, left optical sensor
$z_R(\Delta p, \psi)$	measured reed deflection, right optical sensor
$z(\Delta p, \psi)$	$= 1/2\,(z_L(\Delta p, \psi) + z_R(\Delta p, \psi))$
$S(\Delta p, \psi)$	measured aeraulic section
f_{play}	measured playing frequency

Table 8.1 – List of physical symbols

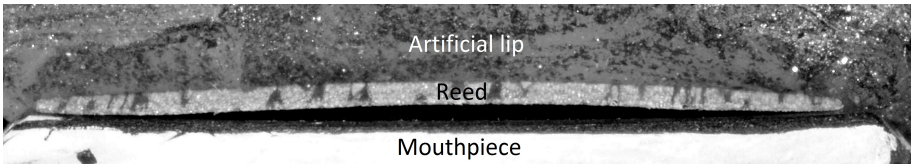

Reed R14 new

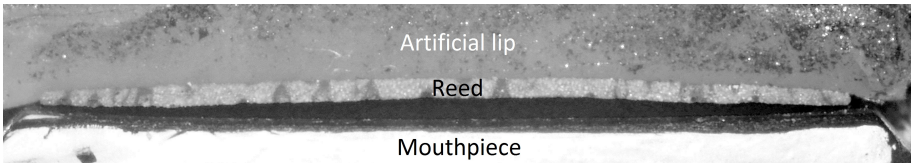

Reed R14 after break-in

Figure 8.2 – Photos of the reed R14 before and after break-in for an embouchure $\psi = 3.0$ mm. The color difference of the silicone, artifical lip is due to the erosion of the graphite after several thousands of manipulations, including 200 bifurcation measurements, where the reeds are played; this graphite was deposited on the artificial lip to make its appearance more matt on the photographs and to facilitate the automated analysis of the photographs. One of the dots with India ink, allowing the centering of the pictures, is visible at the bottom left.

sition), enhancing the contrast on the reed (see Fig. 8.2).

A mask is applied to restrict the analysis area to the relevant region (low-pass filtered, so as not to create a clean cut that would disturb the edge detection) and then the Mathematica `EdgeDetect` procedure is applied, followed by a morphological component analysis of the image (`MorphologicalComponents` procedure), selecting the component with the largest number of points. This gives the outline of the reed. Finally, the lower contour is taken, which corresponds to the lower front edge of the reed. Scaling by the determined size of the pixel, we obtain a scaled graph of the lower contour of the reed. From these about 32'000 pixels, 30 measurements are extracted by averaging over a regularly grid, distributed over the entire width of the reed. The estimated accuracy is of the order of a few microns.

Fig. 8.3 illustrates the contour obtained by this method for the reed R14, in new condition (16 different embouchures) and after break-in (25 different embouchures). The average values observed on 40 reeds is also depicted. The break-in process reduces the opening of the channel by about 0.1 mm. The contour of the reed R14 shows some constancy in the deformation of its tip. After breaking in, the deformation becomes more angular and more pronounced. This is observed practically for all reeds.

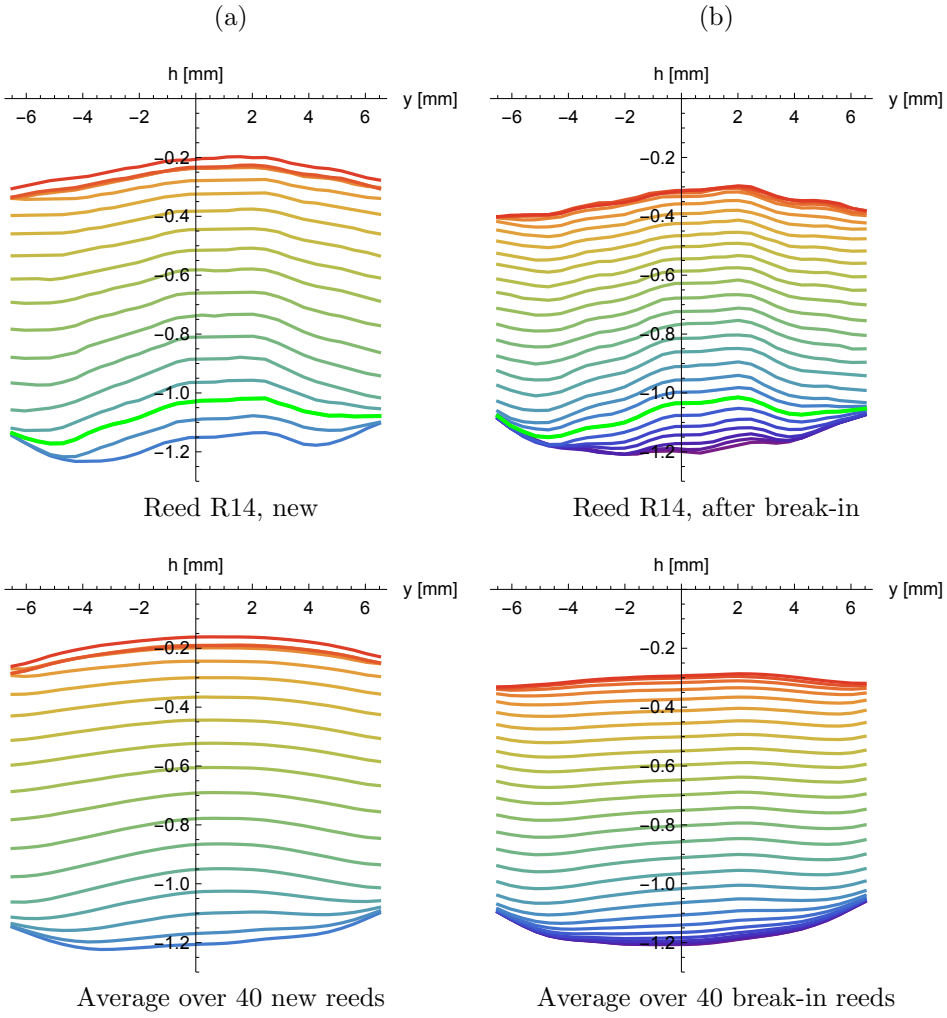

Figure 8.3 – Channel height $h(\psi, y)$ (distance between the tip of the reed and the plane of the lay, depending on the embouchure). The embouchures ψ are encoded by the colors of the rainbow, from red (reed at rest, without contact with the lip) to blue-purple (tight embouchure). (a) new reeds (PhotoNew series): 16 different embouchures (in 0.200 mm increments) and 2 resting positions, without lip pressure (before and after measurement, in red). (b) break-in reeds (PhotoBreakIn series): 25 different embouchures (in 0.125 mm increments) and 2 resting positions. The measurements extracted from the pictures of Fig. 8.2 are shown in thick green lines.

8.3.2 Aeraulic and optical measurements

The measurements of the aeraulic section were performed with the "bottle" technique described in Chapter 4, for 7 different embouchures (ψ varying from 2.500 to 1.750 mm, in steps of 0.125 mm) and discretized for a pressure drop Δp from 0 to 14 kPa, in steps of 0.2 kPa. The optical signals measuring the deflection on the left and on the right (data blocks OptoLeft and OptoRight) of the reed were acquired simultaneously with the aeraulic measurements (data block Aero). They were calibrated according to the photos of the channel made at the end of each aeraulic measurement.

Figs. 8.4 and 8.5 respectively illustrate the aeraulic section $S(\psi, \Delta p)$ and deflection on the left $z_L(\psi, \Delta p)$ and on the right $z_R(\psi, \Delta p)$ for reed R14 and also the average value over 40 reeds.

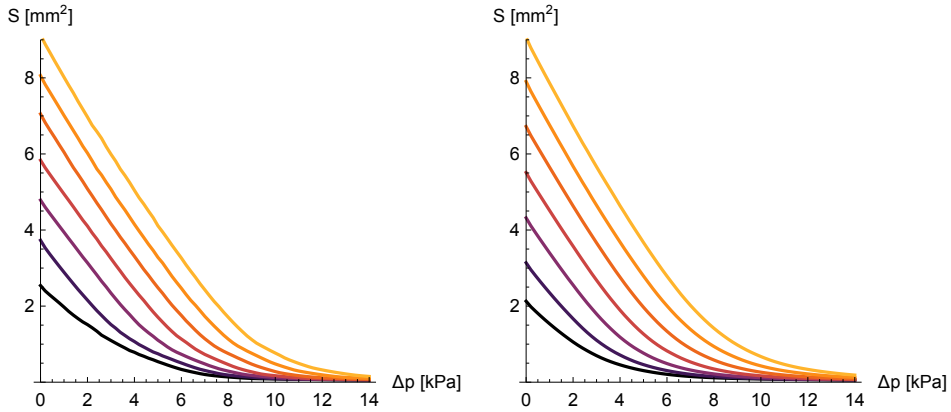

Figure 8.4 – Aeraulic section $S(\psi, \Delta p)$. The 7 embouchures tested are encoded by the colors from yellow (loose embouchure, $\psi = 1.750$ mm) to black (tight embouchure, $\psi = 2.500$ mm).

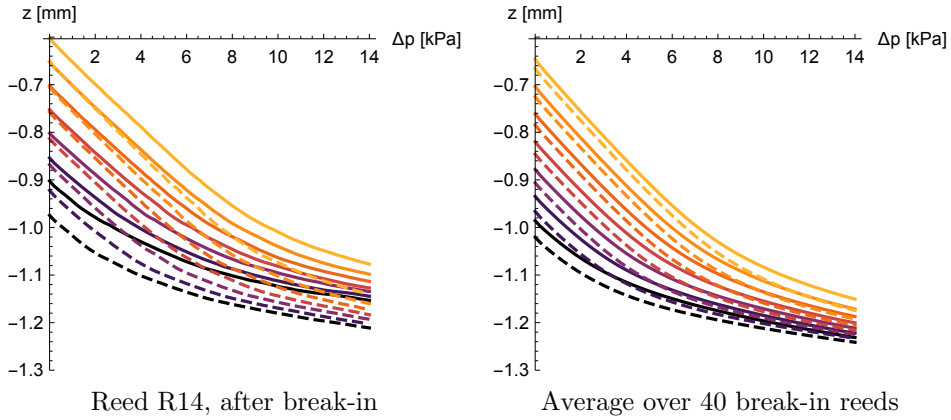

Figure 8.5 – Deflection of the reed on the left $z_L(\psi, \Delta p)$ and on the right $z_R(\psi, \Delta p)$, respectively solid lines and dashed lines, measured by optical sensor during the aeraulic measurements. The 7 embouchures tested are coded by the colors from yellow (loose embouchure, $\psi = 1.750$ mm) to black (tight embouchure, $\psi = 2.500$ mm).

8.3.3 Bifurcation diagrams

A 261 mm long cylinder is played with the artificial mouth (see §8.2.3), increasing the depression in the container until the extinction threshold is reached (*crescendo*), then cock valve is closed and the *decrescendo* is measured (which regulates itself according to the air consumption). The experiment is repeated for 4 different lip positions [5] (ψ ranging from 2.125 to 1.750 mm, in steps of 0.125 mm). The variation of the pressure supply in the *crescendo* phase is approximately equal for all reeds, because the action of the vacuum cleaner is nearly equal in all experiments. In order to accelerate the pressure recovery in the container, a diaphragm (diameter 1 mm) was inserted in the cock valve after closing the valve and the valve was reopened. This "leak" ensures that the inverse threshold is obtained in similar conditions for all reeds (same slope in the pressure supply until the reed reopens). This limits also the duration of one experiment to about 2 minutes and the asymmetry of the pressure supply between *crescendo* and *decrescendo* ramps is reduced. The emergence and extinction thresholds measured with this procedure are fairly comparable between reeds, although they do not coincide with the "true" thresholds which

5. The embouchure $\psi = 2.250$ mm was also measured, but no sound was obtained for some reeds, so these measurements were discarded in the analysis.

are obtained by infinitesimally increasing or decreasing ramps.

8.3.4 Synthesis by physical model

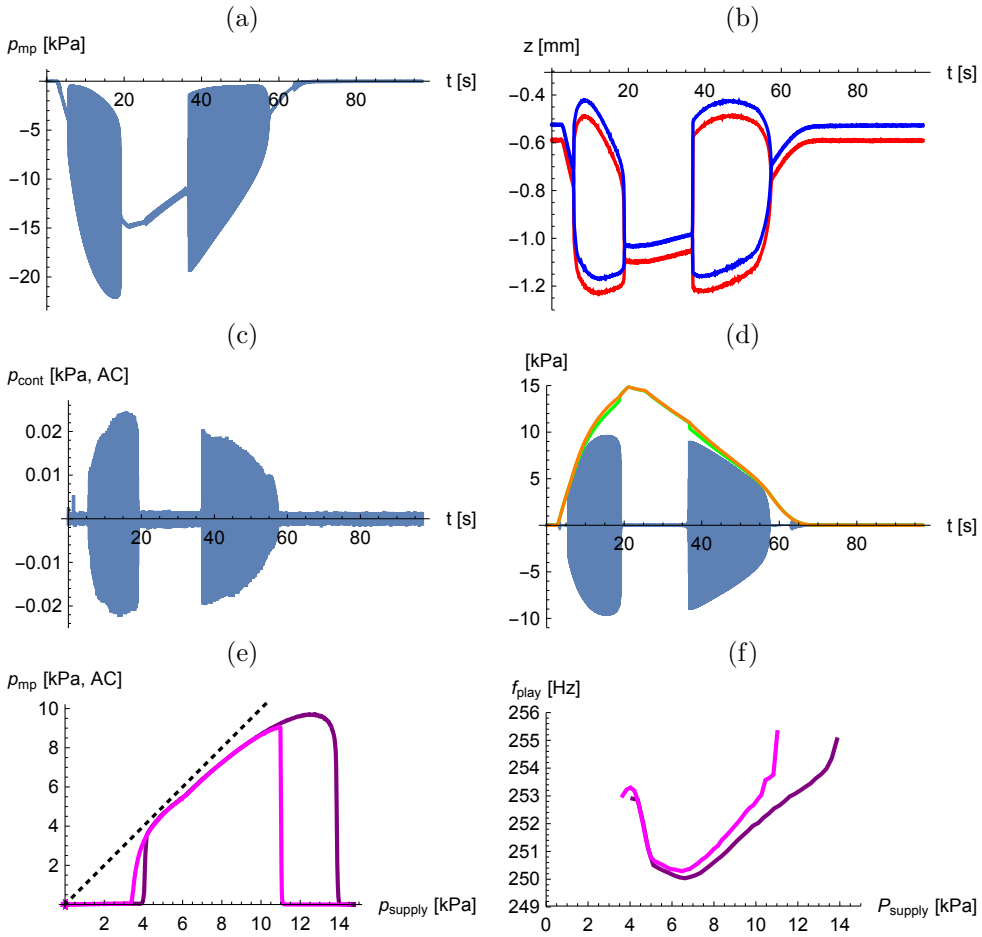

Figure 8.6 – Example of bifurcation measurement (reed R14, with embouchure $\psi = 1.750$ mm). (a) pressure signal p_{mp} measured in the mouthpiece during a *crescendo* / *decrescendo*. (b) deflection of the reed tip (enveloppe of the signals z_R and z_L) measured by the optical sensors R (red) and L (blue). (c) AC component of the pressure signal p_{cont} measured in the container. (d) blue: AC component of signal (a): p_{mp}, green: DC component of signal (a): p_{mp}, orange: pressure supply, i.e. the DC component corresponding to signal (c): p_{cont}. For the orange and green curves, the sign is inverted, in order to correspond to the usual situation (when the pressure supply p_{supply} is the blowing pressure in the mouth of the player). (e) resulting bifurcation diagram, i.e. enveloppe of the AC component of p_{mp} as a function of p_{supply} (purple: *crescendo*, magenta: *decrescendo*). The black dotted line corresponds to the expected asymptotic trend in a lossless case. (f) Playing frequency f_{play} as a function of p_{supply} (purple: *crescendo*, magenta: *decrescendo*).

An example of bifurcation measurement is given on Fig. 8.6. The raw signals are illustrated on the subgraphs (a) pressure in the mouthpiece p_{mp}, (b) deflection of the reed, z_R and z_L, and (c) pressure in the container p_{cont}, AC component. The subgraph (d) show the result of the separation of the "DC" component (i.e. components below 100 Hz) of p_{mp} and p_{cont} and the "AC" component (i.e. components above 100 Hz) of p_{mp}. An intriguing difference has been noted between the DC component of both pressure sensors. It seems that a positive static pressure is present between p_{mp} and p_{cont} when the sound level is high. Is this related to non linear losses at

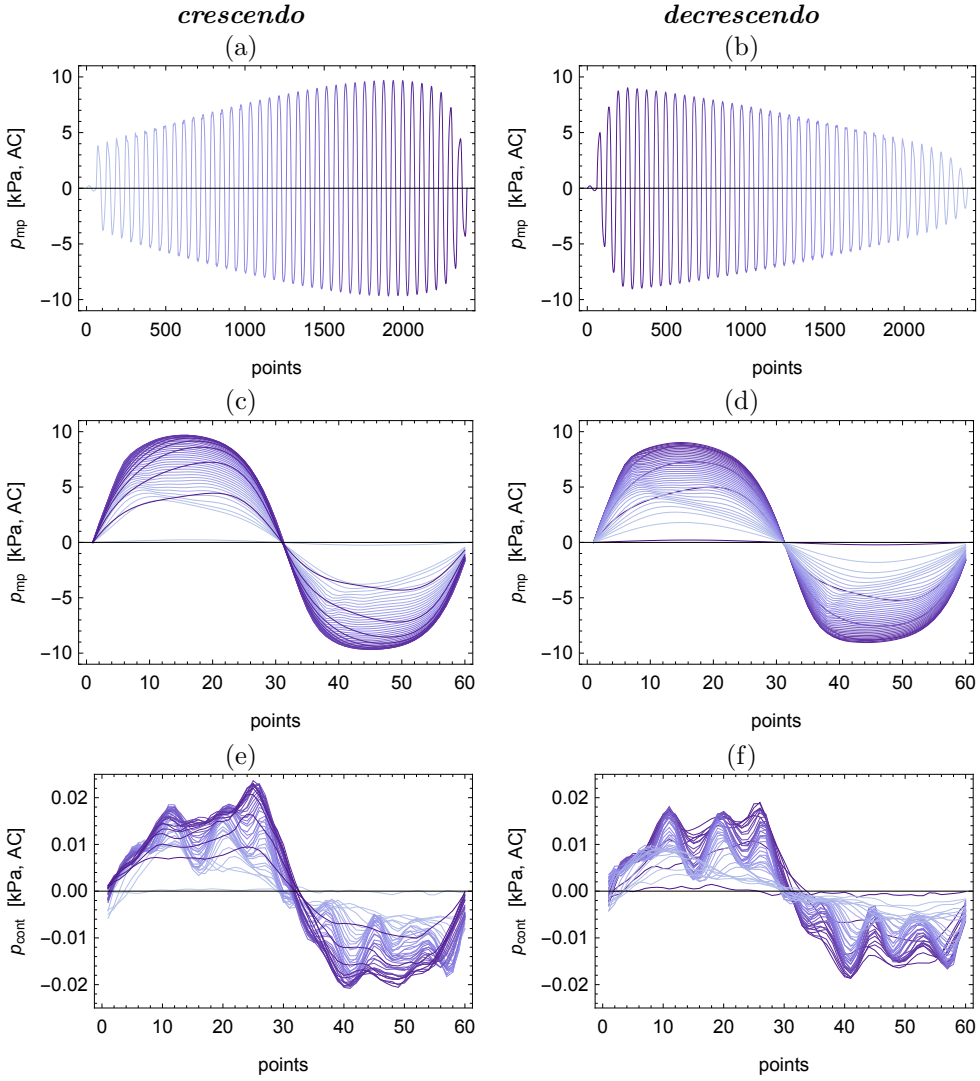

Figure 8.7 – Data processing of the bifurcation measurements of reed R14 illustrated on Fig. 8.6 prior to statistical analyses. Temporal signal (resampled on 60 discrete points) over 1 period for 2×40 blowing pressures regularly distributed between the 2×2 thresholds (respectively for the *crescendo*, left column and the *decrescendo*, right column). The blowing pressure is coded between emergence and extinction thresholds by the colors from light blue (lowest value allowing auto oscillation) to dark blue (highest value allowing auto oscillation). (a) pressure measured in mouthpiece (*crescendo*, AC component of p_{mp}), $40 \times 60 = 2400$ discrete points. (b) *idem* but in *decrescendo*. (c) same data as (a), but partitioned into 40 blowing pressures (over one period, i.e. 60 discrete points). (d) same data as (b), but partitioned into 40 blowing pressures. (e) pressure measured in the container (*crescendo*, AC component of p_{cont}), partitioned into 40 blowing pressures. (f) *idem* but in *decrescendo*.

the output of the instrument or is it merely an artifact of the pressure sensor? Notice that both curves (green and orange) are perfectly superimposed after extinction. The so-called bifurcation diagram is depicted on subgraph (e). The typical hysteresis between the extinction threshold in *crescendo* and the emergence threshold in *decrescendo* (also called inverse threshold) is observed for all reeds. The measured emergence and extinction thresholds are 4.11 and 13.87 kPa for the *crescendo* and 11.02 and 3.65 kPa for the *decrescendo*. The measurement of the "true" emergence and extinction thresholds would require a infinitesimally slow increase or decrease

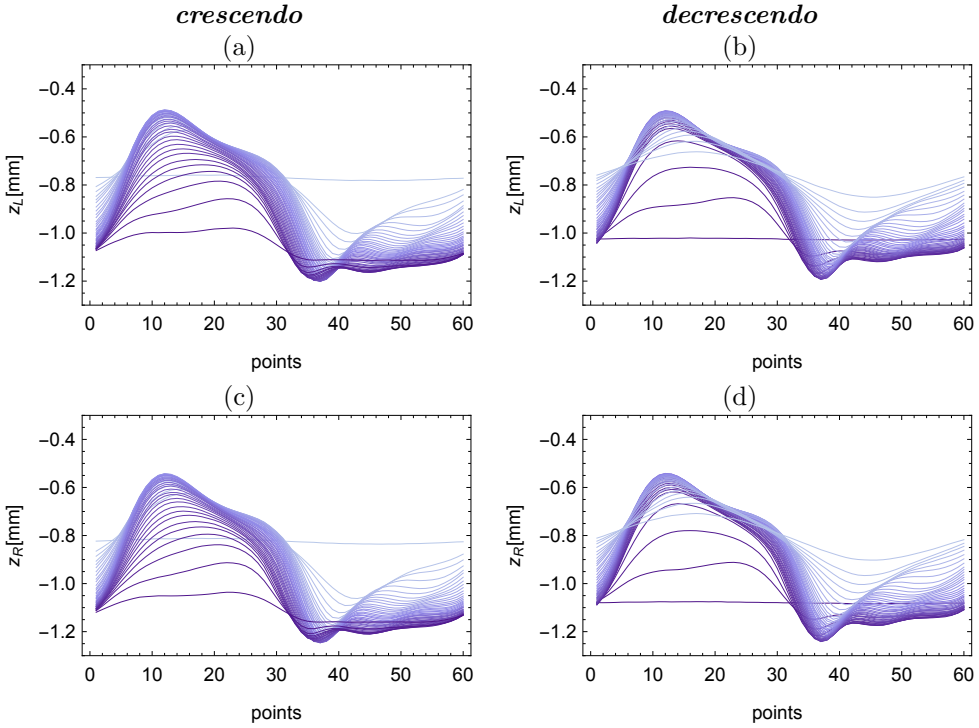

Figure 8.8 – Data processing of the bifurcation measurements of reed R14 prior to statistical analyses (continued). Optical signals partitioned into 40 blowing pressures. (a) deflection of the reed tip, left sensor, z_L (*crescendo*). (b) idem but in *decrescendo*. (c) deflection of the reed tip, right sensor, z_R (*crescendo*). (d) idem but in *decrescendo*.

of the pressure supply. For this reason, the measured emergence threshold in *crescendo* and the extinction threshold in *decrescendo* are not equal. The beating threshold corresponds to the point of the bifurcation diagram which is the closest to the black, dotted line[6]. The air consumption reaches a minimum at this point (see Chapter 1, Fig. 2, Case I). The subgraph (f) illustrates the playing frequency f_{play}. The pitch is higher at low and at high pressure supply. While the increase of the playing frequency is well explained by the model at high pressure, the increase at low pressure is probably related to the acoustical behavior of the mouthpiece. A modest increase was obtained in the simulations (only) with a conical mouthpiece bore (see next § and Fig. 8.9). The discrepancy between *crescendo* and *decrescendo* is probably related to a temperature drop due to the fast decrease of pressure in the container, in the *crescendo* phase, while a partial temperature recovery happened in the slower *decrescendo* phase. A viscoelastic explanation seems less likely: in such a case, both curves in the bifurcation diagram (e) would noticeably diverge in the middle part.

Fig. 8.7 depicts the treatment applied to the measured signals of reed R14 prior to the statistical analysis. In the subgraphs (a) and (b) one period of the pressure signal (AC component of p_{mp}, respectively for the *crescendo* and the *decrescendo* ramp) is collected for 40 blowing pressures regularly distributed between the emergence and extinction thresholds. In the subgraphs (c) and (d) the same data is partitioned into 40 blowing pressures (from light blue: lowest pressure allowing auto-oscillation to dark blue: highest pressure allowing auto-oscillation). In (e) and (f) the same treatment is applied to the AC component of p_{cont}, while Fig. 8.8 shows the same treatment applied to the optical signals z_L and z_R.

Fig. 8.9 illustrates some indicators extracted from the bifurcation measurements (solid lines), averaged over 40 reeds: (a) the playing frequency f_{play}, (b) the envelope of the pressure signal

6. This pragmatic definition of the beating threshold do not correspond necessarily with the theoretic definition given in Chapter 1, because real reeds never close the channel hermetically.

in the mouthpiece (AC component of p_{mp}), (c) the Spectral Centroid (SC) of p_{mp} and (d) the SC of the reed signal $1/2(z_L + z_R)$. The dashed lines correspond to the average of the synthesis model described hereafter.

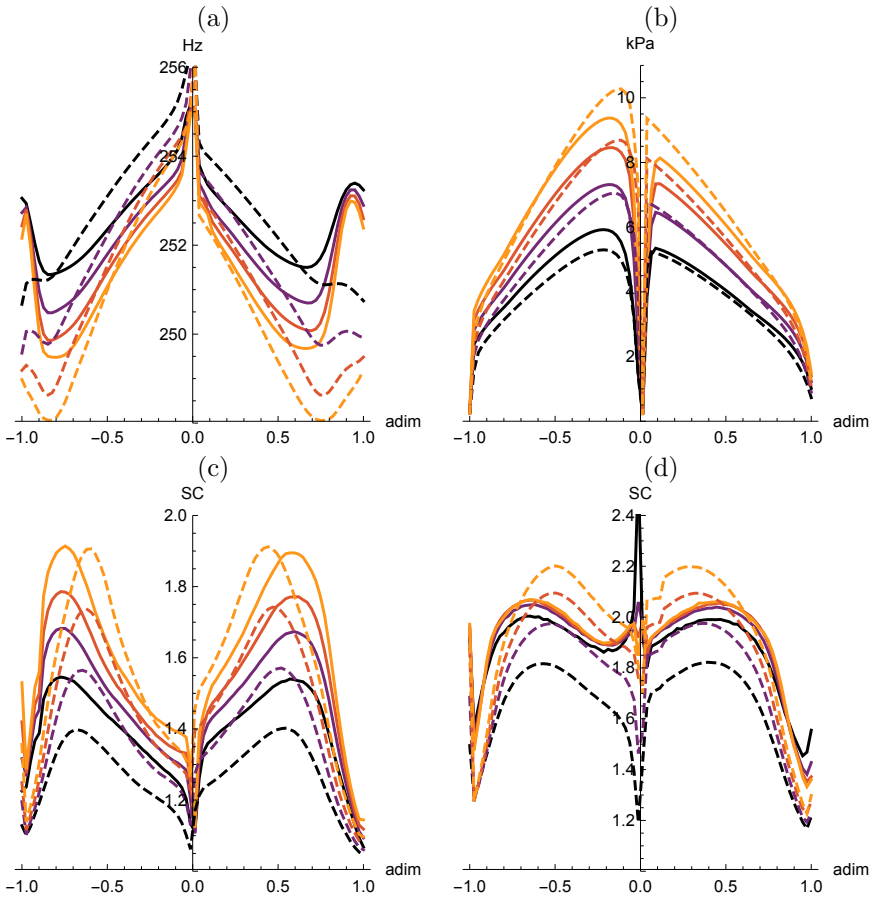

Figure 8.9 – Comparisons between the average of the measurements (solid lines) and the average of the simulations (dashed lines) of the bifurcation diagrams. In each diagram, the pressures (abscissa) are adimensionned by the thresholds of emergence and extinction (between -1 and 0 for the *crescendo* and between 0 and 1 for the *decrescendo*). The 4 embouchures tested are coded by the colors from yellow (loose embouchure, $\psi = 1.750$ mm) to black (tight embouchure, $\psi = 2.125$ mm). (a) playing frequency. (b) envelope of the pressure signal in the mouthpiece. (c) Spectral Centroid (SC) of the pressure signal in the mouthpiece. (d) SC of the reed signal (average between left and right signals).

The "instrument" played by the artificial mouth is simulated by physical model synthesis, using the waveguide techniques detailed in Chapter 7. The aim of the simulations is also to perform a first rough validation of the model, without investing too much time in optimizing the parameters, so as to reproduce the measured signals as accurately as possible. A more elaborate study and a more detailed comparison of the signals must be conducted in the future.

The determination of the geometry of the cylindrical pipe is straightforward, which is not the case for the bore of the mouthpiece. Indeed, in the mouthpiece chamber, the hypothesis of plane (or quasi-spherical) waves is probably no longer valid (J. Kergomard pers. comm.), whereas this hypothesis is probably valid within the bore of the mouthpiece, which is conical. We assume here that the mouthpiece chamber can be modeled by a cone having a downstream diameter equal to that of the input of the conical bore and simulate a few different input diameters (8, 10, 13, 15.5 and 20 mm), keeping the internal volume of the mouthpiece constant (11.2 cm^3, according to volumetric measurements). The results obtained for the diameter of 10 mm were

found to be the most consistent with the measurements. They are depicted for the reed R14 on Fig. 8.11, and compared to measurements and to simulations with a cylindrical mouthpiece model of same volume (and of same diameter than the main bore). Chaziioannou [17] has reached similar conclusions, using other methods.

The geometry of the simulated "instrument" [7] is depicted on Fig 8.10.

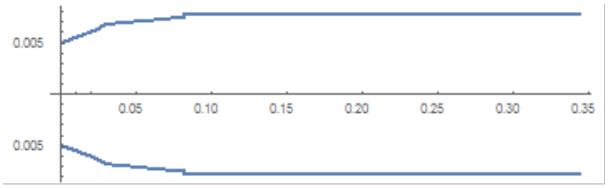

Figure 8.10 – Selected geometry for the simulation of the "instrument" played during bifurcation measurements. The dimensions are in meters.

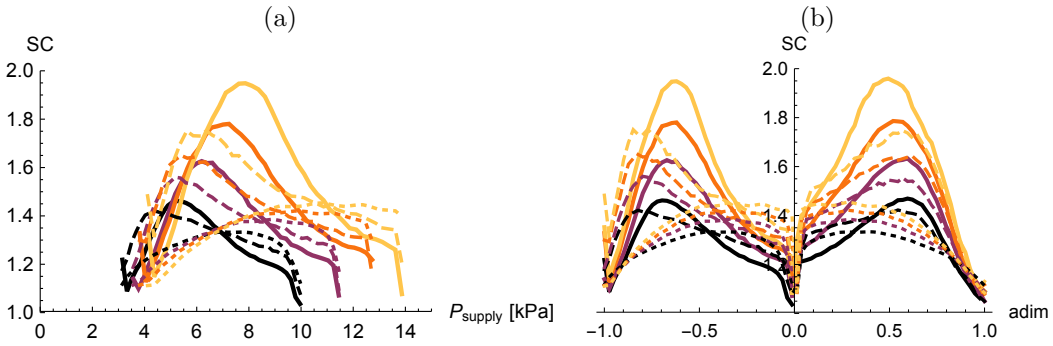

Figure 8.11 – Influence of the mouthpiece model on the Spectral Centroid (SC) of the mouthpiece pressure p_{mp}, in the bifurcation diagrams for the reed R14. Solid thick lines, measurements. Dashed lines, simulations with the proposed conical mouthpiece bore. Dotted lines, simulations with a cylindrical mouthpiece bore (d=15.5 mm). The 4 embouchures are coded by the colors from yellow (loose embouchure, $\psi = 1.750$ mm) to black (tight embouchure, $\psi = 2.125$ mm). (a) SC as a function of the pressure supply (*crescendo* only; the curves in *decrescendo* are practically superimposed and not given here for readability reasons). (b) Same data, prepared for the statistical analysis, adimensioned by the emergence and extinction thresholds. From -1 to 0, *crescendo*. From 0 to 1 *decrescendo*.

The corresponding waveguide involves 3 segments. The first segment lays between the reed and the pressure sensor located in the mouthpiece bore. The 2nd segment simulates the mouthpiece bore, downstream to the sensor, while the 3rd segment simulates the cylinder.

The (linear) input impedance of the simulated instrument is shown in Fig. 8.12.

The nonlinear model of radiation proposed in §A.3.11 is used [8] as well as the nonlinear reed

7. The geometry of the simulated mouthpiece is very similar to the one I determined by optimization from an impedance measurement of the "output" impedance of the mouthpiece, the window of the mouthpiece being rigidly and tightly sealed by a metal reed. With this configuration, the 1D linear acoustical behavior is at least correct when the reed closes the channel. Notice that a mouthpiece with full cylindrical bore fails to reproduce the hump observed on the SC around the beating threshold of the pressure signals measured in the mouthpiece (see Fig. 8.9, bottom left and 8.11). The conical mouthpiece geometry produces also realistic signals in association with the full clarinet model described in B.3.3. This geometry enhances the absolute amplitude of the resonance peaks (except the first peak, which remains almost unchanged). The input impedance at frequencies corresponding to even harmonics of the playing frequency of first regime are considerably increased (because the frequency of the antiresonances is notably lowered by this geometry). The differences among reeds appear also more clearly.

8. It seems that the pressure loss coefficient is overestimated by about 15-20%. To compensate, the output radius of the tube was increased by 10% when calculating the Bernoulli's law, so that the thresholds correspond better to the measured ones (otherwise the extinction is too early, whereas it is much too late and brutal with the linear model, the sound level increasing significantly faster than the measured level).

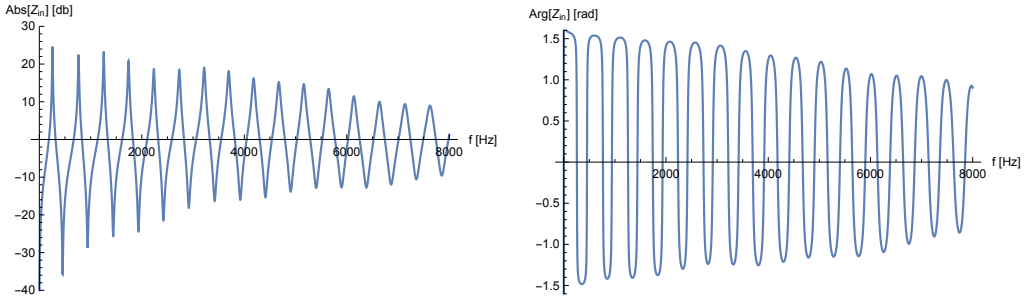

Module Argument

Figure 8.12 – Input impedance of the waveguide, simulated here with a linear radiation impedance. This input impedance corresponds to that of the waveguide with nonlinear radiation impedance, simulated at a very low level.

model, which is described in Chapter 5. In the dynamic model, all reeds are assumed to have the same mass and the same damping. The (unmeasured) value of these parameters was determined very roughly (0.75 mg and 0.0028 kg/s), comparing measurements and simulations. Thus, the first resonance frequency of the reed depends solely on the measured static stiffness. At first sight, the damping parameter seems to be somewhat underestimated.

The blowing pressure (equivalent of the mouth pressure, in the usual playing situation) is determined from the measurements provided by the Endevco sensor located in the container, low-pass filtered with Fourier transform, so as to eliminate completely the components of the sound radiated in the container of frequency higher than 100 Hz (one octave and a half below the playing frequency) and which could otherwise interfere during the synthesis. Thus the conditions of measurements with the artificial mouth are quite perfectly reproduced and the measured and simulated signals can be compared at any moment.

The synthesized data was analyzed with the procedure used to analyze the measured data. The analyzed signals are in principle the same, with 3 differences:

1. The 1D reed model does not differentiate the deflection of the reed on the right and left sides. The simulated reed signal has therefore only one channel.
2. The radiated pressure in the container at the sensor location is not simulated.
3. The calculated flow rate signal in the channel is added to the data .

8.3.5 Subjective musical evaluation

A subjective musical evaluation is performed in blind conditions, based on 4 descriptors allowing absolute comparisons between reeds within the panel [9]. These descriptors include the ability of the reed to meet certain requirements, and not some abstract properties, which are usually imprecisely defined. It is far more relevant to ask the clarinetist to perform some familiar aptitude tests, such as those he uses when selecting his reeds before a concert. An important aspect is often neglected in perceptual studies: the accuracy of intonation, which poses a number of constraints on the embouchure, when playing with other instrumentalists (about the influence of the reed on intonation, see [110, 34, 137, 30, 37]). Three of the four subjective musical descriptors were selected during a preliminary study (from a battery of approximately 40 different descriptors). They proved relatively repeatable: from a panel of 15 reeds, statistically significant correlations were found between two series of tests carried out a few days apart. These descriptors were also selected because they are relatively uncorrelated.

9. Absolute comparisons are more difficult to perform reliably than relative comparisons in pairs, but they are much less demanding to perform. The evaluation of a single descriptor with a panel of 40 reeds requires 40 evaluations instead of 780 (for all possible pairs). On the other hand, it is essential to evaluate the repeatability, in order to verify that the clarinettist presents a certain constancy in his judgments. Another advantage of the absolute comparisons: they allow a comparison between reeds having an equivalent hydric state (the same humidification procedure is used for each reed before the test, which is impossible with pairwise comparisons).

In the present study, each test was repeated 4 times (during 5 consecutive days), for the following descriptors :

1. *StrengthSubj*: The subjective strength of the reed is evaluated, blindly, without knowing its nominal strength (indicated by the manufacturer), but knowing that it is comprised between 2 and 3.5. The purpose of the test is not to retrieve the nominal strength, but to evaluate the subjective strength felt in the playing situation, so as to assess its adequacy with the nominal strength (or not). If necessary, the scale can be extended, so as to signal a particularly weak or strong reed.
2. *Poulenc*: The ability of the reed to play the first lines of the Poulenc sonata, which requires a particularly abrupt and aggressive fortissimo, is evaluated. The reeds are scored on a scale of 1 to 6 (but in practice, the scores 4 and 5 were mainly used). In the 4th evaluation, an alternative test was performed, based on an excerpt from the 3rd movement of the 1st Brahms Sonata (which was statistically significantly correlated with the original test).
3. *Schubert*: The ability of the reed to play the first lines of Schubert's "Der Hirt auf dem Felsen", which requires a soft, expressive sound, is evaluated. The reeds are scored from 1 to 6 (but in practice, the scores 4 and 5 were mainly used). In the 4th evaluation, an alternative test was performed, based on the beginning of Stravinsky's first solo piece for clarinet (which was statistically significantly correlated with the original test).
4. *Intonation*: The fingering G4 (all fingers open) is played for a few seconds, with a full and round sound. When the sound is judged "optimal", the player open his eyes and record the first value read on the chromatic tuner. With a weak reed, the embouchure should not be too loose, so as to limit the flattening of the intonation. With a strong reed, the embouchure should be tighten just what is necessary to diminish the turbulence noise. A small volume of air is exhaled before playing, so as to eliminate the CO_2-poor air contained in the upper airways.

StrengthNom, the nominal strength of the reed, indicated by the manufacturer was included in the analysis. It is merely compared to the measurements.

The test series 2 to 4 have been recorded by an external microphone (to allow a possible future analysis). It turned out that recording is impairing the judgment: the player must focus his attention on playing the right notes, respecting the timing and the tempo, in order to make the audio recording suitable for further analysis. The faculty of judgment is distracted (often, the beginning of the excerpt must be repeated several times to make a more accurate judgment). I quickly decided to assign the scores for the "Poulenc" and "Schubert" descriptors after the end of the recording, by freely testing the reed.

The third series was spread out over 2 days. Between the evaluations of each reed, approximately 15 minutes of manipulations were necessary to carry out the aeraulic measurements for 11 different embouchures (unfortunately unusable). The ambient temperature ranged from 19 to 21°C in this series. A lower repeatability is therefore expected for this series.

During the 4th (and last) series, the "Poulenc" and "Schubert" descriptors were evaluated using alternative musical excerpts (some musical excerpts recorded during the 3rd series seemed to be quite equivalent to the original ones and I wanted to check this point). During this last series, I tried to widen the scale of evaluation (being less restrictive in the evaluation of the scores).

It should be noticed, that the instrumented mouthpiece was not used for the perceptual tests (it was used exclusively for the objective measurements). I played a mouthpiece of the same model (Vandoren M30).

8.3.6 Data acquisition

The reeds were subjected to several measurement sessions [10]. The first session was performed immediately after opening the sealed package, ensuring a stable hygrometry since manufactur-

10. The adopted protocol reflects some imperatives of efficiency : I had to do all the operations myself (preparation of the reeds, perceptual tests, protocol, technical manipulations). The fact that several minutes can pass between two successive subjective evaluations does not improve by the repeatability (but this allows on the other hand to regenerate the concentration)

ing. A series of photos of the channel was made for the new reed, with 16 different embouchures. The reeds have been then subjected to fifteen cycles of humidification (brief soaking in water) and drying (at least one day, with a relative air humidity between 70 and 75%). From the first humidification / desiccation cycle, the author of these lines played each reed for a few minutes. After the 3rd cycle, each reed was played and then subjectively noted. This was repeated during 4 consecutive cycles. The reeds were no longer played by a human in the subsequent cycles, but only by the artificial mouth. At the end of this treatment, the reed is considered to be "break-in", according to the terminology of clarinettists. A series of aeraulic, optical and photographic measurements were carried out at each cycle, but only the last series of measurements is incorporated into the measurement corpus of the present study, for the sake of simplicity [11]. For the bifurcation study, the reeds were played by the artificial mouth in dry conditions (i.e. without humidification). Finally, a series of photographs of the break-in reed were made for 25 different embouchures.

8.4 Data Analysis Methods

An brief introduction to statistical analysis methods is given for readers who are not very familiar with this discipline and with its terminology. Different linear statistical methods are presented, using deliberately similar notations so as to emphasize the similarities among them (see Tables 8.2 and 8.3).

8.4.1 Preparation of data matrices

We aim at analyzing by statistical methods measurements made on a sample of N individuals taken from a population. In our study we have taken $N = 40$ reeds of the brand Vandoren "classic", among those which are put on sale. On each individual reed, we perform P distinct measurements (which are called variables, in statistics). The collected data thus forms a matrix $\boldsymbol{X}$, consisting in N rows and P columns (this is denoted in short form $\boldsymbol{X} : N \times P$).

Prior to processing the data with linear algebra techniques, one of the following treatments is generally applied to $\boldsymbol{X}$, so as to eliminate the affine component:

— **Centering**: the function $\boldsymbol{X} \to \text{center}(\boldsymbol{X})$ subtracts the mean from each variable. This way, the average of each column of $\boldsymbol{X}$ is zero.

— **Standardization**: the function $\boldsymbol{X} \to \text{std}(\boldsymbol{X})$ subtracts the mean from each variable, then divides it by the standard deviation. This way, the average of each column of $\boldsymbol{X}$ is zero and the standard deviation is 1.

In principle, centering is applied to matrices with homogeneous measurements (same physical units, comparable variations among measures). Otherwise, standardization is applied.

In order to obtain a 2D data matrix, notice that the measurement structure must be eventually flattened, so as to obtain a single vector per reed (i.e. one row of the matrix $\boldsymbol{X}$). This is for instance the case for the photos of the channel which repeat similar measurements made on a series of embouchures ψ. After the statistical analysis, the results may be partitioned ("deflattened") in order to recover the orignal measurement structure.

Many statistical analyses do not allow missing data. We have to structure the data in such a way, that measurements are available for all reeds and all variables. For instance, a data structure based on the pressure supply (p_{supply}) is not recommended for the bifurcation analysis, because we have to eliminate the measurements for all pressures for which no sound was obtained for at least one reed. A good practice is to recast p_{supply} by the emergence and extinction thresholds (i.e. to sample the measurements on a dimensionless grid of supply pressures). This way, data is available for all adimensioned pressures and all reeds. Some non-linearities can also be (partially) removed with similar techniques.

11. This is also due to technical problems (disconnection of the calibrated diaphragm and disturbances in the stabilized power supply of the optical sensors). These defects were noticed only after the end of the subjective tests (since the requirements of a blind test prohibit any analysis before the end of the data acquisition). Once the defects were found and repaired, new measurement sessions were carried out. No subjective evaluation has been done since that moment.

Method	Symbol	Dim.	Designation
MLR	N	scalar	number of individuals
MLR	P	scalar	number of variables (predictors)
MLR	P_y	scalar	number of dependent variables
MLR	$\boldsymbol{X}$	$N \times P$	data block
MLR	$\boldsymbol{Y}$	$N \times P_y$	dependent variables
MLR	$\hat{\boldsymbol{Y}}$	$N \times P_y$	linear approximation of $\boldsymbol{Y}$
MLR	$\boldsymbol{A}$	$P \times P_y$	regression coefficients
PCA	N	scalar	number of individuals
PCA	P	scalar	number of variables
PCA	Q	scalar	number of factors taken into account
PCA	$\boldsymbol{X}$	$N \times P$	data block
PCA	$\hat{\boldsymbol{X}}$	$N \times P$	linear approximation of $\boldsymbol{X}$
PCA	$\boldsymbol{Y}$	$N \times P$	principal components scores
PCA	$\boldsymbol{A}$	$P \times P$	component loadings
PCA	λ_q	scalar	qth largest eigenvalue of $\boldsymbol{\Sigma}$
PCA	$\boldsymbol{\Lambda}$	$P \times P$	diagonal matrix of the eigenvalues of $\boldsymbol{\Sigma}$ ($\Lambda_{q,q} = \lambda_q$)
PCA	$\boldsymbol{\Lambda}_Q$	$Q \times Q$	diagonal matrix of the Q largest eigenvalues
PCA	$\boldsymbol{F}$	$N \times Q$	PCA factors : first Q columns of $\boldsymbol{Y}$
PCA	$\boldsymbol{B}$	$P \times Q$	first Q columns of the component loadings
PCA	η_Q	scalar	proportion of variance captured with Q factors
CCA	N	scalar	number of individuals
CCA	J	scalar	number of data blocks
CCA	P_j	scalar	number of variables of the jth data block
CCA	Q	scalar	number of factors taken into account
CCA	$\breve{Q}$	scalar	number of statistically significant factors
CCA	$\boldsymbol{X}_j$	$N \times P_j$	jth data block
CCA	$\hat{\boldsymbol{X}}_j$	$N \times P_j$	linear approximation of $\boldsymbol{X}_j$
CCA	$\boldsymbol{Y}$	$N \times N$	group configuration
CCA	$\hat{\boldsymbol{Y}}_j$	$N \times N$	canonical variates
CCA	$\boldsymbol{A}_j$	$P_j \times N$	canonical weights
CCA	$\boldsymbol{V}_j$	$P_j \times P_j$	reconstruction matrix
CCA	$\boldsymbol{F}$	$N \times Q$	CCA factors : first Q columns of $\boldsymbol{Y}$
CCA	$\boldsymbol{G}$	$N \times N$	$= \sum_{j=1}^{J} \boldsymbol{X}_j \boldsymbol{X}_j^+$
CCA	λ_q	scalar	qth largest eigenvalue of $\boldsymbol{G}$
CCA	$\boldsymbol{\Lambda}$	$Q \times Q$	diagonal matrix of the Q largest eigenvalues ($\Lambda_{q,q} = \lambda_q$)
CCA	$r_{j,q}$	scalar	canonical correlation for block j and factor q
CCA	$\bar{r}_q^2$	scalar	mean square correlation for the qth factor
CCA	$\breve{r}_q^2$	scalar	limit value of statistical significance for $\bar{r}_q^2$
CCA	$\bar{r}_q$	scalar	$=\sqrt{\bar{r}_q^2}$
CCA	$\breve{r}_q$	scalar	$=\sqrt{\breve{r}_q^2}$
CCA	$\eta_{j,q}$	scalar	proportion of variance of the block j captured with q factors
CCA	$\hat{\lambda}_{j,q}$	scalar	$= \eta_{j,q} - \eta_{j,q-1}$

Table 8.2 – Comparison of the symbols used for statistical analyses: Multivariate Linear Regression (MLR), Principal Component Analysis (PCA) and Canonical Correlation Analysis (CCA).

Scores and ranks

If some irregularities (for instance non normal distribution or presence of outliers) are suspected in a variable (i.e. in one of the columns of $\boldsymbol{X}$) , the measured values (called "scores" in statistics) may be transformed into ranks, by sorting the scores in increasing order and replacing the corresponding column in $\boldsymbol{X}$ by the ranks obtained for each individual in the sorted list (in our example the ranks are natural numbers from 1 to 40, because we have 40 reeds). Statistical methods can be applied to ranks instead of to scores. The main advantage is that the results are more robust, while the main drawback is that a part of the information is lost, thus statistical tests become less sensitive. In other words: this technique increases the robustness of the analysis, to the detriment of finesse.

A well known example of application is the Spearman's rank correlation coefficient which may substitute the (usual) Pearson correlation coefficient for the evaluation of the degree of similarity between two variables. The former is actually a Pearson correlation coefficient applied to the ranks obtained by each variable. A "mixed" correlation coefficient could also be evaluated when only one of the variables is transformed into ranks. In this PhD, the word "correlation" always refers to the Pearson correlation formula, while the nature of the analysed variables (scores or ranks) has to be specified.

Identification of outliers

Our aim is to find the individuals who have a preponderant influence on a given statistic we want to compute. One of the simplest methods to identify these outliers is the deviation-based approach: we delete one individual from the database and compute the statistic again and repeat the operation in turn until all individual have been deleted once. The individuals who provoked a noticeable deviation of our statistic may be discarded definitively from the database in the future analyses.

8.4.2 Covariance and Correlation

The covariance (cov) between two vectors $\boldsymbol{x}$ and $\boldsymbol{y}$ is estimated by:

$$\mathrm{cov}(\boldsymbol{x},\boldsymbol{y}) = \frac{1}{N-1}\mathrm{center}(\boldsymbol{x})^T\mathrm{center}(\boldsymbol{y}) \tag{8.1}$$

where $\boldsymbol{x}^T$ is a row vector and $\boldsymbol{y}$ is a column vector.

The correlation ρ between two vectors $\boldsymbol{x}$ and $\boldsymbol{y}$ is estimated by:

$$\rho(\boldsymbol{x},\boldsymbol{y}) = \frac{1}{N-1}\mathrm{std}(\boldsymbol{x})^T\mathrm{std}(\boldsymbol{y}). \tag{8.2}$$

The covariance matrix of the population is estimated from our sample by:

$$\mathrm{cov}(\boldsymbol{X}) = \frac{1}{N-1}\mathrm{center}(\boldsymbol{X})^T\mathrm{center}(\boldsymbol{X}) \tag{8.3}$$

where $\boldsymbol{X}^T$ is the transpose of $\boldsymbol{X}$.

The correlation matrix of the population is estimated from our sample by:

$$\rho(\boldsymbol{X}) = \frac{1}{N-1}\mathrm{std}(\boldsymbol{X})^T\mathrm{std}(\boldsymbol{X}). \tag{8.4}$$

Observe that the covariance and correlation are $P \times P$ matrices. The main diagonal of the correlation matrix is filled with 1 (the correlation of a variable with itself is always 1).

8.4.3 Pseudoinverse of a matrix (inverse of Moore-Penrose)

When the columns of a real matrix $\boldsymbol{X}$ are linearly independent of one another, the matrix $\boldsymbol{X}^T\boldsymbol{X}$ is invertible. Its pseudoinverse $\boldsymbol{X}^+$ is defined as:

$$\boldsymbol{X}^+ = (\boldsymbol{X}^T\boldsymbol{X})^{-1}\boldsymbol{X}^T, \tag{8.5}$$

in which case: $\boldsymbol{X}^+\boldsymbol{X} = \boldsymbol{I}$.

Notice the similarity with the covariance matrix.

The pseudoinverse is commonly used to solve an overdetermined system of linear equations in the sense of least squares.

8.4.4 Linear regression and Multivariate Linear Regression (MLR)

The purpose of linear regression is to provide an estimation (by linear combination) of a vector containing the dependent variables $\boldsymbol{y}$ from a sample matrix $\boldsymbol{X}$ containing the independent variables (regressors, also called predictors) and a vector $\boldsymbol{a}$ containing the regression coefficients. From a random observation $\boldsymbol{x}$, we seek to predict by linear combination a convenient value for y as:

$$y = \boldsymbol{x}^T\boldsymbol{a}. \tag{8.6}$$

How can we estimate an optimal value for $\boldsymbol{a}$?

For our sample matrix of independent variables $\boldsymbol{X}$, this equation reads:

$$\boldsymbol{y} = \boldsymbol{X}\boldsymbol{a}.$$

This system has generally no solution (because $N \gg P$, usually).

We seek a solution that minimizes the quadratic error $S(\boldsymbol{a})$:

$$S(\boldsymbol{a}) = (\boldsymbol{y} - \boldsymbol{X}\boldsymbol{a})^T(\boldsymbol{y} - \boldsymbol{X}\boldsymbol{a}) = \boldsymbol{y}^T\boldsymbol{y} - \boldsymbol{a}^T\boldsymbol{X}^T\boldsymbol{y} - \boldsymbol{y}^T\boldsymbol{X}\boldsymbol{a} + \boldsymbol{a}^T\boldsymbol{X}^T\boldsymbol{X}\boldsymbol{a}.$$

Here, $(\boldsymbol{a}^T\boldsymbol{X}^T\boldsymbol{y})^T = \boldsymbol{y}^T\boldsymbol{X}\boldsymbol{a}$ has the dimension of a scalar. It is therefore equal to its own transpose, hence $\boldsymbol{a}^T\boldsymbol{X}^T\boldsymbol{y} = \boldsymbol{y}^T\boldsymbol{X}\boldsymbol{a}$. The quantity to be minimized becomes:

$$S(\boldsymbol{a}) = \boldsymbol{y}^T\boldsymbol{y} - 2\boldsymbol{a}^T\boldsymbol{X}^T\boldsymbol{y} + \boldsymbol{a}^T\boldsymbol{X}^T\boldsymbol{X}\boldsymbol{a}.$$

Differentiating this with respect to $\boldsymbol{a}$ and equating to $\boldsymbol{0}$ to satisfy the first-order conditions gives

$$-\boldsymbol{X}^T\boldsymbol{y} + (\boldsymbol{X}^T\boldsymbol{X})\boldsymbol{a} = \boldsymbol{0}.$$

A sufficient condition for the satisfaction of the second-order conditions for a maximum is that $\boldsymbol{X}$ have full column rank, in which case $\boldsymbol{X}^T\boldsymbol{X}$ is positive definite. Finally we get:

$$\boldsymbol{a} = (\boldsymbol{X}^T\boldsymbol{X})^{-1}\boldsymbol{X}^T\boldsymbol{y} = \boldsymbol{X}^+\boldsymbol{y}$$

.

This result can be generalized to a multivariate linear regression model (MLR, also called general linear model):

$$\boldsymbol{Y} = \boldsymbol{X}\boldsymbol{A} \tag{8.7}$$

where $\boldsymbol{Y}$ is a data matrix and $\boldsymbol{A}$ is the matrix of the regression coefficients. The minimization problem becomes:

$$\underset{\boldsymbol{A}}{\text{Minimize}} \qquad \operatorname{tr}(\boldsymbol{Y} - \boldsymbol{X}\boldsymbol{A})^T(\boldsymbol{Y} - \boldsymbol{X}\boldsymbol{A}) \tag{8.8}$$

assuming that $\boldsymbol{X}$ is of full column rank.

The least squares solution is:

$$\boldsymbol{A} = \boldsymbol{X}^+\boldsymbol{Y}. \tag{8.9}$$

Regression is often used to predict $\boldsymbol{Y}$ from $\boldsymbol{X}$ or to reconstruct the original data $\boldsymbol{Y}$ from a small set of orthogonal variables, $\boldsymbol{X}$, which are generally obtained by Principal Component Analysis or by Canonical Correlation Analysis (see next paragraphs): $\hat{\boldsymbol{Y}} = \boldsymbol{X}\boldsymbol{A}$.

As explained in §3.6, the affine component may be reintroduced in the regression, by appending a column to $\boldsymbol{X}$ filled with 1. This "variable" bears ordinarily the index 0.

Method	Input	Solution	Projection	Norm.	Minimize
MLR	$\boldsymbol{X}$, $\boldsymbol{Y}$	$\boldsymbol{A} = \boldsymbol{X}^{+}\boldsymbol{Y}$	$\hat{\boldsymbol{Y}} = \boldsymbol{X}\boldsymbol{A}$		$\mathrm{tr}\left(\boldsymbol{Y}-\hat{\boldsymbol{Y}}\right)^{T}\left(\boldsymbol{Y}-\hat{\boldsymbol{Y}}\right)$
PCA	$\boldsymbol{X}$	$\boldsymbol{A}\boldsymbol{\Lambda}\boldsymbol{A}^{T} = \mathrm{cov}(\boldsymbol{X})$ $= \frac{1}{N-1}\boldsymbol{X}^{T}\boldsymbol{X}$	$\boldsymbol{Y} = \boldsymbol{X}\boldsymbol{A}$	$\boldsymbol{A}^{T}\boldsymbol{A} = \boldsymbol{I}$	
CCA	$\boldsymbol{X}_j$	$\boldsymbol{Y}\boldsymbol{\Lambda}\boldsymbol{Y}^{T} = \sum \boldsymbol{X}_j\boldsymbol{X}_j^{+}$ $\boldsymbol{A}_j = \boldsymbol{X}_j^{+}\boldsymbol{Y}$	$\hat{\boldsymbol{Y}}_j = \boldsymbol{X}_j\boldsymbol{A}_j$	$\boldsymbol{Y}^{T}\boldsymbol{Y} = \boldsymbol{I}$	$\mathrm{tr}\sum\left(\boldsymbol{Y}-\hat{\boldsymbol{Y}}_j\right)^{T}\left(\boldsymbol{Y}-\hat{\boldsymbol{Y}}_j\right)$

Table 8.3 – Summary of the essential differences and similarities between the described statistical methods: multivariate linear regression (MLR), Principal Components Analysis (PCA) and Canonical Correlation Analysis (CCA)

8.4.5 Principal component analysis (PCA)

This analysis method is described by Jolliffe, [82], as follows:

The central idea of principal component analysis (PCA) is to reduce the dimensionality of a data set consisting of a large number of interrelated variables, while retaining as much as possible of the variation present in the data set. This is achieved by transforming to a new set of variables, the principal components (PCs), which are uncorrelated, and which are ordered so that the first few retain most of the variation present in all of the original variables.

Having defined PCs, we need to know how to find them. Consider, for the moment, the case where the vector of random variables $\boldsymbol{x}$ has a known covariance matrix $\boldsymbol{\Sigma} : P \times P$. This is the matrix whose (i, j)th element is the (known) covariance between the ith and jth elements of $\boldsymbol{x}$ when $i \neq j$, and the variance of the jth element of $\boldsymbol{x}$ when $i = j$. The more realistic case, where $\boldsymbol{\Sigma}$ is unknown, follows by replacing $\boldsymbol{\Sigma}$ by a sample covariance matrix. It turns out that for $k = 1, 2, \cdots, P$, the kth PC is given by $y_k = \boldsymbol{a}_k^{T}\boldsymbol{x}$ where $\boldsymbol{a}_k$ is an eigenvector of $\boldsymbol{\Sigma}$ corresponding to its kth largest eigenvalue λ_k. Furthermore, if $\boldsymbol{a}_k$ is chosen to have unit length ($\boldsymbol{a}_k^{T}\boldsymbol{a}_k = 1$), then $\mathrm{var}(y_k) = \lambda_k$, where $\mathrm{var}(y_k)$ denotes the variance of y_k.

To derive the form of the PCs, consider first $\boldsymbol{a}_1^{T}\boldsymbol{x}$; the vector $\boldsymbol{a}_1$ maximizes $\mathrm{var}(\boldsymbol{a}_1^{T}\boldsymbol{x}) = \boldsymbol{a}_1^{T}\boldsymbol{\Sigma}\boldsymbol{a}_1$. To maximize $\boldsymbol{a}_1^{T}\boldsymbol{\Sigma}\boldsymbol{a}_1$ subject to $\boldsymbol{a}_1^{T}\boldsymbol{a}_1 = 1$, the standard approach is to use the technique of Lagrange multipliers. Maximize

$$\boldsymbol{a}_1^{T}\boldsymbol{\Sigma}\boldsymbol{a}_1 - \lambda(\boldsymbol{a}_1^{T}\boldsymbol{a}_1 - 1),$$

where λ is a Lagrange multiplier. Differentiation with respect to $\boldsymbol{a}_1$ gives

$$\boldsymbol{\Sigma}\boldsymbol{a}_1 - \lambda\boldsymbol{a}_1 = 0 = (\boldsymbol{\Sigma} - \lambda\boldsymbol{I}_P)\boldsymbol{a}_1.$$

Thus, λ is an eigenvalue of $\boldsymbol{\Sigma}$ and $\boldsymbol{a}_1$ is the corresponding eigenvector. To decide which of the P eigenvectors gives $\boldsymbol{a}_1^{T}\boldsymbol{x}$ with maximum variance, note that the quantity to be maximized is $\boldsymbol{a}_1^{T}\boldsymbol{\Sigma}\boldsymbol{a}_1 = \boldsymbol{a}_1^{T}\lambda\boldsymbol{a}_1 = \lambda\boldsymbol{a}_1^{T}\boldsymbol{a}_1 = \lambda$, so λ must be as large as possible. Thus, $\boldsymbol{a}_1$ is the eigenvector corresponding to the largest eigenvalue of $\boldsymbol{\Sigma}$, and $\mathrm{var}(\boldsymbol{a}_1^{T}x) = \boldsymbol{a}_1^{T}\boldsymbol{\Sigma}\boldsymbol{a}_1 = \lambda_1$, the largest eigenvalue. In general, the kth PC of x is $\boldsymbol{a}_k^{T}x$ and $\mathrm{var}(\boldsymbol{a}_k^{T}x) = \lambda_k$, where λ_k is the kth largest eigenvalue of $\boldsymbol{\Sigma}$, and $\boldsymbol{a}_k$ is the corresponding eigenvector. The proof of this is given in [82], p. 5 ff.

In matrix form, this is written

$$\boldsymbol{Y} = \boldsymbol{X}\boldsymbol{A}, \tag{8.10}$$

where the columns of $\boldsymbol{A}$ are the eigenvectors of $\boldsymbol{\Sigma}$ (i.e. $\boldsymbol{\Sigma} = \boldsymbol{A}\boldsymbol{\Lambda}\boldsymbol{A}^{T}$, where $\boldsymbol{\Lambda}$ is the diagonal matrix of the eigenvalues of $\boldsymbol{\Sigma}$, sorted from the largest to the smallest and $\boldsymbol{A}^{T}\boldsymbol{A} = \boldsymbol{I}$). This orthonormal transformation do not change the total variance of the sample: $\mathrm{tr}\left(\mathrm{cov}\left(\boldsymbol{Y}\right)\right) = \mathrm{tr}\left(\mathrm{cov}\left(\boldsymbol{X}\right)\right) = \mathrm{tr}\left(\boldsymbol{\Lambda}\right)$.

We examine now how to compress the information with minimal loss. For any integer Q, $1 \leq Q \leq P$, let us consider the matrix $\boldsymbol{B} : P \times Q$ of the Q first columns of $\boldsymbol{A}$ and the orthonormal transformation:

$$\boldsymbol{F} = \boldsymbol{X}\boldsymbol{B} \tag{8.11}$$

It can be shown that $\boldsymbol{B}$ maximize $\mathrm{tr}(\mathrm{cov}(\boldsymbol{F}))$, subject to the constraint $\boldsymbol{B}^{T}\boldsymbol{B} = \boldsymbol{I}$, because $\mathrm{cov}(\boldsymbol{F}) = 1/(N-1)\boldsymbol{F}^{T}\boldsymbol{F} = 1/(N-1)\boldsymbol{B}^{T}\boldsymbol{X}^{T}\boldsymbol{X}\boldsymbol{B} = \boldsymbol{B}^{T}\boldsymbol{A}\boldsymbol{\Lambda}\boldsymbol{A}^{T}\boldsymbol{B} = \boldsymbol{\Lambda}_Q$, where $\boldsymbol{\Lambda}_Q$ is the

diagonal matrix of the Q largest eigenvalues of $\boldsymbol{\Sigma}$. Note that $\boldsymbol{F}$ is (generally) of full column rank if $Q \leq \min(N, P)$.

$\boldsymbol{F}$, the $N \times Q$ matrix of the PC scores captures

$$\eta_Q = \frac{\mathrm{tr}\left(\mathrm{cov}\left(\boldsymbol{F}\right)\right)}{\mathrm{tr}\left(\mathrm{cov}\left(\boldsymbol{Y}\right)\right)} = \frac{\mathrm{tr}\left(\mathrm{cov}\left(\hat{\boldsymbol{X}}\right)\right)}{\mathrm{tr}\left(\mathrm{cov}\left(\boldsymbol{X}\right)\right)} = \frac{\mathrm{tr}\left(\boldsymbol{\Lambda}_Q\right)}{\mathrm{tr}\left(\boldsymbol{\Lambda}\right)} = \frac{\sum_{k=1}^{Q} \lambda_k}{\sum_{k=1}^{P} \lambda_k} \tag{8.12}$$

$100 \times \eta_Q$ percent of the variance of $\boldsymbol{X}$. The plot of λ_k as a function of k is called "scree plot". The number Q of factors to retain for an optimal compression of the data can be determined by inspection of the scree plot, by finding an "elbow" in the curve.

The PCA can be viewed as a method of compression of data (from P down to Q components) with minimal loss of information in the sense of least squares. The original data can be approximated (reconstructed) by Multivariate Linear Regression, taking the pseudoinverse of Eq 8.11:

$$\hat{\boldsymbol{X}} = \boldsymbol{F}\boldsymbol{B}^{+} = \boldsymbol{F}(\boldsymbol{B}^T\boldsymbol{B})^{-1}\boldsymbol{B}^T = \boldsymbol{F}\boldsymbol{I}\boldsymbol{B}^T = \boldsymbol{F}\boldsymbol{B}^T \tag{8.13}$$

The reconstructed data is denoted $\hat{\boldsymbol{X}}$.

8.4.6 Canonical-correlation analysis (CCA)

The statistical methods described in the previous § apply to a single set of variables (i.e. to a single data block), $\boldsymbol{X}$. Let us consider now J data blocks $\boldsymbol{X}_j$ of dimension $(N \times P_j)$. We assume that all the columns of $\boldsymbol{X}_j$ are linearly independent of each another. $\boldsymbol{X}_j$ is therefore of full column rank. This implies in particular that $P_j \leq N$. If this is not the case, a PCA can be applied to the data, for instance, in order to get a full column rank matrix $\boldsymbol{X}_j$.

The Canonical Correlation Analysis (CCA) [165, 177, 12, 76, 47, 166, 162, 169, 160, 159, 161, 158] compares $J = 2$ groups of quantitative variables (data blocks) taken on the same individuals. The purpose is to compare these two blocks to see if they describe the same phenomenon. According to [169], the aim of CCA is to find linear combinations for two sets of variables in such a way that the correlation between the two linear combinations is maximal. Let: $\boldsymbol{X}_1 : N \times P_1$ and $\boldsymbol{X}_2 : N \times P_2$ denote centered and standardized data matrices. The idea is to construct $\hat{\boldsymbol{y}}_1 = \boldsymbol{X}_1\boldsymbol{a}_1$ and $\hat{\boldsymbol{y}}_2 = \boldsymbol{X}_2\boldsymbol{a}_2$ so that the correlation between $\hat{\boldsymbol{y}}_1$ and $\hat{\boldsymbol{y}}_2$ is maximal:

$$\begin{array}{ll} \underset{\boldsymbol{a}_j, \hat{\boldsymbol{y}}_j}{\text{Maximize}} & \rho(\hat{\boldsymbol{y}}_1, \hat{\boldsymbol{y}}_2) \\ \text{subject to} & \hat{\boldsymbol{y}}_j^T\hat{\boldsymbol{y}}_j = 1 \end{array} \tag{8.14}$$

The vectors $\hat{\boldsymbol{y}}_1$ and $\hat{\boldsymbol{y}}_2$ are the canonical variates. These canonical variates are standardized: $\hat{\boldsymbol{y}}_j^T\hat{\boldsymbol{y}}_j = 1$. The vectors $\boldsymbol{a}_1$ and $\boldsymbol{a}_2$ are often referred to as canonical weights. Instead of obtaining only two canonical variates, additional variates may be constructed that are orthogonal with respect to the previous ones. Then: $\hat{\boldsymbol{Y}}_1 = \boldsymbol{X}_1\boldsymbol{A}_1$ and $\hat{\boldsymbol{Y}}_2 = \boldsymbol{X}_2\boldsymbol{A}_2$, suject to the constraint $\hat{\boldsymbol{Y}}_j^T\hat{\boldsymbol{Y}}_j = \boldsymbol{I}$.

The **generalized** canonical correlation analysis performs this analysis simultaneously on J data blocks inside the measurement corpus. Many different algorithms have been proposed for this purpose. In an early stage, the methodology described in [160] was applied to our data. Following the advice of a jury member, Jean-François Petiot, the method proposed in 1968 by Carroll was finally retained for the analysis of the data presented here. This method is easy to apply, concise and well suited for our purpose [12].

Crucial in Carroll's method is the introduction of a so-called group configuration $\boldsymbol{Y}$. The canonical variates $\hat{\boldsymbol{Y}}_j = \boldsymbol{X}_j\boldsymbol{A}_j$ are chosen in such a way that the sum of squared correlations between them and the group configuration is at a maximum. This is equivalent to the following minimization problem:

$$\begin{array}{ll} \underset{\boldsymbol{A}, \boldsymbol{Y}}{\text{Minimize}} & \mathrm{tr}\sum_{j=1}^{J}\left(\boldsymbol{Y} - \boldsymbol{X}_j\boldsymbol{A}_j\right)^T\left(\boldsymbol{Y} - \boldsymbol{X}_j\boldsymbol{A}_j\right) \\ \text{subject to} & \boldsymbol{Y}^T\boldsymbol{Y} = \boldsymbol{I} \end{array} \tag{8.15}$$

12. The statistical significance of the results obtained with both method is practically identical. It was tested for both methods with the same algorithm: by Monte-Carlo simulation.

The group configuration matrix $\boldsymbol{Y}$ can be obtained by solving the eigenequation:

$$\boldsymbol{G}\boldsymbol{Y} = \boldsymbol{Y}\boldsymbol{\Lambda} \tag{8.16}$$

where $\boldsymbol{G} = \sum_{j=1}^{J} \boldsymbol{X}_j \boldsymbol{X}_j^+$ and $\boldsymbol{\Lambda}$ is the diagonal matrix of the eigenvalues of $\boldsymbol{G}$. The columns of $\boldsymbol{Y}$ are the eigenvectors of $\boldsymbol{G}$. As before, the eigenvalues are sorted from the largest to the smallest. The matrices $\boldsymbol{A}_j$ can be calculated as

$$\boldsymbol{A}_j = \boldsymbol{X}_j^+ \boldsymbol{Y}.$$

For the jth data bloc, the qth canonical correlation (denoted $r_{j,q}$) is computed as the correlation between the qth column of respectively$\hat{\boldsymbol{Y}}_{\boldsymbol{j}}$ and $\boldsymbol{Y}$:

$$r_{j,q} = \rho(\hat{Y}_{j,\bullet,q}, Y_{\bullet,q}) \tag{8.17}$$

The symbol $\bullet$ indicates that all occurrences of the corresponding index are retained (i.e. the correlation $r_{j,q}$ is computed between two vectors).

The mean square correlation for the qth canonical factor, denoted $\bar{r}_q^2$, is:

$$\bar{r}_q^2 = \frac{1}{J} \sum_{j=1}^{J} r_{j,q}^2 \tag{8.18}$$

Notice that maximizing $\sum_{n=1}^{N} \bar{r}_n^2$ is equivalent to minimizing Eq. 8.15.

Number of statistically significant factors

The probability (P-value) that a mean square correlation greater than the observed value $\bar{r}_q^2$ can be obtained although the null hypothesis H_0 is true (i.e. there is no relationship between the data blocks $\boldsymbol{X}_j$ for the factor q) can be computed by the Monte-Carlo method, for instance. Alternatively, a limit value, $\breve{r}_q^2$, can be determined for a given threshold of significance (for instance at the 1% level). If $\bar{r}_q^2 > \breve{r}_q^2$, H_0 is rejected: the qth CCA factor is statistically significant (or shortly: the qth factor is significant). Once a non-significant factor has been detected, all subsequent factors are considered non-significant [13].

Generally, the threshold of significance is set between 1 and 5%. Here, we are more restrictive: in most cases the 0.1% level is considered. An example of computation of the limit of significance $\breve{r}_q$ by Monte-Carlo with 10'000 random draws (with gaussian distribution) is given on Fig. 8.13 for the case: $N = 40$ reeds, $J = 5$ blocks and $P_j = 15$ variables.

The detection of significant factors is sensitive to the number of variables in each block. This number must be determined carefully, especially when the blocks are compressed by PCA: if too much of meaningless random noise is included in $\boldsymbol{X}_j$, the number of significant factors decreases, because some of the pertinent information which is difficult to detect is drowned in the noise. Similarly, if too less degrees of freedom are given to build $\boldsymbol{Y}$, the number of significant factors decreases. A good balance has to be found between these two extremes. As a rule of thumb, this number should be 2-5 units larger than $\breve{Q}$ (but also not much higher than $N/4$ - $N/3$).

Reconstruction of the information

Once the number Q of retained factors is determined (usually $Q \leq \breve{Q}$), the matrix $\boldsymbol{F}$ of the CCA factors is obtained by taking the Q first columns of $\boldsymbol{Y}$. The matrix $\boldsymbol{F}$ is considered as the quintessence of the data, summarizing the relevant information which is common to all data blocks of the analysis. One expects that every data block can be reconstructed with minimal loss of information by MLR:

$$\hat{\boldsymbol{X}}_j = \boldsymbol{F}\boldsymbol{V}_j \tag{8.19}$$

13. In order to allow a comparison with the magnitude of the correlations, we perform the statistical tests on the **square root** of the mean square correlation: $\bar{r}_q = \sqrt{\bar{r}_q^2}$ and the limit of significance is: $\breve{r}_q = \sqrt{\breve{r}_q^2}$

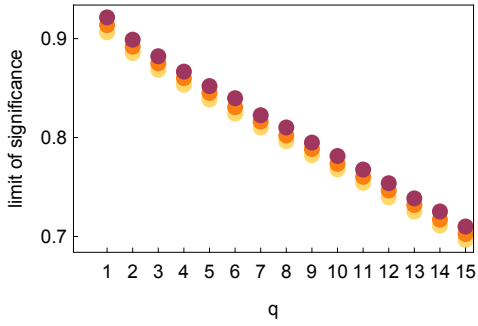

Figure 8.13 – Limit value $\breve{r}_q$ for the thresholds of significance 5%, 1% and 0.1% (respectively from light to dark), for the case: $N = 40$ reeds, $J = 5$ blocks and $P_j = 15$ variables, assuming gaussian distribution. If the observed value of $\bar{r}_q$ is greater than $\breve{r}_q$, the null hypothesis H_0 is rejected (i.e. we admit that the qth canonical correlation is greater than 0 for a least 2 blocks, with a probability of being wrong smaller than the threshold of significance we have chosen). The square root of $\breve{r}_q^2$ is illustrated on this plot, in order to allow a direct comparison with the magnitude of the canonical correlations.

Taking the pseudoinverse, the reconstruction matrix $\boldsymbol{V}_j$ is obtained:

$$\boldsymbol{V}_j = \boldsymbol{F}^T \boldsymbol{X}_j \tag{8.20}$$

because, by construction $\boldsymbol{F}^T \boldsymbol{F} = \boldsymbol{I}$, therefore $\boldsymbol{F}^+ = \boldsymbol{F}^T$.

The MLR can be applied not only to the J data blocks analysed by CCA, but also to every kind of data that could possibly share some common information: raw data, excerpts of data, transformed data, data of other measurements, data from a simulation model, and so on. For instance, the subjective evaluations by the clarinettist can possibly be reconstructed by the matrix $\boldsymbol{F}$ obtained from a CCA made on objective measurements. If this succeeds, $\boldsymbol{F}$ is considered as a relevant indicator for predicting the musical evaluation of the reeds (see §8.5.5). An other concern is to find a measurement method which is able to provide a good estimation of $\boldsymbol{F}$, at minimal cost, in our example for instance by analysis of the photos of the channel made directly by the reed maker in the manufacture (see §D.2). This way a rating method may be developed.

Number of factors to retain for a robust prediction, Scree plot

In order to enhance the robustness of the prediction, the number Q of factors used as predictors should not be taken too large. A reasonable choice is $Q < N/6$, so maximally 6 factors have been retained as predictors for our sample of $N = 40$ reeds, even if more significant factors are available.

The number of factor to retain can also determined by examination of the scree plot (*via* the proportion of explained variance). Similarly to Eq. 8.12, the proportion of variance captured by the reconstruction is:

$$\eta_{j,q} = \frac{\mathrm{tr}\left(\mathrm{cov}\left(\hat{\boldsymbol{X}}_j\right)\right)}{\mathrm{tr}\left(\mathrm{cov}\left(\boldsymbol{X}_j\right)\right)} \tag{8.21}$$

The scree plot is obtained by plotting $\hat{\lambda}_{j,q} = \eta_{j,q} - \eta_{j,q-1}$ as a function of q and j. Similarly to the PCA case, the number of factors to retain can be determined by inspection of the scree plot, by finding an "elbow" in the curve.

It should be mentioned that the amount of reconstructed variance must be considered carefully with respect to the context: for instance the value of $\eta_{j,q}$ may be much higher for a measured quantity than for its *derivative*. The physical context must be considered.

A more didactic introduction to CCA can be found in Appendix C.

8.4.7 Philosophy adopted for the data analysis

Given the considerable amount of data collected (around 100 GB), prior to analysis, it is essential to concentrate the information using parsimonious representations. For physical measurements, which are particularly varied and voluminous - even after linear compression of each collected block of data by Principal Component Analysis (PCA, §8.4.5) - we will take advantage of the diversity of the experiments to gain some knowledge on the hidden structures (CCA factors) common to all data blocks, by Canonical-Correlation Analysis (CCA, §8.4.6). The factors obtained by PCA and by CCA will serve as a basis for further analyses. This supposes a hierarchical organization of the analyses.

Interpretation of the results

The results of a CCA may be interpreted in different ways. In the following, each data matrix $\boldsymbol{X}_j$ included in the analysis is considered as a block (even if it is derived from a group of blocks).

statistical significance The number $\breve{Q}$ of statistically significant factors is a measure of the dimensionality of the redundancy among the analysed blocks. Factors are detected if similar information is present in more than one block. Pertinent information which is present only in one block is discarded by the analysis. We must bear this in mind by the interpretation of the results.

inspection of $r_{j,q}$ The inspection of the canonical correlations $r_{j,q}$ reveals the degree of congruence of each block, within the qth CCA factor. A comparison with the limit value of significance $\breve{r}_q$ is instructive: the contribution of each block to $\bar{r}_q$ can be evaluated. A correlation higher than this value is a signal that the block is well representative of some properties characterizing the reeds for this factor. A relatively low correlation is more difficult to interpret. It may signal:

- presence of irrelevant measures
- presence of artifacts
- human errors in the measurement protocol
- uncertainties on the measured quantities

scree plot The optimal number of factors to retain, Q, can be determined by inspection of the scree plot ($\hat{\lambda}_{j,q}$), by finding "elbows" in the curves.

inspection of $\boldsymbol{V}_j$ The results may also be interpreted in a more intuitive way: in the light of the raw physical measurement, without any compression or treatment of the data, by inspection of the matrix $\boldsymbol{V}_j$, Eq. 8.20.

Designation of the factors

In this PhD, the Principal Component scores (Q first columns of the matrix $\boldsymbol{Y}$, in §8.4.5) are named "PCA factors", in contrast to "CCA factors" (Q first columns of the group configuration matrix $\boldsymbol{Y}$, in §8.4.6).

8.4.8 Database and analyse structure

The database and the analyses are structured according to 3 hierarchical levels of "concentration" of the information:

1. raw data blocks
2. blocks of PCA factors (each block concentrates most of the information of one block of raw data into a matrix of orthogonal PCA factors of full column rank)
3. blocks of CCA factors (each block concentrates most of the information common to all members of a group of blocks, into a matrix of orthogonal CCA factors of full column rank)

Further hierarchical levels could be considered (i.e. groups of groups of blocks of factors). I prefer a "recursive" definition of hierarchical level 3: any group of blocks of factors taken in the hierarchical levels 2 and 3 can be analysed by CCA to form a new group at level 3, concentrating most of the information common to all members of the group, into a matrix of orthogonal CCA factors.

The hierarchical level 1 is never analyzed by CCA for 2 reasons:

1. The number of variables P_j exceeds N in practically all cases. A data compression by PCA is mandatory since Carroll's CCA requires full rank column matrices.
2. The statistical tests I developed require that the variables in each data block are independent from each other (i.e. $\boldsymbol{X}_j$ must be orthogonal).

A hierarchical structuration is also helpful for the following reasons:

In a CCA, all analyzed data blocks are treated with the same weight. The CCA does not make any distinction among data blocks (such as a distinction between predictors and dependent data blocks, like in MLR). The proposed hierarchical structure helps to focus the analysis at the desired level of abstraction. This restores a good balance between the weights of the analysed groups, especially if the number of members of each group is very different (this would not be the case if all blocks were put in one single melting pot for the CCA analysis). Moreover, this structuration helps also the reader to identify easily the members of each group composing an analysis, thanks to a convention about the identifiers of the blocks at the different hierarchical levels:

level 1 First letter of the identifier in uppercase, see Table 8.4.

level 2 First letter and last letter of the identifier in lowercase, see Table 8.5.

level 3 First letter of the identifier in lowercase and last letter of the identifier in uppercase, see Table 8.6. The last letter indicates if the CCA is performed:

"F" : directly on the factor scores of all blocks involved in the analysis.

"R" : after conversion of the factor scores into ranks.

The data blocks containing the raw measurements are detailed in Table 8.4. The number of measurements made for each of the 40 reeds is indicated in the Table. This Table summarizes the first hierarchical level of the data structure (raw measurements).

The raw data blocks are then compressed by PCA to constitute blocks of PCA factors (orthogonal to each other; no rotation of VARIMAX type has been performed). The details can be taken from Table 8.5. This table summarizes the second hierarchical level of the data structure (measurements, compressed by PCA).

The information is then concentrated by CCA, for different groups of PCA blocks. This constitute the superior hierarchical structure of the database. Details are recorded in Table 8.6 (CCA factors).

Table 8.7 presents an overview of the different analyses of hierarchical level 3, according to the category of the analysed data.

8.5 Data analysis

In this section, the corpus of data is analysed with the methods described in the previous section.

8.5.1 Diagnosis about irregularities in the data

In order to detect possible irregularities in the data let us examine the number $\breve{Q}$ of statistically significant factors at the 0.1% level, indicated in Table 8.6, column 4. A very good concordance is observed between all analyses performed on factor scores (identifier ending with letter "F") and the corresponding analyses after transformations of the factor scores into ranks (same identifier ending with letter "R"). As expected, $\breve{Q}$ is sometimes lower for the rank based analyses, since some information is lost in the transformation. The difference is quite marginal: maximally one significant factor less (and this for 3 blocs only: static, subjective and objective).

Identifier	number of measurements	Comment
PhotoNew	540	pictures of the channel for the new reed, 16 embouchures and 2 pictures at rest (before and after measurement)
PhotoBreakIn	810	pictures of the channel for the break-in reed, 25 embouchures and 2 pictures at rest (before and after measurement)
Aero	497	aeraulic section, as a function of ψ and Δp
OptoLeft	497	mechanical deflection of the reed on the left side during the aeraulic measurements, as a function of ψ and Δp
OptoRight	497	mechanical deflection of the reed on the right side during the aeraulic measurements, as a function of ψ and Δp
		Measured diagrams of bifurcation:
MThres	16	Emergence and extinction thresholds (4 embouchures × 2 ramps × 2 thresholds)
MPlayFreq	320	Playing frequencies (4 embouchures × 2 ramps × 40 adim. supply pressures)
M###	32 × 2400	Measured signals (4 sensors × 4 embouchures × 2 ramps) × (40 adimensioned supply pressures × 60 discrete points)
		Synthesized diagrams of bifurcation:
SThres	16	Emergence and extinction thresholds (4 embouchures × 2 ramps × 2 thresholds)
SPlayFreq	320	Playing frequencies (4 embouchures × 2 ramps × 40 adim. supply pressures)
S###	24 × 2400	Synthesized signals (3 signals × 4 embouchures × 2 ramps) × (40 adimensioned supply pressures × 60 discrete points)
ReedDeflec	71	reed deflection: discrete points from which the reed model described in Chapter 5 was fitted for the simulations
ReedAero	71	aeraulic section: discrete points from which the reed model described in Chapter 5 was fitted for the simulations
Test1	4	Subjective evaluation of 4 descriptors, 1st repetition
Test2	4	Subjective evaluation of 4 descriptors, 2nd repetition
Test3	4	Subjective evaluation of 4 descriptors, 3rd repetition
Test4	4	Subjective evaluation of 4 descriptors, 4th repetition
StdSubj	4	Standardized mean of each of the 4 subjective descriptors over the 4 repetitions
StrengthNom	1	Nominal strength of the reed, indicated by the manufacturer

Table 8.4 – Hierarchical level 1: Raw data of the corpus of measurements, collected for each of the 40 reeds. For the bifurcation diagrams: The 4 sensors are 1: pressure in mouthpiece, 2: pressure in container, 3: reed deflection, left optical sensor, 4: reed deflection, right optical sensor. The 3 synthesized signals are 1: pressure in mouthpiece, 2: flow rate in mouthpiece, 3: reed deflection. The 4 embouchures are $1 : \psi_1 = 2.125$ mm, $2 : \psi_2 = 2.000$ mm, $3 : \psi_3 = 1.875$ mm and $4 : \psi_4 = 1.750$ mm. The 2 ramps are: 1: *crescendo*, 2: *decrescendo*.

Identifier	Q	Centered or Standardized	raw data to compress
photoNew	15	C	PhotoNew
photoBreakIn	15	C	PhotoBreakIn
aero	15	C	Aero
optoLeft	15	C	OptoLeft
optoRight	15	C	OptoRight
mThres	15	C	MThres
mPlayFreq	15	C	MPlayFreq
m###	32×15	C	M###
sThres	15	C	SThres
sPlayFreq	15	C	SPlayFreq
s###	24×15	C	S###
reedDeflec	15	C	ReedDeflec
reedAero	15	C	ReedAero
test1	4	S	Test1
test2	4	S	Test2
test3	4	S	Test3
test4	4	S	Test4

Table 8.5 – Hierarchical level 2: blocks of PCA factors. The PCA is computed from the eigenvalues of the covariance matrix for the blocks indicated with "C" in the third column (and of the correlation matrix for the blocks indicated with "S").

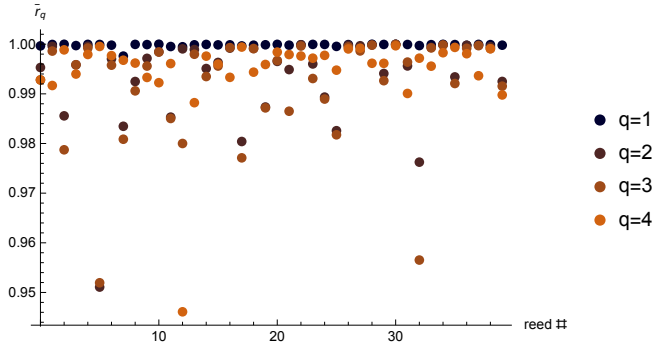

Figure 8.14 – Detection of outliers by a deviation-based approach: for the CCA analysis *staticF*, $\bar{r}_q$ is computed by deleting in turn each reed of the panel. Note the relative importance of the reeds R05, R12 and R32 for the factors $q = 2$ to 4. The limit of significance $\breve{r}_q$ at the 0.1% level is 0.899 for $q = 2$.

We have therefore no serious problems with outliers or with nonlinear distribution of the data. All subsequent analyses can safely be performed exclusively on the factor scores.

In Fig. 8.14, an attempt is made to identify possible outliers among the static measurements by CCA. It is observed that the reeds R05 and R12 have a noticeable influence on the factors 2 and 3 and that the reed R32 has a noticeable influence on the factor 4. This influence is considered to be not problematic (provided $\breve{r}_2 = 0.899$ at the 0.1% level), so the corresponding reeds were not deleted from the data corpus. Note that these reeds are particularly soft or strong: reed R05 is of strength 2, while the 2 others are of strength 3 1/2. Their particular influence in the analyses is probably due to nonlinear effects in the measures.

Identifier	P_j	J	$\breve{Q}$	**Analysed group of data blocks**
staticF	15	5	14	photoNew, photoBreakIn, aero, optoLeft, optoRight
staticR	15	5	13	photoNew, photoBreakIn, aero, optoLeft, optoRight
bifurcationF	15	34	14	mThres, mPlayFreq, m111 to m424 (2+32 blocs)
bifurcationR	15	34	14	mThres, mPlayFreq, m111 to m424 (2+32 blocs)
synthesisF	15	26	15	sThres, sPlayFreq, s111 to s324 (2+24 blocs)
synthesisR	15	26	15	sThres, sPlayFreq, s111 to s324 (2+24 blocs)
reedF	15	2	4	reedDeflec, reedAero
reedR	15	2	4	reedDeflec, reedAero
subjectiveF	4	4	3	test1, test2, test3, test4
subjectiveR	4	4	2	test1, test2, test3, test4
objectiveF	15	6	14	photoNew, photoBreakIn, aero, optoLeft, optoRight, bifurcationF
objectiveR	15	6	13	photoNew, photoBreakIn, aero, optoLeft, optoRight, bifurcationF
objSubjF	6	2	4	objectiveF, subjectiveF
objSubjR	6	2	4	objectiveF, subjectiveF
statSubjF	6	2	4	staticF, subjectiveF
statSubjR	6	2	4	staticF, subjectiveF
bifSubjF	6	2	3	bifurcationF, subjectiveF
bifSubjR	6	2	3	bifurcationF, subjectiveF
synthSubjF	6	2	2	synthesisF, subjectiveF
synthSubjR	6	2	2	synthesisF, subjectiveF
bifSynthF	15	2	13	bifurcationF, synthesisF
bifSynthR	15	2	13	bifurcationF, synthesisF
bifStatF	15	2	11	bifurcationF, staticF
bifStatR	15	2	11	bifurcationF, staticF
statReedF	6	2	5	staticF, reedF
statReedR	6	2	5	staticF, reedF
synthReedF	6	2	5	synthesisF, reedF
synthReedR	6	2	5	synthesisF, reedF
totalF	6	5	6	staticF, bifurcationF, synthesisF, reedF, subjectiveF
totalR	6	5	6	staticF, bifurcationF, synthesisF, reedF, subjectiveF

Table 8.6 – Hierarchical level 3: blocks of CCA factors. **Column 1**: identifer of the CCA analysis. The last letter indicates if the CCA is performed directly on the factor scores of each block ("F") or after conversion of the factor scores of each block into ranks ("R"). **Column 2**: number of variables in each block P_j. **Column 3**: number of blocks J. **Column 4**: number $\breve{Q}$ of statistically significant factors at the 0.1% level. **Column 5**: list of blocks involved in the CCA. The CCAs involving CCA factors are in the lower part of the Table.

Identifier	**objective**	**synthesis**	**subjective**	***static***	***dynamic***
staticF	■			▲	
bifurcationF	■				▲
synthesisF		■			▲
reedF		■		▲	
subjectiveF			■		▲
objectiveF	■			▲	▲
objSubjF	■		■	▲	▲
statSubjF	■		■	▲	▲
bifSubjF	■		■		▲
synthSubjF		■	■		▲
bifSynthF	■	■			▲
bifStatF	■			▲	▲
statReedF	■	■		▲	
synthReedF		■		▲	▲
totalF	■	■	■	▲	▲

Table 8.7 – Hierarchical level 3: overview of the analyses, according to the categories **objective**, **synthesis** and **subjective** and according to the *static* and *dynamic* nature of the data.

Identifier	P_j	J	$\breve{Q}$	**fact. 1**	**fact. 2**	**fact. 3**	**fact. 4**	**fact. 5**	**fact. 6**
staticF	15	5	14	0.9947	0.9757	0.9645	0.9319	0.9104	0.8674
bifurcationF	15	34	14	0.9986	0.9878	0.9666	0.9517	0.9411	0.8993
synthesisF	15	26	15	0.9992	0.9962	0.9877	0.9825	0.9684	0.9678
reedF	15	2	4	0.9995	0.9976	0.9893	0.9727	0.9558	0.8820
subjectiveF	4	4	3	0.9519	0.8808	0.6963	*0.5935*		
objectiveF	15	6	14	0.9952	0.9768	0.9660	0.9339	0.9151	0.8695
objSubjF	6	2	4	0.9880	0.9601	0.9095	0.8848	*0.7916*	*0.7746*
statSubjF	6	2	4	0.9883	0.9571	0.9092	0.8845	*0.7928*	*0.7781*
bifSubjF	6	2	3	0.9840	0.9547	0.9008	*0.8425*	*0.7659*	*0.7184*
synthSubjF	6	2	2	0.9843	0.9347	*0.8722*	*0.8309*	*0.7906*	*0.7491*
bifSynthF	15	2	13	0.9998	0.9986	0.9969	0.9934	0.9905	0.9890
bifStatF	15	2	11	0.9997	0.9983	0.9972	0.9951	0.9917	0.9869
statReedF	6	2	5	0.9989	0.9943	0.9829	0.9756	0.8913	*0.7362*
synthReedF	6	2	5	0.9979	0.9872	0.9742	0.9342	0.8507	*0.7589*
totalF	6	5	6	0.9859	0.9409	0.8827	0.8352	0.7578	0.6816

Table 8.8 – Square root of the mean square correlations $\bar{r}_q = \sqrt{\bar{r}_q^2}$ for all (scores based) CCAs of Table 8.6 for the factors $q = 1, \ldots, 6$. Statistically non significant correlations at the 0.1% level are indicated in *italic*.

P_j	J	**factor 1**	**factor 2**	**factor 3**	**factor 4**	**factor 5**	**factor 6**
15	2	0.997	0.991	0.984	0.975	0.964	0.953
15	5	0.923	0.899	0.883	0.866	0.853	0.839
15	6	0.902	0.879	0.862	0.847	0.833	0.822
15	26	0.772	0.756	0.744	0.734	0.726	0.718
15	34	0.754	0.739	0.729	0.720	0.713	0.706
6	2	0.955	0.921	0.891	0.859	0.825	0.785
6	4	0.832	0.787	0.754	0.726	0.697	0.672
4	2	0.934	0.883	0.842	0.796		
4	4	0.791	0.734	0.694	0.660		
1	4	0.685					

Table 8.9 – Significance limit $\breve{r}_q$ at the 0.1% level ($N = 40$ reeds), assuming gaussian distribution of the data, for scores based CCAs in function of P_j and J. If $\bar{r}_q$ is smaller than the limit, the corresponding factor is statistically non significant. These limits are computed by Monte-Carlo, with 10'000 random draws (although the limit cannot be precisely determined with only 10'000 random draws).

8.5.2 Evaluation of the repeatability of the subjective evaluations

Inside each individual descriptor ($P_j = 1$ variable, $J = 4$ repetitions), very significant mean square correlations are found by a CCA analysis [14]. The values of $\bar{r}_1$ obtained for each descriptor (*ForceSubj*, *Poulenc*, *Schubert* and *Intonation*) are respectively: 0.930, 0.813, 0.807 and 0.868. A value higher than 0.685 is sufficient to assert a statistically significant link between the 4 repetitions of the evaluation of one descriptor, at the 0.1% level (see $\breve{r}_1$, Table 8.9, $P_j = 1$ and $J = 4$). The result is quasi identical, if the analysis is performed on the ranks: $\bar{r}_1 = 0.930$, 0.813, 0.807 and 0.870. $\breve{r}_1$=0.675.

To allow a comparison with the study of Muñoz [105], let us perform a one-way ANOVA for the 4 repetitions of each descriptor (despite the fact that their distributions are possibly not normal, as required by test). We obtain a F-ratio for each respective descriptor of 18.9, 4.9, 4.8 and 5.2, which corresponds - for the worst of them (Schubert) - to a p-value lower than 1.53×10^{-11}. We conclude again that there is indeed a strong link between the 4 repetitions of the test of each descriptor, taken separately.

These analyses showed that the evaluations of the clarinettist are not dictated by chance. Additionally, the fact that the 4th evaluation of the descriptors *Poulenc* and *Schubert* was performed on an alternative test has no major influence on the results, seemingly. This result however did not tell us how many dimensions are present in the data (because each descriptor was taken separately).

For this, we have to analyse by CCA *simultaneously* the 4 repetitions of the 4 subjective tests ($P_j = 4$ variables, $J = 4$ repetitions). For a score based test (see Table 8.6, subjectiveF), a statistically significant link is demonstrated for the first 3 CCA factors at the 0.1% level. For a rank based test (subjectiveR), only 2 factors are significant at the 0.1% level (or 3 significant factors at the 2.5% level). We conclude that we are very confident that at least 2 dimensions are pertinent in the subjective evaluations and that the presence of a third pertinent dimension is very likely.

8.5.3 Inspection of the canonical correlations

The mean square correlations of all CCA listed in Table 8.6 are recorded in Table 8.8, up to the 6th canonical factor. The non significant values at the 0.1% level are indicated in *italic*. The limit of significance at the 0.1% level are computed by Monte-Carlo and are summarized in Table 8.9. A detailed analysis of the canonical correlations is given only for the most important analyses.

14. The reader unfamiliar with the CCA is invited to read the Appendix C, which introduces this analysis technique in a didactic way, developing and commenting the principles underlying the analyzes carried out in this paragraph.

In Fig. 8.22, the canonical correlations are depicted for each individual block of the analyses: *staticF*, *totalF* and *subjectiveF*. The limit of significance is indicated by a dotted gray line. For the *staticF* analysis, the 4th factor is beyond the limit of significance for the block *photoNew*. This is probably related to the break-in process. Indeed, a plastic deformation of the reed caused by the break-in process is observed in Fig. 8.17, between *photoNew* and *photoBreakIn*. The factors 3 and 4 are particularly well related to the aeraulic measurements (*aero*, *optoLeft* and *optoRight*), while the factor 6 is related to the photos of the channel (*photoNew* and *photoBreakIn*). In the *subjectiveF* analysis, the 2 first factors are clearly significant for all repetitions of the subjective tests, while for the 3th factor (the last significant factor), the contribution of the 4th test is under the limit. Only the 2 first factors are above the limit for *subjectiveF*. In the *totalF* analysis, the 4 first factors bind especially well *staticF*, *bifurcationF* and *reedF* (and to a smaller extent *synthesisF*).

In Fig. 8.23, the canonical correlations are depicted for each individual block of the analyses: *bifurcationF* and *synthesisF*. The contribution of all blocks (34 and 26, respectively) are above the limit of significance for the 6 first factors (and mostly well above the limit). No really noticeable differences are observed among sensors, among embouchures or among ramps (*crescendo* and *decrescendo*). The relatively poor contribution of *mThres* (measured emergence and extinction thresholds) to the factors 4 to 7 should be mentioned, while this is not the case for *sThres* (thresholds of the simulations). The factor 8 links all sensors except optoRight. Does this reveal a minor problem with the right optical sensor?

8.5.4 Number of statistically significant factors

For all data blocks of the categories *objective* and *synthesis*, the number of statistically significant factors at the 0.1% level is very high: it is comprised between 13 and 15 factors. This means that practically all PCA factors which have been retained after data compression (at hierarchical level 2) are significant. This is not really a surprise, because the quality of the collected data allows theoretically an individual identification of each reed. Moreover, it is no doubt that the measured quantities are strongly related to one another.

As already mentioned, for *subjectiveF*, 3 factors are significant at the 0.1% level. This seems a quite low number, but it should be remembered that until now, to my knowledge, the existence of only 1 significant factor for subjective evaluations could be demonstrated by other researchers. The subsequent pairwise confrontations of *subjectiveF* with *objectiveF*, *staticF*, *bifurcationF* and *synthesisF* reveal respectively 4, 4, 3 and 2 significant factors. This confirms that the number of significant factors is around 3 for the subjective evaluations. Moreover, this proves the existence of a link between subjective evaluations and objective measurements (and also between subjective evaluations and simulations). Notice that the *static* measurements are particularly well related to the subjective evaluations (which are principally of dynamic nature).

Results for other analyses are found in Table. 8.6.

8.5.5 Relations between objective measurements and subjective evaluations

One of the most tremendous points of the study is to investigate the relations between objective measurements and subjective evaluations. This could have important consequences for the assessment of clarinet reeds, especially for sorting the reeds after manufacture. In order to simplify the analyses, the comparaisons are not performed on each individual test of each subjective descriptor, but on the standardized mean of each descriptor over the 4 repetitions of the test. This data block is denoted *StdSubj*.

Correlations between *staticF* and *StdSubj* are shown in the table 8.10 and graphically illustrated in Fig. 8.15.

Let us refine the CCA analyses [15] and examine in turn each individual block of the static measurements (photoNew, photoBreakIn, aero, optoLeft and optoRight) with *StdSubj*. The aim of these analyses is to examine to which extent each block is related to *StdSubj*, so as to determine

15. These subsequent analyses are not recorded in Table 8.6.

	fact. 1	**fact. 2**	**fact. 3**	**fact. 4**	**fact.5**	**fact.6**
StrengthNom	**0.9100**	-0.1388	0.2823	0.0788	-0.0300	0.061
StrengthSubj	**0.9052**	0.0982	0.1742	0.1270	0.0666	-0.0196
Poulenc	**0.6010**	**0.5071**	**0.3611**	0.1968	0.1679	-0.1273
Schubert	0.1060	**0.3161**	**0.4748**	0.1200	0.2910	0.1498
Intonation	**0.6739**	**-0.4989**	0.1055	-0.0518	-0.0536	0.0101

Table 8.10 – Correlations between the CCA factors *staticF* and *StdSubj* (standardized mean of each subjective descriptor). For comparison, the correlation with *StrengthNom* (nominal strength) is indicated. Noticeable correlations are written in **bold**.

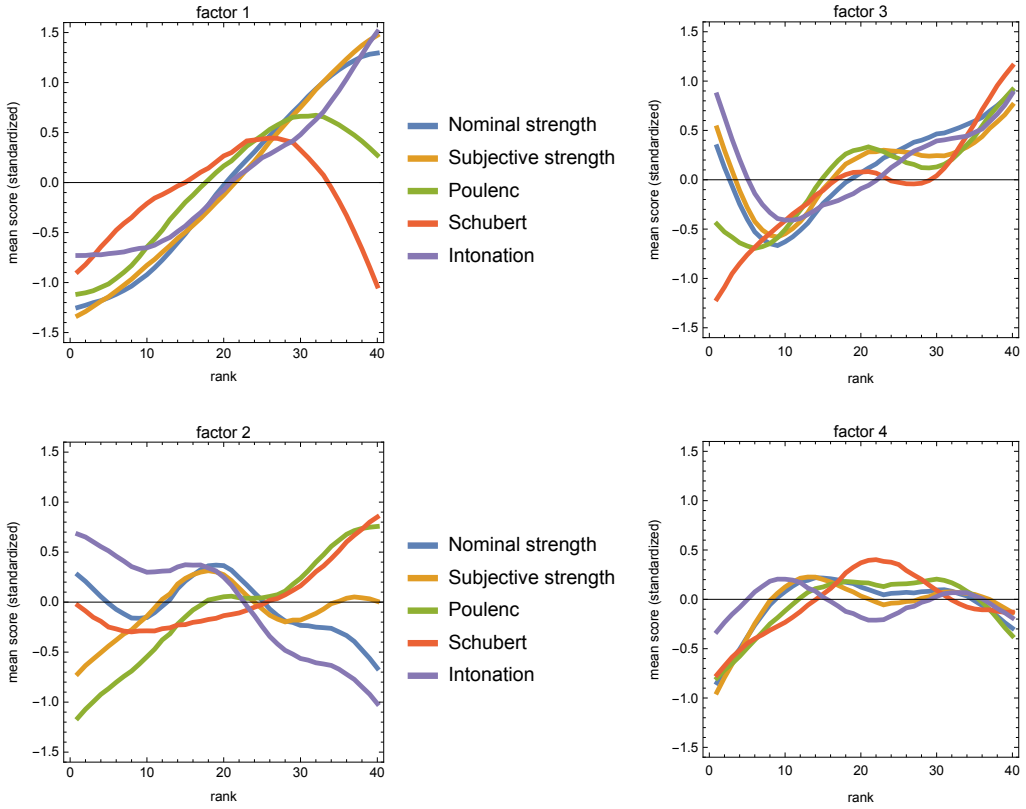

Figure 8.15 – "Moving average" of *StdSubj* (subjective descriptors, standardized mean score for the 4 repetitions of the same test), along the first 4 factors of *staticF*. The reeds are sorted according to the rank obtained inside each factor, and *StdSubj* is smoothed by a Gaussian filter of radius 10. The rank of the reed inside the factor is indicated on the abscissa. The nominal strength (*StrengthNom*) is added to the graph, as information.

the kind of measurements which is best suited to predict the subjective evaluations by the clarinettist.

The results are given in Table 8.11. At the 0.1% level, at least 2 factors are significant for all pairs of blocks, while 3 factors are significant for *photoBreakIn*, *aero* and *optoLeft*. At the 5% level, 3 factors are significant for all pairs of blocks, while 4 factors are significant for *photoNew* and *photoBreakIn*.

This result is important for the clarinettist: a prediction (for at least 3 factors) of his subjective musical evaluation of a wet reed is possible by simple linear regression, from a single objective measurement technique, applied to the dry reed (all 6 proposed techniques are well suited for this task). In particular, the prediction of the musical behavior of the reed after break-in is possible from 4 photos of the channel of the new reed (see D.2). This is decisive for the reed maker,

Block $j=1$	**Block $j=2$**	**fact. 1**	**fact. 2**	**fact. 3**	**fact. 4**
StdSubj	*photoNew*	**0.9857**	**0.9359**	0.8259	0.7716
StdSubj	*photoBreakIn*	**0.9764**	**0.9171**	**0.8734**	0.8187
StdSubj	*aero*	**0.9826**	**0.9147**	**0.8659**	*0.7099*
StdSubj	*optoLeft*	**0.9649**	**0.9497**	**0.8455**	*0.7297*
StdSubj	*optoRight*	**0.9680**	**0.9355**	0.8331	*0.7167*

Table 8.11 – Canonical correlations obtained by performing 5 pairwise CCA between *StdSubj* (standardized mean of the subjective descriptors) and the static, objective measurements, after PCA compression. The significant correlations at the 0.1% level are written in **bold**. The non significant correlations at the 5% level are written in *italic*.

Descriptor	$\sqrt{R^2}$	**coef. 1**	**coef. 2**	**coef. 3**	**coef. 4**
StrengthSubj	0.905	▲			
Poulenc	0.865	▲	▲	▲	
Schubert	0.475			▲	
Intonation	0.838	▲	▲		

Table 8.12 – Linear regression for the prediction of the subjective descriptors *StdSubj* from the first 4 factors of *staticF*. The correlation coefficient for the regression is given and the significant coefficients used for the regression are indicated by ▲. Non significant coefficients are set to 0 in the regression.

which can therefore categorize the reeds immediately after manufacture (if the maturation post production is negligible).

Although a prediction of the first 4 **subjective** factors from 4 individual measurements seems possible for *PhotoNew* a reed categorization by the manufacturer based on **objective** factors is probably more relevant, since they are less affected by errors and do not depend on the personal preferences of the clarinettist who performed the tests.

Let us verify this result by predicting each descriptor in *StdSubj* by linear regression, from the first 4 factors of *staticF* used as predictors. The statistical significance of each regression coefficient is tested by ANOVA at the 0.2% level. The significant regression coefficients are given on Table 8.12.

The corresponding regression plots are given on Fig. 8.16. One outlier (the extremely strong reed R12) is observed in *Schubert* which has an important influence on the correlation.

I renounce giving the numerical values allowing the prediction of the factors, since these are device dependent (in particular on the elasticity, the thickness and the zero position of the artificial lip).

8.5.6 Inspection of the matrix $\boldsymbol{V}_j$

The inspection of the matrix $\boldsymbol{V}_j$, Eq. 8.20, is instructive for many reasons. First of all, this restores an intuitive link with the underlaying physical problem, when this Eq. is applied to the raw data from which the factors are derived.

The columns of matrix $\boldsymbol{V}_j = \boldsymbol{F}^T \boldsymbol{X}_j$ are depicted graphically on Figs. 8.17 to 8.21 for different data blocks. In these Figs. each vector is depicted as a 2D structure. The apparent contradiction (regarding the 1D structure of a vector) must be clarified. For solving Eq. 8.19, the measurement structure must be flattened, so as to obtain a single vector per reed, in order to build the measurement's matrix $\boldsymbol{X}_j$. For the graphical representation, the columns of $\boldsymbol{V}_j$ are then partitioned ("deflattened") in order to recover the measurement structure (for each embouchure ψ).

The vector of the nth factor is normalized by construction so as to correspond to +1 standard deviation of the scores of the nth factor. Thus, the relative weight of each factor for the reconstruction of the variance is well reflected on the graphs Fig. 8.17 to 8.21. The scale is the same for all factors of a data block. For convenience, the mean of the data is stored in the vector $V_{j,\bullet,0}$ (as if it was the 0th factor).

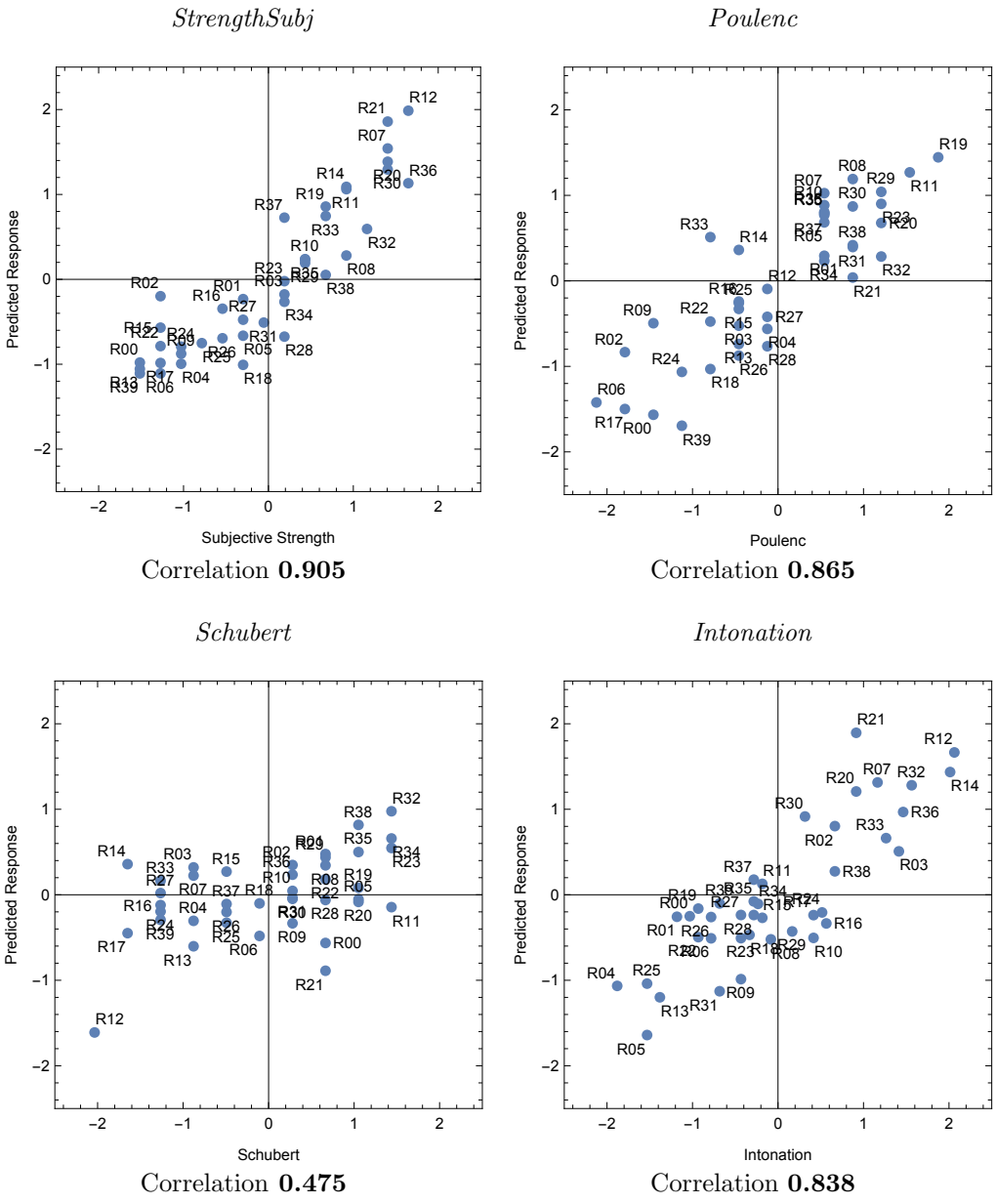

Figure 8.16 – Prediction of the subjective evaluations *StdSubj* from the the first 3 CCA factors of *staticF* . All correlations are statistically significant. The identifiers of each reed are indicated on the plot.

Fig. 8.17 depicts the matrix $\boldsymbol{V}_j$ for the raw data *PhotoNew*, *PhotoBreakIn*, *OptoLeft* and *OptoRight*. Fig. 8.18 depicts the matrix $\boldsymbol{V}_j$ for the raw data *MPlayFreq*, *SPlayFreq* and the spectral centroid (SC) of the measured pressure in mouthpiece in the bifurcation diagrams *M111* to *M142* (and similarly for the synthesized signals *S111* to *S142*). The Fig. 8.19 represents in a similar way the envelope of the pressure in mouthpiece and the SC of the reed signals (measured and synthesized), while the Fig. 8.20 represents one period of the measured optical signals, respectively near beating threshold and near extinction threshold (*M3111* to *M442*). The symmetric (L+R) and the antisymmetric (L-R) components of the optical signals is represented. Finally, Fig. 8.21 presents the components of the reed model described in Chapter 5, fitted from *ReedDeflec* and *ReedAero*.

Didactic examples of interpretation

The reader is encouraged to examine carefully Fig. 8.17 which summarizes one of the most important results of the study. It illustrates graphically the most important differences of static nature observed among reeds (photoNew, photoBreakIn, aero, optoLeft and optoRight). The first raw of the Fig. recall the mean of the observations, already illustrated on Figs. 8.3, 8.4 and 8.5. The 6 lower rows illustrate $\boldsymbol{V}_j$ for the first 6 factors, for each data block j (columns of the Fig.). They are scaled so as to correspond to +1 standard deviation of the factor scores.

Let us explain how to interpret this Fig. For instance, we want to represent mentally how the photos of the channel of a new reed look like, for a reed having a standardized score of 1 for factor 1 and 0 for all other factors. We have simply to add to the top leftmost picture (mean for photoNew) 1 time the leftmost picture of the 2nd row (factor 1 for photoNew). Such a reed has an opening at rest (without lip contact) which is about 0.02 mm more open than average (because a stiffer reed is also stiffer in the radial direction, when compressed by the ligature?). For a quite tight embouchure (depicted in green), the channel is about 0.08 mm more open than average in the middle an 0.06 mm more open than average on the sides. This means that the reed is stiffer than average, especially on the axis.

Let us examine now the aeraulic measurements. We notice that the aeraulic section, column (c), is affected mostly by the factors 1 to 4, while factors 5 and 6 have negligible influence. It is observed that the corresponding reed deflection, column (d), is fairly symmetrical for the left and right optical sensors, while factor 5 affects practically only the left sensor and factor 6 the right sensor.

An interesting observation can be made on Fig. 8.21. Note that the factors 1 to 6 practically do not modify the slope of the aeraulic section $S(y)$. This means that in a rectangular model of the channel, the width is constant for all reeds (about 20 mm). Consequently the air flows also through the sides into the mouthpiece, since the physical width of the reeds at the tip is only 13 mm.

Nonlinearities

The data is known to have nonlinear components, so it is questionable if a linear reconstruction is plausible. In Appendix §D.3, an attempt is made to examine the data along each factor, in order to identify some nonlinear behaviors, by comparing the linear vectors in Fig. 8.17 to 8.21 and their (possibly nonlinear) counterparts in Fig. D.11 and following. Unfortunately, our panel is too small to show such a dependence in a convincing way, because the 2 first factors are quite linear and strongly dominating. The "pollution" of the data by these 2 factors can hardly be removed from the subsequent factors, with such a small number of reeds. As a consequence, the linear model remains useful for interpreting the data.

8.6 Results interpretation

8.6.1 General observations

A good homogeneity is observed in the data distribution of each block and solid inter-block correspondences are noted. The differences between reeds are especially marked for the opening at rest and when the channel section is small. The characteristics of this "leak" have a significant influence on the operation of the instrument, since this determines its efficiency in converting a source of continuous pressure into an oscillating pressure signal in the mouthpiece.

It will be noted (see Fig. 8.3, for example) that the break-in process causes a plastic deformation of the reed at rest, which closes the channel in a relation reasonably well foreseen by the equation $h' = -0.10 + 1.08h$, where h is the average height of the new reed at rest and h' is its average height after break-in (with a maximum error of about 0.02 mm). Plastic deformations are observed on the break-in reed, whose shape corresponds quite exactly to those caused by the lip pressure, on the new reed (see Fig. D.11). On the other hand, surprisingly, none of the first 8 CCA factors shows a divergent evolution of the opening at rest between the new and the break-in reed.

8.6.2 Description of the objective factors

The description of the objective factors (*objectiveF*) is based partly on the inspection of the vectors $V_{j,\bullet,f}$, Figs. 8.17 to 8.21 and partly on the examination of the related (possibly nonlinear) trend along a factor, Figs. D.11 to D.21. The negative direction of a factor is referred to "left" and the positive direction, to "right". It should be remembered that these directions are arbitrary.

Let us perform a detailed analysis for each factor.

1. The factor 1 is strongly correlated with the reed strength (nominal or subjective, which are almost superimposed, see Fig. 8.15). *PhotoNew* and *PhotoBreakIn* show a channel deformation more concave than average for strong reeds and vice versa for weak reeds (see Figs. 8.17 and D.11). We will note the apparent contradiction between the playing frequency (descending, while traversing the factor and very dependent on the embouchure) of the bifurcation measurements (Figs. 8.18 and D.12) and the (ascending) intonation noted during the perceptive tests (Fig. 8.15). The contradiction is explained by the fact that a strong reed must be played with a tighter embouchure, otherwise the turbulence noise is considered too important by the clarinettist, in order to produce an "optimal" sound and vice versa for the weak reed, which would produce a "narrow" sound with a normal embouchure. With the artificial mouth, on the contrary, the same lip position induces a more closed channel with a weak reed than with a strong reed. The examination of Fig. D.14 reveals that this factor has a very important influence on the functioning of the instrument, including for elementary physical models like that of Raman model studied in Chapter 1, because the factor influences at the same time the parameters P_c and ζ, for a constant value of ψ.
2. The factor 2 is characterized by an opening at rest (without lip pressure) which increases linearly along the factor (see Figs. 8.17 and D.11), whereas the opening with a tight embouchure follows a reverse trend . This is interpreted as a more pronounced bending of the reed at rest on the mouthpiece lay, at the "left" end of the factor (examine the evolution of the compliance as a function of Δp in Fig. D.15). The concavity of the channel evolves in the opposite direction, than for the factor 1. The intonation, almost insensitive to the embouchure, decreases linearly through the factor (objective measurements (Figs. 8.18 and D.12), subjective evaluations (Fig. 8.15) and simulations agree on this point), while the SC increases linearly. The reeds which are more open at rest and more flexible (Fig. D.14) are more appreciated by the clarinettist for playing Poulenc and Schubert (Fig. 8.15).
3. The factor 3 links the different blocks of data to the airflow that can enter the instrument (Fig. 8.22), probably also from the sides of the reed (Figs. 8.17, 8.21 and D.11). This may indicate a progressive bending before contact of the tip of the reed with the lay, to "right" of the factor and a more sudden contact of the tip with the lay, with a more linear reed stiffness before contact, to "left" (Fig. D.15). It may be that this is related to a relative difference in stiffness between the tip and the vamp of the reed (in particular in the so-called "heart" region), which provides a rather logical interpretation of the observed differences. The bifurcation diagrams (Figs. D.12) show a gradual and slight increase in brightness (SC of pressure signals) with a tight embouchure (compared to the average) and vice versa for the loose embouchures. The examination of the nonlinear reed model in Fig. D.15 shows that the factor 3 is related to the derivative of the reed compliance around Δp =6 kPa.
4. The factor 4 is related to the break-in process and links the elastic deformation of the new reed with a rather tight embouchure and the plastic deformations at rest observed on the break-in reed (see Figs. 8.17 and D.11 and 8.22). In the linear model, these deformations look like a period of a cosine function. Observed along the factor, these deformations are quite asymmetrical at the 2 ends of the factor and are more regularly concave in the middle of the factor. At "right", the general deformation is convex. It can be seen that a reed at the "left" of the factor modifies its brightness with the embouchure in a much more sensitive way than at the right (Figs. 8.18 and D.12). It is observed in Fig. D.15 that the factor 4 is related to the derivative of the compliance of the reed, for high values of Δp. These differences are probably linked with the stiffness ratio between the axis and the sides of the reed.

5. The factor 5 reveals a bending asymmetry of the reed. In the linear model, these deformations look like a period of a sine function (see Fig. 8.17). Observed along the factor, these deformations are quite antisymmetrical at the 2 ends of the factor(see D.11), while the reeds in the center of the factor are fairly symmetrical. Asymmetry is already present on the new reed (with lip pressure) and a corresponding plastic deformation is observed on the break-in reed. The left and right optical signals confirm the bending asymmetry, in both static and dynamic cases (Figs. 8.20 and D.13). It is observed that the brilliance of the symmetrical reeds is greater than that of the asymmetric reeds (Fig. D.12). These differences are particularly marked near the beating threshold. It can be seen in Fig. D.15 that the factor 5 is related to the derivative of the compliance of the reed, at low Δp. These differences are probably linked with the stiffness ratio between the left and the right side of the reed.
6. The factor 6 is characterized by an antisymmetry (torsion) which is very visible in the dynamics of the reed, played with the artificial mouth (difference between right and left optical signals Figs. 8.20 and D.13). A parabolic trajectory is observed for the brightness along this factor (Fig. D.12), both on the measurements and on the synthesis. This evolution is particularly marked for the tight embouchures, while it is more monotonous for the loose embouchures. Fig. D.15 shows that the factor 6 is related to the compliance of the reed, at relatively strong Δp (around 10 kPa).

8.7 Conclusion

This study demonstrates the essential role of the static features for the playability of the reed and details the diversity and the complexity of the observed behaviors. These features characterize the **exciter** as a whole (reed+mouthpiece+lip) and not merely the reed taken alone. The photos of the channel made with a new reed, varying the embouchures, have a predictive value, which could be useful at the factory for a classification of the reeds, using a fast, automated procedure. The manufacturers could thus propose a categorization based on the feedback returned by their customers. From the measurements made at the factory and the feedback returned by the clients for the same individual reeds, it will be possible to evaluate the relative importance given to each factor by the musicians and to check whether a factor allows a good / bad classification, which is valid for the majority of the musicians or which rather reflects individual, stylistical preferences (or the use of another type of mouthpiece). It remains to show that the measurements made immediately after manufacture are well representative of the state of the reed once arrived at the customer. In particular, it must be verified whether the factor 2 (which characterizes the opening at rest) is already measurable at the manufacturing stage or if it results from a maturation (post-production) of the wood. It could be that a simple retouching of the bottom table would make a number of reeds more playable (adjusting for an optimal opening at rest). The influence of the progressive plastic closure during the aging process should be investigated (in order to give a second youth to reeds, that should be otherwise be discarded).

The perceptual study showed that the 4 proposed perceptive descriptors are correlated in a statistically significant way with the first 4 objective factors (i.e. 2 or 3 more than what could be proved so far from perceptual tests). These factors correspond to: 1) the general stiffness of the reed, especially in its middle part, 2) the opening at rest, 3) the evolution of the stiffness between the tip and the vamp of the reed and 4) the plastic deformations of the break-in reed (linked possibly with the stiffness ratio between sides and axis). Factors 5 and 6 are related to reed antisymmetries that have not been targeted by specific perceptual tests (difference of stiffness between the sides of the reed and (plastic) torsion of the reed). It should be noted that this significant link was established by comparing (essentially *static*) objective measurements, performed on **dry** reeds, with the subjective feeling of a clarinettist *playing* these same reeds in a **wet** state. A detailed analysis make it possible to understand why vague descriptors such as "overall quality" or "brilliance" are poorly adapted, in particular because they do not take into account the multiple (antinomic) influences that come into play. The importance of the constraints related to the playing frequency could be emphasized, in relation with the musical

playability of the reeds. More refined descriptors can be proposed, thanks in particular to the use of the sound synthesis and the precise indications on the differences of functioning between reeds, provided by the photos of the channel. These photos also provide the clarinettist with valuable information on possible corrections to the reed, either by building his own test bench (including a mouthpiece, an artificial lip, and a camera), or by perceiving the related musical differences. The mouthpiece manufacturer can also draw on the developed techniques to optimize the shape of the mouthpiece lay according to a particular reed model (or to develop a wedge of Claripatch type, to optimize the adequation between the lay and the reed which is played).

The simulations made it possible to validate very roughly the relevance of the physical models developed in the preceding Chapters. Further optimization of the parameters, allowing a better match between measurements and simulations, must be carried out and a more thorough comparison of the signals must be undertaken. It is also to clarify what is the missing ingredient in the reed model to get a better match with the spectral centroid of the measured reed signals. Despite this, the proposed 1D nonlinear reed model seems quite representative of the real behavior of the reed. The modeling of the mouthpiece must also be examined. The usual hypothesis - which assimilates it to a cylinder of equivalent volume - must be revised, because the spectral evolution of the signals is poorly reproduced by this simplified model. The simulations made from the measured geometry of a Buffet Crampon clarinet showed that the realism of the synthesized signals depends clearly on the geometry of the mouthpiece and on the incorporation of non linear losses.

First and foremost, this Chapter has presented exploratory studies, performed with a "Vandoren M30" mouthpiece and "Vandoren classic" reeds. Some important directions have been highlighted, but they still need to be confirmed and deepened by a more detailed and rigorous study, with many different mouthpieces and reed designs. In particular, a study of the lip mechanics has yet to be carried out.

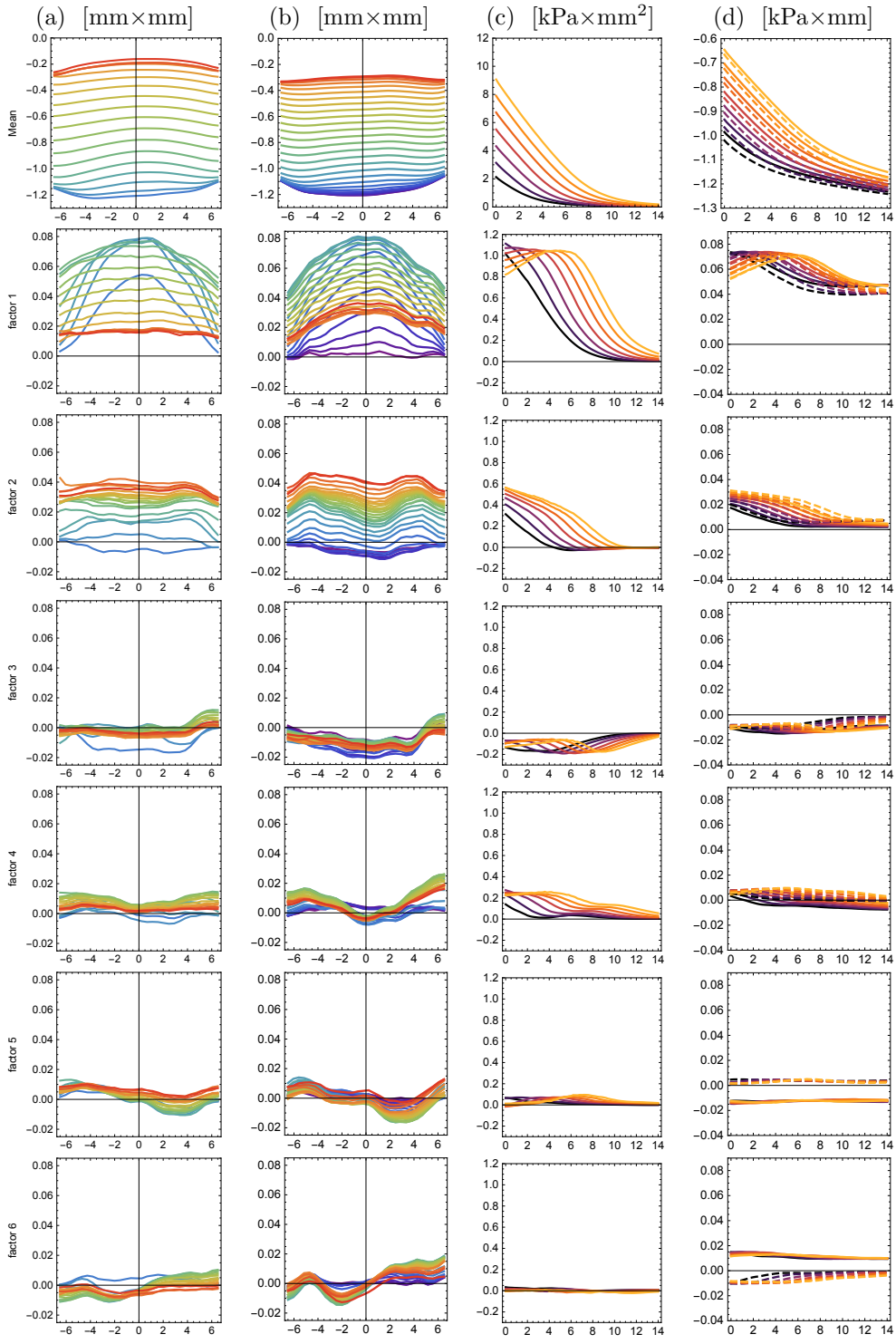

Figure 8.17 – Plot of the vectors $V_{j,\bullet,f}$ (see Eq. 8.20), for the *staticF* CCA factors. Each vector is "deflattened" in order to recover the measurement structure (by embouchures). Columns: measurements blocs j: (a) channel of the new reed (PhotoNew). (b) channel of the reed after break-in (PhotoBreakIn). (c) aeraulic section (Aero). (d) reed deflection (OptoLeft, solid lines, OptoRight, dashed lines). Rows: factors q from 0 (top) to 6 (bottom). Same color code as in Fig. 8.3, 8.4 and 8.5. The vectors $V_{j,\bullet,q}$ are normalized to +1 standard deviation. By convention, $V_{j,\bullet,0}$ represents the mean of the measurements of the jth block.

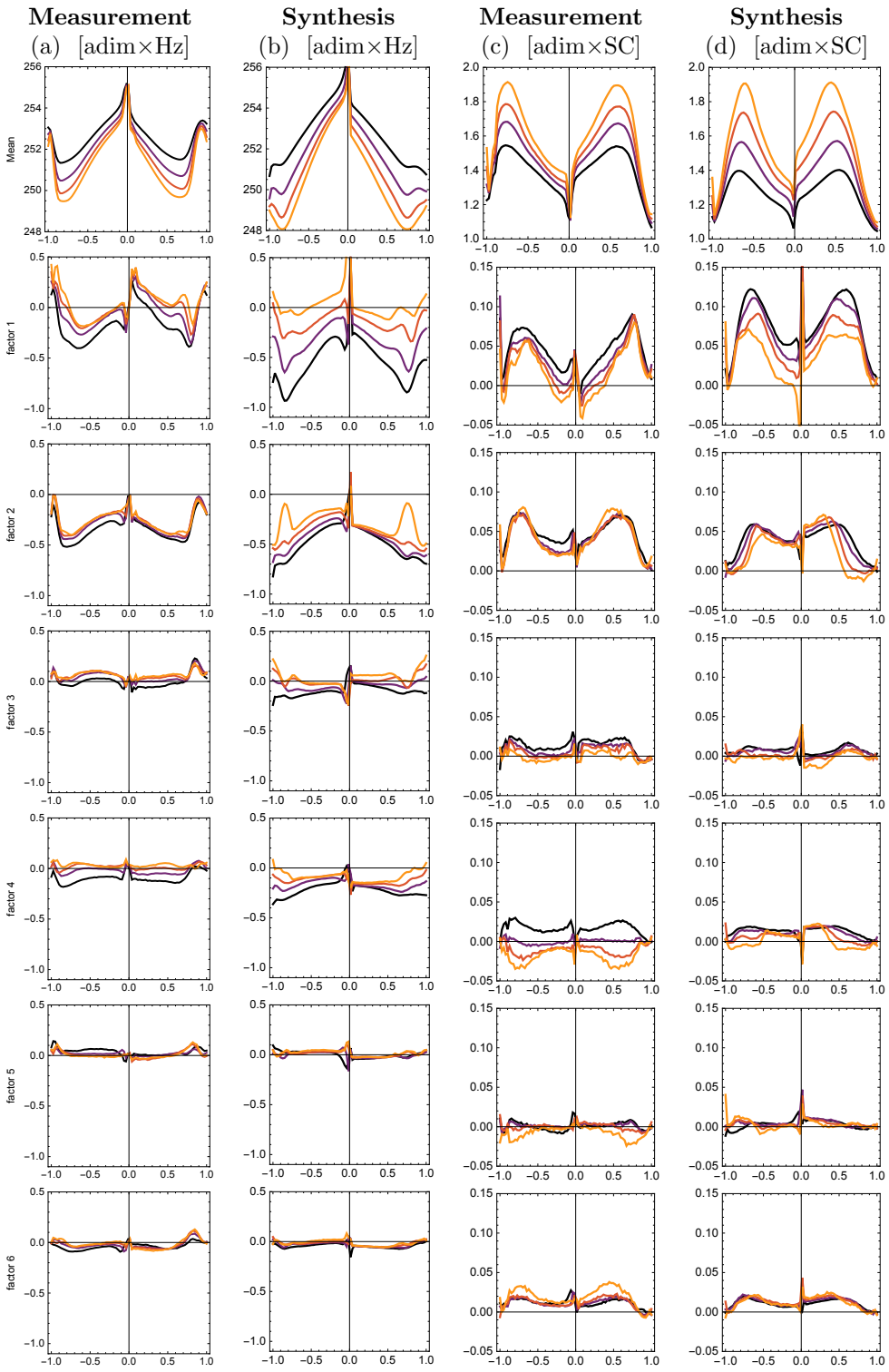

Figure 8.18 – Plot of the vectors $V_{j,\bullet,f}$ (see Eq. 8.20), for the *staticF* CCA factors. Each vector is "deflattened" in order to recover the measurement structure (by embouchures). Bifurcation diagrams. The abscissa of each graph is adimensioned in function of the emergence and extinction thresholds: from -1 to 0, *crescendo*, from 0 to 1, *decrescendo*. Columns: (a) measured playing frequency. (b) synthesized playing frequency. (c) spectral centroid of measured pressure in mouthpiece. (d) *idem* for the synthesis. Rows: factors q from 0 (top) to 6 (bottom). Same color code as in Fig. 8.9.

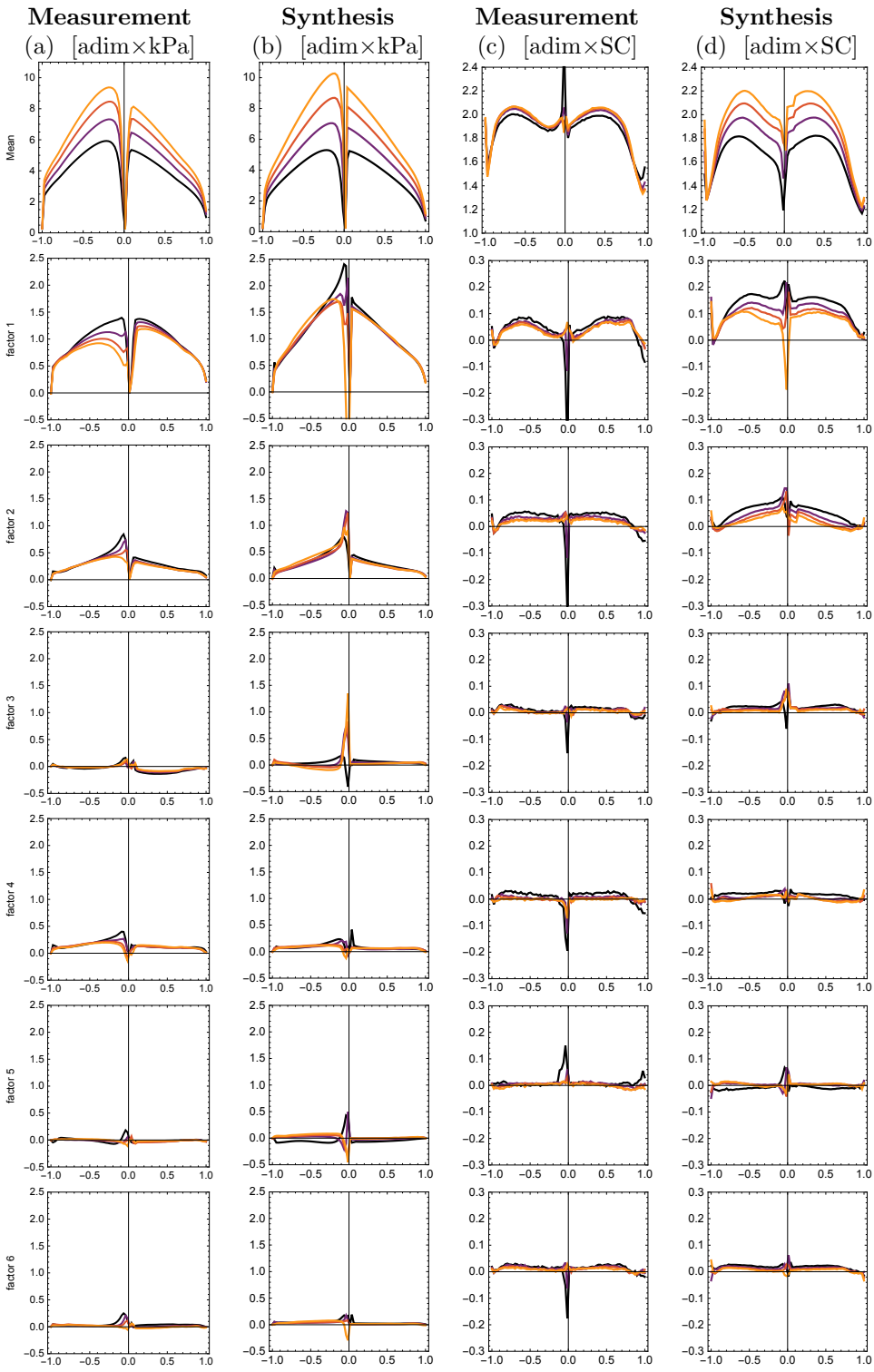

Figure 8.19 – Plot of the vectors $V_{j,\bullet,f}$ (see Eq. 8.20), for the *staticF* CCA factors. Each vector is "deflattened" in order to recover the measurement structure (by embouchures). Columns: (a) enveloppe of the measured pressure signal in the mouthpiece. (b) *idem* for the synthesis. (c) spectral centroid of measured reed signal. (d) *idem* for the synthesis. Rows factors q from 0 (top) to 6 (bottom). Same conventions as in the precedent Fig.

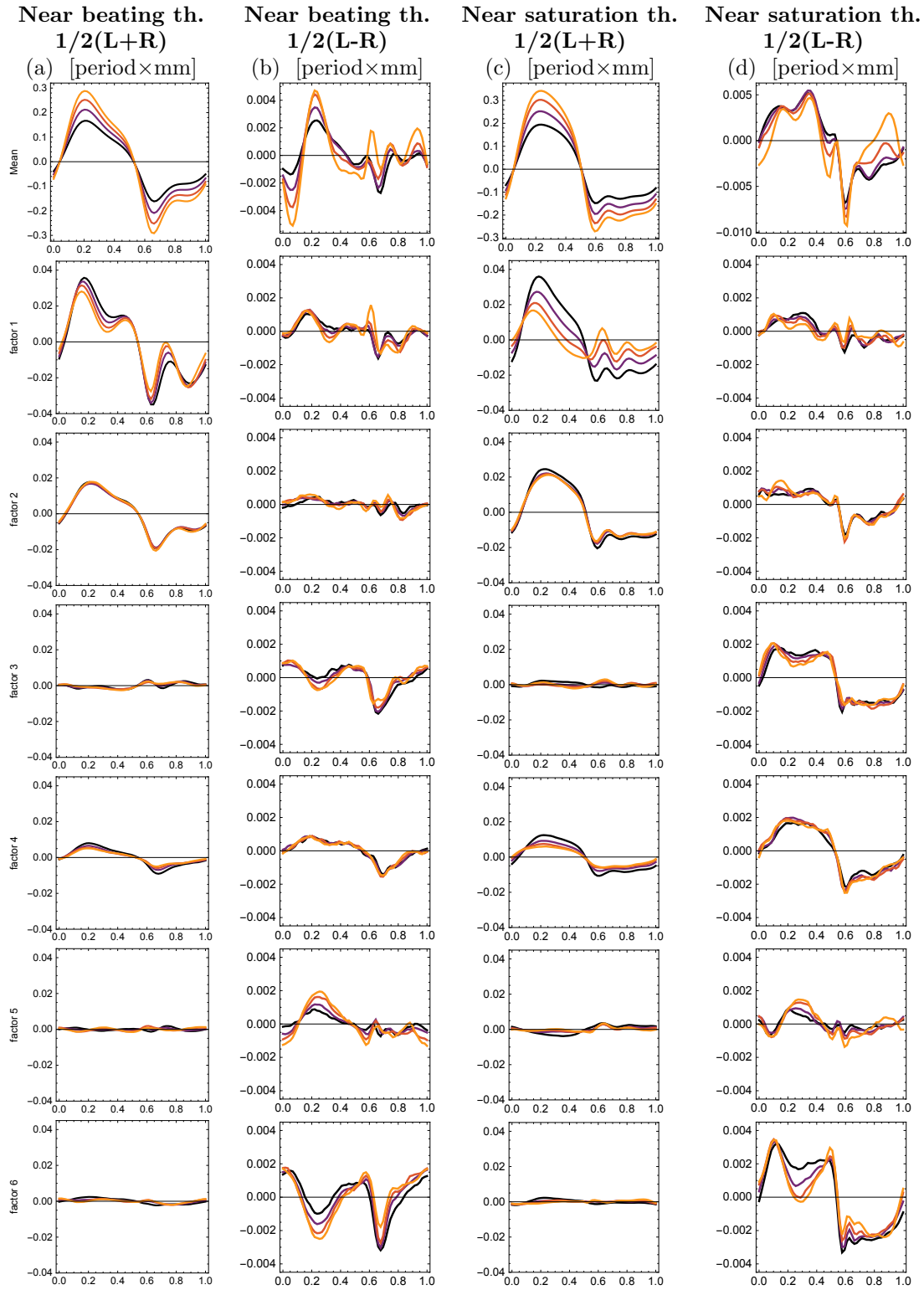

Figure 8.20 – Plot of the vectors $V_{j,\bullet,f}$ (see Eq. 8.20), for the *staticF* CCA factors. Each vector is "deflattened" in order to recover the measurement structure (by embouchures). One period of the measured reed signal (L: left, R: right). Columns: (a) 1/2(L+R) near beating threshold. (b) 1/2(L+R) near saturation threshold. (c) 1/2(L-R) near beating threshold (d) 1/2(L-R) near saturation threshold. Rows: factors q from 0 (top) to 6 (bottom). Same conventions as in the precedent Fig.

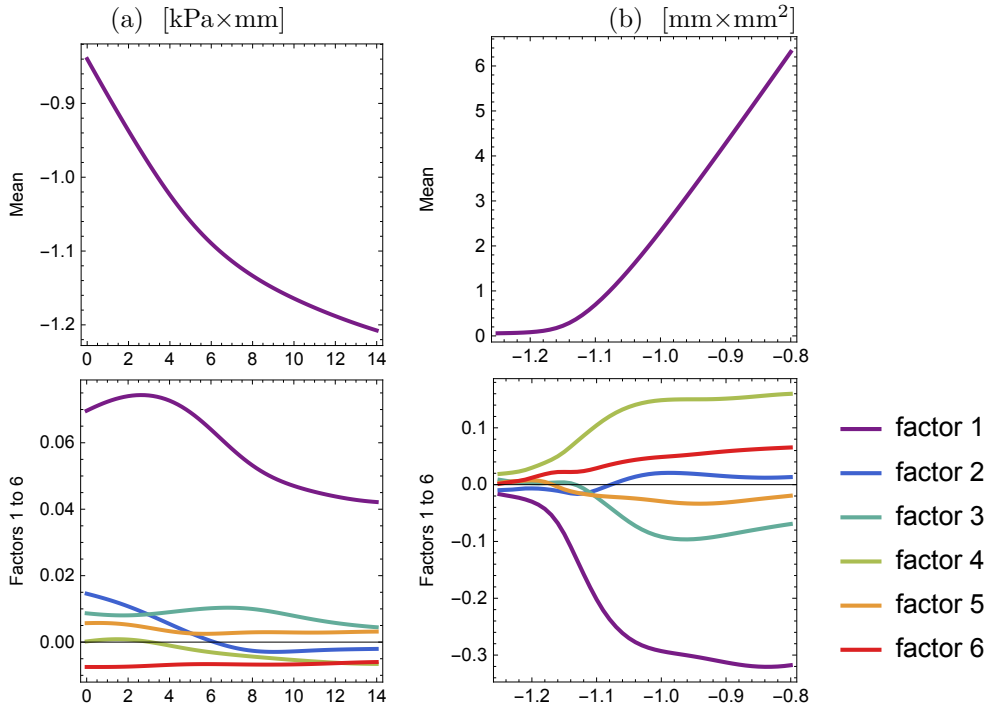

Figure 8.21 – Plot of the vectors $V_{j,\bullet,f}$ (see Eq. 8.20), for the *staticF* CCA factors, for the reconstruction of the reed model proposed in Chapter 5. (a) function $y = f^{-1}(x)$, Eq. (5.6). (b) function $S(y)$, as described in Fig. 5.4. Compare with D.14 to D.16.

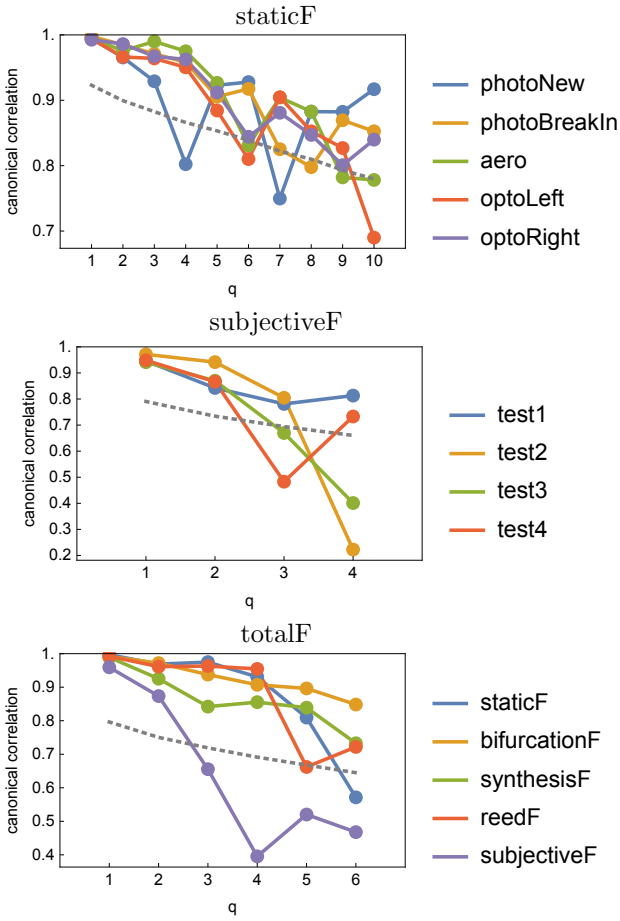

Figure 8.22 – Canonical correlations $r_{j,n}$ for the CCAs **staticF**, **subjectiveF** and **totalF**. The limit of significance $\breve{r}_q$ of $\bar{r}_q$ at the 0.1% level is indicated in grey (dotted line).

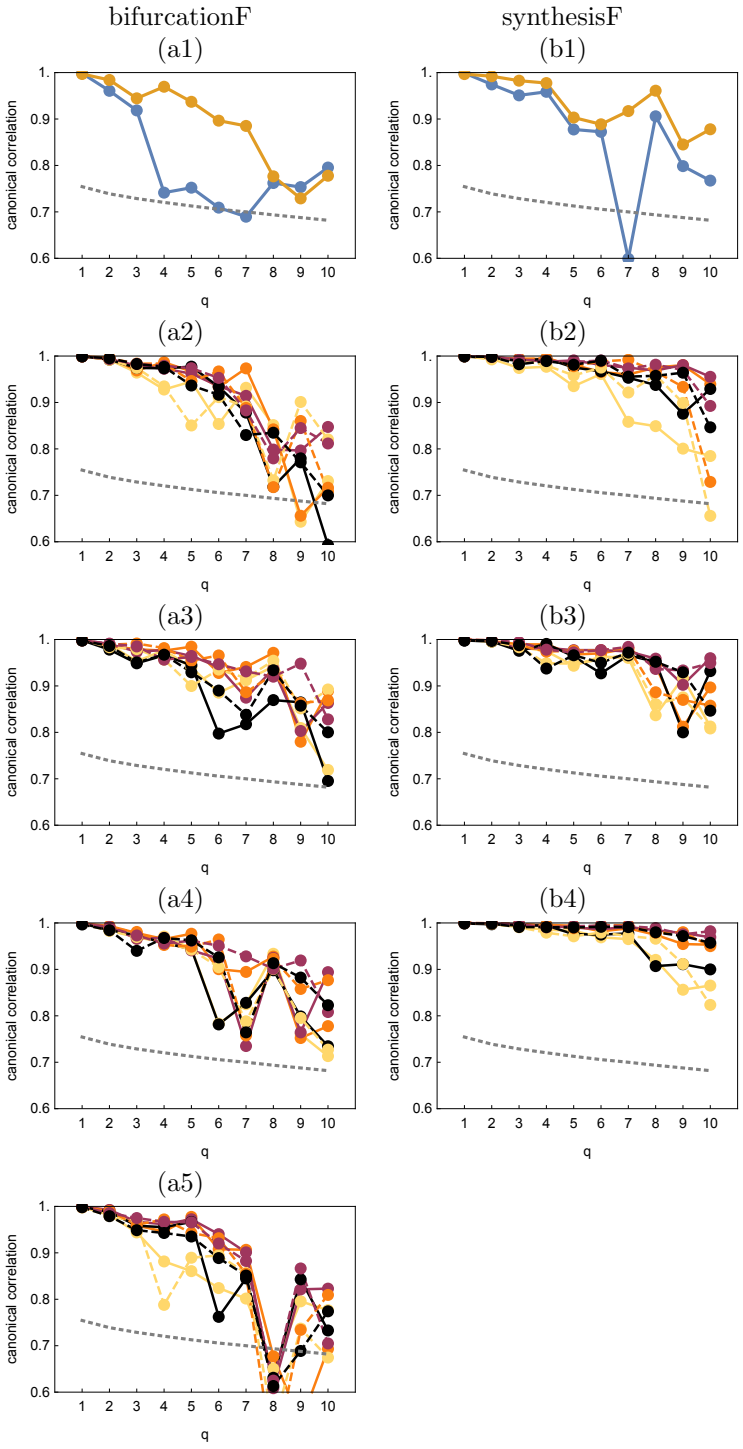

Figure 8.23 – Canonical correlations $r_{j,n}$ for the CCAs of the bifurcation diagrams. The limit of significance $\breve{r}_q$ of $\bar{r}_q$ at the 0.1% level is indicated in grey (dotted line). The embouchures are coded from black (tight embouchure) to light (loose embouchure). Plain lines: *crescendo*. Dashed lines: *decrescendo*, except for (a1) and (b1). Left column: measurements of the bifurcation diagrams. Right column: simulation of the bifurcation diagrams. (a1) MThres (blue) and MPlayFreq (orange). (b1) SThres (blue) and SPlayFreq (orange). (a2) M111 to M142 (measured pressure in mouthpiece). (b2) S111 to S142 (simulated pressure in mouthpiece). (a3) M211 to M242 (measured pressure in container). (b3) S211 to S242 (simulated flow rate in mouthpiece). (a4) M411 to M442 (measured reed deflection Left sensor). (b4) S411 to S442 (simulated reed deflection). (a5) M511 to M542 (measured reed deflection Right sensor).

Part V

General Conclusions

Chapter 9

General Conclusions and future Work

The present conclusions have the character of a postface, reflecting the meandering progress of the study and pointing out the most important findings. The factual conclusions are found at the end of each chapter.

The studies realized on clarinet acoustics over the past 17 years have achieved a number of interesting advances, useful not only in acoustics, but also for the musicians. From the beginning, it seemed obvious to me that the simplified reed models developed by the acousticians (as the one described in Chapter 1) could not reflect all the subtlety of the reed problem and that they could not orient an objective characterization of the reeds different from the one proposed for decades by the reed manufacturers, namely by measuring the "strength" of the reed. This suspicion proved true: parts of the mystery surrounding the reed "problem" could be unveiled, reconciling the perception of the musician with a fairly realistic modeling of the physical problem, while remaining relatively simple and efficient to simulate.

The accomplishment of this task was not easy for a musician, because it required an intensive self-taught training in acoustics during the first years, practically without external help, trying to read and understand many articles and books, sometimes stopping during weeks on a few sentences that I could not grasp, on a typographical error in an equation or an ambiguous notation, trying to redo some calculations, before finally being able to realize my first study, worthy of interest.

My early studies about the Raman model revealed to me the beauty of a rich mathematical world, generated from 2 seemingly very simple equations. The usefulness of these theoretical models for musicians is not obvious to demonstrate, because the sounds produced are very caricatural. Although they do not really tell the difference between the sound of a car horn and that of a clarinet, they do allow a number of interesting conclusions about the functioning of this kind of instruments. Analytical models explain why it is almost impossible to play pianissimo with an instrument having defective keypads. They orient the instrumentalist and the pedagogue towards the playing techniques of the "magical pianissimo" which is idomatic for the instrument, by modulating the loss parameter by means of the texture and the position of the lower lip. The knowledge of these operating regimes is very useful in order to understand and teach important aspects of the sound control by the instrumentalist. The precise knowledge of the physical reasons that authorize or prohibit some behavior, allows the clarinettist to be exonerated in good faith, without rejecting the fault on the reed. The discovery of some "exotic" sounds, as period doubling (discovered by various authors well before my works) was also for me a revelation on the musical usefulness of these simple theoretical models [1].

My first naive attempts to simulate some aspects of reed mechanics using the CATIA software quickly showed me that the reed's secret could not reside in a particular vibrating way, for example through some special harmonic relations between the first resonances: the smallest modification of the boundary conditions destroyed this supposed optimal equilibrium. Static

1. The finding about the musical consequences for the player are summarized in §1.7.3

simulations of the contact between the lay of the mouthpiece and the reed were much more instructive, stirring within me a flicker of suspicion that an important part of the subtlety of the reed problem could lie actually on that side. Unfortunately, instead of continuing my research in this direction, I opted for a study that proved ultimately not very successful: the track of viscoelasticity in the high frequency range.

The study of the resonances of a reed panel by holography revealed a whole bestiary of modal shapes, that were much less regular and symmetrical than expected by the simulations by finite elements, which suppose an ideally homogeneous material. *A posteriori*, it turned out that this approach is not very successful for the characterization of reeds from a musical point of view. While the proposed viscoelastic model reproduces adequately some of the systematic differences observed between reeds, the exploratory studies about the relationships with some subjective musical descriptors did not lead to very convincing results. Most of the performed tests could not prove the existence of statistically significant links: most of the time, the results were located in the "gray" zone of uncertainty. However, the repetition of these "almost significant" results indicates that there is probably "something" behind the parameters of the model. The proposed model does not take into account the inhomogeneities of the material, nor the geometric differences between reeds, inevitable despite all the care taken in their manufacture. However, it is possible that certain parameters (of the proposed viscoelastic model) could influence the static behavior of the exciter and thus play a much more important role than a simple shift in frequency of some modes of high order.

The years following the holographic study led to the development of an efficient instrumented mouthpiece and of a software for the acquisition and analysis of the instrumental gesture in real time (not described in this dissertation), as part of the SDNS-AIMV project. A mathematical method for the approximation of differential equations, which I named Extended Discrete Singular Convolutions (ESDC), was developed during this period. Initially, this method was thought to simulate the contact between reed and lay in a coarse and simplified way, authorizing a real-time calculation. It proved to be efficient in the numerical resolution of fractional partial differential equations or in a calculation of the beam and plate modes, with an unparalleled accuracy, for a given mesh size. Unfortunately, the article devoted to it has never been finalized and published, although most of the work has been done. The lack of interest among acousticians is probably not unrelated to this abandonment. The publication of the unfinished text as an Appendix to this dissertation may save it from oblivion.

The CAGIMA project oriented then my research in a very different direction: the study of the resonator, through the tools of complex analysis, linear transformations (Laplace, in particular), modal decompositions and digital filters. The first two years of the project consisted primarily to learn these methods, which initially seemed beyond my reach. With the means at hand, I tried to understand these quite hermetic topics to my intuition. Gradually, I understood how these areas were interconnected and acquired certain techniques to approach them more safely. More than two years after the official end of the project, I finally realized what was initially expected of me: the development of a method allowing the virtual prototyping of wind instruments. Although there is still a lot of work to be done to validate the developed methods and to finalize the simulator for a broader audience, I hope that my contribution will ultimately be useful to the community and that it will help musicians and instrument makers to design new instruments, more accurate in intonation, more homogeneous and easy to play.

The saga ends with the writing of this dissertation, after about three years as a doctoral student at the University of Maine, which allowed the completion of some projects. Finally, the "secret" of the reed could be partially unveiled, abandoning the almost metaphysical quest about the "vibration" of the reed in favor of a much more basic and elementary approach: observing its static behavior. The "bottle" method allows accurate and repeatable measurement of the static, aeraulic characteristics. This method works very satisfactorily, although some progress in the control and in the modeling of the heat exchanges have yet to be made. The instrumented mouthpiece developed a few years ago, the improvements to the artificial lip developed by A. Muñoz and the devices crafted in my garage have allowed a reliable measurement of the reed deflection. These measurements were supplemented by precise photographs of the channel, which proved very instructive and fairly easy to interpret, after an image processing based on the developed methods. An unsuspected variety of behaviors could be observed, accrediting thus the

clarinettists' testimony about the great variability of the reeds inside a package (of the same brand, model and strength).

However, some clarification is required about the "vibration" of the reed: the study showed the importance of the static aspects, but that does not mean that the dynamic aspects are negligible. They are probably closely related to the static ones, through the material constituting the reed. This should not be minimized when looking for alternative materials for reed making: it is important to reproduce not only the static behavior, but also the frequency of the first reed resonance and its damping, otherwise it will probably not be satisfactory. The damping properties of the reed material are likely important to mitigate any parasitic vibration during operation, without hindering the oscillation of the air column.

The development of a nonlinear reed model (clearly separating the mechanical and aeraulic aspects), combined with the software architecture developed for the simulation of waveguides (including nonlinear effects at the orifices) allowed to verify that an important part of the problem is now scientifically under control. Of course, a number of improvements should perfect the match between measurements and simulations (including the study of the lip mechanics), but this aim seems henceforth easier to achieve.

The canonical correlation analysis proves the existence of a very strong link between all objective physical measurements performed within a panel of 40 reeds. The existence of more than a dozen independent factors has been proved in a statistically significant way. The confrontation between bifurcation measurements and data from sound synthesis has also shown the existence of strong links for at least 13 factors. One of the most thrilling findings of this study is the following one: the 4 most important objective factors detected are correlated in a statistically significant way with the subjective evaluations performed blindly by the clarinettist. This opens the way to an automated selection of the reeds, made directly at the factory. The nature of the descriptors evaluated, the comparison with the measured bifurcation diagrams and the static measurements make it possible to orient the research in directions neglected so far, highlighting the ambivalent character of certain descriptors, when the evaluation context is not clearly defined. These approaches provide relevant insights into the relative failure of some attempts to characterize the reeds by means of subjective descriptors, that are too vaguely defined.

It is to be hoped that the findings of this study will be taken seriously by the reed manufacturers, that they will implement the proposed characterization techniques, improve them and that, in a near future, the clarinettists will get reeds, that are selected in a much more efficient and precise manner than in the past. I also hope that this study will facilitate the development of new models of mouthpieces or reeds, especially trough the use of alternative materials to *Arundo donax*.

Appendix

Appendix A

Dictionary of Junctions

A.1 Structure of the Dictionary and Notations

A.1.1 Structure of the entries

Each entry of the dictionary has the same structure. After a short description of the functionality of a junction, the lists of constants, commands, propagators, reflectors and outputs are given, followed by the equations and the solution of the coupling problem (in generic form, valid for the current discrete time step and the current junction). The equations and solutions are written in a programming style (*c.f.* Mathematica notation), in order to facilitate the implementation. The following generic identifiers refer to values at the current discrete time step and the current junction.

A.1.2 Identifiers related to digital filters

We propose a notation to facilitate the handling of filters, the computations of the interactions between reflectors and propagators, the pre-computation of constants in order to accelerate the computations in real time and the conversion between wave variables and physical variables and vice versa. The first character of the identifier describes the kind of filter, the second character defines the index of the segment and finally a suffix distinguishes the different components of the filters, according to the following tables:

1st char	Description
R	reflector filter
T	propagator filter
Z	impedance filter
Y	admittance filter
D	other filter

2nd char	Description
1	upstream segment (relatively to the current junction)
2	downstream segment (relatively to junction)
3	lateral derivation (chimney)

suffix	Description
V1	coefficient V_1 (affecting the current excitation)
V2	coefficient V_2 (sum of terms from the past)
K1	conversion factor 1
K2	conversion factor 2
In	input value (excitation) sent to the filter
Out	output value (response) of the filter
in	incoming propagator in the junction
out	outgoing propagator in the junction

For instance, T1in refers to the current value of the incoming propagator of the upstream

segment. R1V1 refers to the V_1 component of the upstream reflector and Eq. 7.19 reads: R1out = R1V1 R1in + R1V2. The extra filters (such as integrators or differentiators) are listed among the reflectors with letter D (and the 2 concerned segment numbers). The forward conversion refers to the conversion between wave variables $\{\phi^+, \phi^-\}$ and physical variables $\{P, U\}$, and vice versa for the backward conversion.

A.1.3 Identifiers describing the current acoustical state at the junction

P	Pressure at the junction
U:	Flow rate at the junction
Pexcit:	Blowing pressure imposed to the exciter
W:	Aeraulic section of the exciter
Ur:	Reed induced flow rate (exciter)
Ukey:	Key induced flow rate (tonehole)
θ:	Degree of aperture of a tonehole
r:	radius of the section
rinv:	$=1/r$
Zc:	$= (\rho c)/(\pi r^2)$
Yc:	$= 1/\mathrm{Zc}$
Zr:	$= r\,\mathrm{Zc}$
Yr:	$= 1/\mathrm{Zr}$

If necessary, diverging parameters are distinguished by the segment index, for instance : r1, r2, if the upstream and downstream segments have different radii at the junction.

For the current discrete time step and the current junction, Eq. 7.3 reads:

$$\begin{aligned} r\,P &= \phi^+ + \phi^- \\ \mathrm{Zr}\,U &= \phi^+ - \phi^- \end{aligned}$$

The function RxV2=computeV2(Rx) is called at the beginning of each time step and computes the value of the parameter V_2 (sum of terms from the past) for each reflector (Rx and Dxx filters). The function RxOut = updateR(Rx, TxOut) updates the history of the reflector Rx and computes the output of the filter, RxOut, where x stays for the index of the filter.

A.2 Basic equations

For the segment x (x=1,2,3), using the signed constants SZr1=-r1 Zc1 , SZr2=r2 Zc2 and SZr3=r3 Zc3, the pressure Px and flow rate Ux can be expressed according to Eq. 7.3 as:

$$\begin{aligned} \mathrm{rx\,Px} &= \mathrm{Txout} + (\mathrm{RxV1\,Txout} + \mathrm{RxV2} + \mathrm{Txin}) = \phi_x^+ + \phi_x^- \\ \mathrm{SZrx\,Ux} &= \mathrm{Txout} - (\mathrm{RxV1\,Txout} + \mathrm{RxV2} + \mathrm{Txin}) = \mathrm{sgn(SZrx)}(\phi_x^+ - \phi_x^-) \end{aligned} \tag{A.1}$$

A.2.1 Impedance formulation

Eq. A.1 can be rewritten as an impedance relationship:

$$\begin{aligned} \mathrm{Px} &= \mathrm{ZxV1\ Ux} + \mathrm{ZxV2} \\ \mathrm{ZxV1} &= \frac{(1 + \mathrm{RxV1})\,\mathrm{SZrx}}{(1 - \mathrm{RxV1})\mathrm{rx}} \\ \mathrm{ZxV2} &= \mathrm{ZxK2}\,(\mathrm{RxV2} + \mathrm{Txin}) \\ \mathrm{ZxK2} &= \frac{2}{(1 - \mathrm{RxV1})\,\mathrm{rx}} \end{aligned} \tag{A.2}$$

After solving the coupling problem, the filter Rx is excited by RxIn=Txout and updated:

$$\begin{aligned} \text{Txout} &= \text{ZxK1}(\text{RxV2} + \text{Txin} + \text{SZrx}\,\text{Ux}) \\ \text{ZxK1} &= \frac{1}{1-\text{RxV1}} \\ \text{RxOut} &= \text{updateR}(\text{Rx}, \text{Txout}) \end{aligned} \tag{A.3}$$

The constants used in real-time computations are: SZrx, ZxV1, ZxK1, ZxK2.

A.2.2 Admittance formulation

Eq. A.1 can be rewritten as an admittance relationship:

$$\begin{aligned} \text{Ux} &= \text{YxV1}\ \text{Px} + \text{YxV2} \\ \text{YxV1} &= \frac{(1-\text{RxV1})\,\text{rx}}{(1+\text{RxV1})\text{SZrx}} \\ \text{YxV2} &= \text{YxK2}\,(\text{RxV2} + \text{Txin}) \\ \text{YxK2} &= \frac{-2}{(1+\text{RxV1})\,\text{SZrx}} \end{aligned} \tag{A.4}$$

After solving the coupling problem, the filter Rx is excited by RxIn=Txout and updated:

$$\begin{aligned} \text{Txout} &= \text{YxK1}(\text{Px}\,\text{rx} - \text{RxV2} - \text{Txin}) \\ \text{YxK1} &= \frac{1}{1+\text{RxV1}} \\ \text{RxOut} &= \text{updateR}(\text{Rx}, \text{Txout}) \end{aligned} \tag{A.5}$$

The constants used in real-time computations are: rx, YxV1, YxK1, YxK2.

A.2.3 Special case of cylindrical segments

A cylindrical segment x is simulated with propagators only (no reflectors, consequently no instantaneous reflection). This reverts to set RxV1=RxV2=0 in the equations above.

A.3 Dictionary of Junctions

A.3.1 Flow controlled input junction

The downstream segment (index 2) is excited with a flow U=U2. Typically the flow controlled input junction is used to compute the input impedance of the simulated waveguide, according to its response to a discrete Dirac flow rate impulse.

Constants:	SZr2, Z2V1, Z2K1, Z2K2
Inputs:	U
Propagators:	T2
Reflectors:	R2
Outputs:	P

Equations to solve:

$$\begin{aligned} \text{P2} &= \text{Z2V1}\ \text{U2} + \text{Z2V2} \\ \text{P} &= \text{P2} \\ \text{U} &= \text{U2} \end{aligned}$$

Solution:

$$\mathrm{P} = \mathrm{Z2V1\ U} + \mathrm{Z2V2}$$

A.3.2 Pressure controlled input junction

The downstream segment is excited with a pressure P=P2. Typically the pressure controlled input junction is used to compute the input admittance of the simulated waveguide, according to its response to a discrete Dirac pressure impulse.

Constants:	r2, Y2V1, Y2K1, Y2K2
Inputs:	P
Propagators:	T2
Reflectors:	R2
Outputs:	U

Equations to solve:

$$\begin{aligned} \mathrm{U2} &= \mathrm{Y2V1\ P2} + \mathrm{Y2V2} \\ \mathrm{U} &= \mathrm{U2} \\ \mathrm{P} &= \mathrm{P2} \end{aligned}$$

Solution:

$$\mathrm{U} = \mathrm{Y2V1\ P} + \mathrm{Y2V2}$$

A.3.3 Flow controlled and pressure controlled output junction

The downstream outpout of a waveguide can also be controlled in pressure or flow rate. Typically, a zero flow rate is imposed to each tonehole or output end that remains closed during the simulation. This is more economical in terms of computer resource than simulating a closed tonehole with the junction `JLinearHole`. The equations are straightforward to derive from the input control case: this reverts to substitute the index 2 by 1.

A.3.4 Input coupled with a pressure controlled exciter

The excitation parameters are: Pexcit (excitation pressure, ordinarily the quasi-static pressure inside the mouth), Ur (reed induced flow) and W (aeraulic section).

Constants:	SZr2, Z2V1, Z2K1, Z2K2
Inputs:	Pexcit, W, Ur
Propagators:	T2
Reflectors:	R2
Outputs:	U, P

Equations to solve:

$$\begin{aligned} \mathrm{P2} &= \mathrm{Z2V1\ U2} + \mathrm{Z2V2} \\ \mathrm{U2} = \mathrm{U} &= \mathrm{Ub} + \mathrm{Ur} \\ \mathrm{Ub} &= W \operatorname{sgn}(\mathrm{Pexcit} - \mathrm{P2}) \sqrt{|\mathrm{Pexcit} - \mathrm{P2}|} \end{aligned}$$

Solution:

$$\begin{aligned} \text{b1} &= \text{Pexcit} - \text{Ur}\,\text{Z2V1} - \text{Z2V2} \\ \text{W2} &= W^2\,\text{Z2V1} \\ \text{b2} &= W\sqrt{4\,|\text{b1}| + \text{Z2V1}\,\text{W2}} - \text{W2} \\ \text{U} &= 0.5\,\text{sgn(b1)b2} + \text{Ur} \end{aligned}$$

A.3.5 Exciter inserted between 2 segments

The exciter is driven by the pressure drop $\Delta P = \text{P1} - \text{P2}$ between the upstream and the downstream segments. This is the usual playing situation: the pressure in the mouth is not static and depends from the resonances of the vocal tract and from the quasi-static pressure in the lungs.

Constants:	SZr1, Z1V1, Z1K1, Z1K2, SZr2, Z2V1, Z2K1, Z2K2, V1 = Z1V1 − Z2V1
Inputs:	Pexcit, W, Ur
Propagators:	T1, T2
Reflectors:	R1, R2
Outputs:	U, P1, P2

Equations to solve:

$$\begin{aligned} \text{P1} &= \text{Z1V1 U1} + \text{Z1V2} \\ \text{P2} &= \text{Z2V1 U2} + \text{Z2V2} \\ \Delta P &= \text{P1} - \text{P2} = \text{V1 U} + \text{V2} \\ \text{U1} = \text{U2} = \text{U} &= \text{Ub} + \text{Ur} \\ \text{Ub} &= W\,\text{sgn}(\Delta P)\sqrt{|\Delta P|} \end{aligned}$$

Solution:

$$\begin{aligned} \text{V2} &= \text{Z1V2} - \text{Z2V2} \\ \text{b1} &= \text{Ur V1} + \text{V2} \\ \text{W2} &= W^2\,\text{V1} \\ \text{b2} &= W\sqrt{4\,|\text{b1}| + \text{V1 W2}} + \text{W2} \\ \text{U} &= 0.5\,\text{sgn(b1)b2} + \text{Ur} \\ \text{P1} &= \text{Z1V1 U} + \text{Z1V2} \\ \text{P2} &= \text{Z2V1 U} + \text{Z2V2} \end{aligned}$$

A.3.6 Simple junction of 2 segments

If the 2 segments present a $\mathcal{C}^1$ continuity at the junction or if the 2 segments are cylindrical and present a small difference of section , the acoustic Kirchhoff laws (continuity of the pressure and mass conservation) apply at the junction and therefore the addition of an acoustic mass is not necessary.

Constants:	SZr1, Z1V1, Z1K1, Z1K2, SZr2, Z2V1, Z2K1, Z2K2
	$\mathrm{k1} = \frac{1}{\mathrm{Z1V1}-\mathrm{Z2V1}}$
Inputs:	None
Propagators:	T1, T2
Reflectors:	R1, R2
Outputs:	P, U

Equations to solve:

$$\begin{aligned} \mathrm{P1} &= \mathrm{Z1V1\ U1} + \mathrm{Z1V2} \\ \mathrm{P2} &= \mathrm{Z2V1\ U2} + \mathrm{Z2V2} \\ \mathrm{P} &= \mathrm{P1} = \mathrm{P2} \\ \mathrm{U} &= \mathrm{U1} = \mathrm{U2} \end{aligned}$$

Solution:

$$U = \mathrm{k1}(\mathrm{Z2V2} - \mathrm{Z1V2})$$

A.3.7 Junction of 2 cylindrical segments with added acoustical mass

If the difference in the cross section of the 2 cylinders is important, an acoustical mass should be added to the system in order to simulate adequately the behavior of the junction.

Constants:	SZr1, Z1V1, Z1K1, Z1K2, SZr2, Z2V1, Z2K1, Z2K2,
	$\mathrm{k1} = \frac{1}{-\mathrm{D12V1}+\mathrm{Z1V1}-\mathrm{Z2V1}}$
Inputs:	None
Propagators:	T1, T2
Reflectors:	R1, R2, D12
Outputs:	P1, P2, U

This junction requires additionally a differentiator Eq. 7.28, called D12, in order to simulate the effect of an added acoustical mass across the junction (with gain $k = M_d$). According to Kergomard [16, 42, 38, 43], the discontinuity in the cross section can be approximated for cylindrical, concentric ducts with a low frequency approximation:
$\mathrm{P1}(s) - \mathrm{P2}(s) = M_d\, s\, U(s)$. I propose a new formulation for M_d, which summarizes quite adequately the 2 formulas given by Kergomard:

$$M_d = \frac{\rho}{r_{min}} \left(0.09616\alpha^6 - 0.12386\alpha^5 + 0.03816\alpha^4 + 0.0809\alpha^3 - 0.353\alpha + 0.26164\right) \tag{A.6}$$

$r_{min} = \min(\mathrm{r1}, \mathrm{r2})$, $r_{max} = \max(\mathrm{r1}, \mathrm{r2})$ and $\alpha = r_{min}/r_{max}$.

Equations to solve:

$$\begin{aligned} \mathrm{P1} &= \mathrm{Z1V1\ U1} + \mathrm{Z1V2} \\ \mathrm{P2} &= \mathrm{Z2V1\ U2} + \mathrm{Z2V2} \\ \mathrm{U} &= \mathrm{U1} = \mathrm{U2} \\ \mathrm{P1} - \mathrm{P2} &= \mathrm{D12V1}\, U + \mathrm{D12V2} \end{aligned}$$

Solution:

$$\begin{aligned} \text{U} &= \text{k1}(\text{D12V2} - \text{Z1V2} + \text{Z2V2}) \\ \text{P1} &= \text{Z1V1 U} + \text{Z1V2} \\ \text{P2} &= \text{Z2V1 U} + \text{Z2V2} \end{aligned}$$

A.3.8 Simple junction of 3 segments

We assume that the Kirchhoff laws apply (P=P1=P2=P3 and U1=U2+U3) at the junction.

Constants:	SZr1, Z1V1, Z1K1, Z1K2, SZr2, Z2V1, Z2K1, Z2K2, SZr3, Z3V1, Z3K1, Z3K2, k1=$\frac{-1}{\text{Y1V1}-\text{Y2V1}-\text{Y3V1}}$
Inputs:	None
Propagators:	T1, T2, T3
Reflectors:	R1, R2, R3
Outputs:	P, U1, U2, U3

Equations to solve:

$$\begin{aligned} \text{U1} &= \text{Y1V1 P1} + \text{Y1V2} \\ \text{U2} &= \text{Y2V1 P2} + \text{Y2V2} \\ \text{U3} &= \text{Y3V1 P3} + \text{Y3V2} \\ \text{P} &= \text{P1} = \text{P2} = \text{P3} \\ \text{U1} &= \text{U2} + \text{U3} \end{aligned}$$

Solution:

$$\begin{aligned} \text{P} &= \text{k1}(\text{Y1V2} - \text{Y2V2} - \text{Y3V2}) \\ \text{U2} &= \text{Y2V1 P} + \text{Y2V2} \\ \text{U3} &= \text{Y3V1 P} + \text{Y3V2} \\ \text{U1} &= \text{U2} + \text{U3} \end{aligned}$$

Remark: if a lateral derivation comes back into the main duct, the case U1 + U2 = U3 must also be solved. This reverts to change the sign affecting the filters with index 2 in the equations above.

A.3.9 Junction of 3 segments with added acoustical masses

According to Kergomard the planar mode in the pipe can be linked to the median plane of the tonehole (which is called chimney), thanks to a lower frequency approximation with added acoustical masses, m_a and m_S:

$$\begin{aligned} m_a &= \frac{b(0.087\delta - 0.37)\delta^2\rho}{\pi a^2} \\ m_S &= \frac{\left(-0.71\delta^4 + 1.27\delta^3 - 1.09\delta^2 - 0.193\delta + 0.82\right)\rho}{\pi b} \end{aligned} \tag{A.7}$$

where $\delta = b/a$ is the radius ratio (b and a are the radii of the tonehole and the main duct, respectively). The pressures and the flow rates across junction are linked by:

$$\begin{pmatrix} P_1 \\ U_2 \\ U_3 \end{pmatrix} = \boldsymbol{M} \cdot \begin{pmatrix} U_1 \\ P_2 \\ P_3 \end{pmatrix} \tag{A.8}$$

with

$$\boldsymbol{M} = \frac{1}{m_a + 4m_S} \begin{pmatrix} 4\,s\,m_a m_S & 4m_S - m_a & 2m_a \\ 4m_S - m_a & -4/s & 4/s \\ 2m_a & 4/s & -4/s \end{pmatrix}$$

An inspection of the matrix $\boldsymbol{M}$ reveals the need of 1 differentiator (Eq. 7.28, called D11 hereafter) and 2 integrators (Eq. 7.29, called D22 and D23 hereafter). The gains of these filters are given by Kij $= M_{i,j}$, $s \to 1$. Notice that K12+K13=K21+K31=1 and U1=U2+U3.

Constants: SZr1, Z1V1, Z1K1, Z1K2, SZr2, Z2V1, Z2K1, Z2K2,
SZr3, Z3V1, Z3K1, Z3K2, K12
k1 = 1-K12 , k2 = Z3V1 D23V1, k3 = Z2V1 K12,
k4 = 1 - Z2V1 D22V1 + k2, k5 = 1/k4, k6 = k4 D11V1 + Z3V1 k1^2,
k7 = Z2V1 (-k1 D22V1 + K12 D23V1),
k8 = 1/(k4 - Y1V1 (k6 + k7 Z3V1 + k3 K12)), k9 = K12 + k2,
k10 = 1/(1 + R1V1), k11 = 1/(1 - R2V1), k12 = 1/(1 - R3V1)
Inputs: None
Propagators: T1, T2, T3
Reflectors: R1, R2, R3, D11, D22, D23
Outputs: P1, P2, P3, U1, U2, U3

Equations to solve:

$$\begin{aligned}
\text{U1} &= \text{Y1V1}\,\text{P1} + \text{Y1V2} \\
\text{P2} &= \text{Z2V1}\,\text{U2} + \text{Z2V2} \\
\text{P3} &= \text{Z3V1}\,\text{U3} + \text{Z3V2} \\
\text{P1} &= (\text{D11V1}\,\text{U1} + \text{D11V2}) + \text{K12}\,\text{P2} + (1 - \text{K12})\text{P3} \\
\text{U2} &= (\text{D22V1}\,\text{P2} + \text{D22V2}) + (\text{D23V1}\,\text{P3} + \text{D23V2}) + \text{K12}\,\text{U1} \\
\text{U3} &= -(\text{D22V1}\,\text{P2} + \text{D22V2}) - (\text{D23V1}\,\text{P3} + \text{D23V2}) + (1 - \text{K12})\text{U1}
\end{aligned}$$

Solution:

$$\begin{aligned}
\text{s1} &= \text{D22V2} + \text{D23V2} \\
\text{s2} &= \text{D23V1}\,\text{Z3V2} \\
\text{s3} &= \text{D22V1}\,\text{Z2V2} + \text{s1} \\
\text{s4} &= \text{k1}\,\text{Z3V2} \\
\text{s5} &= \text{D11V2} + \text{K12}(\text{k3}\,\text{Y1V2} + \text{Z2V2}) + \text{k6}\,\text{Y1V2} + \text{s4} \\
\text{s6} &= \text{D23V1}(\text{D11V2} + \text{Z2V2K12}) - \text{k1}\,\text{s3} \\
\text{s7} &= \text{Z2V1}\,(\text{K12}(\text{s1} + \text{s2}) - \text{D22V1}(\text{D11V2} + \text{s4})) \\
\text{P1} &= \text{k8}\,(s7 + \text{Z3V1}(\text{k7}\,\text{Y1V2} + \text{s6}) + \text{s5}) \\
\text{U1} &= \text{Y1V1}\,\text{P1} + \text{Y1V2} \\
\text{U2} &= \text{k5}(\text{k9}\,\text{U1} + \text{s2} + \text{s3}) \\
\text{U3} &= \text{U1} - \text{U2} \\
\text{P2} &= \text{Z2V1}\,\text{U2} + \text{Z2V2} \\
\text{P3} &= \text{Z3V1}\,\text{U3} + \text{Z3V2}
\end{aligned}$$

A.3.10 Output coupled with a linear reflectance and key controlled aperture

With an open tonehole, this case can be viewed as a particular case of a simple junction of 2 segments §A.3.6, where T2in = 0 and the reflectance filter is R2. When the tonehole remains

open all the time, the simulation is more economical this way.

Progressive closure of a tonehole

In our model, the progressive closure of a tonehole is simulated by a diminution of the radius $r = \theta\, \mathrm{r2}$ of an imaginary diaphragm progressively obturating the chimney (or the main pipe) at its downstream output. The "degree of aperture of the tonehole", θ, is a parameter varying between 0 (tonehole closed) and 1 (tonehole open). The output reflectance of the tonehole during closure is interpolated with 2 reflectance filters, R2a and R2b. The reflectance of the open tonehole is simulated in discrete time by R2a, and the reflectance of the partially closed tonehole with degree of aperture θ_1 is simulated by R2b. θ_1 is an arbitrary constant with typical value: $\theta_1 = 0.1$. R2a and R2b are converted to impedance filters with Eq. A.4. For apertures $1 \geq \theta > \theta_1$, the output impedance of the tonehole is approximated with a linear crossfade between the 2 impedance filters [1]. The resulting intermediate filter, Z2c, is written:

$$\mathrm{P2} = \mathrm{Z2cV1\ U2} + \mathrm{Z2cV2},$$

where Z2cVx varies linearly between Z2aVx and Z2bVx, when θ varies from 1 to θ_1.

For $\theta_1 \geq \theta \geq 0$, the flow rate U2 is approximated with a crossfade between the flow rate at $\theta = \theta_1$ and 0 (tonehole hermetically closed). The results are qualitatively similar to the measurements of Terroir [163, 164]. See also [172, 91, 92].

Approximation of the reflectance of small orifices

The LSCE method is not well suited for the approximation of reflectance filters for small orifices, because of passivity issues. An analytical expression is preferable.

We seek a numerical reflectance filter of the form:

$$H(z) = c_1 \left(\frac{1}{1 - y_1 z^{-1}} - \frac{1}{1 - y_1} \right) + c_2 \left(\frac{1}{1 - y_2 z^{-1}} - \frac{1}{1 - y_2} \right) - 1 \tag{A.9}$$

with $y_2 = y_1^*$ and $c_2 = c_1^*$.

It can be verified that with the substitutions:

$$\begin{aligned} z &\rightarrow \exp(j\,\omega) \\ c_1 &\rightarrow \frac{(y_1 - 1)^3 \left(d_2 \left(y_2 - 1\right) + d_1 \left(y_2 + 1\right)\right)}{2 y_1 \left(y_2 - y_1\right)} \\ c_2 &\rightarrow \frac{(y_2 - 1)^3 \left(d_2 \left(y_1 - 1\right) + d_1 \left(y_1 + 1\right)\right)}{2 y_2 \left(y_1 - y_2\right)} \end{aligned}$$

the filter has the following properties:

$$\begin{aligned} H(z)|_{\omega=0} &= -1 \\ \partial_\omega H(z)|_{\omega=0} &= j\, d_1 \\ \partial_\omega^2 H(z)|_{\omega=0} &= d_2 \end{aligned}$$

Approximation of the parameters:

	y_1	c_1
Flanged	$-0.2064 + 0.2797\, j$	$(0.06945 - 0.7939\, j)\, r + (0.1963 + 0.3777\, j)\, r^2$
Unflanged	$-0.4102 + 0.1751\, j$	$(0.2306 + 0.8818\, j)\, r + (0.08649 - 0.5486\, j)\, r^2$

The radius r of the orifice is expressed in mm. The formula for c_1 is obtained with a low frequency estimation of the derivatives d_1 and d_2 (see Eq. 7.11) and with $F_s = 44'100$ Hz and $c = 343.4$ m/s. The filter is passive for $0 < r < 3$mm.

1. The crossfade technique is probably more efficient than updating the filter coefficients during the transition.

Key induced flow

During the closure or the opening phase, the key (or the finger) moves some air flow Ukey inside or outside the tonehole. Similarly to the exciter case, Ukey is assumed to be proportional to the velocity of the key Ukey=$\lambda_{\text{key}} F_s(\theta[n]-\theta[n-1])$, where λ_{key} is a constant proportional to the area of the key.

Constants:	SZr1, Z1V1, Z1K1, Z1K2, SZr2, Z2V1, Z2K1, Z2K2
	SZr3, Z3V1, Z3K1, Z3K2, θ_1,
	k1=1/(Z1V1-Z2aV1), k2=1/(Z1V1-Z2bV1), k3=1/(1-θ_1), k4=1/θ_1
Inputs:	θ, Ukey
Propagators:	T1
Reflectors:	R1, R2a, R2b
Outputs:	P, U1

Equations to solve:

$$
\begin{aligned}
\text{P1} &= \text{Z1V1 U1} + \text{Z1V2} \\
\text{P2} &= \begin{cases} \text{Z2aV1 U2} + \text{Z2aV2}, & \theta = 1 \\ \text{Z2cV1 U2} + \text{Z2cV2}, & 1 > \theta > \theta_1 \\ \text{Z2bV1 U2} + \text{Z2bV2}, & \theta_1 \geq \theta \geq 0 \end{cases} \\
\text{U1} &= \begin{cases} \text{U2} + \text{Ukey}, & \theta > \theta_1 \\ (\theta/\theta_1)\text{U2} + \text{Ukey}, & \theta_1 \geq \theta > 0 \\ 0, & \theta = 0 \end{cases} \\
\text{P} &= \text{P1} = \text{P2} \\
\text{Z2cV1} &= \frac{\theta-\theta_1}{1-\theta_1}\,\text{Z2aV1} + \frac{1-\theta}{1-\theta_1}\,\text{Z2bV1} \\
\text{Z2cV2} &= \frac{\theta-\theta_1}{1-\theta_1}\,\text{Z2aV2} + \frac{1-\theta}{1-\theta_1}\,\text{Z2bV2}
\end{aligned}
$$

Solution:

$$
\begin{aligned}
\text{U2} &= \begin{cases} \text{k1}(\text{Z2aV2} - \text{Z1V2}), & \theta = 1 \\ \frac{\text{Z2cV2}-\text{Z1V2}-\text{Ukey Z1V1}}{\text{Z1V1}-\text{Z2cV1}}, & 1 > \theta > \theta_1 \\ \text{k2}(\text{Z2bV2} - \text{Z1V2} - \text{Ukey Z1V1}), & \theta_1 \geq \theta > 0 \\ \text{Ukey}, & \theta = 0 \end{cases} \\
\text{U1} &= \begin{cases} \text{U2} + \text{Ukey}, & \theta > \theta_1 \\ (\theta/\theta_1)\,\text{U2} + \text{Ukey}, & \theta_1 \geq \theta > 0 \\ \text{Ukey}, & \theta = 0 \end{cases} \\
\text{P} &= \text{Z1V1 U1} + \text{Z1V2}
\end{aligned}
$$

A.3.11 Output coupled with a reflectance with nonlinear losses and key controlled aperture

During clarinet playing, important AC pressure levels are measured inside the clarinet. This causes important flow rates at the orifices of the instrument (mainly in the side toneholes). Relevant nonlinear losses result from this situation. According to Atig [3, 5, 6, 4], these NL losses can be modelled by the addition of a quadratic term (see also Disselhorst [41], Skulina [139] and Temiz [156, 157]). In his model, adapted later by Terroir [163] for the simulation of the progressive closure of a tonehole, the output impedance is assumed to be 0 (i.e. P2=0, whatever the frequency). In our model, the output impedance is assumed to remain that of the linear case (i.e. P2 is frequency dependant, but it still tends to 0 when the frequency tends to 0). As before,

the progressive obturation of the tonehole is modelled with a progressively closing diaphragm. Bernoulli's law is assumed to be valid for the simulation of the effect of the diaphragm:

$$U = \pi(r_2\,\theta)^2\,\mathrm{sgn}(P_1 - P_2)\sqrt{2|P_1 - P_2|/\rho}$$

A vena contracta coefficient may be introduced *via* θ. It may take two different values, αOut or αIn, depending if the flow is outgoing or incoming from the tonehole inside the instrument. This is achieved by the substitution:

$$\theta \to \begin{cases} \alpha\mathrm{Out}\,\theta, & \mathrm{U2} \geq 0 \\ \alpha\mathrm{In}\,\theta, & \mathrm{U2} < 0 \end{cases}$$

This way the simulation scheme remains unmodified by the vena contracta coefficient [2]. These parameters can also be used to simulate the presence of a key pad in rest position in the vicinity of the tonehole.

The model for the progressive closure of the tonehole and for the key induced flow are the same as before.

Constants:	SZr1, Z1V1, Z1K1, Z1K2, SZr2, Z2V1, Z2K1, Z2K2, αIn, αOut, k1=$\rho\,\left(\pi\,\mathrm{r2}^2\right)^{-2}$, k2=1/k1, k3=1/(1-$\theta_1$), k4=1/$\theta_1$
Inputs:	θ, Ukey
Propagators:	T1
Reflectors:	R1, R2a, R2b
Outputs:	P1, P2, U1, U2

Equations to solve:

$$\begin{aligned}
\mathrm{P1} &= \mathrm{Z1V1\ U1} + \mathrm{Z1V2} \\
\mathrm{P2} &= \begin{cases} \mathrm{Z2aV1\ U2} + \mathrm{Z2aV2}, & \theta = 1 \\ \mathrm{Z2cV1\ U2} + \mathrm{Z2cV2}, & 1 > \theta > \theta_1 \\ \mathrm{Z2bV1\ U2} + \mathrm{Z2bV2}, & \theta_1 \geq \theta \geq 0 \end{cases} \\
\mathrm{U1} &= \begin{cases} \mathrm{U2} + \mathrm{Ukey}, & \theta > \theta_1 \\ (\theta/\theta_1)\mathrm{U2} + \mathrm{Ukey}, & \theta_1 \geq \theta > 0 \\ \mathrm{Ukey}, & \theta = 0 \end{cases} \\
2(\mathrm{P1} - \mathrm{P2}) &= \begin{cases} \mathrm{k1}/\theta^4\,\mathrm{U2}^2, & \mathrm{U2} \geq 0 \\ -\mathrm{k1}/\theta^4\,\mathrm{U2}^2, & \mathrm{U2} < 0 \end{cases} \\
\mathrm{Z2cV1} &= \frac{\theta - \theta_1}{1 - \theta_1}\,\mathrm{Z2aV1} + \frac{1 - \theta}{1 - \theta_1}\,\mathrm{Z2bV1} \\
\mathrm{Z2cV2} &= \frac{\theta - \theta_1}{1 - \theta_1}\,\mathrm{Z2aV2} + \frac{1 - \theta}{1 - \theta_1}\,\mathrm{Z2bV2}
\end{aligned}$$

2. A transition model should be considered when the flow inverts its direction. See also the remark about the pressure loss coefficient in §8.3.4

Solution:

$$
\begin{aligned}
\theta &:= \begin{cases} \alpha\mathrm{Out}\,\theta, & \mathrm{Z2aV2} \le \mathrm{Z1V2} \\ \alpha\mathrm{In}\,\theta, & \mathrm{Z2aV2} > \mathrm{Z1V2} \end{cases} \\
\mathrm{d1} &= \begin{cases} (\mathrm{Z2aV1} - \mathrm{Z1V1}), & \theta = 1 \\ \theta^2(\mathrm{Z2cV1} - \mathrm{Z1V1}), & 1 > \theta > \theta_1 \\ \theta_1^2(\mathrm{Z2bV1} - \mathrm{Z1V1}), & \theta_1 \ge \theta > 0 \\ \mathrm{Ukey}, & \theta = 0 \end{cases} \\
\mathrm{d2} &= \begin{cases} 2(\mathrm{Z1V2} - \mathrm{Z2aV2}), & \theta = 1 \\ 2(\mathrm{Ukey}\,\mathrm{Z1V1} + \mathrm{Z1V2} - \mathrm{Z2cV2}), & 1 > \theta > \theta_1 \\ 2(\mathrm{Ukey}\,\mathrm{Z1V1} + \mathrm{Z1V2} - \mathrm{Z2bV2}), & \theta_1 \ge \theta > 0 \\ \mathrm{Ukey}, & \theta = 0 \end{cases} \\
\mathrm{U2} &= \begin{cases} \theta^2\,\mathrm{k2}\left(\sqrt{\mathrm{d1}^2 + \mathrm{k1}\,\mathrm{d2}} - \mathrm{d1}\right), & d2 > 0 \\ \theta^2\,\mathrm{k2}\left(\mathrm{d1} - \sqrt{\mathrm{d1}^2 - \mathrm{k1}\,\mathrm{d2}}\right), & d2 < 0,\ \theta > \theta_1 \\ \theta_1^2\,\mathrm{k2}\left(\mathrm{d1} - \sqrt{\mathrm{d1}^2 - \mathrm{k1}\,\mathrm{d2}}\right), & d2 < 0,\ \theta \le \theta_1 \\ 0, & d2 = 0 \end{cases} \\
\mathrm{U1} &= \begin{cases} \mathrm{U2} + \mathrm{Ukey}, & \theta > \theta_1 \\ (\theta/\theta_1)\,\mathrm{U2} + \mathrm{Ukey}, & \theta_1 \ge \theta > 0 \\ \mathrm{Ukey}, & \theta = 0 \end{cases} \\
\mathrm{P1} &= \mathrm{Z1V1}\ \mathrm{U1} + \mathrm{Z1V2} \\
\mathrm{P2} &= \begin{cases} \mathrm{Z2aV1}\ \mathrm{U2} + \mathrm{Z2aV2}, & \theta = 1 \\ \mathrm{Z2cV1}\ \mathrm{U2} + \mathrm{Z2cV2}, & 1 > \theta > \theta_1 \\ \mathrm{Z2bV1}\ \mathrm{U2} + \mathrm{Z2bV2}, & \theta_1 \ge \theta \ge 0 \end{cases}
\end{aligned}
$$

A.3.12 Junction of 2 segments with a short chimney with nonlinear losses

When the chimney is short comparatively to the wave length corresponding to the sampling period (typically < 30 mm for the usual audio sampling rate), the nonlinear resistance of the tonehole can be approximated at the upstream section of the chimney (instead of the external output of the chimney). This design is more economical in terms of computer resources and avoids the generation of artifacts if the filters are not accurate in the high frequency range. A single reflectance filter replaces the 2 propagators and the radiation reflectance filter. The transition is easier to manage comparatively to the output coupling. No filter for the quasi closed tonehole is required, because no transition to an infinite impedance is needed. Usually two filters are required (one for the open tonehole and one for the closed tonehole). A simple crossfade between the two filters is performed during the transition. In the case of a cylindrical chimney, the filter for the closed case is simply the propagator corresponding to a cylinder of same diameter and twice the acoustical length of the chimney. The acoustical length h' is determined with the length correction proposed in [16] $h' = h + t_w$, with $t_w = \frac{1}{8} b\delta\left(0.207\delta^2 + 1\right)$ (as before, b is the radius of the chimney and δ is ratio of the diameters).

Notice that in the linear case and in absence of key induced flow, the junction with the input reflectance of the chimney can be performed directly with the standard `J3Section` or `J3SectionMass` procedures.

We assume that the Kirchhoff laws apply (P=P1=P2 and U1=U2+U3) at the junction.

Constants:	SZr1, Z1V1, Z1K1, Z1K2, SZr2, Z2V1, Z2K1, Z2K2, SZr3, Z3V1, Z3K1, Z3K2, V1 = -Y1V1 + Y2V1 + Y3V1, k1=1/(2(Y2V1 - Y1V1) Y3V1), k2=1/(Y1V1-Y2V1), k3=1/Y3V1
Inputs:	None
Propagators:	T1, T2, T3
Reflectors:	R1, R2, R3
Outputs:	P, U1, U2, U3

Equations to solve:

$$
\begin{aligned}
\mathrm{U1} &= \mathrm{Y1V1\ P1} + \mathrm{Y1V2} \\
\mathrm{U2} &= \mathrm{Y2V1\ P2} + \mathrm{Y2V2} \\
\mathrm{U3} &= \mathrm{Y3V1\ P3} + \mathrm{Y3V2} \\
\mathrm{P} &= \mathrm{P1} = \mathrm{P2} \\
\mathrm{U1} &= \mathrm{U2} + \mathrm{U3} \\
\mathrm{U3} &= \mathrm{Ukey} + \mathrm{sgn}(\Delta P)\, W \sqrt{|\Delta P|} \\
\Delta P &= \mathrm{P} - \mathrm{P3} \\
W &= S \sqrt{2/\rho}
\end{aligned}
$$

S is the cross section of the (open or partially closed) chimney.

Solution:

$$
\begin{aligned}
\mathrm{b1} &= \mathrm{Y3V1}(\mathrm{Y1V1} - \mathrm{Y2V1})(\mathrm{Ukey\,V1} - \mathrm{Y1V2\,Y3V1} + \mathrm{Y1V1\,Y3V2} - \mathrm{Y2V1\,Y3V2} + \mathrm{Y2V2\,Y3V1}) \\
\mathrm{W2} &= \mathrm{V1}\, W^2 \\
\mathrm{b2} &= W \sqrt{4\,|\mathrm{b1}| + \mathrm{V1W2}} - \mathrm{W2} \\
\mathrm{U3} &= \mathrm{k1\,b2\,sgn(b1)} + \mathrm{Ukey} \\
\mathrm{P} &= \mathrm{k2}\,(\mathrm{U3} - \mathrm{Y1V2} + \mathrm{Y2V2}) \\
\mathrm{U1} &= \mathrm{Y1V1\ P} + \mathrm{Y1V2} \\
\mathrm{U2} &= \mathrm{Y2V1\ P} + \mathrm{Y2V2} \\
\mathrm{P3} &= \mathrm{k3}\,(\mathrm{U3} - \mathrm{Y3V2})
\end{aligned}
$$

Appendix B

Architecture of the synthesizer

Résumé

Cet appendice décrit la structure et les modalités techniques permettant l'implémentation et la simulation d'un instrument à vent numérique. On y décrit également la résolution analytique du problème des boucles sans retard, pour chaque type de jonction proposé dans le dictionnaire de jonctions.

L'instrument numérique est structuré par différents niveaux d'abstraction. Au plus haut niveau, le musicien ne voit que l'instrument numérique, qui peut être joué par un synthétiseur de type Max MSP. Le fabricant d'instruments se situe au second niveau d'abstraction: l'instrument est assemblé et interfacé au moyen de différents objets, de manière similaire à un jeu de construction, en jonctionnant différents segments. Le troisième niveau d'abstraction concerne le traitement du signal. Son objet principal est la construction filtres numériques. L'acousticien gère le niveau d'abstraction le plus bas. Son travail consiste à modéliser les excitateurs et à calculer les fonctions de transfert correspondant à la géométrie de l'instrument dans le domaine fréquentiel et à les ≪traduire≫ dans le domaine temporel, en tant que filtres numériques. Cette tâche, effectuée principalement pour les ondes progressives, est décrite essentiellement au Chapitre 7.

B.1 Introduction

This Appendix describes the structure and the technical aspects related to the implementation and the simulation of a digital instrument. Its main purpose is to solve analytically the problem of delay free loops for each type of junction proposed in the dictionary of junctions.

The digital instrument is structured in different levels of abstraction. At the highest level, the musician see only the digital `Instrument`, which can be played by a synthesizer like Max MSP. The instrument maker is situated at the second highest level of abstraction: the instrument is assembled and interfaced by the mean of the following objects:

- `Section`: cross cut through the instrument's bore at some location, across which the acoustical parameters are to be determined.
- `Segment`: portion of the bore delimited by 2 `Sections`. This is a non local element which simulates the acoustical behavior of this portion of the bore, characterized by a non zero propagation time of the acoustical waves from one section to the other.
- `Orifice`: downstream or upstream end of a wave guide (usually a chimney or the bell of instrument), delimited by a single `Section`. This is a local element, which simulates the acoustical interactions with the outside world.
- `Exciter`: nonlinear, local element interacting with the bore (for instance clarinet mouthpiece and reed)
- `Junction`: binding element between the objects `Exciter`, `Segment` and `Orifice`, which couples locally the waves in order to satisfy the acoustical equations across the `Junction`.

— `Command`: primary playing parameter. Commands are generated for instance by a MIDI device or a command file and define sequentially the playing parameters like the blowing pressure, the lip pressure and the fingering to be played.

— `Action`: user defined procedure, which is performed at each discrete time step. Example: a MIDI code (primary command) is interpreted and executed as a progressive closure or aperture of some toneholes (depending commands). The object `Action` is also used to simulate commands.

— `Output`: channel through which the results of the simulation are sent (for instance a loudspeaker or a WAV file).

The third highest level of abstraction is the signal processing. Its main object is the construction of digital `Filters`.

Last but not least, the acoustician deal with the lowest level of abstraction. His job is to model exciters and to compute the transfer functions corresponding to the instrument's geometry in the frequency domain and to "translate" them into the time domain, as digital filters. This task is described here only for travelling waves, mainly in Chapter 7.

Finally, the digital instrument is simulated by the following procedure:

1. Compute the transfer functions of each segment and the reflectance of each orifice.
2. Perform a modal estimation of these functions, allowing a simulation with digital IIR filters.
3. Implement digital exciters
4. Solve the coupling problem at the junctions. Since the waves travel through a segment with a non zero propagation time, the coupling problem can be solved independently for each junction.
5. Simulate the acoustical response of the instrument to commands and actions.
6. Send the results to the output channels.

B.2 Structure of the digital instrument

The implementation of a digital instrument is realized with the objects listed in the previous section. These objects are of three kinds:

— **Interface objects:** Commands, Actions and Outputs

— **Topological objects:** Sections, Segments, Orifices and Junctions

— **Filter objects:** Filters

Each of these objects are briefly described. The class declaration is given (in C++). A list of the derived classes is given with a comment about the purpose.

B.2.1 The object `Instrument`

The object `Instrument` is the upmost structure and implements the synthesizer itself. The lists of objects {`Command`, `Action`, `Junction` and `Output`} which are stored into the variable `InstrumentData` define the behavior of the instrument. These lists are created by the mean of the functions `incorporateCommand`, `incorporateAction`, `incorporateJunction` and `incorporateOutput`. Any object that is not incorporated into the instrument by the mean of these functions has no effect and is not simulated (except if it is called by one of the incorporated objects).

```
class Instrument {
    public:
    InstrumentData*iData;  //lists of objects
    Instrument();          //constructor
    virtual void play();   //simulate the instrument
};
```

Typically the response of the instrument (member function `play()`) is simulated with the following pseudo code:

```
Initializations
WHILE commands are read() DO
    Perform actions
    Collect next output values of propagators from delay lines
    Solve the coupling problem at the junctions
    Manage output streams
END
Close output streams
```

Depending classes: none.

B.2.2 The object `Command`

At the beginning of each time step, the object `Command` reads an array of commands specifying the values of the playing parameters. Commands are read until the function `read()` return `false`. Theses commands may be the blowing pressure (and other excitation parameters), the lip pressure, the degree of aperture of a key, the state of a valve, the position of a slide, and so on. The mapping between a command and the receiver of the command must be specified by the mean of pointers. This way, any change in the command array is immediately echoed to the objects depending from this command.

```
class Command {
    public:
    double* command;  //ptr to array of commands
    unsigned int len;  //length of the array
    Command(unsigned int);  //constructor (number of commands)
    virtual bool read();  //read next command array
};
```

Depending classes:

Function	Status	Description
CGenerate	Implemented	Generate a stream of commands with fixed length. Each individual command has to be setted by an individual `Action` (with ramps for instance)
CFile	Implemented	Read a binary command file (fingering, blowing pressure, lip pressure) and perform a low pass filtering of the commands, in order to remove the sharp steps between the successive commands.
CMidiFile	Implemented	Read a MIDI file (fingering, blowing pressure, lip pressure) and perform a linear interpolation of the commands, in order to remove the sharp steps between the successive MIDI commands.
CMidiDevice	Project	Read a MIDI device (fingering, blowing pressure, lip pressure) and perform a low pass filtering of the commands, in order to remove the sharp steps between the successive MIDI commands.

B.2.3 The object `Action`

Objects of the class `Action` define procedures which are performed at each discrete time step. Actions may be chained. For instance: a `trill` is activated (which performs in turn 2 distinct actions : up and down `sigmoidRamp`s), the result is low pass filtered with `filterAction` and

the output of the filter is defined (via pointer) as the physical memory address of the parameter `theta` of the junction `JNonLinearHole`, which defines the degree of aperture of a tonehole. The first action of a chain must be incorporated into the instrument before the dependent actions, except if the dependent actions want to refer to the value of the first action one time step behind.

```
class Action {
    public:
    Action(); //constructor
    virtual void start();
    //give the order to start the action
    virtual void update();
    //wait on start or perform next action step
};
```

Depending classes:

Function	Status	Description
waitUntil	Implemented	wait until the settled discrete time is elapsed, then perform the defined action
trill	Implemented	wait until the settled discrete time is elapsed, then perform in turn the 2 defined actions (for instance generate up and down ramps), until stop time is reached
linearRamp	Implemented	Generate a linear ramp
sigmoidRamp	Implemented	Generate a sigmoid-like ramp, implemented with the function $-x^2(2x-3)$.
elbowRamp	Implemented	Generate an elbow shaped ramp, implemented with the function $-\frac{1}{2}x^2(x-3)$.
diracImpulse	Implemented	Generate a discrete Dirac impulse
filterAction	Implemented	Filter a command or any input parameter inside or outside the instrument structure
basicFinger	Implemented	Interpret a MIDI code as a progressive closure or aperture of toneholes or a modification other playing parameters, like the reed frequency

B.2.4 The object `Output`

The class `Output` specifies an array of output channels, opens an output stream for these channels, writes data to the stream and closes the stream. Each `Output` object has its own output stream, so many output files can be created during one simulation.

```
class Output {
    public:
    double** output;
    int len; //number of output channels
    Output(int); //constructor (number of output channels)
    virtual void setOutput(unsigned int, double*);
                        // (channel nr, pointer to output value)
    virtual void write(); //write outputs to stream
    virtual void close(); //close output stream
};
```

Depending classes:

Function	Status	Description
consoleOutput	Implemented	display the output on the console
WAVOutput	Implemented	cast output to integer value (according to conversion factors) and write to WAV file
binaryOutput	Implemented	write to binary file
audioOutput	Project	send output to an audio device

B.2.5 The object `Exciter`

The present application implements only one category of exciters : the reed exciter. In a mono-dimensional implementation, this exciter is modelled by a 1-D mechanical oscillator, driven by the air pressure difference ΔP across the reed, whose position is denoted y_n in discrete time. The aeraulic section of the channel W_n is a function of the position of the oscillator $W_n = S(y_n)$ and the reed flow U_r is proportional to the velocity of the reed $U_r = \lambda(y_n - y_{n-1})F_s$.

The stiffness of the reed is given by the reed-mouthpiece interaction and determines the static mechanical behavior of the reed. Different kind of active controls can be specified in the implementation: lip pressure, reed-lip damping and reed-lip mass, for instance.

The single reed, the double reed and the lip exciter for brass instruments can be simulated with the implemented exciters.

```
class Exciter {
    public:
    double lastInput; //remember last input value
    double W; //Aeraulic cross section
    double ur; //reed flow
    double y1, y2; //reed positions in the near past
    Exciter(); //constructor
    virtual double nextOutput(double input);
                        //(pressure drop across exciter)
    virtual void clearExciter();
};
```

Depending classes:

Function	Status	Description
phantomReed	Implemented	simple reed model with constant stiffness, where the reed is allowed to penetrate inside the mouthpiece
shockReed	Implemented	simple reed model simulating a shock of the reed on the lay
convexReed	Implemented	the simple reed is modelled piecewise with nonlinear springs. The parameters can be fitted according to measurements. Described in Chapter 5.
lippalReed	Implemented	lip model for brass instruments

B.2.6 The object `Section`

The object `Section` stores the parameters of a cross section: radius, characteristic impedance, direction (downstream or upstream) and simulation filters (impedance and admittance virtual filters). It defines a port of a junction.

```
class Section{
    public:
    Section(); //constructor
    double r; //radius of the cross section
    double Zc; //characteristic impedance
```

```
    double SZr; //=r*Zc*direction
    short int direction; //1: downstream, -1:upstream
    Filter*Z,*Y; //impedance and admittance filters
    void setSection(double, short int, Filter*, Filter*);
                //(radius, direction, Z filter, Y filter)
};
```

Depending classes: none.

B.2.7 The object `Orifice`

The object `Orifice` delimits the downstream or the upstream end of a waveguide and simulates the relationships with the external world. This is usually a chimney of a bell, but this can also be the whole bore of the instrument, if the filter Z is simulating the input impedance of the instrument.

```
class Orifice {
    public:
    Section*in;  //downstream end of waveguide
    Section*out;  //upstream end of waveguide
    Orifice(); //constructor
};
```

Depending classes:

Function	**Status**	**Description**
OpenHole	Implemented	interface a single reflectance filter
ChimneyHole	Implemented	interface a variable reflectance filter (usually used in conjunction with `CrossfadeFilter` in order to simulate the progressive closure of a tonehole)
inputImpedance	Implemented	simulates an input impedance

B.2.8 The object `Segment`

The object `Segment` simulates a portion of a bore delimited by 2 `Sections`. It contains 2 propagator filters.

```
class Segment {
    public:
    Section*in,*out;  //input et output sections
    Filter*Tdown,*Tup; //propagators
    Segment(); //constructor
    virtual void computeV2();//forecast next output
};
```

Depending classes:

Function	Status	Description
StdSegment	Implemented	simulate a segment of bore with 4 linear filters (2 reflectors and 2 propagators)
CylSegment	Implemented	simulate a cylindrical segment with 2 linear filters (propagators)
SlideSegment	Implemented	simulate a cylindrical segment with varying length (*c.f.* trombone slide) with 4 linear filters (propagators), crossfade and linear interpolation in delay line (fractional delay)
TuningSegment	Implemented	simulate a cylindrical segment with slightly varying length for tuning purposes (*c.f.* clarinet barrel) with 2 linear filters (propagators) and linear interpolation in delay line (fractional delay)
ValveSegment	Implemented	simulate the transitions between 2 cylindrical segments (*c.f.* trumpet valve) with a crossfade between 2×2 linear filters (propagators)
NLCylSegment	Implemented	simulate the nonlinear propagation of waves in a cylinder (2 NL propagators), with the algorithm proposed by Vergez [175].

B.2.9 The object `Junction`

The object `Junction` binds `Section` objects together and solve the coupling problem at each discrete time step. The `Junction` is responsible for the management and the update of `Exciter` and `Section` objects (i.e. reflectors, propagators and other filters local to the junction, like integrators or differentiators).

```
class Junction {
    public:
    Junction(); //constructor
    virtual void solveCoupling();
};
```

Depending classes:

Function	Status	Ports	Description
JFlowControl	Implemented	1	Flow controlled input junction
JPressureControl	Implemented	1	Pressure controlled input junction
JFlowControlOut	Implemented	1	Flow controlled output junction
JPressureControlOut	Implemented	1	Pressure controlled output junction
JExciterControl	Implemented	1	Input coupled with a pressure controlled exciter
JExciterInserted	Implemented	2	Exciter inserted between 2 segments
J2Segments	Implemented	2	Simple junction of 2 segments
J2SegmentsMass	Implemented	2	Junction of 2 cylindrical segments with added acoustical mass
J3Segments	Implemented	3	Simple junction of 3 segments
J3SegmentsMass	Implemented	3	Junction of 3 segments with added acoustical masses
J3ChimneyNL	Implemented	3	Junction of 2 segments and a short, nonlinear chimney
cLinearHole	Implemented	2	Output coupled with a linear reflectance and key controlled aperture
cNonLinearHole	Implemented	2	Output coupled with a nonlinear reflectance and key controlled aperture

B.2.10 The object `Filter`

The object `Filter` is the foundation of the simulation structure. It implements a linear approximation of the transfer functions in the discrete time domain, as IIR (infinite impulse response) or FIR (finite impulse response) digital filters. Differentiators and integrators are also simulated with the `Filter` structure. A delay line can be coupled to a filter by the mean of the object `CircularBuffer`.

At a given discrete time step, the input and the output of a filter are linked with the linear equation: `output`$= V_1$ `input`$+V_2$ (see Eq. 7.19). This equation is used to solve the coupling problem. A call to the method `computeV2()` computes V_2 according to the history of the filter. Its value is stored in the filter structure. Once the input is determined, the history of the filter must be updated with a call to `output=update(input)`, even if the output value is already known (history update). If the input value is known *a priori*, the slightly faster method `nextOutput` is used instead: `output=nextOutput(input)`. Both approaches cannot be combined during a single time step.

```
class Filter {
    public:
    double V1; //coefficient affecting the present input value
    double  V2; //sum of terms depending from history
    double lastInput; //remember last input
    double lastOutput; //remember last output
    Filter(); //constructor
    virtual void computeV2();
    //compute V2 and update partially the history
    virtual double update(double input);
    //compute the final output from V2 and complete history update
    virtual double nextOutput(double input);
    //compute directly the final output and update history
    virtual void clearFilter();
    //clear history of the filter
};
```

Depending classes:

Function	Status	Description
IIRFilter	Implemented	Infinite Impulse Response Filter
FIRFilter	Implemented	Finite Impulse Response Filter
SymKerFilter	Implemented	FIR filter with symmetrical kernel
OscGuillemain	Implemented	linear oscillator proposed by Ph. Guillemain
DelayedFilter	Implemented	conjugation of a filter and a delay line
CrossfadeFilter	Implemented	performs a crossfade between 2 filters, according to a weight Θ (for filter 2 and $1-\Theta$ for filter 1). If $\Theta = 0$, filter 2 is not simulated; If $\Theta = 1$, filter 1 is not simulated
virtualZFilter	Implemented	virtual impedance filter (see Eq. 7.25)
virtualYFilter	Implemented	virtual admittance filter (see Eq. 7.26)
derivationFilter	Implemented	differentiator
integrationFilter	Implemented	integrator
InstrFilter	Implemented	simulates the input impedance of an instrument from a collection of impedance filters (one for each fingering) and manages the transitions between fingerings
InstrRFilter	Implemented	simulates the input impedance of an instrument from a collection of reflectance filters (one for each fingering) and manages the transitions between fingerings

B.3 Examples of instruments

The purpose of this section is to give a first overview of how to use the software (and not to be a kind of user manual). The 3 examples below show how to define a new class derived from the base class `Instrument` (for instance `lateralHoleInstrument`, in Example 3). The instrument can then be simulated in 2 steps:
1) declare an instrument of the new derived class:

```
lateralHoleInstrument myClarinet;
```

2) simulate the instrument by invoking the method play():

```
myClarinet.play();
```

All objects that have been incorporated to the instrument (during the initialization of the class) are called in turn at each time step during the simulation. In order to understand how the objects are incorporated to the instrument and how the instrument is simulated, it is probably useful to study the source code implementing these methods:

```
void InstrumentData::play() {
discreteTime=0;
while(command->read()){
   for (vector<Action*>::iterator it = actions.begin() ; it != actions.end(); ++it){
     (*it)->update();
   }
   for (vector<Segment*>::iterator it = segments.begin() ; it != segments.end(); ++it){
     (*it)->computeV2();
   }
   for (vector<Junction*>::iterator it = junctions.begin() ; it != junctions.end(); ++it){
     (*it)->solveCoupling();
```

```
   }
   for (vector<Output*>::iterator it = outputs.begin() ; it != outputs.end(); ++it){
     (*it)->write();
   }
   discreteTime++;
}
for (vector<Output*>::iterator it = outputs.begin() ; it != outputs.end(); ++it){
     (*it)->close();
}
```

Compare with the pseudo code in §B.2.1.

Incorporation methods:

```
}
void InstrumentData::incorporateCommand(Command* cmd) {
   command=cmd;
}
void InstrumentData::incorporateSegment(Segment* segment) {
   segments.push_back(segment);
}
void InstrumentData::incorporateAction(Action* action) {
   actions.push_back(action);
}
void InstrumentData::incorporateJunction(Junction* junct) {
   junctions.push_back(junct);
}
void InstrumentData::incorporateOutput(Output* out) {
   outputs.push_back(out);
}
```

B.3.1 Simulation of the impulse response of a cylinder

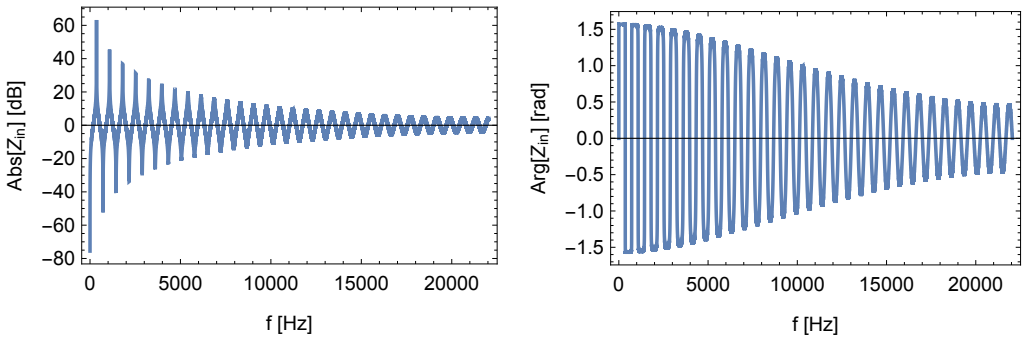

Module Argument

Figure B.1 – Input impedance of the cylinder of Example B.3.1, simulated with a single linear reflector (composed of 1 dipole, 6 monopoles and 1 Dirac).

The following example define a very simple instrument, `testImpulseResponse`, which simulates the response of a cylinder (length 24 cm) to a discrete flow impulse at its input, using a single reflector and a delay line (see discussion in §7.4.5). The filter is automatically converted by the software into an impedance filter, at the junction with the impulse generator. The filter response (in pressure) is exported in two different formats: a WAV file (here mono canal, casted to 16 bits integer values, according to the settled conversion factor) and a binary file (double precision reals). The dimensionless input impedance of the filter (depicted on Fig. B.1) is calculated by a discrete Fourier transform of the impulse response, after dividing the pressure by the characteristic impedance Z_c.

The simulation is about 110 times faster than real time, excluding the time of writing files, or 70 times faster than real time, including the time of writing files. In this example, the simulation time does not depend basically on the length of the cylinder, but only on the number of poles of the reflector, provided the (fractional) delay has been eliminated as described in §7.4.1. The number of poles of the reflector (here 1 dipole, 6 monopoles and 1 Dirac) can then be kept more or less constant (during the modal estimation process), whatever the length of the cylinder. The length of the delay line is modified accordingly.

In order to keep the example simple, the filter coefficients are declared directly in the code. Usually these coefficients are read from a data file. In this example the whole instrument is considered as a single orifice (ChimneyHole), and not as a segment, because no propagator is required : we have to simulate only its input impedance.

```
class testImpulseResponse:
public Instrument{
public:

//Command
CImpulse* myCommand;

//Filters
IIRFilter* filterR;
DelayedFilter* delayFilter;

//Orifice
ChimneyHole* myReflector;

//Junction
JFlowControl* jFlowControl;

//Outputs
WAVOutput* wavOutput;
binaryOutput *binOutput;

testImpulseResponse():
Instrument(){
// create objects
myCommand     = new CImpulse(1);
filterR       = new IIRFilter();
delayFilter   = new DelayedFilter();
myReflector   = new ChimneyHole();
jFlowControl  = new JFlowControl();
wavOutput     = new WAVOutput(1);
binOutput     = new binaryOutput(1);

//parameters of the pipe
double radiusPipe=0.008;
unsigned delay=60;

//initializations

//reset the impulse generator and set the duration of the simulation to 10 seconds
myCommand->resetImpulse(1,10*fe);

//set the reflector filter
filterR->setFilter(&filterRData[0],filterRLen);
//append a delay line to the filter
delayFilter->setFilter(filterR,delay);
//set the input radius of the "orifice" (delayed reflector)
myReflector->set(delayFilter,radiusPipe);

//set the parameters of the junction (flow command and input section)
```

```
jFlowControl->incorporateJunction(iData,&(myCommand->command[0]),
        myReflectance->in);

//export the generated pressure to WAV file
wavOutput->createFile("example.WAV",256,&conversion);
wavOutput->setOutput(0,&(jFlowControl->P));
iData->incorporateOutput(wavOutput);

//export the generated pressure to binary file
binOutput->createFile("example.dat",256);
binOutput->setOutput(0,&(jFlowControl->P));
iData->incorporateOutput(binOutput);
 }

protected:
static const int filterRLen=8;
//filter coefficients
double filterRData[filterRLen*4]=
{     1.56177255682538, 0,                  0, 0,
  -0.00685882662363974, 0, -0.741750668457406, 0,
   0.00187968803501007, 0, -0.846006652548808, 0,
 -0.000415472500341695, 0, -0.912613646131213, 0,
 0.0000781941831989475, 0, -0.953970614839499, 0,
-0.0000108276247890862, 0, -0.978463985204081, 0,
0.00000067960367332951, 0, -0.993366650105859, 0,
     -1.74803256664622, 0.49331398574302,
    -0.598810896410137, 0.0920637930780157};
//conversion factor for WAV export
double conversion = 1/1000.;
};
```

The instrument can be played with a clarinet mouthpiece by replacing the junction `JFlowControl` by a junction `JExciterControl`. Naturally the specification of an exciter is required. This is demonstrated in the next example.

B.3.2 Simulation of a cylindrical clarinet with 1 chimney

The `Instrument` defined in this example simulates 3 cylindrical segments of length 30, 10 and 1 cm. The third segment is a chimney which is connected between the 2 first segments (see scheme on Fig. B.2). A clarinet exciter (of type phantomReed) is connected to the input of the pipe. The outputs of the bore and of the chimney are simulated with nonlinear losses. Because each tonehole can be progressively closed (*via* the value of the parameters theta or thetaEnd), 2 reflectors are required for each tonehole (one for the open tonehole and one for the nearly closed tonehole, see §A.3.10). Two actions are chained in order to obtain the following effect: wait 1 second (action1), then close progressively the tonehole with a linear ramp during 1 second (action2). A third action (not represented on Fig. B.2) computes the external pressure from the pressure signal inside the mouthpiece, with the algorithm described in Chapter 6, Appendix B.

The simulation is about 10 times faster than real time, including the time of writing files.

```
class cylinderWithChimney:
public Instrument{
public:

//Command
CtanhRamp *myCommand;

//Actions
waitUntil *action1;
linearRamp *action2;
filterAction *projectOutside;
```

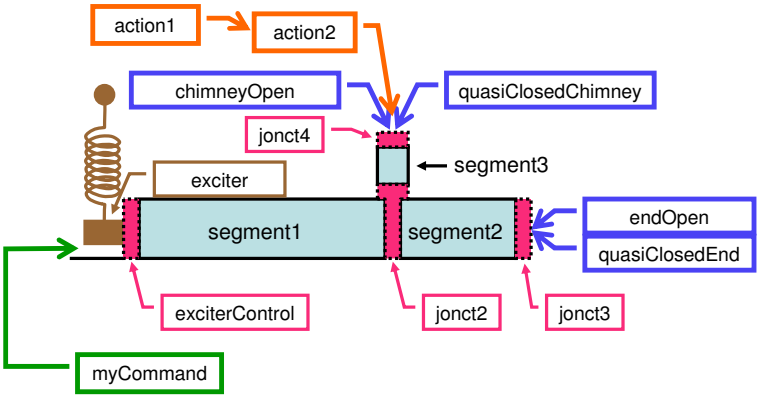

Figure B.2 – Scheme of the instrument defined in Example B.3.2, showing the different kinds of objects involved: Commands in green, Actions in orange, Exciter in brown, Segments in light blue, Orifices in blue, Junctions in magenta (a non zero thickness is given here for graphical reasons, but in reality, a junction is merely a surface). The shape of the arrows distinguishes if informations are exchanged between objects (thick arrows) or if the identifier indicates only the name of the illustrated object (thin arrows).

```
//Exciter
phantomReed *exciter;

//Filter
SymKerFilter*radiation;

//Segments
CylindricalSegment *segment1, *segment2, *segment3;

//Orifices
OpenHole *endOpen, *chimneyOpen, *quasiClosedEnd, *quasiClosedChimney;

//Junctions
JExciterControl *exciterControl;
J3Segments *jonct2;
JNonLinearHole *jonct3, *jonct4;

//Output
WAVOutput *wavOutput;

//parameters
double zeta=0.3, phi=1.0, epsilon=0.04, lambda=0., PMax=6000., fReed=900., qReed=.8,
theta=1., thetaEnd=1., radiusBore=.0075, radiusChimney=.003,
radiusQuasiClosed=.00075, alphaOut=1., alphaIn=1., lambdaKey=0.1, durationRamp=2.;

cylinderWithChimney():
Instrument(){
```

```
// create objects
myCommand          = new CtanhRamp(1);
action1            = new waitUntil();
action2            = new linearRamp();
projectOutside     = new filterAction();
exciter            = new phantomReed();
radiation          = new SymKerFilter();
segment1           = new CylindricalSegment();
segment2           = new CylindricalSegment();
segment3           = new CylindricalSegment();
endOpen            = new OpenHole();
quasiClosedEnd     = new OpenHole();
chimneyOpen        = new OpenHole();
quasiClosedChimney = new OpenHole();
exciterControl     = new JExciterControl();
jonct2             = new J3Segments();
jonct3             = new JNonLinearHole();
jonct4             = new JNonLinearHole();
wavOutput          = new WAVOutput(1);

//initializations

//commands
//simulate the mouthpressure with a tanh ramp
myCommand->incorporateCommand(iData, .05, 3., .8*PMax, 3*fe);

//action1 and action2 : wait 1 s then close the tonehole
action2->set(&theta, 1/(durationRamp*fe), 0.); //set ramp to close tonehole via theta
action1->set(iData, 1*fe, action2);              //wait 1 second until closing tonehole
iData->incorporateAction(action1);

//sound radiation
projectOutside->setFilter(&(exciterControl->P),radiation);
radiation->setFilter(&kerData[0],kerLen);
iData->incorporateAction(projectOutside);

//exciter
zeta=0.3*sqrt(PMax)*square(radiusBore)/rhoCbyPi;
exciter->set(&zeta, &phi, &lambda, &epsilon,1/PMax, fReed, qReed);

//segments
segment1->incorporateSegment(iData, &filterTData[0], filterTLen,  delay1,
    radiusBore);
segment2->incorporateSegment(iData, &filterT2Data[0],filterT2Len, delay2,
    radiusBore);
segment3->incorporateSegment(iData, &filterT3Data[0],filterT3Len, delay3,
    radiusChimney);

//orifices
endOpen->set(&filterRData[0],filterRLen,radiusBore);
chimneyOpen->set(&filterRChimData[0],filterRChimLen,radiusChimney);
quasiClosedEnd->set(&filterRClosedData[0],filterRClosedLen,radiusQuasiClosed);
quasiClosedChimney->set(&filterRClosedData[0],filterRClosedLen,radiusQuasiClosed);

//junctions
exciterControl->incorporateJunction(iData, &(myCommand->command[0]), exciter,
    segment1->in);
jonct2->incorporateJunction(iData, segment1->out, segment2->in, segment3->in);
jonct3->incorporateJunction(iData, &thetaEnd, radiusQuasiClosed/radiusBore,
    alphaOut, alphaIn, lambdaKey, segment2->out, endOpen, quasiClosedEnd);
jonct4->incorporateJunction(iData, &theta, radiusQuasiClosed/radiusChimney,
```

```
    alphaOut, alphaIn, lambdaKey, segment3->out, chimneyOpen,
    quasiClosedChimney);

//export radiated sound as WAV file
wavOutput->createFile("exportSound.WAV",256,&WAVconversion);
wavOutput->setOutput(0,&(projectOutside->lastOutput));
iData->incorporateOutput(wavOutput);

}

protected:
//filter coefficients
static const int filterTLen=15;
static const int delay1=36;
double filterTData[filterTLen*4]              ={/*data deleted*/};

static const int filterRLen=8;
double filterRData[filterRLen*4]              ={/*data deleted*/};

static const int filterRClosedLen=2;
double filterRClosedData[filterRClosedLen*4] ={/*data deleted*/};

static const int filterRChimLen=7;
double filterRChimData[filterRChimLen*4]      ={/*data deleted*/};

static const int delay2=10;
static const int filterT2Len=18;
double filterT2Data[filterT2Len*4]            ={/*data deleted*/};

static const int delay3=1;
static const int filterT3Len=13;
double filterT3Data[filterT3Len*4]            ={/*data deleted*/};

static const int kerLen=49;
double kerData[kerLen]={1., 0.5355,  0.2572,  0.0911, -0.0950, -0.2203, -0.2211,
-0.1484, -0.1093, -0.0745, -0.0377, -0.0603, -0.0996, -0.1088, -0.0989, -0.0682,
-0.0402, -0.0226, -0.0105, -0.0141, -0.0152,  0.0043,  0.0352,  0.0502,  0.0593,
 0.0642,  0.0450,  0.0271,  0.0129,  0.0041,  0.0015, -0.0120, -0.0122, -0.0184,
-0.0182, -0.0211, -0.0180,  0.0072,  0.0070, -0.0023, -0.0072, -0.0255, -0.0250,
-0.0088,  0.0135,  0.0301,  0.0269,  0.0165,  0.0005};

//conversion factor to integer (WAV export)
double WAVconversion = 1.;
};
```

Notice that for a short chimney (like in this example) the junctions junc2 and junc4 could be replaced by a single junction of type `J3ChimneyNL` and the orifices chimneyOpen and quasiClosedChimney and the segment3 could be replaced by 2 orifices of type `ChimneyHole` (tonehole+chimney open or totally closed). The simulation is much more efficient, as described in §A.3.12. This case is shown in the next example.

B.3.3 Generic clarinet with lateral toneholes

This example shows the implementation of a generic wind instrument with lateral toneholes + bell (here blown with the single reed exciter (of type `convexReed`, described in Chapter 5). All lateral toneholes are simulated with nonlinear losses.

Warning: this code is not complete: for sake of concision, some object declarations and initializations were removed. The purpose of this example is only to show the basic structuration of a fully developed instrument.

The structure of the instrument (geometry, number of segments and toneholes) is read from a data file. The user of the synthesizer has to supply this file and the files containing the filter coefficients obtained from to the modal estimation (see §7.4) of the scattering matrices of each segment and the reflectances of the chimneys and the bell. This example demonstrates the use of the short chimneys, which are computationally much more efficient, than the structure shown in Example 2.

This code is used for the simulation of a Buffet Crampon B-Clarinet (instrument measured and described in [154]) with 28 segments and 22 lateral toneholes, playing the beginning of a Brahms sonata from a MIDI file (same data as in Chapter 6, Fig. 8). The simulation is about 1.6 times faster than real time. The simulation of the bifurcation diagrams in §8.3.4 is also based on this code.

```
class lateralHolesInstrument:
public Instrument{
public:

//Commands
CMidiFile          *cmdMidi;

//Actions
sigmoidRamp        *crossfade;
basicFinger        *manageFingerChart;
filterAction       *projectOutside;

//Filters
CrossfadeFilter    *chimneyCross;
DelayedFilter      *chimneyOpen, *chimneyClosed;
IIRFilter          *chimneyOpenIIR, *chimneyClosedIIR;
SymKerFilter       *radiation;

//Exciter
convexReed         *reedExciter;

//Segments
Segment           **pipe;
CylindricalSegment *pipeCyl;
StdSegment         *pipeStd;

//Orifices
ChimneyHole        *chimney;
OpenHole           *endOpen, *quasiClosedEnd;

//Junctions
JExciterControl    *exciterControl;
J2SegmentsMass     *Jpipe;
JLinearHole        *terminationLin;
J3ChimneyNL        *Jchimney;

//Outputs
WAVOutput          *wavOutput;
binaryOutput       *binOutput;


lateralHolesInstrument():   Instrument()
{
////////////////////////////////////
//initialize instrument

//read instrument structure
readStructure("instrStructure.DAT", nbSegm, cylQ, chemQ, noFiltre);
```

```
//incorporate MIDI Command file
cmdMidi->incorporateCommand(iData, "Brahms.MID");

//incorporate fingering chart management
readFinger("fingering.DAT", nbFinger, nbHoles, midiCode, myFingerChart);
manageFingerChart->set(nbHoles, nbFinger, &myFingerChart[0], &midiCode[0], crossfade,
    &(cmdMidi->command[0]), lambdaKey);
crossfade->set(&(manageFingerChart->theta),1/(durationRamp*fe),1.);
iData->incorporateAction(manageFingerChart);

//set exciter
reedExciter->set(reedNr,&(cmdMidi->command[1]),&(cmdMidi->command[2]), &lambda,
    &lambda2,&myNoise,&(exciterControl->U),masse,amor);

////////////////////////////////////
//orifices :  read and set filters

//bell
readFilter("bell.DAT", typePav, nbFiltrersPav, nbCoefTotPav, nbCoefPav, adrCoefPav,
    delaysPav, radiusPav, dataPav);
endOpen->set(&dataPav[0],nbCoefPav[0],radiusPav[0]);
quasiClosedEnd->set(&filterRClosedData[0],filterRClosedLen,radiusQuasiClosed);

//chimneys open
readFilter("chimneysOpen.DAT", type, nbFiltrers, nbCoefTot, nbCoef, adrCoef, delays,
    radius, data);
for(int n=0;n<nbFiltrers;n++){
   chimneyOpenIIR[n].setFilter(&(data[adrCoef[n]]),nbCoef[n]);
   chimneyOpen[n].setFilter(&chimneyOpenIIR[n],delays[n]);
}

//chimneys closed
readFilter("chimneysClosed.DAT", type, nbFiltrers, nbCoefTot, nbCoef, adrCoef, delays,
    radius, data);
for(int n=0;n<nbFiltrers;n++){
   chimneyClosedIIR[n].setFilter(&data[adrCoef[n]],nbCoef[n]);
   chimneyClosed[n].setFilter(&chimneyClosedIIR[n],delays[n]);
   chimneyCross[n].setFilter(&(manageFingerChart->command[n]),&chimneyClosed[n],
       &chimneyOpen[n]);
   chimney[n].set(&chimneyCross[n],radius[n]);
}

////////////////////////////////////
//segments : read filters
readFilter("propagators.DAT", type, nbFiltersTot, nbCoefTot, nbCoef, adrCoef, delays,
    radius, data);
readFilter("reflectionUpstream.DAT", typeUp, nbFiltrersUp, nbCoefTotUp, nbCoefUp,
    adrCoefUp, delaysUp, radiusUp, dataUp);
readFilter("reflectionDownstrean.DAT", typeDown, nbFiltrersDown, nbCoefTotDown,
    nbCoefDown, adrCoefDown, delaysDown, radiusDown, dataDown);

//incorporate segments
int cpte=0;
for(int n=0;n<nbFiltersTot;n++){
   if(cylQ[n]>0){   //Cylindrical segment
      pipeCyl=new CylindricalSegment;
      pipeCyl->incorporateSegment(iData, &data[adrCoef[n]],nbCoef[n], delays[n],
         radius[n]);
      pipe[n] =pipeCyl;
   }
```

```
   else{           //Standard (i.e. non cylindrical) segment
      pipeStd=new StdSegment;
      pipeStd->incorporateSegment(iData, &data[adrCoef[n]],nbCoef[n], delays[n],
         &dataUp[adrCoefUp[cpte]],nbCoefUp[cpte],&dataDown[adrCoefDown[cpte]],
         nbCoefDown[cpte],radiusUp[cpte],radiusDown[cpte]);
      pipe[n] =pipeStd;
      cpte++;
   }
}

////////////////////////////////////
//incorporate junctions
cpte=0;
for(int n=0;n<nbFiltersTot-1;n++){
   if(chemQ[n]>0){
      Jchimney[cpte].incorporateJunction(iData, (pipe[n]->out), (pipe[n+1]->in),
         (chimney[cpte].in),&(manageFingerChart->commandSpeed[cpte]));
      cpte++;
   }
   else{
      Jpipe = new J2SegmentsMass;
      Jpipe->incorporateJunction(iData, (pipe[n]->out), (pipe[n+1]->in));
   }
}
//terminate the bore with the bell
terminationLin->incorporateJunction(iData, &thetaEnd, radiusQuasiClosed/radiusPav[0],
    lambdaKey,(pipe[nbFiltersTot-1]->out), endOpen, quasiClosedEnd);
//command the exciter blowing pressure from MIDI file and
//connect the exciter at the input of the pipe
exciterControl->incorporateJunction(iData, &(cmdMidi->command[1]), reedExciter,
    (pipe[0]->in));

////////////////////////////////////
//incorporate sound radiation
radiation->setFilter(&kerData[0],kerLen);
projectOutside->setFilter(&(exciterControl->P),radiation);
iData->incorporateAction(projectOutside);


////////////////////////////////////
//export results

//export radiated sound as WAV file
wavOutput->createFile("exportSound.WAV",256,&WAVconversion[0]);
wavOutput->setOutput(0,&(projectOutside->lastOutput));
iData->incorporateOutput(wavOutput);

//export data as binary file
binOutput->createFile("exportBinaryData.dat",256);
binOutput->setOutput(0,&(exciterControl->P)); //export mouthpiece pressure
binOutput->setOutput(1,&(exciterControl->U)); //export flow into mouthpiece
binOutput->setOutput(2,&(manageFingerChart->command[0])); //export fingering
// command
binOutput->setOutput(3,&(Jchimney[0].P3)); //export pressure in speaker hole
binOutput->setOutput(4,&(Jchimney[0].U1)); //export flow upstream speaker hole
binOutput->setOutput(5,&(Jchimney[0].U2)); //export flow downstream speaker hole
binOutput->setOutput(6,&(Jchimney[0].U3)); //export flow in speaker hole
iData->incorporateOutput(binOutput);
}};
```

This generic model was modified in order to simulate also brass instrument by adding valves,

slides and nonlinear propagation. This model was tested for the simulation of a Courtois bass trombone and a Blessing trumpet. The geometric measurements of these instruments were kindly provided by Joël Gilbert and René Caussé.

Appendix C

Introduction to the Canonical Correlation Analysis

Résumé

Cet appendice est écrit à l'intention des lecteurs peu familiers avec les techniques d'analyse canonique des corrélations (CCA). Il prend comme exemple didactique l'analyse de répétabilité effectuée à l'intérieur de la catégorie "subjective", au §8.5.2. On passe en revue différentes notions élémentaires liées aux tests statistiques, comme les hypothèses et seuils statistiques, la différence entre statistiques paramétriques et non paramétriques, le problème du nombre de blocs de données indépendants et des simulations Monte-Carlo. On présente succinctement le principe sur lequel est basée la CCA et on discute la différence entre la CCA et l'analyse en composantes principales (PCA).

C.1 Introduction

This appendix is written for readers unfamiliar with CCA techniques. The repeatability analysis performed inside the "subjective" category, in §8.5.2 is taken as a didactic example.

C.2 Statistical hypotheses

Our aim is to evaluate the repeatability of the subjective measures and to check if the judgments made by the clarinettist during the 4 repetitions of the test have a certain reliability or if they are rather dictated by chance. To fix the ideas, let's say that we evaluate the reliability of the descriptor *ForceSubj*. For this, we must determine what is the most likely hypothesis:

— hypothesis H_1: there is a link between the different successive evaluations of the reed strength by the clarinettist. It can be assumed that the mean correlation between the different evaluations of the test is greater than 0.

— hypothesis H_0: there is no link. We will favor this hypothesis if the observed mean correlation has a significant probability of being due to chance

C.3 Significance threshold (or significance level)

To decide which hypothesis we should favor, we set a threshold quantifying the risk of being wrong, say a threshold of 1%. If the observed mean correlation has a probability less than 1% of being due to chance, we reject the hypothesis H_0 and we deduce that the clarinettist is indeed able to discern blindly the different strengths of reed, favoring H_1. The observed correlation is considered to be **statistically significant** at the level of 1%.

C.4 Parametric and non-parametric statistics

What does "chance" mean? For this, we must make an assumption on the statistical distribution of the studied parameter among the population. One could for example assume that the measured parameter has a normal (Gaussian) distribution. In our sample (reed panel) we have a reed strength distribution evenly distributed between 2 and 3.5. We could therefore compare the mean square correlation observed during the 4 repetitions of the test to those obtained by artificially generating 4 tests where the reed strengths are drawn at random, uniformly distributed between 2 and 3.5. By repeating this simulation thousands of times (Monte-Carlo simulation method), we can establish the statistical distribution of the simulated statistic (the mean square correlation, $\bar{r}^2$). A difficulty arises however: how to be sure that the subjective strength of the reed has the same distribution as the nominal strength of the reed indicated by the manufacturer? We do not know it. An elegant way to overcome this difficulty is to perform the statistic not on the **score** attributed by the clarinettist to *ForceSubj*, but on the **rank** occupied by each reed within our panel, by sorting the reeds according to *ForceSubj*, from the weakest to the strongest. Our statistical test is then called "non-parametric".

C.5 Number of independent data blocks

If we have only 2 repetitions of the test to compare, the task is easy: there is only one correlation and it is sufficient to perform the Spearman correlation test. If the studied parameter has a normal distribution, we may perform the Pearson correlation test. Here, we have 4 repetitions of the test: the clarinettist evaluated 4 times the descriptor *ForceSubj* blind.

Carroll's proposed following principle to perform this comparison: we seek a kind of ideal measure of the descriptor (called group configuration, denoted $\boldsymbol{Y}$), which is optimally correlated with all repetitions of the test. In 1 dimension, a good solution is easy to guess because we have no liberty for the choice of a direction in the space: this ideal measure must be something like the mean of *ForceSubj* over all $J = 4$ blocks. Indeed, this guess for $\boldsymbol{Y}$ works well: the canonical correlations (between $\boldsymbol{Y}$ and the canonic variates $\hat{\boldsymbol{Y}}_j$) are respectively: 0.9337, 0.9596, 0.9413 and 0.9413. The mean square correlation is then $\bar{r}_1^2 = 0.8912$ (i.e. $\bar{r}_1^2 = 0.9440$). The optimal choice (determined analytically) is quite near: the optimal canonical correlations are respectively: 0.9459, 0.9714, 0.9413 and 0.9486. The mean square correlation is then $\bar{r}_1^2 = 0.9061$ (i.e. $\bar{r}_1^2 = 0.9518$, wich is the value recorded in Table 8.8, *subjectiveF*).

At first glance, the idea to compute canonical correlations may seem strange. Wouldn't it be easier to compute the correlations directly between $\boldsymbol{Y}$ and $\boldsymbol{X}_j$? This wouldn't work if $\boldsymbol{X}_j$ has more than 1 variable!

In Carroll's proposal, the group configuration is unique for all blocks: $\boldsymbol{Y}$. Notice that other authors propose models of CCA with such a configuration for each block: $\boldsymbol{Y}_j$

C.6 Statistical tests and Monte Carlo Simulations

Once $\boldsymbol{Y}$ has be computed, our aim is now to determine which canonical correlations are statistically significant. For this, we must know the statistical distribution of the mean square correlation when the null hypothesis H_0 is true (i.e. in the case where the blocks are completely independent of each other).

With one dimension, this distribution can be calculated analytically. With several dimensions (in our example: taking into account *simultaneously* 4 descriptors at each repetition of the test), the task is more complicated. I have chosen to perform a Monte Carlo simulation. A new difficulty arises then: during the random draw, it is necessary to take into account the correlation between the different descriptors. The simplest way to overcome this problem is to project the data onto an orthogonal axis system (rotation), where the descriptors are uncorrelated. This reverts to perform beforehand a PCA with the data of each repetition of the test (i.e. take the data blocks test1, test2, test3 and test4, instead of Test1, Test2, Test3 and Test4). Random samples can then be drawn independently for each variable in the Monte Carlo simulation.

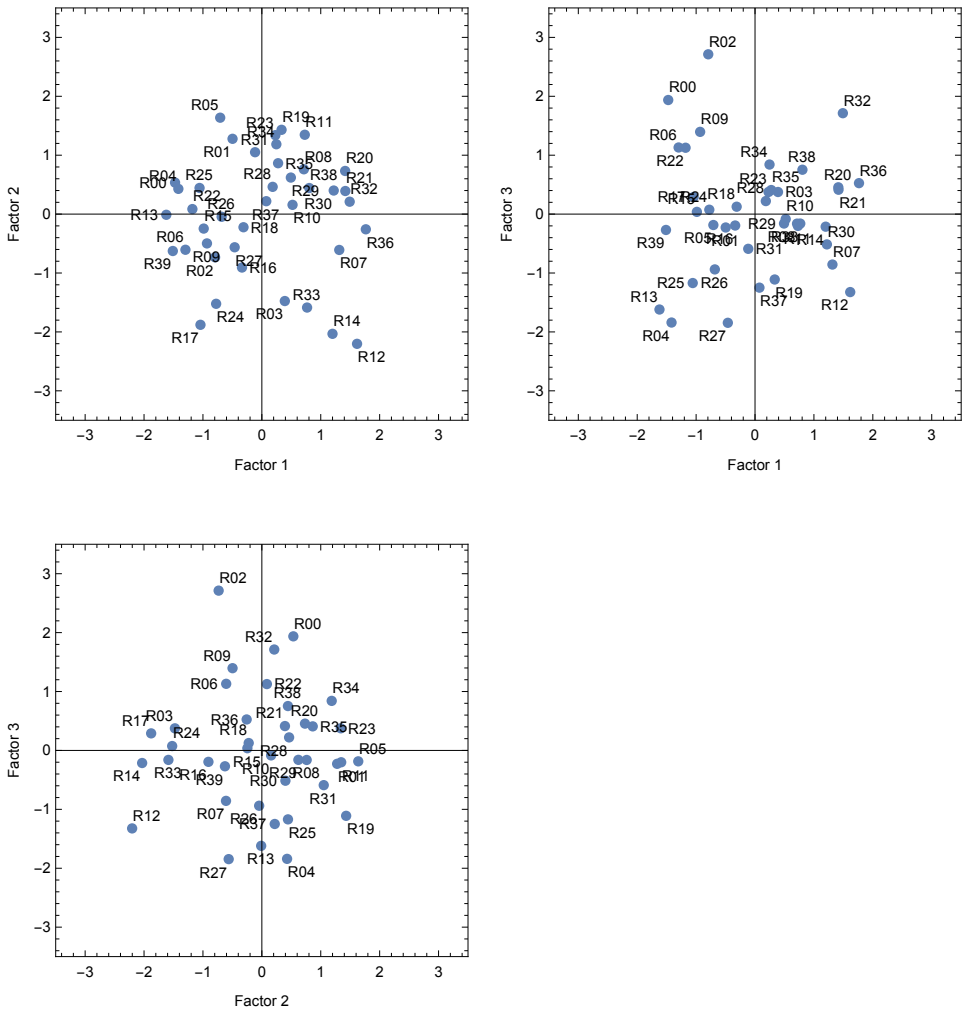

Figure C.1 – Plot of the canonical factors 1 to 3 of *subjectiveF* (after standardization). The identifier of each individual reed is indicated on the graphs.

C.7 Inspection of the canonical factors

A plot of the canonical factors allows to situate each individual reed inside the data corpus. This plot is ordinarily not very easy to interpret, because of the multiple dimensions involved. An example of factor plot is given on Fig. C.1 for the analysis *subjectiveF*, for the 3 significant dimensions (i.e. by plotting all possible pairs of factors: 1×2, 1×3 and 2×3). The inspection of the plot reveals no anomalous behavior: the reeds are distributed quite homogeneously in the 3D space. No reed is clearly an outlier.

At the contrary, the inspection of the first 4 factors of *staticF* on Fig. C.2 reveals clearly a problem of outlier on the factor 3, with the very strong reeds R12 and R21 (which did never completely close the channel in PhotoBreakIn, even with the tightest embouchure). Moreover, a nonlinearity can be noticed in the distribution of factor 1 (the weak reeds are closer together than the strong reeds). For these reasons, all analyses were carried out also on the basis of the ranks and not only on the scores (see Table 8.6).

It seems logical to compare the CCA factors obtained for the analyses *staticF* and *subjectiveF*. The comparison is illustrated on Fig. C.3. Obviously, the factor 1 is quite similar among both analyses, while this relation is less pronounced for the factors 2 and 3. This appears clearly by inspection of the correlation matrix, comparing each factor of *staticF* with each factor of

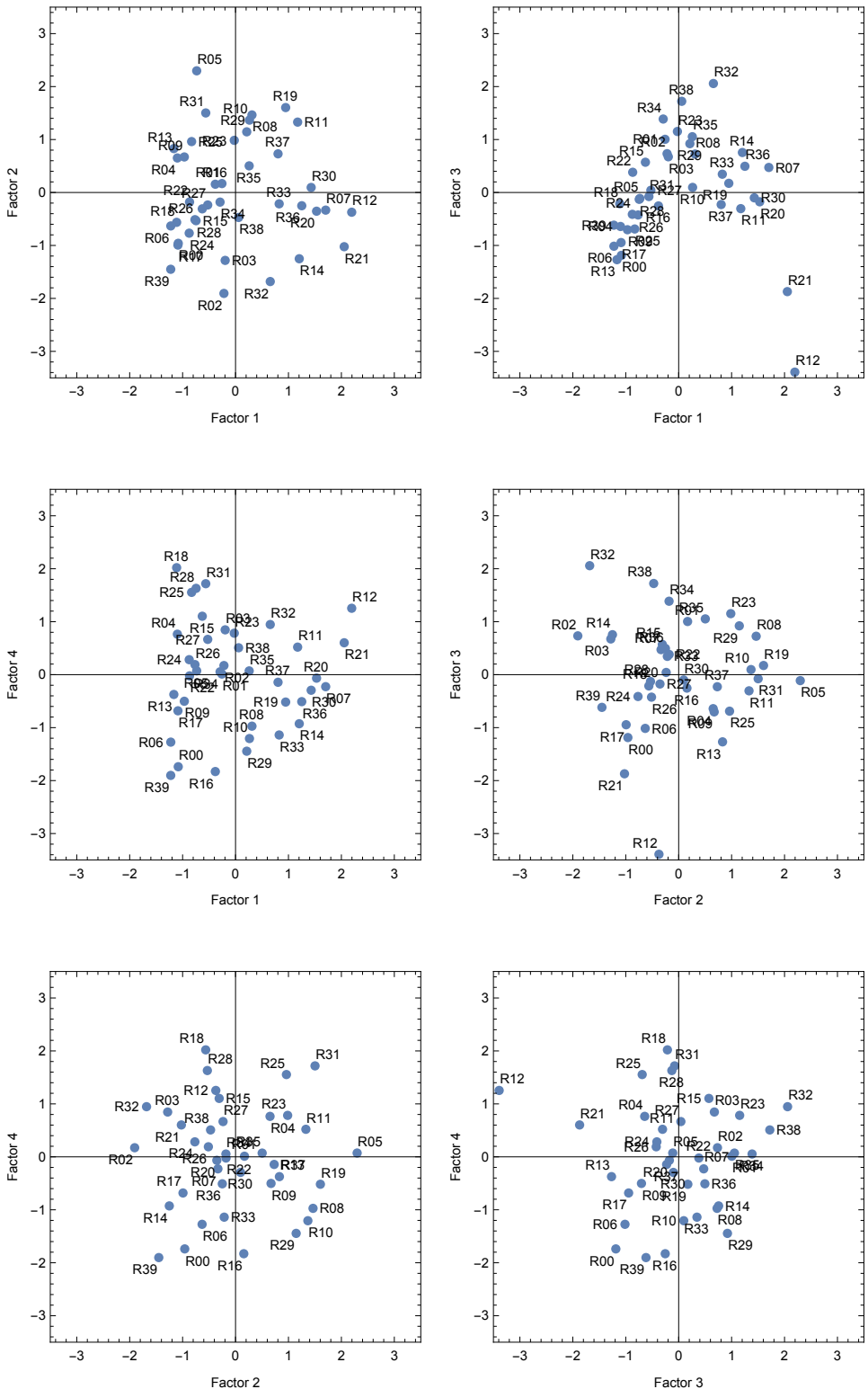

Figure C.2 – Plot of the canonical factors 1 to 4 of *staticF* (after standardization). The identifier of each individual reed is indicated on the graphs. The very strong reeds R12 and R21 appear as outliers for factor 3.

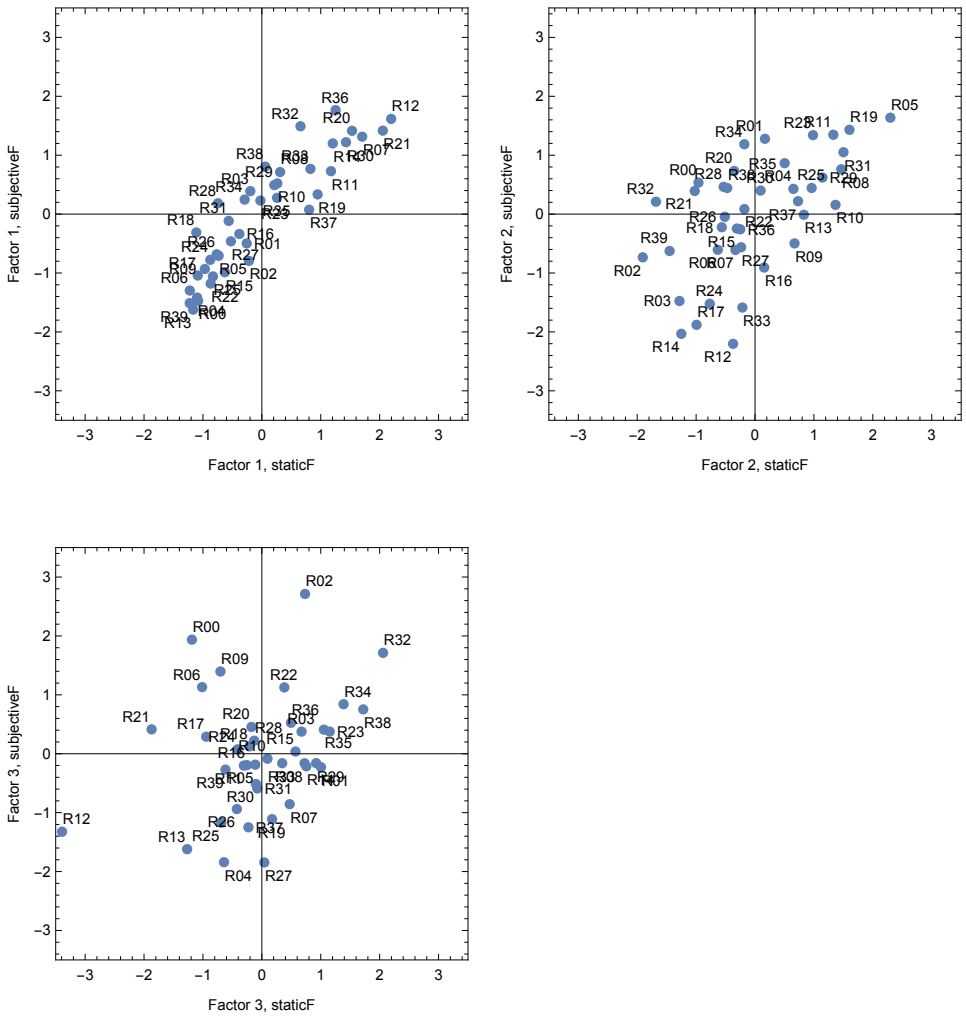

Figure C.3 – Comparison between the CCA factors 1 to 3 of *staticF* and *subjectiveF* (after standardization).

subjectiveF:

$$\rho(\text{staticF}_{\bullet,p}, \text{subjectiveF}_{\bullet,q}) = \begin{pmatrix} 0.903 & -0.025 & -0.111 \\ -0.036 & 0.605 & -0.456 \\ 0.222 & 0.319 & 0.317 \end{pmatrix}$$

The correlation matrix confirms that both factor 1 are well related, while the situation is different for the factors 2 and 3: one observes that an *ad hoc* rotation of the factors of one of the blocks along factor 1 would simplify the interpretation, because the correlation matrix will become essentially diagonal. The next step in the analysis is to find a way for doing this. Actually, this task is easy to do: we have only to apply again a CCA between the blocks *staticF* and *subjectiveF* (which were themselves already obtained by CCA). In Table 8.6, this analysis is called *statSubjF*. Its group configuration $\boldsymbol{Y}$ and its canonical variates $\hat{\boldsymbol{Y}}_j$ are plotted on Fig. C.4 for the 3 first factors.

As before, let us compute the correlation matrix for the 3 first factors (which is now perfectly diagonal):

$$\rho(\boldsymbol{Y}_{\bullet,p}, \hat{\boldsymbol{Y}}_{1,\bullet,q}) = \rho(\boldsymbol{Y}_{\bullet,p}, \hat{\boldsymbol{Y}}_{2,\bullet,q}) = \begin{pmatrix} 0.988 & 0. & 0. \\ 0. & 0.957 & 0. \\ 0. & 0. & 0.909 \end{pmatrix}$$

Both correlation matrices (for $j = 1$ and $j = 2$) are equal, because we have only $J = 2$ blocks.

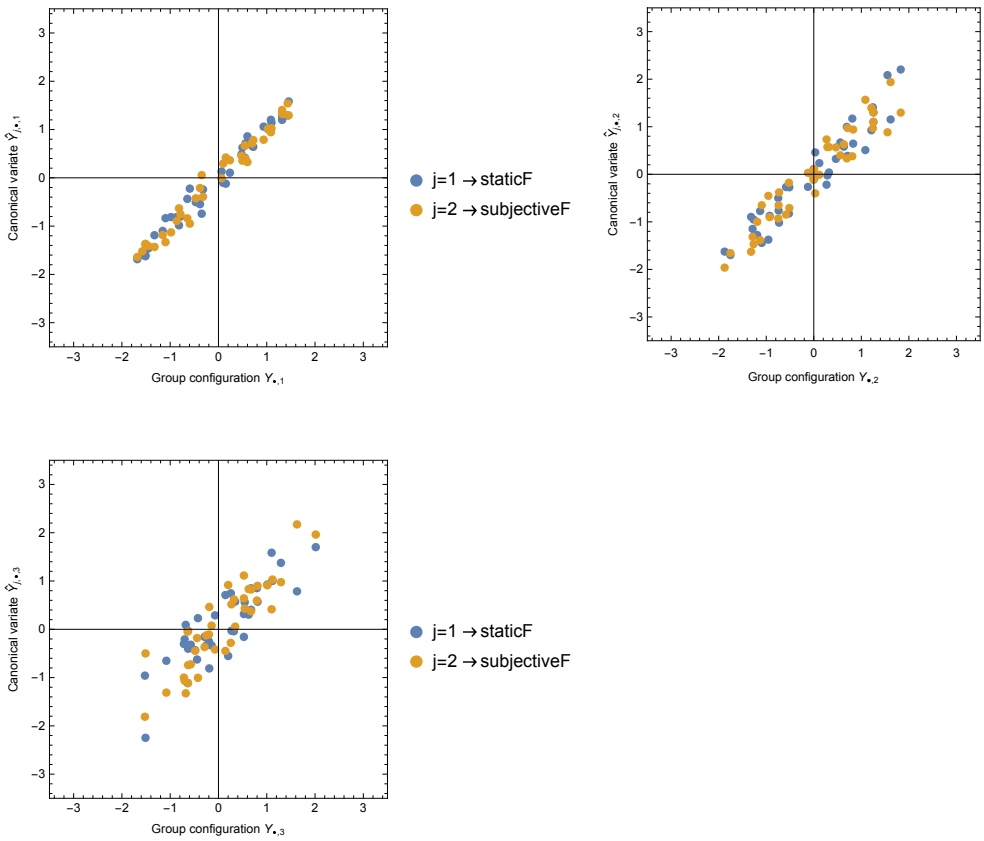

Figure C.4 – Plot of the group configuration $\boldsymbol{Y}$ (CCA factors) and the canonical variates $\hat{\boldsymbol{Y}}_j$ (after standardization) for the analysis *statSubjF*, which which extracts the information common to *staticF* and *subjectiveF*, see Table 8.6.

The diagonal elements of the correlation matrix are therefore equal to $\bar{r}_q$, and can be found in Table 8.8 up to factor $q = 6$ (although only the 4 first factors are significant). Finally the plot of the "new" factors (i.e. the new group configuration $\boldsymbol{Y}$) resuming the information common to *staticF* and *subjectiveF* is depicted on Fig. C.5. As before, the very strong reed R12 appears clearly as an outlier for factor 3.

Facit: a "naive" analysis of the results requires the presentation of many graphs (cf. Fig. C.1 to C.5) that can be advantageously summarized in a single table of correlations (c.f Table 8.8), provided the reader understands the philosophy behind this treatment of the information. I hope that this didactic presentation and the plots of this section will clarify this point.

C.8 Difference between CCA and PCA

What is the difference between CCA and PCA?

The PCA is performed inside a single data block (consisting of a large number of interrelated variables) in order to reduce its dimensionality, while retaining as much as possible of the variation present in the data set. In other words, it seeks to capture so much **variance** of the original data block as possible, on a small number of components.

By contrast, the CCA is performed among J different data blocks and seeks to capture as much of the variation which is **shared** by all data blocks. In other words, it focus on the analysis of the redundancy among data blocks.

Both methods can sometimes lead to similar results, but the PCA is usually much less efficient than the CCA in discovering relevant hidden structures. It is likely to imagine some data where

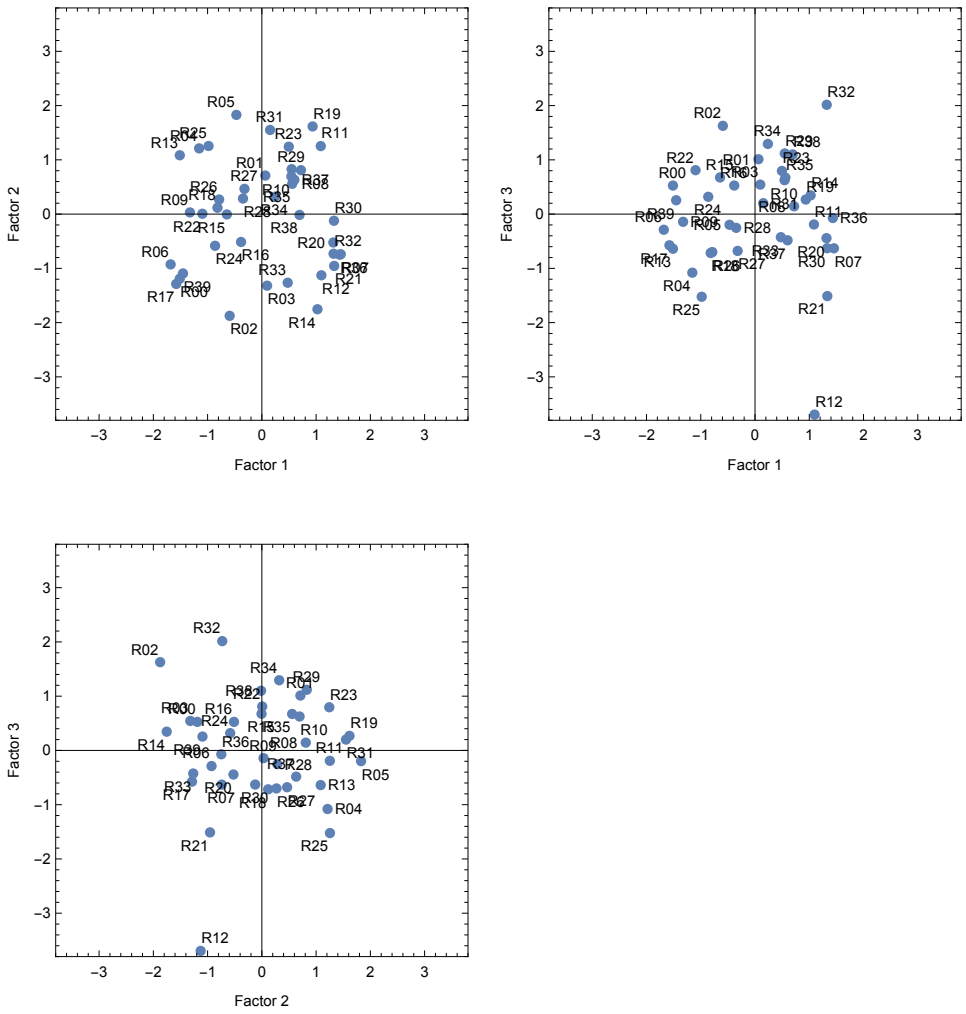

Figure C.5 – Plot of the CCA factors 1 to 3 of *statSubjF* (after standardization). The identifier of each individual reed is indicated on the graphs.

the first PCA factor is composed essentially of unsignificant noise. The CCA seeks exclusively information that is **common** to all data blocks (and tries to ignore noise). This is the reason explaining why its analyzes are often more relevant and easier to interpret than those of the PCA.

Appendix D

Complements to Chapter 8

Résumé

Cet Appendice examine des aspects plus techniques des analyses CCA effectuées au Chapitre 8, notamment ceux liés à la reconstruction des données brutes à partir des facteurs CCA, à la détection de non-linéarités parmi les facteurs à l'aide d'une méthode graphique, à la prédiction des facteurs à l'aide d'un nombre minimal de mesures et à une comparaison entre mesures de bifurcation et simulations.

This Appendix is devoted to the examination of some complementary aspects about nonlinearities, predictions and comparison between measurement and simulations in relation with the CCA.

D.1 Reconstruction of raw data with CCA factors

Let us reconstruct some of our raw data according to §8.4.6. An example of raw data reconstruction is given on Fig. D.1 for the reed R14. The measurements (solid lines) are compared with the reconstruction (dashed lines) for different data blocks. For each data block, a reconstruction with $Q = 2$ and $Q = 6$ factors is given.

The reconstructed variance gives some insight about the relationships among blocks and also about the minimal number of dimensions to retain for an efficient reconstruction. We will see that in all cases 3 or 4 dimensions are necessary in order to capture most of the variance. An "elbow" is observed most of the time around this number of factors on the graphs depicting the proportion of explained variance.

Let us examine first the reconstruction of *staticF* presented on Fig. D.2. The proportion of variance $\hat{\lambda}_{j,n}$ explained by each factor is depicted on the left column of the Fig. while the reconstructed variance $\eta_{j,n}$ is depicted on the right column. The exercice is done from the own "eigenfactors" (i.e. *staticF*) and also for 3 "foreign" CCA factors (*subjectiveF*, *bifurcationF* and *totalF*). Without surprise, the own "eigenfactors" are more efficient for the reconstruction, while *subjectiveF* is less efficient than the others. The variance of the aeraulic measurements (especially that of *aero*) is significantly better reconstructed than that of the photos of the channel. Nevertheless, for the worst case, 4 factors of *subjectiveF* allow to reconstruct about 70% of the variance of *aero* and *photoNew*, 65% of the variance of *optoLeft* and *optoRight* and 50% of the variance of *photoBreakIn*.

Let us repeat the exercice in Fig. D.3 for the subjective evaluations *subjectiveF* (*test1*, *test2*, *test3* and *test4*). The reconstruction of the mean of the descriptors over the 4 repetitions of the test (*StdSubj*) is also depicted on this Fig. About 70% of the variance of *StdSubj* is reconstructed with 4 factors taken among foreign CCA factors (*staticF*, *bifurcationF* and *totalF*), while the 4 own "eigenfactors" reconstruct more than 95% of the variance of *StdSubj*.

The reconstruction of the measured bifurcation diagrams is done with the own "eigenfactors" (i.e. *bifurcationF*) and also with the static factors (*staticF*). This is depicted on Figs. D.4 and D.5. The difference of efficiency is not important. This reveals that the static features determine most

of sound production of the instrument (at least in the first regime). The variance is systematically better reconstructed for the loose embouchures than for the tight ones. The curves are really similar for all sensors. Practically no difference in the reconstruction is observed between the ramps (*crescendo* and *decrescendo*). However, it should be observed that the reconstruction of the measured pressure in the container is significantly determined by the factors 5 to 9. The reasons of this interesting behavior should be examined.

Similarly, the reconstruction of the synthesized bifurcation diagrams is done with the own "eigenfactors" (i.e. *synthesisF*) and also with the static factors (*staticF*). Again, the difference of efficiency of reconstruction is not important, but the curves are quite different of those of the measurements. The differences among embouchures are much more pronounced.

D.2 Prediction of objective factors from a minimum number of measurements

We seek a prediction by Multivariate Linear Regression (MLR) of the first 6 CCA factors of *objectiveF* (called "objective factors") with a minimal number of physical measurements, after selection of the most relevant ones for this task. This selection is performed with a procedure similar to stepwise regression forward. First, the most discriminant measurement for the factor 1 is selected, then the 2nd most discriminating measurement for the factor 2 is selected, when it is associated with the 1st measurement selected, and so on.

Instead of selecting among all **individual** measurements in all data blocks, we seek instead to select more general measurements, such as the **average** channel height or such as some discrete points of the nonlinear reed model (which assumes a linear relation between ψ and Δp).

The following data was used in turn as predictors:

1. Mean channel height
2. Parameters of the nonlinear reed model
3. Bifurcation diagrams

D.2.1 Mean channel height

The mean channel height is calculated for different embouchures, among the PhotoNew and PhotoBreakIn series. We select which embouchures ψ allow an optimal prediction of the first 6 factors. These embouchures are illustrated in Fig. D.8. The associated mean channel height allows to predict by MLR the rank occupied by each reed for the first 6 objective factors with a correlation respectively of 0.96, 0.90, 0.58, 0.62, 0.61 and 0.44, for PhotoNew and 0.95, 0.96, 0.83, 0.69, 0.49 and 0.44, for PhotoBreakIn.

D.2.2 Parameters of the nonlinear reed model

Six of 142 discrete points specifying the nonlinear reed model are selected (blocks *ReedDeflec* and *ReedAero*). The 6 selected values come all from the optical measurements *ReedDeflec* (defining the mechanical stiffness in the reed model). They are illustrated in Fig. D.9 and allow a prediction by MLR of the rank occupied by each reed for the 6 first objective factors with a correlation respectively of 0.98, 0.95, 0.86, 0.84, 0.64 and 0.41.

D.2.3 Bifurcation diagrams

A prediction is possible for different measurements, for instance from the playing frequency f_{play} or from the envelope of the pressure signal in the mouthpiece p_{mp}. The respective correlations for the first 6 objective factors are: 0.92, 0.92, 0.82, 0.67, 0.59 and 0.68 (playing frequency) and 0.98, 0.92, 0.69, 0.73, 0.54 and 0.69 (envelope). The selected points are illustrated in Fig. D.10. These points are located near the emergence or extinction thresholds.

D.3 Detection of nonlinear components among the CCA Factors

In our data, nonlinear relationships are expected among factors, because of the physical nature of the measurements. For examining this topic, a graphical method is proposed in this paragraph. The analysis is based exclusively on raw data, because the interpretation is more intuitive: The reeds are sorted according to the rank obtained for each CCA factor and the trend of the raw measurements along each factor is examined, after smoothing using a Gaussian filter of radius 8. The data is smoothed (in the kind of a moving average) in order to obtain 8 "snapshots" (subgraphs) taken at regular intervals, when going through each factor, after subtracting the average value observed for all reeds (enhancing thus the differences). Such graphs have been established and examined for all data blocks, searching for the most striking features of each factor.

These graphs take up a lot of space and can not all be reproduced here. I chose to present the most outstanding of them. Fig. D.11 illustrates (for the first 6 factors) the evolution of the detected trends for the photos of the channel (PhotoNew and PhotoBreakIn). Fig. D.12 concerns the measurements of the playing frequency and the SC of the pressure signal in the mouthpiece (bifurcation diagrams), while Fig. D.13 shows the asymmetry of the optical signals near the beating and saturation thresholds, for this same series of measurements. Fig. D.14 highlights the differences in the reed model used for the synthesis. These graphs are easier to interpret than the previous ones, because they have one dimension less: the model considers a linear dependence between ψ and Δp. In addition, the differences between reeds are sufficiently visible so that it is not necessary to enhance them by subtracting the average value. Derivatives with respect to Δp (aeraulic and mechanical compliance) are shown in Fig. D.15.

D.4 Summary comparison of time signals between measurement and synthesis

The evolution [1] of time signals along each factor is depicted using the same graphical technique. The smoothing of the data with a Gaussian filter makes it possible to illustrate the (linear or nonlinear) trend within a factor, without disturbing the graphs with noise caused by individual variations between reeds (which may be important for the factors of high rank). Here, unlike the preceding figures, the radius of the Gaussian filter has been reduced to 3 units (instead of 8), which increases the variability while increasing the detection limit of some features. Figs. D.14 to D.21 can be conveniently compared to each other, since they share the same color code to represent the data of each reed, according to its relative ranking inside each factor.

Figs. D.18 and D.19 show the evolution of the *reed signal* within each factor, comparing the signals measured with the artificial mouth (a) and the signals from of the synthesis model (b), this for 2 different blowing pressures [2]. We will notice a fairly good match between measurement and

1. The terms "evolution" or "trend" are used in order to describe how the measured signals are becoming different from one another when the reeds are situated at different locations of a factor, for the same blowing pressure.

2. For readers who may have difficulty reading these graphs, let's perform a detailed interpretation of Fig. D.18 (a), Factor 1. The factor 1 is strongly correlated with the strength of the reed. For the relatively loose embouchure ($\psi = 1.250$ mm) and for a blowing pressure of 4 kPa corresponding to the measured signal, one expects a quasi-sinusoidal signal for a strong reed, since the oscillation threshold should be close to this pressure. There is indeed such a signal, illustrated in dark green. This curve is very close to the one obtained by averaging the signals observed for the 7 strongest reeds, located at the "right" end of the factor (the Gaussian filter is a kind of improved version of a moving average). For the weakest reeds, it is expected on the contrary to observe a beating reed regime for this blowing pressure. It can be seen that the yellow curves exceed the coordinate $z = 1.2$ mm, signaling a contact between the reed and the lay. For reeds of intermediate strength, an intermediate behavior is expected, represented by shades of green. Let's continue our interpretation for factor 2: from Fig. D.11, we find that, for the embouchure corresponding to the signal we are studying ($\psi = 1.250$ mm, in light green in Fig. D.11 (b), Factor 2, which color corresponds to an opening of about -0.7 mm according to Fig. 8.3 (b), illustrating the average opening of the break-in reeds), the reeds "left" to the factor have an opening (at $\Delta p = 0$) which is about 0.06 mm more closed than at the opposite end of the factor. In Fig. D.18 (a), Factor 2, there is indeed a difference of this order of magnitude when the reed is in the opening phase, (around the coordinate -0.7 mm). According

synthesis, when we compare the relative trend within each factor. Some systematic differences in the rebound of the reeds suggest that the damping parameter is probably underestimated in the simulations.

Figs. D.20 and D.21 allow the same comparison at the level of the *pressure signals* measured and synthesized in the mouthpiece. For the lowest blowing pressure (4 kPa), the proximity of the oscillation threshold (causing pronounced nonlinearity) makes the comparisons more delicate, especially for very strong reeds (R07, R12 and R21), of which the data has been eliminated in the graphical representation. Similarly, for the high blowing pressure (10 kPa), the 3 weakest reeds (R00, R06 and R39) had to be removed from the graphs, because the extinction threshold is exceeded. The very low variability between reeds for the blowing pressure of 8 kPa is striking (not shown here, but still much lower than at 10 kPa, as depicted; seemingly, all reeds have the same sound at this pressure for this embouchure), while the reed signal has a much greater variability. Systematic differences in the aspect of the temporal signal between measurement and synthesis are quite obvious. Further study should be conducted to better understand the origin of these differences, in particular by clarifying the role of the mouthpiece geometry in the model.

We will observe in Fig. D.12 the marked (negative) correlation between the playing frequency and the SC of the pressure signal in the mouthpiece, for all factors. This correlation is even clearer for tight embouchures.

It should be noted, however, that the synthesis model has not been optimized very extensively, particularly with respect to reed dynamics (the mass and damping parameters are considered constant for all reeds). There are examples in the literature ([17] and [105]) where the match between measurement and simulation is better, but these examples concern a single reed, mouthpiece and blowing pressure for which the parameters of the model have been optimized. Here, the model has a much more general validity, largely independent of the blowing pressure and the embouchure. The reed parameters were determined by static measurements, performed independently of the bifurcation measurements in question, without any optimization between simulations and measurements.

to Fig. D.15 (a), Factor 2, we note that this factor is also related to a more or less pronounced bending of the reed on the lay, as indicated by the difference in slope observed. For this, it is necessary to evaluate the value of Δp, which is obtained by subtracting the pressure in the mouthpiece (indicated in Fig. D.14 (a), Factor 2) to the blowing pressure (here 4 kPa), in order to compare two curves of the same color.

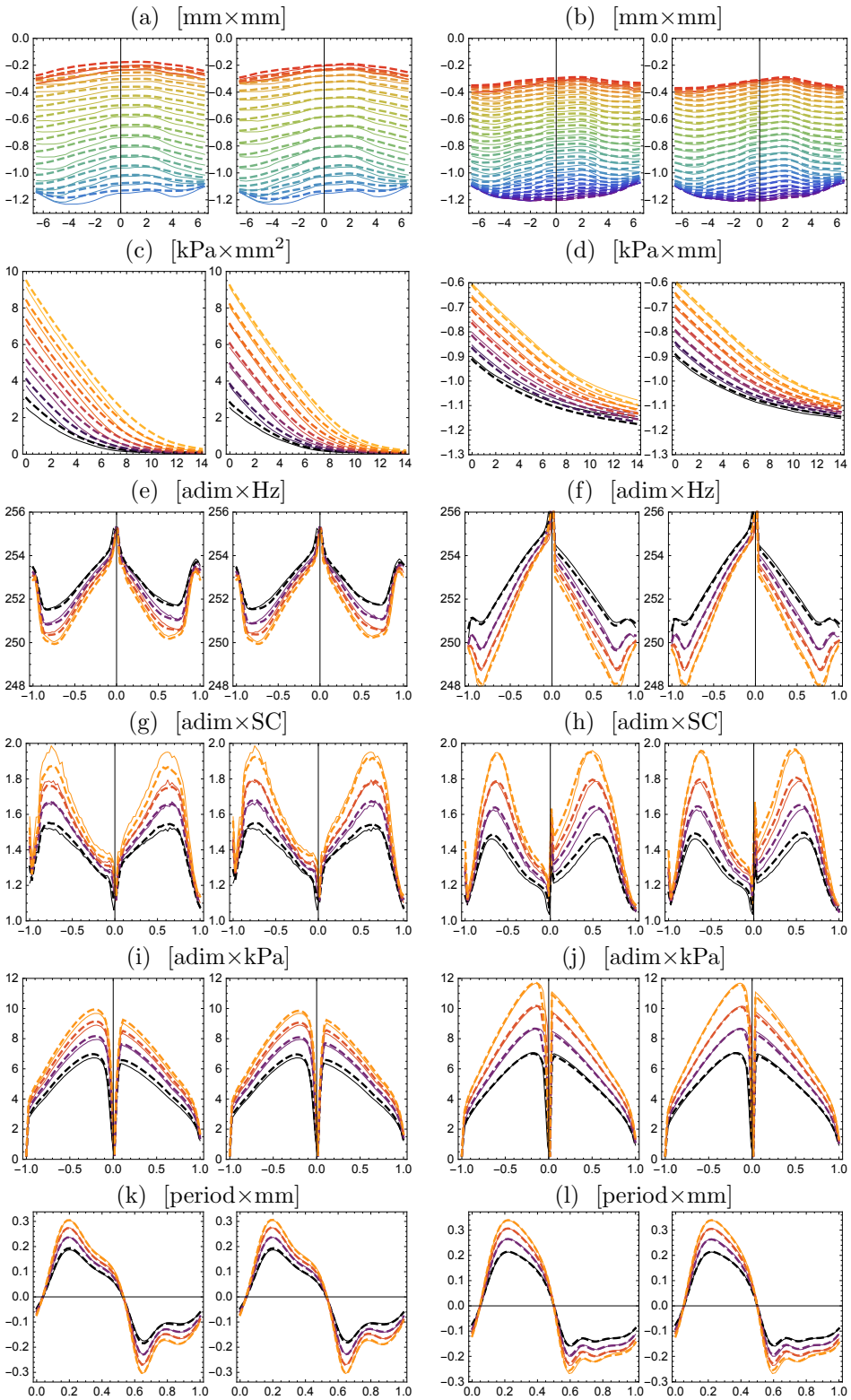

Figure D.1 – Reconstruction of the raw data of the reed R14 by *staticF*: (see Eq. 8.20) with $Q = 2$ factors (left picture) or $Q = 6$ factors (right picture) for the matrix $\boldsymbol{F}$. Solid lines: measurement $X_{j,14}$. Dashed lines: reconstruction $\hat{X}_{j,14}$. (a) *PhotoNew*. (b) *PhotoBreakIn* (c) *Aero*. (d) *OptoLeft*. (e) *MPlayFreq* (playing frequency, measure). (f) Idem synthesis. (g) SC pressure in mouthpiece, measure. (h) Idem synthesis. (i) Enveloppe pressure in mouthpiece, measure. (j) Idem synthesis. (k) reed signal 1/2(L+R) near beating threshold, measure. (l) reed signal 1/2(L+R) near saturation threshold, measure. Same conventions as in the precedent Figs.

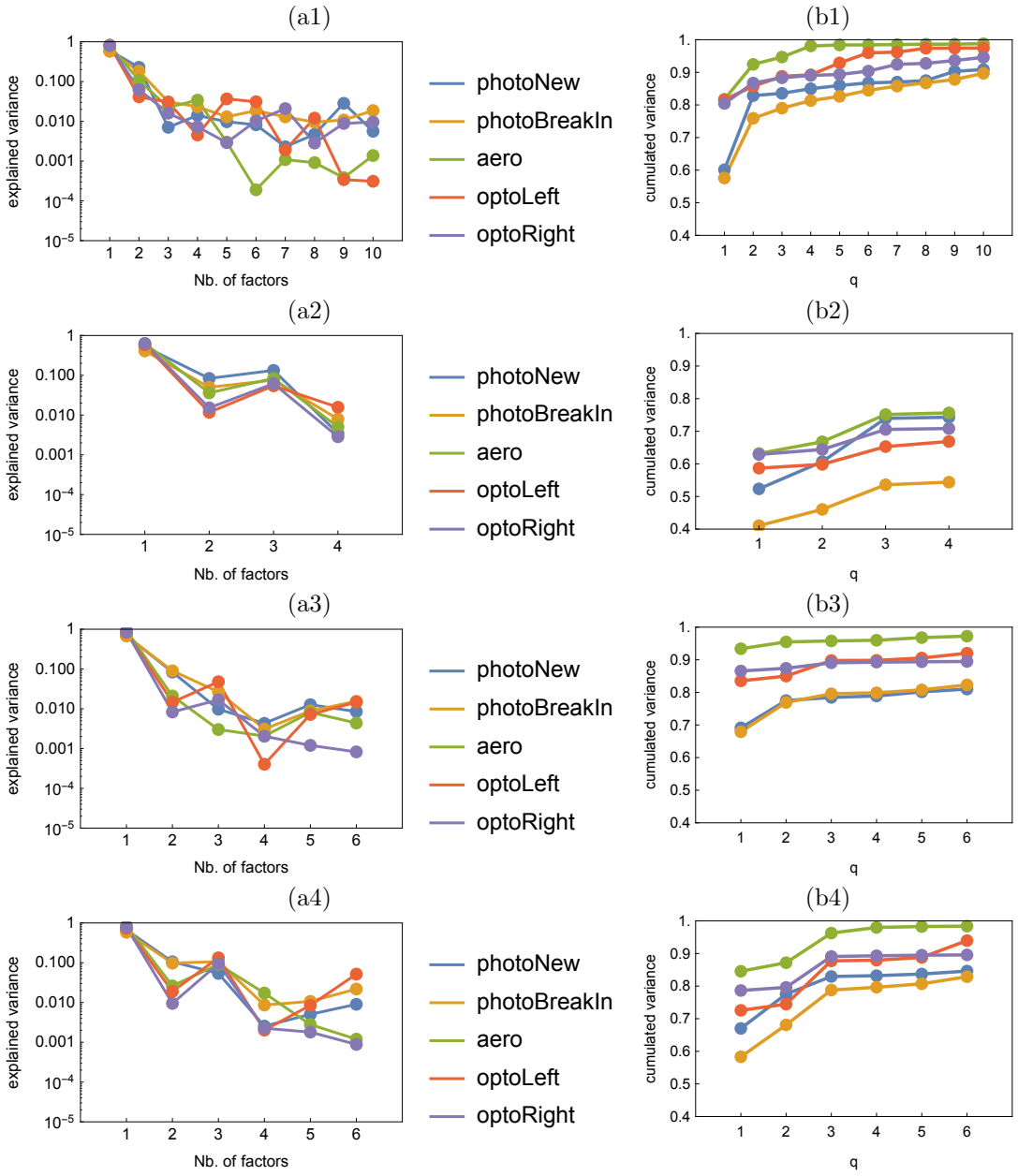

Figure D.2 – **Reconstruction of the *objective* static measurements: *staticF*.**
(a1) to (a4): Proportion of variance $\hat{\lambda}_{j,n}$ explained by each factor. For the computation of this proportion, the total variance of the *raw* data of each block was taken into account.
(b1) to (b4): Reconstructed variance $\eta_{j,n}$, as a function of the number of factors taken into account. This graph cumulates the variance $\hat{\lambda}_{j,q}$ explained by each factor.
(a1) and (b1): Reconstruction with ***staticF*** (*own* "eigenfactors").
(a2) and (b2): Reconstruction with ***subjectiveF*** (*foreign* factors).
(a3) and (b3): Reconstruction with ***bifurcationF*** (*foreign* factors).
(a4) and (b4): Reconstruction with ***totalF*** ("mixture" of factors of all categories).

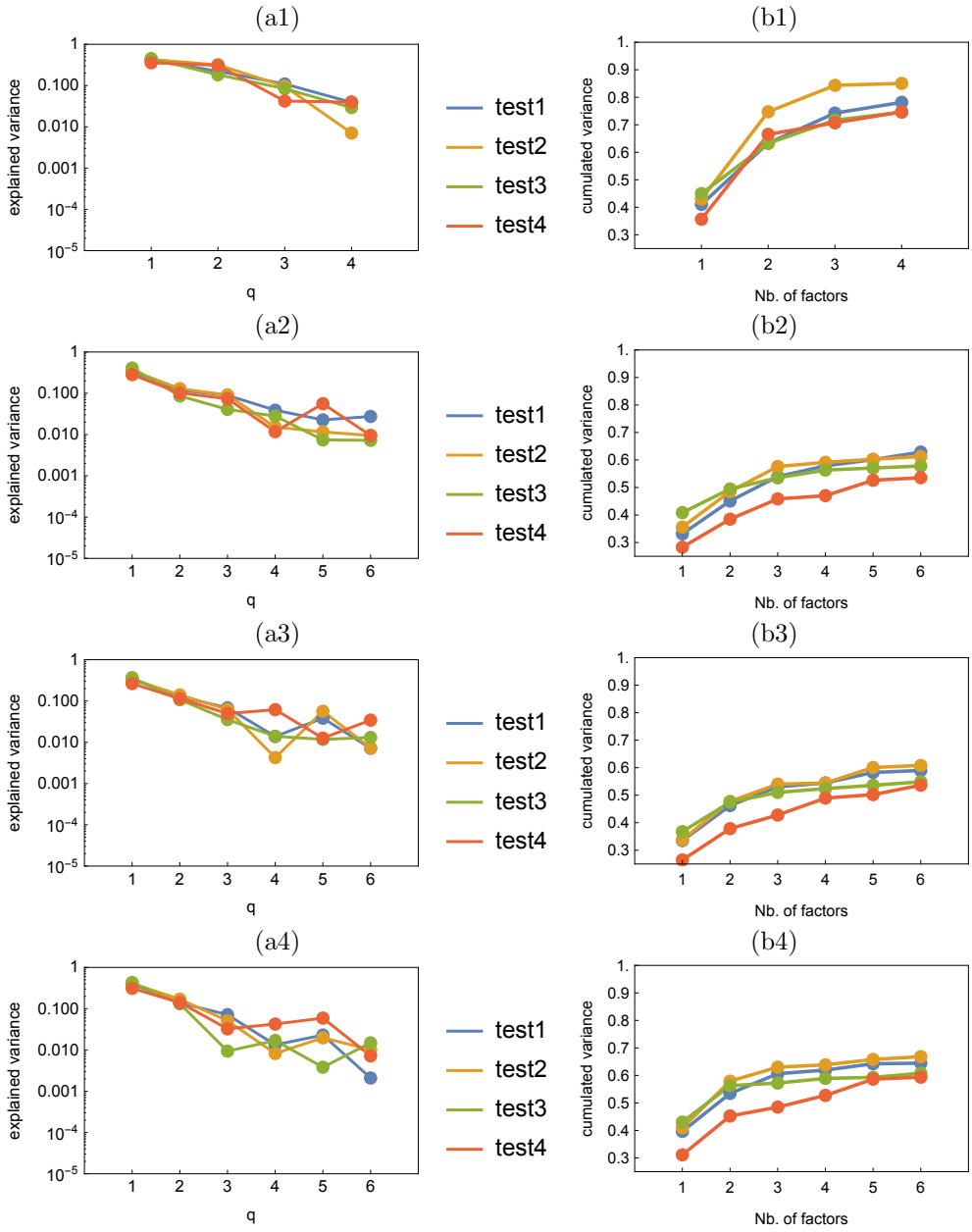

Figure D.3 – **Reconstruction of the *subjective* musical evaluations: *subjectiveF* and *StdSubj* (standardized mean of each subjective descriptor).**
(a1) to (a4): Proportion of variance $\hat{\lambda}_{j,q}$ explained by each factor. For the computation of this proportion, the total variance of the *raw* data of each block was taken into account.
(b1) to (b4): Reconstructed variance $\eta_{j,q}$, as a function of the number of factors taken into account. This graph cumulates the variance $\hat{\lambda}_{j,q}$ explained by each factor.
(a1) and (b1): Reconstruction with ***subjectiveF*** (*own* "eigenfactors").
(a2) and (b2): Reconstruction with ***staticF*** (*foreign* factors).
(a3) and (b3): Reconstruction with ***bifurcationF*** (*foreign* factors).
(a4) and (b4): Reconstruction with ***totalF*** ("mixture" of factors of all categories).

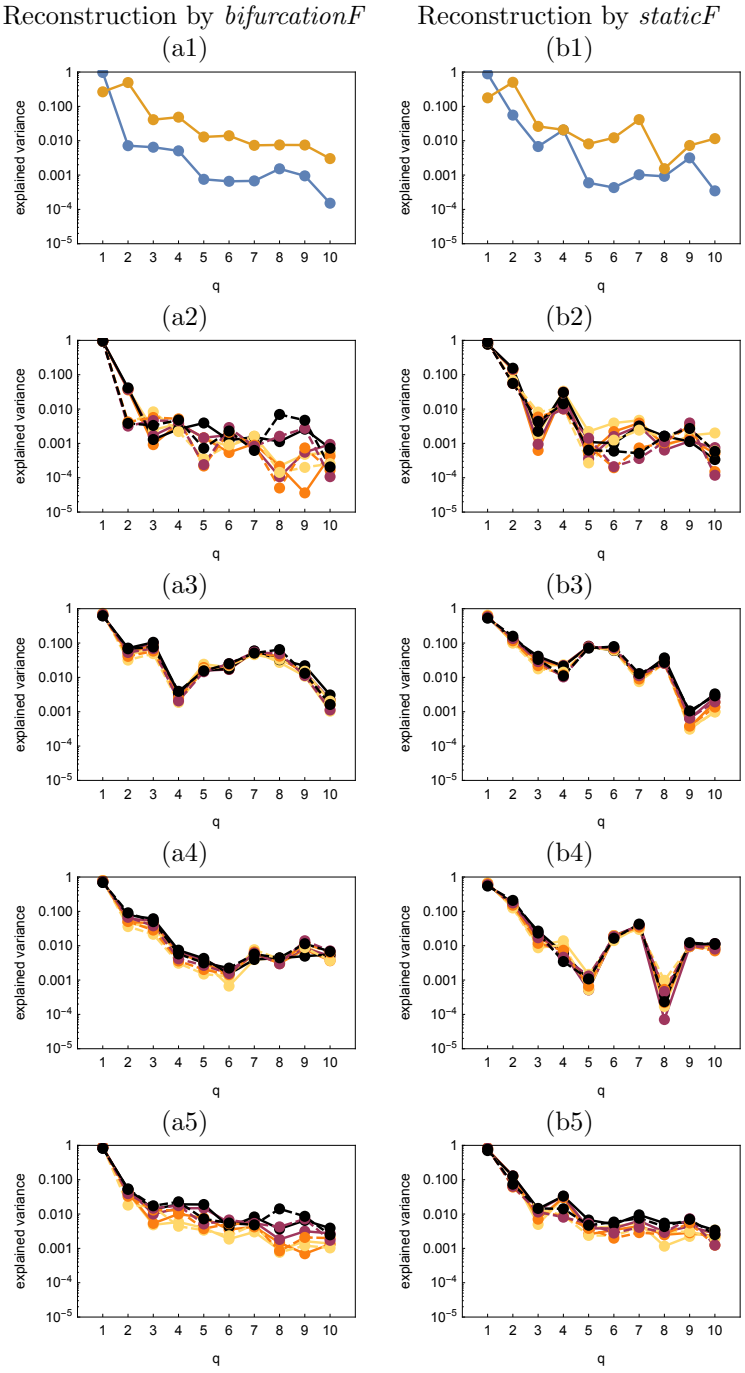

Figure D.4 – **Reconstruction of the measured bifurcation diagrams**, with the *own* "eigenfactors" (*bifurcationF*) and with *foreign* factors (*staticF*). Proportion of variance $\hat{\lambda}_{j,q}$ explained by each factor. For the computation of this proportion, the total variance of the *raw* data of each block was taken into account. The embouchures are coded from black (tight embouchure) to light (loose embouchure). Plain lines: *crescendo*. Dashed lines: *decrescendo*, except for the first line. Column (a): measurements of the bifurcation diagrams, reconstructed with *bifurcationF*. Column (b): measurements of the bifurcation diagrams, reconstructed with *staticF*. (a1) and (b1) *MThres* (blue) and *MPlayFreq* (orange). (a2) and (b2) *M111* to *M142* (measured pressure in mouthpiece). (a3) and (b3) *M211* to *M242* (measured pressure in container). (a4) and (b4) *M411* to *M442* (measured reed deflection Left sensor). (a5) and (b5) *M511* to *M542* (measured reed deflection Right sensor).

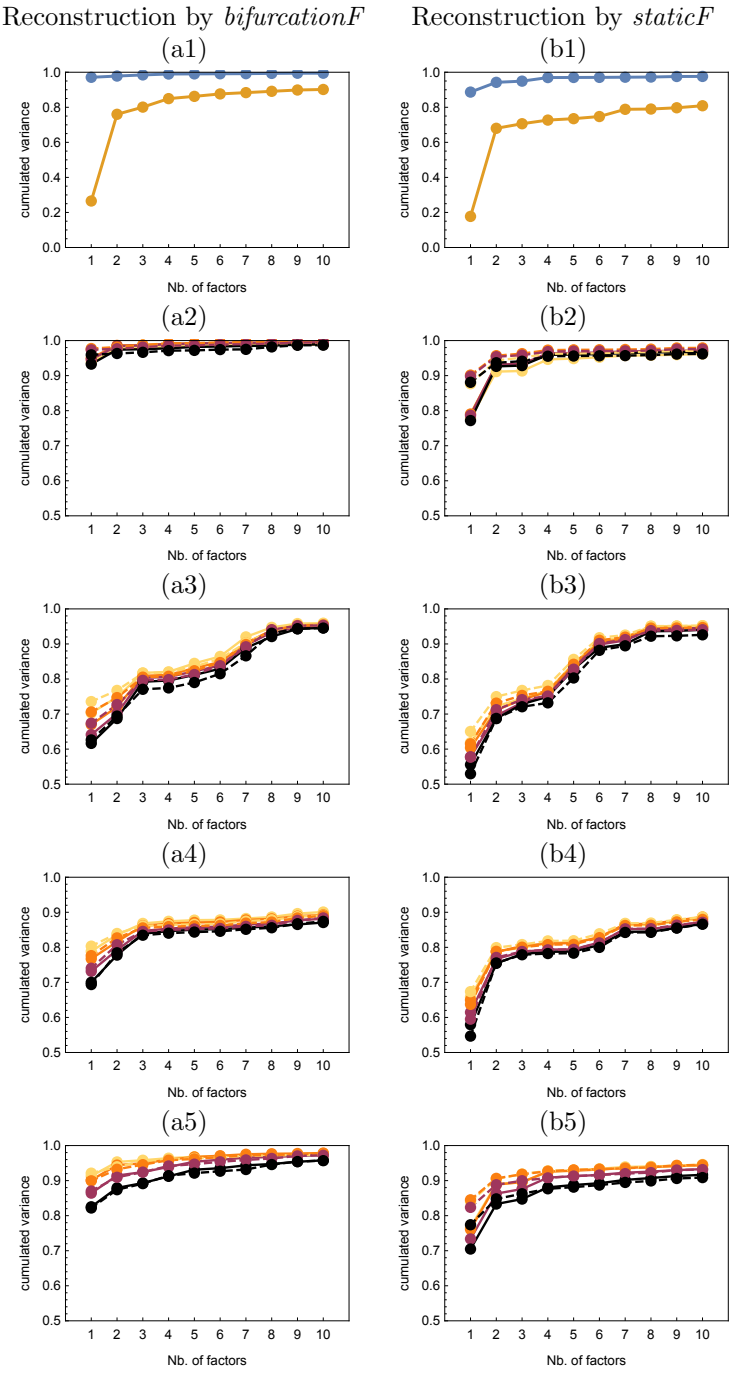

Figure D.5 – **Reconstruction of the measured bifurcation diagrams**, with the *own* "eigenfactors" (bifurcationF) and with *foreign* factors (staticF). Reconstructed variance $\eta_{j,q}$, as a function of the number of factors taken into account. This graph cumulates the variance $\hat{\lambda}_{j,q}$ explained by each factor (see Fig. D.4). The embouchures are coded from black (tight embouchure) to light (loose embouchure). Plain lines: *crescendo*. Dashed lines: *decrescendo*, except for the first line. Column (a): measurements of the bifurcation diagrams, reconstructed with bifurcationF. Column (b): measurements of the bifurcation diagrams, reconstructed with staticF. (a1) and (b1) MThres (blue) and MPlayFreq (orange). (a2) and (b2) M111 to M142 (measured pressure in mouthpiece). (a3) and (b3) M211 to M242 (measured pressure in container). (a4) and (b4) M411 to M442 (measured reed deflection Left sensor). (a5) and (b5) M511 to M542 (measured reed deflection Right sensor).

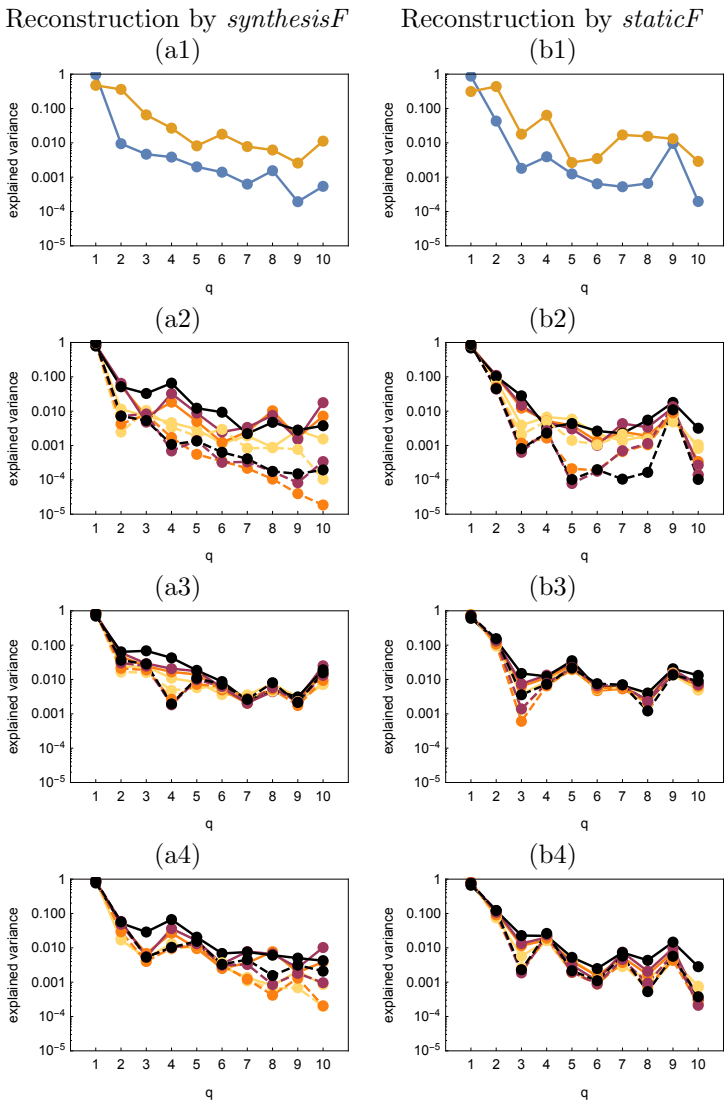

Figure D.6 – **Reconstruction of the synthesized bifurcation diagrams**, with the *own* "eigenfactors" (*synthesisF*) and with *foreign* factors (*staticF*). Proportion of variance $\hat{\lambda}_{j,q}$ explained by each factor. For the computation of this proportion, the total variance of the *raw* data of each block was taken into account. The embouchures are coded from black (tight embouchure) to light (loose embouchure). Plain lines: *crescendo*. Dashed lines: *decrescendo*, except for the first line. Column (a): measurements of the bifurcation diagrams, reconstructed with *bifurcationF*. Column (b): measurements of the bifurcation diagrams, reconstructed with *staticF*. (a1) and (b1) *SThres* (blue) and *SPlayFreq* (orange). (a2) and (b2) *S111* to *S142* (simulated pressure in mouthpiece). (a3) and (b3) *S211* to *S242* (simulated flow rate in mouthpiece). (a4) and (b4) *S311* to *S342* (simulated reed deflection).

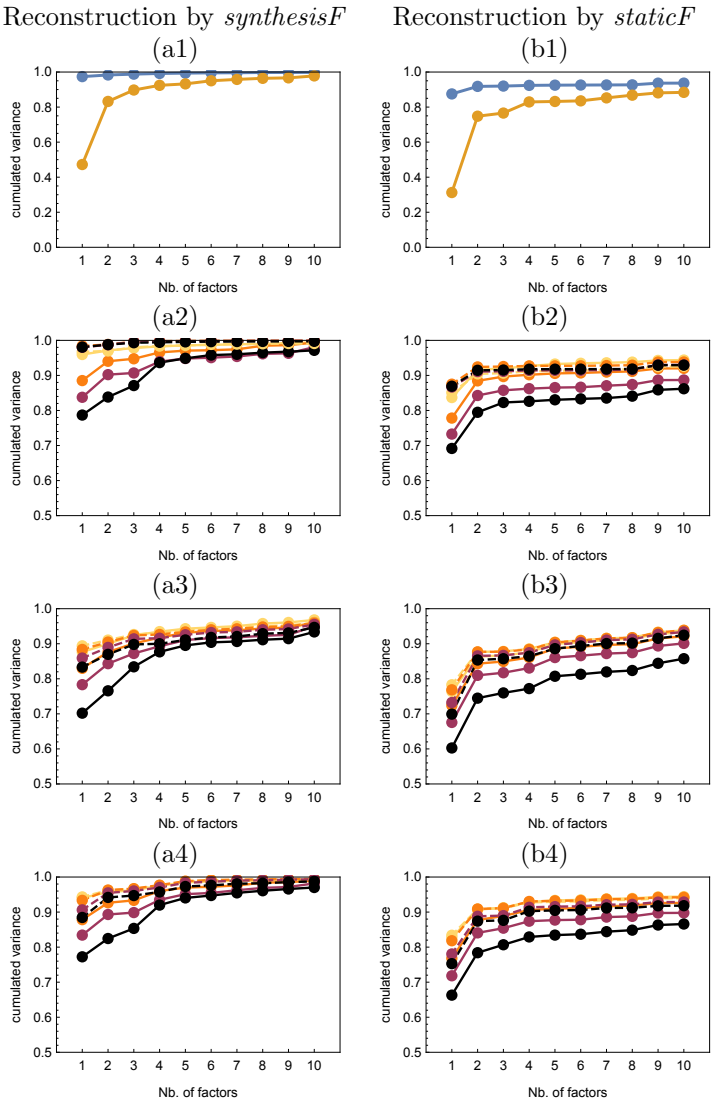

Figure D.7 – **Reconstruction of the synthesized bifurcation diagrams**, with the *own* "eigenfactors" (synthesisF) and with *foreign* factors (staticF). Reconstructed variance $\eta_{j,q}$, as a function of the number of factors taken into account. This graph cumulates the variance $\hat{\lambda}_{j,q}$ explained by each factor (see Fig. D.6). The embouchures are coded from black (tight embouchure) to light (loose embouchure). Plain lines: *crescendo*. Dashed lines: *decrescendo*, except for the first line. Column (a): measurements of the bifurcation diagrams, reconstructed with *bifurcationF*. Column (b): measurements of the bifurcation diagrams, reconstructed with *staticF*. (a1) and (b1) *SThres* (blue) and *SPlayFreq* (orange). (a2) and (b2) *S111* to *S142* (simulated pressure in mouthpiece). (a3) and (b3) *S211* to *S242* (simulated flow rate in mouthpiece). (a4) and (b4) *S311* to *S342* (simulated reed deflection).

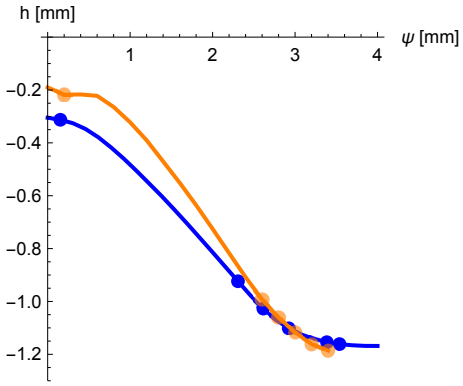

Figure D.8 – Mean channel height (average over the width of the reed, for all reeds) as a function of the embouchure ψ showing the location of the 6 embouchures selected to optimally predict the classification of the reeds reeds for the first 6 CCA factors of *objectiveF*. In orange: PhotoNew (new reed). In blue: PhotoBreakIn (break-in reed)

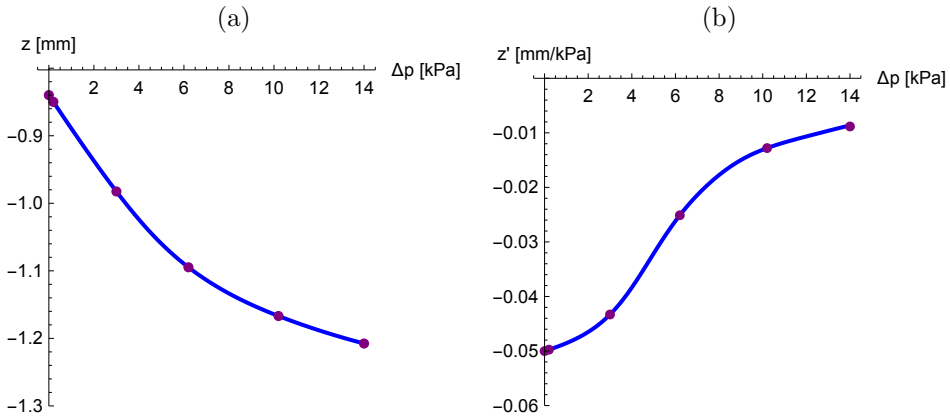

Figure D.9 – Mean value (over all reeds) of the nonlinear mechanical model Eq. 5.6 (see §5.2) showing the location of the 6 selected points allowing an optimal prediction of the ranking of the reeds, for the first 6 CCA factors of *objectiveF*. These points are discriminant respectively for the objective factors 2, 5, 1, 3, 6 and 4, taken in the order of increasing pressures. The proximity of the first 2 selected points reveals that the second derivative of the mechanical deflection (thus the first derivative of the mechanical compliance around $\Delta p = 0$) is discriminating for the factor 5 (see Fig. D.15). (a) mechanical deflection of the reed with respect to Δp. (b) corresponding mechanical compliance.

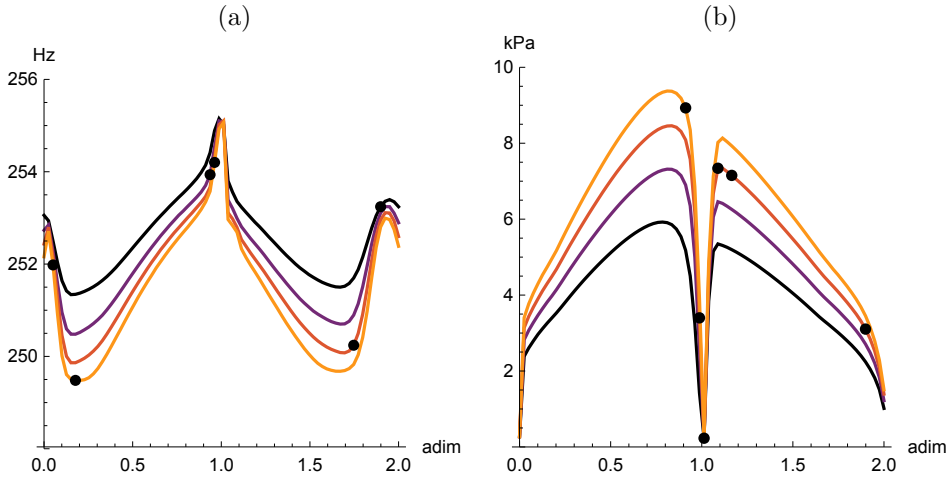

Figure D.10 – Bifurcation diagrams (mean values over all reeds) showing the location of the 6 selected points allowing an optimal prediction of the ranking of the reeds, for the first 6 CCA factors of *objectiveF*. In each diagram, the pressures (abscissa) are adimensionned by the thresholds of emergence and extinction (between 0 and 1 for the *crescendo* and between 1 and 2 for the *decrescendo*). The 4 embouchures are coded by the colors from yellow (loose embouchure, $\psi = 1.250$ mm) to black (tight embouchure, $\psi = 2.000$ mm). (a) prediction from the playing frequency; (b) prediction from the envelope of the pressure signal in the mouthpiece.

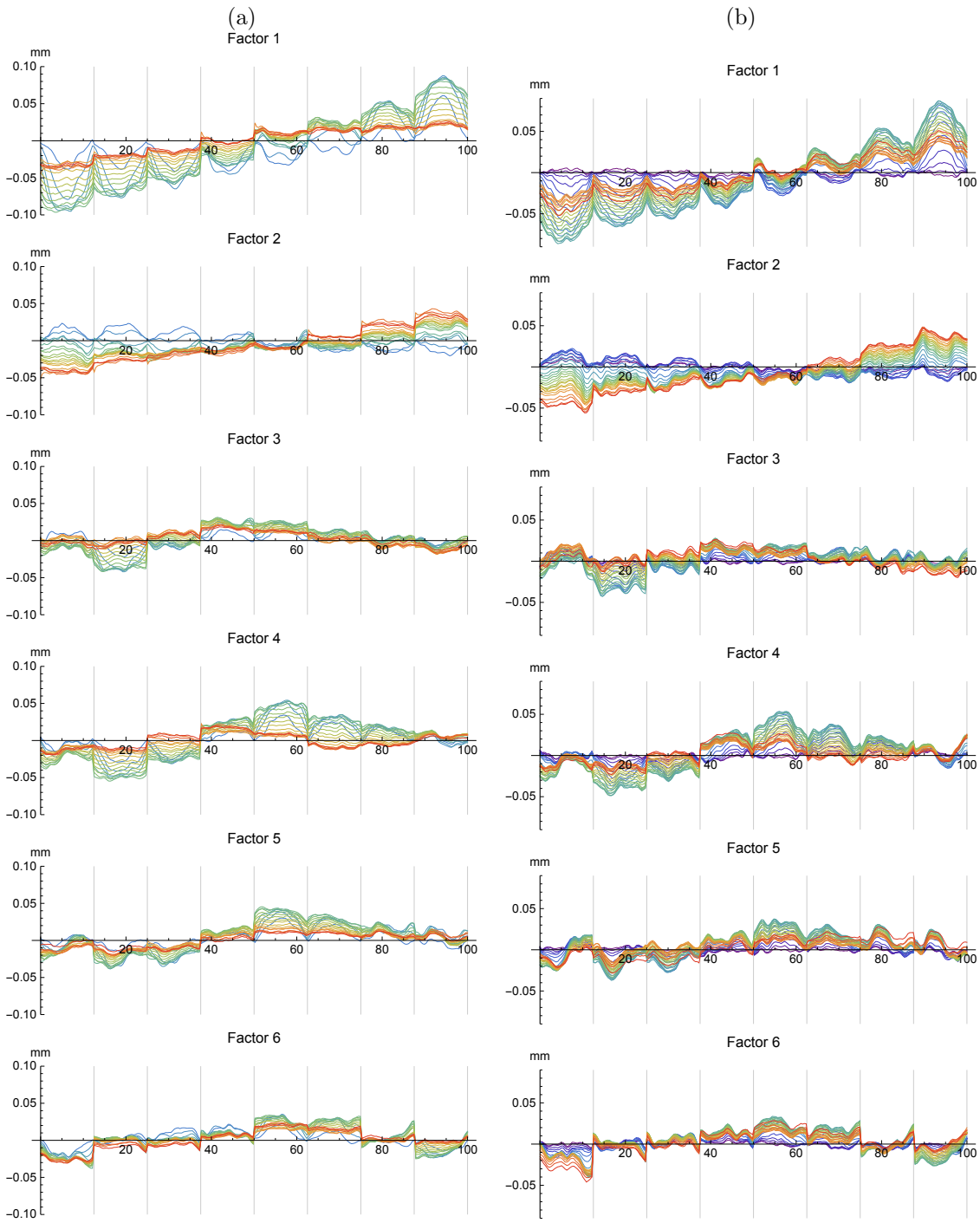

Figure D.11 – Channel height, measured by photo, for the reed seen frontally. (a) new reed (PhotoNew), (b) break-in reed (PhotoBreakIn). The trend of the channel section (in relation to the average section, given in Fig. D.11) is represented by ranking the reeds (from 0 to 100%) according to the first 6 CCA factors of *objectiveF* (objective factors). Each graph is divided into 8 sub-graphs, which illustrate the trends observed among the reeds, when they are sorted from the "left" to the "right" of the factor (i.e. from the first to the last reed inside a factor). The embouchures are coded by the colors of the rainbow, from red (reed at rest) to violet (very tight embouchure)

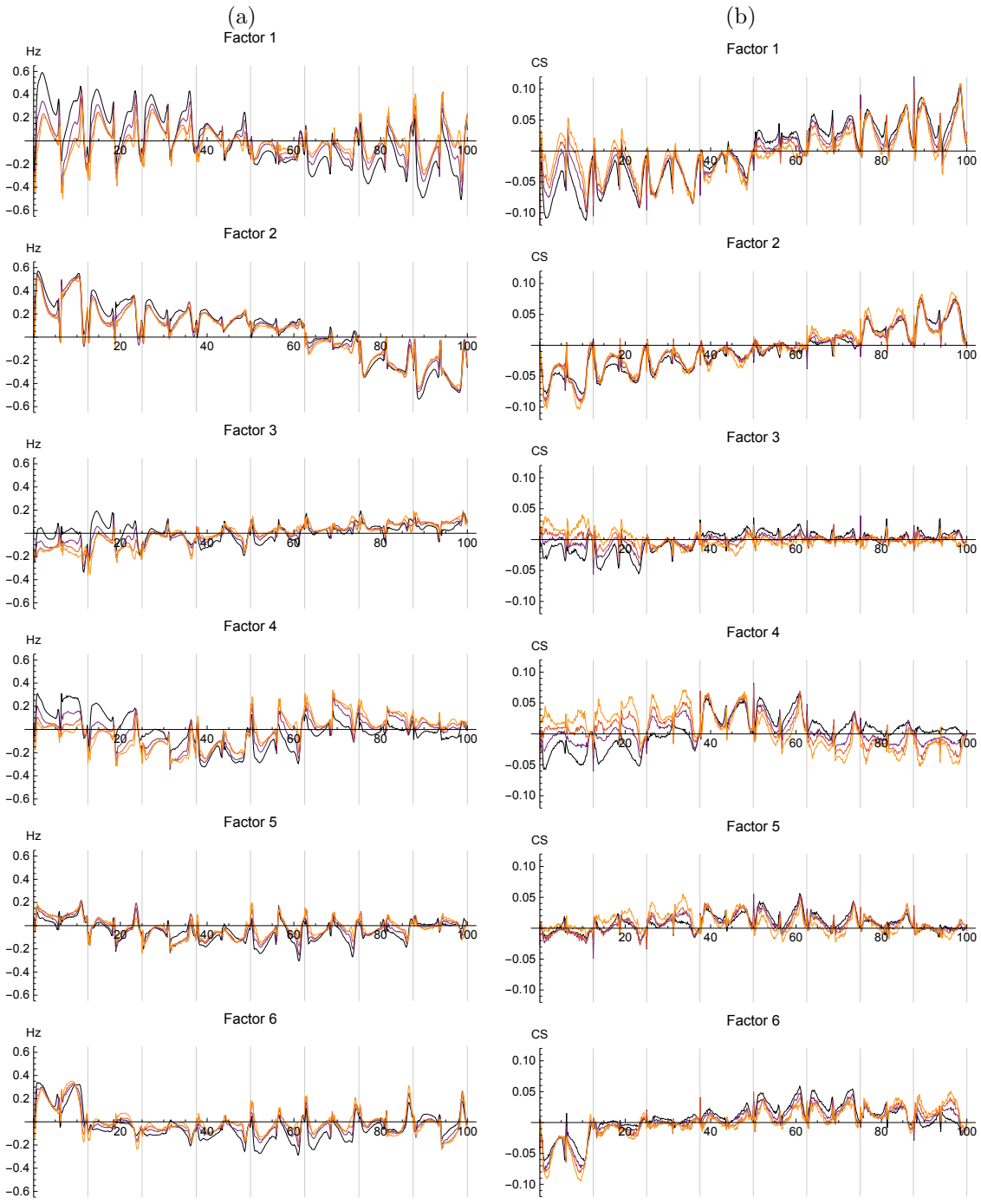

Figure D.12 – Bifurcation diagrams: (a) playing frequency, (b) spectral centroid (SC) of the pressure signal in the mouthpiece. Each graph is divided into 8 subgraphs, which illustrate the trends observed among the reeds, sorted from "left" to "right" (i.e. from first (0%) to last reed (100%) of each objective factor). Each subgraph represents the trend (with respect to the average, given in Fig. D.12) during a *crescendo* and *decrescendo* (adimensionned by the pressures of the thresholds of emergence and extinction). The embouchures are coded by the colors of the sunset, from yellow (loose embouchure) to black (tight embouchure)

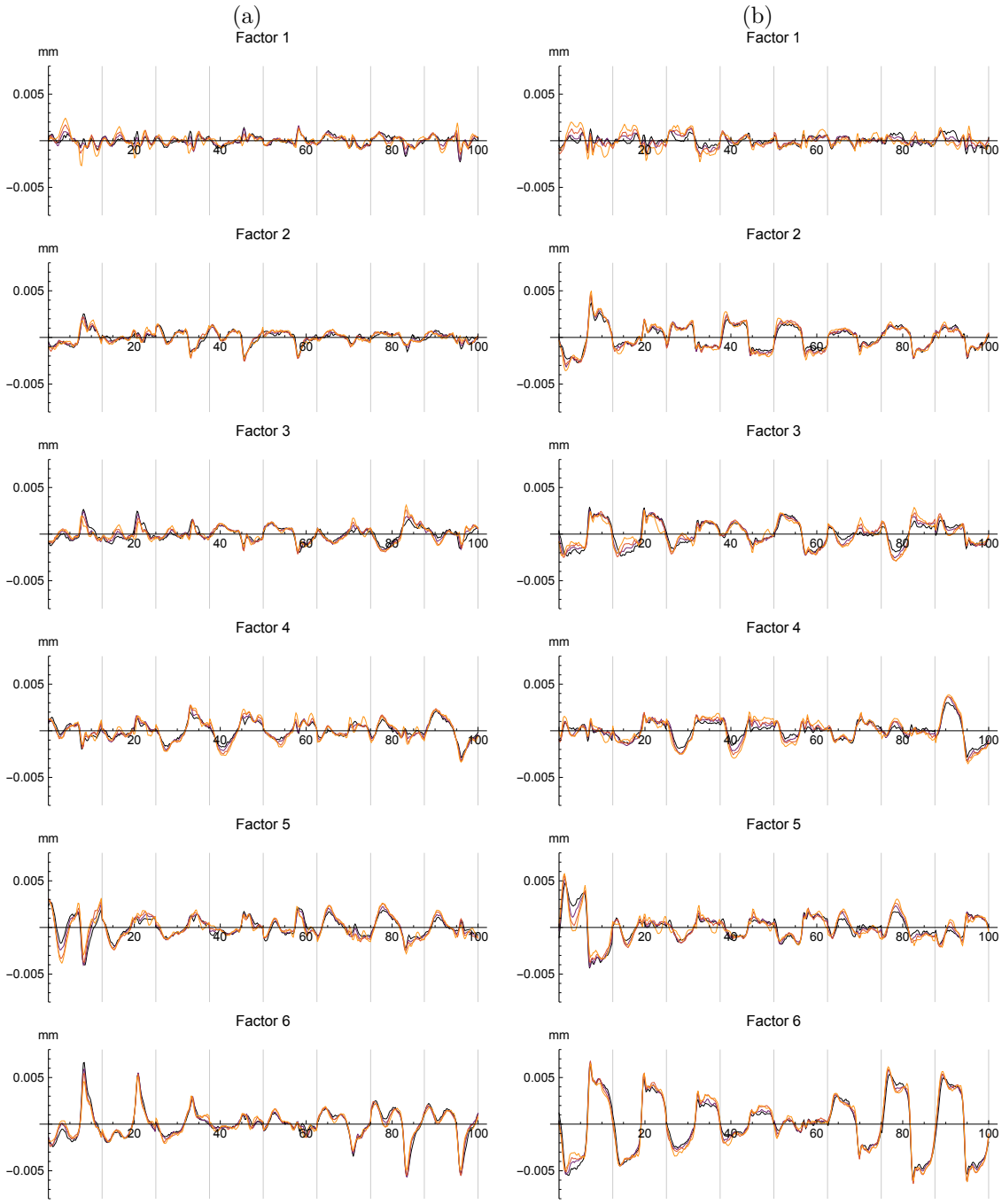

Figure D.13 – Bifurcation diagrams (asymmetry of optical signals): difference between left and right optical channel. (a) near the beating threshold, (b) near the saturation threshold. Each graph is divided into 8 subgraphs, which illustrate the trends observed among the reeds, sorted from "left" to "right" (i.e. from first (0%) to last reed (100%) of each objective factor). Each subgraph represents the difference to the average for all reeds during one oscillation period. The embouchures are coded by the colors of the sunset, from yellow (loose embouchure) to black (tight embouchure)

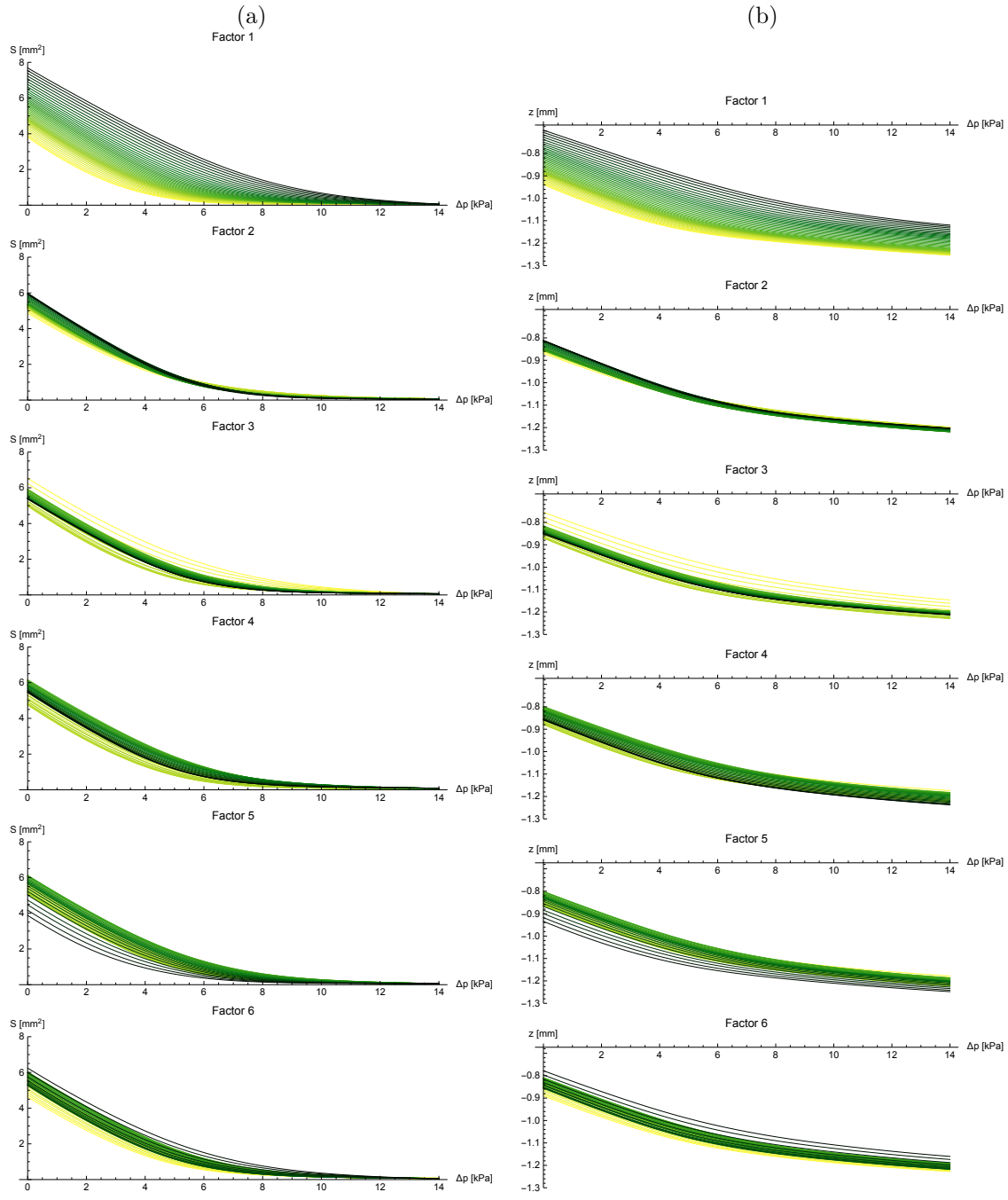

Figure D.14 – Nonlinear reed model used for the synthesis (corresponding to an intermediate embouchure: $\psi = 2.125$ mm). (a) aerodynamic section S, as a function of Δp, (b) mechanical deflection z, as a function of Δp. The model considers a linear relationship between Δp and ψ (position of the lip support). The rank of each reed inside the factor is coded by the colors of the avocado, from light yellow (first reed of the factor) to black (last reed of the factor), this for each objective factor. Compare with Fig. D.9 (a), which indicates the location of the most discriminating points for the different factors.

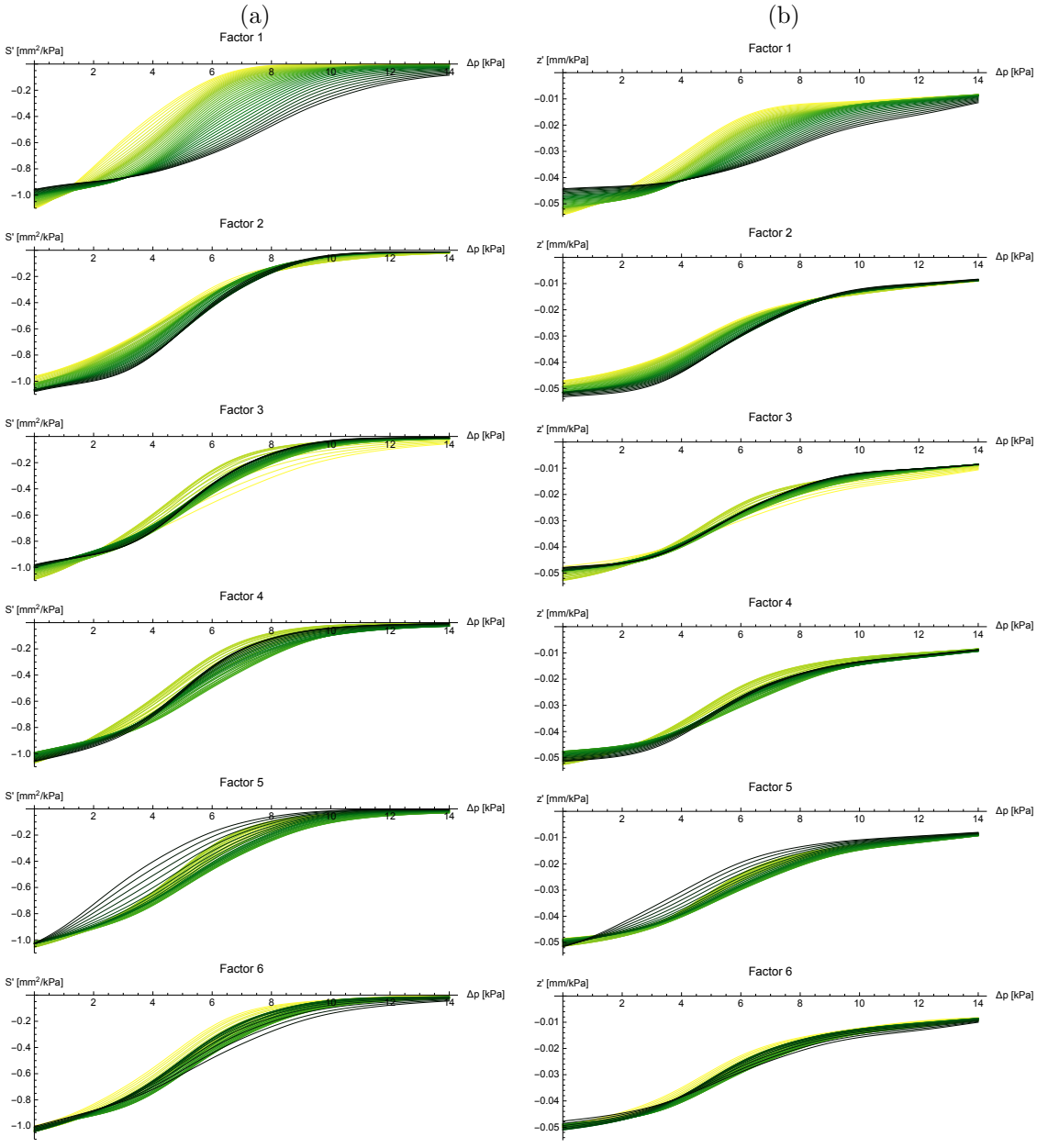

Figure D.15 – Nonlinear reed model used for synthesis (corresponding to an intermediate embouchure: $\psi = 2.125$ mm). (a) aeraulic compliance as a function of Δp, (b) mechanical compliance of the reed as a function of Δp. These graphs correspond to the derivatives with respect to Δp of those illustrated in Fig. D.14 and share the same color code. Compare with Fig. D.9 (b), which indicates the location of the most discriminating points for the different factors.

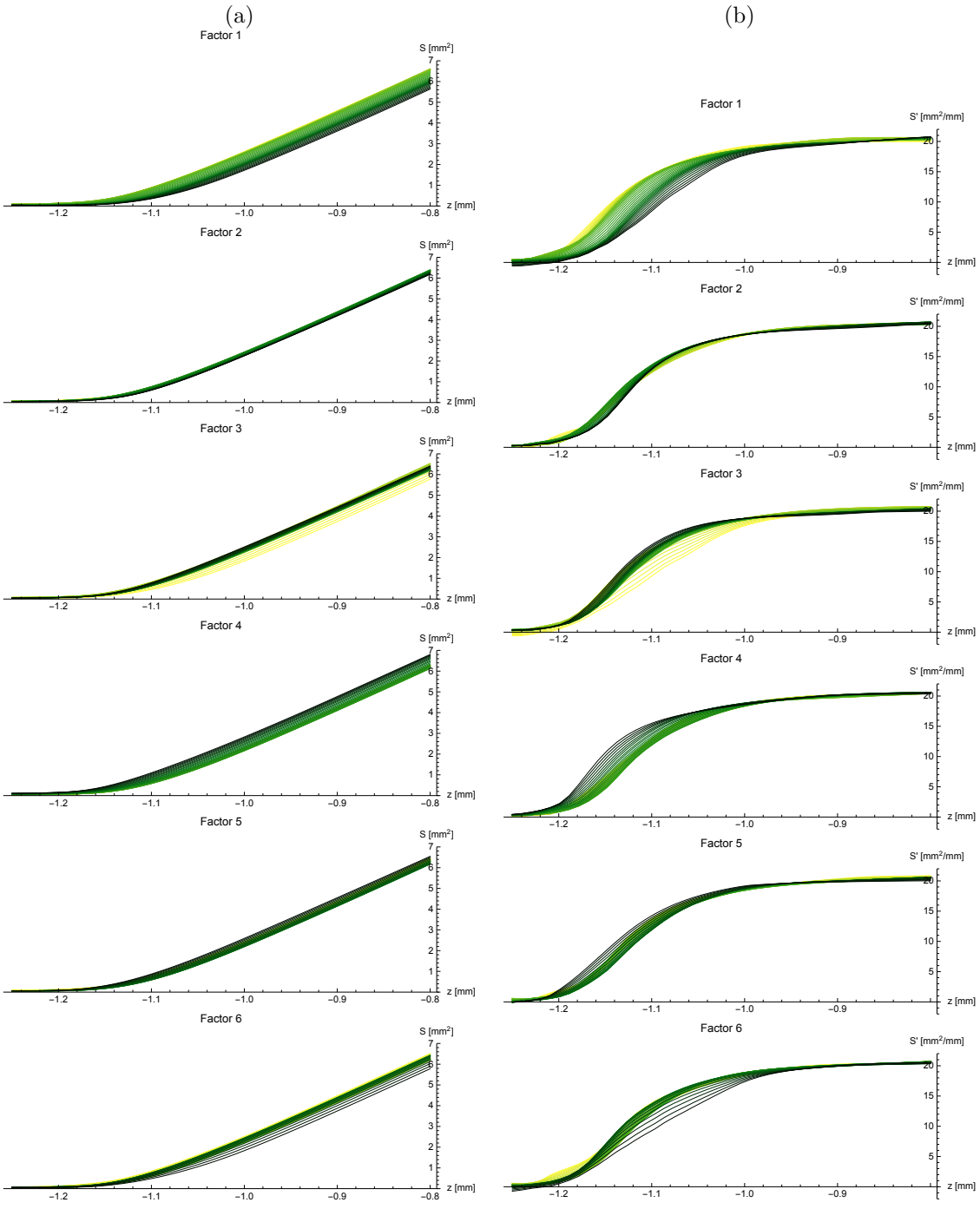

Figure D.16 – Nonlinear reed model used for synthesis (corresponding to an intermediate embouchure: $\psi = 2.125$ mm). (a) Aeraulic section $S(z)$ as a function of the channel height z, according to Fig. 5.4. (b) first derivative $S'(z)$. With a rectangular model of the channel, this corresponds to the effective width of the reed. Notice that the actual width of the reeds is 13 mm. The additional width accounts for the air entering from the sides of the reed. Same color code as the 2 preceding Figs.

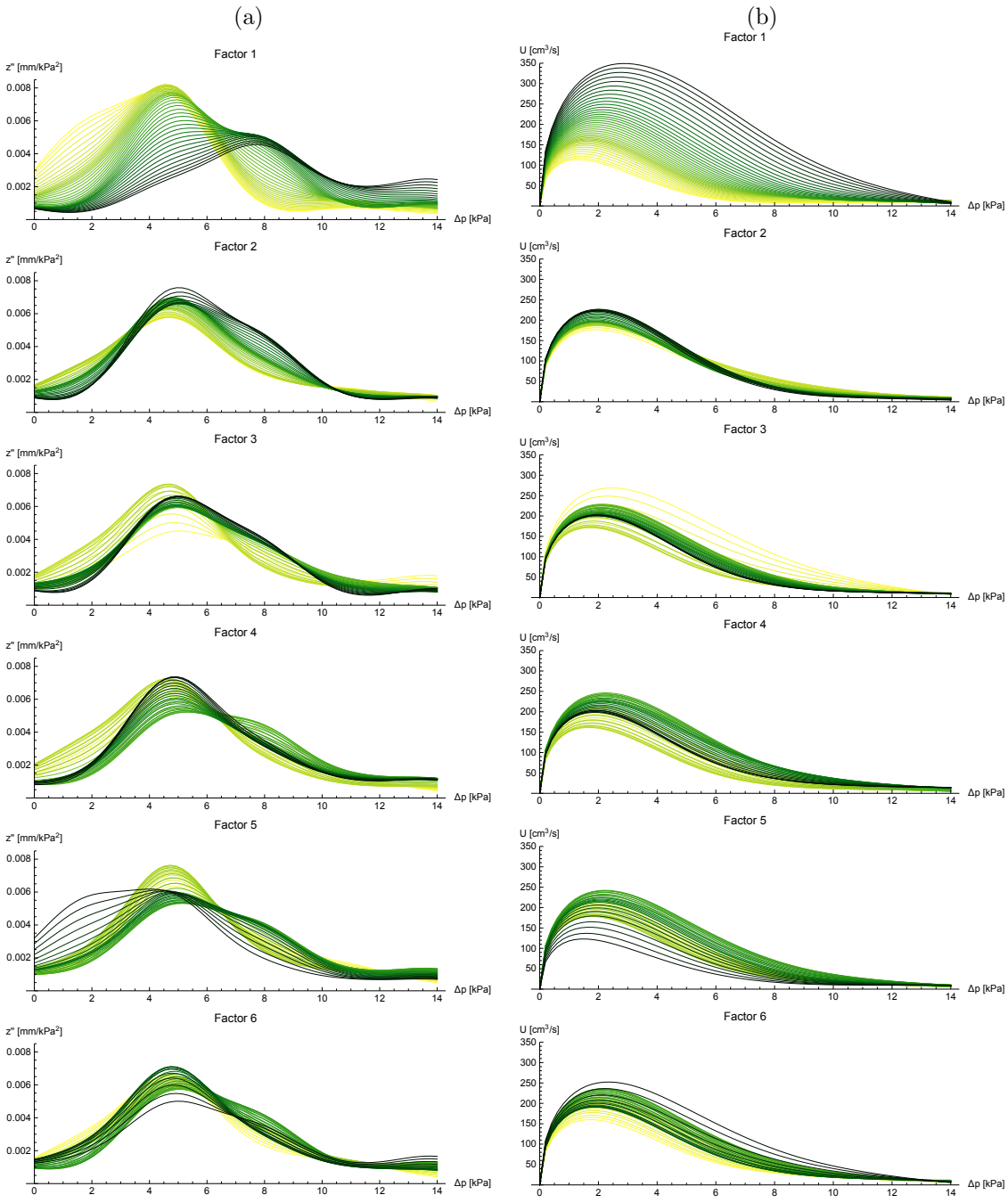

Figure D.17 – Nonlinear reed model used for synthesis (corresponding to an intermediate embouchure: $\psi = 2.125$ mm). (a) 1st derivative of the compliance as a function of Δp, (b) flow rate as a function of Δp (nonlinear characteristic), according to Bernoulli's law. Same color code as the 3 preceding Figs.

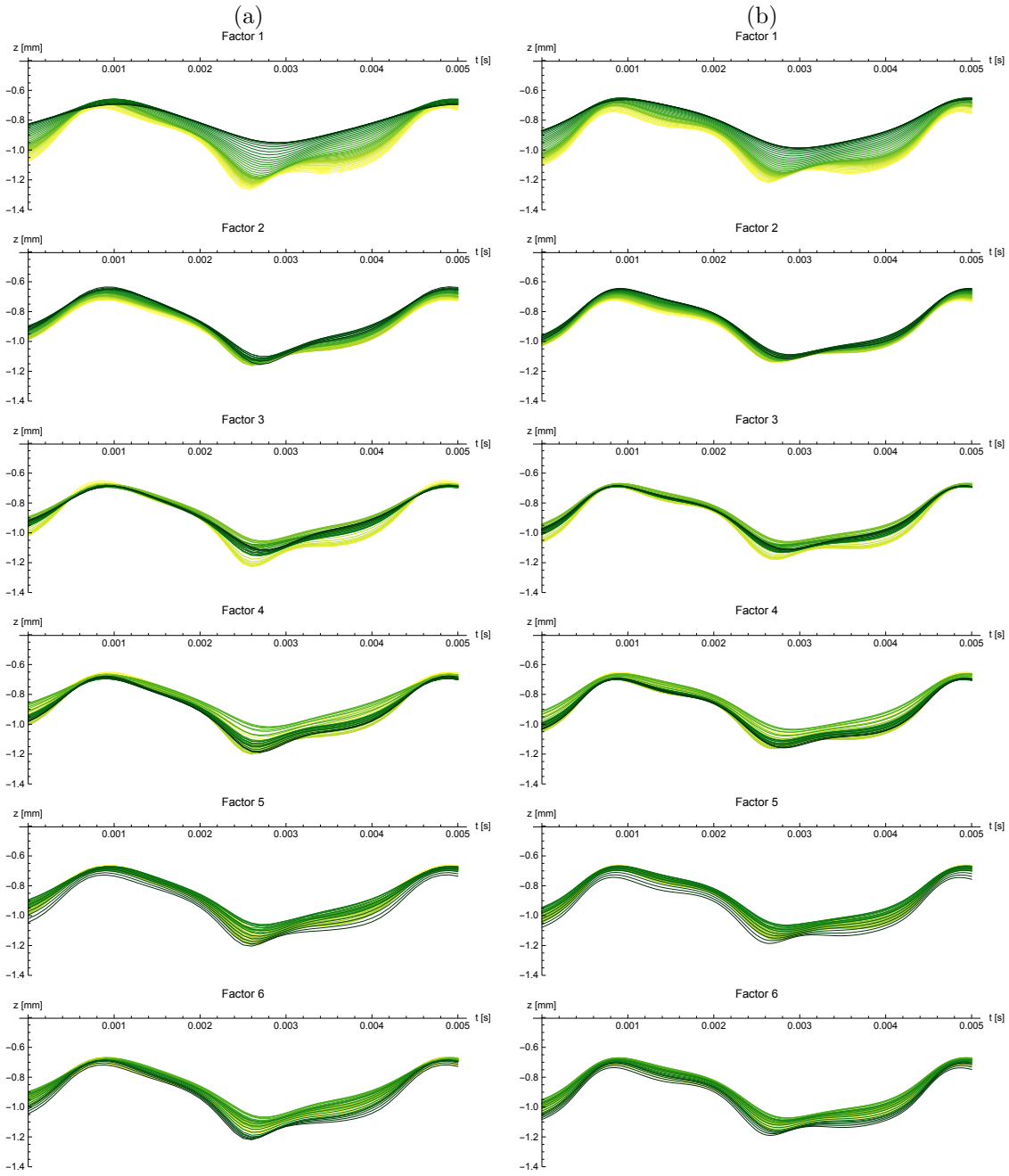

Figure D.18 – Trend (within each factor) of the deflection signal of the reed, for a blowing pressure of **4 kPa**, with a loose embouchure ($\psi = 1{,}250$ mm). (a) measured with the artificial mouth. (b) according to the synthesis model. Same color code as the 4 preceding Figs.

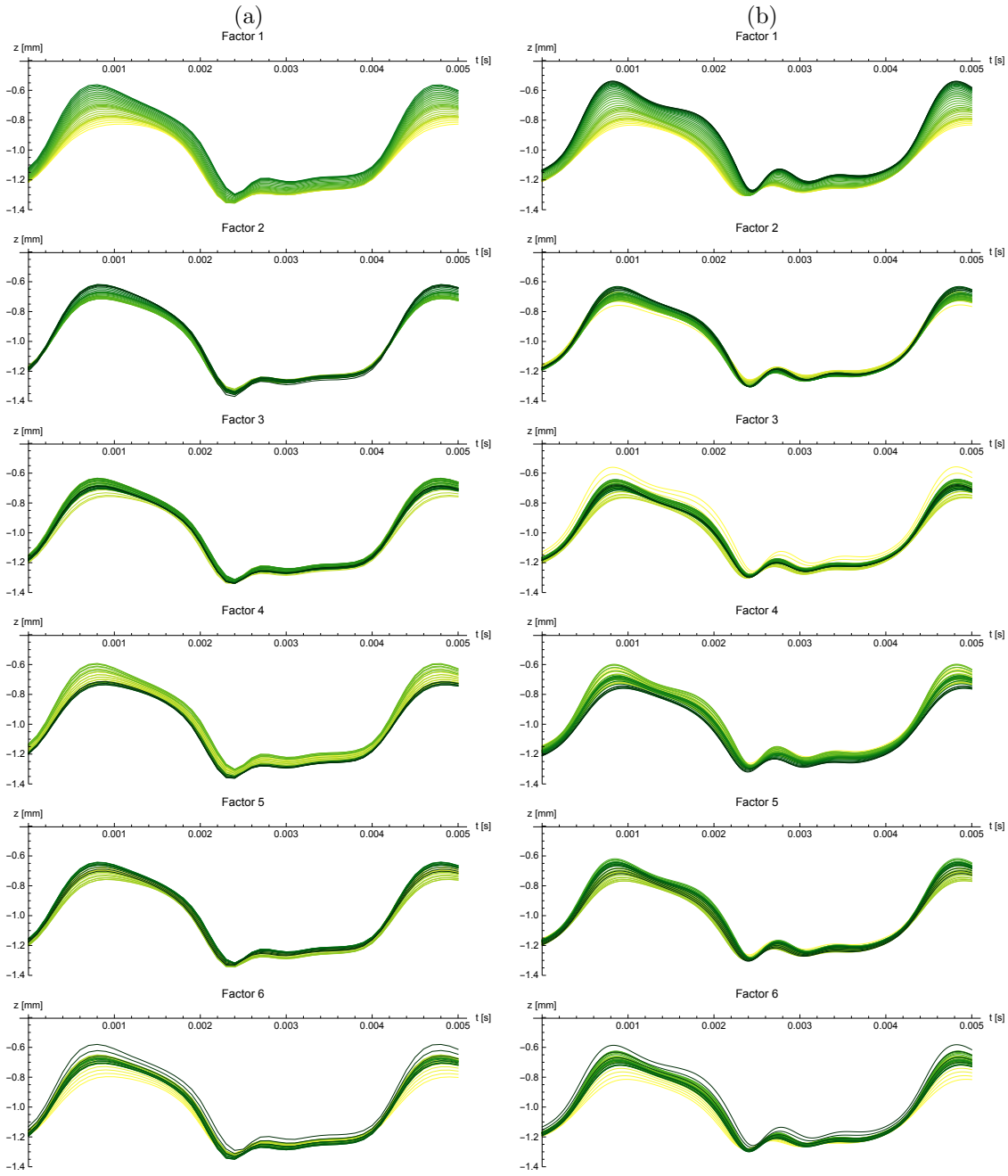

Figure D.19 – Trend (within each factor) of the deflection signal of the reed, for a blowing pressure of **10 kPa**, with a loose embouchure (ψ =1,250 mm). (a) measured with the artificial mouth. (b) according to the synthesis model. Same color code as the 5 preceding Figs.

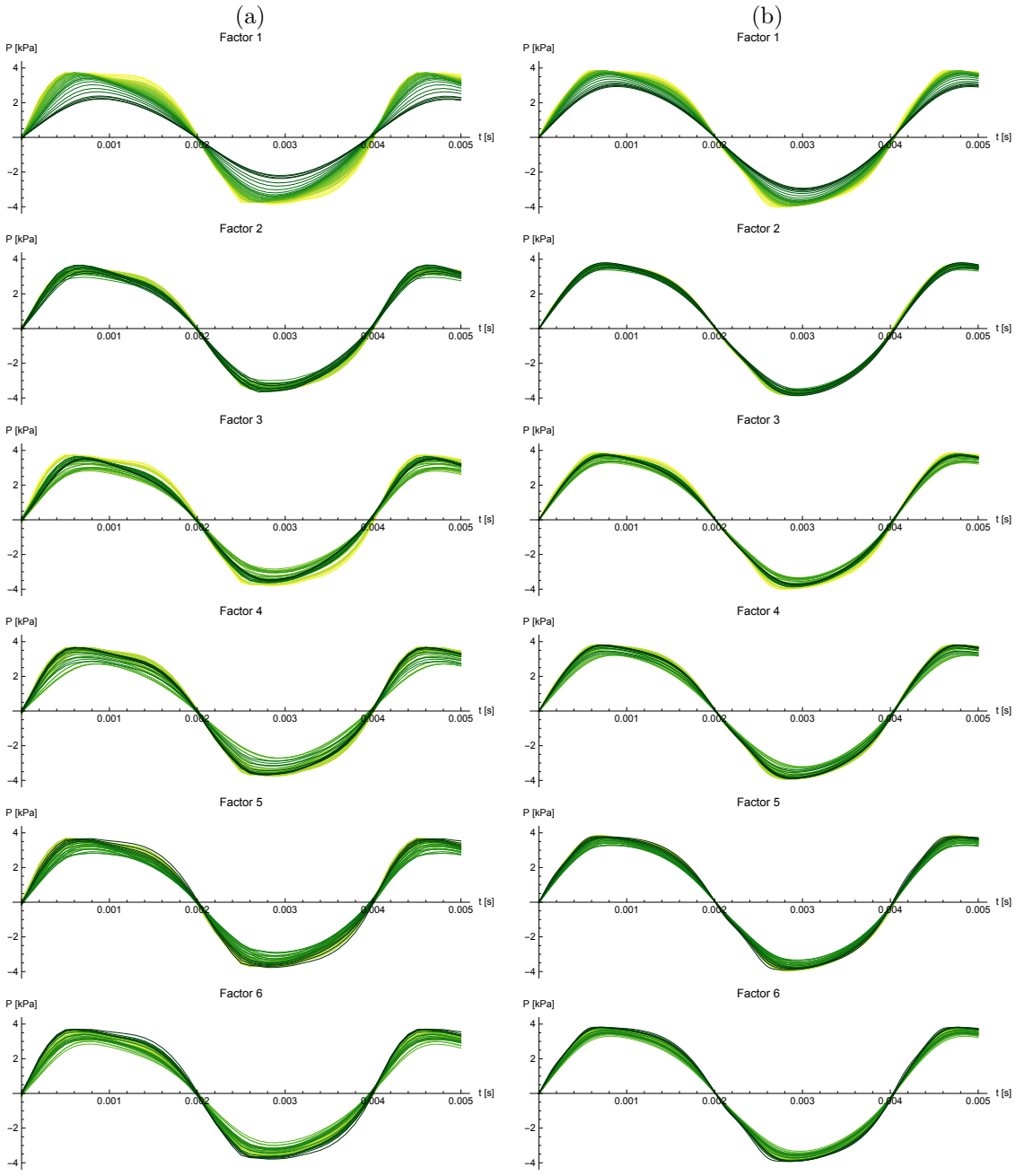

Figure D.20 – Trend (within each factor) of the pressure signal in the mouthpiece, for a blowing pressure of **4 kPa**, with a loose embouchure ($\psi = 1,250$ mm). (a) measured with the artificial mouth. (b) according to the synthesis model. Same color code as the 6 preceding Figs.

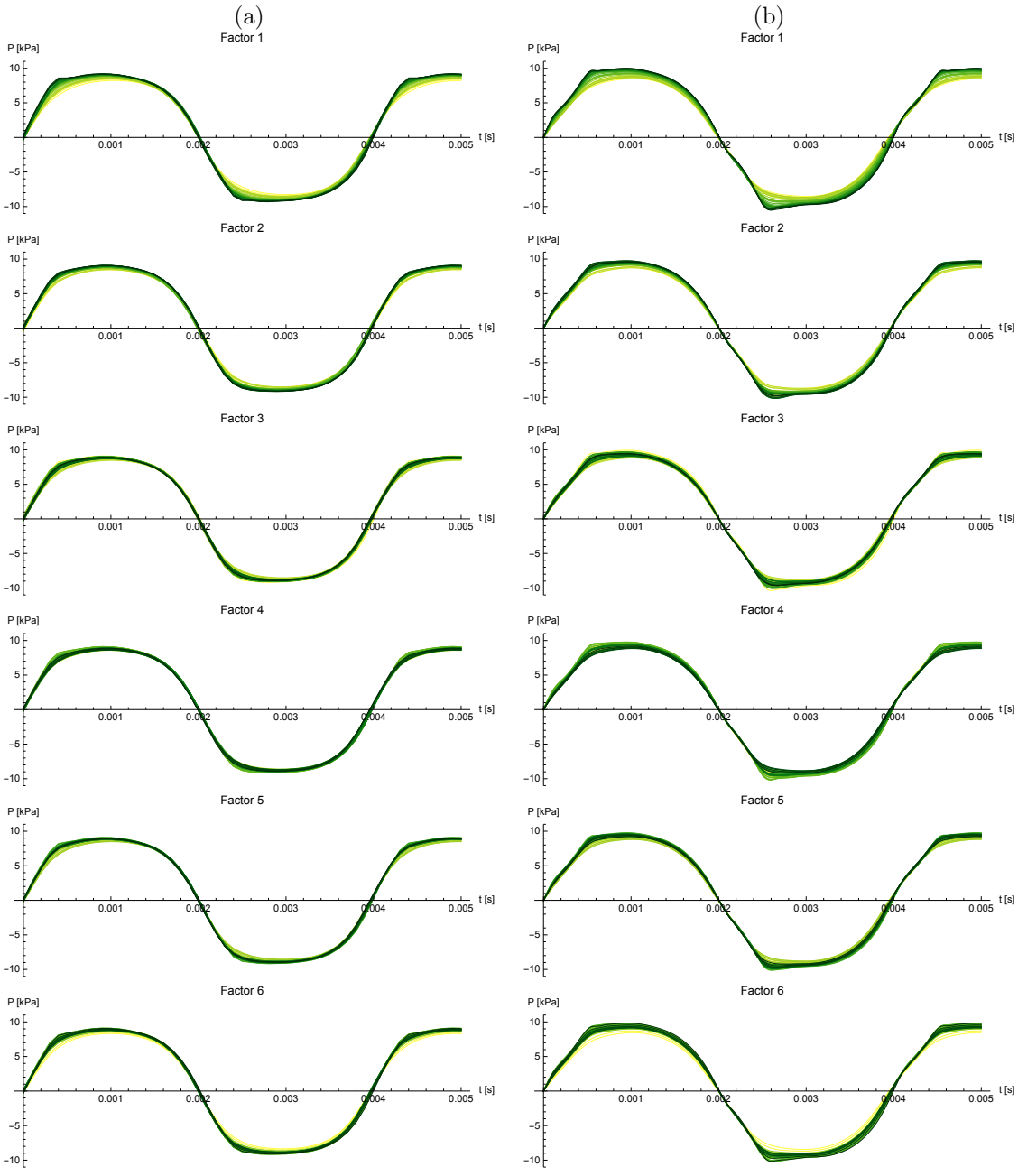

Figure D.21 – Trend (within each factor) of the pressure signal in the mouthpiece, for a blowing pressure of **10 kPa**, with a loose embouchure ($\psi = 1.250$ mm). (a) measured with the artificial mouth. (b) according to the synthesis model. Same color code as the 7 preceding Figs.

Appendix E

Improvements to the Discrete Singular Convolution method and application to beam analysis

Résumé

Ce projet d'article propose une introduction simplifiée à l'algorithme Discrete Singular Convolution, incluant plusieurs améliorations. Grâce à l'utilisation d'un noyau régularisé pouvant être analytiquement intégré, cette méthode baptisée EDSC (Extended Discrete Singular Convolution) ouvre de nouveaux champs d'application, comprenant tout type de transformations linéaires (dérivées et intégrales, transformées de Fourier et de Laplace et leurs inverses, par exemple), et offre simultanément une flexibilité supplémentaire, associée à une précision numérique souvent meilleure que la méthode originelle, selon les tests de benchmark effectués à l'aide de différents problèmes de mécanique des poutres dont on connaît la solution analytique. Une approche unifiée et simplifiée est également développée pour la mise en œuvre de points fictifs pouvant prendre en compte des conditions aux limites d'ordre arbitraire. L'EDSC apparaît comme une méthode numérique fiable pour intégrer, dériver et interpoler une fonction à bande limitée, définie par une série tronquée de points discrets, de même que pour résoudre numériquement des équations différentielles .

Improvements to the Discrete Singular Convolution method and application to beam analysis

Pierre-André Taillard[1], Bruno Gazengel[2], André Almeida[2]
and Jean-Pierre Dalmont[2]
[1] Schola Cantorum Basiliensis, Fachhochschule Nordwest-Schweiz;
Leonhardstrasse 6; 4003 Basel; Switzerland;
[2] Laboratoire d'Acoustique de l'Université du Maine (UMR CNRS 6613)
Université du Maine; Le Mans; France;

December 3, 2013

Abstract

This paper proposes a simplified introduction to the Discrete Singular Convolution algorithm, including several improvements. Through the use of a regularized kernel that can be analytically integrated, this Extended Discrete Singular Convolution (EDSC) method opens new fields of application, including any kind of linear transformations (i.e. derivatives and integrals, Fourier and Laplace transforms and their inverses), and offers simultaneously an additional flexibility, combined with a numerical accuracy favorably comparable to the original method, according to various benchmark beam problems. A unified, simplified approach is also developed for implementing fictitious points with any number of boundary conditions. The EDSC appears as a reliable numerical method for integrating, differentiating and interpolating a band limited function defined as a truncated series of discrete points, and for solving numerically differential equations.

1 Introduction

Whenever the mathematical distributions involved in a given scientific problem are thought to be band limited, the Discrete Singular Convolution method (DSC) should be considered, especially for solving numerically differential equations. This algorithm emerged in the early 2000's as a wavelet collocation scheme for the computer realization of singular convolutions [1, 2]. Its foundation is the Shannon theorem and the theory of distributions [3] and it is therefore optimally suited for handling such functions. Zaho et al.[4] describe its main features as follows: " The DSC algorithm has the global methods' accuracy and the local methods' flexibility for handling complex geometry and boundary conditions in the analysis of fluid dynamics [5] and electrodynamics problems [6]. It is a simple and robust approach for structural analysis, and has found its success in structural analysis, including the vibration and buckling of beams [7], plate vibration under various edge and internal supports [8, 9, 10, 11, 12, 13, 14, 15, 16]. The DSC algorithm was extensively validated by analytical and exact solutions and carefully compared with other existing methods, including the series expansion [17], integral equation approach [18, 19], finite strip and finite element methods [20, 21, 22], Galerkin methods [23], differential quadrature methods [24, 25, 26], and Rayleigh-Ritz variational methods [27, 28, 29]. The most distinguished feature of the DSC algorithm is its high level of accuracy and reliability. At present,

it is the only available method that is able to predict accurately thousands of vibration modes of plates and beams without encountering numerical instability [7, 13].

This method can be used for other kinds of problems, for instance when a compact and parsimonious support is needed for a smooth, continuous interpolation of a multidimensional measurement data set or for capturing the main features of a complex physical model with a simple mathematical model (metamodel). For example we used this method for modeling the static bending of a clarinet reed with only 12 points from a Finite Element Method computation involving more than 4'000 points [30]. Throughout the analytical nature of the equation, a continuous interpolation of the function and its derivatives and integrals is possible.

Until now, the method was difficult to apply without a fairly good understanding of the underlying mathematics and without some previous experience with numerical solving of differential equations. Its application for an arbitrary number of boundary conditions was not described. We wish to introduce this method to a broader public, proposing a formulation based only on elementary matrix operations. We try to show the essential features through an intuitive and direct approach, without overwhelming the reader with mathematical details, which can be found in the appendix or in the original publications.

In the DSC algorithm, differential equations are numerically solved through the derivatives of a kernel of delta type. This gives rise to principally two types of difficulties :

- When an integration is required, the matrix of the differential operator must be inverted and this may impact negatively upon the accuracy of the computation. Besides the required computing power, the inversion can be critical to achieve, especially for differential operators of odd orders.

- When the function is truncated, the accuracy of the DSC method near the boundary of the computation domain is highly corrupted by the phenomenon of ripple, which is especially important when the derivation order is high. The function must be extended beyond the truncation with fictitious points (FPs) to retrieve a good accuracy [14]. Typically, 25 FPs are added on the left and on the right of the computation domain, which leads to a substantial inflation in the size of matrices, growing moreover exponentially with the number of variables of the problem.

One of the goals of the present paper is to investigate if the primitives of the kernel help to eliminate these drawbacks. To our knowledge, theses primitives have never been used with the DSC method, allowing on one hand to build directly the desired integral operator, and on the other hand, to lower the number of required FPs. Indeed, the phenomenon of ripple decreases as the order of integration rises, allowing sometimes a quite accurate computation without FPs. Unfortunately, no analytical primitive of the Regularized Shannon Kernel (RSK) is known so far. A numerical integration of the kernel is possible, but this may be difficult to achieve up to the required accuracy. We propose to use a new kernel, written as a rapidly convergent series, which can be integrated analytically. This new kernel also permits the analytical calculation of many kinds of integral transformations.

The application of the method is illustrated with some elementary 1D beam analysis problems and the results are compared to the analytical solutions.

The theoretical background to the DSC and the EDSC algorithms are succinctly presented in §2.1. The accuracy of the new kernel for interpolating, differentiating and integrating a band limited function is studied, and a numerical method for solving differential equations is sketched in §2.2. A novel approach for implementing FPs is proposed in §2.3, which allows an implicit formulation for any number of boundary conditions. Finally, the method is validated in §3 with some problems having a known analytical solution and the results compared to those of the

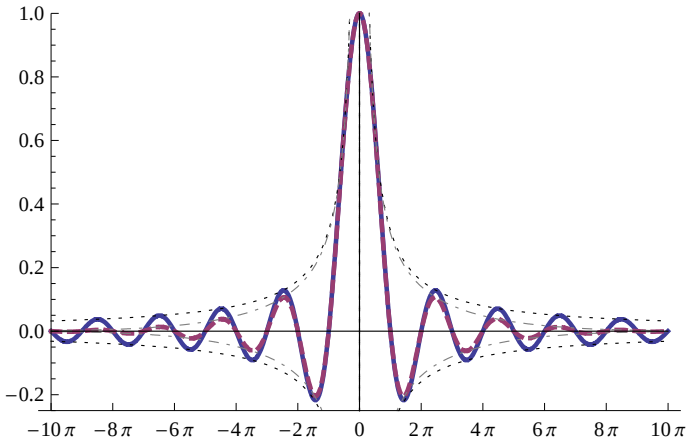

Figure 1: Plot of the Sinus Cardinal function (thick line), the Regularized Shannon Kernel (RSK) Equation (3), with $\sigma = 4\pi$ (dashed line) and the envelope of both functions: (respectively dotted and dash-dotted lines).

standard DSC method. These problems include the bending of beams under transverse load (§3.1) and free vibrations of beams (§3.2). Conclusions are the subject of §4.

2 Extended Discrete Singular Convolution method

2.1 Method

The Nyquist–Shannon sampling theorem states that, if a continuous function[1] $\check{y}[\check{t}]$ contains no frequencies higher than F, it is completely determined by giving its ordinates at a series of points spaced $T = 1/(2F)$ seconds apart. T is the sampling interval. For convenience, let us normalize the variable $t \equiv \check{t}/T$ and center the function: $y[t] \equiv \check{y}[\check{t} + \tau]$. The constant τ allows to shift the function if necessary, to center its region of interest around 0. The variable t can describe the time or any other parameter like the space coordinate as shown in some following examples. The Whittaker–Shannon interpolation formula [31] permits the reconstruction of the band limited function as a discrete convolution:

$$y[t] = \sum_{m=-\infty}^{\infty} y_m \cdot \mathrm{Sinc}\left[\pi(t-m)\right] \tag{1}$$

with $y_m = y[m]$. This equation is exact for all $t \in \mathbb{R}$. The Sinus cardinal function [32, 33, 34] is defined as: $\mathrm{Sinc}[x] \equiv \mathrm{Sin}[x]/x$. Notice that $\mathrm{Sinc}[\check{t}/T]/T$ tends to the Dirac δ distribution when

[1] Notation conventions: In this paper, the arguments of a function are systematically enclosed between square brackets []. If necessary, the constant parameters of the function are given as indices. $f_a^{(d)}[x]$ denotes the d^{th} derivative with respect to x of a function $f[x]$ having a constant parameter a. A sequence of scalars is denoted by curly brackets {}; this notation is also used for vectors and matrices. For instance $\boldsymbol{v} = \{m^2\}$, $m \in \{0, .., 2\}$ denotes the vector $\boldsymbol{v} = \begin{pmatrix} 0 \\ 1 \\ 4 \end{pmatrix}$. The components of $\boldsymbol{v}$ are referred by an index, as usual. The notation above is equivalent to $v_{m+1} = m^2$; it avoids the problem of translation of the indices in the vector, in order to ensure that the first component of the vector has index 1. If 2 indices are involved, this notation builds a matrix.

T tends to 0 and Equation (1) tends consequently to $y[t] = \int_{-\infty}^{\infty} y[t] \cdot \delta\left[(t-m)\right] \mathrm{d}m = y * \delta$, the δ distribution being the neutral element of the convolution product [33]. Notice also that the envelope of the $\mathrm{Sinc}[x]$ function decreases according to $1/x$. The formula is therefore extremely sensitive to truncations of the infinite series. For a numerical interpolation of $y[t]$ with 15 digits of precision (the usual machine precision), for a particular value of t, at least 2×10^{15} terms around t should be taken into account in the truncated series. The Sinc kernel can be replaced by any other kernel of δ type, such that $\delta_{kernel}[0] = 1$ and $\delta_{kernel}[\pi n] = 0$, $\forall n \in \mathbb{Z}^*$. Wei et al. [14] give many examples of such kernels. This leads to:

$$y[t] \simeq \sum_{m=-M}^{M} y_m \cdot \delta_{kernel}\left[\pi(t-m)\right] \tag{2}$$

This equation is slightly inexact[2] except for the integer values of $-M \leq t \leq M$, whereas outside this interval (i.e. outside the computational domain) it is inexact. It is desirable to choose a kernel which tends rapidly to 0 when $|x| \to \infty$, in order to lower the number $2M+1$ of terms in the series. Wei [9] propose to use the Regularized Shannon Kernel (RSK, shown in Figure 1)

$$\mathrm{RSK}[x] = \mathrm{Sinc}[x]\ \mathrm{Exp}\left[-\frac{x^2}{2\sigma^2}\right] \tag{3}$$

This lowers considerably the number of terms to take into account, with negligible loss of precision. The parameters M and σ can be adapted to the desired computational accuracy. Wei [9] found an approximate formula to determine them. With $\sigma = 3\pi$, $|\mathrm{RSK}(\pi x)| < 8.6 \times 10^{-15}$ for $|x| > 22.5$, reaching the order of magnitude of the machine precision, therefore the value for an optimal precision around $t = 0$ should be at least $M = 23$ (in other words: the first 15 digits remain practically unchanged if $M > 23$). In practice, the value taken as M is much larger than this, in order to extend the interval on which the accuracy is optimal (i.e. the interval on which Equation (2) is translation invariant, with respect to the accuracy determined by the choice of σ) and the effective kernel support can be truncated around this value, to reduce the computational burden, without loss of precision.

Equation (2) can be generalized to any linear transformation $\mathscr{L}$ of $y[t]$, including the Fourier transform, the bilateral Laplace transform, the Hartley transform, the Weierstrass transform and the Hilbert transform:

$$\mathscr{L}y[t] \simeq \sum_{m=-M}^{M} y_m \cdot \mathscr{L}\delta_{kernel}\left[\pi(t-m)\right] \tag{4}$$

In particular, for derivatives ($d > 0$) and antiderivatives ($d < 0$) this equation can be written:

$$y^{(d)}[t] \simeq \pi^d \sum_{m=-M}^{M} y_m \cdot \delta_{kernel}^{(d)}\left[\pi(t-m)\right] \tag{5}$$

Again, the accuracy of this equation is excellent in the middle of the computational domain but may be poor near the boundaries, especially for the derivatives. An example is given on Fig. 2 in which the interpolation of a truncated Cosine function and some of its derivatives and antiderivatives are depicted. The error of this interpolation compared to the analytic derivatives and antiderivatives (relative to the maximum amplitude of these analytical derivatives and antiderivatives) is also given. The accuracy is optimal in the interval $-M + 23$ to $M - 23$; the

[2]The proof of this is beyond the scope of this paper. The problem can be addressed via the distribution theory or (Philippe pourrait donner quelques références sur Galerkin).

error increases considerably from the boundaries of this interval to the boundaries of the computational domain ($|t| = M$). The antiderivatives are always more precise than the derivatives. Near the boundaries, the 4^{th} antiderivative is about 3×10^6 times more accurate than the 4^{th} derivative, because antiderivatives are far less sensitive to the phenomenon of ripple. For a precise numerical computation, the computation domain has to be extended by adding fictitious points (FPs), which are eliminated after computation. This is the subject of § 2.3.

Observe that Equation (5) builds formally a discrete convolution. The use of a dedicated convolution algorithm reduces significantly the computing time, especially for big values of M.

EDSC Method Equation (5), with $d \geq 0$, correspond to the standard DSC method, as described in [9]. The scope of the DSC method can be extended through different improvements. Let us examine how to use Equation (5) analytically also with $d < 0$. So far, our equation has no constants of integration: $y^{(d)}[t]$ is merely one out of an infinity of antiderivatives. In order to build a convenient function $y_C^{(d)}[t]$ matching given boundary conditions, $|d|$ constants of integration a_i must be introduced into the equation, as a polynomial $p_d[x]$ of degree $|d| - 1$:

$$\begin{gathered} y_C^{(d)}[t] = y^{(d)}[t] + p_d[t] \\ p_d[x] = \begin{cases} 0, & d \geq 0; \\ \sum_{i=0}^{|d|-1} 1/i!\ a_{|d|-1-i}\ x^i, & d < 0. \end{cases} \end{gathered} \tag{6}$$

The integration constants a_i are solutions of a system of $|d|$ equations, according to $|d|$ conditions given on the derivatives of $y_C^{(d)}[t]$. Example: for a bar clamped at its extremities at $x = -M$ and $x = M$, the boundary conditions are $y_C^{(-4)}[-M] = 0$, $y_C^{(-4)}[M] = 0$, $y_C^{(-3)}[-M] = 0$ and $y_C^{(-3)}[M] = 0$. Applying 4 times Equation (6), we get 4 equations: $\frac{1}{6}a_0(-M)^3 + \frac{1}{2}a_1(-M)^2 + a_2(-M) + a_3 + y^{(-4)}[-M] = 0$, *etc...* The solutions are easily found: $a_0 \to 3(M(y^{(-3)}[-M] + y^{(-3)}[M]) + y^{(-4)}[-M] - y^{(-4)}[M])/(2M^3)$, *etc...* Notice that the solutions depend on y_m, since $y^{(-3)}[t]$ and $y^{(-4)}[t]$ depend on y_m.

There is now the limitation that the antiderivatives of the function RSK are not known analytically and a numerical integration must be carefully conducted, in order to reach a sufficient precision. In order to avoid this numerical integration we define a new kernel (with a supplementary parameter $N \in \mathbb{N}^*$):

$$\mathrm{RSK}_N[x] = \frac{\mathrm{RSK}[x]}{\mathrm{Sinc}\,[x/(2\mathrm{N})]} \tag{7}$$

which can be integrated analytically, as:

$$\mathrm{RSK}_N[x] = \frac{1}{\mathrm{N}} \sum_{n=\frac{1}{2}}^{\mathrm{N}-\frac{1}{2}} \Re\left[\mathrm{Exp}\left[\frac{inx}{\mathrm{N}} - \frac{x^2}{2\sigma^2}\right]\right] \tag{8}$$

with $i = \sqrt{-1}$ (see proof in Appendix A.1, Equation (36)).

Equation (7) shows that the RSK_N is a kernel close to RSK and tends to RSK when $N \to \infty$, because $\mathrm{Sinc}\,[0] = 1$. It can be shown that $\mathrm{RSK}_{N,\sigma_2}[x] \simeq RSK[x]$ where $\sigma_2 = \left(1/\sigma^2 + 1/(12N^2)\right)^{-1/2} \approx \sigma(1 - \frac{\sigma^2}{24N^2})$ with an absolute difference lower than 0.000007 for $N = 15$ and $\sigma = 3\pi$, for instance. It should be emphasized that this kernel exhibits a numerical accuracy comparable (or sometimes even better) than the RSK-Kernel (see Fig. 3, down). Optimal values for N have linear dependence on σ in the range $\sigma = 2.5\pi$ ($\Rightarrow N \geq 10$) to $\sigma = 4\pi$ ($\Rightarrow N \geq 25$).

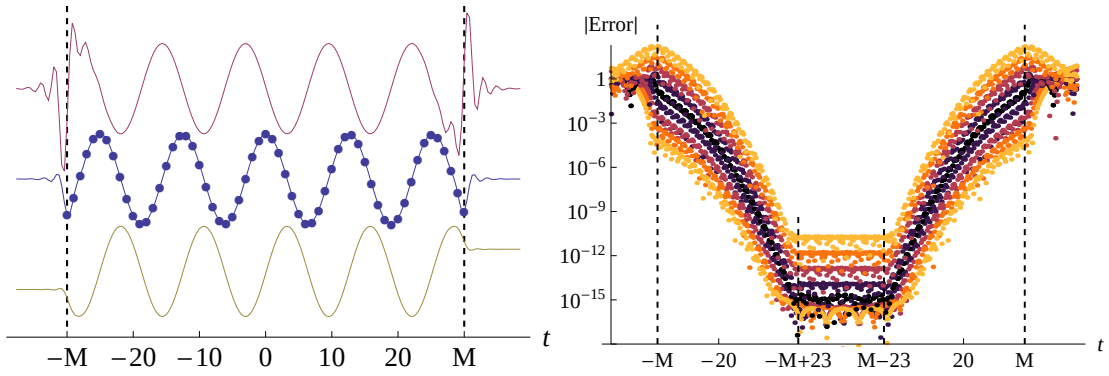

Figure 2: Interpolation and extrapolation of a sampled truncated Cosine function and of some of its derivatives and antiderivative, computed according to Equation (5) with RSK_N-Kernel, $\sigma = 3\pi$, $M = 30$ and $N = 15$. **Left:** From top to bottom: derivatives 1, 0 (with sampled points as blue dots) and -1 (i.e. 1^{st} antiderivative). The Gibbs phenomenon appears clearly especially for the 1^{st} derivative. **Right:** Absolute value of the error between the interpolated and the analytic normalized derivatives of the same function. Interpolation (and extrapolation) grid: from -38 to 38 by 0.2. Antiderivatives 0 to 4 (from dark to light, smaller values of the error). Derivatives 0 to 4 (from dark to light, higher values). Near the boundaries ($t \simeq -M$ or $t \simeq M$), the 4^{th} antiderivative is up to 3×10^6 times more accurate than the 4^{th} derivative because derivatives are more sensitive to the Gibbs phenomenon than antiderivatives.

With this formulation, the derivatives and especially the antiderivatives of RSK_N can be evaluated to an arbitrary precision. They are given in Appendix A for integer values of d, $-4 \leq d \leq 4$. In our computations, the kernel is sampled with 40 significant digits and the computations are performed with this precision, in order to ensure an irreproachable final accuracy in any cases.

In Fig. 3, the accuracy of Equation (5) is evaluated with a truncated $\mathrm{Cos}[2\pi\,\phi\,t]$ and different values of the frequency ϕ. The frequencies are normalized according to the Shannon theorem: 1 corresponds to the Nyquist rate (2 samples per period). $M = 219$ was used in all cases and the standard deviation of the error was computed for 75 points in the center of the computation domain. Upper left: the order of the derivative is varied between -4 and 4 and the error is normalized according to a relative amplitude of 1. It shows clearly that the antiderivatives are more precise in all cases. For low frequencies the 4^{th} antiderivative is up to 10^{15} more precise than the 4^{th} derivative. Of course, this result can only be achieved if the computations are performed with 30 or 40 significant digits. Upper right: the influence of the parameter σ is depicted ($N = 40$ in all cases). As expected, the maximum absolute precision (10^{-36}) is reached for the highest value of σ (4π). Again, this requires a computation with at least 40 significant digits and about 130 points have to be dropped on each side of the computation domain, in order to reach the sector of optimal precision. All curves converge for the Nyquist rate to a value of about 0.677. Bottom: the influence of N (number of terms in the series) is depicted ($\sigma = 3\pi$ in all cases). The result with $N = 15$ is up to 3.3 times better than with $N = \infty$ (RSK-Kernel, therefore without respect to the correction $\sigma \to \sigma_2$ proposed above, which explains mainly this difference). Values of $N < 15$ are not optimal.

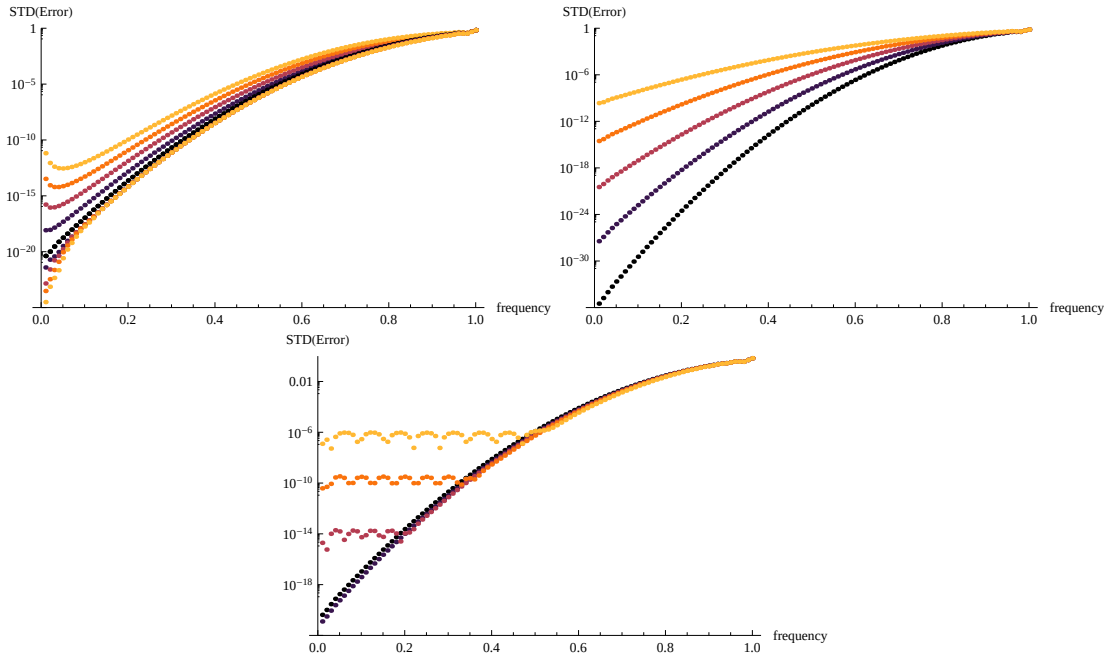

Figure 3: Frequency dependence of the standard deviation of the relative error in the optimal sector (75 central points with $M = 219$), between the interpolated and the analytic derivatives and antiderivatives of a truncated sampled $\mathrm{Cos}[2\pi\,\phi\,t]$ computed with Equation (5) and different values of the frequency ϕ; freq=1 correspond to the Nyquist frequency (2 samples per period). **Upper left**: Influence of the derivative (same colors as Figure 2). **Upper right**: Influence of the parameter σ: From dark to light: $\sigma = 4\pi, 3.5\pi, 3\pi, 2.5\pi$ and 2π, with $N = \infty$. **Bottom**: Influence of the number of terms in Equation (8): From dark to light: $N = \infty$, $N = 15$, $N = 12$, $N = 10$ and $N = 8$, with $\sigma = 3\pi$.

2.2 Solving differential equations and linear transformations with EDSC

In a linear problem (with a source term f) of the form $\mathscr{L}y = f$ in which the operator $\mathscr{L}$ cannot be analytically inverted, it is necessary to discretize the computational domain. With the DSC method, the solution $y[t]$ of the linear equation is presumed to be bandlimited. This assumption implies that $y[t]$ can be approximated with Equation (2). The left member of the differential equation may be written by discretizing the independent, continuous variable[3] t in Equation (4):

$$\mathscr{L}y[t] = f[t], \qquad \Rightarrow \qquad \boldsymbol{L} \cdot \boldsymbol{y} \simeq \boldsymbol{f} \tag{9}$$

where $\boldsymbol{f}$ is a discrete source term and $\boldsymbol{L}$ is a square Toeplitz matrix, implementing the discrete linear operator:

$$\boldsymbol{L} = \left\{ \mathscr{L}\delta_{kernel}[\pi(i-j)] \right\}, \qquad -M \leq i, j \leq M \tag{10}$$

If the matrix $\boldsymbol{L}$ is invertible, Equation (9) can be solved for $\boldsymbol{y}$:

$$\boldsymbol{y} \simeq \boldsymbol{L}^{-1} \cdot \boldsymbol{f} \tag{11}$$

The solution $\boldsymbol{y}$ is however merely one out of an infinity of solutions of the linear equation[4]. The particular solution respecting the boundary conditions $\boldsymbol{y}_c$ is obtained by adding an integration vector $\boldsymbol{c}$, satisfying $\boldsymbol{L} \cdot \boldsymbol{c} \simeq \boldsymbol{0}$, cf. continuous problem, Equation (6). We obtain finally:

$$\boldsymbol{y}_c \simeq \boldsymbol{L}^{-1} \cdot \boldsymbol{f} + \boldsymbol{c} \tag{12}$$

Practical remarks: For the particular case of the derivative operator of order d, ($i.e. \mathscr{L}y[t] \rightarrow y^{(d)}[t]$), we denote the corresponding discrete operator of derivation $\boldsymbol{L} \rightarrow \boldsymbol{A}^{(d)}$. This notation remembers that the discrete operator is built on the d^{th} derivative of the kernel. Observe that $\left(\boldsymbol{A}^{(d)}\right)^{-1} \simeq \boldsymbol{A}^{(-d)}$.

When the order of the derivative or of the antiderivative is odd, the number of discrete points must be even, since Equation (10) can produce a skew-symmetric matrix and skew-symmetric matrices of odd rank are singular (after Jacobi's theorem). Moreover some matrices can be badly conditioned and therefore difficult to invert.

Examples: The differential equation $\frac{\partial^4}{\partial x^4} w[x] = f[x]$, may be written:

$$\frac{\partial^4}{\partial x^4} y[x] = f[x], \quad y[x] = w[x]$$

$$\frac{\partial^3}{\partial x^3} y[x] = f[x], \quad \int y[x]\, dx = w[x]$$

$$\frac{\partial^2}{\partial x^2} y[x] = f[x], \quad \int\int y[x]\, dx = w[x]$$

$$\dots$$

These cases can be expressed with Equations (9 or 11) for the unknowns $\boldsymbol{w}$ and $\boldsymbol{y}$. Ignoring the integration vector $\boldsymbol{c}$, we may write:

$$\boldsymbol{w} \simeq \boldsymbol{A}^{(0)} \cdot \boldsymbol{y} \simeq \boldsymbol{A}^{(0)} \cdot (\boldsymbol{A}^{(4)})^{-1} \cdot \boldsymbol{f}$$

[3] In the present paper, for sake of simplicity, only equations with one independent variable are treated. A multivariate formulation of the DSC-Method is however possible (see for instance Wei et al. [14]).

[4] From now, without loss of generality, we consider that the linear operator is a derivative or an antiderivative.

$$\boldsymbol{w} \simeq \boldsymbol{A}^{(-1)} \cdot \boldsymbol{y} \simeq \boldsymbol{A}^{(-1)} \cdot (\boldsymbol{A}^{(3)})^{-1} \cdot \boldsymbol{f}$$
$$\boldsymbol{w} \simeq \boldsymbol{A}^{(-2)} \cdot \boldsymbol{y} \simeq \boldsymbol{A}^{(-2)} \cdot (\boldsymbol{A}^{(2)})^{-1} \cdot \boldsymbol{f}$$
$$\dots$$

The cases $\boldsymbol{A}^{(0)} \cdot (\boldsymbol{A}^{(4)})^{-1} = (\boldsymbol{A}^{(4)})^{-1}$ and $\boldsymbol{A}^{(-4)} \cdot (\boldsymbol{A}^{(0)})^{-1} = \boldsymbol{A}^{(-4)}$ are particularly interesting, numerically, and are studied in §3.

Other example (see hereafter beam problem § 3): $EI \frac{\partial^4 w}{\partial x^4} + 2 \frac{\partial EI}{\partial x} \frac{\partial^3 w}{\partial x^3} + \frac{\partial^2 EI}{\partial x^2} \frac{\partial^2 w}{\partial x^2}$ can be implemented alternatively as:

$$\boldsymbol{L} = \boldsymbol{EI}^{(0)} \cdot \boldsymbol{A}^{(4)} + 2\boldsymbol{EI}^{(1)} \cdot \boldsymbol{A}^{(3)} + \boldsymbol{EI}^{(2)} \cdot \boldsymbol{A}^{(2)}, \quad \text{if } y[x] = w[x]$$

or as:

$$\boldsymbol{L} = \boldsymbol{EI}^{(0)} \cdot \boldsymbol{I} + 2\boldsymbol{EI}^{(1)} \cdot \boldsymbol{A}^{(-1)} + \boldsymbol{EI}^{(2)} \cdot \boldsymbol{A}^{(-2)}, \quad \text{if } \int\int\int\int y[x]\, dx = w[x]$$

with $\boldsymbol{EI}^{(d)} = \text{Diag}[\{EI^{(d)}[m]\}],\ m \in \{-M, \dots, M\}$. Both options are compared in §3.1.2.

2.3 Implementation of boundary conditions

When $\boldsymbol{L}^{-1} \to \boldsymbol{A}^{-d}$, the boundary conditions can be implemented easily via the integration vector $\boldsymbol{c}$, by solving Equation (6). With this method, a computation is possible without using fictitious points (FPs) outside the boundary, with a reasonable accuracy (cf. Fig. 2 and 3). However, this might be insufficient when a high precision is required. The precision can be notably increased by the use of FPs, which allows a correct implementation of a translation invariant kernel near the boundaries of the linear problem. Both difficulties of implementation (writing the boundary conditions implicitely and implementing a translation invariant kernel near the boundaries) can be solved at the same time. For this, the right member of Equation (12) needs to be written as a product. We have then to deduce some properties of this product, to expand the size of the computational domain, to compute the required matrix and finally, we have to reduce this matrix back to the original size of the problem. Let us examine each step with more details:

The coordinate system of our linear problem must be chosen such that the problem is strictly linear (i.e. if $\boldsymbol{f} = \boldsymbol{0} \quad \Rightarrow \quad \boldsymbol{y}_c = \boldsymbol{y} + \boldsymbol{c} = \boldsymbol{0}$: Any affine component must be removed). This implies that the integration vector $\boldsymbol{c}$ depends linearly on $\boldsymbol{f}$ (otherwise the problem would not be strictly linear), according to some matrix $\boldsymbol{C}$ (*a priori* unknown): $\boldsymbol{c} = \boldsymbol{C} \cdot \boldsymbol{f}$. As already mentioned, the integration vector has the property $\boldsymbol{L} \cdot \boldsymbol{c} \simeq \boldsymbol{0}$. This implies that:

$$\boldsymbol{L} \cdot \boldsymbol{C} \cdot \boldsymbol{f} \simeq \boldsymbol{0}, \quad \forall \boldsymbol{f} \qquad \Rightarrow \qquad \boldsymbol{L} \cdot \boldsymbol{C} \simeq \boldsymbol{O} \tag{13}$$

where $\boldsymbol{0}$ is the null vector and $\boldsymbol{O}$ is the null matrix. Moreover, Equation (12) can be written:

$$\boldsymbol{y}_c \simeq (\boldsymbol{L}^{-1} + \boldsymbol{C}) \cdot \boldsymbol{f} = (\boldsymbol{I} + \boldsymbol{C} \cdot \boldsymbol{L}) \cdot \boldsymbol{L}^{-1} \cdot \boldsymbol{f} = \boldsymbol{B}^{-1} \cdot \boldsymbol{L}^{-1} \cdot \boldsymbol{f} \tag{14}$$

with $\boldsymbol{B}^{-1} \equiv \boldsymbol{I} + \boldsymbol{C} \cdot \boldsymbol{L}$.

We demonstrate now that the inverse of $\boldsymbol{B}^{-1}$ is $\boldsymbol{B} \simeq \boldsymbol{I} + \boldsymbol{C} \cdot \boldsymbol{L}$:

$$\boldsymbol{B}^{-1} \cdot \boldsymbol{B} \simeq (\boldsymbol{I} + \boldsymbol{C} \cdot \boldsymbol{L}) \cdot (\boldsymbol{I} - \boldsymbol{C} \cdot \boldsymbol{L}) = \boldsymbol{I} - \boldsymbol{C} \cdot \boldsymbol{L} \cdot \boldsymbol{C} \cdot \boldsymbol{L} \simeq \boldsymbol{I} \tag{15}$$

because $\boldsymbol{B}^{-1} \cdot \boldsymbol{B} = \boldsymbol{I}$ and because $\boldsymbol{L} \cdot \boldsymbol{C} \simeq \boldsymbol{O}$. Thus, Equation (9) and its solution, Equation (12), may be written:

$$\boldsymbol{L} \cdot \boldsymbol{B} \cdot \boldsymbol{y}_c \simeq \boldsymbol{f} \qquad \Leftrightarrow \qquad \boldsymbol{y}_c \simeq \boldsymbol{B}^{-1} \cdot \boldsymbol{L}^{-1} \cdot \boldsymbol{f} \tag{16}$$

Writing explicitly the expression of matrix $\boldsymbol{B}$ is however not straightforward. This can be achieved by extending the computation domain outside the boundaries of the linear problem. This allows simultaneously a correct implementation of a translation invariant kernel near the boundaries of the linear problem. An expression of this matrix in the computational domain extended by FPs, called $\boldsymbol{B}_{FP}$, satisfying Equation (15) *stricto sensu*, is given in Appendix B. Two different methods are proposed, called the Simple Extension (SX) and the Polynomial Extension (PX).

The idea is to increase the size of the vector $\boldsymbol{y}_c$ by zero-padding (i.e. extending a vector of size $Inner$ by concatenating $Left$ zeros to the left and $Right$ zeros to the right): $\boldsymbol{y}_c \rightarrow \boldsymbol{y}_{zp}$ and then replace the padded 0's by fictitious points (FPs) extrapolated with respect to the boundary conditions of the problem: $\boldsymbol{y}_{zp} \rightarrow \boldsymbol{y}_{FP}$. The zero-padding ensures that the FPs depend only on the $Inner$ points of vector $\boldsymbol{y}_c$, as required by an implicit implementation. If a matrix $\boldsymbol{B}_{FP}$ holds the coefficients defined in Appendix B for the required boundary conditions, then $\boldsymbol{y}_{FP} = \boldsymbol{B}_{FP} \cdot \boldsymbol{y}_{zp}$. Let us rewrite Equation (16) in the extended computational domain as:

$$\boldsymbol{f}_{FP} = \boldsymbol{L}_{ext} \cdot \boldsymbol{B}_{FP} \cdot \boldsymbol{y}_{zp} \tag{17}$$

$\boldsymbol{L}_{ext}$ is a version of the discrete linear operator extended to the *ad hoc* size (i.e. $2M + 1 = Left + Inner + Right$). We compute the product $\boldsymbol{L}_{FP} \equiv \boldsymbol{L}_{ext} \cdot \boldsymbol{B}_{FP}$. The resulting equation $\boldsymbol{f}_{FP} = \boldsymbol{L}_{FP} \cdot \boldsymbol{y}_{zp}$ can be viewed as a system of R equations with R unknowns (R is the rank of the matrix $\boldsymbol{L}_{FP}$). By extending the computational domain, we have introduced new unknowns in the problem: the values of the components of the source term $\boldsymbol{f}_{FP}$ outside the boundaries of the linear problem. The system can be resolved only after elimination of all these "unnecessary" equations. These are easily identified as the lines where the value 0 was imposed in the vector $\boldsymbol{y}_{zp}$, either because of the zero padding for creating the FPs or because the boundary conditions require this value (for instance: simply supported or clamped condition in a beam problem). We have then simply to drop all corresponding lines and columns in $\boldsymbol{L}_{FP} \rightarrow \boldsymbol{L}_B$, $\boldsymbol{f}_{FP} \rightarrow \boldsymbol{f}$ and $\boldsymbol{y}_{zp} \rightarrow \boldsymbol{y}_c$. Finally, solving for $\boldsymbol{y}_c$ leads to:

$$\boldsymbol{y}_c = \boldsymbol{L}_B^{-1} \cdot \boldsymbol{f} \tag{18}$$

Notice that the expression of the matrix $\boldsymbol{B} = \boldsymbol{L}^{-1} \cdot \boldsymbol{L}_B$ in Equation (16) does not need to be known explicitly.

If $\mathscr{L}$ can be analytically inverted, a matrix inversion is not required, however the "unnecessary" equations must be eliminated with Gaussian elimination in order to obtain $\boldsymbol{L}_B^{-1}$. With an auxiliary matrix $\boldsymbol{K} \equiv \boldsymbol{B}_{FP}^{-1} \cdot \boldsymbol{L}_{ext}^{-1}$ and $R = \mathrm{rank}(\boldsymbol{K})$, compute:

$$K_{n,m} := K_{n,m} - K_{1,m} K_{n,1} / K_{1,1} \quad \text{for } n, m \in \{2 \dots R\},$$

then drop line 1 and column 1 in $\boldsymbol{K}$. Repeat this operation for each equation to eliminate.

3 Validation with benchmark beam problems

For an Euler-Bernoulli 1D-beam, the governing equation is:

$$EI \frac{\partial^4 w}{\partial x^4} + 2 \frac{\partial EI}{\partial x} \frac{\partial^3 w}{\partial x^3} + \frac{\partial^2 EI}{\partial x^2} \frac{\partial^2 w}{\partial x^2} = f \tag{19}$$

where the function $w[x]$ represents the deflection of the beam. The function $EI[x]$ is called the flexural rigidity of the beam. It is composed as the product of the Young modulus $E[x]$ and

the moment of inertia of the cross section $I[x]$. If the beam has uniform section and constant Young modulus, $EI[x]$ is constant. In this case, we take a value of $EI = 1$ for the benchmark tests.

f is a source term, depending on the problem under consideration.

In the benchmark beam problems, we used 3 different boundary conditions:
the simply supported condition:

$$w = 0 \quad ; \quad \frac{\partial^2 w}{\partial x^2} = 0 \tag{20}$$

the clamped condition:

$$w = 0 \quad ; \quad \frac{\partial w}{\partial x} = 0 \tag{21}$$

and the free condition:

$$\frac{\partial^2 w}{\partial x^2} = 0 \quad ; \quad \frac{\partial^3 w}{\partial x^3} = 0 \tag{22}$$

at the boundaries (in our problem (without FPs), at $x = -M$ or $x = M$)

Hereafter, we use the abbreviation S, C and F for refering to these boundary conditions (S: simply supported, C: clamped, F: free).

3.1 Bending under transverse load

3.1.1 Uniform thickness

In this paragraph, cases with uniform thickness (i.e. with constant flexural rigidity $EI[x]$) and sinusoidal load are explored. The source term in Equation (19) is $f[x] = \sin[\alpha x + \beta]$. The generic solution of the differential equation has the form:

$$w[x] = a_3 x^3 + a_2 x^2 + a_1 x + a_0 + \frac{\sin[\beta + \alpha x]}{\alpha^4 \mathrm{EI}} \tag{23}$$

The values of the constants of integration a_i are easily determined for the boundary conditions selected in our benchmark tests: SS, CS, CC and CF. The maximum admissible value for α in the DSC algorithm is π (the Nyquist rate for the sinusoidal load). In the benchmark tests, the values $1/25 \leq \alpha \leq 1$ (by steps of $1/25$) and $\beta = 1$ were used. This ensures that the analytical solution is neither a pure, even function, a pure, odd function, nor a pure polynomial (i.e. the simple extension or the polynomial extension cannot be the exact continuation of the analytical solution of the equation).

Let us examine concretely how to perform such a computation with the DSC algorithm for the boundary condition FC (free/clamped). First, we have to set the desired precision (for machine precision, typically $\sigma = 3\pi$ and $N = 15$) and the size of the computational domain (i.e. we have to set values for $Left$, $Inner$ and $Right$; M is then determined as $2M+1 = Left+Inner+Right$). Next, we have to choose the linear operator (let us take $\boldsymbol{A}^{(4)}$, like in the standard DSC method) and the kind of extension. We take for this example the polynomial extension (PX) for realizing the free condition at $x = -(M - Left)$ and the simple extension (SX) for realizing the clamped condition at $x = (M - Right)$. For the PX, a value for K has to be chosen (how many points in the inner zone next to the boundary are taken into account in the interpolation/extrapolation polynomial).

The construction of the discrete linear operator of derivation $\boldsymbol{A}^{(4)}$ with Equation (10) is straightforward; the 4^{th} derivative of the RSK_N kernel is given by Equation (48). Our differential equation has only one operator (since $EI[x]$ is constant), thus $\boldsymbol{L}_{ext} = \boldsymbol{A}^{(4)}$, cf. § 2.3. The construction of the matrix $\boldsymbol{B}_{FP}$ is described in Appendix B. The main difficulty consists in the

implicit formulation of a polynomial of degree $K+2$ having its 2^{nd} and 3^{rd} derivatives vanishing at $x = -(M - Left)$, as required by the free condition, Equation (22). The construction of such a polynomial is explained in Appendix B.2. In our example, we have: $\boldsymbol{d} = \{2, 3\}$ and $D = Length[d] = 2$. Equation (53) gives the analytical expression of such a polynomial (however relatively to a boundary at $x = 0$). The matrix $\boldsymbol{L}_B$ is computed with the procedure described in § 2.3 and finally, the solution $\boldsymbol{y}_c$ is obtained according to Equation (18), for any load $\boldsymbol{f}$. In the benchmark tests, we set $f_m = \sin[\alpha m + \beta]$ in order to compare the result with the analytical solution.

Let us detail the construction of the matrix $\boldsymbol{B}_{FP}$ with a minimal, numerical example (however much too small to allow a precise computation with the DSC algorithm, because the assumptions behind the truncation of the series in Equation (2) are strongly violated). Following values are used for this pedagogical example: $Left = Right = 3$, $Inner = 5$ and $K = 3$, thus $M = 5$.

From Equation (53), we get the expression of the Lagrange polynomials respecting the boundary condition "free end at $x = 0$":

$$\begin{aligned}
p_{3,\boldsymbol{d},0}[x] &= -\frac{1}{102}(x-1)(x-2)(x-3)(5x^2+12x+17) \\
p_{3,\boldsymbol{d},1}[x] &= \frac{1}{510}x(x-2)(x-3)(57x^2+90x+108) \\
p_{3,\boldsymbol{d},2}[x] &= -\frac{1}{510}x(x-1)(x-3)(39x^2+36x+27) \\
p_{3,\boldsymbol{d},3}[x] &= \frac{1}{510}x(x-1)(x-2)(7x^2+6x+4)
\end{aligned}$$

It is easy to verify that the 2^{nd} and 3^{rd} derivatives of these polynomials vanish at $x = 0$ and that they fulfill the properties required in Appendix B.2 for the interpolating/extrapolating function $P_{K,\boldsymbol{d}}[x]$, Equation (52). These polynomials are discretized for $x \in \{-Left, .., -1\}$, in order to obtain the sub-matrix $\boldsymbol{G}$, composing the matrix $\boldsymbol{B}_{FP}$, as described in Appendix B:

$$\boldsymbol{B}_{FP} = \begin{pmatrix}
1 & 0 & 0 & \frac{520}{17} & -\frac{1053}{17} & \frac{648}{17} & -\frac{98}{17} & 0 & 0 & 0 & 0 \\
0 & 1 & 0 & \frac{130}{17} & -\frac{208}{17} & \frac{111}{17} & -\frac{16}{17} & 0 & 0 & 0 & 0 \\
0 & 0 & 1 & \frac{40}{17} & -\frac{30}{17} & \frac{8}{17} & -\frac{1}{17} & 0 & 0 & 0 & 0 \\
0 & 0 & 0 & 1 & 0 & 0 & 0 & 0 & 0 & 0 & 0 \\
0 & 0 & 0 & 0 & 1 & 0 & 0 & 0 & 0 & 0 & 0 \\
0 & 0 & 0 & 0 & 0 & 1 & 0 & 0 & 0 & 0 & 0 \\
0 & 0 & 0 & 0 & 0 & 0 & 1 & 0 & 0 & 0 & 0 \\
0 & 0 & 0 & 0 & 0 & 0 & 0 & 1 & 0 & 0 & 0 \\
0 & 0 & 0 & 0 & 0 & 0 & -1 & 0 & 1 & 0 & 0 \\
0 & 0 & 0 & 0 & 0 & -1 & 0 & 0 & 0 & 1 & 0 \\
0 & 0 & 0 & 0 & -1 & 0 & 0 & 0 & 0 & 0 & 1
\end{pmatrix}$$

The basics of the implicit implementation of boundary conditions and FPs can be well understood with this example: multiply this matrix with the corresponding zero-padded vector

$$\boldsymbol{y}_{zp} = \{0, 0, 0, y_0, y_1, y_2, y_3, 0, 0, 0, 0\}$$

and observe the result, $\boldsymbol{y}_{FP}$. Notice that $y_4 = 0$, because the clamped condition requires this value.

The first 3 lines and columns and the last 4 lines and columns (because $y_4 = 0$) of the matrix $\boldsymbol{L}_{FP} = \boldsymbol{A}^{(4)} \cdot \boldsymbol{B}_{FP}$ have to be dropped, in order to get an invertible matrix (i.e. eliminate a division by 0 at the clamped boundary) and to reduce the size of the matrix to the points inside

the beam. Notice that in this case, the final size of the matrix is $Inner - 1$ (unless a line and a column filled with 0 is added at the clamped boundary, subsequently to the matrix inversion).

In the benchmark tests, following values were used for the computations: $Left = Right = 58$, $Inner = 61$ and $K = 25$. The relative error of our algorithm (compared to the maximum deflection of the beam according to the analytical solution) is depicted in Fig. 4, for 2 constructions of the linear operator ($\boldsymbol{A}^{(-4)}$ or $(\boldsymbol{A}^{(4)})^{-1}$), 2 kinds of extensions (SX and PX) and 4 boundary conditions (SS, CS, CC and CF). For $\alpha/\pi \leq 0.1$, $\boldsymbol{A}^{(-4)}$ associated with PX gives the best results (up to 22 correct digits), whereas both linear operators are quasi equivalent for higher values of α and the boundary conditions never significantly affect the precision (with PX). The results for SX are mostly many orders of magnitude less precise, except near $\alpha/\pi = 0.3$. No noticeable differences were found between linear operators for SX. The boundary conditions SS and CS exhibit similar (lack of) precision for all values of α, whereas CC is often about 2 digits more precise.

3.1.2 Parabolic thickness

If the thickness of the beam is parabolic: $H[x] = \kappa_0 + \kappa_1 x/L + \kappa_2 (x/L)^2$, the differential equation can be solved analytically. In this case: $EI[x] = E\ b\ H[x]^3/12$, where E is the Young Modulus and b the width of the beam. We examine only the boundary conditions "clamped" at $x = L$ and "free" at $x = 0$:

$$\begin{aligned}
w[x] &= 3\left(L^3\left(f_1(L-x)\left(f_2 + f_3 x + f_4 x^2\right) - f_5\ f_6\right)\right)/\left(f_7\ E\ b\right) \\
f_1 &= \sqrt{-\kappa_1^2 + 4\kappa_0\kappa_2} \\
f_2 &= \kappa_0\left(\kappa_1\left(6\kappa_0^2 + 9\kappa_0\kappa_1 + 2\kappa_1^2\right) + \kappa_1(10\kappa_0 + \kappa_1)\kappa_2 + 8\kappa_0\kappa_2^2\right) L^2 \\
f_3 &= \left(4\kappa_0^3\kappa_2 + \kappa_1^3(2\kappa_1 + \kappa_2) + \kappa_0^2\left(5\kappa_1^2 + 4\kappa_1\kappa_2 + 4\kappa_2^2\right) + \kappa_0\kappa_1\left(8\kappa_1^2 + 9\kappa_1\kappa_2 + 8\kappa_2^2\right)\right) L \\
f_4 &= \kappa_2\left(\kappa_0^2(6\kappa_1 - 4\kappa_2) + \kappa_1^2(3\kappa_1 + 2\kappa_2) + 2\kappa_0\left(5\kappa_1^2 + 3\kappa_1\kappa_2 + 2\kappa_2^2\right)\right) \\
f_5 &= 4(\kappa_0 + \kappa_1 + \kappa_2)^2\left(3\kappa_0\kappa_1 L + \kappa_1^2 x + 2\kappa_0\kappa_2 x\right)\left(\kappa_0 L^2 + x(\kappa_1 L + \kappa_2 x)\right) \\
f_6 &= \mathrm{ArcTan}\left[\frac{\kappa_1 + 2\kappa_2}{f_1}\right] - \mathrm{ArcTan}\left[\frac{\kappa_1 L + 2\kappa_2 x}{f_1 L}\right] \\
f_7 &= (\kappa_0 + \kappa_1 + \kappa_2)^2 f_1^5\left(\kappa_0 L^2 + x(\kappa_1 L + \kappa_2 x)\right)
\end{aligned} \tag{24}$$

Three different profiles are tested: profile P1: $\kappa_0 = 0.025$, $\kappa_1 = 10^{-9}$ and $\kappa_3 = 0.975$; profile P2: $\kappa_0 = 0.08$, $\kappa_1 = 0.92$ and $\kappa_3 = 10^{-9}$; profile P3: $\kappa_0 = 0.1$, $\kappa_1 = 1.6$ and $\kappa_3 = -0.8$. These profiles are depicted on Fig. 5, left. We examined 3 options for the construction of the linear operator:

$$\begin{aligned}
\boldsymbol{L}_1 &= \boldsymbol{EI}^{(0)} \cdot \boldsymbol{A}^{(4)} + 2\boldsymbol{EI}^{(1)} \cdot \boldsymbol{A}^{(3)} + \boldsymbol{EI}^{(2)} \cdot \boldsymbol{A}^{(2)} \\
\boldsymbol{L}_2 &= \left(\boldsymbol{EI}^{(0)} \cdot \boldsymbol{I} + 2\boldsymbol{EI}^{(1)} \cdot \boldsymbol{A}^{(-1)} + \boldsymbol{EI}^{(2)} \cdot \boldsymbol{A}^{(-2)}\right) \cdot \boldsymbol{A}^{(4)} \\
\boldsymbol{L}_3 &= \left(\boldsymbol{EI}^{(0)} \cdot \boldsymbol{I} + 2\boldsymbol{EI}^{(1)} \cdot \boldsymbol{A}^{(-1)} + \boldsymbol{EI}^{(2)} \cdot \boldsymbol{A}^{(-2)}\right) \cdot \left(\boldsymbol{A}^{(-4)}\right)^{-1}
\end{aligned}$$

In the construction of the linear operators, 3 kinds of difficulties are encountered:

1. The use of FPs requires that a value for the flexural rigidity $EI[x]$ outside the boundaries must be defined. Our function $EI[x]$ is a polynomial of the 6^{th} degree and may vary up to 10 orders of magnitude within the computational domain (extended by the FPs). Moreover the values may be negative, which is physically a nonsense. In order to test the algorithm under rough conditions, we choose one of the worst options: use the function $EI[x]$ as defined above, without any modification.

2. The matrices of the operators $\boldsymbol{L}_2$ and $\boldsymbol{L}_3$ are badly conditioned. In many cases, they cannot be inverted up to the required precision, despite of the use of 40 digits in the computations.

3. For the case $\boldsymbol{L}_2$, the multiplication by $\boldsymbol{A}^{(4)}$ generates very strong ripples near the boundaries of the matrix. Extra FPs (30 points on each side) must be introduced prior to the multiplication. These extra FPs must be eliminated before multiplication by $\boldsymbol{B}_{FP}$.

The relative precision of the algorithm (compared to the maximum deflection of the beam according to the analytical solution) is depicted on Fig. 5, for different sizes of the computational domain ($31 \leq Inner \leq 301$, with $Left = Right = 35$ and PX with $K = 25$). The option $\boldsymbol{L}_1$ is reliable for all tested values of $Inner$ and the computations are less time consuming than for the other options. As expected, the general accuracy is many orders of magnitude smaller than for the beam with uniform thickness. The option $\boldsymbol{L}_2$ gives very coarse results if $Inner < 100$ (not depicted); this option is always less precise than $\boldsymbol{L}_1$. The option $\boldsymbol{L}_3$ is slightly more precise for the profiles P2 and P3, but the matrix could not be inverted with a satisfactory accuracy for $Inner > 101$.

3.2 Free vibrations of beams

Considering the dynamic problem of the free vibrations of a beam of uniform section, an inertial term must be added to the beam equation. This is achieved by equating the source term according to Newton's 2nd law:

$$f = -\rho S \frac{\partial^2 w}{\partial t^2} \tag{25}$$

where ρ is the density of the material, t is the time and S is the area of the cross section. Assuming that the solution has the form: $\mathrm{Cos}[\omega t]\ w[kx]$, Equations (19 and 25) can be rewritten as:

$$EI\ \mathrm{Cos}[\omega t] \frac{\partial^4}{\partial x^4} w[kx] = \omega^2 \rho S\ \mathrm{Cos}[\omega t]\ w[kx]$$

or, with $\omega^2 = \frac{k^4 EI}{\rho S}$:

$$\frac{\partial^4}{\partial x^4} w[kx] = k^4 w[kx] \tag{26}$$

The general solution is found to be:

$$w[kx] = \beta_1 \mathrm{Cosh}[kx] + \beta_2 \mathrm{Sinh}[kx] + \beta_3 \mathrm{Cos}[kx] + \beta_4 \mathrm{Sin}[kx] \tag{27}$$

The β_n coefficients of a particular solution can be deduced from the boundary conditions. The angular eigenfrequencies ω can be numerically computed from an analytical formula: see Table 1.

This problem can also be solved numerically with the EDSC method, since the solutions (and their derivatives) are bandlimited, as recognized from the analytic solutions. Equation (26) can be written in discrete form as an eigenvalue problem, using Equation (18):

$$\boldsymbol{L}_B \cdot \boldsymbol{w} = k^4 \boldsymbol{w} \tag{28}$$

The unknown function $w[kx]$ is identified as $\boldsymbol{y}_c$, the source term $k^4 w[kx]$ as $\boldsymbol{f}$ and the differential operator $\frac{\partial^4}{\partial x^4}$ as $\boldsymbol{L}_B$, in which the boundary conditions are implemented implicitely according to Equation (18). The eigenvalues v_n of matrix $\boldsymbol{L}_B$ are determined with an eigenvalue solver and compared to the corresponding analytical values, denoted k_n.

Boundary conditions	Eigenfrequencies depend from:
SS	$\sin kL = 0$
CF	$\cos kL \cosh kL = -1$
CC and FF	$\cos kL \cosh kL = 1$
CS and SF	$\tan kL = \tanh kL$

Table 1: The angular eigenfrequencies $\omega = k^2\sqrt{\frac{EI}{\rho S}}$ are solution of the equations above, for a thin, freely vibrating beam of uniform thickness, constituted from an homogeneous elastic material. L is the length of the beam.

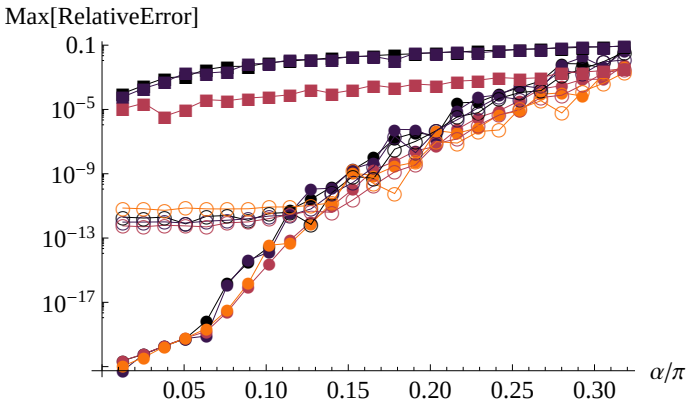

Figure 4: Maximum relative error in the deflection of a beam with uniform thickness under sinusoidal load: $f = \sin[\alpha x + \beta]$, computed according to Equation (18), 58 FPs on each side, $Inner = 61$, $N = 15$, $\sigma = 3\pi$ and $\beta = 1$. The parameter α varies from $1/25$ to 1. Dividing α by π normalizes the load relative to the Nyquist frequency of the sampled load (2 samples per period). Filled circles: computation with $\boldsymbol{A}^{(-4)}$ and polynomial extension ($K = 25$); Empty circles: computation with $(\boldsymbol{A}^{(4)})^{-1}$ and polynomial extension ($K = 25$). Filled squares: computation with $\boldsymbol{A}^{(-4)}$ and simple extension (the computation with $(\boldsymbol{A}^{(4)})^{-1}$ gives approximately the same result). From dark to light: boundary conditions SS, SC, CC and CF. The condition CF cannot be realized with the simple extension.

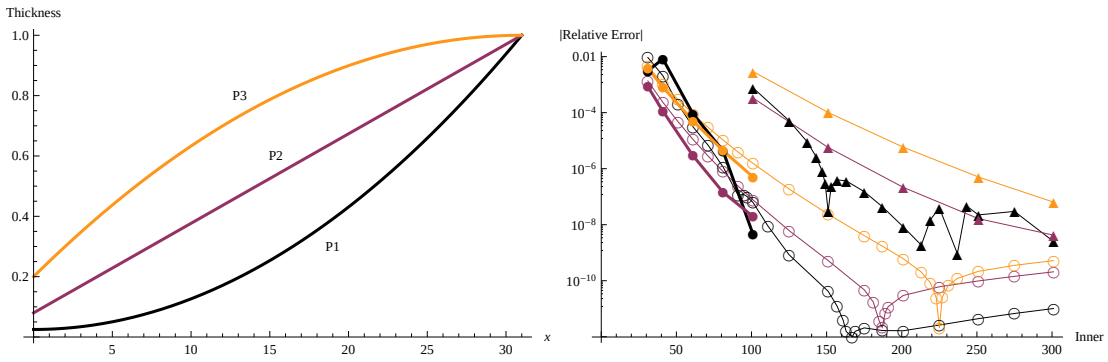

Figure 5: **Left**: parabolic profiles P1, P2 and P3, defining the thickness of the beam (here with $Inner = 31$). **Right**: Maximum relative error of the deflection, for different sizes of the computational domain ($31 \leq Inner \leq 301$), for each parabolic profile (from dark to light: P1, P2, P3), under uniform load, for the clamped/free condition, computed according to Equation (18), with 35 FPs on each side, $\sigma = 3\pi$, $N = 30$, PX with $K = 25$. Empty circles: computation with $\boldsymbol{L}_1$. Filled triangles: computation with $\boldsymbol{L}_2$. Filled circles and thick lines: computation with $\boldsymbol{L}_3$.

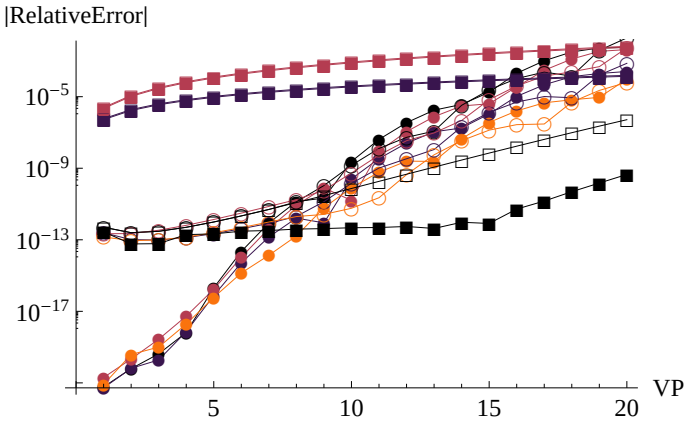

Figure 6: Relative error in the first 20 eigenvalues (EV) of the matrix $\boldsymbol{L}_B$ in Equation (28), with 58 FPs on each side, $Inner = 61$, $N = 15$ and $\sigma = 3\pi$. Same linear operators, boundary conditions and symbols as in Fig. 4

.

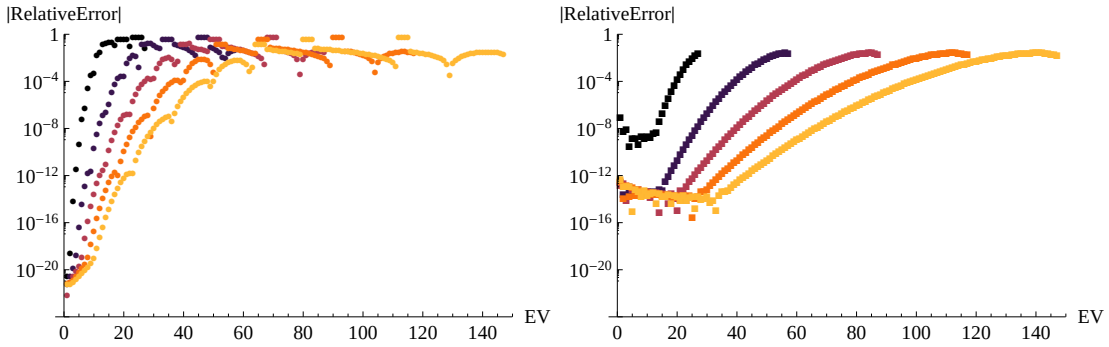

Figure 7: Influence of the size of the computational domain on the relative precision of the eigenvalues (EV), computed according to Equation (28), with 58 FPs on each side, $N = 15$, $\sigma = 3\pi$ and SS boundary condition. From dark to light: $Inner = 31, 61, 91, 121, 151$. **Left**: computation with $\boldsymbol{A}^{(-4)}$ and polynomial extension ($K = 25$). **Right**: computation with $\boldsymbol{A}^{(-4)}$ and simple extension.

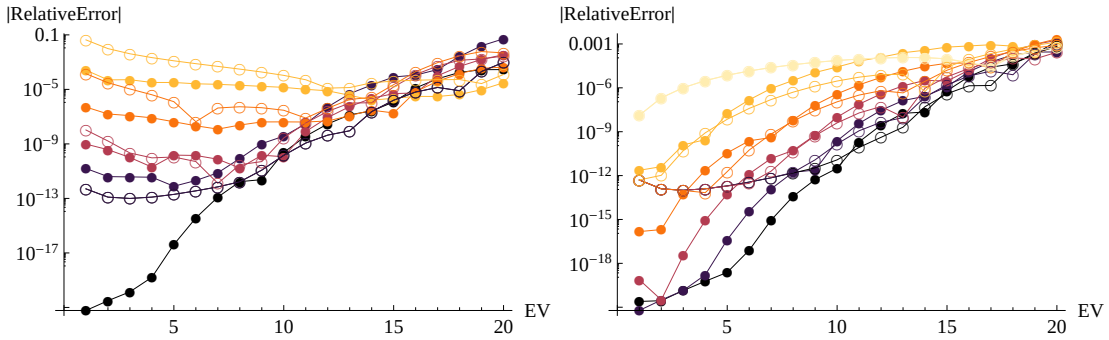

Figure 8: **Left**: Influence of the number of FPs on the relative error in the first 20 eigenvalues (EV), with $Inner = 61$, $N = 15$, $\sigma = 3\pi$ and SS boundary condition. From dark to light: $Left = Right = 58, 25, 17, 10, 5$. Filled circles: computation with $\boldsymbol{A}^{(-4)}$ and polynomial extension ($K = 25$); Empty circles: computation with $(\boldsymbol{A}^{(4)})^{-1}$ and polynomial extension ($K = 25$). **Right**: Influence of the degree of the polynomial used for the PX, on the relative error in the first 20 eigenvalues, with $Inner = 61$, $N = 15$, $\sigma = 3\pi$ and SS boundary condition. From dark to light: $K = 30, 25, 20, 15, 10, 5$. Filled circles: computation with $\boldsymbol{A}^{(-4)}$; Empty circles: computation with $(\boldsymbol{A}^{(4)})^{-1}$.

The relative precision of the algorithm (i.e. $v_n^{1/4}/k_n - 1$) is depicted in Fig. 6, for 2 constructions of the linear operator ($\boldsymbol{A}^{(-4)}$ or $(\boldsymbol{A}^{(4)})^{-1}$), 2 kinds of extensions (SX and PX) and 4 boundary conditions (SS, CS, CC and CF). The discrete linear operators are therefore exactly the same as in § 3.1.1. The similarity with Fig. 4 is striking for the PX. The results differ somehow for the SX, especially for the condition SS. The good result for SS has an explanation: the SX imposes a characteristic of the analytical solution: the function is odd, relatively to each boundary. Notice the positive influence of the operator $\boldsymbol{A}^{(-4)}$ for this case, whereas it has almost no influence for the CS and CC conditions (with SX).

The influence of the size of the computational domain is studied on Fig. 7, for the SS condition and the operator $\boldsymbol{A}^{(-4)}$. The polynomial extension confirms its extreme accuracy for the first eigenvalues, whatever the size of the computational domain (at least for $31 \leq Inner \leq 151$). The increase of precision for the first ($Inner/2$) eigenvalues is approximately proportional to $Inner$, in the studied domain. The simple extension confirm also the good results obtained for this special case (the analytical solution is an odd function), also for quite high eigenvalues (not depicted on Fig. 6).

The influence of 2 other parameters (number of fictitious points and degree of the polynomial for the PX) are illustrated on Fig. 8. In the studied range, increasing the number of FPs or increasing the degree of the polynomial enhances favorably the accuracy of the computations. Most of the time the computations with the operator $\boldsymbol{A}^{(-4)}$ are more precise than with the operator $(\boldsymbol{A}^{(4)})^{-1}$. This is particularly striking for the first 8 eigenvalues, $Left = Right = 58$ and $K = 30$. As expected, the computations based on antiderivatives are more precise than the computations based on derivatives, when the number of FPs is small (as a result of the sensitivity to the phenomenon of ripple). The fact that the computations were conducted with 40 significant digits must be emphasized. With a standard machine precision (15 digits), the advantages of the antiderivatives become less obvious. If possible, the operator $\boldsymbol{L}_B$ should be constructed with high precision computations, especially if the FPs are numerous and if high values of K are used. Otherwise, the substraction of the integration polynomial can degrade notably the final numerical precision of the operator. Afterwards, the operator can be rounded down to standard machine precision, for further use.

4 Conclusions

The proposed improvements of the DSC method could be positively evaluated. The new RSK_N kernel exhibits an accuracy comparable to that of the RSK kernel (standard DSC method). The analytical integrability of the proposed kernel opens new fields of application, including any kind of linear transformations. This offers a new flexibility in the construction of discrete operators. In particular, the proposed kernel allows the construction of integration operators with an arbitrary precision. This avoids a numerical inversion of the operator in some cases. The structured description of the implementation of fictitious points facilitates the use of the DSC method. Moreover the proposed formulation of the polynomial extension has proved its flexibility and its reliability in all performed benchmark tests. The benchmark results published by Wei [8] and Zhao et al. [4] show approximately the same precision than our results with the derivatives of the RSK_N kernel. In the low frequency range, the computations based on the antiderivatives of the RSK_N kernel can be up to 8 digits more precise than those based on derivatives. The EDSC appears therefore as a reliable numerical method for integrating, differentiating and interpolating a band limited function defined as a truncated series of discrete points, and for solving numerically differential equations.

5 Acknowledgments

This work was supported by the French National Agency ANR within the SDNS-AIMV project. We thank also the high school ARC-Engineering in Neuchâtel. Finally we wish to thank Martin Pring for linguistic corrections to the manuscript.

APPENDICES

A Analytic expressions for $\mathbf{RSK}_N$

A.1 Analytic proofs

Proposition:

$$2\ \mathrm{Sin}\left[x/(2\mathrm{N})\right]\sum_{n=1}^{\mathrm{N}} e^{-ix(n-1/2)/\mathrm{N}} = \mathrm{Sin}[x] + i(\mathrm{Cos}[x]-1) \tag{29}$$

We assume that: $x \in \mathbb{R},\ \mathrm{N}, n \in \mathbb{N}^*$

Proof. The equation above is a geometric series of the form:

$$b\sum_{n=N_1}^{N_2} e^{an} = b\frac{e^{a(N_2+1)} - e^{aN_1}}{e^a - 1} = b\frac{e^{a(N_2+1/2)} - e^{a(N_1-1/2)}}{e^{a/2} - e^{-a/2}} \tag{30}$$

with $a = -ix/\mathrm{N}$, $b = 2\ \mathrm{Sin}\left[x/(2\mathrm{N})\right] = i(e^{a/2} - e^{-a/2})$, $N_1 = 1/2$ and $N_2 = \mathrm{N} - 1/2$. This equation can therefore be simplified as:

$$i\left(e^{-ix} - 1\right) = \mathrm{Sin}[x] + i(\mathrm{Cos}[x]-1) = \mathrm{Sin}[x] - 2\ i\ \mathrm{Sin}\left[\frac{x}{2}\right]^2 \tag{31}$$

□

Corollary:
According to our assumptions, $x(n-1/2)/\mathrm{N}$ is real. This implies that:

$$2\ \mathrm{Sin}\left[x/(2\mathrm{N})\right]\sum_{n=1}^{\mathrm{N}} \mathrm{Cos}\left[x(n-1/2)/\mathrm{N}\right] = \mathrm{Sin}[x] \tag{32}$$

$$\mathrm{Sin}\left[x/(2\mathrm{N})\right]\sum_{n=1}^{2\mathrm{N}} \mathrm{Sin}\left[x(n-1/2)/\mathrm{N}\right] = \mathrm{Sin}[x]^2 \tag{33}$$

Dividing both sides of these equations respectively by

$$\begin{gathered} xSinc\left[x/(2\mathrm{N})\right] \\ x^2 Sinc\left[x/(2\mathrm{N})\right] \end{gathered} \tag{34}$$

we get finally:

$$\begin{aligned} \frac{1}{\mathrm{N}}\sum_{n=1}^{\mathrm{N}} \mathrm{Cos}\left[x(n-1/2)/\mathrm{N}\right] &= \frac{\mathrm{Sinc}[x]}{\mathrm{Sinc}\left[x/(2\mathrm{N})\right]} \\ \frac{1}{2x\ \mathrm{N}}\sum_{n=1}^{2\mathrm{N}} \mathrm{Sin}\left[x(n-1/2)/\mathrm{N}\right] &= \frac{\mathrm{Sinc}[x]^2}{\mathrm{Sinc}\left[x/(2\mathrm{N})\right]} \end{aligned} \tag{35}$$

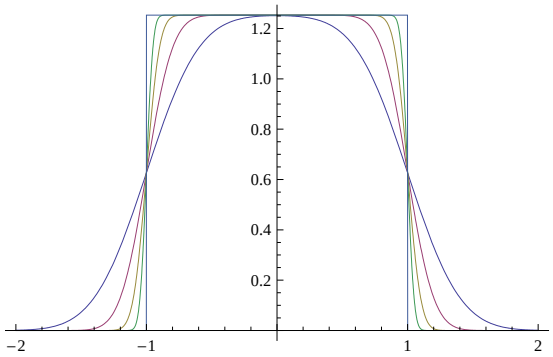

Figure 9: Fourier Transform of RSK_N Equation(37), for $\sigma \in \{\pi, 2\pi, 4\pi, 8\pi, \infty\}$ and $N = 50$. The last case corresponds to the Fourier Transform of the function Sinc.

Notice that $\lim_{\mathrm{N}\to\infty} \mathrm{Sinc}\,[x/(2\mathrm{N})] = 1$. We could not find these series developments for the Sinc and the Sinc^2 functions in the literature.

Equation (35) implies that:

$$\frac{\mathrm{Sinc}[x]\ \mathrm{Exp}\left[-\frac{x^2}{2\sigma^2}\right]}{\mathrm{Sinc}\,[x/(2\mathrm{N})]} = \frac{\mathrm{RSK}[x]}{\mathrm{Sinc}\,[x/(2\mathrm{N})]} = \frac{1}{\mathrm{N}} \sum_{n=\frac{1}{2}}^{\mathrm{N}-\frac{1}{2}} \Re\left[\mathrm{Exp}\left[\frac{inx}{\mathrm{N}} - \frac{x^2}{2\sigma^2}\right]\right] \tag{36}$$

The similarity between our formula

$$\sum_{n=-\mathrm{N}+\frac{1}{2}}^{\mathrm{N}-\frac{1}{2}} e^{inx} = 2\ \sum_{n=1}^{\mathrm{N}} \mathrm{Cos}\,[x(n-1/2)] = \frac{\mathrm{Sin}[\mathrm{N}x]}{\mathrm{Sin}[x/2]}$$

and the Dirichlet kernel

$$\sum_{n=-\mathrm{N}}^{\mathrm{N}} e^{inx} = 1 + 2\sum_{n=1}^{\mathrm{N}} \mathrm{Cos}[nx] = \frac{\mathrm{Sin}[(\mathrm{N}+1/2)x]}{\mathrm{Sin}[x/2]}$$

should be emphasized. Both formulas exploit the fact that:
$\mathrm{Cos}[x] + \mathrm{Cos}[-x] = 2\mathrm{Cos}[x]$ and $\mathrm{Sin}[x] + \mathrm{Sin}[-x] = 0$.

A.2 Fourier Transform

We refer to the following definition of the Fourier Transform:

$$\widetilde{f}[\omega] = \frac{1}{\sqrt{2\pi}} \int_{-\infty}^{\infty} f[t] e^{-i\omega t} dt$$

The Fourier transform of $\mathrm{Sinc}[t]$ is a rectangular function: $\frac{1}{2}\sqrt{\frac{\pi}{2}}(\mathrm{Sign}[1-\omega] + \mathrm{Sign}[1+\omega])$. The Fourier transform of RSK_N (see Fig. 9) can be evaluated analytically using Equation (8):

$$\widetilde{\mathrm{RSK}}_N[\omega] = \frac{\sigma}{2\mathrm{N}} \sum_{n=-\mathrm{N}+\frac{1}{2}}^{\mathrm{N}-\frac{1}{2}} \mathrm{Exp}\left[-\frac{\sigma^2}{2}\left(\frac{n}{\mathrm{N}} + \omega\right)^2\right] \tag{37}$$

The Fourier Transform of Equation (5) is then:

$$\widetilde{y}^{(d)}[\omega] = \frac{(i\omega)^d}{\pi}\widetilde{\mathrm{RSK}}_N[\frac{\omega}{\pi}] \sum_{m=-M}^{M} y_m \cdot e^{-im\omega} \tag{38}$$

It is the Centered Discrete Fourier Transform of the sampled data $\boldsymbol{y}$ multiplied by the Fourier Transform of the d^{th} derivative of $\mathrm{RSK}_N[\pi x]$.

A.3 Antiderivatives

The antiderivatives of Equation (8) can be written as:

$$\mathrm{RSK}_N^{(d)}[x] = \frac{1}{\mathrm{N}} \sum_{n=1}^{\mathrm{N}} \Re\left[D^{(d)}[x]\right] \tag{39}$$

with $D[x] = \mathrm{Exp}\left[-ibx - \frac{x^2}{2\sigma^2}\right]$ and b=(n-1/2)/N.

The first 4 antiderivatives of D are:

antiderivative 1

$$D^{(-1)}[x] = \sqrt{\frac{\pi}{2}}\sigma \ \mathrm{Exp}\left[-\frac{1}{2}b^2\sigma^2\right] \mathrm{Erf}\left[\frac{x+ib\sigma^2}{\sqrt{2}\sigma}\right]] \tag{40}$$

antiderivative 2

$$D^{(-2)}[x] = D^{(-1)}[x]\, g^{(2)}[x] + \sigma^2 D[x] \tag{41}$$

antiderivative 3

$$D^{(-3)}[x] = D^{(-1)}[x]\, g^{(1)}[x] + \frac{1}{2}\sigma^2 g^{(2)}[x] D[x] \tag{42}$$

antiderivative 4

$$D^{(-4)}[x] = D^{(-1)}[x]\, g[x] + \frac{1}{6}\left(\sigma^4 + 2\sigma^2 g^{(1)}[x]\right) D[x] \tag{43}$$

with

$$\begin{aligned} g[x] &= \frac{1}{6}\left(x+ib\sigma^2\right)\left(3\sigma^2 + \left(x+ib\sigma^2\right)^2\right) \\ g^{(1)}[x] &= \frac{1}{2}\left(\sigma^2 + \left(x+ib\sigma^2\right)^2\right) \\ g^{(2)}[x] &= x + ib\sigma^2 \end{aligned} \tag{44}$$

A.4 Derivatives

The derivatives of RSK_N, Equation (8) are:
derivative 1

$$\begin{aligned} \mathrm{RSK}_N^{(1)}[x] = \frac{k_1 k_2}{4\sigma^2 \mathrm{N}^2}\left(2\mathrm{N}\sigma^2 \mathrm{Cos}[x] - \left(2\mathrm{N}x + \sigma^2 k_3\right)\mathrm{Sin}[x]\right) \\ k_1 = e^{-\frac{x^2}{2\sigma^2}} \\ k_2 = \frac{1}{\mathrm{Sin}\left[x/(2\mathrm{N})\right]} \\ k_3 = \frac{1}{\mathrm{Tan}\left[x/(2\mathrm{N})\right]} \end{aligned} \tag{45}$$

derivative 2

$$\begin{aligned}
\mathrm{RSK}_N^{(2)}[x] &= \frac{k_1 k_2}{8\sigma^4 \mathrm{N}^3}\left(a_1 \mathrm{Cos}[x] + a_2 \mathrm{Sin}[x]\right) \\
a_1 &= -4\mathrm{N}\sigma^2\left(2\mathrm{N}x + 9\pi^2 k_3\right) \\
a_2 &= 81\left(-1 + 2k_1^2\right)\pi^4 + 4\mathrm{N}^2\left(-9\left(\pi^2 + 9\pi^4\right) + x^2\right) + 36\mathrm{N}\pi^2 x k_3
\end{aligned} \tag{46}$$

derivative 3

$$\begin{aligned}
\mathrm{RSK}_N^{(3)}[x] &= \frac{k_1 k_2}{16\sigma^6 \mathrm{N}^4}(b_1 \mathrm{Cos}[x] + (b_2 + b_3)\ \mathrm{Sin}[x]) \\
b_1 &= -6\mathrm{N}\left(81\left(1 - 2k_2^2\right)\pi^4 - 36k_3\mathrm{N}\pi^2 x + 4\mathrm{N}^2\left(9\pi^2 + 27\pi^4 - x^2\right)\right)\sigma^2 \\
b_2 &= 2\mathrm{N}x\left(243\left(1 - 2k_2^2\right)\pi^4 + 4\mathrm{N}^2\left(27\left(\pi^2 + 9\pi^4\right) - x^2\right)\right) \\
b_3 &= -27k_3\pi^2\left(27\left(-1 + 6k_2^2\right)\pi^4 + 4\mathrm{N}^2\left(-9\left(\pi^2 + 9\pi^4\right) + x^2\right)\right)
\end{aligned} \tag{47}$$

derivative 4

$$\begin{aligned}
\mathrm{RSK}_N^{(4)}[x] &= \frac{k_1 k_2}{32\sigma^8 \mathrm{N}^5}\left(8\mathrm{N}\ \sigma^2(c_1 + c_2)\ \mathrm{Cos}[x] + (c_3 + c_4 + c_5)\mathrm{Sin}[x]\right) \\
c_1 &= 2\mathrm{N}x\left(243\left(1 - 2k_2^2\right)\pi^4 + 4\mathrm{N}^2\left(27\pi^2 + 81\pi^4 - x^2\right)\right) \\
c_2 &= -27k_3\pi^2\left(27\left(-1 + 6k_2^2\right)\pi^4 + 4\mathrm{N}^2\left(-9\left(\pi^2 + 3\pi^4\right) + x^2\right)\right) \\
c_3 &= 6561\pi^8 + 16\mathrm{N}^4\left(243\left(\pi^4 + 18\pi^6 + 27\pi^8\right) - 54\pi^2\left(1 + 9\pi^2\right)x^2 + x^4\right) \\
c_4 &= 8k_3\mathrm{N}x\left(81\left(-1 + 6k_2^2\right)\pi^4 + 4\mathrm{N}^2\left(-27\left(\pi^2 + 9\pi^4\right) + x^2\right)\right)\sigma^2 \\
c_5 &= 54k_2^2\pi^2\sigma^2\left(54\left(-5 + 6k_2^2\right)\pi^4 - 2\mathrm{N}^2\left(9\pi^2 + 81\pi^4 - x^2\right)\left(3 + \mathrm{Cos}\left[\frac{x}{\mathrm{N}}\right]\right)\right)
\end{aligned} \tag{48}$$

At $x = 0$ these derivatives have to be evaluated to their limit values, respectively as:

$$\begin{aligned}
\mathrm{RSK}_N^{(1)}[0] &= 0 \\
\mathrm{RSK}_N^{(2)}[0] &= -\frac{1}{3} - \frac{1}{\sigma^2} + \frac{1}{12\mathrm{N}^2} \\
\mathrm{RSK}_N^{(3)}[0] &= 0 \\
\mathrm{RSK}_N^{(4)}[0] &= \frac{1}{5} + \frac{3}{\sigma^4} + \frac{2}{\sigma^2} - \frac{3 + \sigma^2}{6\mathrm{N}^2\sigma^2} + \frac{7}{240\mathrm{N}^4}
\end{aligned} \tag{49}$$

A.5 Fractional derivatives and antiderivatives

Taking the inverse Fourier transform of the derivative of the kernel in Equation (38) leads an analytical expression for the fractional derivatives and antiderivatives of the kernel:

$$\mathrm{RSK}^{(d)}[t] = \frac{2^{\frac{d-2}{2}}\pi^{d-\frac{5}{2}}\sigma^{2-d}}{9N}\left(\cos\left(\frac{\pi d}{2}\right)u[t,0] + d\sin\left(\frac{\pi d}{2}\right)u[t,1]\right) \tag{50}$$

with

$$u[t,s] = \Gamma\left(\frac{d+1-s}{2}\right) \sum_{n=\frac{1}{2}-N}^{N-\frac{1}{2}} e^{-\frac{n^2\sigma^2}{2N^2}} \nu[t]^s \, {}_1F_1\left[\frac{1}{2}(d+s+1); s+\frac{1}{2}; -\nu[t]^2\right]$$

$$\nu[t] = \frac{-Nt - in\sigma^2}{\sqrt{2}N\sigma} \quad ; \quad \Gamma[t] = \int_0^\infty x^{t-1}e^{-x}\,dx$$

$${}_1F_1[a;b;z] = \sum_{k=0}^{\infty} \frac{a_k z^k}{b_k k!} \quad ; \quad a_0 = 1 \quad ; \quad a_k = a(a+1)(a+2)...(a+k-1)$$

This formula is valid for all reals d, except zero and negative integers, for which the Γ function tends to infinity. In this case, the limit leads to Equation (39). The computing time for one discrete point is about 0.09 seconds (machine precision), or about 0.2 seconds with 40 significant digits.

As a conclusion of this section, the new RSK_N kernel allows to express analytically with Equation (5) any integer or fractional (anti-)derivative of any bandlimited function, up to any arbitrary precision.

B Implementation of fictitious points

The matrix $\boldsymbol{B}_{FP}$ from § 2.3 is structured with $Left$ FPs on the left of the left boundary, $Inner$ inner points including both boundaries and $Right$ FPs on the right of the right boundary:

$$\boldsymbol{B}_{FP} = \begin{pmatrix} \boldsymbol{I}_{Left} & \boldsymbol{G} & \boldsymbol{0} \\ \boldsymbol{0} & \boldsymbol{I}_{Inner} & \boldsymbol{0} \\ \boldsymbol{0} & \boldsymbol{D} & \boldsymbol{I}_{Right} \end{pmatrix} \tag{51}$$

where $\boldsymbol{I}_{Left}$, $\boldsymbol{I}_{Inner}$ and $\boldsymbol{I}_{Right}$ are identity matrices of rank $Left$, $Inner$, and $Right$.

In the following subsections, only the content of the rectangular ($Left \times Inner$) matrix $\boldsymbol{G}$ will be described. Matrix $\boldsymbol{D}$ is built exactly in the same way, but the order of the lines and columns has to be reversed afterward. In other words, if a matrix $\boldsymbol{D'}$ is computed with the procedure described for $\boldsymbol{G}$, the components of matrix $\boldsymbol{D}$ are $D_{n,m} = D'_{Right+1-n,Inner+1-m}$.

By default, $G_{n,m} = 0$, if not otherwise specified.

B.1 simple extension (SX)

An even, bandlimited function has the properties $f(x) = f(-x)$ and $f'(0) = 0$. This case applies for the clamped condition at $x = 0$ and matrix $\boldsymbol{G}$ is written: $G_{n,Left+2-n} = 1$. An odd, bandlimited function has the properties $-f(x) = f(-x)$ and $f''(0) = 0$. This case applies for the simply supported condition and matrix $\boldsymbol{G}$ is written: $G_{n,Left+2-n} = -1$. The SX did not apply for the free condition. For details, see Wei et al. [14].

Remark: The SX imposes some additional (probably unwanted) conditions on the derivatives, because an even, bandlimited function has also the property that all derivatives of odd order vanish at $x = 0$ (respectively all derivatives of even order, for an odd, bandlimited function).

Appendix F

Numerical Computation of the Transfer Functions of an Axisymmetric Duct with the Extended Discrete Singular Convolution Method

Résumé

Ce travail [149] s'inscrit dans le cadre du projet "CAGIMA" (soutenu par l'agence de recherche française ANR) qui étudie la justesse des instruments de musique à anche ainsi que leur homogénéité d'émission et de timbre. L'objectif consiste à remplacer l'approche incrémentielle traditionnellement adoptée par les facteurs d'instruments par une approche globale et rationnelle dans la conception de nouveaux instruments *ab initio* (appelés «instruments logiques»), en minimisant certains défauts identifiés. Dans ce contexte, un modèle virtuel interactif, prédictif et configurable est proposé. Plusieurs approches sont décrites dans la littérature pour simuler ce type de modèle, mais la difficulté principale consiste à concevoir des instruments numériques à la fois précis (selon les calculs analytiques ou les mesures) et pouvant être simulés en temps réel. Dans cet article, une approche basée sur la méthode Extended Discrete Singular Convolution (EDSC) est proposée. L'opérateur temporel (incluant un terme avec dérivée fractionnaire pour les pertes viscothermiques) est implémenté selon le formalisme EDSC. La méthode permet un calcul rapide, direct et précis des fonctions de transfert d'un conduit axisymétrique ayant un profil arbitraire. Le calcul du cas où les pertes dépendent du diamètre ne provoque aucune difficulté notable. Les résultats sont comparés aux mesures de l'impédance d'entrée d'un pavillon de trombone.

Numerical Computation of the Transfer Functions of an Axisymmetric Duct with the Extended Discrete Singular Convolution Method

P.-A. Taillard, T. Hélie and J. Bensoam
IRCAM, 1, place Igor-Stravinsky, 75004 Paris, France
taillard@hispeed.ch

This work takes part of the "cagima" project (supported by the ANR) which investigates the defects of the tuning of reed musical instruments as well as their homogeneity of emission and timbre. The goal consists in replacing the traditional approach adopted by instrument makers by a global and rational approach in the design of new instruments /ab initio/ (called "logical instruments"), minimizing some identified defects. In this context, an interactive virtual model, predictive and configurable is proposed. Several approaches are available in the literature but the main difficulty is to design digital instruments that are accurate (according to measurements) and that can be implemented in real-time. In this paper, an approach based on the Extended Discrete Singular Convolution method (EDSC) is proposed. The temporal operator (including the fractional derivative term for viscothermal losses) is implemented according to the EDSC formalism. The method allows a fast, straightforward and accurate computation of the transfer functions of an axisymmetric duct with an arbitrary profile. The computation of the case where the losses are dependent from the diameter causes no noticeable difficulty. The results are compared to measurements of a trombone bell.

1 Introduction

This work takes part of the "Cagima" project (supported by the French national research agency ANR) which investigates the defects of the tuning of reed musical instruments as well as their homogeneity of emission and timbre. The goal consists in replacing the traditional approach adopted by instrument makers by a global and rational approach in the design of new instruments *ab initio* (called "logical instruments"), minimizing some identified defects. In this context, an interactive virtual model, predictive and configurable has to be developed. Several approaches are available in the literature but the main difficulty is to design digital instruments that are accurate (according to measurements) and that can be implemented in real-time.

The present paper investigates how the Extended Discrete Singular Convolution (EDSC) method [1] can be used for the acoustical simulation of the bore of wind instruments. This method is an extension of the original DSC method proposed by Wei et al. [2], which has proved its efficiency and accuracy for solving differential equations. Technically, this method is based on a "well-suited" family of time-continuous interpolation kernels (delta sequence kernels), which provide the continuous signal from its sampled version. Here, this is used to simulate a 1D model of acoustic propagation in axisymmetric lossy pipes, established in [3] and validated in [4] for straight, conical and flared pipes: the Webster-Lokshin model with curvilinear abscissa (named WL model in the sequel). In this context, the main interest of EDSC (besides accuracy and parsimony) is that the fractional derivative of a signal (operator involved in the model) is derived from the interpolation formula by using the fractional derivative of the kernel, that makes the computation easy. With this method, simulations are performed in the time domain, from which the acoustic transfer functions are deduced in the spectral domain.

This paper is organized as follow: in section 2, the principles of the EDSC method are presented. The section 3 is devoted to the application of this method to the Webster-Lokshin equation. In section 4, a method is given for obtaining numerically the transfer functions from the EDSC simulations. Section 5 is dedicated to the validation of the results with some known analytical results and with measurements of a trombone bell, followed by the conclusions, Section 6.

2 Kernel methods and EDSC

Ideal bandlimited signals $y \in L^2(\mathbb{R})$ (finite energy) with a frequency range included in $[-1/2, 1/2]$ are known to be such that

$$y(t) = \sum_{m\in\mathbb{Z}} y(m)\,\mathrm{sinc}\left(\pi(t-m)\right), \tag{1}$$

where $\mathrm{sinc}(x) = \sin(x)/x$ is the Shannon-Whittaker interpolation kernel [5, 6]. The sampling period is therefore $\Delta t = 1$. This kernel is non causal and with infinite support.

The DSC method has been built in a practical way, so that: (i) an interpolation formula similar to (1) is fulfilled; (ii) the band-limited property is numerically satisfied up to a fixed precision (typically, that of floats); (iii) the kernel magnitude is larger than the fixed precision, on a bounded centered support ($-M \leq t \leq M$). Such approximations can be recasted in the general framework of Reproducing Kernel Hilbert Spaces [7, cf. p.433] [8], which is not investigated here. The generic formula for the continuous interpolation $\tilde{y}(t)$ of a bandlimited function $y(t)$, its derivatives of order $d > 0$ and its antiderivatives ($d < 0$) is

$$\tilde{y}^{(d)}(t) = \sum_{m=-M}^{M} y(m)\cdot k^{(d)}\left(t-m\right). \tag{2}$$

Different functions can implement the kernel $k(t)$. If $k(t) = \mathrm{sinc}(\pi x)$, $d = 0$ and $M \to \infty$, Eq (1) is retrieved. The kernel has to satisfy (at least up to a fixed precision)

$$\lim_{\alpha\to\infty} \alpha\, k(\alpha t) = \delta(t) \tag{3}$$

where $\delta(t)$ is the Dirac delta distribution. In [2], many kernels are proposed. Among them, an interesting family of symmetrical kernels, efficiently focusing the energy close to $t = 0$, allowing a control of the bandlimited approximation, is defined by the following Regularized Shannon Kernels (labeled RSK in the sequel), for $\sigma > 0$,

$$\mathrm{RSK}(x) = \mathrm{Sinc}(x)\ \mathrm{Exp}(-\frac{x^2}{2\sigma^2}) \tag{4}$$

Note that with $k(t) = \mathrm{RSK}(\pi t)$, $\tilde{y}$ and y coincide at each sample $t = m$ and that, tuning σ and M, their

difference can be made as small as wanted. For a relative level of numerical precision η, the length of the effective numerical kernel support is defined as follows: if $|t| > \ell_k$ then $k(t) < \eta$. Typical value for double precision[1] reals, $\eta \simeq 10^{-15}$, gives rise to $\sigma = 3\pi$ and $\ell_k \simeq 23$.

Because a general expression for $k^{(d)}$ is difficult to find with the RSK kernel, we propose to use another kernel [1]

$$\mathrm{RSK}_N(x) = \frac{1}{2\mathrm{N}} \sum_{n=-\mathrm{N}+\frac{1}{2}}^{\mathrm{N}-\frac{1}{2}} \mathrm{Exp}\left(\frac{inx}{\mathrm{N}} - \frac{x^2}{2\sigma^2}\right) = \frac{\mathrm{RSK}(x)}{\mathrm{sinc}\,(x/(2\mathrm{N}))} \tag{5}$$

with $i = \sqrt{-1}$. Notice that $\mathrm{RSK}_\infty(x) = \mathrm{RSK}(x)$ and, if $k(t) = \mathrm{RSK}_N(\pi t)$, $d = 0$ and $M, N, \sigma \to \infty$, Eq (1) is also retrieved.

This series (5) is rapidly convergent. Moreover it can be shown that a value as small as $N = 15$ builds a kernel which has a numerical accuracy in Eq (2) comparable to that of the RSK kernel (with $\sigma = 3\pi$). In the sequel, the kernel $k(t) = \mathrm{RSK}_N(\pi t)$ with parameters $\sigma = 3\pi$ and $N = 15$ is used, and simply denoted k for sake of conciseness. All numerical examples are computed with this kernel. A general expression for $k^{(d)}$ is given in Appendix A (see also figure 1). For the discrete times

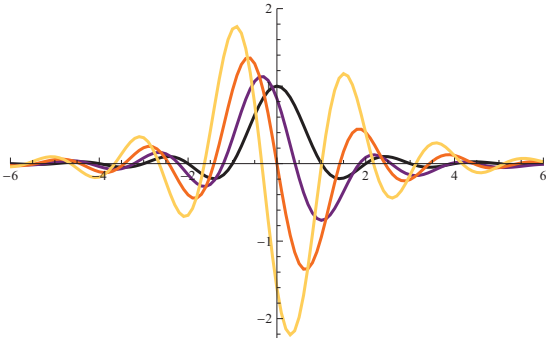

Figure 1: Kernel $k(t) = \mathrm{RSK}_N(\pi t)$ and its derivatives of order $d = \frac{1}{2}$, 1 and $\frac{3}{2}$, according to Eq(13) (from dark to light).

$t = m$, the interpolation formula (2) can be written in vector form as a convolution, $\tilde{\boldsymbol{y}}^{(d)} = \boldsymbol{k}^{(d)} * \boldsymbol{y}$, with $k_j^{(d)} = k(t)^{(d)}|_{t=j}$ and $j = -2M$ to $2M$ by step 1. The vector $\boldsymbol{y}$ has to be padded with M zeros on the left and M zeros on the right, in order to meet the size of the vector $\boldsymbol{k}^{(d)}$. Efficient numerical techniques based on the Fast Fourier Transform can be used to compute this convolution. Doing so, the computing time has approximately linear dependence to M (and not to M^2, as it could be suggested by Eq (2)).

The range $[-M \dots M]$ is called "computing domain". The formula has an optimal accuracy in the "optimal domain" $[-M + \ell_k \dots M - \ell_k]$, whereas in the "truncation domain" $[-M \dots -M + \ell_k,\ M - \ell_k \dots M]$, it may have a poor accuracy, except if $y(m)$ displays small values in this range. This is the main drawback of the method. In the EDSC method, fictitious points are generally implemented in this range [1], in order to perform the most relevant part of the computation in the optimal domain, for instance as

[1]Notice that with $k(t) = \mathrm{sinc}(\pi t)$, a numerical computation up to that precision would be difficult because $\ell_k = 10^{15}$.

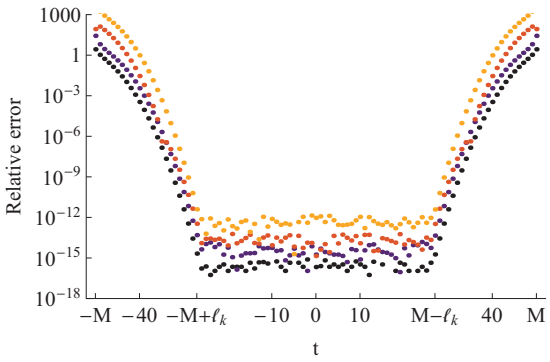

Figure 2: Numerical computation of the derivatives $d = 1, 2, 3, 4$ of a cosine function with Eq (2): Relative error $\left|y^{(d)}(t) - \tilde{y}^{(d)}(t)\right|$, with $y(t) = \cos(t)$ and $M = 50$, comparatively to the exact analytical derivatives $y^{(d)}(t) = \cos(t + d\pi/2)$. From dark to light: derivatives 1 to 4. Length of the effective numerical kernel support: $\ell_k \simeq 23$. The plateau of the "optimal domain" appears clearly.

a polynomial continuation of $y(t)$, which fulfills some boundary conditions, or with the requirement that $y(t)$ is symmetrical or antisymmetrical at the boundaries of the physical problem (located generally at $-M + \ell_k$ and at $M - \ell_k$). These different domains appear clearly in Fig. 2 where the cosine function is chosen as an example (however with $\Delta t = 1/4$, in order to be representative of the accuracy of Eq (2) in the low frequency range).

3 Application to the WL equation

3.1 The Webster-Lokshin equation

The Webster-Lokshin equation (hereafter abreviated WL equation) [4, 9] describes the behavior of the acoustic pressure waves $p(x,t)$ in an 1D axisymmetric duct

$$\left(\partial_x^2 + \frac{2r'(x)}{r(x)}\partial_x\right) p(t,x) = \frac{1}{c^2}\left(\partial_t^2 + 2\epsilon(x)\partial_t^{3/2}\right) p(t,x) \tag{6}$$

and the flow $u(x,t)$, dual quantity to the pressure, is described by the Euler equation

$$-\frac{\rho}{A(x)}\partial_t u(t,x) = \partial_x p(t,x) \tag{7}$$

with parameters $r(x)$: radius of the duct, $A(x) = \pi r^2(x)$: area of the cross section, ρ: density of air, $\epsilon(x) = \kappa_0\sqrt{1 - r'(x)^2}/r(x)$: coefficient of viscothermal losses, and $\kappa_0 \simeq 3.5 \times 10^{-4}$ m$^{1/2}$. The curvilinear abscissa is denoted x in this paper. In order to simplify the discussion, the speed of sound is considered to be $c = 1$.

The analytical solution of this equation for constant $\epsilon(x)$ and constant $\frac{r''(x)}{r(x)}$ is described in [9] and the transfer functions for an arbitrary profile are approximated by concatenation of pieces of pipe with constant curvature and $\mathcal{C}^1$ regularity.

In the present paper we investigate purely numerical solutions of the WL equation for an arbitrary

bandlimited function describing the radius of the duct $r(x)$. A numerical solution can be approximated with the EDSC method. This solution is accurate up to approximately half the Nyquist rate of the temporal mesh.

3.2 Numerical solution with EDSC

We propose an explicit scheme, mixing the ability of the EDSC method for approximating the temporal derivative (including the fractional derivative) and the classical finite differences scheme for the spatial derivative. In order to avoid the problems of accuracy in the "truncated domain" (see Fig. 2), the computing domain must be broad enough to ensure that the acoustic waves have always negligible values in the "truncation domain". A consequence of this choice is that the initial conditions can be specified only for the spatial variable x. This correspond to the physical situation where the pressure and the flow signals are known at a particular coordinate x_0 (or equivalently: where the pressure signals are known at the particular coordinates x_0 and $x_0 - h$, h being a small distance, because flow and pressure are bounded by Eq (7)).

If the signals $p(t, x = x_0)$ and $p(t, x = x_0 - h)$ are bandlimited, Eq (2) permits to approximate the right member of the WL equation (6), at the coordinates $x = x_0$ and $x = x_0 - h$ for all times t (in particular for the discrete times m from $-M$ to M). Let us write these signals in discrete form as a vectors: $\boldsymbol{p}_j = \{p(t = m, x = j)\}$, for all discrete steps m defined above. For any coordinate x, the left member of Eq (6) can be approximated with a classical finite differences centered scheme. This gives rise to the discretization of the WL equation

$$\frac{\boldsymbol{p}_{x-h} - 2\,\boldsymbol{p}_x + \boldsymbol{p}_{x+h}}{h^2} + \frac{r_p(x)\,\left(\boldsymbol{p}_{x+h} - \boldsymbol{p}_{x-h}\right)}{h} \simeq \frac{1}{c^2}\left(\boldsymbol{k}^{(2)} * \boldsymbol{p}_x + 2\epsilon(x)\,\boldsymbol{k}^{(3/2)} * \boldsymbol{p}_x\right) \tag{8}$$

and leads to the explicit scheme for the propagation of the signal in forward direction

$$\boldsymbol{p}_{x+h} \simeq \frac{(h\,r_p(x) - 1)\,\boldsymbol{p}_{x-h} + 2\,\boldsymbol{p}_x + h^2\,\boldsymbol{k}_x * \boldsymbol{p}_x}{h\,r_p(x) + 1} \tag{9}$$

with $r_p(x) = \frac{2r'(x)}{r(x)}$ and $\boldsymbol{k}_x = \frac{1}{c^2}\left(\boldsymbol{k}^{(2)} + 2\epsilon(x)\,\boldsymbol{k}^{(3/2)}\right)$. The spatial progression of the waves in the (infinite) duct can be computed for any arbitrary, bandlimited initial condition $(\boldsymbol{p}_{x_0}, \boldsymbol{p}_{x_0-h})$, by applying the scheme (9) for each spatial step, starting from x_0 and progressing in forward or in backward direction. Since the classical finite differences scheme is much less precise than the EDSC scheme, the spatial step h must be notably smaller than Δt (approximately $h = \Delta t/10$ to $\Delta t/20$), in order to ensure the numerical stability of the scheme[2].

[2]The EDSC scheme has a remarkable, numerical stability, because the RSK kernel damps the high frequency components.

3.3 Practical considerations

In our simulations, the arbitrary initial conditions are defined as a "RSK-impulses":

$$\begin{aligned} p(t, x = 0) &= \mathrm{RSK}(\pi t/\gamma) \\ p(t, x = h) &= \mathrm{RSK}(\pi(t - h)/\gamma) \\ &\text{or} \\ p(t, x = L) &= \mathrm{RSK}(\pi(L - t)/\gamma) \\ p(t, x = L - h) &= \mathrm{RSK}(\pi(L - h - t)/\gamma) \end{aligned}$$

with $\gamma = 1.5$. This choice is motivated by the following considerations: the duration of the RSK-impulse is optimally short (only 70 points are numerically non zero) and it contains all frequencies up to 2/3 of frequency bound of the kernel. The impulse is not centered on zero, because $\boldsymbol{k}_x$ is strongly asymmetrical. On the contrary, the impulse is placed to the leftmost position ensuring that no noticeable numerical reflection occurs on the left boundary. With this placement, the "viscothermal relaxation" due to the "memory" of fractional derivative can be optimally developed.

Despite of this manoeuvre, some numerical reflection occurs on the right boundary, because the "memory" of the 3/2 derivative is very long. This happens even if a temporal mesh of many thousands of points is used, although this makes little sense and wastes computer power only to simulate a sum of decreasing exponentials. The following procedure is more efficient and falsifies the results in a very marginal manner (only on the very low frequency range, where the WL equation has no validity anyway): compute the wave propagation with a quite small value of M (800 or less), cut away the pollution due to the numerical reflection on the right boundary, fit a recursive linear filter according to the "clean" portion of the relaxation "tail" (where the computed signal looks like a decreasing exponential) and extrapolate the decreasing exponential until very small values are reached. In our simulations we used the following recursive linear filter:

$$p(m) = a_1 p(m-n_1) + a_2 p(m-n_2) + a_3 p(m-n_3) + a_4 p(m-n_4) \tag{10}$$

For the trombone bell simulation (see hereafter), the numerical values are: $M = 800$, $n_1 = 1$, $n_2 = 2$, $n_3 = 645$, $n_4 = 1291$. The simulation of the wave propagation was conducted on 20 spatial unities (by steps $h = 1/20$). The RSK-impulse used as initial condition (at $x = 0$ or at $x = L$) was centered 81 points away from the left boundary. The 40 rightmost points of the signal were cut away. The relaxation "tail" was extrapolated up to a total length of 8192 points.

4 Transfer functions

According to the theory of wave guides, the acoustic behavior of a piece of tube of length L (as seen from the input of the piece of tube at $x = 0$ and from the output at $x = L$) can be linked in the frequency domain by a scattering matrix:

$$\begin{pmatrix} U_0 \\ U_L \end{pmatrix} = \begin{pmatrix} H_{11} & H_{12} \\ H_{21} & H_{22} \end{pmatrix} \begin{pmatrix} P_0 \\ P_L \end{pmatrix} \tag{11}$$

When this system of equations is solved for U_0 and U_L (like here), it is named "scattering matrix with

admittance representation". We refer to the functions H_{11}, H_{12}, H_{21} and H_{22} with the generic denomination "transfer functions".

Our concern now is to obtain a discrete numerical version of these transfer functions, computed according to our scheme (9). For this, we have to compute the wave propagation in the piece of tube between $x = 0$ and $x = L$ for 2 different arbitrary initial conditions A and B. The corresponding flows are computed with Eq (7). We notate P_{0A} the Discrete Fourier Transform of the pressure signal $\boldsymbol{p}_0$ for the arbitrary initial condition A, and similarly for P_{0B}, P_{1A} and P_{1B}. The corresponding flows are denoted: U_{0A}, U_{0B}, U_{1A} and U_{1B}. Applying Eq (11) for the arbitrary initial conditions A and B leads to:

$$\begin{aligned} H_{11} &= (-P_{2B}U_{1A} + P_{2A}U_{1B})/C \\ H_{12} &= (P_{1B}U_{1A} - P_{1A}U_{1B})/C \\ H_{21} &= (-P_{2B}U_{2A} + P_{2A}U_{2B})/C \\ H_{22} &= (P_{1B}U_{2A} - P_{1A}U_{2B})/C \\ C &= (P_{1B}P_{2A} - P_{1A}P_{2B}) \end{aligned} \tag{12}$$

5 Validation

5.1 Comparison with the analytic formula

We conducted many simulations for different pieces of pipe with constant curvature and compared the results with the analytical formula given in [9]. The following parameters are used: length of the pipe $L = 70$cm, spatial step $h = 1/20$cm, $M = 400$, extrapolation of the relaxation "tail" on 16384 points. We observed practically no differences in the precision reached by the simulations, between the different curvatures and the different loss coefficients ϵ.

Results: inside the frequency band of validity of the WL equation (about up to 2kHz), the deviation for all transfer functions compared to the analytic formula do not exceed 0.015dB on the module and 0.003rad on the argument. Up to 8kHz, the maximal deviation is: 0.6dB on the module and 0.12rad on the argument.

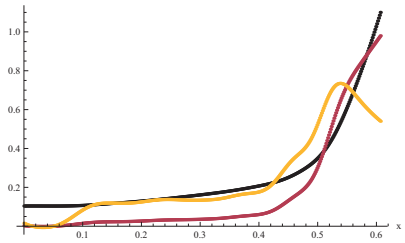

Figure 3: **Bell profil of a trombone**. Abscissa x [in m] and from dark to light: profile of the bell $r(x)$ [in dm], $r'(x)$ and $r'(x)/r(x)$ [arbitrary units].

5.2 Validation with measurements of a trombone bell

The simulation results are compared to the measurements of the input impedance published in [10]

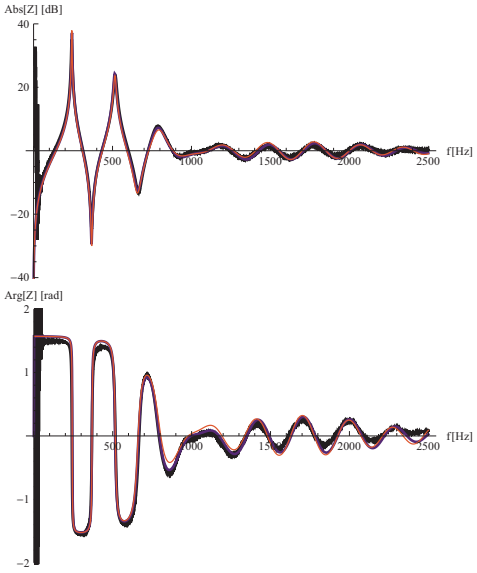

Figure 4: Normalized input impedance of the bell. **Top**: modulus in dB ($20\log_{10}$) **Bottom**: phase in radians. From dark to light: measurement, simulation with the EDSC method and simulation with 5 pieces of pipe with constant curvature, according to [4]

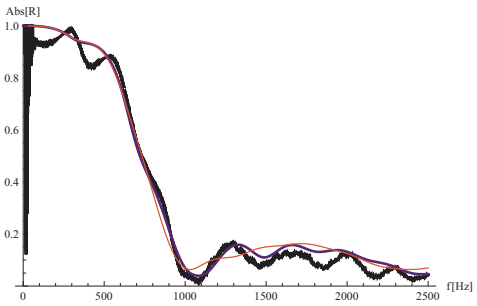

Figure 5: Modulus of the reflection coefficient of the bell. From dark to light: measurement, simulation with the EDSC method and simulation with 5 pieces of pipe with constant curvature, according to [4]

for a trombone bell (Courtois 155R). The curvilinear abscissa x is extracted from the measurements of the radius of the bore (43 points unequally spaced). The radius $r(x)$ and its first derivative $r'(x)$ are interpolated according to Eq (2). The length of the bore is divided in 20 equally spaced steps (plus 5 fictitious points on each side). The corresponding weights $y(m)$ (equally spaced) are obtained by a least squares fit. Fig. 3 illustrates the radius of the trombone bell $r(x)$, its first derivative $r'(x)$ and the ratio $r_p(x) = \frac{2r(x)}{r'(x)}$, plotted along the axis x.

The radiation impedance was simulated according to the model Z_5 used in [4, 11]. The results for the normalized input impedance $Z_{in} = A(0)/(\rho c)P_{in}/U_{in}$ are depicted on Fig. 4. The accuracy is very satisfactory and even better than the best model ($M_\star$) in [4], especially for the phase (between 800 and 1300Hz) and for the reflection coefficient $R_{in} = (Z_{in} - 1)/(Z_{in} + 1)$ (see Fig. 5). We explain this result because the loss coefficient $\epsilon(x)$ varies with the diameter in our model, while in [4], it was taken constant for each piece of pipe constituting the trombone bell.

5.2.1 Computing time

In the context of an interactive design of wind instruments, the recomputing time after a modification of the bore has to be short. We give here some indications of the computing time for the transfer functions of the trombone bell on a quite archaic PC with Intel processor 2.66 GHz. Simulation of 2 propagations with different initial conditions: 0.546 s. Extrapolation of the signals, Fourier Transform and computation of the transfer functions: 0.421 s. Total computing time. 0.967 s.

Computing time of the transfer functions according to [4], as a concatenation of 5 pieces of pipe with constant curvature, according to the analytical formula: 1.186 s. The computing time for the division of the bell into 5 pieces with constant curvature and $\mathcal{C}^1$ regularity is not included.

6 Conclusions

The EDSC method appears to be efficient and accurate for the computation of the transfer functions with the proposed algorithm. The duct has not to be subdivided as usual into different pieces of pipe, which have to be concatenated afterwards. Any bandlimited function can be used in order to define the radius of the duct. The simulation of the wave propagation in the duct requires the computation of one convolution per spatial step. Efficient algorithms are available for this task. The only delicate step is the accurate discretization of $\partial_t^{3/2}\mathrm{RSK}_N(t)$ with the analytical Eq (13), which has to be performed only once and can be stored as a lookup table (see Appendix). The method is promising for solving other equations with fractional derivatives.

Acknowledgments

This work is supported by the French Research National Agency ANR within the CAGIMA project. We also thank the high school ARC-Engineering in Neuchâtel.

References

[1] P.-A. Taillard, B. Gazengel, A. Almeida, and J.-P. Dalmont. Improvements to the discrete singular convolution method and application to beam analysis. *submitted to Journal of Sound and Vibration, available on the HAL server*, 2014.

[2] GW Wei, YB Zhao, and Y Xiang. Discrete singular convolution and its application to the analysis of plates with internal supports. part 1: Theory and algorithm. *International Journal for Numerical Methods in Engineering*, 55(8):913–946, 2002.

[3] Thomas Hélie. Mono dimensional models of the acoustic propagation in axisymmetric waveguides. *J. Acoust. Soc. Amer.*, 114:2633–2647, 2003.

[4] Thomas Hélie, Thomas Hézard, Rémi Mignot, and Denis Matignon. One-dimensional acoustic models of horns and comparison with measurements. *Acta Acustica united with Acustica*, 99(6):960–974, 2013.

[5] John Macnaughten Whittaker. On the cardinal function of interpolation theory. In *Proc. Edinburgh Math. Soc*, volume 1, pages 41–46. Cambridge Univ Press, 1929.

[6] William B Gearhart and HS Schultz. The function sin (x)/ x. *The College Mathematics Journal*, 2:90–99, 1990.

[7] K Yao. Applications of reproducing kernel hilbert spaces–bandlimited signal models. *Information and Control*, 11(4):429–444, 1967.

[8] Nachman Aronszajn. Theory of reproducing kernels. *Transactions of the American mathematical society*, pages 337–404, 1950.

[9] Rémi Mignot, Thomas Hélie, and Denis Matignon. From a model of lossy flared pipes to a general framework for simulation of waveguides. *Acta Acustica united with Acustica*, 97(3):477–491, 2011.

[10] P Eveno, J-P Dalmont, R Caussé, and J Gilbert. Wave propagation and radiation in a horn: Comparisons between models and measurements. *Acta Acustica united with Acustica*, 98(1):158–165, 2012.

[11] Thomas Hélie and Xavier Rodet. Radiation of a pulsating portion of a sphere: Application to horn radiation. *Acta Acustica united with Acustica*, 89(4):565–577, 2003.

A Derivatives of the RSK_N kernel

The RSK_N kernel (5) can be analytically integrated. Moreover, for real values of d (fractional derivatives and antiderivatives), the general expression is

$$\left(\mathrm{RSK}_N(\pi t)\right)^{(d)} = \frac{2^{\frac{d-2}{2}}\pi^{d-\frac{5}{2}}\sigma^{2-d}}{9N}\left(\cos\left(\frac{\pi d}{2}\right)\psi(t,0) + d\sin\left(\frac{\pi d}{2}\right)\psi(t,1)\right) \quad (13)$$

with

$$\psi(t,s) = \Gamma_s \sum_{n=\frac{1}{2}-N}^{N-\frac{1}{2}} e^{-\frac{n^2\sigma^2}{2N^2}}\nu(t)^s\,{}_1F_1\left(\frac{1}{2}(d+s+1), s+\frac{1}{2}, -\nu(t)^2\right)$$

$$\Gamma(t) = \int_0^\infty x^{t-1}e^{-x}\,dx \quad , \quad \Gamma_s = \Gamma\left(\frac{d+1-s}{2}\right)$$

$$\nu(t) = \frac{-Nt - in\sigma^2}{\sqrt{2}N\sigma} \quad , \quad {}_1F_1(a,b,z) = \sum_{k=0}^{\infty}\frac{a_k z^k}{b_k k!}$$

$$a_0 = 1 \quad , \quad a_k = a(a+1)(a+2)...(a+k-1)$$

Notice that the formula (13) is not valid for zero and negative integer values of d, because the Γ function is not defined (analytical formulas for these cases can be found in [1]). The function ${}_1F_1$ is called "Kummer confluent hypergeometric function".

Bibliography

[1] Andre Almeida, David George, John Smith, and Joe Wolfe. The clarinet: how blowing pressure, lip force, lip position and reed "hardness" affect pitch, sound level, and spectrum. *The Journal of the Acoustical Society of America*, 134(3):2247–2255, 2013.

[2] André Almeida, Christophe Vergez, René Caussé, and Xavier Rodet. Physical study of double-reed instruments for application to sound-synthesis. In *International Symposium in Musical Acoustics*, pages 1–1, 2002.

[3] Mérouane Atig. *Non-linéarité acoustique localisée à l'extrémité ouverte d'un tube. Mesure, modélisation et application aux instruments à vent.* PhD thesis, Université du Maine, 2004.

[4] Mérouane Atig, Jean-Pierre Dalmont, and Joël Gilbert. Impedance terminale d'un tuyau cylindrique ouvert à fort niveau sonore. *Comptes rendus-Mecanique*, 4(332):299–304, 2004.

[5] Mérouane Atig, Jean-Pierre Dalmont, and Joël Gilbert. Saturation mechanism in clarinet-like instruments, the effect of the localised non-linear losses. *Applied Acoustics*, 65(12):1133–1154, 2004.

[6] Mérouane Atig, Jean-Pierre Dalmont, and Joël Gilbert. Termination impedance of open-ended cylindrical tubes at high sound pressure level. *Comptes Rendus Mécanique*, 332(4):299–304, 2004.

[7] Federico Avanzini and Maarten van Walstijn. Modelling the mechanical response of the reed-mouthpiece-lip system of a clarinet. part i. a one-dimensional distributed model. *Acta Acustica united with Acustica*, 90(3):537–547, 2004.

[8] John Backus. Small-vibration theory of the clarinet. *The Journal of the Acoustical Society of America*, 35(3):305–313, 1963.

[9] Mathieu Barthet, Philippe Guillemain, Richard Kronland-Martinet, and Sølvi Ystad. From clarinet control to timbre perception. *Acta Acustica united with Acustica*, 96(4):678–689, 2010.

[10] Arthur H Benade. *Fundamentals of musical acoustics*. Courier Corporation, 1990.

[11] David P Berners. *Acoustics and signal processing techniques for physical modeling of brass instruments*. PhD thesis, Citeseer, 1999.

[12] VK Bhatia. Canonical correlation analysis, 1998.

[13] Stefan Bilbao, Alberto Torin, and Vasileios Chatziioannou. Numerical modeling of collisions in musical instruments. *Acta Acustica united with Acustica*, 101(1):155–173, 2015.

[14] Henri Boutin, Sandie Le Conte, Benoît Fabre, and Jean-Loïc Le Carrou. Comment l'état de surface du bois modifie les caractéristiques des résonances dans la perce des instruments à vent. In *M02 Mini symp. Mécanique des Instruments de Musique*. AFM, Association Française de Mécanique, 2015.

[15] Donald Jay Casadonte. *The clarinet reed: an introduction to its biology, chemistry, and physics*. PhD thesis, The Ohio State University, 1995.

[16] Antoine Chaigne and Jean Kergomard. *Acoustics of musical instruments*. Springer, 2016.

[17] Vasileios Chatziioannou. *Forward and inverse modelling of single-reed woodwind instruments with application to digital sound synthesis*. PhD thesis, Queen's University Belfast, 2011.

[18] Vasileios Chatziioannou and Alex Hofmann. Physics-based analysis of articulatory player actions in single-reed woodwind instruments. *Acta Acustica united with Acustica*, 101(2):292–299, 2015.

[19] Vasileios Chatziioannou and Alex Hofmann. Single-reed woodwinds: From physical modeling to sound radiation. *The Journal of the Acoustical Society of America*, 142(4):2510–2510, 2017.

[20] Vasileios Chatziioannou and Maarten van Walstijn. Extraction of lumped clarinet reed model parameters from numerically synthesised sound. *Journal of the Acoustical Society of America*, 123(5):3123, 2008.

[21] Vasileios Chatziioannou and Maarten van Walstijn. A refined physical model of the clarinet using a variable air jet height. In *Communications, Control and Signal Processing, 2008. ISCCSP 2008. 3rd International Symposium on*, pages 1297–1301. IEEE, 2008.

[22] Vasileios Chatziioannou and Maarten van Walstijn. Inverting the clarinet. In *12th Int. Conference on Digital Audio Effects (DAFx-09)*, 2009.

[23] Vasileios Chatziioannou and Maarten van Walstijn. Estimation of clarinet reed parameters by inverse modelling. *Acta Acustica united with Acustica*, 98(4):629–639, 2012.

[24] Vasileios Chatziioannou and Maarten van Walstijn. Discrete-time conserved quantities for damped oscillators. *Proceedings of the Third Vienna Talk on Music Acoustics*, 16:19, 2015.

[25] Vasileios Chatziioannou and Maarten van Walstijn. Energy conserving schemes for the simulation of musical instrument contact dynamics. *Journal of Sound and Vibration*, 339:262–279, 2015.

[26] Whitney Coyle, J Kergomard, P Guillemain, C Vergez, and A Guilloteau. An attempt at predicting the variation in playing frequencies for clarinets. In *Proceedings of the Stockholm Music Acoustics Conference*, pages 350–357, 2013.

[27] Whitney L Coyle. The clarinet: Past, present, and future. *The Journal of the Acoustical Society of America*, 138(3):1913–1913, 2015.

[28] Whitney L Coyle. *A study of the acoustical properties of the clarinet in order to predict playing frequencies*. The Pennsylvania State University, 2016.

[29] Whitney L Coyle, Philippe Guillemain, Jean-Baptiste Doc, Alexis Guilloteau, and Christophe Vergez. Descriptive maps to illustrate the quality of a clarinet. *The Journal of the Acoustical Society of America*, 136(4):2283–2283, 2014.

[30] Whitney L Coyle, Philippe Guillemain, Jean Kergomard, and Jean-Pierre Dalmont. Predicting playing frequencies for clarinets: A comparison between numerical simulations and simplified analytical formulas. *The Journal of the Acoustical Society of America*, 138(5):2770–2781, 2015.

[31] Jean-Pierre Dalmont. *Etude et realisation de capteurs d'impedance: application a la mesure d'elements localises, etude et realisation d'une terminaison anechoique basses frequences*. PhD thesis, Le Mans, 1988.

[32] Jean-Pierre Dalmont, Cyril Frappé, Joël Gilbert, Jean Kergomard, and Sébastien Ollivier. Dynamique de jeu de la clarinette: le modèle de raman à l'épreuve de l'expérience dans. *Actes du 8ème Congrès Français d'Acoustique*, pages 387–390, 2006.

[33] Jean-Pierre Dalmont and Cyrille Frappe. Oscillation and extinction thresholds of the clarinet: Comparison of analytical results and experiments. *The Journal of the Acoustical Society of America*, 122(2):1173–1179, 2007.

[34] Jean-Pierre Dalmont, Bruno Gazengel, Joël Gilbert, and Jean Kergomard. Some aspects of tuning and clean intonation in reed instruments. *Applied acoustics*, 46(1):19–60, 1995.

[35] Jean-Pierre Dalmont, Joel Gilbert, Jean Kergomard, and Sebastien Ollivier. An analytical prediction of the oscillation and extinction thresholds of a clarinet. *The Journal of the Acoustical Society of America*, 118(5):3294–3305, 2005.

[36] Jean-Pierre Dalmont, Joël Gilbert, and Sébastien Ollivier. Nonlinear characteristics of single-reed instruments: Quasistatic volume flow and reed opening measurements. *The Journal of the Acoustical Society of America*, 114(4):2253–2262, 2003.

[37] Jean-Pierre Dalmont, Philippe Guillemain, and Pierre-André Taillard. Influence of the reed flow on the intonation of the clarinet. In *Acoustics 2012*, 2012.

[38] Jean-Pierre Dalmont, Cornelis J Nederveen, Véronique Dubos, Sébastien Ollivier, Vincent Meserette, Edwin te Sligte, et al. Experimental determination of the equivalent circuit of an open side hole: linear and non linear behaviour. *Acta Acustica united with acustica*, 88(4):567–575, 2002.

[39] Andre Goios Borges de Almeida. *The physics of double-reed wind instruments and its application to sound synthesis*. PhD thesis, 2006.

[40] Vincent Debut. *Deux études d'un instrument de musique de type clarinette: analyse des fréquences propres du résonateur et calcul des auto-oscillations par décomposition modale*. PhD thesis, Université de la Méditerranée-Aix-Marseille II, 2004.

[41] JHM Disselhorst and L Van Wijngaarden. Flow in the exit of open pipes during acoustic resonance. *Journal of Fluid Mechanics*, 99(2):293–319, 1980.

[42] V Dubos, J Kergomard, A Khettabi, J-P Dalmont, DH Keefe, and CJ Nederveen. Theory of sound propagation in a duct with a branched tube using modal decomposition. *Acta Acustica united with Acustica*, 85(2):153–169, 1999.

[43] Véronique Dubos. *Etude de l'effet d'une cheminee laterale sur un guide d'onde acoustique. Etude theorique de l'interaction de deux cheminees*. PhD thesis, Le Mans, 1996.

[44] Eric Ducasse. *Modélisation et simulation dans le domaine temporel d'instruments à vent à anche simple en situation de jeu: méthodes et modèles*. PhD thesis, Le Mans, 2001.

[45] Pauline Eveno. *L'impédance d'entrée pour l'aide à la facture des instruments de musique à vent: mesures, modèles et lien avec les fréquences de jeu*. PhD thesis, Université Pierre et Marie Curie-Paris VI, 2012.

[46] Matteo Facchinetti, Xavier Boutillon, and Andrei Constantinescu. Application of modal analysis and synthesis of reed and pipe to numerical simulations of a clarinet. *The Journal of the Acoustical Society of America*, 108(5):2590–2590, 2000.

[47] Xitao Fan and Timothy R Konold. Canonical correlation analysis. *Quantitative methods in the social and behavioral sciences: A guide for researchers and reviewers*, pages 29–34, 2010.

[48] S Félix, J.-B. Doc, and M. A. Boucher. Modeling of the multimodal radiation from an open-ended waveguide. *submitted to The Journal of the Acoustical Society of America*, 2018.

[49] Didier Ferrand, Thomas Hélie, Christophe Vergez, Baptiste Véricel, and René Caussé. Bouches artificielles asservies: étude de nouveaux outils pour l'analyse du fonctionnement des instruments à vent. In *10ème Congrès Français d'Acoustique*, 2010.

[50] Didier Ferrand, Fabrice Silva, and Christophe Vergez. Seuils d'oscillation de la clarinette: validité de la représentation excitateur-résonateur. In *10ème Congrès Français d'Acoustique*, pages CD–ROM, 2010.

[51] Neville H Fletcher. Air flow and sound generation in musical wind instruments. *Annual Review of Fluid Mechanics*, 11(1):123–146, 1979.

[52] Neville H Fletcher. Autonomous vibration of simple pressure-controlled valves in gas flows. *The Journal of the Acoustical Society of America*, 93(4):2172–2180, 1993.

[53] Neville H Fletcher and Thomas D Rossing. *The physics of musical instruments*. Springer Science & Business Media, 2012.

[54] OMEGA Complete Flow. Level measurement handbook and encyclopedia®, 1995.

[55] Claudia Fritz. La clarinette et le clarinettiste: Influence du conduit vocal sur la production du son. *These de Doctorat, Université Paris*, 6, 2004.

[56] Claudia Fritz, René Caussé, Jean Kergomard, and Joe Wolfe. Experimental study of the influence of the clarinettist's vocal tract. In *Proc. Forum Acusticum*, 2005.

[57] Claudia Fritz and Joe Wolfe. How do clarinet players adjust the resonances of their vocal tracts for different playing effects? *The Journal of the Acoustical Society of America*, 118(5):3306–3315, 2005.

[58] Claudia Fritz, Joe Wolfe, Jean Kergomard, and René Caussé. Playing frequency shift due to the interaction between the vocal tract of the musician and the clarinet. In *Proc. Stockholm Music Acoustics Conference (SMAC 03)*, pages 6–9, 2003.

[59] Bruno Gazengel. *Caractérisation objective de la qualité de justesse, de timbre et d'émission des instruments à vent à anche simple*. PhD thesis, Université du Maine, 1994.

[60] Bruno Gazengel and Jean-Pierre Dalmont. Mechanical response characterization of saxophone reeds. In *Forum Acusticum*, page 000124, 2011.

[61] Bruno Gazengel, Jean Pierre Dalmont, and Jean Francois Petiot. Link between objective and subjective characterizations of bb clarinet reeds. *Applied Acoustics*, 106:155–166, 2016.

[62] Bruno Gazengel, Joël Gilbert, and Noam Amir. Time domain simulation of single-reed wind instrument. from the measured input impedance to the synthesis signal. where are the traps? *Acta Acustica*, 3:445–472, 1995.

[63] Bruno Gazengel, Thomas Guimezanes, Jean-Pierre Dalmont, Jean Baptiste Doc, Sylvain Fagart, and Y Léveillé. Experimental investigation of the influence of the mechanical characteristics of the lip on the vibrations of the single reed. In *Proceedings of the International Symposium on Musical Acoustics, Barcelona, Spain*, 2007.

[64] J Gilbert, JP Dalmont, B Gazengel, F Giroud, and Franck Durand. Etude de la clarinette à partir de la mesure de l'impédance d'entrée. *Le Journal de Physique IV*, 4(C5):C5–581, 1994.

[65] Joël Gilbert. *Etude des instruments de musique à anche simple: extension de la méthode d'équilibrage harmonique, rôle de l'inharmonicité des résonances, mesure des grandeurs d'entrée*. PhD thesis, Le Mans, 1991.

[66] Michel Gross, Fadwa Joud, Michael Atlan, Pierre-Andre Taillard, Frederic Verpillat, and Nicolas Verrier. Vibration motions studied by heterodyne holography. In *Digital Holography and Three-Dimensional Imaging*, pages DTh3A–5. Optical Society of America, 2013.

[67] Philippe Guillemain. *Analyse et modélisation de signaux sonores par des représentations temps-frequence linéaires*. PhD thesis, Aix-Marseille 2, 1994.

[68] Philippe Guillemain and Jean Kergomard. Generic resonator models for real-time synthesis of reed and brass instruments. In *6th Forum Acusticum*, 2011.

[69] Philippe Guillemain, Jean Kergomard, and Thierry Voinier. Real-time synthesis of clarinet-like instruments using digital impedance models. *The Journal of the Acoustical Society of America*, 118(1):483–494, 2005.

[70] Philippe Guillemain and Fabrice Silva. De l'utilisation de la décomposition modale pour la synthèse sonore temps réel: écueils et solutions. In *10ème Congrès Français d'Acoustique*, pages CD–ROM, 2010.

[71] Alexis Guilloteau. Détection de défauts dans un instrument de type clarinette par impédancemétrie. *rapport de stage Master*, 2, 2011.

[72] Alexis Guilloteau. *Conception d'une clarinette logique*. PhD thesis, Aix-Marseille, 2015.

[73] Alexis Guilloteau, Philippe Guillemain, and J Kergomard. Dependence of the acoustic power produced by a woodwind on the tonehole size. In *International symposium on musical acoustics*, pages 241–245, 2014.

[74] Alexis Guilloteau, Philippe Guillemain, Jean Kergomard, and Michael Jousserand. The effect of the size of the opening on the acoustic power radiated by a reed woodwind instrument. *Journal of Sound and Vibration*, 343:166–175, 2015.

[75] Thomas Guimezanes. *Etude expérimentale et numérique de l'anche de clarinette*. PhD thesis, Thèse de doctorat, Université du Maine, 2008.

[76] Wolfgang Karl Härdle and Léopold Simar. Canonical correlation analysis. In *Applied Multivariate Statistical Analysis*, pages 443–454. Springer, 2015.

[77] Thomas Hélie. *Modélisation physique d'instruments de musique en systèmes dynamiques et inversion.* PhD thesis, Université Paris-Sud, Orsay, 2002.

[78] Thomas Hélie, Thomas Hézard, Rémi Mignot, and Denis Matignon. One-dimensional acoustic models of horns and comparison with measurements. *Acta Acustica united with Acustica*, 99(6):960–974, 2013.

[79] Thomas Hélie and Xavier Rodet. Radiation of a pulsating portion of a sphere: Application to horn radiation. *Acta Acustica united with Acustica*, 89(4):565–577, 2003.

[80] Thomas Hézard. *Production de la voix: exploration, modèles et analyse/synthèse.* PhD thesis, Université Pierre et Marie Curie-Paris VI, 2013.

[81] A Hirschberg, RWA Van de Laar, JP Marrou-Maurieres, APJ Wijnands, HJ Dane, SG Kruijswijk, and AJM Houtsma. A quasi-stationary model of air flow in the reed channel of single-reed woodwind instruments. *Acta Acustica united with Acustica*, 70(2):146–154, 1990.

[82] Ian Jolliffe. Principal component analysis. In *International encyclopedia of statistical science*, pages 1094–1096. Springer, 2011.

[83] F Joud, F Verpillat, P-A Taillard, M Atlan, N Verrier, and M Gross. Mouvements de vibrations etudies par holographie heterodyne. In *3ème rencontre francophone d'holographie numérique appliquée à la métrologie des fluides*, 2014.

[84] Fadwa Joud, Frédéric Verpillat, Michael Atlan, Pierre-André Taillard, and Michel Gross. Shot noise in digital holography. In *Information Optics and Photonics*, pages 163–175. Springer, 2010.

[85] Jean Kergomard. *Champ interne et champ externe des instruments à vent.* PhD thesis, Université Pierre et Marie Curie, Paris 6, 1981.

[86] Jean Kergomard, A Hirschberg, and G Weinreich. Mechanics of musical instruments. *Lecture notes CISM*, 1995.

[87] Jean Kergomard, Elise Moers, Jean-Pierre Dalmont, and Philippe Guillemain. Cutoff frequencies of a clarinet. what is acoustical regularity? In *6th Forum Acusticum*, pages 533–538, 2011.

[88] Jean Kergomard and Marc Pachebat. Low frequency coupling and mode interference in an inhomogeneous lattice of finite length. In *Forum Acusticum*, volume 1, pages 6–pages, 2014.

[89] Peter Kolesik, Alan Mills, and Margaret Sedgley. Anatomical characteristics affecting the musical performance of clarinet reeds made from arundo donax l.(gramineae). *Annals of Botany*, 81(1):151–155, 1998.

[90] G Le Vey. Graph-based models for woodwinds. In *Stockholm Music Acoustics Conference 2013*, 2013.

[91] Antoine Lefebvre and Gary P Scavone. Refinements to the model of a single woodwind instrument tonehole. In *Proceedings of 20th International Symposium on Music Acoustics (Associated Meeting of the International Congress on Acoustics), Sydney and Katoomba, Australia*, 2010.

[92] Antoine Lefebvre and Gary P Scavone. Characterization of woodwind instrument toneholes with the finite element method. *The Journal of the Acoustical Society of America*, 131(4):3153–3163, 2012.

[93] Antoine Lefebvre, Gary P Scavone, and Jean Kergomard. External tonehole interactions in woodwind instruments. *Acta Acustica united with Acustica*, 99(6):975–985, 2013.

[94] Harold Levine and Julian Schwinger. On the radiation of sound from an unflanged circular pipe. *Physical review*, 73(4):383, 1948.

[95] Esteban Maestre and Gary P Scavone. Experimental modal analysis/synthesis of saxophone input impedances. *The Journal of the Acoustical Society of America*, 140(4):3092–3092, 2016.

[96] Esteban Maestre, Gary P Scavone, and Julius O. Smith. Joint modeling of impedance and radiation as a recursive parallel filter structure for efficient synthesis of wind instrument sound. In *Proceedings of the 21th International Conference on Digital Audio Effects (DAFx-18), Aveiro, Portugal*, 2018.

[97] Esteban Maestre, Julius O Smith, and Gary P Scavone. Analysis-synthesis of saxophone input impedances via recursive parallel filters. In *Proceedings of the 2017 International Symposium on Musical Acoustics, Montreal, Canada*, 2017.

[98] Michael E McIntyre, Robert T Schumacher, and James Woodhouse. On the oscillations of musical instruments. *The Journal of the Acoustical Society of America*, 74(5):1325–1345, 1983.

[99] Rémi Mignot. *Réalisation en guides d'ondes numériques stables d'un modèle acoustique réaliste pour la simulation en temps-réel d'instruments à vent.* PhD thesis, Télécom ParisTech, 2009.

[100] Rémi Mignot, Thomas Hélie, and Denis Matignon. From a model of lossy flared pipes to a general framework for simulation of waveguides. *Acta Acustica united with Acustica*, 97(3):477–491, 2011.

[101] Elise Moers and Jean Kergomard. On the cutoff frequency of clarinet-like instruments. geometrical versus acoustical regularity. *Acta Acustica united with Acustica*, 97(6):984–996, 2011.

[102] Philippe Morel. *Hauterive-Champréveyres. 11. Un campement magdalénien au bord du lac de Neuchâtel: étude archéozoologique (secteur 1).* Ed. du Ruau, 1997.

[103] Philippe Morel, Pierre-André Taillard, and Éric Taillard. Le problème de l'état de fragmentation en archéologie. proposition d'un procédé mathématique d'évaluation du degré de fragmentation. *Ann. Soc. Suisse Préhist. et Arch*, 69:221–224, 1986.

[104] Subhas Chandra Mukhopadhyay, Gourab Sen Gupta, Jonathan D Woolley, and Serge N Demidenko. Saxophone reed inspection employing planar electromagnetic sensors. *IEEE Transactions on Instrumentation and Measurement*, 56(6):2492–2503, 2007.

[105] Alberto Muñoz Arancón. *New techniques for the characterisation of single reeds in playing conditions.* PhD thesis, Université du Maine, 2017.

[106] Alberto Muñoz Arancón, Bruno Gazengel, and Jean Pierre Dalmont. In vivo and in vitro characterization of single cane reeds. *SMAC 2013*, 2013.

[107] Alberto Muñoz Arancón, Bruno Gazengel, and Jean-Pierre Dalmont. Caractérisation objective des anches de saxophone en situation de jeu: Etude comparative des modeles physiques décrivant le comportement de l'anche. In *Congres Français d'Acoustique*, pages 22–25, 2014.

[108] Alberto Muñoz Arancón, Bruno Gazengel, Jean-Pierre Dalmont, and Ewen Conan. Estimation of saxophone reed parameters during playing. *The Journal of the Acoustical Society of America*, 139(5):2754–2765, 2016.

[109] Alberto Muñoz Arancón, Bruno Gazengel, Jean Pierre Dalmont, and Guy Plantier. Comparative study of different physical models describing the reed behaviour in artificial playing conditions. In *International Symposium on Musical Acoustics*, 2014.

[110] CJ Nederveen. Influence of reed motion on the resonance frequency of reed-blown woodwind instruments. *The Journal of the Acoustical Society of America*, 45(2):513–514, 1969.

[111] Cornelis Johannes Nederveen. Acoustical aspects of woodwind instruments. 1969.

[112] Daniel Noreland, Sergio Bellizzi, Christophe Vergez, and Robert Bouc. Nonlinear modes of clarinet-like musical instruments. *Journal of Sound and Vibration*, 324(3-5):983–1002, 2009.

[113] Daniel Noreland, Jean Kergomard, Franck Laloë, Christophe Vergez, Philippe Guillemain, and Alexis Guilloteau. The logical clarinet: numerical optimization of the geometry of woodwind instruments. *Acta Acustica united with Acustica*, 99(4):615–628, 2013.

[114] Eiichi Obataya and Misato Norimoto. Acoustic properties of a reed (arundo donax l.) used for the vibrating plate of a clarinet. *The Journal of the Acoustical Society of America*, 106(2):1106–1110, 1999.

[115] Sébastien Ollivier. *Contribution à l'étude des oscillations des instruments à vent à anche simple*. PhD thesis, Université du Maine, 2002.

[116] Alfred Olza, JC Diethelm, Freddy Taillard, and E Vautravers. *Tables numériques et formulaires*. Spes, 1978.

[117] Marc Pachebat and Jean Kergomard. Propagation of acoustic waves in two waveguides coupled by perforations. ii. application to periodic lattices of finite length. *arXiv preprint arXiv:1603.03395*, 2016.

[118] Montserrat Pàmies-Vilà, Alexander Mayer, Alex Hofmann, and Vasileios Chatziioannou. Measurement of dynamic bending and displacement of clarinet reeds. In *7th Congress of Alps-Adria Acoustics Association, Ljubljana, Slovenia*, 2016.

[119] Jean Francois Petiot, Pierric Kersaudy, Gary Scavone, Stephen McAdams, and Bruno Gazengel. Modeling of the subjective quality of saxophone reeds. In *Proceedings of Meetings on Acoustics ICA2013*, volume 19, page 035028. ASA, 2013.

[120] Fabrice Pinard, Benoit Laine, and Holger Vach. Musical quality assessment of clarinet reeds using optical holography. *The Journal of the Acoustical Society of America*, 113(3):1736–1742, 2003.

[121] Benjamin Ricaud, Philippe Guillemain, Jean Kergomard, Fabrice Silva, and Christophe Vergez. Behavior of reed woodwind instruments around the oscillation threshold. *Acta Acustica united with Acustica*, 95(4):733–743, 2009.

[122] Junich Saneyoshi, H Teramura, and S Yoshikawa. Feedback oscillations in reed woodwind and brasswind instruments. *Acta Acustica united with Acustica*, 62(3):194–210, 1987.

[123] Gary P Scavone. Digital waveguide modeling of the non-linear excitation of single-reed woodwind instruments. In *ICMC*, 1995.

[124] Gary P Scavone. Modeling and control of performance expressin in digital waveguide models of woodwind instruments. In *ICMC*, 1996.

[125] Gary P Scavone. Modeling wind instrument sound radiation using digital waveguides. In *ICMC*, 1999.

[126] Gary P Scavone. Time-domain synthesis of conical bore instrument sounds. In *ICMC*. Citeseer, 2002.

[127] Gary P Scavone and Julius O Smith. A stable acoustic impedance model of the clarinet using digital waveguides. In *Proc. of the 9th Int. Conference on Digital Audio Effects (DAFx-06)*, pages 89–94. Citeseer, 2006.

[128] Gary Paul Scavone. *An acoustic analysis of single-reed woodwind instruments with an emphasis on design and performance issues and digital waveguide modeling techniques*. PhD thesis, Citeseer, 1997.

[129] RT Schumacher. Self-sustained oscillations of the clarinet: An integral equation approach. *Acta Acustica united with Acustica*, 40(5):298–309, 1978.

[130] RT Schumacher. Ab initio calculations of the oscillations of a clarinet. *Acta Acustica united with Acustica*, 48(2):71–85, 1981.

[131] Andrey Ricardo da Silva, Gary P Scavone, and Arcanjo Lenzi. Numerical investigation of the mean flow effect on the acoustic reflection at the open end of clarinet-like instruments. *Acta Acustica united with Acustica*, 96(5):959–966, 2010.

[132] Fabrice Silva. *Émergence des auto-oscillations dans un instrument de musique à anche simple*. PhD thesis, Université de Provence-Aix-Marseille I, 2009.

[133] Fabrice Silva, Vincent Debut, Jean Kergomard, Christophe Vergez, Aude Deblevid, and Philippe Guillemain. Simulation of single reed instruments oscillations based on modal decomposition of bore and reed dynamics. *arXiv preprint arXiv:0705.2803*, 2007.

[134] Fabrice Silva, Didier Ferrand, and Christophe Vergez. Seuils d'oscillation d'un instrument de musique à anche simple: protocole expérimental & instrumentation d'une bouche artificielle. In *XIXème Congrès Français de Mécanique*, pages CD–ROM, 2009.

[135] Fabrice Silva, Ph Guillemain, Jean Kergomard, Bastien Mallaroni, and Andrew N Norris. Approximation formulae for the acoustic radiation impedance of a cylindrical pipe. *Journal of Sound and Vibration*, 322(1-2):255–263, 2009.

[136] Fabrice Silva, Philippe Guillemain, Jean Kergomard, and Jean-Pierre Dalmont. Synthèse sonore de la clarinette avec modèle de résonateur à trous latéraux optimisé sur des impédances d'entrée d'une clarinette réelle. In *8ème Congrès Français d'Acoustique*, 2006.

[137] Fabrice Silva, Jean Kergomard, Christophe Vergez, and Joël Gilbert. Interaction of reed and acoustic resonator in clarinetlike systems. *The Journal of the Acoustical Society of America*, 124(5):3284–3295, 2008.

[138] Fabrice Silva, Ch Vergez, Ph Guillemain, Jean Kergomard, and Vincent Debut. Moreesc: a framework for the simulation and analysis of sound production in reed and brass instruments. *Acta Acustica united with Acustica*, 100(1):126–138, 2014.

[139] David John Skulina. *A study of non-linear acoustic flows at the open end of a tube using particle image velocimetry*. PhD thesis, University of Edinburgh, 2005.

[140] Julius Orion Smith. Physical modeling using digital waveguides. *Computer music journal*, 16(4):74–91, 1992.

[141] Julius Orion Smith. *Introduction to digital filters: with audio applications*, volume 2. Julius Smith, 2007.

[142] Scott D Sommerfeldt and William J Strong. Simulation of a player–clarinet system. *The Journal of the Acoustical Society of America*, 83(5):1908–1918, 1988.

[143] Karl A Stetson. Study of clarinet reeds using digital holography. *Optical Engineering*, 53(11):112305, 2014.

[144] Stephen E Stewart and William J Strong. Functional model of a simplified clarinet. *The Journal of the Acoustical Society of America*, 68(1):109–120, 1980.

[145] Pierre-André Taillard. Etude biométrique de l'astragale de quelques rongeurs de suisse romande et de france limitrophe (mammalia, rodentia). *Verhandl. Naturf. Ges. Basel*, 96:27–40, 1986.

[146] Pierre-André Taillard. Lip element for instrument with flapping reed, July 26 2005. US Patent 6,921,853.

[147] Pierre-André Taillard and Jean-Pierre Dalmont. Scraping technique for clarinet reeds derived from a static bending simulation. In *Acoustics 2012*, 2012.

[148] Pierre-André Taillard, Jean-Pierre Dalmont, Bruno Gazengel, and Alberto Muñoz Arancón. Analysis of nonlinear characteristics of the clarinet exciter obtained via a new measurement method. In *ISMA Montreal*, 2017.

[149] Pierre-André Taillard, Thomas Hélie, and Joël Bensoam. Numerical computation of the transfer functions of an axisymmetric duct with the extended discrete singular convolution method. In *International Symposium on Musical Acoustics*, pages 159–164, 2014.

[150] Pierre-André Taillard and Jean Kergomard. An analytical prediction of the bifurcation scheme of a clarinet-like instrument: Effects of resonator losses. *Acta Acustica united with Acustica*, 101(2):279–291, 2015.

[151] Pierre-André Taillard, Jean Kergomard, and Franck Laloë. Iterated maps for clarinet-like systems. *Nonlinear dynamics*, 62(1-2):253–271, 2010.

[152] Pierre-André Taillard, Jean Kergomard, Franck Laloë, and Sami Karkar. Cartes itérées appliquées à un instrument de type clarinette. In *10ème Congrès Français d'Acoustique*, 2010.

[153] Pierre-André Taillard, Franck Laloë, Michel Gross, Jean-Pierre Dalmont, and Jean Kergomard. Statistical estimation of mechanical parameters of clarinet reeds using experimental and numerical approaches. *Acta Acustica united with Acustica*, 100(3):555–573, 2014.

[154] Pierre-André Taillard and Sanchez Patrick. Comparaison de deux clarinettes séparées par deux cent ans d'évolution: Tentative d'hybridation amusante et instructive entre facture instrumentale, modèles physiques et synthèse sonore. *CFA/VISHNO 2016*, 2016.

[155] Pierre-Andre Taillard, Fabrice Silva, and Philippe Guillemain. Simulation en temps réel de l'impédance d'entrée mesurée ou calculée des instruments à vent. In *13ème Congrès Français d'Acoustique*, 2016.

[156] MA Temiz, I Lopez Arteaga, and A Hirschberg. Non-linear behaviour of tone holes in musical instruments: an experimental study. In *French Acoustic Congress (CFA 2016)*. Université du Maine, 2016.

[157] Muttalip Aşkın Temiz, Jonathan Tournadre, Ines Lopez Arteaga, and Avraham Hirschberg. Non-linear acoustic transfer impedance of micro-perforated plates with circular orifices. *Journal of Sound and Vibration*, 366:418–428, 2016.

[158] Arthur Tenenhaus, Cathy Philippe, and Vincent Frouin. Kernel generalized canonical correlation analysis. *Computational Statistics & Data Analysis*, 90:114–131, 2015.

[159] Arthur Tenenhaus, Cathy Philippe, Vincent Guillemot, Kim-Anh Le Cao, Jacques Grill, and Vincent Frouin. Variable selection for generalized canonical correlation analysis. *Biostatistics*, 15(3):569–583, 2014.

[160] Arthur Tenenhaus and Michel Tenenhaus. Regularized generalized canonical correlation analysis. *Psychometrika*, 76(2):257, 2011.

[161] Arthur Tenenhaus and Michel Tenenhaus. Regularized generalized canonical correlation analysis for multiblock or multigroup data analysis. *European Journal of operational research*, 238(2):391–403, 2014.

[162] Michel Tenenhaus, Vincenzo Esposito Vinzi, Yves-Marie Chatelin, and Carlo Lauro. Pls path modeling. *Computational statistics & data analysis*, 48(1):159–205, 2005.

[163] Jonathan Terroir. *Mesures, modélisation et synthèse des transitions entre notes et des sources de bruit dans les instruments à anche simple.* PhD thesis, Université de la Méditerranée-Aix-Marseille II, 2006.

[164] Jonathan Terroir and Philippe Guillemain. A simple dynamic tonehole model for real-time synthesis of clarinet-like instruments. In *ICMC*, 2005.

[165] Bruce Thompson. Canonical correlation analysis. *Encyclopedia of statistics in behavioral science*, 2005.

[166] Robert M Thorndike. Canonical correlation analysis. In *Handbook of applied multivariate statistics and mathematical modeling*, pages 237–263. Elsevier, 2000.

[167] Vesa Välimäki. *Discrete-time modeling of acoustic tubes using fractional delay filters.* Helsinki University of Technology, 1995.

[168] Vesa Välimäki, Jyri Pakarinen, Cumhur Erkut, and Matti Karjalainen. Discrete-time modelling of musical instruments. *Reports on progress in physics*, 69(1):1, 2005.

[169] Michel van de Velden. On generalized canonical correlation analysis. In *Proceedings of the 58th World Statistical Congress*, 2011.

[170] Maarten van Walstijn. *Discrete-time modelling of brass and reed woodwind instruments with application to musical sound synthesis.* PhD thesis, University of Edinburgh, 2002.

[171] Maarten van Walstijn and Federico Avanzini. Modelling the mechanical response of the reed-mouthpiece-lip system of a clarinet. part ii: A lumped model approximation. *Acta Acustica united with Acustica*, 93(3):435–446, 2007.

[172] Maarten van Walstijn and Gary P Scavone. The wave digital tonehole model. In *ICMC*, 2000.

[173] J Van Zon, A Hirschberg, J Gilbert, and APJ Wijnands. Flow through the reed channel of a single reed music instrument. *Le Journal de Physique Colloques*, 51(C2):C2–821, 1990.

[174] JPC van Zon. Stromingsgeinduceerde klepinstabiliteiten. *Rapport de stage, Vakgroep Transport Fysica, Eindhoven University of Technology*, 1989.

[175] Christophe Vergez. *Trompette et trompettiste: un système dynamique non linéaire à analyser, modéliser et simuler dans un contexte musical.* PhD thesis, Paris 6, 2000.

[176] Hermann von Helmholtz. *Die Lehre von den Tonempfindungen als physiologische Grundlage für die Theorie der Musik.* 1863.

[177] David Weenink. Canonical correlation analysis. In *Proceedings of the Institute of Phonetic Sciences of the University of Amsterdam*, volume 25, pages 81–99. University of Amsterdam, 2003.

[178] Theodore A Wilson and Gordon S Beavers. Operating modes of the clarinet. *The Journal of the Acoustical Society of America*, 56(2):653–658, 1974.

[179] Peter Ernst Zingg. *Eine Methode zur akustischen Artidentifikation von Fledermäusen (mammalia: chiroptera) und ihr Einsatz bei der ermittlung der Artvorkommen im Val Bregaglia/GR*. PhD thesis, Universität Bern, 1990.

[180] William E Zorumski. Generalized radiation impedances and reflection coefficients of circular and annular ducts. *The Journal of the Acoustical Society of America*, 54(6):1667–1673, 1973.

Remark: see also the bibliography of the enclosed papers.

UNIVERSITE BRETAGNE SCIENCES LOIRE POUR L'INGENIEUR

Titre : Étude théorique et expérimentale du rôle de l'anche dans le jeu de la clarinette

Mots clés : Instruments à vent, clarinette, caractérisation des anches, estimation modale, synthèse sonore par modèle physique, guide-ondes

Résumé : Ce mémoire traite de l'acoustique de la clarinette et du rôle de l'anche, résumant des travaux menés entre 2001 et 2018 sur divers sujets:

I) Étude de modèles analytiques élémentaire focalisée sur: 1) le rôle des pertes. 2) les cartes itérées, mettant en évidence divers régimes de fonctionnement, utiles aussi pour la pédagogie instrumentale.

II) Étude de caractérisation des anches: 1) Étude dynamique des résonances de l'anche réalisée par holographie. Elle conduit à un modèle de matériau viscoélastique expliquant certaines différences observées dans les fréquences des 15 premiers modes de l'anche. 2) Étude statique des caractéristiques mécaniques et aérauliques de l'excitateur (anche+bec+lèvre). La méthode mesure précisément la quantité d'air entrant dans l'instrument en fonction de la pression de lèvre et d'air.

III) Synthèse sonore par modèle physique en temps réel: 1) Modélisation mécanique et aéraulique de l'anche, d'après mesure. Le modèle de ressort raidissant non linéaire proposé autorise une simulation dynamique efficace. 2) Estimation modale de l'impédance d'entrée (mesurée) des instruments à vent. On montre les techniques de conception de filtres numériques précis et passifs à toute fréquence. 3) Modélisation et simulation instruments à vent au moyen de guide-ondes, par estimation modale, implémentée dans un logiciel en C++.

IV) Une étude de jouabilité d'un panel de 40 anches par analyse canonique des corrélations révèle des liens statistiquement solides entre mesures physiques, évaluations subjectives et synthèse sonore. Elle autorise une caractérisation des anches pouvant être réalisé par le fabricant, selon au moins 4 facteurs indépendants.

Title : Theoretical and experimental study of the role of the reed in clarinet playing

Keywords : Wind instruments, clarinet, reed characterization, modal estimation, sound synthesis by physical model, waveguides

Abstract : This thesis deals with the acoustics of the clarinet and the role of the reed, summarizing studies carried out between 2001 and 2018 on various topics:

I) Study of elementary analytical models, focused on 1) role of losses. 2) iterated maps, highlighting various operating regimes, which are also useful for the instrumental pedagogy.

II) Reed characterization study : 1) Dynamic study of the reed resonances, by holography. It leads to a model of viscoelastic material explaining some differences observed in the frequencies of the first 15 modes of the reed. 2) Static study of the mechanical and aeraulic characteristics of the exciter (reed + mouthpiece + lip). The method accurately measures the airflow entering the instrument as a function of lip and air pressure.

III) Sound synthesis by physical model in real time: 1) Mechanical and aeraulic modeling of the reed, according to measurements. The proposed nonlinear stiffening spring model allows for an efficient dynamic simulation. 2) Modal estimation of the (measured) input impedance of wind instruments. Design techniques for accurate digital filters, passive at any frequency, are described. 3) Modal estimation and simulation of wind instruments by waveguides, implemented in C ++ software.

IV) A playability study of a panel of 40 reeds by canonical correlation analysis reveals statistically strong links between physical measurements, subjective evaluations and sound synthesis. It allows a characterization of the reeds that can be made by the manufacturer, according to at least 4 independent factors.